MANUFACTURING MODIFICATION THROUGH PROCESS MANIPULATION IN INERTIA FRICTION WELDING: ENHANCED FUNCTIONALITY ROTARY FRICTION WELDING.

By

RICHARD CHRISTOPHER ASHWELL

A thesis submitted to the University of Birmingham for the degree of

DOCTOR OF ENGINEERING

Volume 1

Department of Metallurgy and Materials

School of Engineering and Physical Sciences

University of Birmingham

March 2021

UNIVERSITY OF
BIRMINGHAM

University of Birmingham Research Archive

e-theses repository

This unpublished thesis/dissertation is copyright of the author and/or third parties. The intellectual property rights of the author or third parties in respect of this work are as defined by The Copyright Designs and Patents Act 1988 or as modified by any successor legislation.

Any use made of information contained in this thesis/dissertation must be in accordance with that legislation and must be properly acknowledged. Further distribution or reproduction in any format is prohibited without the permission of the copyright holder.

Word count: 42876

Excludes: title pages including abstract, acknowledgements and contents pages, appendices, tables, diagrams, equations and figures (including associated legends), bibliography and footnotes.

Table of contents

Table of contents 3

List of figures 7

List of tables 28

Nomenclature 30

Mathematical symbols 31

Abstract 34

Acknowledgements 35

1 Introduction 1

1.1 Introduction to the thesis 1

1.2 The engineering doctorate degree 1

1.3 Introduction to the process 3

1.4 Aims and objectives 11

2 Friction welding process literature review 14

2.1 Rotary friction welding 14

2.2 Metallurgical weld characteristics 36

2.3 Friction welding of steel 42

2.4 Friction welding of Ti-6Al-4V 57

2.5 Modelling 79

2.6 State of the art 79

2.7 Research link 82

3 Research approach 84

3.1 Explanation of enhanced functionality welding 84
3.2 Experimental methodology 87
4 Inertia welding enhanced functionality initial capability assessment on S355 Steel. 105
4.1 Aim 105
4.2 Summary 105
4.3 Methodology 105
4.4 Nominal results 107
4.5 Torque modulation inertia results 117
4.6 Pressure modulation inertia 124
4.7 Orientation control inertia 132
4.8 Enhanced functionality review 142
4.9 Review of the torque modulated welds 143
4.10 Conclusion 163
5 Microstructural impact and upset accuracy of proportionally modified energy friction welds. 165
5.1 Aim 165
5.2 Introduction 165
5.3 Summary 165
5.4 Enhanced functionality - Final length control in industry 167
5.5 Objectives 167
5.6 Experimental methods 167
5.7 Nominal weld results 173

5.8 Nominal weld analysis 187
5.9 Final length control results 192
5.10 Final length control analysis 233
5.11 Conclusions and recommendations 246
5.12 Industrial recommendations 248
5.13 Future work 248
6 Impact of simulated inertias upon the residual stress in inertia friction welded Ti-6Al-4V. 250
6.1 Aim 250
6.2 Summary 250
6.3 Research approach 250
6.4 Experimental background 251
6.5 Experimental methodology 253
6.6 Results 256
6.7 Analysis 280
6.8 Discussion 296
6.9 Conclusions 303
7 Conclusion 304
7.1 Inertia welding enhanced functionality capability assessment 304
7.2 Proportionally modified energy friction welds 305
7.3 Simulated inertia impact upon residual stress 306
7.4 Enhanced functionalities and potential industrial applications 307

7.5 Final conclusion 308

8 Bibliography 309

9 Appendix 320

9.1 Chapter 5 320

9.2 Chapter 6 322

List of figures

Figure 1-1: Rotary friction welding example with one piece rotating against the second stationary piece while axial pressure is applied creating flash, visible at the centre (Kallee & Nicholas, 1999). 5

Figure 1-2: Continuous drive friction weld parameter trace example showing the optional 1st friction reduced pressure and/or elevated speed through stage 1 in order to prevent machine stall (Adapted from M Maalekian (2007); (Manufacturing Technology Inc, 2012; L. Yang, 2010)). 7

Figure 1-3: Inertia friction weld parameter trace example (Adapted from M Maalekian (2007) and (L. Yang, 2010)). 8

Figure 2-1: Parameter effects on the weld interface viscoplastic material (Linnert, 1994) 19

Figure 2-2: Effect on axial shortening of square of rotational speed for different axial pressures (F. F. Wang *et al.*, 2014). 20

Figure 2-3: Experimental results of rubbing speed vs upset rate at various axial pressures during the linear equilibrium upset phase performed on a continuous drive welding machine (Healy *et al.*, 1976). 21

Figure 2-4: Effects of axial pressure (*P*) and kinetic energy (*E*) on axial shortening(F. F. Wang *et al.*, 2014). 22

Figure 2-5: Effect of moment of inertia on axial shortening for constant initial flywheel kinetic energy (F. F. Wang *et al.*, 2014) 23

Figure 2-6: Parameter window showing the upset produced by various combinations of rotational speed and pressure produced from a finite element model using a neural network (W. Liu *et al.*, 2013). 24

Figure 2-7: Tube to tube weld in stainless steel showing the incomplete bonding of a re-entrant notch, circled in red, and the formation of a central column of flash, shown for ease on a sectioned weld (Adams & Miller, 2013). 25

Figure 2-8: Cross section of a tubular steel friction weld. Welding flash and notch have been highlighted (Işık & Özes, 2016). 25
Figure 2-9: Schematic joining mechanism demonstration of the first stage of the friction model. a) low pressure b) high pressure. (Kimura *et al.*, 2010)..... 31
Figure 2-10: Efficiency of the inertia friction welding as a function of (a) the flywheel moments of inertia or (b) the initial angular velocity for two axial compression forces (Senkov, Mahaffey, Tung*, et al.*, 2017)..... 34
Figure 2-11: Time dependence of the energy ES, consumed by samples during IFW conducted with different welding parameters: (a) I = 0.166 kg·m2, E_o = 23.6 kJ, various P; (b) various I, E_o = 23.6 kJ, P = 64.9 kN; (c) I = 0.166 kg·m2, various E_o, P = 38.7 kN (Senkov, Mahaffey, & Semiatin, 2017)..... 35
Figure 2-12: Weld zones diagram of a Rotary Friction Weld (Maalekian, 2007) 37
Figure 2-13: A) Weld zone regions related to the cycle conditions and basic resultant microstructure: WL – Weld Line, FPZ – Fully Plasticised Zone, PDZ – Partially Deformed Zone, UZ – Undeformed Zone. B) weld zones related to the physical shape of a weld.(Iracheta *et al.*, 2015) 38
Figure 2-14: Welding temperatures normalised to the solidus temperature (Li *et al.*, 2016). 39
Figure 2-15: Mechanisms for dynamic recrystallisation (Huang & Logé, 2016). 41
Figure 2-16: Typical section of a mild steel tubular friction weld. In this case from a continuous drive machine. A) tubular cross section B) A close up image of the previous cross section showing the contact zone, recrystallised zone (RZ), TMAZ and HAZ (Duffin & Bahrani, 1973). 44
Figure 2-17: A) Contact zone of an austenitic stainless steel (ASS) joined to medium carbon steel (MCS) friction weld. B) the HAZ of the MCS component of the friction weld (Paventhan *et al.*, 2011)..... 45
Figure 2-18: Micrograph of an austenitic-ferritic stainless steel friction weld, showing high deformation but with recrystallisation only on the bond line in the austenite side, while a large

area of recrystallisation and TMAZ deformation is visible on the ferritic side (Satyanarayana *et al.*, 2005)..... 46
Figure 2-19: Macro-section of a mild steel rod to HSLA plate friction weld showing HAZ shape and flash. Letters indicate hardness trace locations: M - midsection, Q - quarter section and S - near surface (Bhole, 1991). 47
Figure 2-20: Schematic diagram of thermomechanically controlled processing, in this case rolling and cooling of micro alloyed steel (Baker, 2016). 48
Figure 2-21: Effect of friction time on the average width of Region I and Region II in HNS joints (I. Woo *et al.*, 2002). 49
Figure 2-22: S355 Basic/Parent microstructure consisting of light grained ferrite and dark grained pearlite in rolled induced banding (Ni & Abdel Wahab, 2017). 55
Figure 2-23: SVh40c micro alloyed steel hot rolled microstructure at A) 50x and B) 500x magnification (Y. Chen *et al.*, 2016). 56
Figure 2-24: Two main crystal structures in Titanium (Pederson, 2002). 58
Figure 2-25: A mostly equiaxed Ti-6Al-4V in an annealed state with ~90% α phases and ~10% β phase (Reddy *et al.*, 2008). 59
Figure 2-26: Ti-6Al-4V inertia friction welds produced with variable parameter sets resulting in similar upsets (Turner *et al.*, 2016)..... 59
Figure 2-27: CCT curves of Ti-6Al-4V (Sieniawski *et al.*, 2013)..... 60
Figure 2-28: LFW Ti-6Al-4V weld microstructures. a) Widmanstätten Ti-6Al-4V morphology. b) Martensite Ti-6Al-4V morphology. From McAndrew *et al.* (2018), originally from McAndrew *et al.* (2014) 61
Figure 2-29: a) A typical backscattered SEM image of the friction stir welded stir zone showing equiaxed cells containing a fine intergranular Widmanstätten phase b) A typical optical micrograph of the same microstructure stir zone, collated from Tchein *et al.* (2018). 61

Figure 2-30: Optical micrograph of a LFW Ti-6Al-4V TMAZ structure clearly showing the transition into the weld centre zone (WCZ) (recrystallised zone) and the deformation of the TMAZ grains towards the exterior surface of the weld (McAndrew *et al.*, 2018). 62
Figure 2-31: Thermal profiles of Ti-6Al-4V inertia friction welds where the pressure is varied, modelled by Turner *et al.* (2016). 64
Figure 2-32: Thermal profiles of Ti-6Al-4V inertia friction welds where the initial rotational speed is varied, modelled by Turner *et al.* (2016). 65
Figure 2-33: Etched weld zone macrographs of Ti-6Al-4V continuous drive friction welds showing the result of parameter changes. Friction time: 2s (a), 4s (b), 6s (c). Friction speed: 1500r/min (d), 2000r/min (e), 2500r/min (f). (H.-Y. Chen *et al.*, 2015). 65
Figure 2-34: Slip planes in HCP crystal structures (Raabe, 2017). 66
Figure 2-35: A) Directions in LFW. Adapted from Karadge *et al.* (2007); L. Yang (2010), B) Coordinate geometry directions on a rotary friction welded sample. Extrapolated from Attallah *et al.* (2012). 68
Figure 2-36: The {0 0 0 2}α, {1 1 2$\bar{}$ 0}α, {1 1 0}β, and {1 1 1}β pole figures recorded at WL in sample P, 2.2P, 5P and 9P showing the influence of the pressure on the weld line texture development in the α and β phases. (Romero *et al.*, 2009) 69
Figure 2-37: The principal causes of residual stresses and the interactions between the affected areas. Adapted from (N. Kumar *et al.*, 2014). 70
Figure 2-38: Comparison between synchrotron and contour residual stress measurements, in the transverse direction, in an as welded LFW component (Frankel *et al.*, 2009). 73
Figure 2-39: Synchrotron residual stress measurements in the principal directions as welded and after various heat treatments (Z is supposed to be Y, Y is supposed to be X and X is supposed to be Z) (Frankel, 2017; Frankel *et al.*, 2009) 74
Figure 2-40: The α-Ti residual stresses (following d0 corrected) distribution in AW condition (located at +2mm [OD], 0mm [CD], and –2mm [ID] from the centre of the cylinder thickness):

(a) hoop α stress (including an uncorrected trace CD-unc), (b) axial α stress (Attallah *et al.*, 2012). 76

Figure 2-41: Influence of the d0-correction on the calculated residual stress components (x, y, z) in the P and 9P-welds (Romero *et al.*, 2009). 77

Figure 2-42: LFW thermal weld profiles away from the weld interface of Ti-6Al-4V (McAndrew *et al.*, 2015)..... 78

Figure 2-43: Appearances of welded interfaces after welding in friction pressure of 30Mpa and friction speed of 27.5s^{-1}. Wear can be seen starting at the periphery working inwards up to 0.5s, after which seizure can be seen expanding outwards from the centre (Kimura *et al.*, 2003). 80

Figure 2-44: Comparison of (a) the conventional continuous drive welding method (b) the LHI method and (c) the improved LHI method, adapted from (M. Kimura, M. Kusaka*, et al.*, 2005a). 81

Figure 3-1: Upset scaling during the weld cycle. Scaled energy input coming from the profile weld's linear upset phase resulting in the machine using torque modulation to influence the rotational speed. Adapted from (Lovin *et al.*, 2004b; Manufacturing Technology Inc, 2012). 86

Figure 3-2: Diagrams of weld profiles exhibiting initial speed changes proportional to the energy change required to adjust the resultant upset to the desired amount, adapted from (Lovin *et al.*, 2004b) 86

Figure 3-3. Example of parts geometry; a) tubular and b) solid – the step down in diameter allows for an interface sizing suitable for current study while the larger diameter section is sized to the nearest collet tooling size to eliminate the need for individual part tooling. 89

Figure 3-4: Model 125 Ton Tri-Mode RFW machine at the MTC. 91

Figure 3-5: Energy changes experienced by the system during welding. The flywheel measures the overall system change. The other sources are denoted with upwards arrows for energy out and downwards arrows for energy into the system. The remaining energy is into

the weld. a) deceleration and braking, b) motor input during deceleration, c) constant speed, d) acceleration. 95
Figure 3-6: Example energy input and outputs during an enhanced functionality inertia weld. 96
Figure 3-7: Example weld energy input rate and cumulative energy during an enhanced functionality inertia cycle. 97
Figure 3-8: Example energy inputs and outputs during a continuous drive weld. 97
Figure 3-9: Example weld energy input rate and cumulative energy during a continuous drive cycle. 98
Figure 3-10: An example of the flywheel energy rates from an enhanced functionality inertia weld. Each progressive overlay shows further smoothing of the data using a 3-point moving average..... 99
Figure 3-11: An example of a weld mosaic of an IFW Ti-6Al-4V weld. Multiple images were taken at 50x magnification and automatically stitched together. The microscopes inbuilt scale was used to take weld zone and TMAZ measurements. The outside diameter re-entrant notch tip is highlighted 101
Figure 3-12: The method of the residual stress contour method (VEQTER Ltd, 2018). 104
Figure 4-1: Weld curves from the weld RFWCRP80-010 for later comparison. 107
Figure 4-2: In-process vs post-process nominal weld upset measurements compared to a matched upset. 108
Figure 4-3: Macrograph of the weld intersection of the IFW nominal weld RFWCRP80-010. 109
Figure 4-4: Etched optical micrographs of RFWCRP80-010: (a) The weld cross section (b& c) 500x magnification of the parent material. Micrograph location highlighted in red on the weld cross section, with labels on (b) to distinguish the ferrite and pearlite grains. 110

Figure 4-5: Etched optical micrographs of RFWCRP80-010: (a) the weld cross section, OD TMAZ with (b) at 50x magnification and (c-e) 500x magnification. Area of magnification highlighted in red. 111
Figure 4-6: Etched optical micrographs of RFWCRP80-010: Centreline TMAZ with (a-c) at 50x magnification and (d-f) 500x magnification. Area of magnification highlighted in red. 112
Figure 4-7: Etched optical micrographs of RFWCRP80-010: ID TMAZ with (a-c) at 50x magnification and (d-f) 500x magnification. Area of magnification highlighted in red. 113
Figure 4-8: Stress strain data for the nominal weld set. 116
Figure 4-9: IFW nominal weld cycle tensile test results (RFWCRP80- 006-010) 116
Figure 4-10: Comparison of torque modulated weld RFWCRP80-016 against the profile weld RFWCRP80-010. 117
Figure 4-11: IFW torque modulation % feedback and upset weld record of RFWCRP80-015-022 and weld upset trace of RFWCRP80-010 for comparison with respect to spindle rotational speed. 118
Figure 4-12: The in-process and post-process upset measurement comparison of the torque modulated and nominal inertia welds. The profile weld is highlighted with the larger star marker and yellow background. 119
Figure 4-13: Graphs to show A) Machine and B) Cold measured upset values for torque modulated welds (RFWCRP80-015-022) and nominal IFW upset values (RFWCRP80-010) with three standard deviations for comparison. 120
Figure 4-14: A series of spindle run down tests to compare the effect of the upset measurement device probe being in contact and not in contact. 124
Figure 4-15: Weld cycle comparison of the profile weld (RFWCRP80-043) to a pressure modulated weld (RFWCRP80-044). 125
Figure 4-16: IFW profile and pressure modulated weld cycle upset curves (RFWCRP80- 043, 044-047) with respect to spindle rotational speed. Upset tracing from the bottom left to top right, pressure traces horizontally. 126

Figure 4-17: Machine, Cold measured and Upset Measurement Device upset values for pressure modulated welds (RFWCRP -044 to 047) Included are three standard deviation error bars and the nominal IFW upset three standard deviation limits (RFWCRP80 – 006 to 010). 127

Figure 4-18: A comparison of the machine and UMD measured upset when referenced against the cold measured upset of the profile and pressure modulated welds. Lines of best fit have been applied with their R^2 number shown. A hypothetical line of matched upset has been included for comparison where the in-process upset is equal in value to the post-process CMM cold upset. The nominal welds have been included for comparison. For easy identification the profile weld is a cross marker with a yellow background. 128

Figure 4-19: Plot showing the final spindle orientation for the pre-welding spindle tests, as measured by the RFW machine, including the target orientation. 133

Figure 4-20: Weld cycle properties for the IFW profile weld (RFWCRP80- 027) and orientation-controlled weld RFWCRP80- 034 133

Figure 4-21: Spindle position, motor torque and speed data for orientation-controlled weld RFWCRP80-034, from part contact. 134

Figure 4-22: Plot showing the final spindle orientation for the orientation-controlled welds RFWCRP80- 034, 036 & 037, as measured by the RFW machine, including a line showing the profile weld orientation that was used as a target..... 135

Figure 4-23: Plot showing the offset from the profile spindle position for the orientation-controlled welds RFWCRP80- 034, 036 & 037, as recorded by three different measurement systems in each instance. 135

Figure 4-24: Comparison of the in-process and post-process upset measurements of the orientation-controlled welds, the profile weld and the nominal welds..... 136

Figure 4-25: A Graph to show both post-process cold and in-process machine measured upset values for orientation controlled welds (RFWCRP - 034, 036 & 037) with error bars of ± 3 SD.

Included are the upper and lower upset limits (± 3 SD of the average) for the nominal IFW welds (RFWCRP80 – 006 - 010). 137
Figure 4-26: Weld energy results showing the energy transfer rate and cumulative energy amounts during the nominal inertia welds. 144
Figure 4-27: Weld energy results showing the energy transfer rate and cumulative energy amounts during the torque modulated inertia welds. 144
Figure 4-28: Weld energy rates shown alongside the upset progress of the torque modulated inertia welds. 145
Figure 4-29: Macro-images of IFW nominal weld cross-section, unetched (RFWCRP80- 010, 019, 021 & 022). 147
Figure 4-30: a) mounted sample and b) etched optical micrograph of RFWCRP80-019 parent material at 500x magnification with the white ferrite grains and dark pearlite banding visible, red box is provided for location reference. 148
Figure 4-31: Etched optical micrographs of RFWCRP80-019: OD TMAZ to weld line transition with (a) at 50x magnification and (b) TMAZ at 500x magnification (c) weld zone at 500x magnification, weld sample and red boxes are provided for location reference. 149
Figure 4-32: Etched optical micrographs of RFWCRP80-019: Centreline weld zones with (a) TMAZ to Weld zone transition at 50x magnification and (b) TMAZ and (c) weld line at 500x magnification, weld sample and red boxes are provided for location reference. 149
Figure 4-33: Etched optical micrographs of RFWCRP80-019: (a) ID weld overview at 50x magnification, (b, c & d) TMAZ to weld zone to TMAZ transition at 500x magnification, weld sample and red boxes are provided for location reference. 150
Figure 4-34: Graph to show OD, CL and ID TMAZ widths for IFW torque modulated welds (RFWCRP80- 019, 021 & 022) and for average nominal welds (RFWCRP80- 006-010) with 3 standard deviation error bands. 151
Figure 4-35: Bifurcation width and distance from the OD for IFW torque modulated welds (RFWCRP80- 019, 021 & 022) with 3 standard deviation error bars and for average nominal

welds (RFWCRP80- 006-010) with 3 standard deviation error bands of the nominal welds. 152
Figure 4-36: Graph to show the OD and ID re-entrant notch depths (where a positive value is representative of a non-re-entrant notch) for IFW torque modulated welds (RFWCRP80- 019, 021 & 022) and for average nominal welds (RFWCRP80- 006-010) with 3 standard deviation error bands. 152
Figure 4-37: Hardness survey traces across the OD, centreline, and ID of the nominal and torque modulated inertia welds. Profile weld - 10 on the graph. Torque modulated welds - 19, 21 & 22 on the graph. 1 standard deviation of all parent material results has been plotted as error bars on all measurements. 154
Figure 4-38: Maximum OD, Centreline and ID hardness values for the IFW torque modulated weld cross-sections (RFWCRP80 -019, 021 & 022), the profile weld cross sections (RFWCRP80-010) and average nominal weld cross-sections (RFWCRP80-006-010) with 3 standard deviation limit lines. 155
Figure 4-39: IFW torque modulated weld cycle stress strain results from tensile testing (RFWCRP80-019 to 022) compared to the nominal weld (RFWCRP80-010). 156
Figure 4-40: IFW torque modulated weld tensile results..... 156
Figure 4-41: Frictional stress at the interface of two IFW torque modulated welds. 158
Figure 4-42: Continuous cooling transformation diagram of the structural steel alloy S355N (Ponge, 2005). 160
Figure 5-1. Weld identification system. 168
Figure 5-2. Profile parameter weld curves of MAIRFWS004 for the inertia solid components. 173
Figure 5-3. Profile parameter weld curves of MAIRFWT001 for the inertia tube components. 174
Figure 5-4. Profile parameter weld curves of MACDFWS005 for the continuous drive solid components. 174

Figure 5-5. Profile parameter weld curve for MACDFWT005, for the continuous drive tube components. 175
Figure 5-6. Micro-alloyed steel repeated parameter weld samples: a) MAIRFWS001, b) MAIRFWT001, c) MACDFWS005 and d) MACDFWT005. 176
Figure 5-7: The microstructural changes from the parent material to the centre of the weld zone of MAIRFWT 003. Images at 50x and 500x mag (shrunk for reproduction). 177
Figure 5-8: The microstructural changes from the parent material to the centre of the weld zone of MAIRFWS 005. Images at 50x and 500x mag (shrunk for reproduction). 178
Figure 5-9: The microstructural changes from the parent material to the centre of the weld zone of MACDFWT 005. Images at 50x and 500x mag (shrunk for reproduction). 179
Figure 5-10: The microstructural changes from the parent material to the centre of the weld zone of MACDFWS 006. Images at 50x and 500x mag (shrunk for reproduction)..... 180
Figure 5-11: Centreline hardness trace of the IFW tube nominal weld. Error bars of 1 standard deviation of the base material measurements displayed. 181
Figure 5-12: Centreline hardness trace of the CDFW tube nominal weld. Error bars of 1 standard deviation of the base material measurements displayed. 182
Figure 5-13: Centreline hardness trace of the IFW solid nominal weld. Error bars of 1 standard deviation of the base material measurements displayed. 182
Figure 5-14: Centreline hardness trace of the CDFW solid nominal weld. Error bars of 1 standard deviation of the base material measurements displayed. 183
Figure 5-15: Micro-alloyed steel SVH40C average bend test results with error bars. 183
Figure 5-16: Micro-alloyed steel SVH40C nominal weld average bend test pieces. 184
Figure 5-17: Stress strain results from the tensile testing of the nominal welds..... 185
Figure 5-18: Average tensile test results of the micro-alloyed steel SVH40C nominal weld samples including one standard deviation error bars. 185
Figure 5-19: Representative micro-alloyed steel SVH40C tensile samples showing failure location. Weld line indicated by black mark. 186

Figure 5-20: Micro-alloyed steel SVH40c nominal weld charpy impact testing results including error bars. 187
Figure 5-21: Nominal weld average charpy impact test pieces. 187
Figure 5-22: Parameter weld curves for a) MAIRFWTFL001, and b) MAIRFWTFL002, both from components +2mm greater than nominal. 193
Figure 5-23: Parameter weld curves for a) MAIRFWTFL003, and b) MAIRFWTFL004 both from components +1mm greater than nominal. 193
Figure 5-24: Parameter weld curves for a) MAIRFWTFL005, and b) MAIRFWTFL006, both from components -1mm less than nominal. 194
Figure 5-25: Parameter weld curves for a) MAIRFWTFL007, and b) MAIRFWTFL008, both from components -2mm less than nominal. 194
Figure 5-26: Parameter weld curves for a) MAIRFWSFL001, and b) MAIRFWSFL002, both from components +2mm greater than nominal. 195
Figure 5-27: Parameter weld curves for a) MAIRFWSFL003, and b) MAIRFWSFL004, both from components +1mm greater than nominal. 195
Figure 5-28: Parameter weld curves for a) MAIRFWSFL005, and b) MAIRFWSFL006, both from components -1mm less than nominal. 196
Figure 5-29: Parameter weld curves for a) MAIRFWSFL007, and b) MAIRFWSFL008, both from components -2mm less than nominal. 196
Figure 5-30: Parameter weld curves for a) MACDRFWTFL001, and b) MACDRFWTFL002, both from components +2mm greater than nominal. 198
Figure 5-31: Parameter weld curves for a) MACDRFWTFL003, and b) MACDRFWTFL004, both from components +1mm greater than nominal. 198
Figure 5-32: Parameter weld curves for a) MACDFWTFL005, and b) MACDFWTFL006, both from components -1mm less than nominal. 199
Figure 5-33: Parameter weld curves for a) MACDRFWTFL007, and b) MACDRFWTFL008, both from components -2mm less than nominal. 199

Figure 5-34: Parameter weld curves for a) MACDRFWSFL001, and b) MACDRFWSFL002, both from components +2mm greater than nominal. 200
Figure 5-35: Parameter weld curves for a) MACDRFWSFL003, and b) MACDRFWSFL004, both from components +1mm greater than nominal. 200
Figure 5-36: Parameter weld curves for a) MACDRFWSFL005 and b) MACDRFWSFL008, both from components -1mm less than nominal. 201
Figure 5-37: Parameter weld curves for a) MACDRFWSFL006, d b) MACDRFWSFL007, from components -2mm less than nominal. 201
Figure 5-38: Inertia solid final length control cold measurements compared to the targets, a) with the undersized part welds included outlined in a red circle, b) with the undersized part welds removed and a linear trend line applied. 202
Figure 5-39: Inertia tube final length control cold measurements compared to the targets, a) with the impossible welds included outlined in a red circle, b) with the impossible welds removed and a linear trend line applied. 203
Figure 5-40: Continuous drive solid final length control cold measurements compared to the targets. 203
Figure 5-41: Continuous drive tube final length control cold measurements compared to the targets. 204
Figure 5-42: The energy input rate and cumulative energy of the IFW solid FLC welds. 204
Figure 5-43: The energy input rate and cumulative energy of the IFW tube FLC welds..... 205
Figure 5-44: The energy input rate and cumulative energy of the CDFW solid FLC welds. 206
Figure 5-45: The energy input rate and cumulative energy of the CDFW tube FLC welds. 206
Figure 5-46: Micro alloyed steel inertia rotary friction welding final length control weld tubes: a) MAIRFWTFL001 with part length 108.1mm, b) MAIRFWTFL003 with part length 107.1mm, c) MAIRFWTFL005 with part length 105.1mm, and d) MAIRFWTFL007 with part length 104.1mm. 207

Figure 5-47: Micro alloyed steel inertia rotary friction welding final length control weld solids: a) MAIRFWSFL001 with part length 108.1mm, b) MAIRFWSFL003 with part length 107.1mm, c) MAIRFWSFL005 with part length 105.1mm, and d) MAIRFWSFL007 with part length 104.1mm..... 208
Figure 5-48: Micro alloyed steel continuous drive rotary friction welding final length control weld tubes: a) MACDFWTFL001 with part length 108.1mm, b) MACDFWTFL003 with part length 107.1mm, c) MACDFWTFL005 with part length 105.1mm, and d) MACDFWTFL007 with part length 104.1mm. 208
Figure 5-49: Micro alloyed steel continuous drive rotary friction welding final length control weld solids: a) MACDFWSFL001 with part length 108.1mm, b) MACDFWSFL003 with part length 107.1mm, c) MACDFWSFL005 with part length 105.1mm, and d) MACDFWSFL007 with part length 104.1mm. 209
Figure 5-50: The microstructural changes from the parent material to the centre of the weld zone of MAIRFWSFL001. Images at 50x and 500x mag (shrunk for reproduction). 210
Figure 5-51: The microstructural changes from the parent material to the centre of the weld zone of MAIRFWSFL003. Images at 50x and 500x mag (shrunk for reproduction). 211
Figure 5-52: The microstructural changes from the parent material to the centre of the weld zone of MAIRFWSFL005. Images at 50x and 500x mag (shrunk for reproduction). 212
Figure 5-53: The microstructural changes from the parent material to the centre of the weld zone of MAIRFWSFL007. Images at 50x and 500x mag (shrunk for reproduction). 213
Figure 5-54: The microstructural changes from the parent material to the centre of the weld zone of MAIRFWTFL001. Images at 50x and 500x mag (shrunk for reproduction). 214
Figure 5-55: The microstructural changes from the parent material to the centre of the weld zone of MAIRFWTFL003. Images at 50x and 500x mag (shrunk for reproduction). 215
Figure 5-56: The microstructural changes from the parent material to the centre of the weld zone of MAIRFWTFL5. Images at 50x and 500x mag (shrunk for reproduction). 216

Figure 5-57: The microstructural changes from the parent material to the centre of the weld zone of MAIRFWTFL7. Images at 50x and 500x mag (shrunk for reproduction). 217
Figure 5-58: The microstructural changes from the parent material to the centre of the weld zone of MACDFWSFL1. Images at 50x and 500x mag (shrunk for reproduction). 218
Figure 5-59: The microstructural changes from the parent material to the centre of the weld zone of MACDFWSFL3. Images at 50x and 500x mag (shrunk for reproduction). 219
Figure 5-60: The microstructural changes from the parent material to the centre of the weld zone of MACDFWSFL5. Images at 50x and 500x mag (shrunk for reproduction). 220
Figure 5-61: The microstructural changes from the parent material to the centre of the weld zone of MACDFWSFL7. Images at 50x and 500x mag (shrunk for reproduction). 221
Figure 5-62: The microstructural changes from the parent material to the centre of the weld zone of MACDFWTFL1. Images at 50x and 500x mag (shrunk for reproduction)..... 222
Figure 5-63: The microstructural changes from the parent material to the centre of the weld zone of MACDFWTFL3. Images at 50x and 500x mag (shrunk for reproduction)..... 223
Figure 5-64: The microstructural changes from the parent material to the centre of the weld zone of MACDFWTFL5. Images at 50x and 500x mag (shrunk for reproduction)..... 224
Figure 5-65: The microstructural changes from the parent material to the centre of the weld zone of MACDFWTFL7. Images at 50x and 500x mag (shrunk for reproduction)..... 225
Figure 5-66: Comparison of the inertia solid final length control welds centreline hardness traces. 1 standard deviation error bars from the base material measurements displayed. . 226
Figure 5-67: Comparison of the inertia tube final length control welds centreline hardness traces. 1 standard deviation error bars from the base material measurements displayed. . 227
Figure 5-68: Comparison of the continuous drive solid final length control welds centreline hardness traces. 1 standard deviation error bars from the base material measurements displayed. 227

Figure 5-69: Comparison of the continuous drive tube final length control welds centreline hardness traces. 1 standard deviation error bars from the base material measurements displayed. 228
Figure 5-70: Bend test results of inertia rotary friction final length control welds..... 229
Figure 5-71: Bend test results of continuous drive rotary friction final length control welds. 229
Figure 5-72: Tensile test results of inertia rotary friction final length control welds. 230
Figure 5-73: Stress strain curves of the inertia rotary friction final length welds..... 230
Figure 5-74: Tensile test results of continuous drive rotary friction final length control welds. 231
Figure 5-75: Stress strain curves of the continuous drive rotary friction final length welds . 231
Figure 5-76: Charpy impact test results of inertia rotary friction final length control welds. . 232
Figure 5-77: Charpy impact test results of continuous drive rotary friction final length control welds. 232
Figure 5-78: In-process and post-process upset measurements of the IFW solid final length control welds plotted against the total weld energy input..... 237
Figure 5-79: In-process and post-process upset measurements of the IFW tube final length control welds plotted against the total weld energy input..... 237
Figure 5-80: In-process and post-process upset measurements of the CDFW tube final length control welds plotted against the total weld energy input..... 238
Figure 5-81: In-process and post-process upset measurements of the CDFW solid final length control welds plotted against the total weld energy input..... 238
Figure 5-82: a) low energy - weld zone is thin and even across most of the weld sample with small amounts of flash b) high energy - large changes in weld zone width across the weld sample with larger amounts of flash thereby distorting the edge of the weld zone near the flash (adapted from Linnert (1994) with results seen in the work above). 241
Figure 6-1: Schematic diagram of the tested weld cycles showing the intended deceleration and predicted torque profiles..... 253

Figure 6-2: Photo of the welded components clearly showing the keyway machined into the rear of the parts and the small clamping area visible from the collet marks on the surface. 254
Figure 6-3: Schematic diagram of tracked weld pieces for temperature measurement (not to scale). 255
Figure 6-4: Weld traces of the rotational speed of representative cycles for comparison. .. 256
Figure 6-5: Weld traces of the torque feedback percentage of representative cycles for comparison. 256
Figure 6-6: Weld traces of the machine pressure of representative cycles for comparison. 257
Figure 6-7: Weld traces of the upset of representative cycles for comparison. 257
Figure 6-8: Weld traces of the upset rate (smoothed) of representative cycles for comparison. 257
Figure 6-9: Machine upset measurements for each weld including the average and three standard deviation upper and lower lines. The error bars indicate measurement deviation of the machine to the post weld measurement. Resolution of the machine measurement was +/-0.01mm. Resolution of the post weld height gauge measurement was +/-0.01mm. 258
Figure 6-10: Post weld upset measurements for each weld including the average and three standard deviation upper and lower lines. The error bars indicate measurement deviation of the post weld to the machine measurement. Resolution of the post weld height gauge measurement was +/-0.01mm. 259
Figure 6-11: Calculated instantaneous energy input traces of the representative welds from each cycle. 260
Figure 6-12: Calculated cumulative energy input traces of the representative welds from each cycle. 260
Figure 6-13: Temperature traces of the simulated inertia and fast deceleration weld 4's starting at 8mm from the weld line. 261
Figure 6-14: Temperature traces of the simulated inertia and fast deceleration weld 4's starting at 12mm from the weld line. 261

Figure 6-15: Comparison of the three weld modes. Fast deceleration on the left, Nominal in the centre and Simulated inertia on the right. 262
Figure 6-16: Close up of the simulated inertia weld flash. 262
Figure 6-17: Close up of the fast deceleration weld flash. 263
Figure 6-18: Close up of the nominal weld flash. 263
Figure 6-19: Simulated inertia weld zone mosaic image at 50x magnification (resized). 264
Figure 6-20: Simulated inertia TMAZ transition to weld zone from the outside diameter at 50x magnification. 265
Figure 6-21: Simulated inertia weld zone from the outside diameter at 50x magnification on the left and 500x magnification on the right. 265
Figure 6-22: Simulated inertia weld zone from the centre line at 50x magnification on the left and 500x magnification on the right. 266
Figure 6-23: Simulated inertia weld zone from the inside diameter at 50x magnification on the left and 500x magnification on the right. 266
Figure 6-24: Fast deceleration weld zone mosaic image at 50x magnification (resized). 267
Figure 6-25: Fast deceleration TMAZ transition to weld zone and flash from the outside diameter at 50x magnification. 267
Figure 6-26: Fast deceleration weld zone from the outside diameter at 50x magnification on the left and 500x magnification on the right. 268
Figure 6-27: Fast deceleration weld zone from the centre line at 50x magnification on the left and 500x magnification on the right. 268
Figure 6-28: Fast deceleration weld zone from the inside diameter at 50x magnification on the left and 500x magnification on the right. 269
Figure 6-29: Nominal weld zone moasic image at 50x magnification (resized). 270
Figure 6-30: Nominal weld zone to TMAZ transition from the OD at 50x magnification. 270
Figure 6-31: Nominal weld zone from the outside diameter at 50x magnification on the left and 500x magnification on the right. 271

Figure 6-32: Nominal weld zone from the centre line at 50x magnification on the left and 500x magnification on the right. 271
Figure 6-33: Nominal weld zone from the inside diameter at 50x magnification on the left and 500x magnification on the right. 272
Figure 6-34: Results of the weld region measurements from the optical micrograph mosaics. As the test pieces are cylindrical, the data has been flipped and repeated to provide a through thickness view..... 273
Figure 6-35: Contour map of the fast deceleration hardness survey. 274
Figure 6-36: Map of the nominal hardness survey. 275
Figure 6-37: Map of the simulated inertia hardness survey. 275
Figure 6-38: Hardness trace across the weld zone at the outer diameter. 276
Figure 6-39: Hardness trace across the weld zone at the centre line. 276
Figure 6-40: Hardness trace across the weld line at the inside diameter 276
Figure 6-41: Hoop stresses from the three cycles shown as coloured areas on the mesh map. 277
Figure 6-42: Hoop stress measurements across the weld diameter through the contact zone from the contour method. The drop in stress visible in the simulated inertia ID at -15 to -10mm was caused by a wire snap on the EDM machine at the -14mm point. 278
Figure 6-43: Evidence of the wire cut restarting due to the wire breakage in the simulated inertia sample. Visible in the upper portion as the light-coloured line. 278
Figure 6-44: Axial stresses from the three cycles shown as coloured areas on the part map. 279
Figure 6-45: Axial stress measurements from across the horizontal weld diameter relative to the above orientation. 280
Figure 6-46: The conditioning energy of the enhanced cycles. 284
Figure 6-47: Apparent coefficients of friction determined from the weld parameters and calculated input power. A representative weld from each cycle is shown. 285

Figure 6-48: Apparent shear stress values across the weld interface derived from the power input. 286
Figure 6-49: Apparent coefficient of friction plotted against angular velocity. 287
Figure 6-50: Apparent coefficient of friction plotted against upset, with 75 rad/s marked on each line with a red star. 288
Figure 6-51: Probe temperatures plotted against the distance to the approaching weld interface. 290
Figure 6-52: Temperature vs upset rate of the simulated inertia and fast deceleration weld. 290
Figure 6-53: Rate of temperature change of the 8mm and 12mm probes throughout the weld cycles. 291
Figure 6-54: Continuous cooling curves of Ti-6Al-4V with air cooling estimated at ~20°C/s (Zhong *et al.*, 2020). 293
Figure 6-55: Cut through diagram of the weld pieces and tooling displaying the potential temperature flow from the interface through the part. Red indicating higher temperatures with orange ,yellow and blue indicating progressivly colder temperatures. 298
Figure 6-56: Residual stress measurements compared to the weld zone widths across the weld interface. 300
Figure 9-1. Part drawings: Solid MA steel. 320
Figure 9-2. Part drawings: Tubular MA steel. 321
Figure 9-3: Weld traces of the simulated inertia cycles. 322
Figure 9-4: Weld traces of the fast deceleration cycles. 323
Figure 9-5: Weld traces of the nominal weld cycles. 323
Figure 9-6: Collection of the upset rate from each weld cycle for comparison. 324
Figure 9-7: Calculated energy data from the simulated inertia cycles. 325
Figure 9-8: Calculated energy data from the fast deceleration weld cycles. 325
Figure 9-9: Calculated energy data from the nominal weld cycles. 326

Figure 9-10: Temperature traces from SI4 during the simulated welding cycle, denoted by their initial position from the weld line. Compared against the upset curve from the same weld. 327
Figure 9-11: Temperature traces from FD4 during the fast deceleration welding cycle, denoted by their initial position from the weld line. Compared against the upset curve from the same weld. 328

List of tables

Table 2-1: S355 Chemical Composition 55

Table 2-2: Material chemical composition of SVh40c supplied by Nissan (Y. Chen *et al.*, 2016). 56

Table 2-3: Ti-6Al-4V Composition. 57

Table 3-1: Final length control welds summary. 88

Table 3-2. Material chemical composition of S355 from supplier. 89

Table 3-3. Material chemical composition of SVH40C as supplied by Nissan. 89

Table 3-4: Material chemical composition of Ti-6Al-4V from supplier. 89

Table 3-5. Inertia rotary friction welding parameters. 92

Table 3-6. Continuous drive rotary friction welding parameters. 92

Table 4-1: Weld parameters and set sizes for the nominal weld set and three enhanced functionality weld sets. 106

Table 4-2: Upset values for the nominal IFW welds RFWCRP80- 006-010 for comparison. 108

Table 4-3: Thermo-mechanically affected zone (TMAZ) width, bifurcation width / location and re-entrant notch (where a positive value is representative of a non-re-entrant notch) measurements taken from IFW nominal weld cross-sections (RFWCRP80- 006-010) for comparison. 114

Table 4-4: Maximum OD, centreline and ID values for the IFW nominal weld cross-section (RFWCRP80-010) for comparison. 115

Table 4-5: Upset in-process and post-process measurements for the torque modulated weld set compared to the nominal weld RFWCRP80-010. 121

Table 4-6: Table of final spindle speeds at the data acquisition cut off point. 125

Table 4-7: Upset values for the profile weld RFWCRP80-043 and pressure modulated IFW welds RFWCRP80-044 to 047 127

Table 4-8: Orient spindle tests at 30 and 5rpm detailing the accuracy of the machine for part loading. 132
Table 4-9: Spindle position data for the IFW profile weld RFWCRP80–027, and the orientation controlled IFW welds RFWCRP80-034, 036 & 037 134
Table 4-10: Upset values for the IFW profile weld RFWCRP80 - 027, and the orientation controlled IFW welds RFWCRP80 - 034, 036 & 037 137
Table 4-11: Nominal and Torque modulated weld energy peak rates and total amounts. Red cells indicate values above the nominal weld three standard deviation upper limit (3SD upper) while yellow cells indicate values below the nominal weld three standard deviation lower limit (3SD lower). 145
Table 4-12: Thermo-mechanically affected zone (TMAZ) width, bifurcation width / location and re-entrant notch (where a positive value is representative of a non-re-entrant notch) measurements taken from IFW torque modulated weld cross-sections (RFWCRP80- 019, 021 & 022). 153
Table 5-1.Final length control welds summary 168
Table 5-2. Final length control parts geometry summary. 169
Table 5-3. Inertia friction welding final length parameters. 171
Table 5-4. Continuous drive rotary friction welding parameters. 171
Table 6-1: Weld parameters developed through prior testing 254
Table 6-2: TMAZ widths across the weld zone. 273

Nomenclature

RFW	Rotary friction welding
IFW	Inertia friction welding
CDFW	Continuous drive friction welding
DDFW	Direct drive friction welding
LFW	Linear friction welding
ID	Internal diameter
OD	Outside diameter
TMAZ	Thermo-mechanically affected zone
HAZ	Heat affected zone
RZ	Recrystallised zone
LHI	Low heat input
FEM	Finite element modelling
MCS	Medium carbon steel
HSLA	High strength low alloy
OC	Orientation controlled
FLC	Final length controlled
SI	Simulated inertia
FD	Fast deceleration

Nom Nominal

Mathematical symbols

T_{nr} Static recrystallisation temperature

A_{r3} Austenite to ferrite transformation start temperature

A_{r1} Austenite to ferrite transformation finish temperature

E Energy

E_f Energy of the flywheel system

E_m Energy from the motor

E_{fric} Energy from frictional losses

E_w Energy into the weld

I Moment of Inertia

ω Rotational speed

ω_v Angular velocity

ω_s Surface speed of the rotating component

r Radial distance from the central axis

r_o External surface radius of component

r_i Internal surface radius of component

U_T Upset target

π Pi

p_c Internal ram cylinder pressure

p_i Component interface pressure

A_c Area of the ram piston inside the ram cylinder

A_i Area of the component interface

F Normal force

F_f Frictional force

t_f Frictional stress

μ Coefficient of friction

$\dot{P}$ Heat input rate / internal interface power rate

t_y Shear yield stress

σ_y Tensile yield stress

n Process efficiency factor

δ Frictional stress to plastic deformation transition factor

q Heat flux

P_w Power into the weld

T Torque

T_w Weld torque

T_s System friction torque

M_{JB} Moment of the journal bearing

M_{JB0} Initial moment of the journal bearing

M_{TB} Moment of the thrust bearing

M_{TB0} Initial moment of the thrust bearing

v Lubricating oil viscosity

R_1 Shaft radius

R_2 Surface radius

L Length

h_1 Radial clearance of the bearing

h_2 Oil film thickness of the thrust bearing

M_M Machine friction moment

M_{Mo} Initial machine friction moment

Z_h Zener-Hollman parameter

d Sub-grain diameter

ε Strain

$\bar{\varepsilon}$ Strain rate

Q Activation energy for deformation

T_{temp} Temperature

Tm Solidus Temperature

R_{gas} Gas constant

σ_o Material initial dislocation movement stress,

K_y Material specific strengthening coefficient

G Shear modulus,

b Burgers vector

$\rho_\perp$ Dislocation density

τ Stress for dislocation movement

r_{par} Particle radius,

γ Surface energy,

L_{pps} Pinning point spacing

C solute concentration

Abstract

Rotary friction welding has been around since the end of the Second World War. Until recently machines and the process have only improved with the introduction of easier control systems and more accurate instrumentation. Recently, however, Manufacturing Technology Inc developed a range of enhanced functionalities based on combining the two fundamental processing options: Inertia and Continuous drive. The aim of this thesis is to explore the new enhanced functionalities and gain an understanding of their influence on the weld to examine potential process improvements.

Initially all the various forms of enhanced functionality are reviewed in order to assess the potential for further use. Torque modulation, where the rotational speed can be modified mid cycle in reference to a profile, was found to have the greatest impact on the standard cycle,

substantially reducing the variation in upset, with no noticeable impact on the weld microstructure. Final length control demonstrated an impact on the microstructure away from the nominal if large energy inputs were utilized. Simulated inertia profiles used large energy inputs to purposefully modify the process and resulting microstructure. Links were found between the process, corresponding weld zone widths and resultant residual stresses in Titanium 6Al 4V.

Acknowledgements

To my friends and family, who without, it just would not have been possible.

To my industrial supervisor, Hannah, who guided, supported, and kept me afloat throughout all my challenges.

To my academic supervisor, Moataz, for supplying the walls I had to climb and thankfully taught me how to climb them.

To Coventry Universities Prof Xiang Zhang and Dr Bilal Ahmed who graciously helped in providing the contour method residual stress results.

1 Introduction

1.1 Introduction to the thesis

Friction welding is a process that has been around since the 1940's (Morton, 1944). It has been used mainly in the production of vehicle and aerospace engines. When the Manufacturing Technology Centre (MTC) was founded a 125T Rotary Friction Welding (RFW) machine was ordered from Manufacturing Technology, Inc (MTI) of South Bend, Illinois. The research machine included several enhanced functionalities that do not appear on production machines. This thesis is an exploration of the new functionalities and an investigation into the initial development of using these capabilities in an updated novel method of rotary friction welding in order to explore potential process improvements.

1.1.1 Background to the thesis

The work herein represents a collaboration between the University of Birmingham and the MTC, who sponsored the doctorate. As the MTC was the only place with such advanced rotary friction welding machines (a 300T machine from MTI was also at the MTC), the collaboration afforded opportunities of study that would not have been possible elsewhere. Characterisation of the work was carried out by the author at the MTC and University of Birmingham in order to bring together a range of analysis capabilities directly suitable for the work undertaken. Coventry Universities Prof Xiang Zhang and Dr Bilal Ahmed worked with the author to produce the residual stress results in Chapter 6.

1.2 The engineering doctorate degree

This degree was orchestrated by the Manufacturing Technology Engineering Doctorate Centre (MTEDC). A collaboration between the University of Birmingham, the University of Nottingham and Loughborough University. The Engineering Doctorate (EngD) is similar to the traditional PhD but more suited to those looking to progress in industry rather than academia.

1.2.1 Development modules

Throughout the course a selection of compulsory and optional modules from various areas and institutions, equalling a minimum of 120 credits, were taken.

Compulsory Modules

Management and Professional Development:

1. Satisfying the Customer
2. Research and Professional Skills

Advanced Technical Skills:

3. Materials for Manufacturing
4. Advanced Manufacturing Process & Technology

Elective Modules

Management and Professional Development Skills:

5. Innovation and Technology Transfer

Contextual Skills:

6. Sustainable Development: the Engineering Context

Advanced Technical Skills:

7. Intermetallics
8. Physical Metallurgy of Titanium and Nickel
9. Netshape Manufacture
10. Polymer Science and Soft Matter

These modules were completed over the first two years of the programme with the majority occurring in the first two semesters. A master's style project was also conducted and submitted early on, this work was fed into the torque modulation chapter.

1.3 Introduction to the process

1.3.1 Process origin

Rotary friction welding (RFW) is a technique for welding cylindrical parts that was developed in Russia in the mid 1950's using a modified lathe, (M Maalekian, 2007; Morton, 1944). This later became known as continuous drive or direct drive friction welding (CDFW or DDFW). Soon after, the Caterpillar Tractor Company developed a competing version using a flywheel to drive the rotation called Inertia Friction Welding (IFW) (K. Wang & Lin, 1974). This was patented in the United States of America in the 1960's with commercial machines being sold from 1965 in order to manufacture, as Caterpillar put it, "simple, clean, efficient, economical, safe, versatile, and high quality" joints in similar and dissimilar materials. (Caterpillar, 2020; Milton & Lynn, 1966; Milton & Robert, 1968; Morris & Bernard, 1969)

1.3.2 Process fundamentals

Solid state welding relies on the application of pressure or pressure and heat combined to join two materials. It differentiates itself from fusion and other welding techniques through two points; the temperature of the process stays below the melting temperature of the metals being joined and the absence of requiring any filler material (Hashmi, 2014). Friction welding is a solid state technique utilising the heat generated from the surface deformation of the soon to be joined surfaces moving over each other.

Solid-state joining based on friction heat generation has become popular due to its ability to produce high-quality joints in the difficult to weld aerospace materials (Grant et. al. 2009). All variants use friction at an interface to plasticise the weld region. The form of motion used to create the friction and plasticise the interface defines the process. Rotary friction welding spins

one axisymmetrical component against a secondary stationary one. Orbital friction welding (OFW) rotates one component on an offset axis to the stationary one, bringing the two together at the end of the cycle. Linear friction welding (LFW) moves the parts in a straight-line in-plane with the interface again aligning the parts at the cycle's end. All rely on the friction between the two components under an axial pressure, whereas, Friction Stir Welding (FSW) uses a shaped probe to interact with the weld region and plasticise the material while not being consumed (M Maalekian, 2007; Mishra & Ma, 2005).

In RFW once one component has reached sufficient rotational speed, the components are brought into contact and an axial force great enough to generate friction at the interface is applied. The rotational energy is transferred into thermal energy from the friction between the weld surfaces providing a quick rise in the temperature at the weld surface. The rise in temperature reduces the yield stress of the material creating a plasticised region at the weld interface. The axial force ejects some of the material forming a curled back feature, called flash, on the exterior of the component. Flash formation consumes weld energy and helps cool the interface region by taking the heated material at the centre of the interface and depositing the material on an exterior surface.(Romero *et al.*, 2009). Once the rotation stops and the axial force is removed the process is completed. If the axial force is increased after the rotation stops this increases the cooling rate and thereby produces a higher hardness at the centre of the weld as seen in CCT diagrams of steel (Ponge, 2005).

In RFW, OFW and LFW the majority of the plasticised material is ejected from the weld interface, transporting surface impurities and contaminants creating an essentially self-cleaning process. The clean material remaining forms the joint. The basic premise of the RFW technique is shown in Figure 1-1. The process is fundamentally controlled by the application of axial force and the rate of rotation of the spinning component. The amount of movement of the components towards each other, as flash is produced, is known as upset.

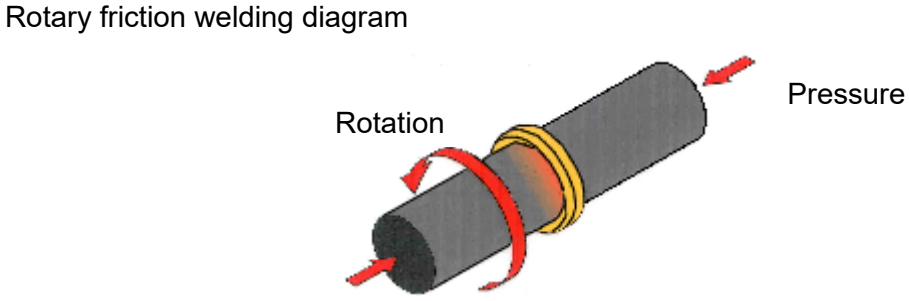


Figure 1-1: Rotary friction welding example with one piece rotating against the second stationary piece while axial pressure is applied creating flash, visible at the centre (Kallee & Nicholas, 1999).

1.3.3 Torque at the interface

Understanding the interface is critical in friction welding. Tracking the power input into the weld is a common method and helps when determining parameters for new geometries or materials (MTI, 2012).

Knowing the torque at the interface and ultimately the power into the weld allows for direct comparison of the efficiency of various parameter combinations in producing desired weld cycles.

Currently the two standard methods of transferring rotational energy to the component comes from either; the storage and release of energy in large flywheels or continuous input from a motor. Utilising a flywheel is termed Inertia Friction Welding (IFW) while employing a motor is called Continuous Drive Friction Welding (CDFW). The power into the weld, $\dot{P}$, can be calculated by measuring the torque, T, on the fixed part and multiplying by the rotational speed ω_v (angular velocity). The torque on the part is the rotational force transferred through the interface.

$$\dot{P} = T\omega_v \tag{1-1}$$

If torque is not directly measured, then experimentally torque can be calculated from an inertia friction weld if the rotational speed throughout the cycle is recorded. Torque is equal to the product of the flywheel inertia and angular acceleration α.

$$T = I\alpha \tag{1-2}$$

The alternative is to calculate the drop in energy in the flywheel over the period of a second (Attallah & Preuss, 2012) as in equation (2-2).

1.3.4 Continuous drive friction welding

A hydraulic or electric motor supplies the energy that is initially converted into thermal energy via friction at the interface of two cylindrical components. One is connected to the spindle while the other is placed in a fixture and prevented from rotating. Either the spindle end or fixture end can be mounted on a slide and connected to a hydraulic ram. The ram provides the axial force for the frictional heat generation and, once the motor has been disengaged, the consolidation of the weld. The weld process can be detailed in a few steps as seen in the parameter traces of Figure 1-2. The motor spins the component up to speed. The ram brings the components into contact and applies a force great enough to generate friction at the interface, stage 1. The continuous energy input from the motor is transferred into thermal energy from the frictional interface increasing the temperature at the weld surface. A plasticised region at the weld interface is created due to reduction in the materials yield stress from the increase in temperature, stage 2. Flash is formed from any material in the plasticised layer with a yield stress less than the pressure from the ram. The ram pressure is increased to a forging pressure either once the rotation has stopped or during the deceleration, stage 3. (Johnson & Daines, 1973; M Maalekian, 2007; Manufacturing Technology Inc, 2013a; Ponge, 2005).

Example continuous drive friction welding parameter trace

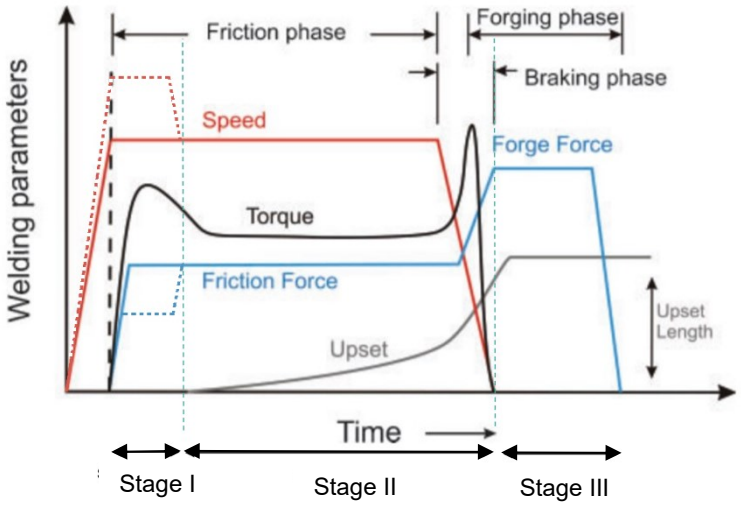


Figure 1-2: Continuous drive friction weld parameter trace example showing the optional 1st friction reduced pressure and/or elevated speed through stage 1 in order to prevent machine stall (Adapted from M Maalekian (2007); (Manufacturing Technology Inc, 2012; L. Yang, 2010)).

1.3.5 Inertia friction welding

Inertia differs from Continuous Drive initially in the method of supplying energy to the part. In IFW a flywheel of specific mass is pre-chosen and attached to the machine spindle. The flywheel is then spun up to a predetermined speed. The motor is disconnected, and the components are forced together with either a single or dual phase force, stage 1, Figure 1-3. The generation of heat at the interface, which plasticises the weld surfaces, extracts energy from the flywheel causing the spindle to slow down, stage 1 and 2. Once the rotation ceases the forge phase begins, stage 3. Here the forge force is maintained or increased to help consolidate the weld (Attallah & Preuss, 2012; Manufacturing Technology Inc, 2013a, 2013b).

Throughout the process the power input of IFW into the weld interface changes to meet the requirements at that stage but is limited in total energy whereas in CDFW the total input into the weld interface is determined by the amount of burn off (stage II, Figure 1-2). CDFW is controllable up to the burn off point but is limited in interface area by the capability of the motor, whereas the total stored energy of IFW is pre-determined by the choice of flywheel inertia and

initial speed. When more energy is required, for either more upset or a greater interface area, a flywheel with a greater moment of inertia is used or it is spun at a faster speed (Attallah & Preuss, 2012; Manufacturing Technology Inc, 2012).

Example inertia friction welding parameter trace

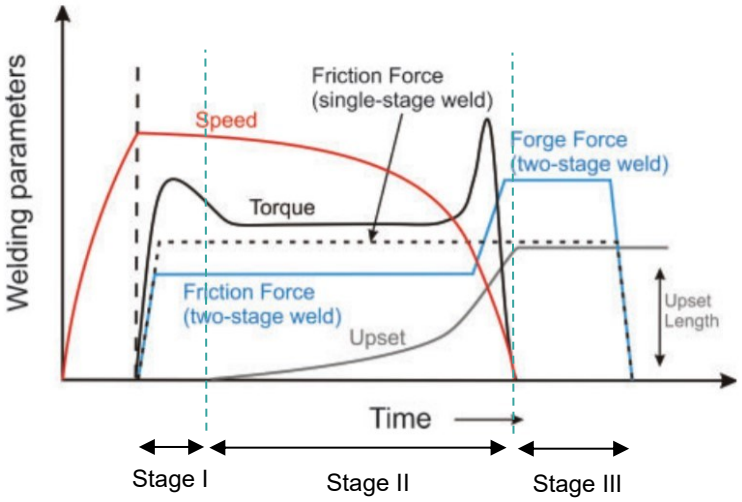


Figure 1-3: Inertia friction weld parameter trace example (Adapted from M Maalekian (2007) and (L. Yang, 2010)).

1.3.6 Process benefits

Compared to similar processes friction welding has several benefits:

- Shielding gasses and pre-preparation not always required. In the majority of cases the interface is isolated from the atmosphere and self-cleaning (TWI, 2014).
- Self-cleaning – surface contaminants are removed from the interface through material movement (TWI, 2014).
- Minimal number of variables – IFW has three pre-set variables. Compared to Fusion welding the friction process is much simpler and could be viewed as easier to setup and maintain (NASA, 2014)
- Near net shape production can be used to simplify a production route – Several castings or forgings can be made and friction welded together decreasing the complexity and cost of the component parts and reducing the amount of machining

required afterwards further reducing costs (AFW, 2016; B. Kumar, 2013; Richards, 2009).

- Capable of welding the entire interface in one pass – This can produce a high rate of production. (Serva-Tech Systems Inc, 2006)
- Quality is not dependant on operator skill. (Serva-Tech Systems Inc, 2006)
- High quality welds are possible in materials normally found to be difficult using fusion techniques – Materials such as nickel-based superalloys, titanium alloys and steel alloys can be successfully welded. The compressive forge forces eliminate the formation of pores while the lack of melting reduces the chances of experiencing hot-cracking (TWI, 2014).
- Monitor and adjust parameters – It is possible to monitor welding parameters during the welding and review post-process. Control during production is also possible especially during a continuous drive cycle. Welders such as the M125T hybrid machine (at the MTC) utilise both modes for an even more controllable, precise and accurate process (MTI, 2013a&b).

1.3.7 Current process applications

Rotary friction welding can be used to join two components of varying shape and size if the part to be rotated is of circular geometry. Dissimilar metals can also be joined using this method. Examples have included: drill pipe screw ends, bosses being welded onto a main part and nickel-superalloy turbine blades being welded onto a steel shaft for a turbocharger.

It can also be used in the pursuit of near net shape manufacture. Small parts can be welded together to produce complex components saving material, machining and associated costs (B. Kumar, 2013; Richards, 2009)

Friction welding can also replace mechanical joints which allow the component to utilise less material. In rotating situations this is extremely useful as the inertia of the part can be reduced

helping to improve the performance or increase product lifespans. In LFW Blisks are a prime example of this situation (B. Kumar, 2013).

1.3.8 Industry standards

The industry standard during the degree for RFW was BS EN 15620:2000 (BSI, 2000) an update was produced in 2019 (BSI, 2019) The documents detail production and testing of welds to ensure welds are fit for purpose. Periodic schedules for testing of mechanical and metallographic properties and non-destructive testing help with ensuring ongoing quality control. Suggested documentation is also included to assist with process control, setup and production recording.

1.4 Aims and objectives

Aim: To assess the utility of enhanced control approaches during friction welding

Objectives:

1. To understand the role of enhanced control mechanisms on weld repeatability (Chapter 4).
2. To study the influence of mid-cycle energy modification on the weld microstructure and component geometry (Chapter 5).
3. To evaluate the impact of artificial deceleration profiles on the weld energy input and associated residual stress state (Chapter 6).

1.4.1 Research approach

Chapter 4: Inertia welding enhanced functionality initial capability assessment on S355 Steel.

To meet the initial objective and provide a baseline performance of the enhanced welds each weld set was analysed according to weld cycle variation, upset variation and in the case of orientation welds the angular deviation. From this point the torque modulation functionality was down-selected for further analysis, based on providing the greatest upset control performance while also not requiring secondary measurement tooling, thereby allowing a greater use of part geometries in future. Until the introduction of the M125T friction welder at the MTC modulated inertia weld profiles were not possible and had not been investigated.

To further understand the torque modulated functionality's impact upon the weld further testing was completed to see, if the modulated energy input rate had influenced the resulting microstructure. The energy input was calculated from the change in energy of the flywheel system, the input from the motor and the losses due to friction in the bearings. Optical micrographs were taken of the weld microstructure and used to measure the weld regions. These were compared with hardness results from across the weld line for better understanding

of the morphology. Finally, tensile testing was used to confirm the strength of the welded samples.

Chapter 5: Microstructural impact and upset accuracy of proportionally modified energy friction welds.

To assess the impact of modifying the energy input mid-weld, two cycles were studied.

The final length control in inertia mode where the energy input was modified after the conditioning phase in order to increase or decrease the upset to meet the required amount to produce final parts of identical length.

The upset controlled friction limit in continuous drive mode where the friction phase utilised a fixed point on the machine upset scale to initiate the forge phase, thereby automating the upset produced.

The M125T is the first machine capable of mid-weld proportionally modified inertia deceleration profiles which had not been investigated prior to this work. Analysis was conducted using the energy input calculations, upset measurements, microstructure analysis and mechanical testing.

Chapter 6: Impact of simulated inertias upon the residual stress in inertia friction welded Ti-6Al-4V.

In order to see if novel welding cycles can improve the weld performance and reduce the need for post processing, three weld profiles were created with a nominal profile compared to a virtual inertia deceleration profile and a twin inertia deceleration profile, in essence changing the flywheel inertia midway through the weld. These novel cycles were analysed using the energy input calculated from weld curves, and temperature measurements taken of the outer

surface. Further analysis of the weld zones, their hardness and microstructure were compared to stress measurements, provided by contour mapping the stress relaxations when the welds were cut through.

The research focused on determining, if artificially controlling the deceleration profile of the weld manipulated the upset rate. Thereby modifying the temperature of the weld interface and subsequent heat input into the surrounding material, in order to lessen post weld residual stresses. The M125T friction welder was the first machine capable of fully artificial deceleration profiles and previously had not been investigated.

2 Friction welding process literature review

The literature review builds on the understanding of the basic process, looking at the parameters and their role in controlling the weld interface. The focus is on inertia friction welding (IFW) as this is the primary mode used in the research. However, when evaluating the literature, research conducted in both inertia and continuous drive modes is used to gain a greater breadth of study. The review moves onto the welded microstructure of the materials studied and finally looks at the current research trends.

2.1 Rotary friction welding

2.1.1 Stages of a friction weld

Tracking the process parameters provides a clear depiction of the process and the two forms, IFW and continuous drive friction welding (CDFW).

Commonly the welding cycle is split into 3 stages that apply in both forms: 1- Initial contact, 2 - Transition Stage and 3 - Forge Stage as shown in Figure 1-2 and Figure 1-3. Sometimes a pre-stage is considered where the spindle or flywheel is spun up to speed. Just prior to the third stage the forging pressure is applied before the rotation stops creating a larger second torque peak. This extra work refines the microstructure, through dynamic recrystallisation, along with further joint cleaning from increased flash formation which removes any impurities such as oxides or inclusions L. Yang (2010).

Stage 1 – Conditioning (also known as Initial Contact): The components are brought together creating a sharp increase in frictional torque causing a deceleration in spindle speed. Joining between the surfaces does not occur until the two surfaces soften and plasticise from the increase in temperature coinciding with a decrease in torque. Prior to this, unevenness and irregularities in the surfaces are worn away until the two reach total contact. In IFW the point of maximum energy transfer is during this stage due to the high spindle speeds and high

torques. In CDFW a higher initial speed, lower pressure or both can be used to prevent the machine from stalling.

Stage 2 – Transition Stage (also known as Burn Off): Here the strain hardening is supressed by the frictional heating. The upset slowly increases to a constant rate as the flash starts to form and material is extruded. In inertia the spindle speed drops proportionally to the energy transferred to the weld. The torque stays constant while the plasticised region becomes wider due to the frictional heating. In CDFW a feedback loop keeps the speed constant while adjusting the motor torque in response to the changing frictional torque at the interface. The burn-off point can be time or upset based and triggers the switch from friction to forging forces. In CDFW it also triggers the spindle deceleration.

Stage 3 – Forging Stage (also known as Consolidation): This starts when the forge pressure has been reached such as in CDFW. In an IFW weld it is when the torque increases as the spindle speed decreases rapidly. As the final upset is attained in this stage slightly more flash is formed which helps to cool the interface. The forging force is sustained until the weld has cooled, known as dwell time (Attallah & Preuss, 2012; I Bhamji *et al.*, 2011; M Maalekian, 2007; Uday *et al.*, 2010; Vairis *et al.*, 2016; L. Yang, 2010)

2.1.2 Process parameters

Although the two processes are similar the parameters which control them are different. IFW is controlled by:

- *Flywheel energy.*
- *Forging pressure*.

The flywheel energy (E) is a product of its rotational speed (ω) and moment of inertia (I) which can be considered as separate parameters, as in equation (2-1) (Attallah & Preuss, 2012).

$$E = \frac{1}{2} I \omega^2 \tag{2-1}$$

As flywheel size is a discreet variable and therefore the moment of inertia is discreet the speed, as a continuous variable, is used to easily affect the stored energy. The forging pressure are usually single or dual phase. The two phases are referred to as Friction and Forge (L. Yang, 2010). In IFW, the energy in the flywheel is predetermined by the flywheel inertia and rotational speed, no energy is added or subtracted during the cycle, hence the spindle speed gradually decelerates as energy is transferred into the weld interface, whereas CDFW has a controllable spindle speed throughout the process.

By tracking the deceleration of the flywheel over a defined time gap the rate of energy transfer from the flywheel can be calculated. If system frictions are assumed to be negligible then this energy becomes the input rate into the weld. As in equation (2-2), ΔE change in energy, Δt change in time, subscript 1 denoting the initial condition, E_1 initial energy, t_1 initial time and ω_1 initial rotational speed, with subscript 2 denoting the second condition, E_2, t_2 *and* ω_2 (Manufacturing Technology Inc, 2012).

$$\frac{\Delta E}{\Delta t} = \frac{E_2 - E_1}{t_2 - t_1} = \frac{\frac{1}{2} i(\omega_2^2 - \omega_1^2)}{t_2 - t_1} \tag{2-2}$$

CDFW is more complicated than IFW but as events during the weld trigger further actions, it is more controllable. Parameters include:

- *Rotational speed* during the friction stage.
- *Friction pressure* during the friction stage.
- *Ramp rates* for the speed and pressure throughout the process.
- *Burn off* - the trigger to switch from the friction to forge stage which can be time or axial shortening based.

- *Forge pressure*.
- *Forge duration*.

In some scenarios there can also be two friction pressures and two friction speeds, normally the first friction speed is higher while the first friction pressure is lower than the following values in order to prevent the motor from stalling (Manufacturing Technology Inc, 2012).

Output variables apply to both modes. They can be measured or calculated by the machine thereby providing a basic form of quality control as they respond to changes in the input variables.

- *Upset* – the amount of axial shortening.
- *Torque* – the rotational force generated at the interface.
- *Upset rate* – the rate of axial shortening.
- *Weld time* – the actual time from the parts contacting to the forge pressure dropping.

In order to build up parameter knowledge or transfer parameters between geometries the size of the component is removed from the values. Energy becomes energy per unit area E_A.

$$E_A = \frac{E}{\pi r^2} \tag{2-3}$$

Rotational speed, ω, (in revolutions per minute) is converted to surface speed per min, ω_s, by multiplying by the circumference of the surface.

$$\omega_s = 2\omega\pi r \tag{2-4}$$

While the cylinder pressure, p_c, on the machine can easily be converted to weld interface pressure, p_i, if the area of the piston inside the cylinder, A_c, and the weld interface area, A_i, are known (Attallah & Preuss, 2012; Manufacturing Technology Inc, 2012).

$$p_i = \frac{p_c A_c}{A_i} \tag{2-5}$$

Figure 2-1 shows the effects of high, medium and low inputs of the parameters from IFW on solid pieces. The centre of the weld shown is the viscoplastic material, which has been deformed and displaced during the process. Increasing the energy input into the weld, in this case by increasing the flywheel inertia, allows more of the material to be deformed so generates a larger amount of flash as the forge phase forces a greater amount of material away from the interface. Low pressure indicates that the force applied is not enough to deform the material and move material away from the interface, which allows the heat to build up at the interface, hence the wider plastic region at the centre. Too much pressure and the effect is reversed. The hot material is moved to the outside diameter (OD) before heat energy can be transferred to the non-rotating centre leaving a centre defect where the centre is insufficiently formed of plastic material. Low speeds and high pressures produce similar effects as do high speeds and low pressures. At low speeds, the frictional and shearing heating methods only generate adequate heat to plasticise the material towards the outer diameter where the relative surface velocity is high enough. This area is too far away to transfer heat to the centre. At high speed the inverse occurs. However as rotational speed and energy are linked it can be difficult to separate the effects of parameter changes. Normally a compromise is used due to the limited number of flywheel sizes available. Once the ideal parameters have been chosen, usually producing a theoretical flywheel size, the closest actual flywheel size is chosen and the speed adjusted to keep the energy the same (Attallah & Preuss, 2012; Linnert, 1994; Manufacturing Technology Inc, 2012).

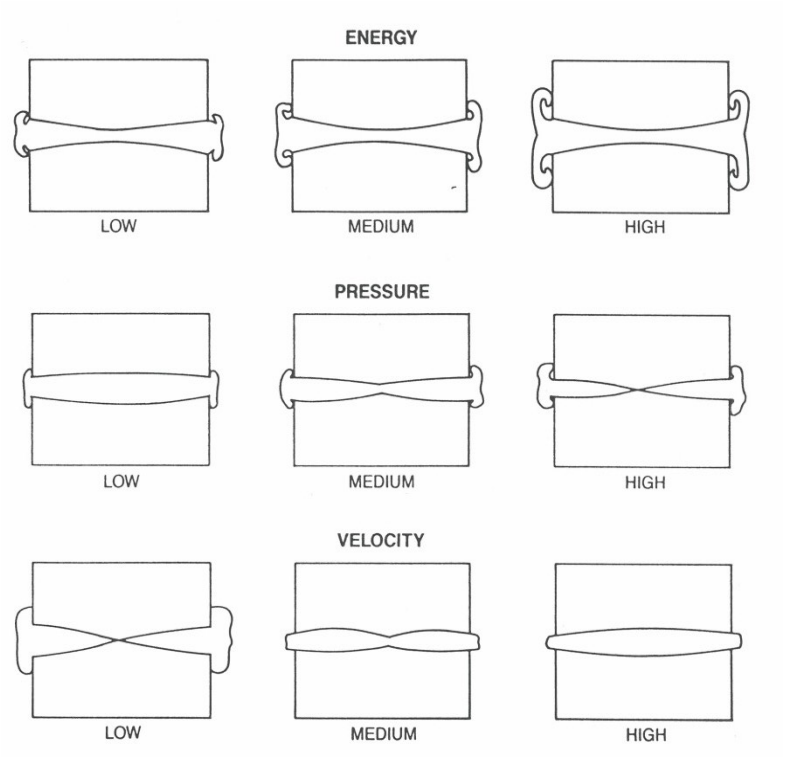


Figure 2-1: Parameter effects on the weld interface viscoplastic material (Linnert, 1994)

2.1.3 Effect of energy

Energy stored in the flywheel is a product of the rotational speed and flywheel inertia, adjusting the stored energy requires changes to one or the other. At set pressures the modelling by F. F. Wang *et al.* (2014) in Figure 2-2 shows a linear relationship with the square of rotational speed, which is directly proportional to energy. As the lines cross through the x-axis, a minimum energy is suggested to start generating upset at the various pressures.

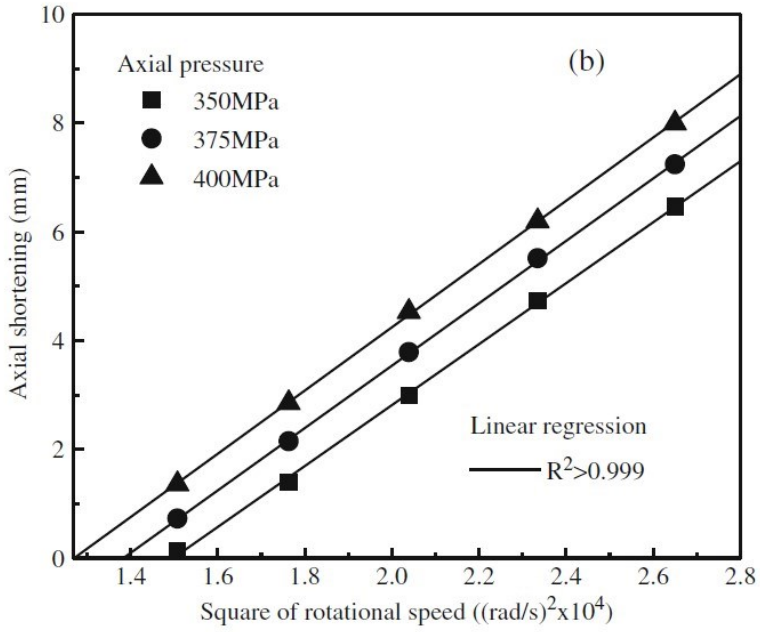


Figure 2-2: Effect on axial shortening of square of rotational speed for different axial pressures (F. F. Wang *et al.*, 2014).

Modelling and experimental work of the continuous drive process Healy *et al.* (1976) of the linear equilibrium phase indicated a relationship between the rotational speed and the upset rate. At low rotational speeds, an optimum could be found which maximised the production of flash. At higher speeds, regardless of pressure, the trend was towards lower upset rates suggesting a lower process efficiency, Figure 2-3. The upsets rates showed strong correlation with torque, plasticised layer and interface temperature. Faster rubbing speeds predicted higher interface temperatures that matched with the lower torque and a thinner plasticised layer. The same effects were also seen by Özdemir *et al.* (2007) but due to the increased temperature and slower ejection of material, heat affected zone (HAZ) widths increased.

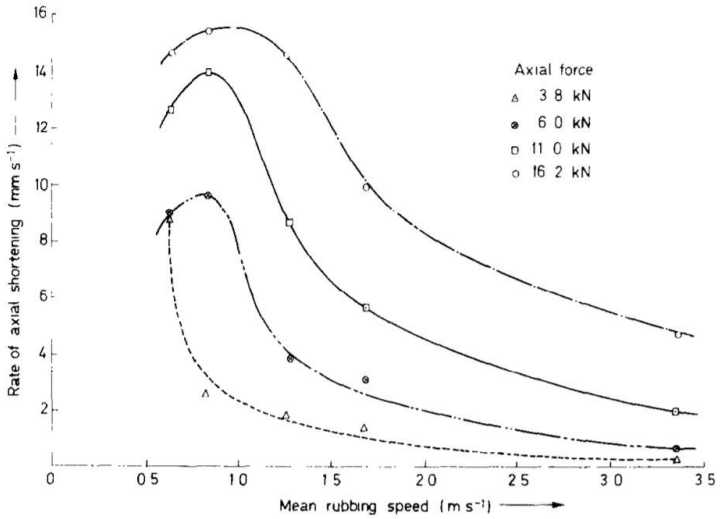


Figure 2-3: Experimental results of rubbing speed vs upset rate at various axial pressures during the linear equilibrium upset phase performed on a continuous drive welding machine (Healy *et al.*, 1976).

2.1.4 Effect of pressure

Tumuluru (1984) showed that it was only the inertia and rotational speed, which affected the weld microstructure through manipulation of available energies, which indicated that they relate to cooling rates and hence phase development in different regions. Pressure was shown to have limited effect and only changed the amount of material forced out of the weld zone as flash. However, the work was conducted on high carbon steels that only showed a final martensite structure, possibly making it difficult to identify any microstructural differences. F. F. Wang *et al.* (2014) produced a finite element model of the IFW process in GH4169 nickel superalloy performing a sensitivity study of the parameters on the model. A logarithmic relationship is found between increasing a combined pressure and energy factor and increasing axial upset as seen in Figure 2-4, showing that the two parameters are linked in the generation of upset, a lack of one can be compensated for by an increase in the other.

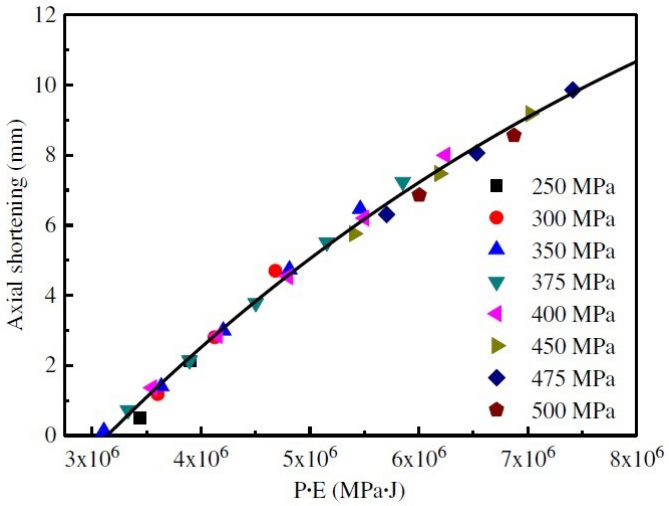


Figure 2-4: Effects of axial pressure (*P*) and kinetic energy (*E*) on axial shortening(F. F. Wang *et al.*, 2014).

In continuous drive the effects of pressure and time on ferritic stainless steel welds were tested with higher friction and forge pressures combined with shorter processing times producing tensile and impact properties closer to the parent material Sathiya, Aravindan, and Haq (2007). However, no combination of short times and low pressures or long times and high pressures were tested to separate the effect of the processing time and pressures. Neither were the friction stage and forge stage tested independently.

Alavala (2016) modelled the effect of parameters in continuous drive welding in a finite element model. Initial predictions suggested rotational speed and friction pressure have the greatest influence on the welding temperature but in trials, it was the friction pressure and friction time. Further work indicated that as long as a sufficient temperature is reached during the friction phase, it is the friction and forge pressure, which have the most effect on the axial upset.

2.1.5 Effect of flywheel inertia vs rotational speed

The model by Wang et al. (2014) allows evaluation of the change in flywheel inertia by small incremental amounts, which if proven by experimentation would be extremely costly. Figure

2-5 shows the decrease in energy efficiency of conversion to axial shortening with the increasing flywheel inertia F. F. Wang *et al.* (2014). It was also claimed that the interface temperature increased faster and the cycle times decreased when the flywheel inertia was reduced, matching the information from MTI and supporting earlier findings (Manufacturing Technology Inc, 2012); L. Wang *et al.* (2005).

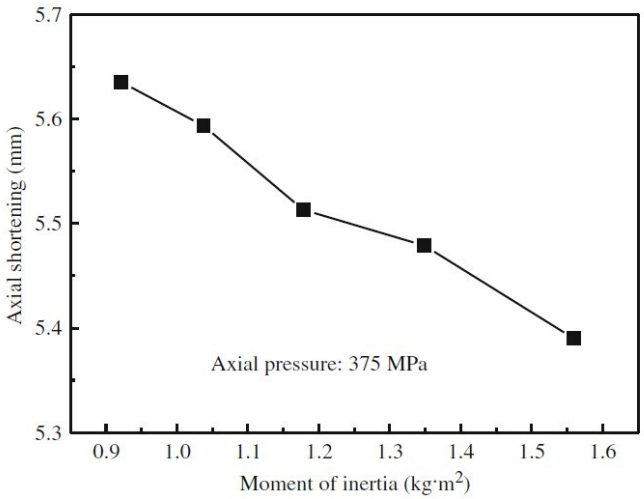


Figure 2-5: Effect of moment of inertia on axial shortening for constant initial flywheel kinetic energy (F. F. Wang *et al.*, 2014)

2.1.6 Optimising parameters

As noted above, various combinations of inertia and rotational speed can be used to create the same energy levels and various combinations of pressure and energy can produce the same upset amount. Either through empirical testing or verified models, a parameter window such as in Figure 2-6, can be produced for a certain welding scenario. This allows desired upsets to be produced with a high certainty of the outcome. Further testing is required to link upset to material microstructure and performance. Once all data has been collected the ideal parameters can be selected to balance performance, material costs and processing time. Weighted statistical methods have been used to good effect (Sathiya, Aravindan, & Haq, 2007; Sathiya *et al.*, 2006) The Taguchi method weights outputs and highlights the value of an individual parameter that gave the best result, of those tested, while only requiring a minimal

number of test samples. Basic modelling of the process before commencing weld trials is becoming more popular as it can provide initial parameters for a trial, reducing the cost and complexity for the customer. Neural network modelling has also been used to assist in parameter optimisation with minimal trial expense by (Sathiya *et al.*, 2009) and W. Liu *et al.* (2013).

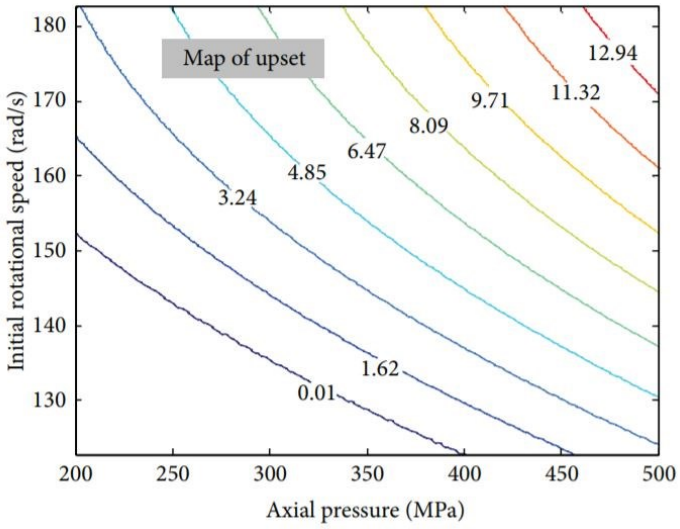


Figure 2-6: Parameter window showing the upset produced by various combinations of rotational speed and pressure produced from a finite element model using a neural network (W. Liu *et al.*, 2013).

Without cutting up the weld the only visual indication of a good weld, other than upset, is the flash size, shape and texture. Sathiya *et al.* (2006) measured the flash height, width across both sides and the individual thickness from the interface but did not measure roughness or colour. They produced welds in the continuous drive mode and found a general relationship between increased parameters (time and pressure) and overall flash size. The exception was flash width which experienced a minimum in the middle of the data set under medium pressure (friction and forge) and time (again friction and forge).

Other visible features include re-entrant notches and internal flash columns. Re-entrant notches form, when a lack of bonding occurs across the interface, , as circled in red in Figure 2-7 (Adams & Miller, 2013). Similar cracking across the interface was contributed to a lack of heat generation from insufficient friction pressure (Selvamani *et al.*, 2015). In ideal conditions the material at the interface bonds enough to be ejected as a homogenous piece before splitting and curling away. Thereby increasing the bonded interface area, Figure 2-8 (Işık & Özes, 2016).

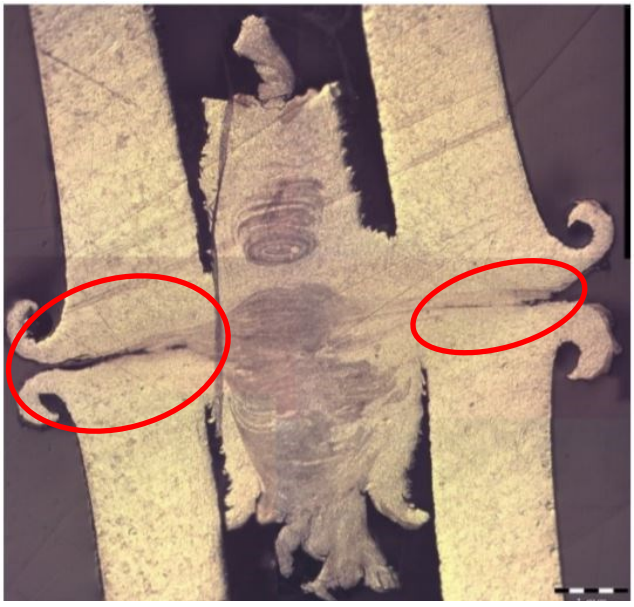


Figure 2-7: Tube to tube weld in stainless steel showing the incomplete bonding of a re-entrant notch, circled in red, and the formation of a central column of flash, shown for ease on a sectioned weld (Adams & Miller, 2013).

Central flash columns form on welds where the material expelled onto the inside diameter (ID) is great enough to join and create a column. This can be due to a large upset or a small ID in comparison to the weld area.

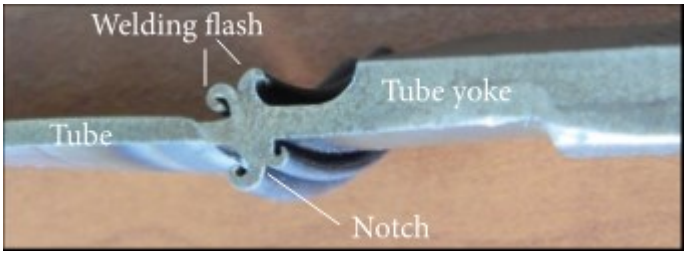


Figure 2-8: Cross section of a tubular steel friction weld. Welding flash and notch have been highlighted (Işık & Özes, 2016).

2.1.6.1 Required upset

Part of defining a parameter window is to determine how much upset is required to ensure a weld of acceptable quality. As the process is generally defined as self-cleaning (M Maalekian, 2007; Uday *et al.*, 2010), movement of the material at the interface to ensure clean material bonding can be a critical factor in weld quality. The industry standard for ensuring enough material is removed from the interface to guarantee a cleaned interface is based on upsetting 1/5th of the components thickness, plus a small amount extra to increase the reliability of achieving a suitably strong weld (Attallah & Preuss, 2012; MTI, 2012).

For tubes $U_T = 3.81 + 0.2 \times (r_o - r_i)$ in millimetres (2-6)

For solid bar $U_T = 1.27 + 0.2 \times 2r_o$ in millimetres (2-7)

With U_T being the upset target, $r_o$the outer surface radius and r_i the inner surface radius. The 3.81mm comes from the imperial 0.15” that is added on to the formula, the 1.27mm from the imperial 0.05”.

In rotary friction welding (RFW) studies into a Low Heat Input (LHI) method M. Kimura, M. Kusaka*, et al.* (2005a); (Kimura *et al.*, 2003) (discussed in detail in 2.6.1 Low heat input welding) by testing welds essentially stopped at progressively further points through the cycle. Although not specifically looking at surface contaminants the performance of the welds was evaluated. Welds that have passed through the initial high torque peak performed reliably at 100% base material strength, it suggests either that the interface has been completely cleaned, or that the remaining contaminants are not detrimental to the strength of the weld. Further work would be needed to confirm whether this phenomenon is coincidental or not. What it is suggested is, that it is possible to use torque as a performance indicator instead of upset.

2.1.7 Frictional heat at the interface

Under Coulomb's friction law heat generation rate at the interface $\dot{P}$ is a product of the input parameters; the pressure applied at the interface p_i, the angular velocity ω_v, and the coefficient of friction between the two surfaces μ and can be modelled across an annulus at a radial distance from the central axis r. It comes from the frictional force F_f which, is a product of the coefficient of friction and the normal force F. The normal force resulting from the pressure applied over a small annulus area A. Converting the equation into a differential characterisation of the area creates;

$$dF = p_i \, dA \tag{2-8}$$

$$dA = 2\pi r \;\; dr \tag{2-9}$$

$$dF_f = \mu p_i 2\pi r \;\; dr \tag{2-10}$$

Heat generation rate being proportional to the frictional force and the velocity of the surface ω_s;

$$d\dot{P} = dF_f(\omega_s) \tag{2-11}$$

Surface speed being the product of angular velocity and radial distance;

$$\omega_s = r\omega_v \tag{2-12}$$

Combining these equations together;

$$d\dot{P} = 2\pi\mu p_i r^2 \omega_v \;\; dr \tag{2-13}$$

Integrated for all values of r the equation becomes;

$$\dot{P} = \int_0^R 2\pi\mu p_i r^2 \omega_v \; dr = \frac{2}{3}\pi\mu p_i \omega_v R^3 \tag{2-14}$$

Providing the power input $\dot{P}$ required to rotate the work piece under pressure (C. Bennett *et al.*, 2007); Li *et al.* (2016); Seli *et al.* (2010). Similar equations have been produced for orbital friction welding M. Maalekian *et al.* (2008). The equation for heat flux, q, is found by dividing the internal power by the annulus area.

$$q(r) = \frac{d\dot{P}}{dA} = \frac{2\pi\mu p_i r^2 \omega_v \; dr}{2\pi r \; dr} = \mu p_i \omega_v r \tag{2-15}$$

Under coulombic friction law τ_f is proportional to the normal pressure p_i through the coefficient of friction μ M. Maalekian *et al.* (2008).

$$\tau_f = \mu p_i \tag{2-16}$$

However, if it is assumed that the process is operating entirely in the plastic deformation regime, the frictional stress τ_f is equal to the shear yield stress τ_y. The shear yield stress is related to the tensile yield stress σ_y through the Von Mises relationship.

$$\tau_f = \tau_y = \frac{1}{\sqrt{3}}\sigma_y \tag{2-17}$$

Combining equations (2-15), (2-16) and (2-17) gives an equation for the heat generation under plastic shear stress;

$$d\dot{P} = \frac{2}{\sqrt{3}}\sigma_y \omega_v \pi r^2 \; dr \tag{2-18}$$

This assumes that the coefficient of friction also does not change which is viable during the dynamic equilibrium region of stage II, however during the initial contact and deceleration the torque is much higher as depicted in the cycle diagrams (Figure 1-3, L. Yang (2010)) indicating that the energy input during these sections is not a constant rate. A transition equation that covers the transition between the frictional stress and shear stress regimes would be;

$$d\dot{P} = \left((1-\delta) 2\pi\mu p_i r^2 \omega_v \; + \delta n \frac{2}{\sqrt{3}} \sigma_y \pi r^2 \omega_v \right) \; dr \tag{2-19}$$

Integrated for all values of *r*

$$d\dot{P} = \int_0^R \left((1-\delta) 2\pi\mu p_i r^2 + \omega_v \; \delta n \frac{2}{\sqrt{3}} \sigma_y \pi r^2 \omega_v \right) \; dr \tag{2-20}$$

$$\dot{P} = (1-\delta) \frac{2}{3} \pi\mu p_i \omega_v r^3 + \delta n \frac{2}{3\sqrt{3}} \sigma_y \pi r^3 \omega_v \tag{2-21}$$

Where n is the efficiency of the process of mechanical energy into heat energy and δ is a factor between 0 and 1 defining the transition between the two states, 0 being fully in the frictional stress regime and 1 being in the fully plastic deformation regime, as covered by M. Maalekian *et al.* (2008).

For a more accurate measurement of the power transfer into the weld, a flywheel run down can be performed detailing the deceleration of the flywheel when no load is placed upon the parts. This allows the friction of the system to be detailed and the system friction torque T_s calculated. When the power is calculated the weld torque T_w can be combined with the system torque and the correct power into the weld P_w calculated (Senkov, Mahaffey, Tung*, et al.*, 2017).

$$T = T_w + T_s \tag{2-22}$$

$$P_w = (T - T_s)\omega_v \tag{2-23}$$

Kimura *et al.* (2010) produced a similar model based on CDFW primarily concentrating on the conditioning phase and transition of the material into the plastic region, defining the states as friction and seizure where the criteria between the two is temperature. Earlier work, (Kimura *et al.*, 2003), on developing a new welding method using a clutch mechanism that can, in

essence, pause the weld, helped guide the authors. When the entire weld has reached a state of seizure, the weld is in dynamic equilibrium and the model is stopped. Figure 2-9 shows the model's transition through the initial weld phases under high and low pressure weld scenarios. Both creating a state of wear starting at the OD surface and working towards the centre due to the requirement for differential speed between the two faying surfaces. This is visible in steps i – iii. Low pressure continues the transition of the wear interface towards the centre and builds a seizure scenario out from the centre. High pressure rapidly converts the wear surface at the outer circumference into a seizure mode whilst developing the internal circumference of the seized area into a wear state. This seized area grows towards the centre preceded by an inner circumference of wear until the entire surface has moved to the seized mode. The difference occurs due to the high pressure's ability to rapidly raise the temperature of the surface into the seizure mode. Whereas in the low pressure weld seizure starts initially at the centre as the weld surface temperature is slowly increased allowing the wear regime to expand and reduce energy losses from the centre increasing the centre point's transition rate into the seizure mode. IFW speed decelerates non-linearly, with respect to time, due to changes in the frictional torque at the interface because of the material response to the initial parameters; initial speed, pressure, and flywheel inertia, and subsequently the temperature and torque at the interface.

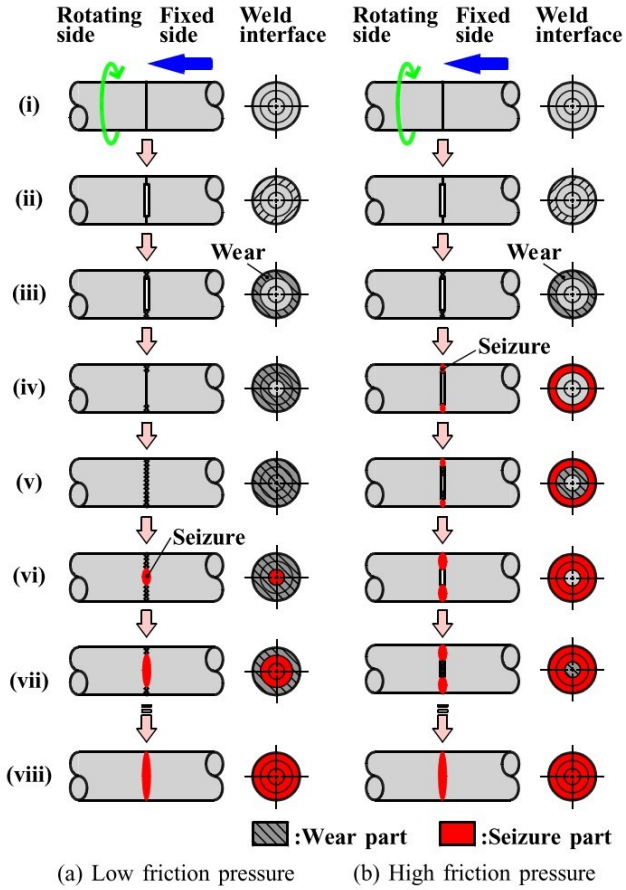


Figure 2-9: Schematic joining mechanism demonstration of the first stage of the friction model. a) low pressure b) high pressure. (Kimura *et al.*, 2010)

2.1.8 Energy efficiency

The total energy contained in a rotating flywheel system, noted in equation (2-1), is only the total stored energy and is not the energy transferred into the weld piece. Energy efficiency has largely been ignored until recently with a few papers investigating the relationship between parameters and energy input into the weld of a dissimilar nickel superalloy joint (Mahaffey *et al.*, 2016; Senkov, Mahaffey, & Semiatin, 2017; Senkov, Mahaffey, Tung, *et al.*, 2017). Torque measurements of the fixture part were detracted from the torque decelerating the flywheel separating energy into the sample and energy lost into the machine. As is already known multiple combinations of parameters can produce the same result normally measured by the

amount of upset produced. These papers primarily measured the total energy input and energy input rates to evaluate the effect of parameters. Efficiency of the process was defined as the energy consumed by the sample over the total energy stored in the flywheel at the start of the process. Upset was found to increase with increasing amounts of inertia when the total initial energy was kept the same indicating high inertia and low speeds produce the more energy efficient method of welding. Peak temperatures were also shown to increase with increasing amounts of inertia, which was attributed to the increased efficiency. Defects were seen in the two lower inertia welds conducted by (Mahaffey *et al.*, 2016) suggesting that the drop in efficiency reduces the energy below the minimum required to make a sound weld. The minimum weld energy factor is identified and discussed further by (Senkov, Mahaffey, & Semiatin, 2017) and fits with the modelling by (F. F. Wang *et al.*, 2014) while also matching with the minimum upset criteria by Attallah and Preuss (2012).

In order to quantify and calculate the torque characteristics of the parasitic energy loses multiple methods were presented. Flywheel rundowns were initially employed where the flywheel decelerates without any load applied and no parts are in contact. As the machine contains a thrust and a journal bearing the frictional torque is a linear function of the velocity (Mahaffey *et al.*, 2016; Senkov, Mahaffey, & Semiatin, 2017).

$$M_{JB} = \left(\frac{2\pi v R_1^3 L}{h_1}\right)\omega + M_{JB0} \tag{2-24}$$

$$M_{TB} = \left(\frac{2\pi v R_2^4}{3h_2}\right)\omega + M_{TB0} \tag{2-25}$$

M_{JB} is the moment of the journal bearing, M_{TB} is the moment of the thrust bearing, v – the lubricating oil viscosity, R_1 – shaft radius, L – length of the journal bearing, h_1 – radial clearance of the journal bearing, R_2 is the surface radius of the oil film of the thrust bearing while h_2 is the

oil film thickness of the thrust bearing. Added together these two moments make the machine friction momentum. Rearranged you can combine the initial moments M_{TB0} and M_{JB0} into one machine initial moment, $\mathrm{M_{mo}}$, and the other factors as a function of ω.

$$M_M = a\omega + M_{M0} \tag{2-26}$$

Machine friction moment can then be substituted into the equation defining the deceleration of the flywheel rundown with different flywheels.

$$\frac{d\omega}{dt} = \frac{M_M}{I} \tag{2-27}$$

And then integrated into a time dependant function of ω.

$$\omega = -\frac{M_{M0}}{a} + \left(\omega_0 + \frac{M_{M0}}{a}\right) e^{\left(\frac{-at}{I}\right)} \tag{2-28}$$

To gain a and M_{M0} the equation can be fitted to the run-downs recorded. The difficulty is this approach does not consider the bearing performance under load as it would be exceptionally difficult to separate out these two bearing performances. Use of the torque cell to separate the machine frictional torque agreed with the linear equation of M_M allowing easy identification of *a* and M_{M0} as gradient and intercept respectively. The parasitic loses subsequently could be compared between each welding scenario.

Further analysis detailed by Senkov, Mahaffey, Tung*, et al.* (2017) has shown pressure to effect the parasitic loses in the machine, with increasing pressure also increasing the energy loses to the machine. However, in comparison to the relationship between energy efficiency and rotational speed the effect of pressure on efficiency is small as seen in Figure 2-10. Interestingly the torque experienced at the sample interface was not seen to be dependent on pressure while temperature measurements did show that higher pressures increased the rate of temperature rise and the peak temperature experienced. This contradicts the suggestion of a cold weld forming from the pressure increase seen by Romero *et al.* (2009). Potentially this

is because the pressures tested by Romero *et al.* (2009) were significantly above the known nominal whereas here the pressures appear to be around the nominal value. There are also no temperature measurements to compare only microstructural evidence and the process is LFW instead of IFW.

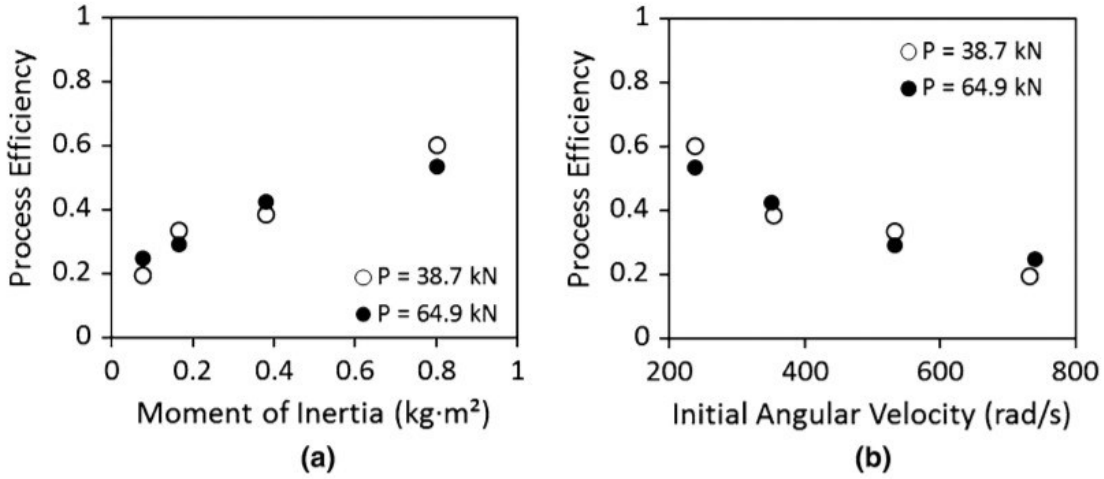


Figure 2-10: Efficiency of the inertia friction welding as a function of (a) the flywheel moments of inertia or (b) the initial angular velocity for two axial compression forces (Senkov, Mahaffey, Tung*, et al.*, 2017).

The effects of parameter choices on the energy input into the sample is summarised in Figure 2-11 by Senkov, Mahaffey, and Semiatin (2017). In part (a) pressure is shown to affect the total amount of energy input but not the rate. Part (b) shows that the combination of flywheel inertia and rotational speed to achieve a set initial energy has large effects on the efficiency of the process but again does not change the input rate, while part (c) reveals the inefficiency of increasing initial energy by increasing rotational speed with the secondary effect of impacting on the input rate.

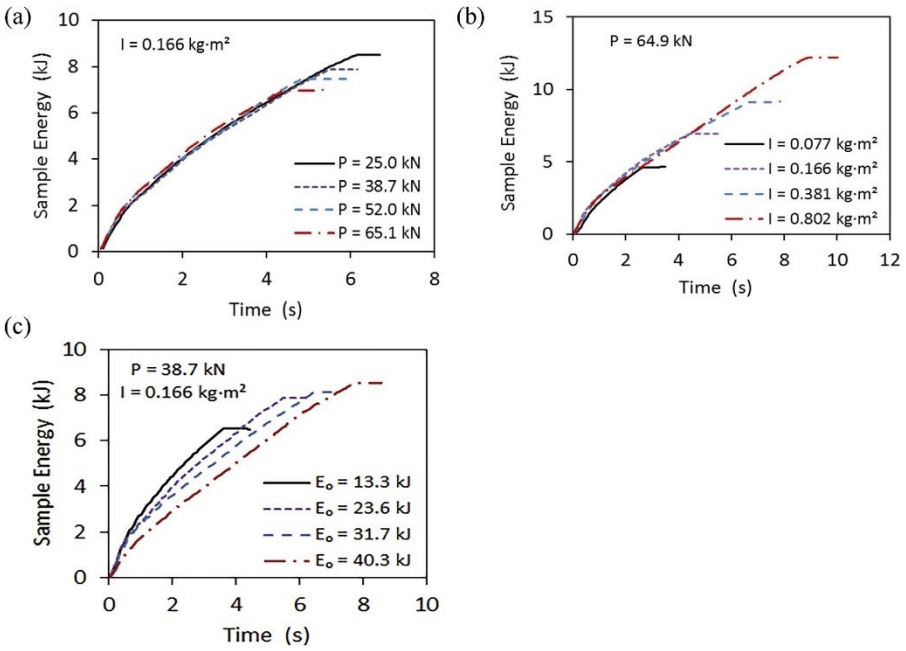


Figure 2-11: Time dependence of the energy ES, consumed by samples during IFW conducted with different welding parameters: (a) I = 0.166 kg·m2, E_o = 23.6 kJ, various P; (b) various I, E_o = 23.6 kJ, P = 64.9 kN; (c) I = 0.166 kg·m2, various E_o, P = 38.7 kN (Senkov, Mahaffey, & Semiatin, 2017).

2.1.9 Comparison of inertia and continuous drive friction welding

As there are two process forms, manufacturers need to know the benefits of one option over the other. Below is a combined view of the advantages of each process over the other.

2.1.9.1 Advantages of CDFW over IFW

Lower weld forces therefore bigger parts on the same tonnage machine.

Weld torque peak is smaller therefore fixturing is put under less stress, therefor lasts longer.

Better overall length control and greater ability to accept part length variation.

No lengthy flywheel changes required.

(Manufacturing Technology Inc, 2013a)

2.1.9.2 Advantages of IFW over CDFW

IFW can produce improved properties in numerous materials compared to CDFW due to shorter weld times and a narrower HAZ.

IFW creates helical weld flow patterns from differences in deceleration, which can improve weld strength.

The process is scalable as the parameters are pre-set. e.g a small part can be used as proof of concept for larger parts.

IFW machines do not have a clutch or brake, therefore reduced cost and simpler programing.

IFW generally utilises a higher force during upset generation as there are no issues with motor stall, leading to narrower weld zones.

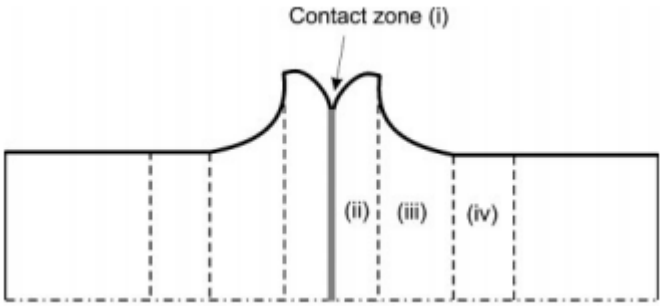
(Attallah & Preuss, 2012; Chaturvedi, 2011; Manufacturing Technology Inc, 2013c)

2.2 Metallurgical weld characteristics

2.2.1 Weld zones

For clarification, the weld is split into several weld zones as seen in Figure 2-12. These are dependent on the characteristics found in the zones. In simple terms the unaffected region is called the Parent Material. The area affected by the heat input alone is named the Heat Affected Zone (HAZ) (region iv). The next area affected by the mechanical deformation and heat is known as the Thermo-mechanically affected zone (TMAZ) (region iii). The join at the centre of the weld is called the Bond Line or Contact Zone (CZ) (region i) and the material around this area can be called the Recrystallised Zone (RZ) (region ii) though in some cases is included in the TMAZ. Occasionally, the bond line and recrystallised zone are combined into one zone known as the weld zone. In friction welding, the HAZ is generally quite small, no plastic deformation is present in this zone. If the peak temperature is high enough a phase transformation can occur, and some grain growth may also occur. In the TMAZ the grains start

deforming from the input of strain energy in the form of plastic deformation. The grains can be seen to be elongated and orientated in the direction of the material flow. Some grain coarsening may be visible. At the centre of the TMAZ the RZ has undergone dynamic recrystallisation and a new equiaxed fine grain structure is visible. The CZ experiences high deformation rates from the rotation of the parts, resulting in dynamic recrystallisation that is more continuous, producing a very fine microstructure (M Maalekian, 2007; Özdemir *et al.*, 2007; Uday *et al.*, 2010). Due to the large variation visible within one zone, Yates (2015) ends up describing the TMAZ and HAZ as having inner and outer regions; primarily due to the change in grain size and change in secondary phases visible in Ti-6Al-4V friction welds.



(i) Contact Zone; (ii) recrystallised zone / fully plasticised zone (iii) thermo-mechanically-affected-zone / partly deformed zone (iv) heat-affected –zone / undeformed zone

Figure 2-12: Weld zones diagram of a Rotary Friction Weld (Maalekian, 2007).

Alternative naming conventions exsist such as that used by (Iracheta *et al.*, 2015) in Figure 2-13 which are defined by the state during the cycle and resultant microstructure rather than purely the microstructure visible after the process. The weld line (WL) is the interface between the two parts where heat is initially generated by friction before moving to a shear deformation mechanism. The fully plasticised zone (FPZ) is characterised by high temperatures, strains and strain rates and is the equivalent of the recrystalised zone displaying refined grains compared to the parent material. The partialy deformed zone (PDZ) is the equivalent of the TMAZ where grain growth is evident due to high heat input but low strain and strain rates. The

undeformed zone is the same as the HAZ where heat energy can cause some grain growth or dissolution. Phase A is the parent material, Phase B the region effected by the slow heating and cooling of transferred energy from the interface and Phase C is the region where the peak temperature experienced is above a phase transformation temperature leading to a new phase upon cooling.

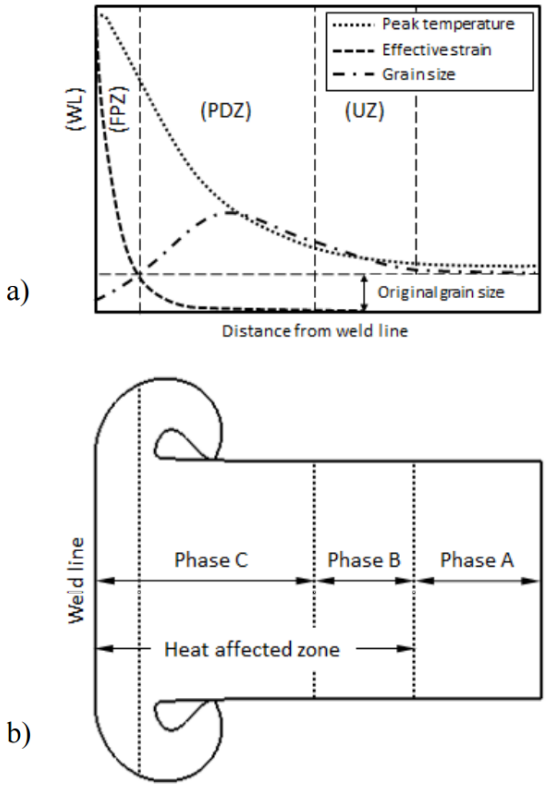


Figure 2-13: A) Weld zone regions related to the cycle conditions and basic resultant microstructure: WL – Weld Line, FPZ – Fully Plasticised Zone, PDZ – Partially Deformed Zone, UZ – Undeformed Zone. B) weld zones related to the physical shape of a weld.(Iracheta *et al.*, 2015)

When comparing materials and interface temperatures the coallated data by Li *et al.* (2016) in Figure 2-14 shows that regardless of material the relative interface temperatures are similar occuring between 0.75 and 0.95 of the solidus temperature (*Tm*). The lower relative temperature of titanium alloys being suggested because of the materials lower thermal diffusivity and reduced strength at higher temperatures.

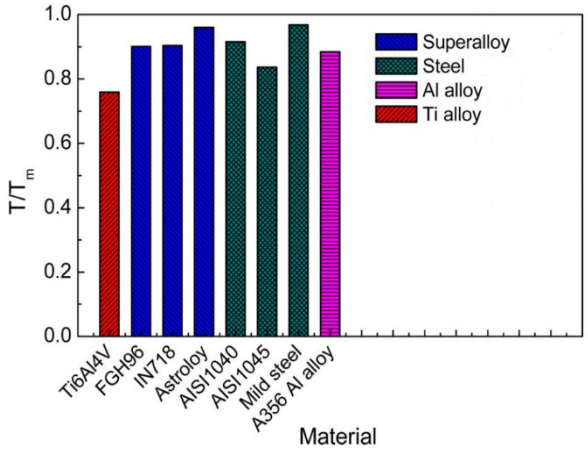


Figure 2-14: Welding temperatures normalised to the solidus temperature (Li *et al.*, 2016).

2.2.2 Recrystallisation

In the centre of a rotary friction weld the zone either side of the interface is known as the fully plasticised or recrystallisation zone. Recrystallisation is the formation of a new set of strain free equiaxed grains from a previously strained structure by the formation and migration of high angle grain boundaries (~10^{o} to 15^{o} misorientation) without the need for the material to enter a liquid phase.

The mechanism of recrystallisation has been subdivided into multiple types depending on the type of processing steps undertaken. When the deformation occurs prior to heating it is known as static recrystallisation. When the deformation occurs during the heating phase the term dynamic recrystallisation is used. In friction welding the deformation and heat occur at the same time defining it as dynamic (M Maalekian, 2007). The process is then further divided dependant on the formation of the new grains, into discontinuous and continuous.

Discontinuous is used to describe when recrystallisation occurs due to a two-step route of nucleation followed by grain growth. Nucleation occurs in regions highly misoriented compared to the surrounding material. The high degree of misorientation then provides the needed mobility for growth. Grain growth or coarsening is driven by the reduction in grain boundary area resulting in a larger mean grain size. Either the smallest grains can be absorbed or a few grains can become disproportionately large (Doherty *et al.*, 1997).

Continuous recrystallisation involves the gradual localised migration of sub-grains with low angle boundaries, which are formed due to very high levels of deformation, into grains with high angle boundaries (Alaneme & Okotete, 2019; Heidarzadeh *et al.*, 2014). The sub-grains absorb dislocations, which provide the energy for them to rotate further. As they become further miss-orientated the boundary becomes more mobile allowing the grain to grow faster until it can be recognised as a new strain free grain (Jata & Semiatin, 2000; Su *et al.*, 2003).

In dynamic recrystallisation the discontinuous mechanism is generally found in materials with a low stacking fault energy with nucleation sites on prior grain boundaries, forming a necklace pattern, and growth at the expense of dislocation full regions. While continuous is found in high stacking fault energy materials with sub-grains forming across the entire grain. However, a third option of geometric dynamic recrystallisation is also possible, Figure 2-15 (Huang & Logé, 2016).

In geometric dynamic recrystallisation the deformation elongates the grains while containing local serrations. As the grains elongate and the thickness reduces to 1-2 sub-grains the serrations pinch together forming equiaxed high angle boundary grains.

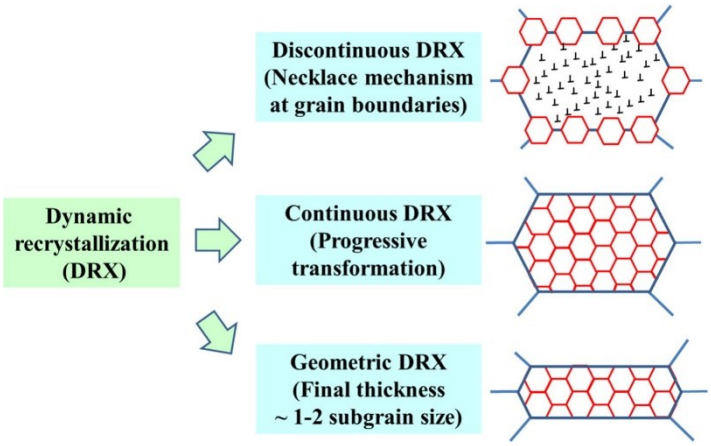


Figure 2-15: Mechanisms for dynamic recrystallisation (Huang & Logé, 2016).

The energy for the process is provided by the stored energy of deformation. The deformation leads to excess volume energy which is stored in the stress fields around the increasing density of dislocations (Alaneme & Okotete, 2019; Doherty *et al.*, 1997). A source of heat then provides the necessary energy to release the stored energy as activation energy levels are met. During dynamic recrystallisation the external deformation during heating reduces the recrystallisation temperature, (the temperature required for recrystallisation to fully occur in 1 hr) due to the increase in stored strain energy. The alloy composition also effects the recrystallisation temperature with pure materials recrystallizing from as low as $0.3\,Tm$ and alloying raising the temperature up to $0.7\,Tm$ (Callister Jr, 1994). Friction welding temperatures of several commonly weld materials as a percentage of the solidus temperature are shown in Figure 2-14. As all the materials are processed above $0.7\,Tm$ recrystallisation is experienced in all. It is generally accepted that the recrystallisation seen around the interface of friction welds is continuous and dynamic (M Maalekian, 2007; Uday *et al.*, 2010).

2.2.2.1 Recrystallisation in friction welds

The microstructural evidence observed by Jata and Semiatin (2000) during friction stir welding of a wide spread of miss-orientation angles of sub-grains and the appearance of high density dislocation boundaries in the cell-like substructure at the same time as sub-grains with

dislocation free boundaries strongly suggests a continuous dynamic mechanism. This leads to the small grain sizes seen at the centre of the welds as new grains would be recrystallised as the process continues. Ćirić and Radović (2005) link the small grain size found in M2 tool steels to the large number of preferential nucleation sites: grain boundaries, sub grain boundaries, twins and deformation bands, leading to a much faster rate of nucleation when compared to grain growth in the austenite phase. Work by Fu and Du (2006) has shown that application of an electric field during the friction welding process can alter the recrystallisation process; negative electrostatic fields increasing grain size and homogeneous distribution while an alternating current reduced the grain size and enhanced diffusion. The effects were attributed to changes in the initial energy required for recrystallisation and changes in the degree of plastic deformation.

Recrystallisation is very closely linked to recovery and grain growth. During recovery, the high angle grain boundaries are static instead of mobile and the only driving force for grain growth is the reduction in grain boundaries and hence reduction in free surface energy to a more thermodynamically stable state (Callister Jr, 1994; Doherty *et al.*, 1997).

2.3 Friction welding of steel

2.3.1 Weldability

Friction welding of similar and dissimilar steel combinations has widely been carried out with strong joint capabilities possible once the right parameters have been found (Ananthapadmanaban *et al.*, 2009; Celik & Ersozlu, 2009; Ćirić & Radović, 2005; Handa & Chawla, 2014; Kimura *et al.*, 2010; Moat *et al.*, 2009; Moat *et al.*, 2008; Özdemir *et al.*, 2007; Sathiya, Aravindan, & Haq, 2007; Satyanarayana *et al.*, 2005; Tumuluru, 1984; Uday *et al.*, 2010; I. Woo *et al.*, 2002). Dissimilar bonding to aluminium and titanium alloy systems has also proven possible with strengths being dependant on diffusion of elements across the interface and in certain cases the extent of detrimental heating effects, in these scenarios parameters

require careful consideration and control (Dey *et al.*, 2009; Fu & Du, 2006; Fuji *et al.*, 1992; S Fukumoto *et al.*, 2010; Gan *et al.*, 2017; Kim *et al.*, 1995; Luo *et al.*, 2012; Nguyen-Dinh, 2001; Seli *et al.*, 2010; Taban *et al.*, 2010; Uday *et al.*, 2010; Wu *et al.*, 2011).

2.3.2 Microstructure

Due to the wide variety of steels available and their complex nature when subjected to heat and pressure, combined with the potential to have undergone various parameter combinations, a single example of a typical steel friction weld is not possible. Therefore, one single steel friction weld is not capable of covering all areas. Instead listed below, after the table, are examples from the literature of steel sub-groups.

2.3.2.1 Mild steel/ low carbon steel

Figure 2-16 shows the cross section from a mild steel (En 3B) tube weld 19mm OD and 12.7mm ID, axial shortening 4.5mm, axial force of 6KN and a rubbing speed of 3.36m/s at the mean radius. Within the Contact zone and recrystallised zone (RZ) an upper bainite morphology was seen moving to a lower bainite structure as the material temperature further away reached 950^{O}C. In the TMAZ when the temperature was above the austenite starting temperature carbon rich pearlite was austenised while below, it simply became spheroidised. The ferrite was not transformed. In the HAZ ferrite crystals exhibited some recrystallisation and grain growth.

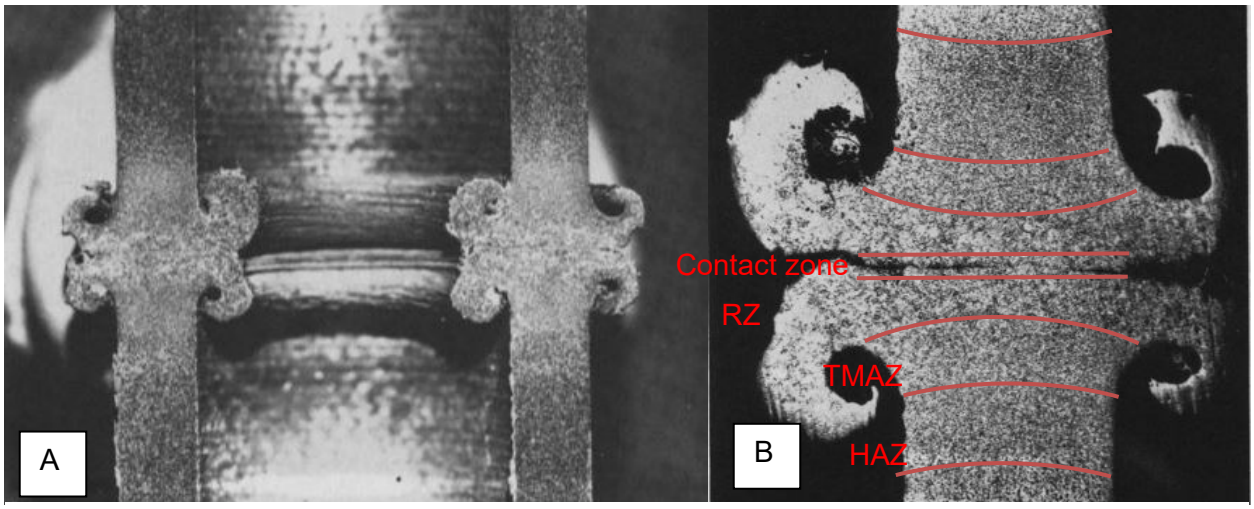


Figure 2-16: Typical section of a mild steel tubular friction weld. In this case from a continuous drive machine. A) tubular cross section B) A close up image of the previous cross section showing the contact zone, recrystallised zone (RZ), TMAZ and HAZ (Duffin & Bahrani, 1973).

2.3.2.2 Medium carbon steel

Sahin (2005) joined medium carbon steel AISI 1040 to high speed steel HSS-S 6-5-2 using a continuous drive machine testing the influence of friction time and friction pressure. Sahin and Erol Akata (2004) also welded medium carbon steel to stainless steel under a similar testing regime but with different parameter values. Paventhan *et al.* (2011) welded the same AISI 1040 grade medium carbon steel to 304 grade stainless steel. The results produced a refined microstructure within the weld zone of ferrite and pearlite in all scenarios, with carbon diffusion at the contact zone having an impact on the hardness due to the dissimilar material joint.

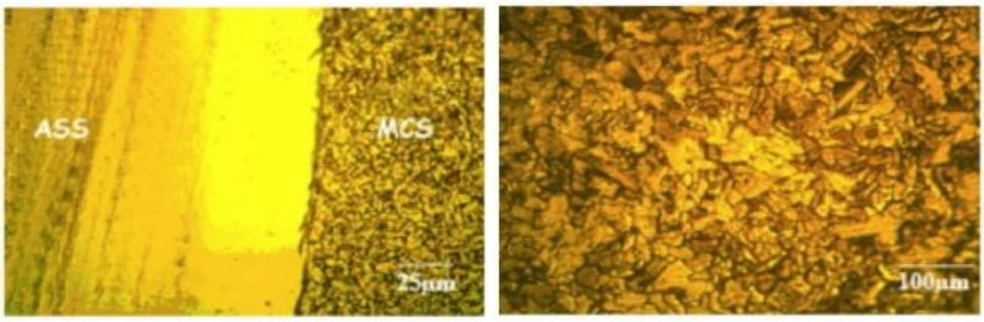


Figure 2-17: A) Contact zone of an austenitic stainless steel (ASS) joined to medium carbon steel (MCS) friction weld. B) the HAZ of the MCS component of the friction weld (Paventhan *et al.*, 2011).

2.3.2.3 Stainless Steel

Predominant research has been centred on investigating the weldability of the austenitic stainless steel AISI 304 and the ferritic stainless steel AISI 430 to each other and other metals such as Aluminium and Titanium alloys.

Satyanarayana *et al.* (2005) joined austenitic stainless steel to ferritic stainless steel as shown in Figure 2-18**.** The ferritic material displays the characteristic weld zones with recrystallised fine grains at the interface surrounded by coarser recrystallised grains. Further out the deformation is apparent from the elongated and rotated grains found in the TMAZ. Due to the austenite material's higher strength at temperature, there is almost no recrystallisation visible away from the interface, only displaying heavy deformation close to the bond line. These characteristics are also visible when joining to other materials as long as the temperature at the interface is sufficient to produce similar deformation (Ananthapadmanaban *et al.*, 2009; Dey *et al.*, 2009; Fuji *et al.*, 1992; S. Fukumoto *et al.*, 1998; Handa & Chawla, 2014; Lippold & Odegard, 1984; Sahin & Erol Akata, 2004; Sathiya, Aravindan, & Haq, 2007; I. Woo *et al.*, 2002).

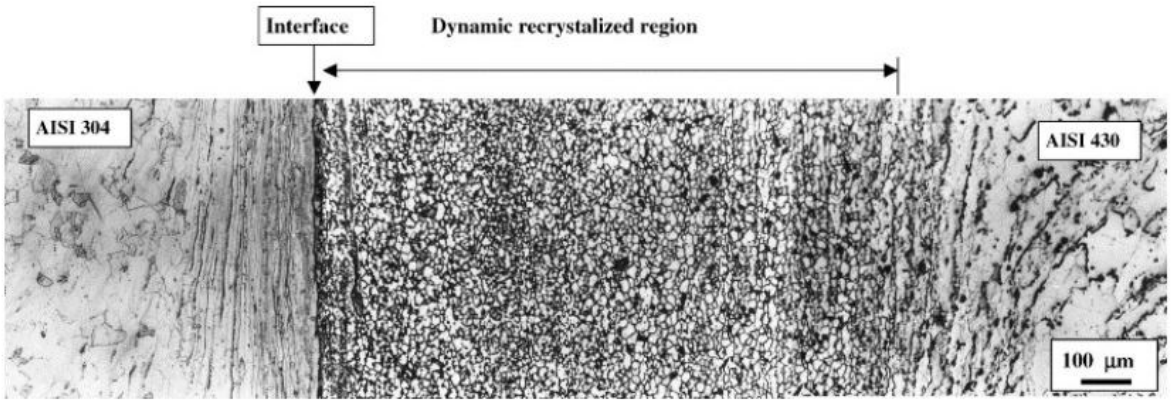


Figure 2-18: Micrograph of an austenitic-ferritic stainless steel friction weld, showing high deformation but with recrystallisation only on the bond line in the austenite side, while a large area of recrystallisation and TMAZ deformation is visible on the ferritic side (Satyanarayana *et al.*, 2005).

2.3.2.4 Micro alloyed / High strength low alloyed steel

Friction welding of high strength low alloyed steel (HSLA) is sparse within the literature when considering rotary or linear conditions. Bhole (1991) welded a mild steel rod onto a HSLA plate. Due to the highly convex shape of the weld zone within the mild steel rod the parameters were suggested to be of relatively low speed and high pressure for the geometric and material combination, as shown in Figure 2-19.

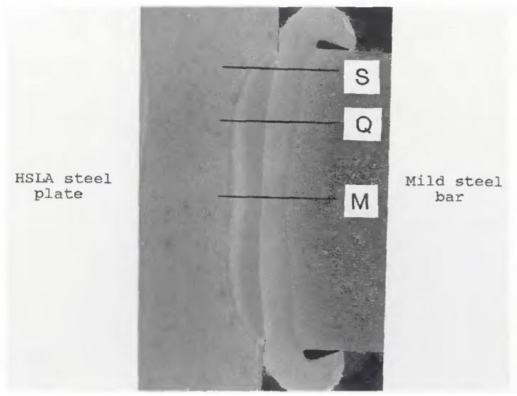


Figure 2-19: Macro-section of a mild steel rod to HSLA plate friction weld showing HAZ shape and flash. Letters indicate hardness trace locations: M - midsection, Q - quarter section and S - near surface (Bhole, 1991).

The mild steel rod displayed a classic microstructure of highly deformed grains in the TMAZ moving to recrystallised refined grains in the weld zone. In the HSLA plate a fine microstructure of potentially bainite or low carbon martensite was recorded, further away a ferrite-pearlite, similar to the base material was present but with a refined grain size. A slight hardness rise from 185Hv up to an average of 205Hv was seen in the mild steel while in the HSLA plate the hardness near the weld interface was between 500-550Hv with higher peak values and slower drop off rates taken from the quarter section and mid-section when compared to the near surface results. The weld interface was recorded at 485Hv suggesting some intermixing. The high increase in the HSLA hardness advocates confirmation of the transformation towards the martensitic microstructure as seen by Tumuluru (1984) and C. Bennett *et al.* (2007). Fitting with characteristic microstructures seen when cooling micro alloyed steel as shown in Figure 2-20. Hardness's of 320Hv maximum were seen by Wei and Nelson (2011) in a mixed

microstructure of ferrite and bainite within the weld nugget centre of HSLA-65 that had been friction stir welded.

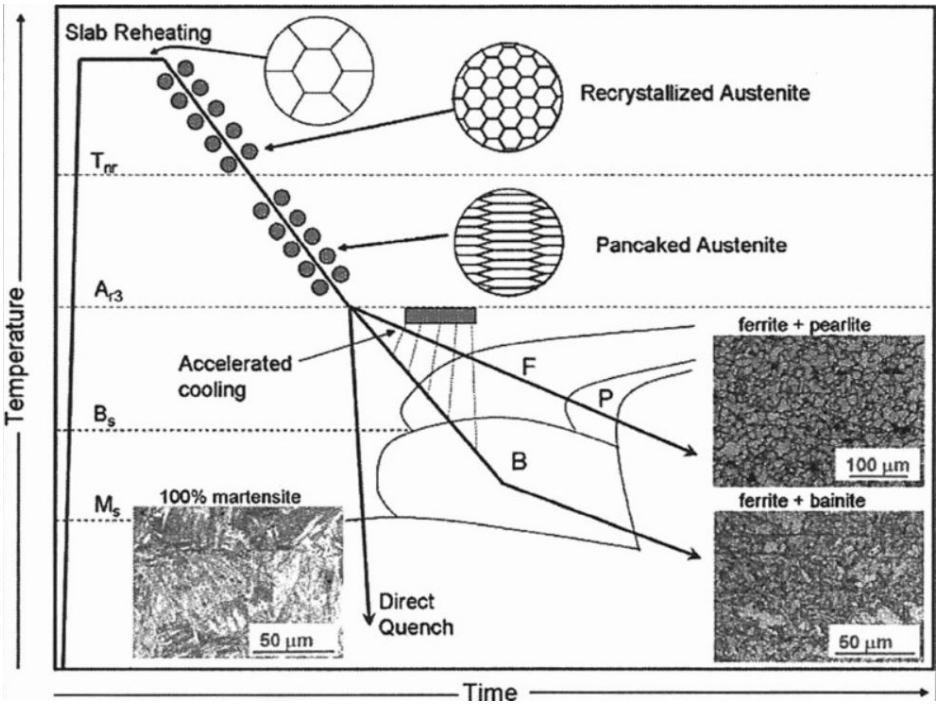


Figure 2-20: Schematic diagram of thermos-mechanically controlled processing, in this case rolling and cooling of micro alloyed steel (Baker, 2016).

Further investigation of the material through mapping the thermal processing routes indicates the scenarios under which various microstructures occur. Reviewing the process cycle of the weld and comparing to others against thermal processing maps such as Figure 2-20 can help to direct the user towards the desired final microstructure. In the thermal processing map T_{nr} is the temperature below which complete static recrystallisation begins to occur between times of high deformation such as hot rolling. A_{r3} is the starting transformation temperature of austenite to ferrite during cooling. A_{r1} is the finish temperature of the austenite to ferrite transformation.

2.3.3 Parameter effects on weld zones

As seen in Figure 2-1 the parameters chosen for an inertia weld have a direct outcome on the size and shape of the overall weld zone. Less information, however, exists on the parameters effect on the individual weld zones. Potentially this is due to the difficulty in accurately marking

the transition Doherty *et al.* (1997). Some papers have studied the effect of parameter changes on weld zones in a select number of alloys. I. Woo *et al.* (2002) measured the fully plasticised / recrystallised zone (region I) and the TMAZ (region 2) of high nitrogen stainless steels (HNS) when continuous drive friction welded. They made a link between friction time and the zone/region widths on two materials, Figure 2-21. HNS-1 contained less nitrogen and carbon than HNS-2 and so upset more material during the friction phase, due to its lower high temperature strength. The faster upsetting material HNS-1 produced a wider recrystallised zone but a smaller TMAZ when compared to the slower upsetting HNS-2 while the offset stayed roughly constant between the two materials suggesting it to be potentially upset rate or material dependant. However, both materials showed an increase in the recrystallised zone with a corresponding decrease in TMAZ the longer the welds took.

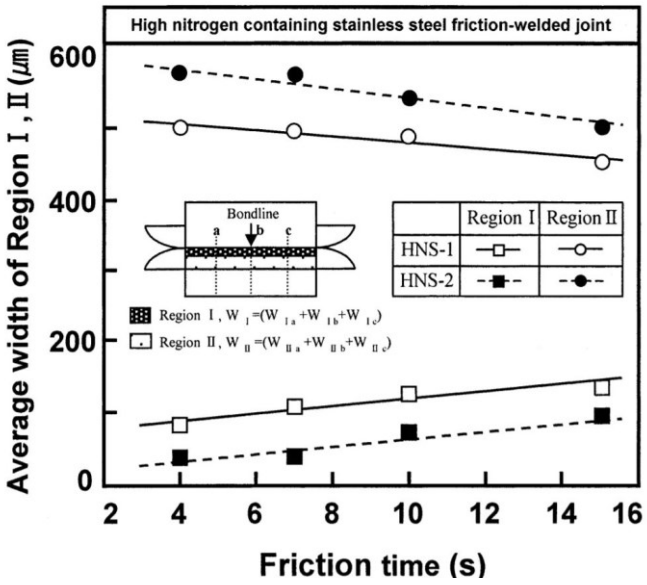


Figure 2-21: Effect of friction time on the average width of Region I and Region II in HNS joints (I. Woo *et al.*, 2002).

A time-based continuous drive machine was used to investigate rotational speed, with all other parameters left constant, on AISI 304L to AISI 4340 stainless steel joints Özdemir *et al.* (2007). Increasing rotational speed was linked to decreased contact zone width combined with increased upset due to suggested higher temperatures at the weld line. HAZ widths were

shown to widen due to the dissipation of the heat energy into the adjacent material. While increasing percentages of martensite in the contact zone of the initial welds support the idea of higher temperatures over the austenite start temperature for the material to transform into martensite upon cooling. Aided by the narrower contact zone and associated steeper temperature gradient.

Duffin and Bahrani (1973) investigated rotational speed and axial pressure on mild steel tubes that were continuous drive welded. Their findings were based on a similar premise to Kimura *et al.* (2010) who further developed work by Hirst and Lancaster (1960) and Kerridge and Lancaster (1956). During phase I of initial contact, adhesion junctions are formed between asperities on both parts. Some junctions shear away from the interface transferring material between the two surfaces. As the pressure increases, during the process, and the temperature at the interface increases the adhesion and shearing becomes more common increasing the frictional force and raising the temperature further. Higher axial forces and lower rubbing speeds transferred thicker material fragments, that were joined over a larger area with higher torque requirements as a result. While lower axial forces and higher rotational speeds reduced the fragment sizes and associated torque.

The initial thickness of the contact layer goes onto explain the difference in weld region thickness seen above Duffin and Bahrani (1973). The fragmenting surface will eventually fully plasticise in the equilibrium phase. Low speeds produced larger fragments and hence a thicker plasticised layer. The thicker layer is easy to squeeze out under the axial force while the plasticised material is constantly replaced, requiring high torques, producing a high rate of upset and therefore steep temperature gradients leading to smaller TMAZ regions but larger recrystallised zones. Increasing the pressure also increased the temperature gradient as material is forced out faster. Fast speeds produce a thin plasticised layer from the previous thin fragment layer, needing low torque hence material is ejected at a slower rate giving the

heat longer to penetrate the surrounding material thereby increasing the TMAZ and HAZ regions. Lower axial forces produced the same result as higher speeds.

2.3.4 Understanding the microstructural changes

During the welding process, the material is subjected to varying degrees of heat input and deformation. The precise location of the material under study determines the mix of heat and strain, resulting in a proportional change to the microstructure and associated properties. Linking the properties through the microstructural change can help identify the processing route and hence the nature of the friction welding process.

2.3.4.1 The Zener-Holloman parameter

The Zener-Holloman (Z_h) parameter is used in hot working to help determine the sub-grain diameter (d) and hence structure of the material.

$$d^{-m} = a + b \log Z_h \tag{2-29}$$

Here a and b are experimental constants and m is an exponent. The equation for Z_h is

$$Z_h = \bar{\varepsilon} + \exp\left(\frac{Q}{R_{gas}T_{temp}}\right) \tag{2-30}$$

$\bar{\varepsilon}$ is strain rate, Q is activation energy for deformation, T_{temp} is temperature (absolute) and R_{gas} is the gas constant (I. Woo *et al.*, 2002). The outcome of a change in strain rate or temperature, which is possible in friction welding, determines a change in the sub-grain size. Higher temperatures or lower strain rates create larger sub-grains while lower temperatures or higher strain rates will create finer sub-grain structures.

2.3.4.2 Grain Refinement and the Hall-Petch Relationship

This well-known effect is known as grain boundary strengthening. Dislocation movement through a material is plastic deformation. Grain boundaries are the lines between two neighbouring crystal lattices with large atomic mismatch. Grain boundaries pin dislocations causing pile ups. The repulsive stress field caused by each dislocation will build at these pile ups. Once the stress field is large enough it provides enough driving force to reduce the energetic diffusion barrier at the grain boundary and a dislocation can diffuse across. By reducing the available size of dislocation pile-ups at grain boundaries through smaller grain sizes, the applied energy required for dislocations to diffuse across a grain boundary is increased as the energy from the dislocation pile-up stress field is reduced. The recrystallisation in the weld gives a refined structure. This greater number of grain boundaries provides more resistance to the movement of dislocations and hence is stronger than the parent material (aluMatter, 2010; Smith & Hashemi, 2003).

The Hall-Petch equation describes the relationship between yield stress σ_y, material initial dislocation movement stress σ_o, material specific strengthening coefficient K_y and average grain diameter d.

$$\sigma_y = \sigma_0 + \frac{K_y}{\sqrt{d}} \tag{2-31}$$

Below about 10nm grain size strength ceases to increase as grain boundary sliding and other mechanisms become prevalent. As detailed in the inverse Hall-Petch relationship (Rollet, 2007; Volpp *et al.*, 1997).

2.3.4.3 Work Hardening

Interaction of dislocations increases yield stress. The stress fields surrounding the two interacting dislocations will reduce the movement of dislocations and hence resist deformation. If two dislocations entangle then they can act as pinning points and further restrict dislocation movement. The more dislocations present the greater the effect.

$$\Delta\sigma_y = Gb\sqrt{\rho\perp} \tag{2-32}$$

$\triangle\sigma_y$ is change in yield stress, G is shear modulus, b is burgers vector and $\rho\perp$ is dislocation density. The highly deformed regions of the TMAZ would experience work hardening and therefore increase the TMAZ's yield strength (Roters *et al.*, 2000).

2.3.4.4 Alloying

Adding elements to a metal can increase the yield stress. If the amount of alloy is above a critical value it can form its own second phase, called Precipitation Hardening. Mechanical and thermal treatments also introduce secondary phases. These secondary phases can also pin dislocations. They cause the dislocation to either cut through the phase or elongate and bow around it joining up on the other side. Due to the energy differences of achieving each method, if the phase is small it will be cut, while large phases will be bowed. Both increase the stress required for dislocation to move.

For cutting: $$\Delta\tau = \frac{\pi r_{par}\gamma}{bL_{pps}} \tag{2-33}$$

For bowing: $$\Delta\tau = \frac{Gb}{L_{pps} - 2r_{par}} \tag{2-34}$$

Where change in stress $\triangle\tau$, particle radius r_{par}, surface energy γ and pinning point spacing L

Below critical concentrations it is called Solid Solution Strengthening. The elements either go interstitially or substitutionally into the crystal lattice. They create lattice distortions which again impede dislocations increasing yield stress.

$$\Delta\tau = Gb\sqrt{c\epsilon^{3/2}} \quad (2\text{-}35)$$

Where solute concentration is c and strain caused by the solute ϵ (Callister Jr, 1994).

2.3.5 S355 Structural steel

Structural Steel has a classification system to help easily identify its properties and processing route.

- S – Signifies it is structural steel.
- 355 – Denotes the minimum yield stress.
- J2/K2/JR/JO these relate to the material toughness as measured with a charpy impact test or 'v' notch test.
- W – Weathering steel i.e Corrosion resistant within atmosphere.
- Z – Structural steel with its perpendicular surface strength enhanced.
- C – Cold formed.
- N – Normalised / normalised and rolled.

2.3.5.1 Composition

S355 is a high strength low alloy steel gaining its strength primarily from grain refinement. The composition is denoted in

S355 composition by weight percentage						
Constituents	**C**	**Si**	**Mn**	**P**	**S**	**Fe**
Content (wt%)	0.23	0.05	1.60	0.05	0.05	Balance

. S355 denotes that it is a structural steel with a minimum yield stress of 355 MPa. The equivalent US grade is A572Gr50 as set by the American Society for Testing and Materials.

S355 has reported ultimate tensile strengths of 470 – 630 MPa (Gilbert, 2012; Metric-Metal, 2018; West-Yorkshire-Steel, 2018).

Table 2-1: S355 Chemical Composition

S355 composition by weight percentage						
Constituents	**C**	**Si**	**Mn**	**P**	**S**	**Fe**
Content (wt%)	0.23	0.05	1.60	0.05	0.05	Balance

2.3.5.2 Microstructure

S355 comes under the hot rolled low alloy system, which in the UK is controlled by BS EN 10025. The current standard was published in 2004 and various sections control the material delivery conditions whether normalised or with improved corrosion resistance (BSI, 2004).

S355 consists of a ferrite and pearlite mixed microstructure with influence from the rolling visible by the clear banding of the distinct regions as in Figure 2-22 (Ni & Abdel Wahab, 2017).

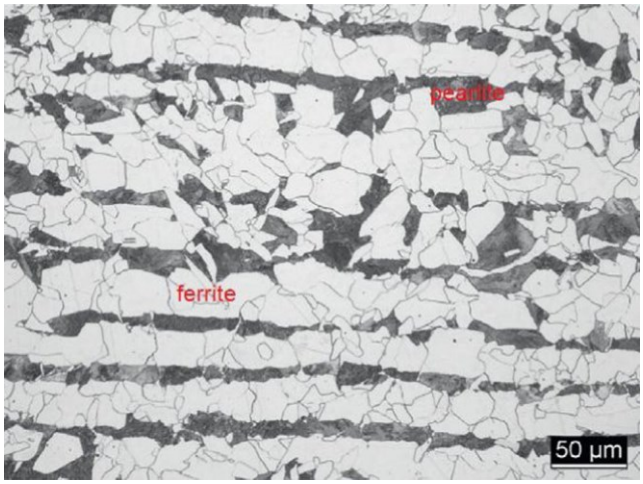


Figure 2-22: S355 Basic/Parent microstructure consisting of light grained ferrite and dark grained pearlite in rolled induced banding (Ni & Abdel Wahab, 2017).

2.3.6 SVh40c

SVh40c is a hot rolled high strength steel produced by BAOSTEEL for Nissan and China Dongfeng Motor Co. It is designed for use within the crankshaft assembly (Alloypipes, 2012).

2.3.6.1 Composition

The material composition of SVh40c is detailed in Table 2-2 as supplied by the Nissan Motor Company Ltd to the Manufacturing Technology Centre (Y. Chen *et al.*, 2016).

Table 2-2: Material chemical composition of SVh40c supplied by Nissan (Y. Chen *et al.*, 2016).

SVh40c composition by weight percentage										
Constituents	**C**	**Cu**	**Si**	**Mn**	**Cr**	**Ni**	**S**	**V**	**P**	**Fe**
Content (wt%)	0.39	0.1	0.2	0.7	0.2	0.05	0.02	0.05	0.02	Bal

2.3.6.2 Microstructure

As SVh40c is a hot rolled low alloy steel it also comes under the micro-alloyed steel section similar to the S355 above. Base microstructures present a ferrite-pearlite mix with the grains slightly elongated in the rolling direction, which is visible due to the layered bands of ferrite and pearlite, seen in Figure 2-23. The layered bands also match the rolling direction. (Alloypipes, 2012; Baker, 2016; Y. Chen *et al.*, 2016).

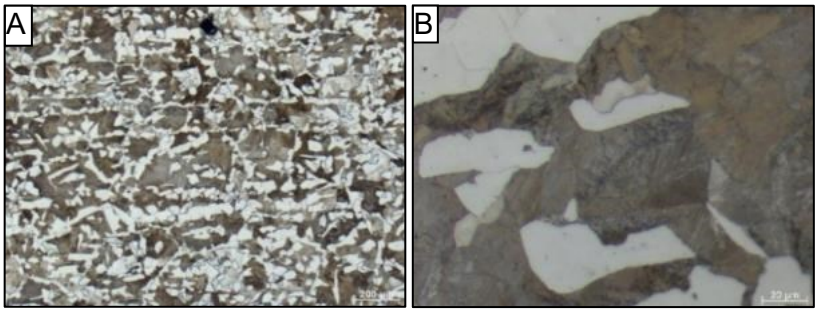


Figure 2-23: SVh40c micro alloyed steel hot rolled microstructure at A) 50x and B) 500x magnification (Y. Chen *et al.*, 2016).

2.4 Friction welding of Ti-6Al-4V

Predominantly the work conducted in friction welding Ti-6Al-4V has been directed through the linear welding of blisks (bladed disks) assemblies within the compressor section of an aero engine. The welded structure removes the need for a mechanical connection reducing the associated weight and complexity; with the knock-on effect of reducing the stress throughout the surrounding areas of the engine further reducing the weight of the supporting structure. This allows aero engine manufacturers to produce lighter, more powerful and fuel efficient engines (I Bhamji *et al.*, 2011; B. Kumar, 2013).

Ti-6Al-4V is comprised of primarily 6% Aluminium, 4% Vanadium and a balance of Titanium with other trace elements such as Carbon, Iron, Nitrogen, Oxygen and Hydrogen all below 0.25%, Table 2-3.

Table 2-3: Ti-6Al-4V Composition.

Ti-6Al-4V composition by weight percentage								
Constituents	**C**	**Fe**	**N_2**	**O_2**	**Al**	**V**	**H_2**	**Ti**
Content (wt%)	<0.08%	<0.25%	<0.05%	<0.2%	5.5 - 6.76%	3.5 – 4.5%	<0.0125%	Bal

2.4.1 Titanium alloy groups

Titanium alloys are classified into three groups by the predominant phase at room temperature: α alloys, α+β alloys and β alloys. Titanium transforms from a hcp structure (α phase) to bcc (β phase), see Figure 2-24, when passing 882°C (1155°K), known as the α-β transition temperature. The stable room temperature phase depends on the dissolved alloying elements, which either raise the transition temperature (α stabilisers), lower the transition temperature (β stabilisers) or act as solid solution strengtheners. Increasing the concentration of the stabilisers increases the width of the combined α+β phase which is found separating the α phase and β phase (Pederson, 2002).

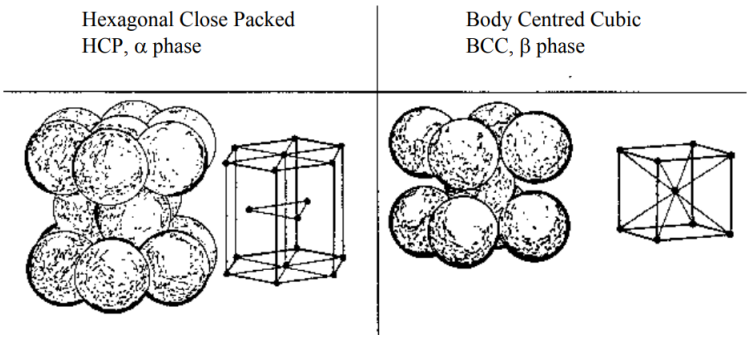


Figure 2-24: Two main crystal structures in Titanium (Pederson, 2002).

Most titanium alloys have been produced with a view to increasing the maximum working temperature. Increasing the number of interstitial elements increases the strength of the alloy but at the expense of ductility and risk of embrittlement. As most interstitial elements and simple metals are α stabilisers, β stabilisers, which are mostly transition metals, are included in the alloy composition to control the α-β transition temperature while still benefiting from the increase in strength (Pederson, 2002).

Ti-6Al-4V is an α+β alloy containing, as hinted in the name, 6wt% Aluminium and 4wt% Vanadium, with the former being an α stabiliser and the later a β stabiliser (McAndrew *et al.*, 2018). The alloy falls in the α+β group thereby containing a mixture of both phases at room temperature but primarily the α phase, for example see Figure 2-25. Depending on the thermal history the material can produce various microstructures; allotriomorph α, primary α (bi-modal when the globular α is surrounded by widmanstätten platelets), widmanstätten or basketweave and martensitic (Pederson, 2002).

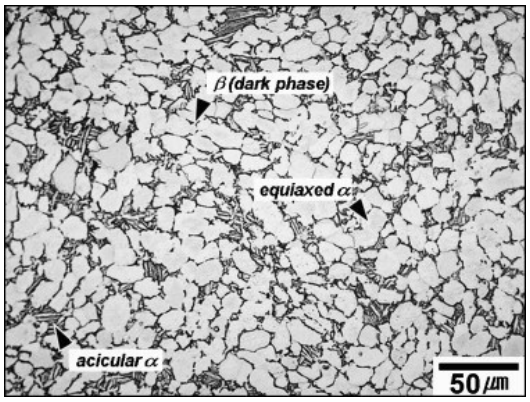


Figure 2-25: A mostly equiaxed Ti-6Al-4V in an annealed state with ~90% α phases and ~10% β phase (Reddy *et al.*, 2008).

2.4.2 Weldability

Friction welding of Ti-6Al-4V has shown wide parameter windows, as in Figure 2-26, with marginal reductions in properties until extreme parameters were used (Nessler *et al.*, 1971; Threadgill & Russel, 2007). Generally tensile testing has produced results indicating the yield and ultimate tensile strength of the welded region are equal and above that of the parent material. Impact toughness has also been shown to improve in the weld region with machined cracks in the weld centre deviating towards the parent material rather than continue through the weld region. These improvements are due to grain refinement and work hardening close to the interface (I Bhamji *et al.*, 2011). Experts in the field generally describe Ti-6Al-4V as eminently weldable (Sketchley, 2013; Threadgill & Russel, 2007).

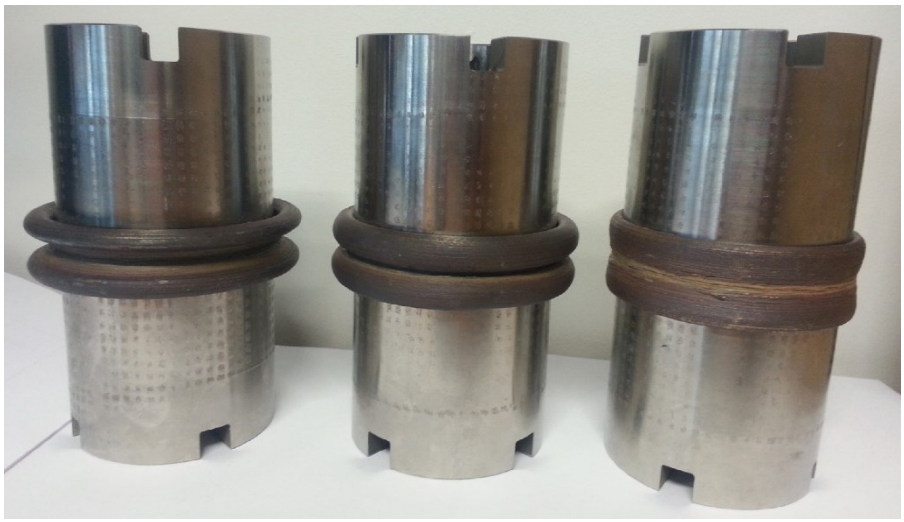


Figure 2-26: Ti-6Al-4V inertia friction welds produced with variable parameter sets resulting in similar upsets (Turner *et al.*, 2016).

2.4.3 Weld microstructure

Ti-6Al-4V constitutes a bimodal structure (α and β) which transforms in the weld region displaying as a lath-type morphology. The transformation suggests that welding temperatures are above the β transus (~1000°C, depending on the exact amount of interstitial elements, transforming α grains into β grains (McAndrew *et al.*, 2018)), Figure 2-27, with cooling rates slow enough not to form martensitic formations (α'). This produces a visible TMAZ/HAZ in the order of a few millimetres (~2mm) from the weld line (Avinash *et al.*, 2007; Wisbey *et al.*, 1999).McAndrew *et al.* (2018) notes that it is often difficult to detect the HAZ on its own due to the structural stability of TI6Al-4V below 800°C. English (1995) reports of Widmanstätten α found in the HAZ weld region of Ti-6Al-4V inertia friction welds (IFW). In IFW if the parameters are adjusted to increase the speed of the heating and cooling cycle (Zulu & Mashinini, 2018), the visible weld region is smaller with a higher chance of martensite (α') and retained metastable β formations An effect that is also visible in LFW where the process is much shorter in time and the cooling rates are faster (I Bhamji *et al.*, 2011; Wisbey *et al.*, 1999).

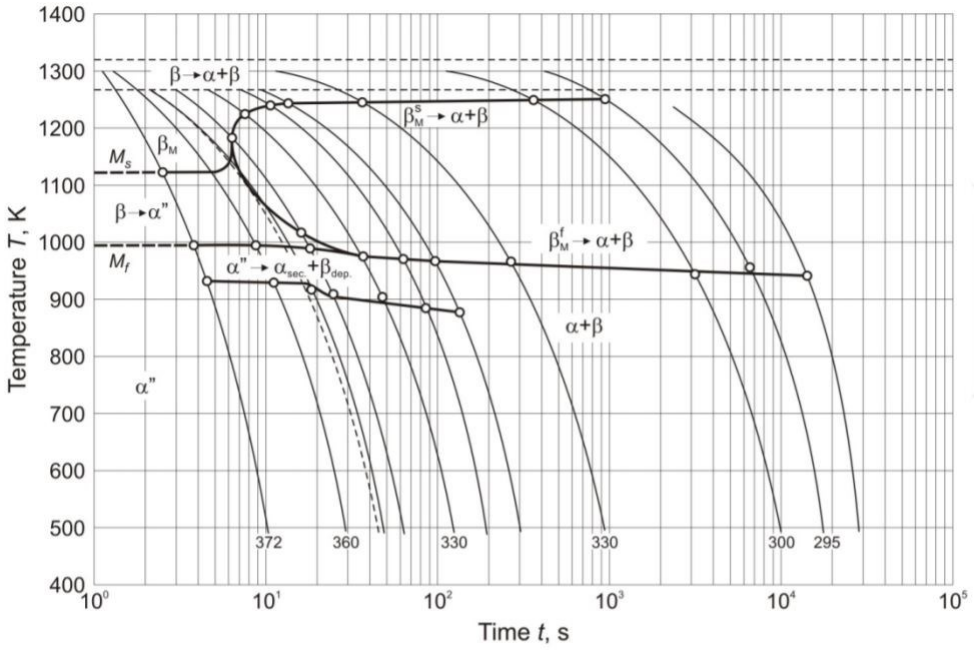


Figure 2-27: CCT curves of Ti-6Al-4V (Sieniawski *et al.*, 2013).

A review by McAndrew *et al.* (2018) reports that according to Ahmed and Rack (1998) below a cooling rate of 410°C/s diffusion can occur leading to a Widmanstätten morphology, as in Figure 2-28(a), while above that rate a diffusionless transformation leads to Martensite morphology, as in Figure 2-28(b).

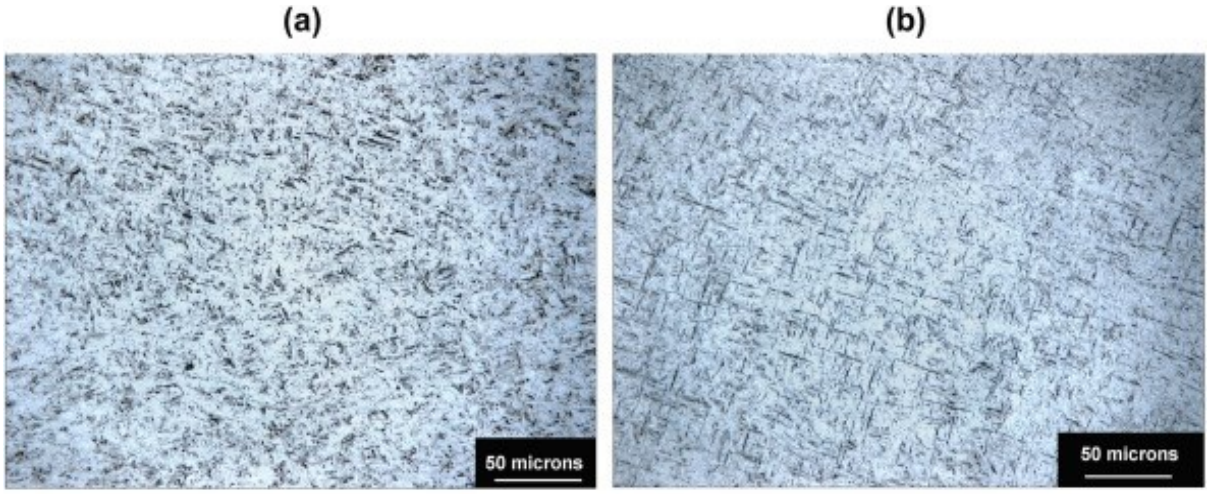


Figure 2-28: LFW Ti-6Al-4V weld microstructures. a) Widmanstätten Ti-6Al-4V morphology. b) Martensite Ti-6Al-4V morphology. From McAndrew *et al.* (2018), originally from McAndrew *et al.* (2014) .

Tchein *et al.* (2018) conducted friction stir welding trials showing that prior morphology was not important to the resultant microstructure of the stir zone within the parameters tested. Each time producing a basket weave structure as in Figure 2-29.

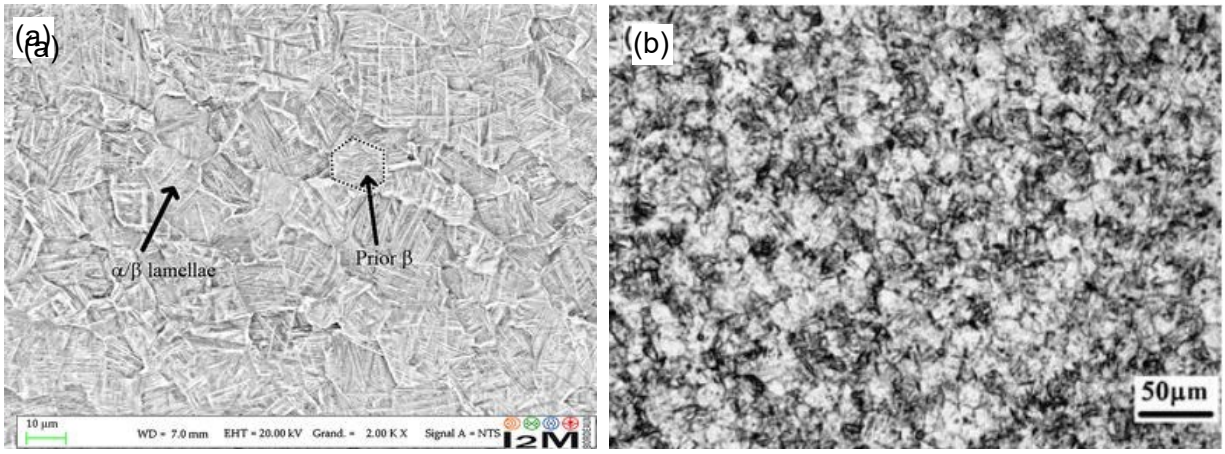


Figure 2-29: a) A typical backscattered SEM image of the friction stir welded stir zone showing equiaxed cells containing a fine intergranular Widmanstätten phase b) A typical optical micrograph of the same microstructure stir zone, collated from Tchein *et al.* (2018).

This suggests that as long as the material undergoes dynamic recrystallisation the cooling rate can override the influences from the prior microstructure and parameters.

Figure 2-30 displays the transition of a linear friction weld from the parent material through the TMAZ and into the central weld region. Deformation within the TMAZ is visible, elongating and rotating the grains towards the right where material will be ejected as flash. As mentioned by McAndrew *et al.* (2018) the HAZ isn't visible as the deformed region transitions directly to unmodified parent material.

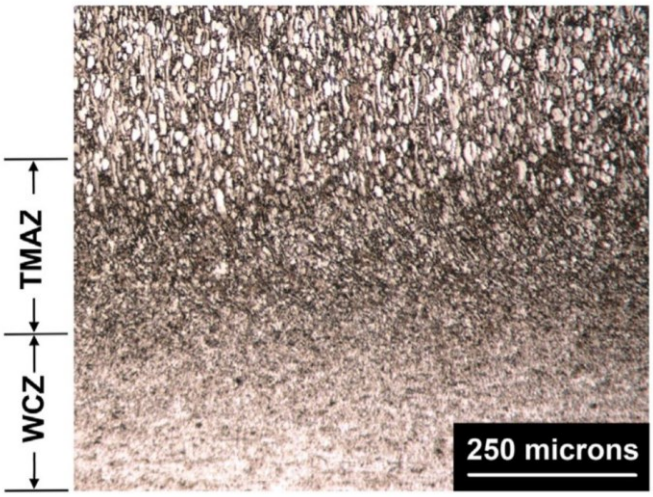


Figure 2-30: Optical micrograph of a LFW Ti-6Al-4V TMAZ structure clearly showing the transition into the weld centre zone (WCZ) (recrystallised zone) and the deformation of the TMAZ grains towards the exterior surface of the weld (McAndrew *et al.*, 2018).

Across the region, the change in microstructure and grain size contributed to the rise in hardness seen in the weld zone. Böhme *et al.* (2009) using a continuous drive machine, recorded parent material Vicker's hardness values of 310 -330Hv rising to 385Hv within the weld zone, but this was reduced, down to 365Hv when longer friction times and lower pressures were used. Zulu and Mashinini (2018) saw similar results with a drop in peak hardness seen when rotational speeds were increased, down from 375.9Hv to 365.0Hv over an 1100rpm increase on 25.4mm rods. Hardness was also reduced when friction pressure was reduced, 360.2Hv at 80Mpa down to 346.5 at 25Mpa.

2.4.4 Effects of parameters

The influence of parameters has been reported through real world studies. Nessler *et al.* (1971) performed a study investigating the IFW parameter effects on properties in Ti alloys. In the initial work parameters were varied by +/- 10% from nominal. In Ti-6Al-4V Speed was found to be the greatest influencer on upset followed by area and then pressure, moment of inertia wasn't altered, meaning the speed change led directly to an energy change. It was noted that a difference in upset, and hence difference in properties, would exist between two welds made with the same energy, but differing inertia and speed combinations. This was due to other welds with the same upset showing varying properties based on the unique parameters chosen. No statistically noticeable effects in the materials UTS or yield strength were noted. Elongation was found to be statistically affected but not in an engineering sense. Low speeds and low thrusts were associated with reductions in elongation of 1-3%. The amount of upset was related to the consistency of the results. Low upset welds produced properties that are more variable while higher upset welds produce properties that are more consistent.

Turner *et al.* (2016) produced and modelled inertia welds, using high speed photography to focus on and mark the transition from conditioning to upsetting. Conditioning was defined as the energy required to form a temperature profile within the specimen suitable for upsetting to commence. Initial rotational speed and pressure were changed, inertia was kept constant, and energy was left as a product of the rotational speed and inertia. Results from the modelling suggested a strong profile dependence on the pressure. Reducing pressure increased heat penetration into the part. Increasing pressure reduced heat input into the part with further increments having steadily limited effectiveness, Figure 2-31.

Rotational speed had an impact on the interface temperature with higher speeds increasing the temperature until a max around 1300^{O}C, while also lowering the heat penetration into the part, Figure 2-32. A similar phenomenon was noted by Zulu and Mashinini (2018) where reduced speed and higher pressure both increased the heating and cooling rates within an

RFW leading to more visible fine martensitic α grains in the weld zone. Comparing Figure 2-31 and Figure 2-32, higher pressures increased the gradient of the thermal profiles while maintaining the same intercept while lower speeds reduced the gradient and lowered the intercept (interface temperature). The result of the lower speeds matches the phenomenon recorded by McAndrew *et al.* (2015) in LFW whereas when the pressure was changed it was the intercept which moved not the gradient of the profile. Parameters have also shown to have a direct impact on the formation of the flash, Figure 2-26, but no direct links were made between parameter sets and the resulting flash.

Avinash *et al.* (2007) conducted a study in CDFW and showed an increase in grain size in the weld zone along with a reduction in HAZ size when the rotational speeds were increased, however this does not consider the extra energy input or change in energy input efficiency. According to the Zener-Hollomon parameter this would indicate higher temperatures and reduced strain rates.

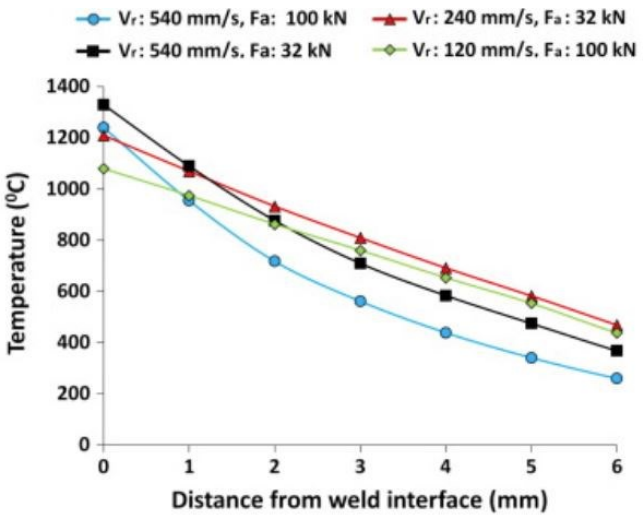


Figure 2-31: Thermal profiles of Ti-6Al-4V inertia friction welds where the pressure is varied, modelled by Turner *et al.* (2016).

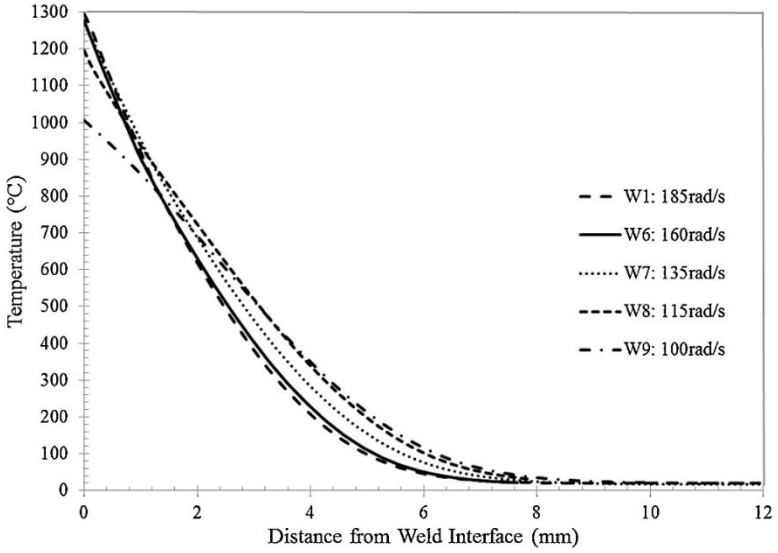


Figure 2-32: Thermal profiles of Ti-6Al-4V inertia friction welds where the initial rotational speed is varied, modelled by Turner *et al.* (2016).

H.-Y. Chen *et al.* (2015) produced welds using a continuous drive machine, as seen in Figure 2-33. Increase of the friction speed shows a thickening of the central weld zone in line with the expected transformation from Linnert (1994), Figure 2-1. However, in Figure 2-33, the increase in friction time somehow shows a reduction in flash shape and volume from four to six seconds, which does not fit with earlier reported results.

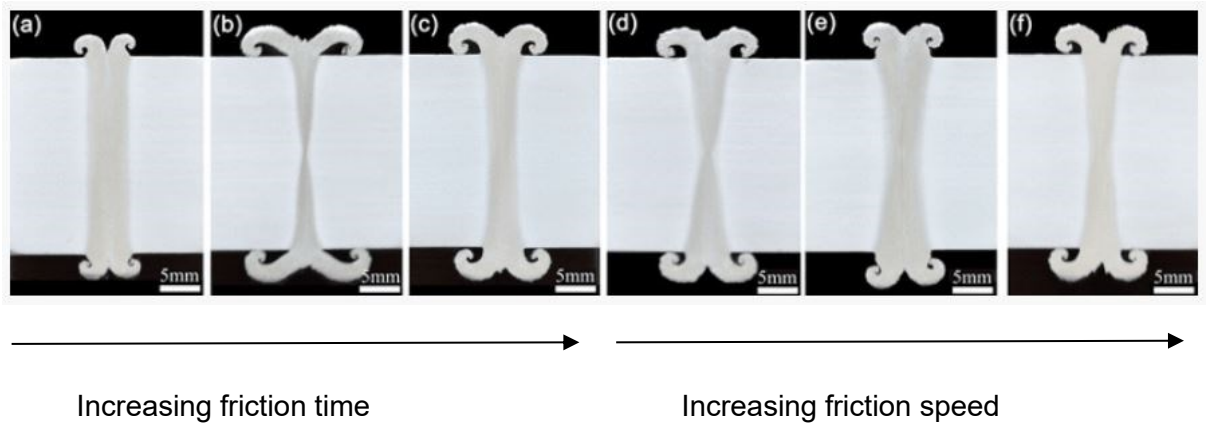


Figure 2-33: Etched weld zone macrographs of Ti-6Al-4V continuous drive friction welds showing the result of parameter changes. Friction time: 2s (a), 4s (b), 6s (c). Friction speed: 1500r/min (d), 2000r/min (e), 2500r/min (f). (H.-Y. Chen *et al.*, 2015).

2.4.5 Texture

Mechanical properties are strongly influenced by the texture of the α phase due to the anisotropic nature of the hcp crystal structure. Work by Bache and Evans (2001) conducted upon a highly textured rolled sheet of Ti-6Al-4V showed directional dependant properties. Higher yield strengths and ultimate tensile strengths (UTS) presented when loaded perpendicular to the basal plane (direction C in Figure 2-34) while under stress controlled fatigue loading applying the load perpendicular to the prismatic planes (directions a_1,a_2,a_3 in Figure 2-34) produced the optimum results. As also noted by (Bowen, 1978; Lütjering, 1998; Peters *et al.*, 1984). Bowen (1978) did point out however that it is due to the exposure to the atmosphere that the fatigue results were best perpendicular to the prismatic planes; under vacuum the best results were shown perpendicular to the basal plane.

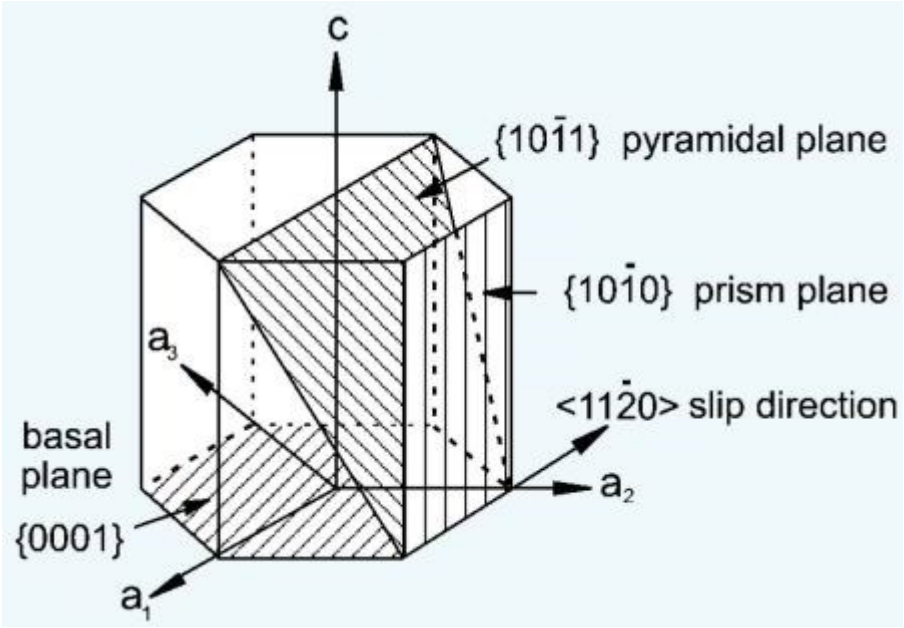


Figure 2-34: Slip planes in HCP crystal structures (Raabe, 2017).

Heng *et al.* (2015) report a cohesive texture in the normal direction [0001] of the weld zone when Linear friction welding Ti-6Al-4V. Whereas Karadge *et al.* (2007) noted a strong transverse texture throughout the weld region in full scale welds while seeing a transition from

almost random in the weld zone to transverse in the TMAZ in lab scale welds; with the difference being attributed to the variant selections during β to α transformation.

The strong transverse texture seen in LFW's of Ti-6Al-4V has also been seen by Guo *et al.* (2017) in similar Ti-6Al-4V welds and again in dissimilar Ti-6Al-4V to Ti-6246 in both sides of the weld (Guo *et al.*, 2012) and Ti-6Al-4V to Ti-6242 (Frankel *et al.*, 2009).

Attallah *et al.* (2012) investigated the texture development of TI-6246 Inertia Friction Welds showing a strong texture in the radial direction within the dynamically recrystallized region in both the as-welded and post-weld heat treated samples. Further work using energy-dispersive synchrotron X-ray diffraction (EDXRD) confirmed the existence of the radial texture across the weld zone with overlapped $\{0004\}_{\alpha}$ peaks and $\{220\}_{\beta}$ peaks in the as-welded condition. While the post-weld heat treated sample showed distinct $\{0004\}_{\alpha}$ and $\{220\}_{\beta}$ peaks with an increase in the intensity of the alpha phase and a decrease in beta phase compared to the as-welded sample.

The strong radial texture seen in the IFW Attallah *et al.* (2012) matches well with the strong transverse texture seen in the LFW (Frankel *et al.*, 2009; Guo *et al.*, 2017; Guo *et al.*, 2012); Karadge *et al.* (2007). Both are perpendicular to the applied load (normal direction) and the direction of motion (hoop direction in IFW and reciprocating in LFW); comparable in Figure 2-35.

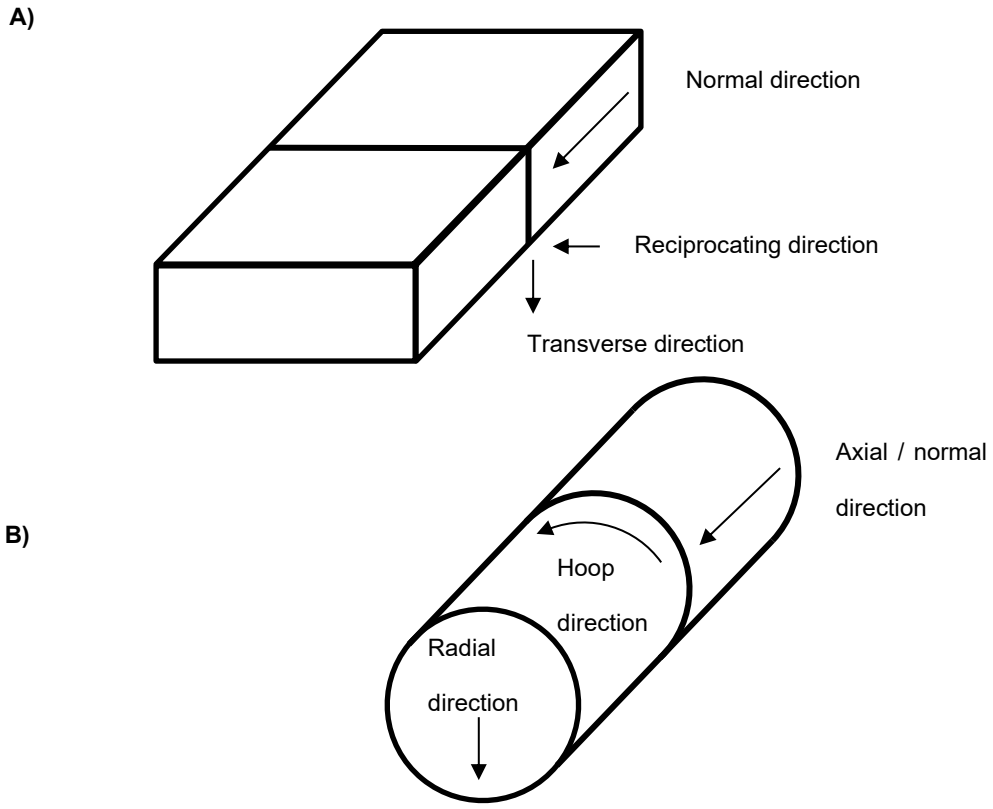


Figure 2-35: A) Directions in LFW. Adapted from Karadge *et al.* (2007); L. Yang (2010), B) Coordinate geometry directions on a rotary friction welded sample. Extrapolated from Attallah *et al.* (2012).

Parameter studies have looked into the effect pressure has on the resultant texture. Romero *et al.* (2009) tested 4 levels of pressure (P, 2.2P, 5P and 9P) and reported strong textures in both the α and β phases at normal pressure, p. The act of increasing the pressure led to reductions in the strength of the texture until it was essentially random at 9P as seen in Figure 2-36. A result confirmed by energy dispersive synchrotron X-ray diffraction comparisons of integrated peak intensity variations between the weld line and base material of the welds. Drawing on work by (Lütjering, 1998) it is suggested that the principal driving force for the differing textures is the temperature of the material experienced under the differing parameters. This is due to temperature effecting the deformation modes and therefore the texture development. Deformation occurring above but near the β transus produces the strong transverse texture as previously seen. Whereas deformation in the cooler α+β phase produces

a random texture which leads the author to suggest that higher pressure welds lower the temperature at the weld interface, with welds at and above 9P being below the β transus temperature.

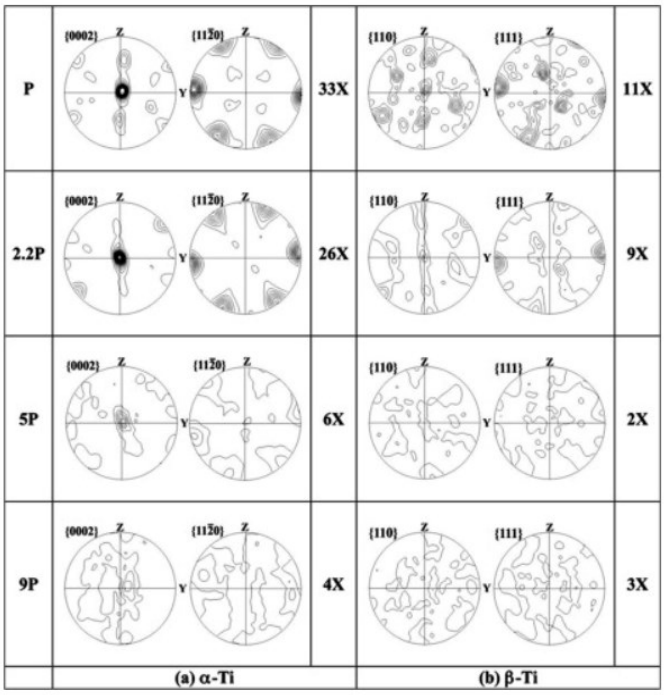


Figure 2-36: The {0 0 0 2}α, {1 1 2̄ 0}α, {1 1 0}β, and {1 1 1}β pole figures recorded at WL in sample P, 2.2P, 5P and 9P showing the influence of the pressure on the weld line texture development in the α and β phases. (Romero *et al.*, 2009)

2.4.6 Residual stresses

Residual stresses are the self-equilibrating stresses that exist even without external loads in an elastic body (N. Kumar *et al.*, 2014). They occur when an object is stressed beyond its elastic limit and plastically deforms. The three principal causes are thermal variations, phase transformations and plastic deformation (TWI, 2021; Williams & Steuwer, 2010).

Thermal variations are the differing heating or cooling rates experienced across an object. As an object changes temperature, it correspondingly changes size. The local variations in temperature change induce non-uniform volumetric changes. Where differing volumetric changes meet, they prevent either one from completely changing, thereby causing residual stresses.

Phase transformations create residual stresses due to the volumetric change associated with the transformation. Where one area has undergone a phase transformation next to an area of untransformed material, a volumetric mismatch is created, resulting in residual stresses.

Plastic deformations create residual stresses when they occur non-uniformly such as in a mechanical process or machining operation. As the stresses causing the deformation are removed the elastic deformation stresses are prevented from being fully removed by neighbouring areas of plastic deformation (N. Kumar *et al.*, 2014; TWI., 2021; Williams & Steuwer, 2010). The three principal causes and six interactions are displayed in Figure 2-37.

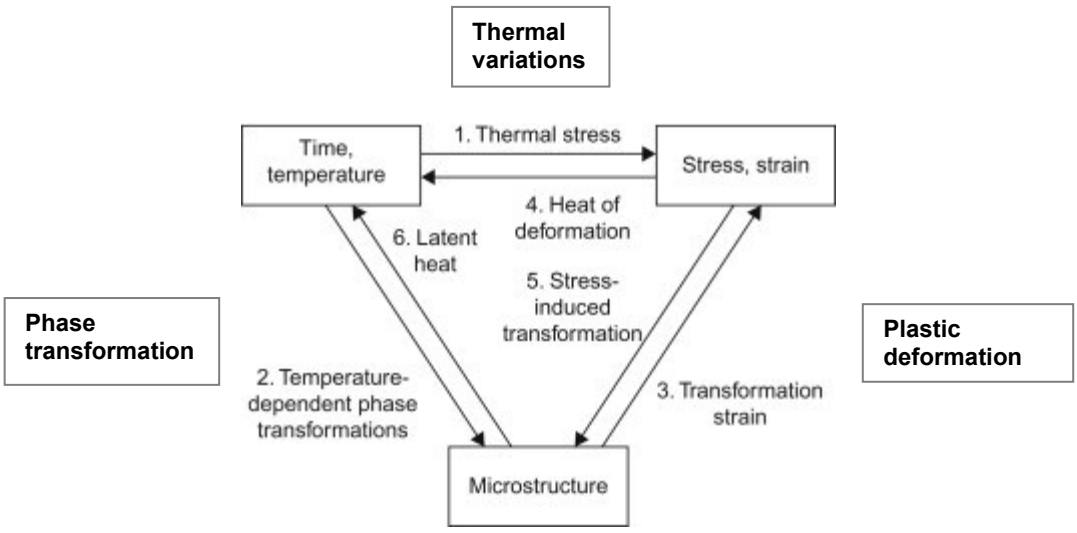


Figure 2-37: The principal causes of residual stresses and the interactions between the affected areas. Adapted from (N. Kumar *et al.*, 2014).

Residual stresses can also be characterised by the scale they interact over.

- Type I are macroscopic and cover areas over several grains.
- Type II are found between grains or over areas of sub-grains.
- Type III are inter-atomic e.g. those exhibited around inclusions.

With respect to welding, it is the type I stresses that are generally of most importance as they deform components and can impact upon the service performance.

2.4.6.1 Residual stresses in welds

When concerned with residual stresses the weld cycle can be divided into three phases: welding, initial cooling, and final cooling. During the welding phase the low yield stress of the plasticised material prevents residual stress build up through material movement. Within the initial cooling period the weld piece experiences high cooling rates creating large inelastic thermal strains, primarily near the weld line. Once in the final cooling regime, cooling rates across the weld have equalised and reduced. Instead, material phases transformations become the primary contributor such as those found in CrMoV steels where the volumetric change in the lattice, upon the transformation from austenite to martensite, can reduce hoop stresses near the weld line (C. J. Bennett *et al.*, 2013; C. J. Bennett *et al.*, 2007; Iracheta *et al.*, 2015).

Due to the heat losses to the environment peak temperatures are seen at the mean diameter rather than at the OD as would be suggested from the power input's dependence on radial distance, equation (2-21). During the initial cooling heat losses at the surface continue to be greater than at the mean diameter with the material away from the weld zone acting as a heat sink. This creates a thermal boundary where the material near the weld is cooling and contracting whereas the material away from the weld is warming and therefore expanding. As the weld zone area is contracting restrained by the material away from the weld zone this thermal strain creates tensile stresses. As the ID and OD experience greater cooling rates, creating the characteristic curved HAZ shape, the tensile stresses are greater towards the weld surfaces (Iracheta *et al.*, 2015).

Of the three stress directions hoop stresses have generally found to be the highest, being tensile in nature and reaching peak values near to the inner diameter. The yield strength of the material limiting the maximum for the developed stresses (Attallah & Preuss, 2012). Axial stresses have been found at lower intensities than hoop stress. Across the interface the stress swaps from tensile at the ID to compressive at the OD creating a bending moment. This has

been attributed to either a tourniquet effect from the hoop stresses (F. F. Wang *et al.*, 2014), a temperature difference between the two surfaces (Preuss *et al.*, 2006), from the clamping forces of the machine(Pang *et al.*, 2003) or from opposing thermal strains which swap when beyond a thermal barrier away from the weld zone (Grant *et al.*, 2009; Iracheta *et al.*, 2015). Radial stresses were minimal in comparison.

2.4.6.2 Residual stresses in Titanium welds

Work conducted into Ti-6Al-4V friction welded residual stress measurements has mainly been carried out by those also interested in texture measurement, again primarily in LFW. Frankel *et al.* (2009) used synchrotron x-ray diffraction and the contour method to evaluate the stresses in a dissimilar Ti-6Al-4V to Ti-6242 linear weld, Figure 2-38. Synchrotrons use a method of measuring the material lattice spacing and comparing the strained lattice spacing of interest to the unstrained in order to calculate the stresses. The large power of a synchrotron enables high penetration into the material and bulk material measurements to be taken. The contour method is a destructive technique, first proposed by Prime and Gonzales (2000) which measures the relaxation movement of a part when cut in order to calculate the original residual stresses. Compared to neutron diffraction techniques which require exponentially longer interaction times and deep hole drilling which only gives a 1D profile, the contour method can easily and efficiently provide a 2D map of multiple residual stress components as the stresses are calculated directly from the measurements. Other sectioning techniques that rely on multiple cuts, inverse calculations and strain gauges can determine a 3D state but are more complicated and therefore time consuming (Pagliaro *et al.*, 2010; Prime & Gonzales, 2000; Y. Zhang *et al.*, 2005).

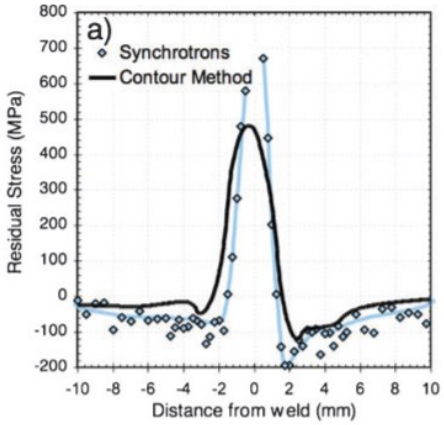


Figure 2-38: Comparison between synchrotron and contour residual stress measurements, in the transverse direction, in an as welded LFW component (Frankel *et al.*, 2009).

Frankel *et al.* (2009) reported that though the trends between the synchrotron and contour method agreed the values were in disagreement with peak stresses over 180MPa different in the transverse direction as in Figure 2-38.

Both techniques however highlighted the appearance of stresses beyond the visible plastically deformed regions suggesting that it is the thermal history, which has the greater impact. There does appear to be some disagreement within the paper. The synchrotron results show axial (z) direction stresses being the largest followed by transverse (y) and then reciprocating (x) as in Figure 2-39, while the conclusion claims that it is the transverse which is the largest followed by reciprocating and the axial direction stresses barely exist. This is due to incorrect labelling of the directions on the graph. Z should be Y, Y should X and X should be Z as discussed with the author (Frankel, 2017). These stresses match the strong textures seen above.

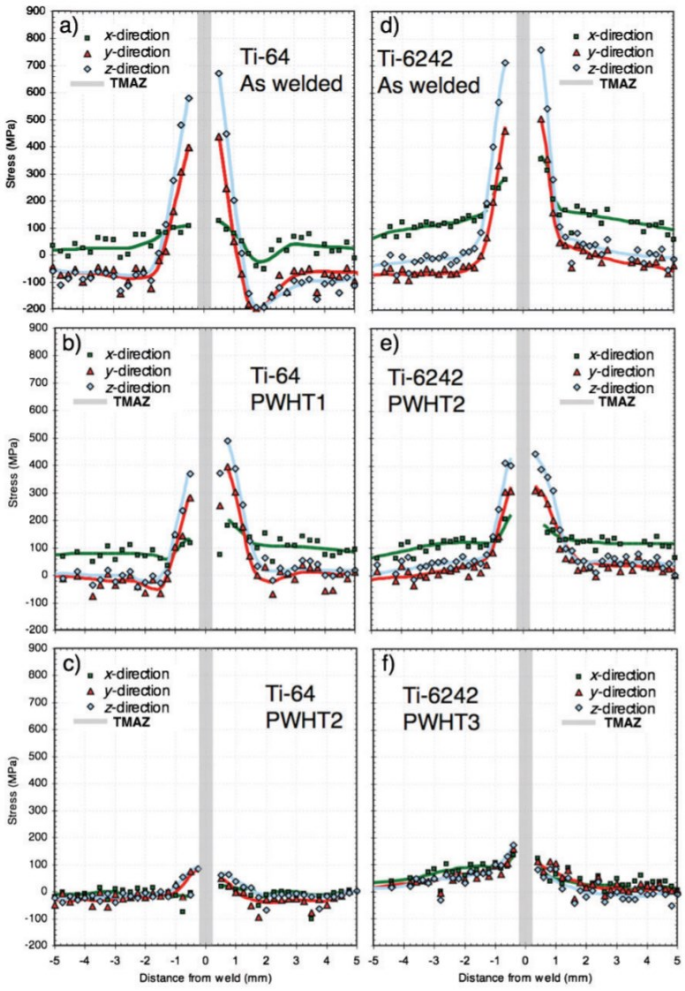


Figure 2-39: Synchrotron residual stress measurements in the principal directions as welded and after various heat treatments (Z is supposed to be Y, Y is supposed to be X and X is supposed to be Z) (Frankel, 2017; Frankel *et al.*, 2009) .

Attallah *et al.* (2012) investigated the residual stress development in IFW Ti-6246 using synchrotron X-ray diffraction and neutron diffraction techniques. Strain distributions were measured in both the α and β phases. The maximum stresses were measured in the hoop direction within the β phases suggesting that the β phase is the primary load bearer. Hoop stresses are also seen as the largest stress component in other material IFW's: nickel based superalloys (Karadge *et al.*, 2011; Preuss *et al.*, 2006), high strength steels (Moat *et al.*, 2009). Further analysis of the axial and radial β phases was not possible due to difficulty in acquiring quality data. From the initial data however, it is shown that the axial and radial stresses in the

β phase are roughly equal and inverse to those in the α phase which, Attallah *et al.* (2012) points out, cannot be explained as it would require different thermal expansion coefficients. A stress balance in the axial direction allowed chemically induced α lattice parameter variation to be calculated across the weld zone. A drop in lattice size was seen in the HAZ, which was attributed to Al segregation due to the β transus temperature not being reached. Al being known to reduce α-lattice spacing according to Vegard's law (Denton & W. Ashcroft, 1991). Calculation of the strain free lattice parameter has also been shown to be of high importance in other friction-based welding processes (Altenkirch *et al.*, 2008; Prime *et al.*, 2006; Staron *et al.*, 2004). Whereas others have only found minor variation which would lead to micro strain variations in the results (Lombard *et al.*, 2009) or using a variation of the method where it isn't needed (W. Woo *et al.*, 2007).

In Figure 2-40, the hoop stresses show a maximum at +/-4mm from the weld. The dip towards the weld is suggested to be due to the α'' formation from the β phase field upon fast cooling. The distorted crystal structure being an expansion from the β phase providing tensile reducing compressive stresses, matching similar transformations in steel welds (C. Bennett *et al.*, 2007; Moat *et al.*, 2009).

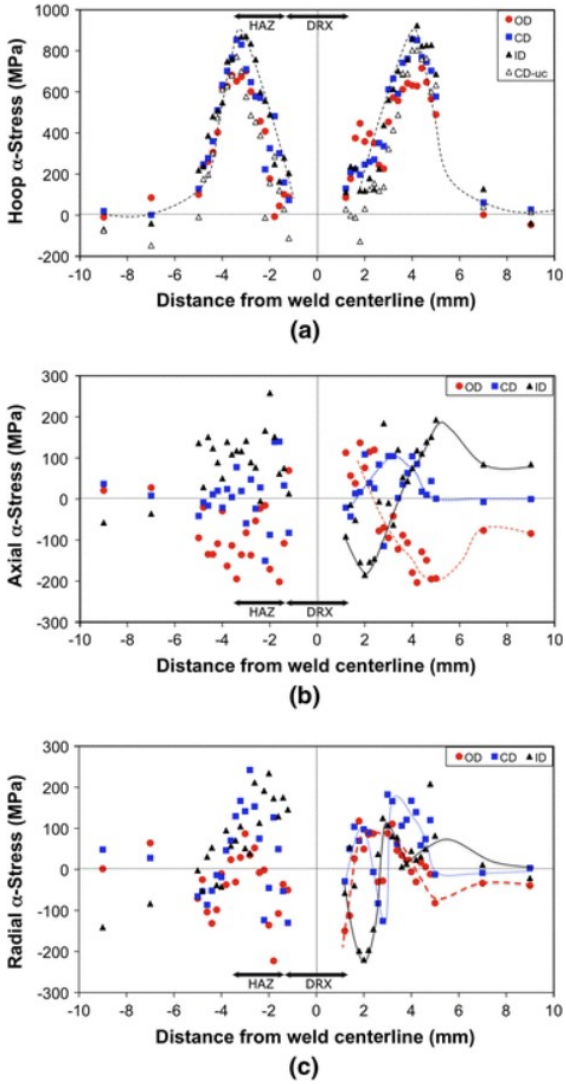


Figure 2-40: The α-Ti residual stresses (following d0 corrected) distribution in AW condition (located at +2mm [OD], 0mm [CD], and –2mm [ID] from the centre of the cylinder thickness): (a) hoop α stress (including an uncorrected trace CD-unc), (b) axial α stress (Attallah *et al.*, 2012).

For the axial direction the transition from tensile in the ID to compressive in the OD and further swapping away from the weld line is suggested to be due to a tourniquet effect (Preuss *et al.*, 2006) and the tooling (Pang *et al.*, 2003). The radial stresses show a similar dip as seen in the hoop stresses while also balancing a moment between the ID and OD similar to the axial stresses. The increasing scatter in the radial and axial directions is attributed to the longer path lengths of the measurement method.

Work by Romero *et al.* (2009), Figure 2-41, studied the effect of pressure on residual stresses in linear welds using energy dispersive X-ray diffraction (EDXRD). Strain free lattice

measurements were taken across the weld line noting an influence wider than the HAZ seen in that weld. The LFW here produced an increase in the strain free lattice parameter unlike the reduction seen in work by Attallah *et al.* (2012) above, suggesting an decrease in Al close to the weld line.

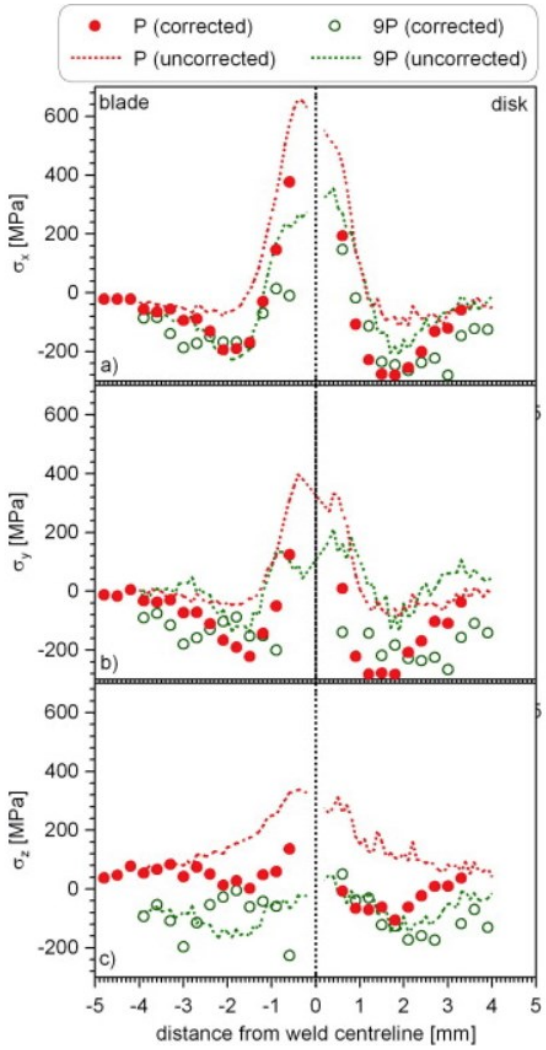


Figure 2-41: Influence of the d0-correction on the calculated residual stress components (x, y, z) in the P and 9P-welds (Romero *et al.*, 2009).

Both the x and y direction show tensile stresses towards the centre of the weld before becoming compressive and then reducing to zero away from the weld. The z direction shows scatter around the unstrained level. It is suggested that the formation of the tensile strains is caused by the thermomechanical deformation and constraint to thermal expansion. With the

size of the x direction (transverse) being larger than the y (reciprocating) a greater thermal gradient could be established and thereby produce greater stresses. The increase in pressure and subsequent reduction in residual stresses is contributed to a “colder” weld. The shorter welding times and accelerated material flow suggesting a reduction in total weld energy and thermal exposure, which matches the reduction in TMAZ width seen in the microstructure. Increased pressure was also seen to lead to a reduction in HAZ size due to a reduction in interface temperatures (blue vs black line in Figure 2-42). Although the increase in pressure would increase the energy into the weld it also increases the expulsion of material. As the flash generation increased a greater amount than the energy input, the heat energy has less time to conduct into the bulk material, keeping the bulk at a lower temperature and providing a cooling result when it reached the interface. A phenomenon also seen by Romero *et al.* (2009). Unlike early work such as Linnert (1994), which generalised lower speeds and higher pressures, and vice versa, as being synonymous, as seen depicted in Figure 2-1, the work by McAndrew *et al.* (2015) shows that higher pressures lower the thermal profile across the entire weld piece whilst lower speeds reduce the gradient of the thermal profile across the entire weld piece.

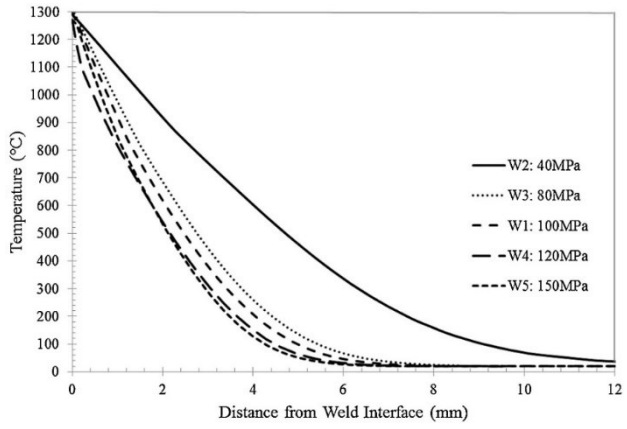


Figure 2-42: LFW thermal weld profiles away from the weld interface of Ti-6Al-4V (McAndrew *et al.*, 2015).

2.5 Modelling

Friction welding models convert potential energy either stored in the flywheel or available from a motor into deformed material, through the frictional interaction at the rotating rubbing surface. Understanding and representing the frictional interaction is key to a successful and accurate model (C. Bennett *et al.*, 2007).

Modelling of the friction process can be split into two primary routes. A representative modelling technique and a predictive modelling technique. Representative models also known as analytical models are based on real world welds. The welding process is deconstructed, and equations are generated to describe the stages. The resulting model can be checked against welding scenarios within the original parameter window and then used to predict new results. Numerical models generally build equations from the authors understanding of the process. Material data and behaviour can be fed into the model to make predictions, which can be checked against real world welds. Primarily models use upset as the definitive output. It is easy to quantify and therefore compare against. Other factors such as temperature profiles, stress-strain distributions and flash formation can also be predicted but can be much harder and/or expensive to accurately quantify (C. Bennett *et al.*, 2013; C. Bennett *et al.*, 2007; D'Alvise, 2002; D'Alvise *et al.*, 2002; Grant *et al.*, 2009; Iracheta *et al.*, 2015; L. Wang *et al.*, 2005; L. Yang, 2010; Y.-C. Yang *et al.*, 2011; Q. Z. Zhang *et al.*, 2006).

2.6 State of the art

Friction welding as a process has not changed greatly since its inception. Over time the systems for recording and controlling the parameters have improved allowing for greater accuracy and repeatability, but the process itself has not changed.

Only a limited number of people are engaged in developing the process. There has been development of a low heat input (LHI) variant of the process. Deformation during braking is avoided due to the utilisation of a near instantaneous de-clutch mechanism holding the non-

rotating work piece within a continuous drive machine (Kimura *et al.*, 2006; Kimura *et al.*, 2010; M. Kimura, M. Kusaka*, et al.*, 2005a, 2005b; M. Kimura, S. Nakamura*, et al.*, 2005; Kimura *et al.*, 2003). While, Manufacturing Technology, Inc has developed a combined inertia and continuous drive machine. The outcome is a machine that mixes the power and simple operation of an inertia machine with the accuracy and precision of a continuous drive machine, through what have been termed enhanced functionalities and hybrid welds (Lovin *et al.*, 2004a, 2004b; Manufacturing Technology Inc, 2012, 2016, 2017a, 2017b, 2017c, 2017d).

2.6.1 Low heat input welding

De-clutching the stationary work piece causes it to rotate and reduce the relative speeds of the work pieces far quicker than a traditional braking system in essence pausing the weld. Initially suggested and reviewed by Kimura *et al.* (2003) when welding low carbon steel (mild steel), the group used the clutch mechanism to investigate the development of the process through stage one, containing the initial torque peak and into stage two, eventually producing a model of the interface heat production and joining progress (Kimura *et al.*, 2010). Dissection of the weld interface, Figure 2-43, revealed the progress of wear at the periphery working inwards and converting to seizure moving outwards from the centre until full seizure had occurred at 1.1s, which coincided with the start of flash formation.

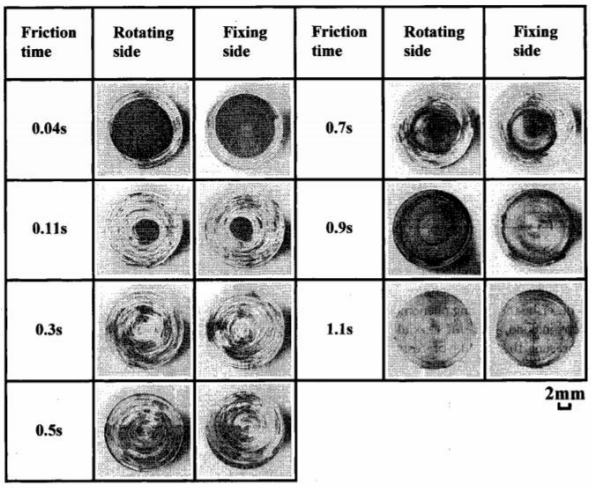


Figure 2-43: Appearances of welded interfaces after welding in friction pressure of 30Mpa and friction speed of 27.5s^{-1}. Wear can be seen starting at the periphery working inwards up to 0.5s, after which seizure can be seen expanding outwards from the centre (Kimura *et al.*, 2003).

At 1.3s the welding reached peak torque. Tensile testing of samples taken from different points in the weld cycle indicated that 100% joint efficiency could be achieved; producing welds that fractured in the parent material with minimal scatter of results, once torque peak had been reached. The initial testing suggested that the lengthy friction phases and forge stage were unnecessary when producing strong joints. The LHI method is shown compared to the standard continuous drive system in Figure 2-44.

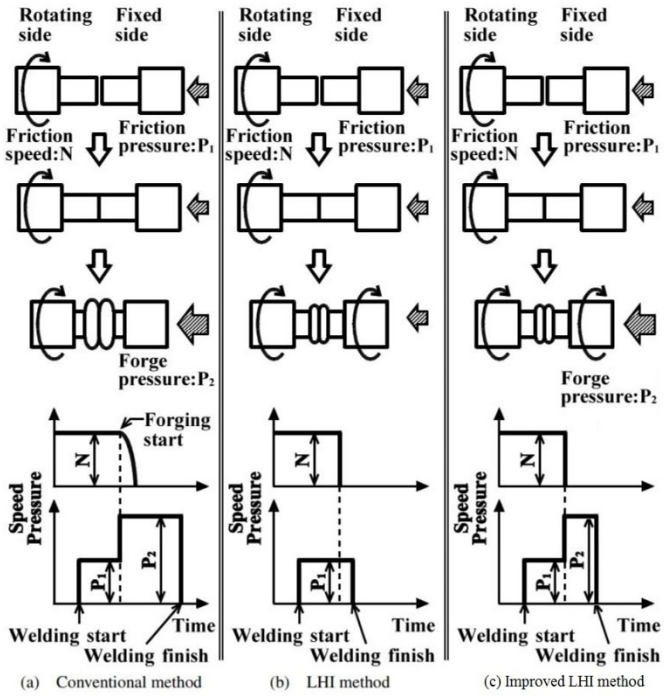


Figure 2-44: Comparison of (a) the conventional continuous drive welding method (b) the LHI method and (c) the improved LHI method, adapted from (M. Kimura, M. Kusaka*, et al.*, 2005a).

Further work in M. Kimura, M. Kusaka*, et al.* (2005a) indicated that the LHI method created a spike in the hardness in the centre of the weld zone compared to the dip seen in CDFW due to the lack of heat entering the sample and associated slow cooling rates. However, either side of the central spike was a reduction in hardness creating a potential focal point for fracture caused by the dissipation of the small amount of heat into the base material. Introduction of the improved LHI method where a forge phase was introduced, Figure 2-44(c), eliminated the drop in hardness by removing the small amount of softened material as flash. This change allowed the entire weld region to strengthen above that of the base material removing the

previous preferential fracture points exhibited during the tensile testing. The improved LHI method was used to reduce the softening at the weld interface when friction welding aluminium alloys to Ti-6Al-4V (M. Kimura, S. Nakamura*, et al.*, 2005) enabling 100% joint efficiency to be achieved under specific conditions. In Aluminium to Aluminium welds 100% joint efficiency was possible when the base material exhibited isotropic properties (Kimura *et al.*, 2006). What has not been proven with this technique yet is whether the interface undergoes complete cleaning of any contaminants. Arguably, as the materials tested so far have reached 100% efficiency it is not needed but this may become important when testing more exotic material combinations.

2.7 Research link

With the aim to assess the utility of enhanced control approaches during friction welding the literature has covered aspects directly related to the work undertaken. The development of the weld has been studied along with the parameters directly influencing that development. Models have been created and validated in order to further understand the mechanisms at the interface, but no one has currently investigated variable energy input in an inertia weld. The work conducted so far should help to understand the role of enhanced control mechanisms on weld repeatability. Energy input has been reviewed, along with sources of energy loss, during a welding cycle. Parameter studies have been conducted to work out their significance on energy losses but there has been no work carried out experimenting with substantial energy changes mid-process. The closest is the Low Heat Input method where the energy input is suddenly stopped. The review continues into texture development and residual stresses of friction welds. In high performance components residual stresses are important to quantify and ensure they are not detrimental to the role of the part. So far, the work on residual stresses has primarily been conducted in nickel superalloys, the work on titanium is limited therefore studies in LFW have been included. Although some progress has been made in reducing residual stresses in LFW through utilising pressures much higher than normal this approach is

potentially prohibitive due to the associated machine costs. So far work has not been widely conducted into alternative methods for stress reduction.

Due to the nature of the EngD with the work coming from multiple projects the materials studied have not been consistent. For this, the response of the individual materials used in the assessments, has been studied during friction welding.

3 Research approach

The literature review has investigated and evaluated the current understanding of the friction welding process in general and upon the specific materials acquired for each experimental section. This understanding was used to guide the experimental direction. First the enhanced functionalities are explained followed by the methodology for each technique used.

3.1 Explanation of enhanced functionality welding

3.1.1 Upset control

Inertia welding utilises stored energy in the form of a rotating flywheel to transfer into the weld pieces for welding. Local variations in the material properties of the weld piece change the amount of energy consumed to heat the material to a temperature at which the applied pressure can extrude it. The result is different amounts of extrusion occurs in each weld from the same initial speed and flywheel inertia due to the variation in transfer of energy during the weld. Two methods of controlling the weld exists.

Torque modulation (TM) is a method to counter the changing energy requirements through supplementing and removing the energy stored in the flywheel with an electric motor.

Pressure modulation (PM) is the alternative method. The applied pressure is changed as a result of the variations in energy to produce upset, with the pressure dropping when the energy required drops and the pressure increasing when the energy required increases. Torque modulation has a response time that is up to ten times faster and therefore is more accurate (Manufacturing Technology Inc, 2017d). Pressure modulation also sufferers from tooling compression changes as the pressure varies leading to further inaccuracies (Manufacturing Technology Inc, 2017c).

Both methods require a previous weld to follow, known as a profile weld. From that weld set points between the speed, time and upset are logged. This relationship is then used in the

modulated weld's feedback loop to determine what progress the weld should have made by each specific point in the cycle and the required response needed to bring the current weld to a matching point if it is not already there. This response relies on two parts; a proportional response and integral response, controlled through what is commonly known as a PID (proportional-integral-derivative) controller. The proportional section looks at how far the measured value is from the set point and applies a response directly related to how far apart the two are. The integral section looks at how far the measured value is from the set point and how long the measured value has been different. The response applied is related to both factors. The user can set a value for each, which controls how strongly the two responses react (Manufacturing Technology Inc, 2012).

The result is a weld cycle that adjusts the parameters during the cycle in response to the resulting progress compared to the profile weld. Natural variation is therefore compensated for and the deviation from the profile weld is reduced.

Once in-process control of the upset has been established the method can be extrapolated for employment in various situations. Both torque modulation and pressure modulation allow welding to a predetermined upset utilising data from a previous weld. Scaling the energy input of the profile weld allows the user to weld to self-defined upsets, as in Figure 3-1 . This can be either welding so that a desired amount of upset or parts of a certain total length are produced. Scaling can either be to adjust the linear equilibrium phase by changing the torque or pressure during the weld or by adjusting the initial speed of the weld, as in Figure 3-2. Using modulation throughout the weld then drives the weld towards a precise upset amount (Lovin *et al.*, 2004b; Manufacturing Technology Inc, 2017a).

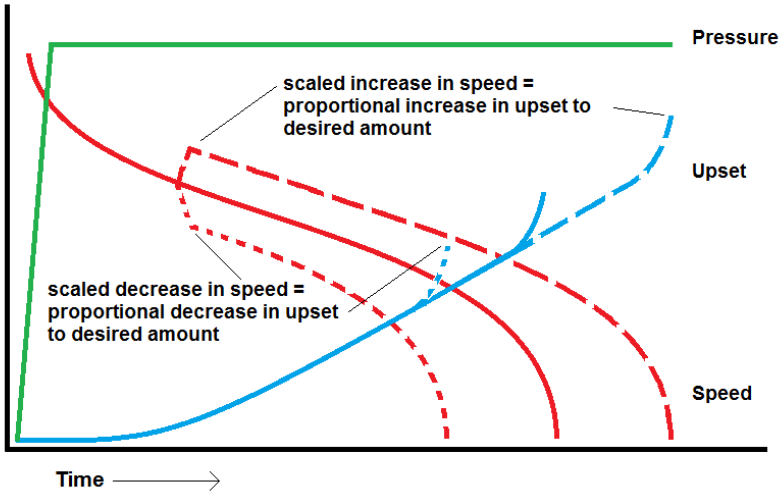


Figure 3-1: Upset scaling during the weld cycle. Scaled energy input coming from the profile weld's linear upset phase resulting in the machine using torque modulation to influence the rotational speed. Adapted from (Lovin *et al.*, 2004b; Manufacturing Technology Inc, 2012).

Within continuous drive welding upset control is built in as a control measure. The trigger from the friction to the forge stage can be based on upset distance instead of time, ensuring that up to the end of the friction phase, the upset between welds is identical. However, once in the forge phase there is no control over the resultant upset. Compared to a standard inertia process the standard continuous drive process is more repeatable due to the control during the weld (Manufacturing Technology Inc, 2016).

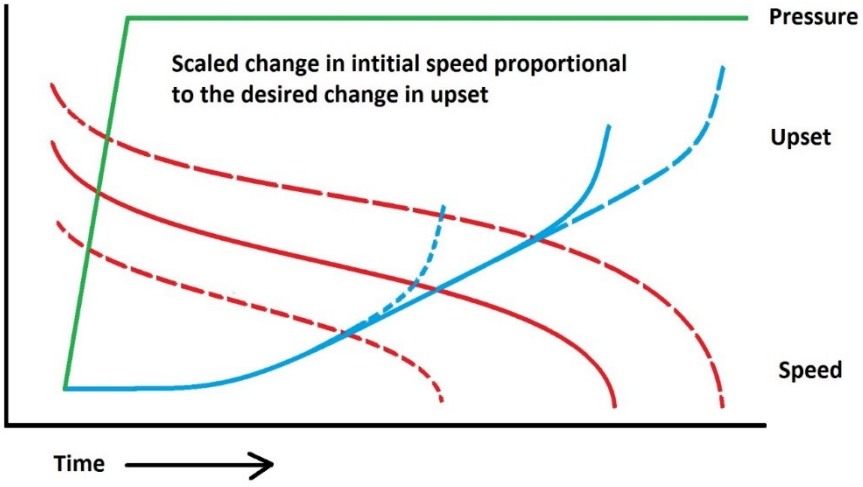


Figure 3-2: Diagrams of weld profiles exhibiting initial speed changes proportional to the energy change required to adjust the resultant upset to the desired amount, adapted from (Lovin *et al.*, 2004b) .

3.1.2 Orientation control

In orientation-controlled (OC) welds, torque is dynamically added to or subtracted from the spindle in order to track to the spindle orientation of a previous (profile) weld. This process utilises a closed loop control algorithm, which calculates the torque required as a function of the difference between the commanded and the actual spindle position.

The aim of this functionality is to force the actual spindle position to exactly match the commanded value. If the commanded value is achieved at all instances during the deceleration period, then the final orientation of the spindle should match the targeted orientation. By adjusting the Velocity Feed Forward Gain parameter (VFF) the orientation of the welds can be dialled in to match the profile orientation as closely as possible (Lovin *et al.*, 2004a; Manufacturing Technology Inc, 2012).

3.2 Experimental methodology

The experimental approach is based on ISO 15620:2000 Welding – Friction welding of metallic materials.

For each results chapter certain aspects of the research methodology are repeated. The common aspects are covered below. When non-standard analysis methods are used these are detailed in each chapter.

Pre/post-weld part geometry, weld record, mechanical properties and metallurgy for all welds was recorded and analysed. Pre/post weld measurement was conducted primarily using height gauges. Weld records were collected from the machine and processed in Microsoft Excel. Mechanical testing was conducted at UKAS accredited test facilities, either at The Test House, Cambridge or Special Testing, Sheffield. This included bend tests, charpy tests and tensile tests.

Metallographic testing was primarily conducted at the Manufacturing Technology Centre (MTC). In most cases a selection of weld's were down selected for further examination including; micro-structure, Thermal-Mechanically Affected Zone (TMAZ) measurement, interface characteristic identification (grain structure, inclusions and defects) and hardness surveys of the weld region. One joint cross-section per weld was prepared, ground and polished for metallographic examination.

3.2.1.1 Weld matrix

For each experimental situation, a weld matrix is derived to detail the production of the welded

Table 3-1: Final length control welds summary.

	Example weld matrix							
	IFW				**CDFW**			
Geometry	**Tubular**	**No. of welds**	**Solid**	**No. of welds**	**Tubular**	**No. of welds**	**Solid**	**No. of welds**
Part deviation from nominal (mm)	+2	2	+2	2	+2	2	+2	2
	+1	2	+1	2	+1	2	+1	2
	-1	2	-1	2	-1	2	-1	2
	-2	2	-2	2	-2	2	-2	2
Total no. of welds		8		8		8		8

samples. Table 3-1 is an example weld matrix table from Chapter 5.

3.2.1.2 Materials

Each chapter focuses on a different material due to the availability and focus of the individual CRP projects the work comes from. Chapter 4 uses S355, a micro alloyed structural steel, Table 3-2. Chapter 5 uses SVH40C a specialised micro-alloyed steel developed by Nissan, Table 3-3. Chapter 6 uses the popular titanium alloy Ti-6Al-4V, Table 3-4.

Table 3-2. Material chemical composition of S355 from supplier.

Chemical composition of S355 steel (wt. %)					
C	**Si**	**Mn**	**P**	**S**	**Fe**
0.23	0.05	1.60	0.05	0.05	Balance

Table 3-3. Material chemical composition of SVH40C as supplied by Nissan.

Chemical composition of SVH40C steel (wt. %)									
C	**Cu**	**Si**	**Fe**	**Mn**	**Cr**	**Ni**	**S**	**V**	**P**
0.39	0.1	0.2	Balance	0.7	0.2	0.05	0.02	0.05	0.02

Table 3-4: Material chemical composition of Ti-6Al-4V from supplier.

Chemical composition of Titanium Ti-6Al-4V (wt. %)							
C	**Fe**	**N_2**	**O_2**	**Al**	**V**	**H_2**	**Ti**
<0.08%	<0.25%	<0.05%	<0.2%	5.5 - 6.76%	3.5 – 4.5%	<0.0125%	Bal

Prior to welding the material blanks are machined into the appropriate tubular or solid geometries. Examples are shown in Figure 3-3. Part geometries are given in each chapter. Pre-weld part geometry is measured using a TESA Hite 700 height gauge. Post weld heights of the components were measured using a height gauge and subtracted from the combined pre-weld part measurements to produce a cold upset measurement.

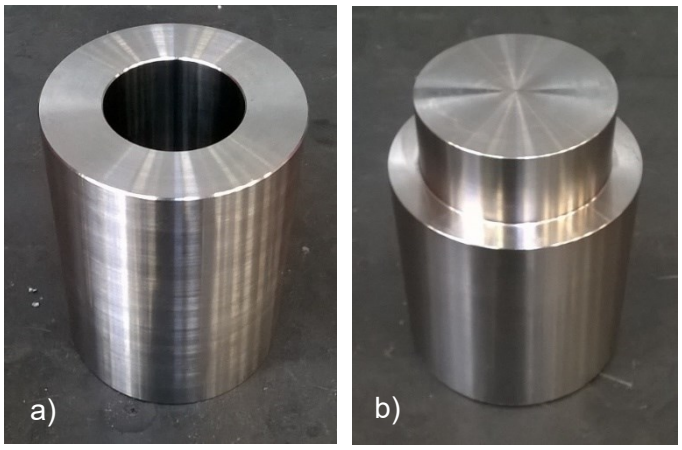


Figure 3-3. Example of parts geometry; a) tubular and b) solid – the step down in diameter allows for an interface sizing suitable for current study while the larger diameter section is sized to the nearest collet tooling size to eliminate the need for individual part tooling.

Cold measurement is preferentially given in the report as it is the final size. Hot upset can be taken from the cycle graphs. The difference between hot and cold upset is a product of the elastic de-compression of the part and the thermal contraction of the heated proportion of the part.

3.2.1.3 Welding equipment

All welds were performed on the 125 Ton Tri-Mode Rotary Friction Welding (RFW) machine at the MTC (Figure 3-4).

A tri-mode machine combines the inertia and continuous drive energy input systems, into one machine. This enables the machine to provide programme options that are not normally available. Some of these options and what can be developed from them is the focus of this thesis.

Primary measurements are:

- Rotational speed – RPM
- Cylinder Pressure – Bar
- Torque feedback – % (This is a percentage of the motors capability)
- Upset –mm
- Time – s

These parameters were tracked up to 200 times a second. In a production environment limits can be set to provide immediate indication of out of tolerance welds. The interface pressure can be calculated from the specific geometry of the component and the cylinder area of the machine and is given in all parameter tables. Upset measurements were taken from an upset zero position created prior to welding through full forge pressure being applied to compensate for any tooling compression. Final upset is taken during the forge dwell period. This produces an in-process hot upset measurement. With the M125 it is possible to operate the machine

with data from a secondary Upset Measuring Device (UMD). This can be in the form of laser measurements or utilising contact probes. With tubular components, at the MTC, it is possible to utilise a separate UMD installed directly behind the components which utilises a contact probe that passes through the centre of the component. This allows measurements to be taken directly from the back surface of each component and therefore does not have to compensate for flex in the tooling.



Figure 3-4: Model 125 Ton Tri-Mode RFW machine at the MTC.

3.2.1.4 Weld parameters

When working within a core research program (CRP) each combination had an original set of parameters suggested by the steering group. These were tested and incrementally optimised. Outside of a CRP parameters are based on previous accumulated knowledge at the MTC and published data. If required, a representative weld was chosen to act as a profile by reviewing the weld response and upset curves in addition to evaluating the flash. When available, the microstructure data was included within the evaluation. Profile welds were selected in order to represent the average weld produced by a parameter set. They were then used as baseline performances to control the subsequent enhanced welds.

For welds with a target upset or final length the progress and success criteria is based upon the machine measured upset values (hot measurements). Values either come from a required amount or profile weld. Once cooled the part will have deformed; average cooling deformations

are applied to the hot target to produce a cold target. This can work in reverse to define the hot target.

Example parameters used in the trials are presented in Table 3-5, for inertia mode, and in Table 3-6, for continuous drive mode.

Table 3-5. Inertia rotary friction welding parameters.

Example inertia friction weld parameter matrix			
Geometry		**Solid**	**Tube**
Inertia Weld Parameters	**Weld Speed [RPM]**	2000	2000
	Forge Interface Pressure [MPa]	254.99	184.21
	Total Inertia [kg.m^2]	18.6	18.6

Table 3-6. Continuous drive rotary friction welding parameters.

Example continuous drive weld parameter matrix			
Geometry		**Solid**	**Tube**
Continuous Drive Weld Parameters	**1st Friction speed [RPM]**	650	800
	2nd Friction speed [RPM]	486	488
	1st Friction interface pressure [MPa]	38.98	57.40
	2nd Friction interface pressure [MPa]	124.99	114.80
	Burn off [mm]	5	8.4
	Forge interface pressure [MPa]	169.34	179.51
	Forge time [s]	6.5	5.0
	Brake torque [%]	50%	50%
	Machine inertia [kg.m^2]	18.6	18.6

3.2.2 Weld analysis

3.2.2.1 Weld curve analysis

Weld curves are analysed with focus on the following:

- Weld upset: identification of weld phases, repeatability, amount and rates.
- Pressure at the weld contact interface: consistency.
- Rotational speed: accuracy of start speeds, deceleration rates.
- Torque feedback: levels in relation to the required speed and upset profile.
- Burn-off: consistency of triggering at the correct point.

3.2.2.2 Weld energy measuring methodology

As stated in the literature review the potential energy of a rotating flywheel is $E = \frac{I\omega^2}{2}$ with I being inertia in kgm^2 and ω being angular velocity in rad/s. This states the energy stored at the start of the process but does not cover the losses due to friction or the influence of the motor during the process. Data available from the machine allows tracking of the spindle speed, and torque feedback; a demand value for the motor, both measured against time. Measuring the change in spindle speed can be equated to the change in energy of the flywheel. Once the energy change from frictional losses and motor inputs have been accounted for the remaining difference in energy can contributed to the weld.

When the flywheel is decelerating, it is due to energy being removed from it. If no weld or braking action is occurring, then the energy removed is purely from the friction in the hydrostatic bearings and system. This situation is called a flywheel run down and is how the frictional energy losses with respect to speed are quantified. Mahaffey *et al.* (2016); Senkov, Mahaffey, and Semiatin (2017); Senkov, Mahaffey, Tung*, et al.* (2017) all show that frictional losses are proportional to the speed of the rotating system and are the most significant losses in the system and the biggest factor to energy efficiency of the inertia welding process.

Motor inputs and outputs were characterised in a similar way. Set amounts of torque were run while measuring the changing energy input/output on the flywheel. The factors controlling the shape of the trend line for each scenario were plotted and the equations for those factors used to link torque percentage and rotational speed to create an energy change equation. This energy rate was used to calculate the motors energy input/output over a single time step.

Combing the energy change in the flywheel, the motor energy change and the energy lost to friction the weld energy equation is:

$$E_w = E_f - E_m - E_{fric} \quad (3\text{-}1)$$

With energy of the flywheel system as E_f, energy from the motor as E_m, energy from frictional losses as E_{fric} and energy into the weld as E_w.

Energy out of the system is positive with energy being put into the system as negative.

During deceleration and braking, the equation is as above, in equation (3-1). The motor cannot remove more energy than the flywheel is losing, otherwise energy from the weld would be travelling out of the weld. This is shown in Figure 3-5a. In a standard inertia weld, where the motor is not used during the cycle, the motor element of the equation would be zero. This leaves the flywheel energy minus the friction energy to determine the energy going into the weld.

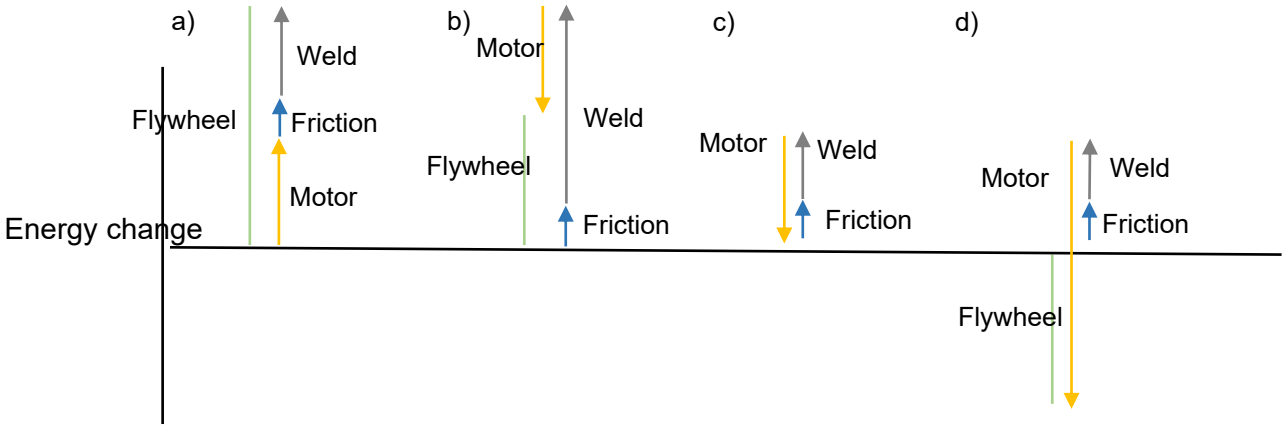


Figure 3-5: Energy changes experienced by the system during welding. The flywheel measures the overall system change. The other sources are denoted with upwards arrows for energy out and downwards arrows for energy into the system. The remaining energy is into the weld. a) deceleration and braking, b) motor input during deceleration, c) constant speed, d) acceleration.

When the motor is adding energy into the system but less than that required to keep the flywheel at constant speed it will decelerate. Here the negative motor energy in the equation is added to the flywheel energy, minus the friction energy, to leave the remaining weld energy, creating

$$E_w = E_f + E_m - E_{fric} \tag{3-2}$$

As in Figure 3-5b.

During constant speed, Figure 3-5c, such as in the friction stage of a continuous drive weld there is no change in stored energy in the flywheel, therefore the energy coming from the motor must match the frictional losses and the energy being transferred into the weld. In this situation the equation becomes:

$$E_w = -E_m - E_{fric} \tag{3-3}$$

During a period of flywheel acceleration, the potential energy in the flywheel is increasing which comes from the motor input. The motor also needs to put in enough energy to overcome the

frictional losses and the energy transferred to the weld. Here, in Figure 3-5d, As the flywheel and motor energies are negative the equation becomes:

$$E_w = -E_f + E_m - E_{fric} \tag{3-4}$$

Once the energy input has been calculated for every point in the weld the energy input can be tracked and cumulated. The combination of flywheel energy, motor energy and friction energy are combined throughout the cycle to produce an energy trace for the specific energy put into the weld. This weld energy trace can be converted into energy rates using the time step duration while also being sequentially added together to find the total amount of energy consumed by the weld pieces during the cycle. Examples are shown for enhanced functionality inertia welds in Figure 3-6 and Figure 3-7.

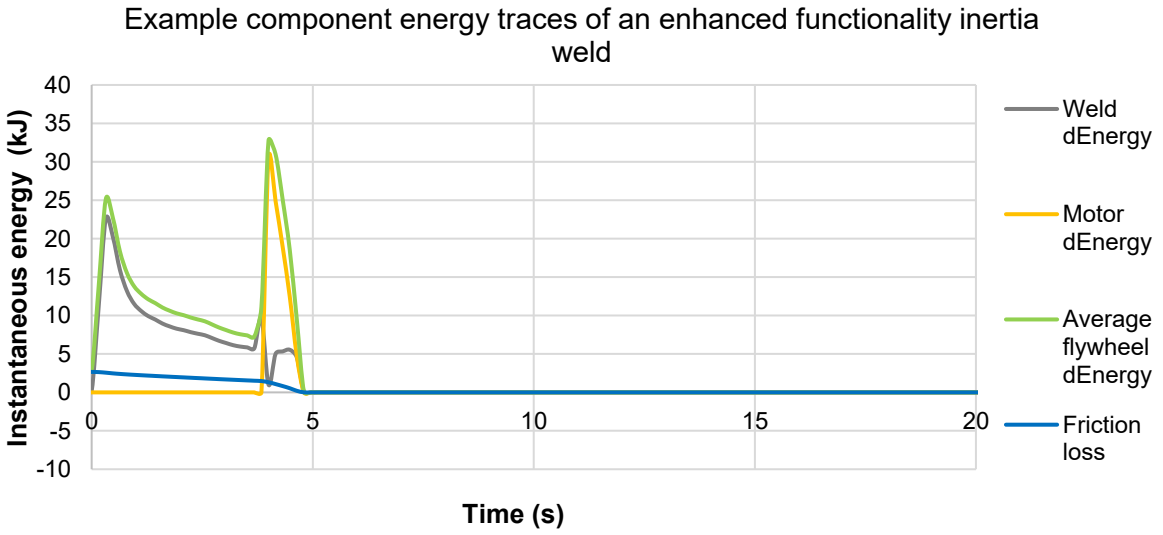


Figure 3-6: Example energy input and outputs during an enhanced functionality inertia weld.

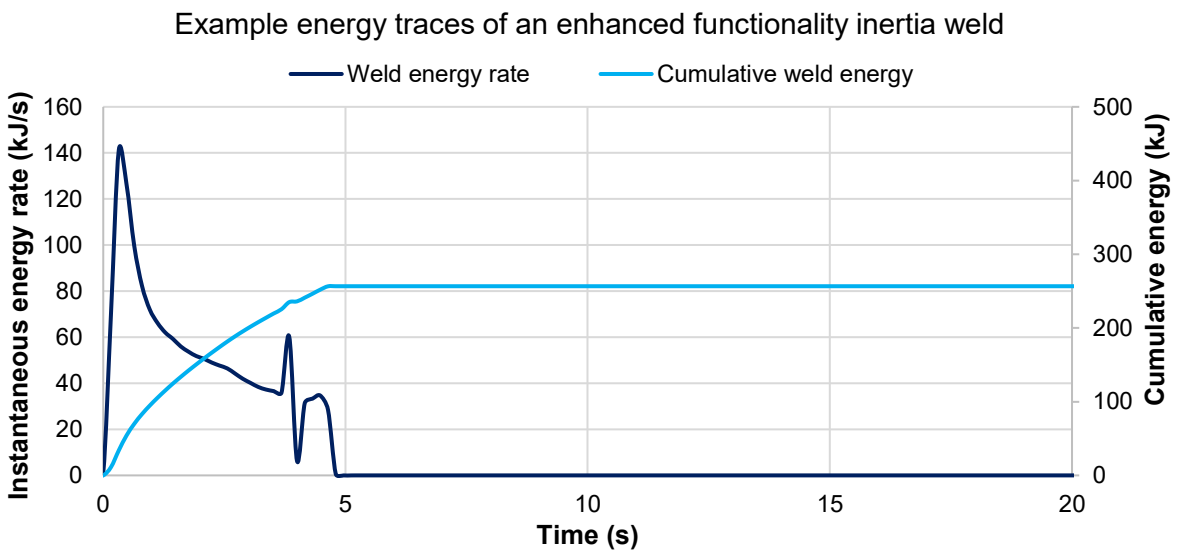


Figure 3-7: Example weld energy input rate and cumulative energy during an enhanced functionality inertia cycle.

While continuous drive weld examples are in Figure 3-8 and Figure 3-9.

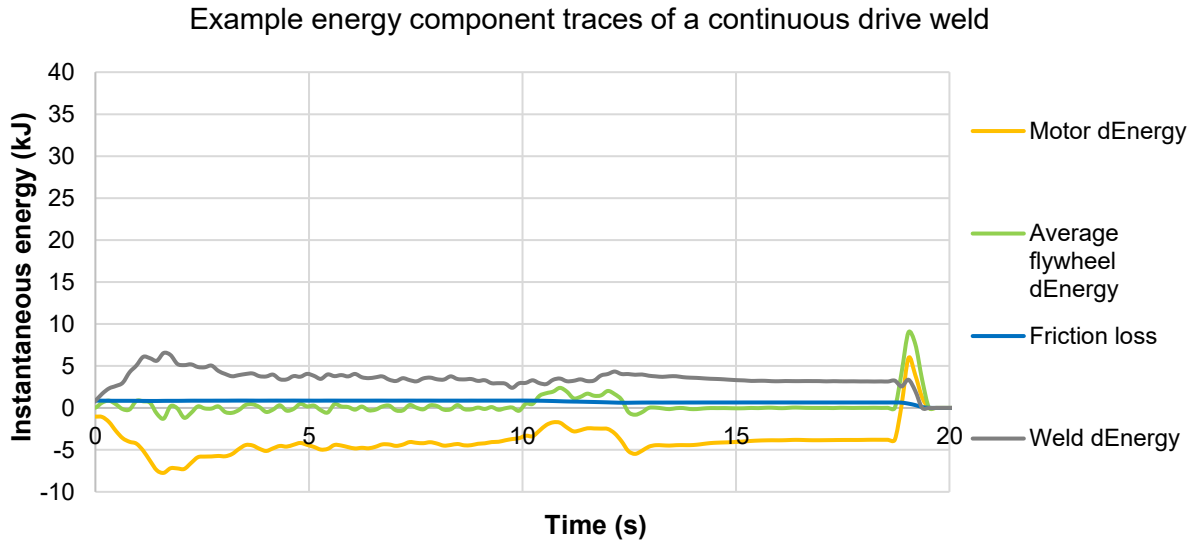


Figure 3-8: Example energy inputs and outputs during a continuous drive weld.

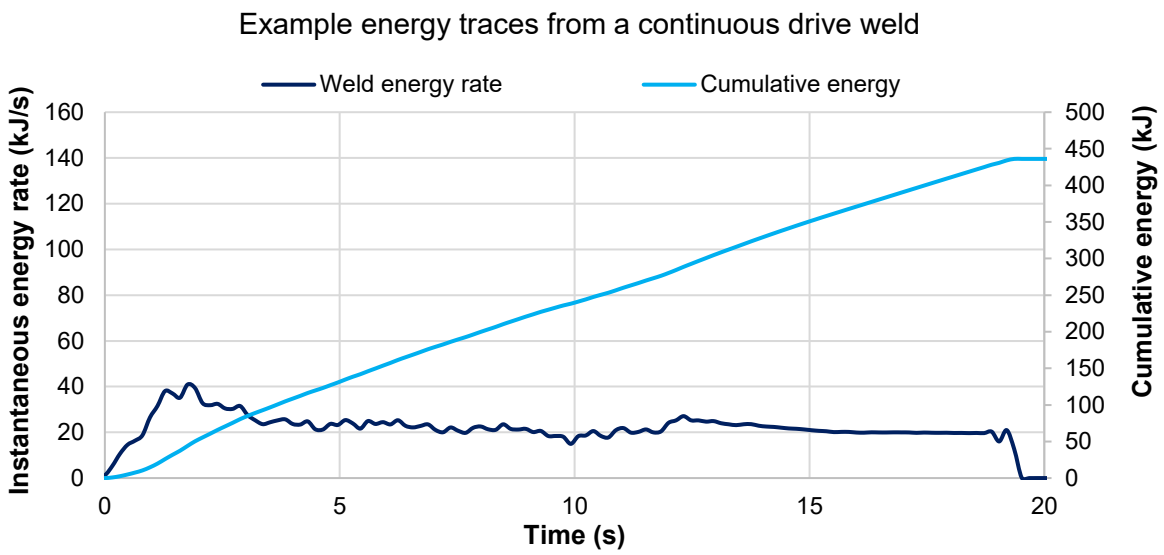


Figure 3-9: Example weld energy input rate and cumulative energy during a continuous drive cycle.

The M125T rotary friction welder records data nominally at 200Hz, however it is not a constant time gap with durations ranging up to 0.015 seconds. This variation appeared to be due to a buffer overload in the recording software causing a repeating pattern of standard durations followed by a long and then short duration gap. When converted to rates the pattern was still visible suggesting the data collection is not spread smoothly over the moving time gaps, as can be seen in Figure 3-10. To combat this the original energy change was converted into an energy rate and then smoothed with a double 3-point moving average. A new time step was introduced of constant proportion to base the friction and motor equations on. The flywheel energy rates within each time step were collected, averaged and converted to an amount of energy for use in calculating the weld energy in that time step. The constant time step also allows the torque feedback to be offset. Although termed feedback it is in fact a calculated feedback of how much percentage effort the motor needs to put into the flywheel and as such would better be described as a torque demand value. It was noted that there was a delay between the demand being made and the response appearing as a change of speed in the

flywheel. Therefore, to accurately align the motor's energy input and the flywheel's response to the input a delay of 0.084s was introduced on the motor torque feedback value.

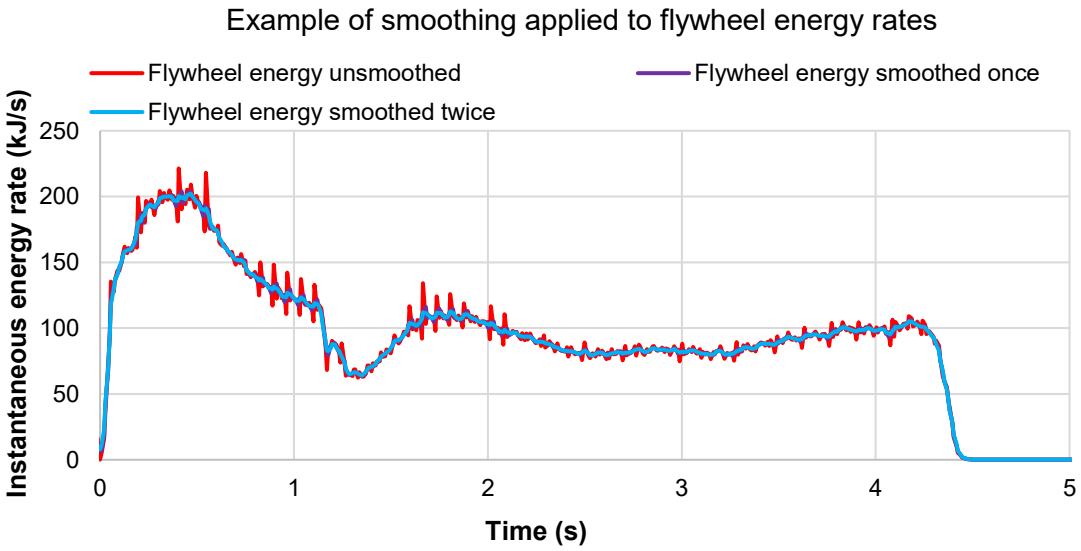


Figure 3-10: An example of the flywheel energy rates from an enhanced functionality inertia weld. Each progressive overlay shows further smoothing of the data using a 3-point moving average.

3.2.2.3 Metallurgical assessment

Sections for metallographic analysis were taken from the weld pieces at the same time as the mechanical testing sample blanks. All metallography analysis samples were prepared and inspected at the MTC. Images focused on the parent material, transition to the heat affected zone (HAZ), transition to the thermo-mechanically affected zone (TMAZ) and the weld region (recrystallised zone) including the bond line. Size and microstructure of the weld zones are identified to allow for comparison between welds.

3.2.2.3.1 Visual inspection

As a preliminary method of quality assessment, visual inspection is carried out. Flash shape, volume and aspect are assessed. Any abnormalities are noted.

3.2.2.3.2 Optical micrographs

Micro-scale images covering the parent material, ID/OD flash and images across the weld TMAZ at the centreline, ID and OD were taken using a Keyence VHX-600 digital microscope system with the VHZ50L lens at 50x and 500x magnifications. Samples were mounted in bakerlight or epoxy and polished on Struers automated machines using the Struers recommended procedure route. Etchants were chosen based on the material to be etched by the MTC's metallurgy lab team.

3.2.2.3.3 Weld zone widths

For TMAZ measurements a mosaic of images taken at 50x magnification was produced, an example is shown in Figure 3-11. The edge of the TMAZ was identified at the ID, CL and OD on both sides of the weld. The inbuilt microscope scale was used to measure the width of the TMAZ zones. For bifurcation measurements the point in the TMAZ where the weld zone material swapped from moving to the ID to the OD was identified. The point was measured relative to the OD. The TMAZ width at the bifurcation point was also measured. For the re-entrant notch feature a line was constructed along the component surface across the weld zone. The notch tip was identified and the distance from the tip to the weld surface measured. If the notch was inside the component weld area it was given a negative value and a positive value if outside.

Macro-scale images of the joint and surrounding weld area were taken using a Nikon digital camera and an Axiom digital microscope system at x5 magnification.

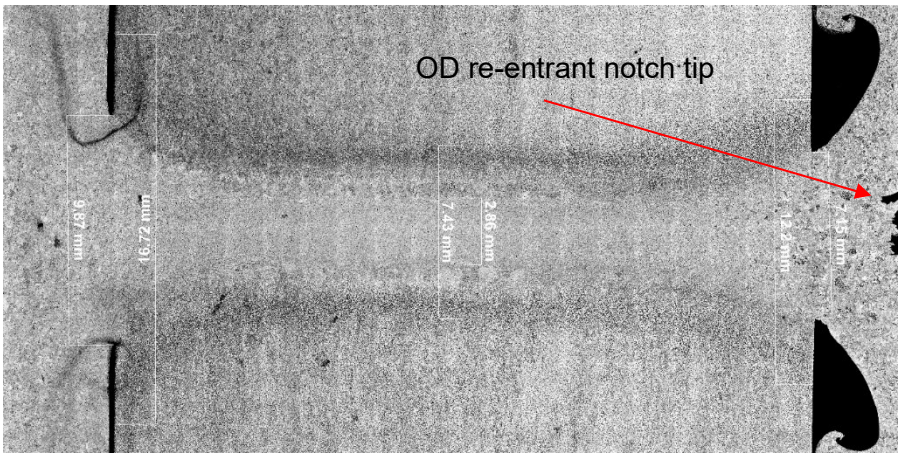


Figure 3-11: An example of a weld mosaic of an IFW Ti-6Al-4V weld. Multiple images were taken at 50x magnification and automatically stitched together. The microscopes inbuilt scale was used to take weld zone and TMAZ measurements. The outside diameter re-entrant notch tip is highlighted

3.2.2.3.4 Hardness testing

Hardness surveys of the welded region of the macro-samples were taken at the wall thickness centreline (CL), 1mm from the internal diameter (ID), and 1mm from the outer diameter (OD) in accordance with the British Standard EN ISO 6507-1: 2005. Low-force Vickers hardness testing with aHv1 indenter was used with a minimum of 0.5mm between indents. A spacing of two times the diameter of the indents is required to ensure induced micro-stresses around the indentation are not able to influence the result of the next indent. A force of 1kgf, was used as indents covered multiple grains in the parent material thereby removing error from only measuring a single grain. Error bars are calculated as 1 standard deviation of the parent material values.

For hardness mapping, measurements across the weld zone using columns 1mm apart and offset rows 0.5mm apart were taken. The offset rows were used to increase the resolution across the weld zone and more accurately pinpoint changes between zones without increasing

processing time. The collated data was used to populate a grid with 0.5mm spacing between columns and rows. The interstitial data was interpolated from the surrounding data points. A downside of this method is that erroneous results influence the surrounding interpolated data points creating what appears to be a large area of inaccurate data. Once erroneous results were smoothed out a contour plot can be made of the weld area.

3.2.2.4 Mechanical testing

Weld samples were delivered to the Test House, Cambridge, and Special Testing, Sheffield, both UKAS test facility with ISO 17025 quality standards. The methods of mechanical testing employed in this study and the standards followed where possible:

- Bend testing – BS EN ISO 7438 2005
- Tensile testing – ASTM A370 2014
- Charpy testing – ASTM E23 – 12c

Sample blanks were taken from the mid-wall thickness on tubular components and at the midpoint of the radius on solid components. The blanks were machined into the required form for the individual test.

For tensile testing, the stress strain plots were calculated from load displacement traces. 0.2% proof strength, ultimate tensile strength, elongation and reduction in area were recorded.

3.2.2.5 Residual stress – Contour method

Although relatively new the contour method is commonly used in industry. First proposed by Prime and Gonzales (2000) the technique directly calculates the stresses within a component from the relaxation movement of a part generated when released after being slowly cut. The contour method easily produces multiple residual stress components in a 2D plane with relative time efficiency. 3D stress results can be produced by combining the data from multiple cuts

but requires significantly more processing power and time. (Pagliaro *et al.*, 2010; Prime & Gonzales, 2000; Y. Zhang *et al.*, 2005).

To conduct the contour method components are rigidly held in a fixture while the cut is slowly made with a wire cutting electro discharge machine (EDM). To minimize heat input into the part and therefore unwanted distortions a fine brass EDM wire is used of 250 - 500μm using low energy settings (VEQTER Ltd, 2018). The rigid fixture prevents the component moving and thereby contains the residual stresses, until the cut is complete, while the slow movement of the wire reduces induced stresses. The relaxed cut surface is then measured by co-ordinate measuring machine (CMM) or lasers to create a surface contour. This contour is superimposed upon an original stress free body; a variation of Bueckner's superposition principle (Bueckner, 1973). The relaxed component is forced back to the stress free shape thereby allowing the calculation of the residual stresses normal to the surface using a finite element model, Figure 3-12 (C. Liu & Dong, 2014; Pagliaro *et al.*, 2010; Prime, 2001). In this form it is assumed that the shear stresses are zero or conversely the fact that they are anti-symmetrical can be used to average out the shear stress effect by measuring both sides of the cut to produce a contour as if the shear stresses were not present (Pagliaro *et al.*, 2010).

It is important to note the limitations of the technique. The resultant stress map is only as good as the computational algorithms and the quality of the cut surface available to work from. Differences in the surface quality of the cut are known as EDM artefacts. These primarily come from changes in the material removal rate. Entry and exit points of the wire can change the removal rate, however this can be overcome by adding sacrificial layers to the surface. Wire breakages also cause EDM artefacts as cutting has to restart which can significantly alter the resultant stress calculations (Ahmad & Fitzpatrick, 2016; Bouchard *et al.*, 2012).

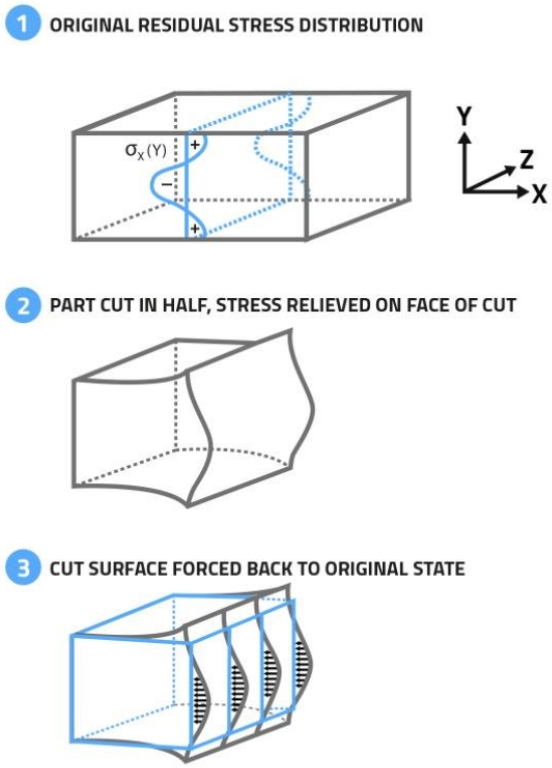


Figure 3-12: The method of the residual stress contour method (VEQTER Ltd, 2018).

4 Inertia welding enhanced functionality initial capability assessment on S355 Steel.

4.1 Aim

To understand the role of enhanced control mechanisms on weld repeatability

4.2 Summary

Four sets of welds were preformed using the enhanced functionalities of the M125T rotary friction welding (RFW) machine. Three functionalities were investigated: torque modulation, pressure modulation and orientation control, all in inertia mode. They were compared back to the standard inertia friction welds and the control capability was quantified in terms of upset produced. Both in-process and post-process

Each enhanced functionality controlled the weld cycle, through a closed loop feedback system using a selected weld as a profile. Torque modulation and pressure modulation actively reduced the upset variation while orientation control, which was producing welds of matched rotation, and therefore potentially controlled upset was not successful in this aim. Torque modulation reduced the in-process variation the most down to a range of 0.03mm.

As torque modulation produced the lowest variation and the highest scope for novel research, it was selected for further investigation. Energy calculations showed greater variation during the cycle as expected to compensate for the natural fluctuation in the process. This did not have a statistically significant impact on the microstructure, resulting properties, or weld shape.

4.3 Methodology

Welds were undertaken to establish the difference in mechanical and metallurgical properties under enhanced functionality conditions compared to a common set of inertia friction welding (IFW) nominal welds. The parameters of each weld set are listed in Table 4-1.

Table 4-1: Weld parameters and set sizes for the nominal weld set and three enhanced functionality weld sets.

Enhanced functionality capability weld matrix				
	Weld set			
Parameter	**Nominal**	**Torque modulated**	**Pressure modulated**	**Orientation controlled**
Weld Speed (rpm)	1118	1118	1118	1118
Inertia (kg.m^2)	68.6	68.6	68.6	68.6
Interface Pressure (MPa)	218	218	218	218
Proportional response	N/a	200%	200%	N/a
Integral response	N/a	200%	200%	N/a
Feed forward gain	N/a	N/a	N/a	84
Modulation start point	N/a	0.6mm upset	2mm upset	Start of weld
Additional profile weld required	N/a	No	Yes	Yes
Number of welds	5	8	4	3

Components were produced from s355 structural steel, the composition of which can be found in Table 3-2.

Parts were tubular with an outside diameter of 80mm and a wall thickness of 19mm. The interface roughness was machined down to an RA of 3.2. To suit the machine and provide adequate clamping area parts were 106.1mm long. Dimensional tolerances were +/-0.05mm.

Each functionality produced several welds which were scrutinised for performance differences in the weld cycle results, post weld CMM measurements and in the case of orientation control rotational position. From these initial findings a functionality was selected to pursue with further testing conducted for a more in-depth comparison to the nominal welds.

Welds with attributes at the edge of the observed limits were chosen and underwent destructive testing at the accredited testing facility, The Test House in Cambridge. While all metallographic testing was conducted at the Manufacturing Technology Centre (MTC). Sample preparation was conducted by the MTC metallurgy team and the author while all imaging and measurements were conducted by the author.

4.4 Nominal results

The results from the nominal welding characterise the capability of the inertia process. The results of each section were compared back to these with the aim of determining the effect of the enhanced functionality on the weld and the process.

4.4.1 Weld data

4.4.1.1 Weld curves

Parameter traces of the nominal IFW RFWCRP80-010 are shown in Figure 4-1.

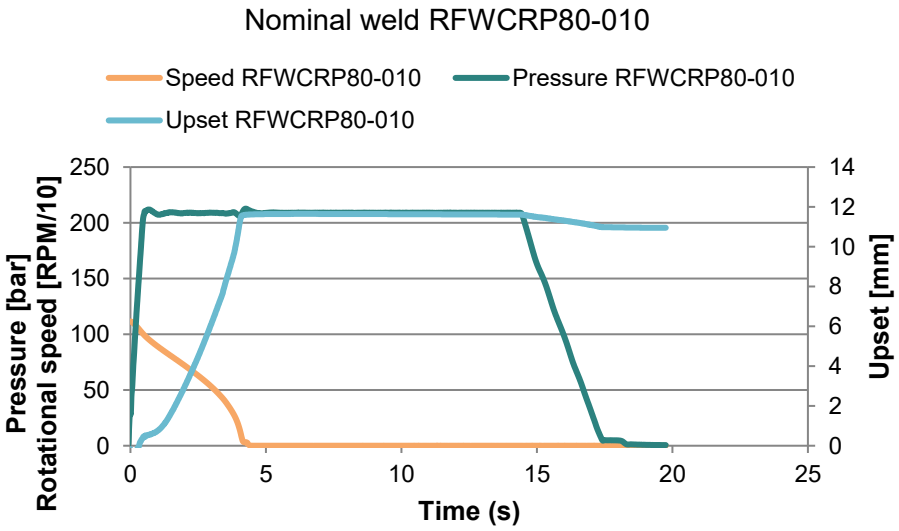


Figure 4-1: Weld curves from the weld RFWCRP80-010 for later comparison.

4.4.1.2 Upset measurement

The upset produced by the IFW nominal welds is displayed in Figure 4-2 and Table 4-2 .

The welds produced a three standard deviation of 0.35mm when measured in-process and 0.309mm when measured post process with a CMM. When comparing the two measurements the correlation is close to an ideal where both measurements are matched. The gradient of the line is 1.108 with an intercept at -1.038 showing the in-process measurement will be undervalued at low upset amounts but at higher values will over measure. The crossover is at 0.936mm when measured post process. The R^2 value suggests a good fit of the line.

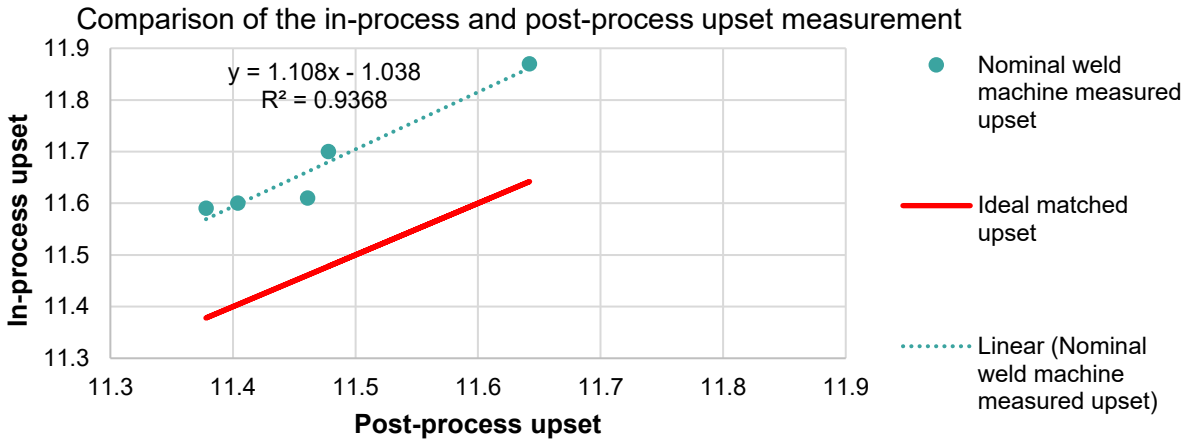


Figure 4-2: In-process vs post-process nominal weld upset measurements compared to a matched upset.

Variances in upset in a single pressure inertia weld could be attributed to a number of reasons, from energy losses in the machine system to changes in the material such as areas of variable hardness or yield strength for example. Variation in inertia friction welding can be used as a form of process control to identify sub-standard welds if the natural variation of the specific weld scenario is known Manufacturing Technology Inc (2012).

Table 4-2: Upset values for the nominal IFW welds RFWCRP80- 006-010 for comparison.

Comparison of nominal IFW weld upset measurements		
Weld number: RFWCRP80-	**In-process machine measured upset**	**Post-process cold measured upset**
	(mm)	**(mm)**
006	11.70	11.478
007	11.87	11.642
008	11.60	11.404
009	11.59	11.378
010	11.61	11.461
Average	**11.67**	**11.473**
Maximum Value	11.87	11.642
Minimum Value	11.59	11.378
Range	0.28	0.264
Standard Deviation	0.12	0.103
3 SD	0.35	0.309

4.4.2 Microstructural investigation

4.4.2.1 Micrograph images of IFW nominal weld RFWCRP80-010 microstructure

Weld 010 was chosen as the representative weld of the set owing to consistent results close to the average for each division. The macrograph (Figure 4-3) shows the cross section of the tubular weld wall. The joint appears vertically in the centre, with the bond line, recrystallised zone and TMAZ (Thermo-Mechanically Affected Zone) visible but faint.

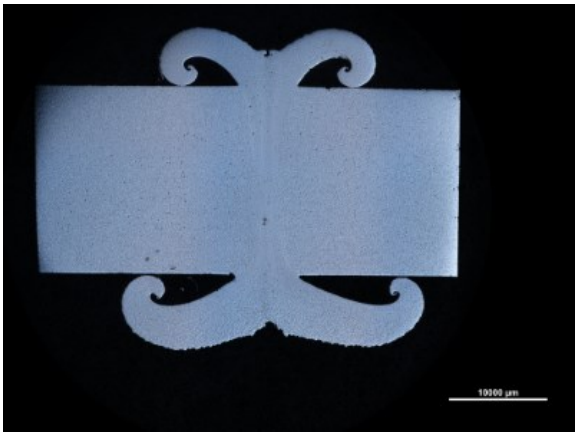
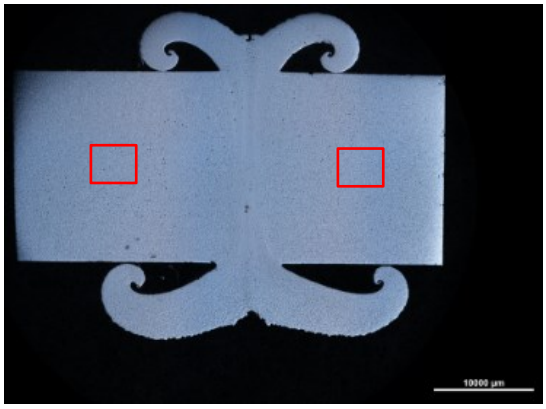


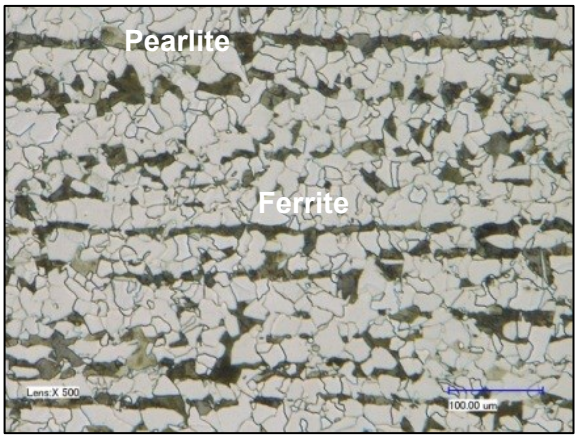
Figure 4-3: Macrograph of the weld intersection of the IFW nominal weld RFWCRP80-010.

Extending either side of the joint are the extruded flashes. The smaller cross section flash being on the outside diameter.

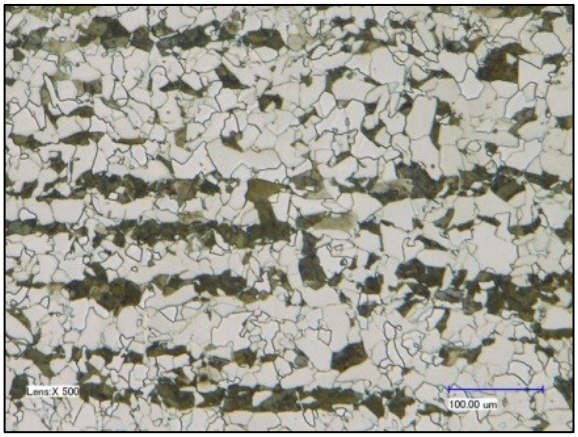
Figure 4-4 shows the parent material microstructure taken from areas far away from the weld zone. The rolling direction from the manufacture of the billets can clearly be seen as the aligned groupings of the dark pearlite grains among the light ferrite grains.



(a)



(b)



(c)

Figure 4-4: Etched optical micrographs of RFWCRP80-010: (a) the weld cross section (b& c) 500x magnification of the parent material. Micrograph location highlighted in red on the weld cross section, with labels on (b) to distinguish the ferrite and pearlite grains.

Figure 4-5 to Figure 4-7 shows the weld region including the transition to the TMAZ at the OD, centre, and ID. The lower magnification micrographs show the weld line with the transitions to the TMAZ on either side. The centre of the weld appears as a recrystallised region with fine microstructure of mixed bainite, pearlite and ferrite. The transition regions of the TMAZ are visible as the prior microstructure has not been fully obliterated and is still visible while also displaying recrystallised grains. This transition appears characteristic: matching those reviewed by M Maalekian (2007).

The TMAZ near the OD shows high amounts of deformation angled towards the OD with a highly recrystallised weld zone.

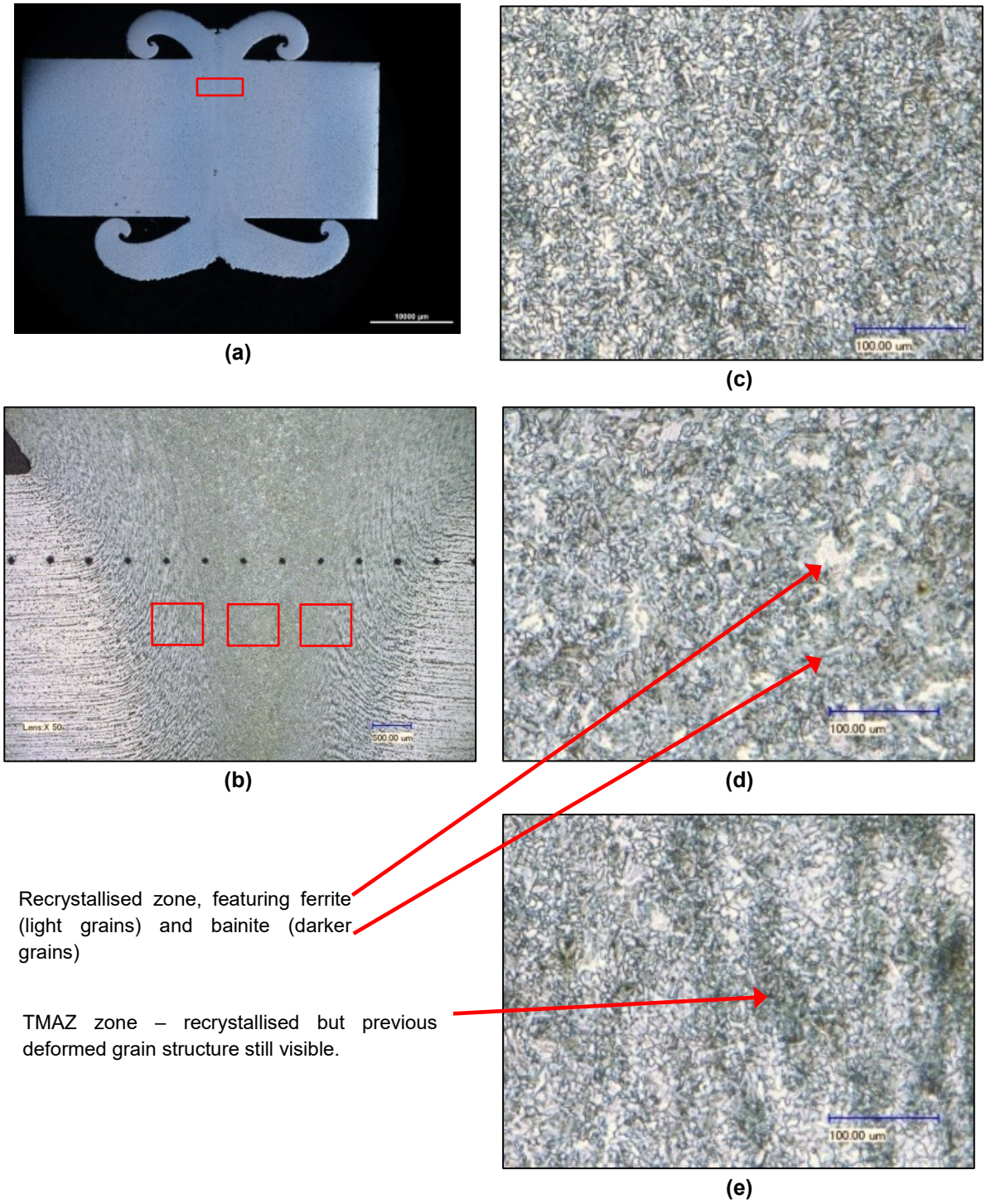


Figure 4-5: Etched optical micrographs of RFWCRP80-010: (a) the weld cross section, OD TMAZ with (b) at 50x magnification and (c-e) 500x magnification. Area of magnification highlighted in red.

The weld zone at the CL shows very high levels of recrystallisation evident by the small grain size. In Micrograph (b) at 50x magnification at the centre the TMAZ deformation direction can be seen to swap from the OD to the ID.

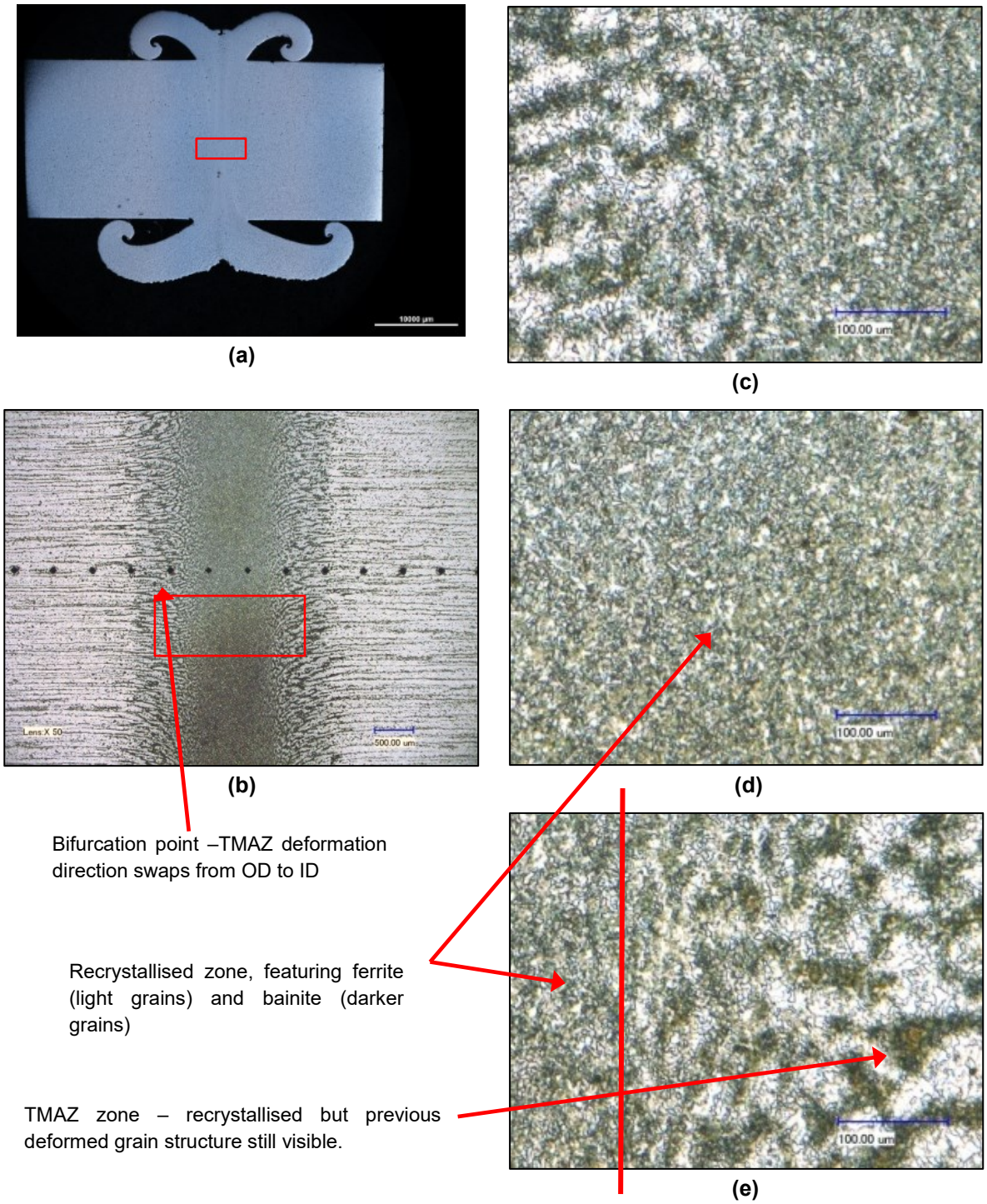
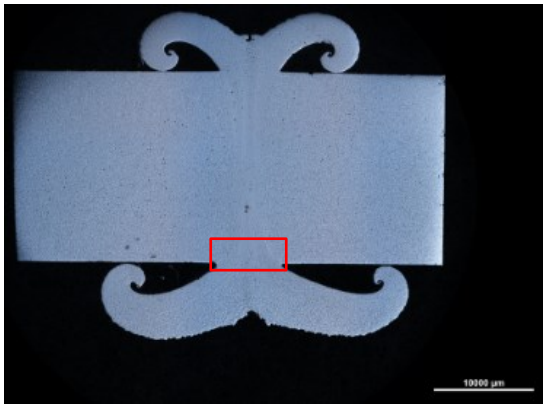
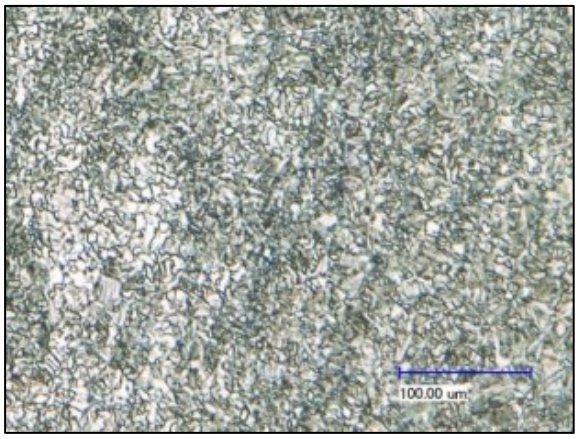


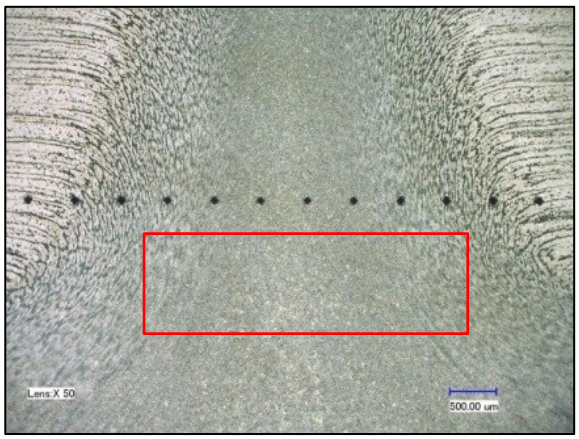
Figure 4-6: Etched optical micrographs of RFWCRP80-010: Centreline TMAZ with (a-c) at 50x magnification and (d-f) 500x magnification. Area of magnification highlighted in red.



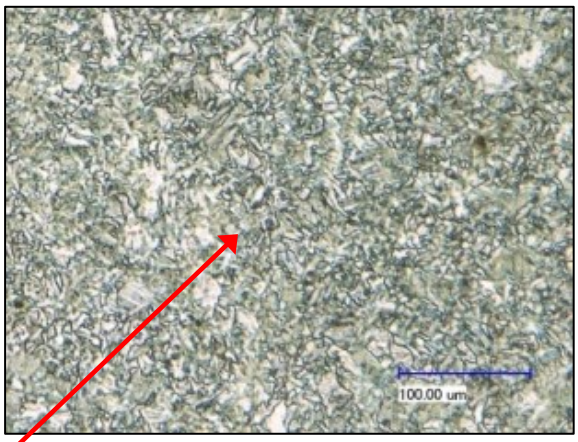
(a)



(c)

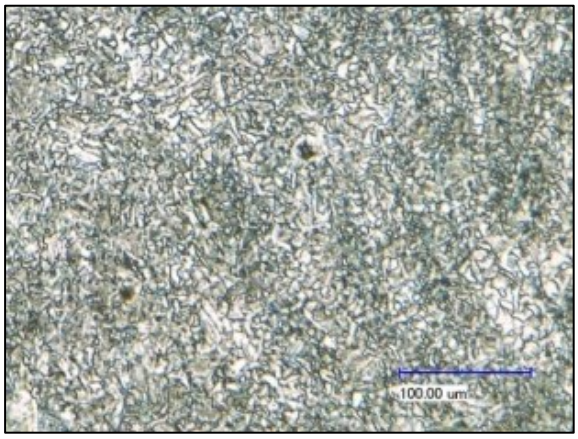


(b)



(d)

Weld zone grain structure displays larger grain size suggesting less recrystalisation compared to the centreline.



(e)

Figure 4-7: Etched optical micrographs of RFWCRP80-010: ID TMAZ with (a-c) at 50x magnification and (d-f) 500x magnification. Area of magnification highlighted in red.

4.4.2.2 Weld zone measurements

Table 4-3: Thermo-mechanically affected zone (TMAZ) width, bifurcation width / location and re-entrant notch (where a positive value is representative of a non-re-entrant notch) measurements taken from IFW nominal weld cross-sections (RFWCRP80- 006-010) for comparison.

Nominal IFW weld zone feature measurements							
Weld Number: RFWCRP80-	**TMAZ Width (mm)**			**Distance of Bifurcation Location from OD (mm)**	**Bifurcation Width (mm)**	**Depth of Re-entrant Notch Feature (mm)**	
	OD	**CL**	**ID**			**OD**	**ID**
006	4.64	2.37	4.69	9.48	2.47	3.39	4.37
007	4.19	2.45	4.16	9.22	2.37	3.46	4.86
008	4.11	2.38	4.55	9.40	2.36	3.44	4.47
009	4.16	2.41	4.14	9.29	2.32	3.31	4.65
010	4.15	2.41	4.36	9.39	2.33	3.61	4.62
Average	**4.25**	**2.40**	**4.38**	**9.36**	**2.37**	**3.44**	**4.59**
Maximum Value	4.64	2.45	4.69	9.48	2.47	3.61	4.86
Minimum Value	4.11	2.37	4.14	9.22	2.32	3.31	4.37
Range	0.53	0.08	0.54	0.26	0.15	0.3	0.49
Standard Deviation	0.22	0.03	0.24	0.10	0.06	0.11	0.18
3SD	0.66	0.09	0.71	0.31	0.18	0.34	0.55

4.4.2.3 Hardness testing

Hardness was shown to be greater at the centre of the weld corresponding with the smaller TMAZ width, indicating a faster cooling rate due to smaller amount of surrounding hotter material as seen by Duffin and Bahrani (1973). No difference was visible between the inside and outside diameter despite the larger cross section of flash on the inside diameter suggesting that in this scenario flash influence on the bond line cooling rate is minimal.

Table 4-4: Maximum OD, centreline and ID values for the IFW nominal weld cross-section (RFWCRP80-010) for comparison.

Nominal IFW weld zone hardness measurements			
Weld Number: RFWCRP80-	Maximum Hardness (Hv1)		
	Outer Diameter	Centreline	Inner Diameter
006	234.6	269.7	239.0
007	247.0	271.0	236.8
008	241.3	275.1	242.4
009	247.0	277.9	248.2
010	245.0	269.0	240.0
Average	243.0	272.5	241.3
Maximum Value	247.0	277.9	248.2
Minimum Value	234.6	269.0	236.8
Range	12.4	8.9	11.4
Standard Deviation	5.2	3.8	4.4
3 SD	15.7	11.4	13.1

4.4.3 Mechanical testing

4.4.3.1 Tensile testing

Through tensile testing it is confirmed that the microstructural changes present in the weld region increase the strength of the weld region compared to the parent material as all welds broke in the parent material. A situation also witnessed by others Ragu Nathan *et al.* (2015); Sathiya, Aravindan, and Noorul Haq (2007). Weld 007 has the smallest proof strength value along with being the furthest from the average, which combined with being the most upset weld could suggest a trend but in UTS, elongation and reduction in area it is not an outlier and matches other welds from the set. Weld 008 has a visibly higher elongation, Figure 4-9.

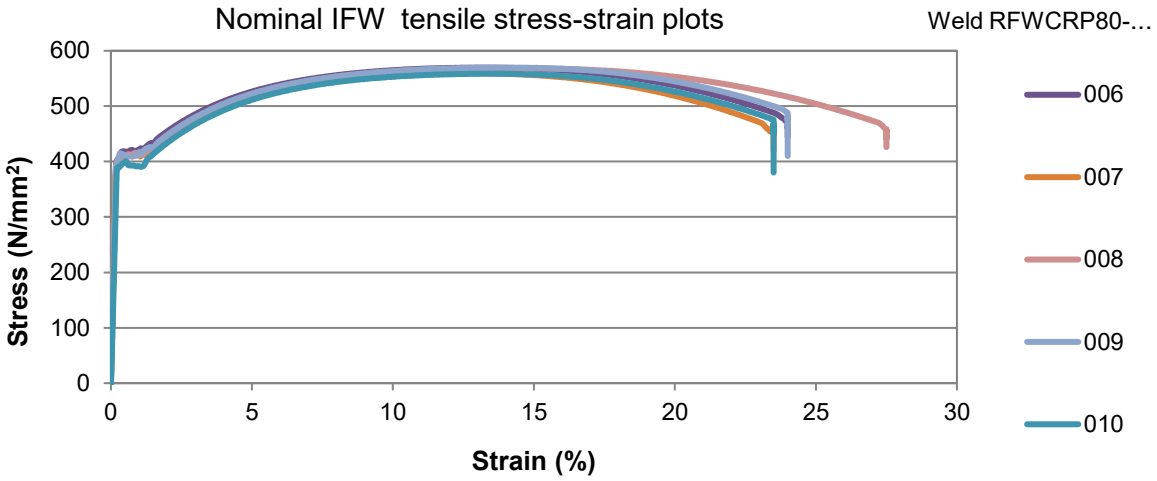


Figure 4-9: Stress strain data for the nominal weld set.

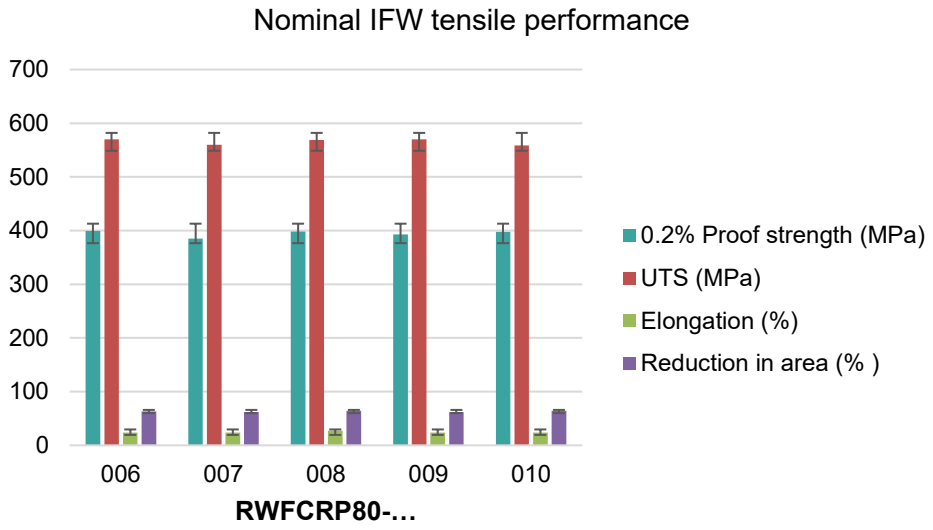


Figure 4-8: IFW nominal weld cycle tensile test results (RFWCRP80- 006-010)

4.5 Torque modulation inertia results

The torque modulation results are shown here, followed by an analysis to compare the against the pressure modulated and orientation control welds.

4.5.1 Weld data

4.5.1.1 Weld records

In process weld data has been used to compare the upset generation from each weld cycle. Figure 4-10 compares an example torque modulated inertia weld with the nominal profile weld.

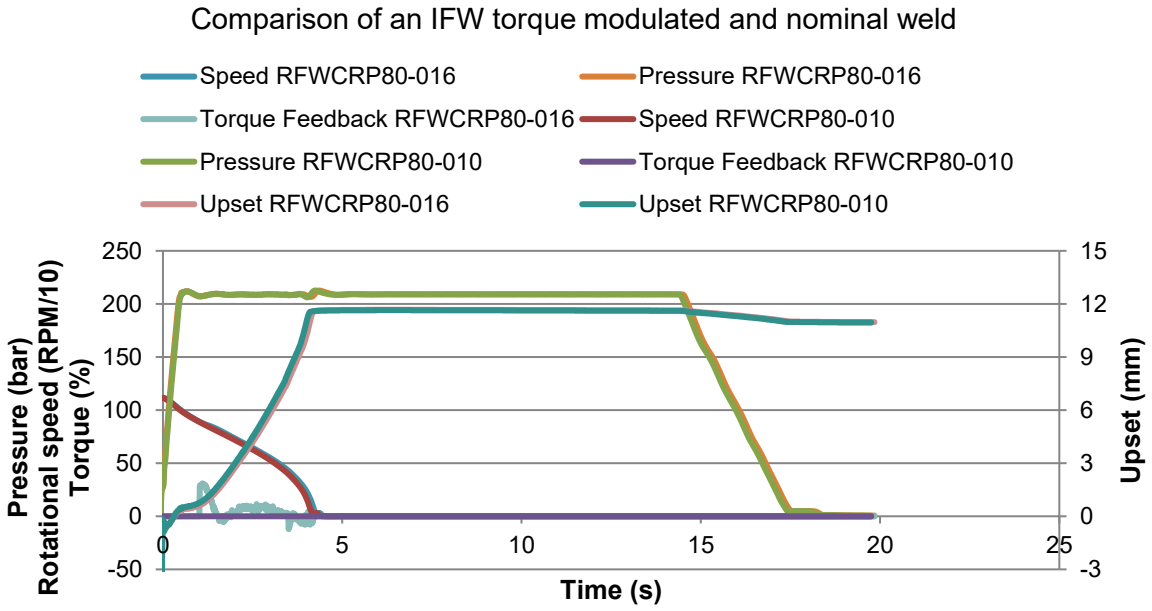


Figure 4-10: Comparison of torque modulated weld RFWCRP80-016 against the profile weld RFWCRP80-010.

Figure 4-11 shows the overlapped upset and torque modulation amounts of the modulated welds and nominal weld cycles. The torque modulation initiated when the weld reached 0.6mm of upset. As can be seen this occurs between 922 and 889rpm suggesting that the first contact and initial conditioning between parts does not transfer the same energy into the weld each time. Various amounts of positive and negative torque inputs were then observed which produced closely matching upset curves.

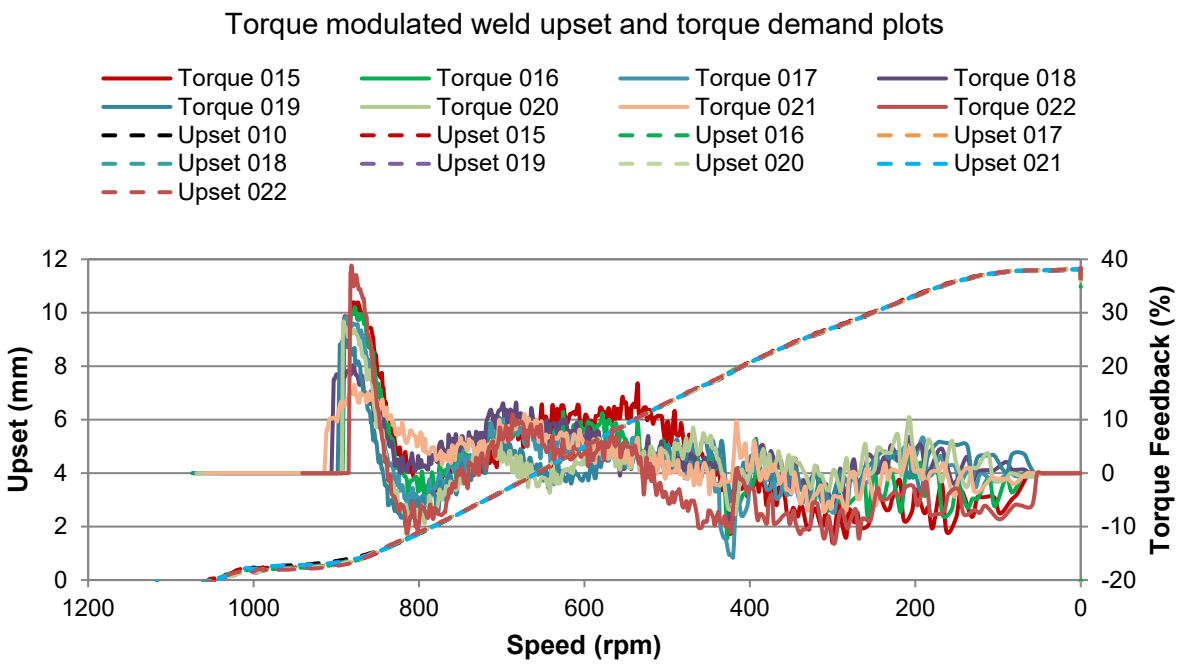


Figure 4-11: IFW torque modulation % feedback and upset weld record of RFWCRP80-015-022 and weld upset trace of RFWCRP80-010 for comparison with respect to spindle rotational speed.

4.5.1.2 Upset measurement

Presented are the two measurement methods of the upset from the IFW torque modulated welds compared to the corresponding measurement data from the nominal IFW welds. The in-process measurement data shows a greater reduction in variability than the post-process measurements. However, it is only weld RFWCRP80-021 that causes the post-process variability to be so great.

Figure 4-12 shows the comparison of the upset measurements. The reduction in post-process CMM measurements is evident by the reduction in horizontal spread with most welds over upsetting compared to the profile. The lack of vertical spread highlights the reduction of in-process upset variability. Both the nominal and torque modulated welds show a greater upset when measured at the end of the weld compared with a measurement taken over 24hrs later in a temperature controlled CMM lab. Further comparison is in Figure 4-13 and Table 4-5.

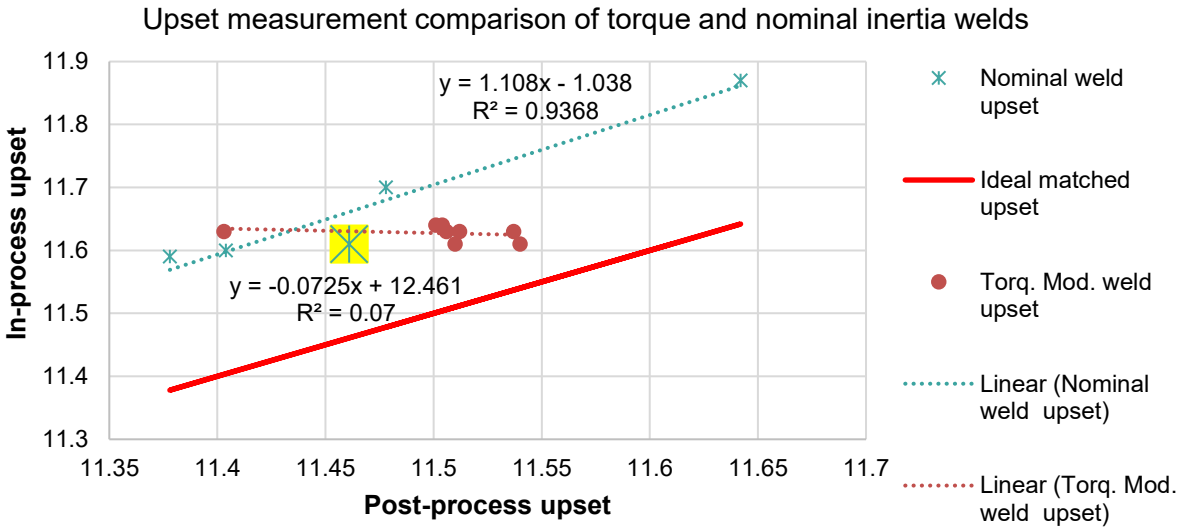
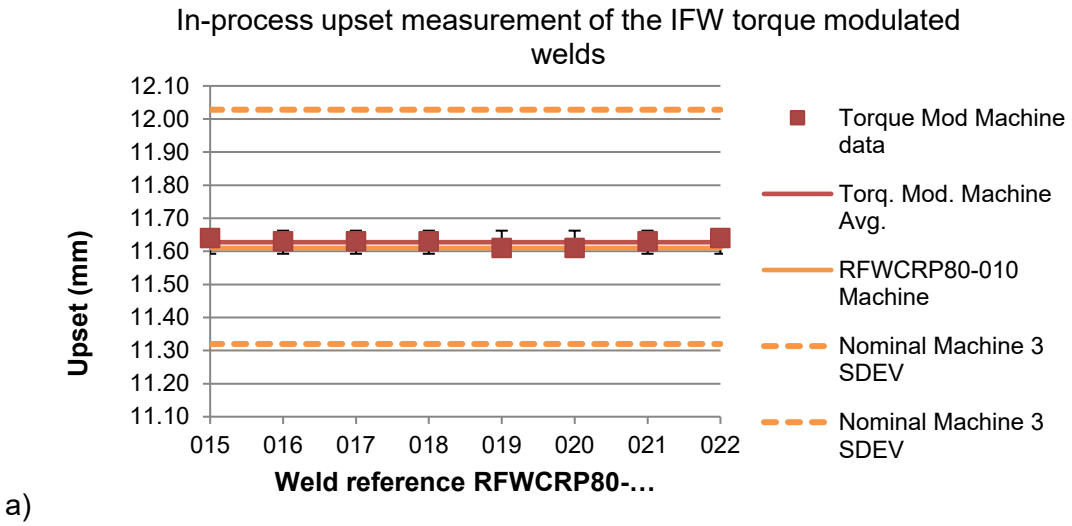
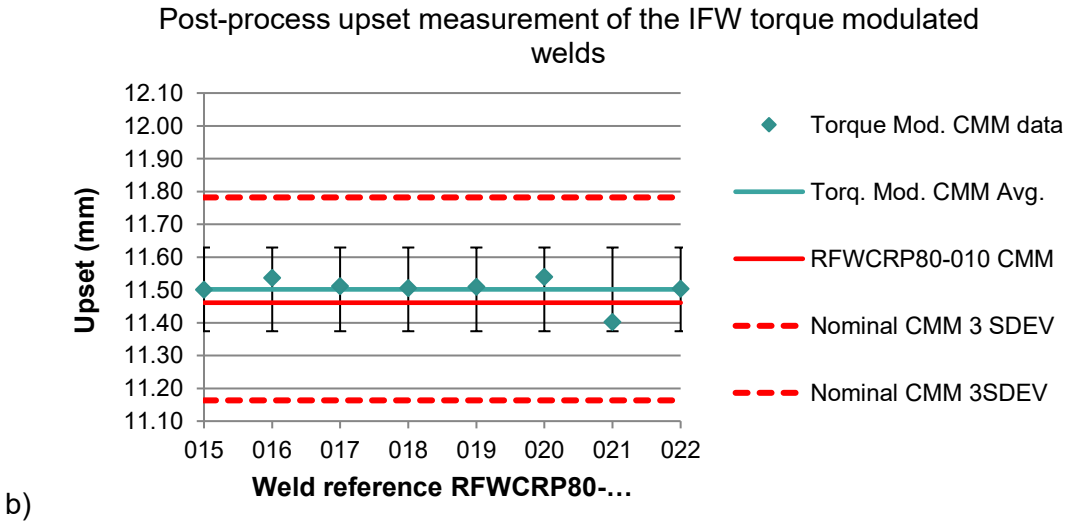


Figure 4-12: The in-process and post-process upset measurement comparison of the torque modulated and nominal inertia welds. The profile weld is highlighted with the larger star marker and yellow background.



a)



b)

Figure 4-13: Graphs to show A) Machine and B) Cold measured upset values for torque modulated welds (RFWCRP80-015-022) and nominal IFW upset values (RFWCRP80-010) with three standard deviations for comparison.

Table 4-5: Upset in-process and post-process measurements for the torque modulated weld set compared to the nominal weld RFWCRP80-010.

Upset measurement comparison of the IFW torque modulated welds				
Weld Number: RFWCRP80-	**In-process Machine Measured Upset**	**Machine Deviation from Nominal**	**Post-process Cold Measured Upset**	**Cold Measured Deviation from Nominal**
	(mm)	**(mm)**	**(mm)**	**(mm)**
015	11.64	0.03	11.501	0.040
016	11.63	0.02	11.537	0.076
017	11.63	0.02	11.512	0.051
018	11.63	0.02	11.506	0.045
019	11.61	0.00	11.510	0.049
020	11.61	0.00	11.540	0.079
021	11.63	0.02	11.403	0.058
022	11.64	0.03	11.504	0.043
Average	**11.63**	**0.02**	**11.502**	**0.055**
Maximum Value	11.64	0.03	11.540	0.079
Minimum Value	11.61	0.00	11.403	0.040
Range	0.03	0.03	0.137	0.039
Standard Deviation	0.01	0.01	0.043	0.015
3SD	0.03	0.03	0.128	0.045

4.5.2 Weld analysis

4.5.2.1 Weld record analysis

The upset curves for the torque modulated welds were typical and representative to the nominal IFW profile weld. The curves only show minor variation from the profile weld. As the torque value oscillations reduce as the weld progresses this indicates the gain factors are suitable Manufacturing Technology Inc (2012).

Figure 4-11 shows the overlay of the weld upset traces with respect to spindle speed. The torque modulation input effect is clearly visible on the upset curves due to the lack of variability between them.

The torque input can be seen to change in line with the amount of upset error between the torque modulated upset and profile upset as the amount of upset error increases a proportional

torque input is applied to the motor to bring the torque modulated weld upset to the same value as the profile upset. As the torque modulated upset increases above that of the profile weld a negative torque is applied to slow the spindle, while a positive torque is applied if the current upset falls below the profile upset as defined by Manufacturing Technology Inc (2012, 2017d).

Using an upset measurement device that measures from the backup of the fixture to the backup of the spindle could further improve the ability of the modulation and therefore the accuracy of the process.

4.5.2.2 Upset measurement analysis

The M125T RFW machine measured upset and cold measured upset values of the torque modulated welded parts (Figure 4-13) show that all welds produced upset values within three standard deviations of the profile weld part. Both measurement methods show a marked decrease in the upset variability of the torque modulation process compared to the nominal IFW welds, with a smaller spread of the three standard deviations around the average values. The machine measured three standard deviation values reduced from 0.35mm down to 0.03mm, a reduction of 91%, while the CMM measured three standard deviations reduced from 0.309mm down to 0.128mm, a reduction of 58% compared with the nominal weld set. This would have been further reduced to 0.044mm without the inclusion of the anomaly of RFWCRP80-021 in the post-process cold measured data set. RFWCRP80-021 achieved an upset of 10.403mm which was 0.058mm below the profile weld. All other welds recorded upsets greater than the profile weld. The maximum deviation from the profile upset was 0.03mm measured on the machine and 0.079mm cold measured with the CMM.

4.5.3 Conclusions

Initially eight inertia friction welds utilising torque modulation to a profile weld (RFWCRP80-010) were undertaken. The torque modulated IFW welds were compared against the average

IFW welds to investigate how this enhanced functionality mode would alter the weld record and upset repeatability.

CMM measured and in-process measured upset values for the welds showed a reduction in variation compared to the nominal weld set. In-process measured variation was reduced from 0.28mm to 0.03mm and CMM variation reduced from 0.264mm to 0.137mm, with potential for a greater reduction of the CMM results.

The torque modulated welds undertaken within this study show a greatly reduced variation of the upset due to the modulated parameters from both the machine scale and post weld CMM data.

4.6 Pressure modulation inertia

4.6.1 Weld data

4.6.1.1 Weld records

Figure 4-14 & Table 4-6 show the difference between a set of spindle run down tests when the UMD is in contact and not in contact. Figure 4-15 shows an overlap of a modulated weld and the nominal weld cycle aligned at the point of part contact. Figure 4-16 shows how the pressure modulation affected the upset generation during the weld with respect to spindle speed. The start of modulation at 2mm of upset is clearly visible as the separation in the target pressure lines.

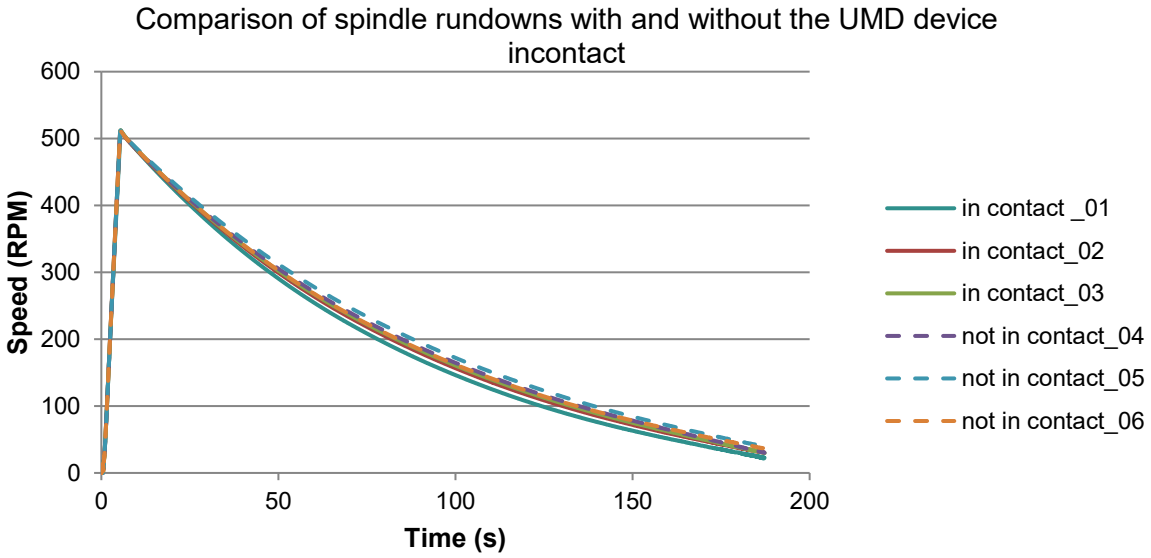


Figure 4-14: A series of spindle run down tests to compare the effect of the upset measurement device probe being in contact and not in contact.

Table 4-6: Table of final spindle speeds at the data acquisition cut off point.

Spindle run down tests comparing the impact of the UMD device			
Test	**Probe**	**Final spindle speed (rpm)**	**Average Final Spindle Speed (rpm)**
1	in contact	22.76	27.74
2	in contact	30.86	
3	in contact	29.60	
4	not in contact	30.19	35.16
5	not in contact	38.91	
6	not in contact	36.37	

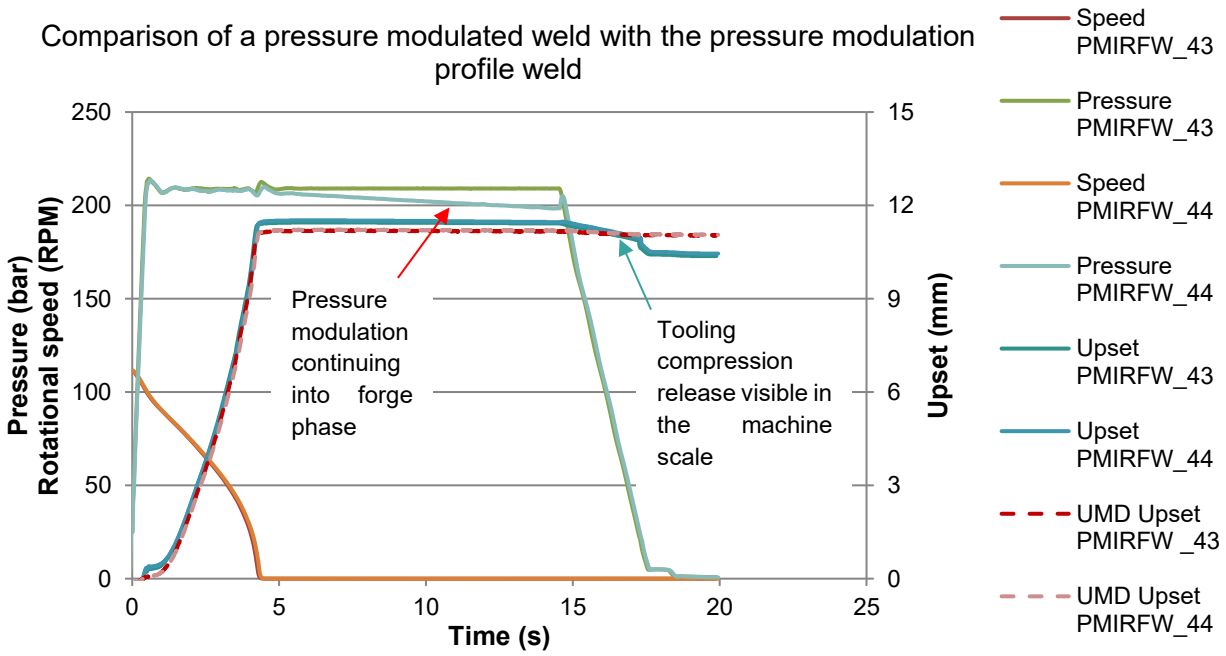


Figure 4-15: Weld cycle comparison of the profile weld (RFWCRP80-043) to a pressure modulated weld (RFWCRP80-044).

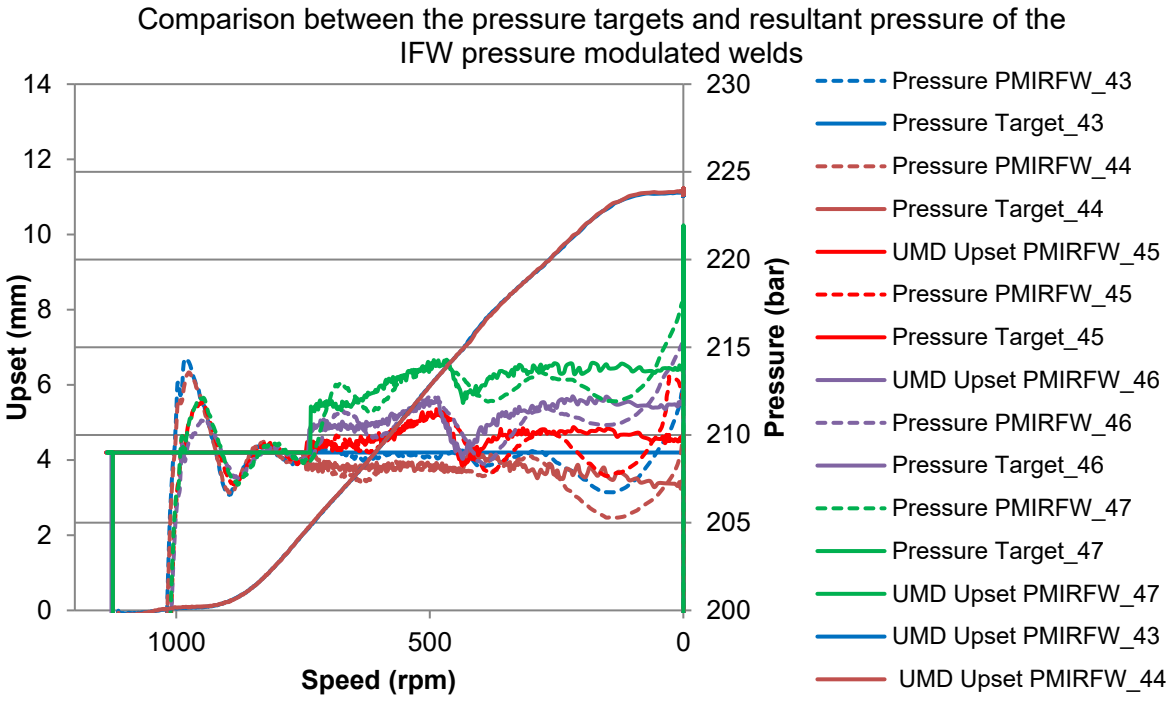


Figure 4-16: IFW profile and pressure modulated weld cycle upset curves (RFWCRP80- 043, 044-047) with respect to spindle rotational speed. Upset tracing from the bottom left to top right, pressure traces horizontally.

4.6.1.2 Upset measurement results

Table 4-7 details the upset amounts from the pressure modulated. Machine measured upset is calculated from pre- and post-weld slide positions of the fixture during the cycle. The CMM measurements are calculated from the pre-weld part heights and the post weld component height once it had cooled. The CMM measurements were taken after the parts had sat in the temperature-controlled lab for a minimum of 24hrs to allow them to stabilise. Figure 4-17shows the reduction in the variability of the process when using pressure modulation, both from the machine measured data and the CMM data. Figure 4-18 displays the correlation between the UMD measurements and machine measured upset measurements against the cold measured upset. A matched upset line was also included where the in-process measured upset would equal the post-process cold measured upset for comparison.

Table 4-7: Upset values for the profile weld RFWCRP80-043 and pressure modulated IFW welds RFWCRP80-044 to 047

In process and post-process upset measurement comparison and deviation to the profile weld						
Weld Number: RFWCRP80-	**Machine Measured Upset**	**Machine Deviation from Profile**	**UMD Measured Upset**	**UMD Deviation From Profile**	**Cold Measured Upset**	**Cold Measured Deviation from Profile**
	(mm)	**(mm)**	**(mm)**	**(mm)**	**(mm)**	**(mm)**
Profile						
43	11.42		11.066		11.383	
Modulated Welds						
44	11.46	0.04	11.113	0.047	11.450	0.067
45	11.44	0.02	11.074	0.008	11.383	0.000
46	11.42	0.00	11.020	-0.046	11.327	-0.056
47	11.44	0.02	11.020	-0.046	11.327	-0.056
Average	**11.44**	**0.02**	**11.057**	**-0.009**	**11.372**	**-0.011**
Maximum Value	11.46	0.04	11.113	0.047	11.450	0.067
Minimum Value	11.42	0.00	11.020	-0.046	11.327	-0.056
Range	0.04	0.04	0.093	0.093	0.123	0.123
Standard Deviation	0.02	0.02	0.045	0.045	0.058	0.058
3 SD	0.05	0.05	0.135	0.135	0.175	0.175

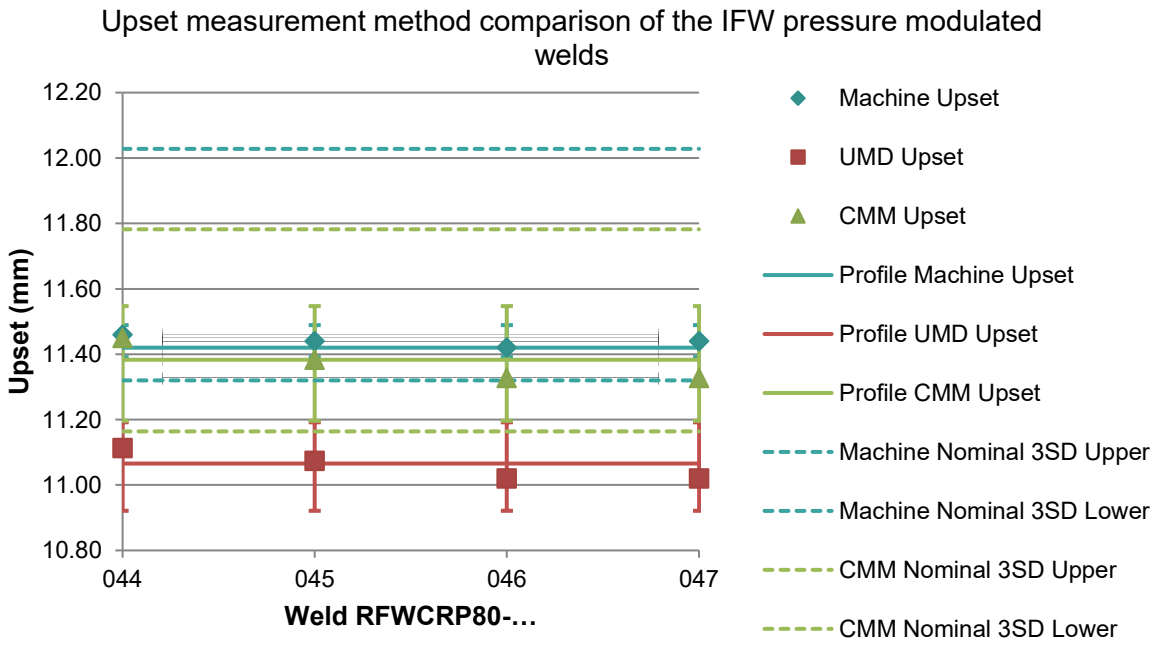


Figure 4-17: Machine, Cold measured and Upset Measurement Device upset values for pressure modulated welds (RFWCRP -044 to 047) Included are three standard deviation error bars and the nominal IFW upset three standard deviation limits (RFWCRP80 – 006 to 010).

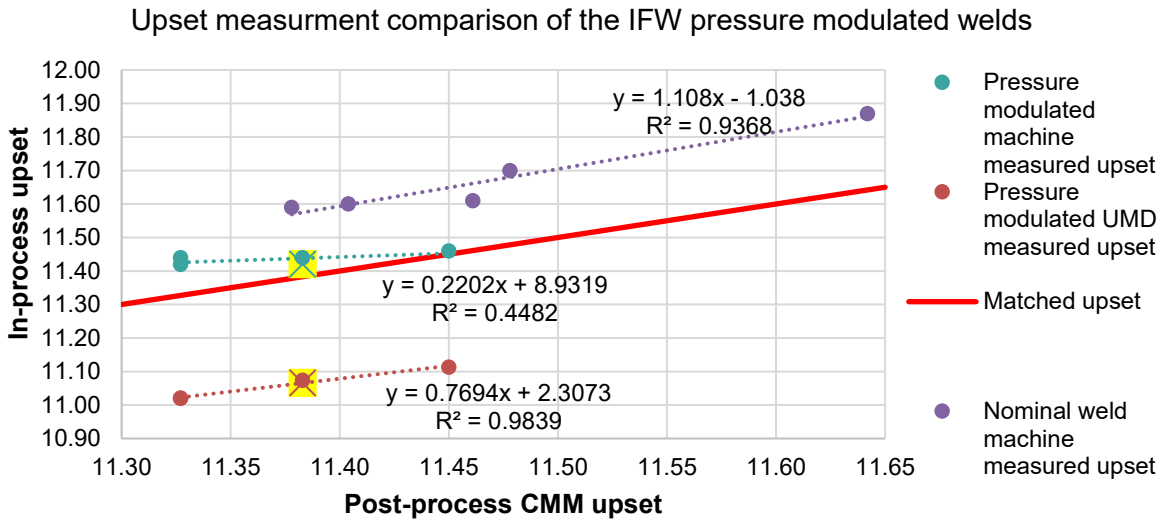


Figure 4-18 Error! Reference source not found.**: A comparison of the machine and UMD measured upset when referenced against the cold measured upset of the profile and pressure modulated welds. Lines of best fit have been applied with their R^2 number shown. A hypothetical line of matched upset has been included for comparison where the in-process upset is equal in value to the post-process CMM cold upset. The nominal welds have been included for comparison. For easy identification the profile weld is a cross marker with a yellow background.**

4.6.2 Weld analysis

4.6.2.1 Weld record analysis

The run-down tests (Table 4-6 and Figure 4-14) with the UMD in contact and not in contact indicate that a small amount of energy is extracted from the flywheel system when the UMD is in use. It is possible that at the higher pressures experienced during the welding cycle that the friction of the in-contact UMD is enough of an energy extractor to explain the lower-than-average upset produced by the profile weld compared to the nominal welds. However, as the profile weld upset is within the natural variation seen in the nominal welds it is also possible that the low upset is not due to the UMD and is natural. The UMD is required to accurately measure the upset of the weld in order to remove inaccuracies from the tooling due to varying compression and flex created by the modulated pressure changes (Manufacturing Technology Inc, 2012, 2017c).

The upset curves for the pressure modulated welds RFWCRP80- 044-047 were typical and representative of the profile IFW weld RFWCRP80-043 (Figure 4-15). The upset curves only show minor variation from the profile weld. This is expected as the machine modulates the pressure to achieve these curves. The pressure input can be seen to change in line with the amount of upset error between the current upset and profile upset. As the amount of upset error increases a proportional counteracting pressure input is applied to the ram to bring the current upset to the same value as the profile upset (Figure 4-16). As the current upset rises above that of the profile weld a reduction in pressure is applied to slow the rate of increase of upset, while an increase in pressure is applied if the current upset falls below the profile upset. The parameters for the rotating phase of the modulation appear to be effective.

It can also be seen that the modulation continues into the forge phase. The effectiveness of the modulation during this phase appears to be limited. During welds 044, 046 and 047 the pressure continues to change at a steady rate attempting to change the amount of upset reached by the end of this stage. If modulation were effective during this stage a return towards nominal pressure would be visible as the upset approached the profile value. Higher modulation parameters during this phase potentially could make it effective. If the parameters were set high enough that a suitable change in pressure resulted in a change in upset whilst the material was still hot enough then a greater accuracy could be achieved, though this may be more effective when greater pressure is required rather than less. However, there is the risk that the pressure could continue to rise or lower dramatically thereby fundamentally changing the dwell period of the cycle possibly affecting the resulting microstructure whilst not having an impact on the upset. However, Tumuluru (1984) suggests that pressure influences microstructure far less than rotational speed or inertia when welding low alloy steels.

Tooling compression can be seen when the pressure is applied and removed by comparing the upset results from the UMD and the machine. The UMD does not appear to be affected by the changes in pressure in the same magnitude as the machine slide measurement device.

4.6.2.2 Upset measurement analysis

The machine measured upset and cold measured upset values of the pressure modulated welded parts (Table 4-7 and Figure 4-13) show that all welds produced upset values within three standard deviations of the profile welded part (RFWCRP80-043) (Table 4-7). Both measurement methods show a marked decrease in the variability of the pressure modulated IFW process with a much-reduced spread of the three standard deviations around the average values when compared to standard IFW welds. For the machine measured values this reduced from 0.35mm down to 0.05mm, 14.3% of the original variation. While the CMM measured three standard deviations reduced from 0.309mm down to 0.175mm, a 56.6% of the nominal weld set variation. The Upset Measurement Device (UMD) controlling the modulation measured three standard deviations of 0.135mm. The maximum deviation from the profile upset was 0.04mm measured on the machine and 0.067mm cold measured with the CMM. The UMD measured a maximum deviation of 0.047mm. Overall the UMD shows a stronger correlation to the CMM results than the machine measured results indicating the effectiveness of the UMD.

In Figure 4-18 the final in-process machine measured and UMD upset measurements are compared to the post process cold upset measurements. The higher R^2 value of the UMD line shows less variation indicating a more consistent measurement. The gradient is much closer to 1, the value of a line where the upsets have matched. The UMD gradient being 0.7694 vs the machine measured gradient of 0.2202. This means that at values further from the measurement's interception with the ideal line the UMD would give less variation. However, of the upsets reached the machine results have less direct variation to the matched line. The UMD also under-measures the upset when compared to the CMM values. This suggests either the UMD needs further calibration or the weld is expanding upon cooling. It is known that the transition from austenite to martensite in steel welds can reduce the hoop residual stresses found in the weld due to the volumetric lattice expansion (C. Bennett *et al.*, 2013), however in

the nominal welds no martensite was seen, suggesting the UMD needs some further calibration.

4.6.3 Conclusions

Initially one profile inertia friction weld was conducted. Four welds were produced modulated to the profile weld to investigate how this enhanced functionality mode would alter the weld record and upset repeatability.

The four pressure-modulated IFW welds were compared against the average IFW welds (RFWCRP80 - 006 to 010) from the nominal welds and specifically their own profile weld (RFWCRP80 - 043). The findings from this investigation were compared to within three standard deviations of the nominal weld findings, with the following conclusions:

1. Cold measured and machine measured upset values for the welds showed a reduction in variation compared to the nominal weld set. Machine variation was down from 0.35mm to 0.05mm and CMM variation down from 0.309mm to 0.175mm
2. The separate UMD upset measurements showed a stronger correlation to the CMM measured upset than the machine measured upset and showed reduced impact from tooling flex. However, it appears to under-measure the upset produced suggesting further calibration is necessary.

The welds RFWCRP80-044 to 047 show a greatly reduced variation of the upset due to the modulated parameters from both the machine scale and post weld CMM data.

4.7 Orientation control inertia

4.7.1 Weld data

The loading accuracy and initial position of the components has an impact upon the orientation repeatability. Results of the pre-process orientation are included ahead of the weld data.

4.7.1.1 Pre-process orientation

Table 4-8 and Figure 4-19 show the variation in the spindle test, prior to part loading and the effect of reducing the spindle orient speed.

Table 4-8: Orient spindle tests at 30 and 5rpm detailing the accuracy of the machine for part loading.

Spindle orient position comparisons								
Orient speed (rpm)	**30**			**Orient speed (rpm)**	**5**			
Orient aim	**176**			**Orient aim**	**176**		**Results without no. 2**	
Repeat	**Position**	**Deviation from aim**		**Repeat**	**Position**	**Deviation from aim**	**Position**	**Deviation from aim**
1	176.17	0.17		**1**	176.43	0.43	176.43	0.43
2	176.58	0.58		**2**	175.19	-0.81	N/A	
3	175.3	-0.7		**3**	176.42	0.42	176.42	0.42
4	176.66	0.66		**4**	176.42	0.42	176.42	0.42
5	175.84	-0.16		**5**	176.4	0.4	176.4	0.4
6	175.66	-0.34		**6**	176.48	0.48	176.48	0.48
7	175.8	-0.2		**7**	176.56	0.56	176.56	0.56
8	176.41	0.41		**8**	176.55	0.55	176.55	0.55
9	176.48	0.48		**9**	176.18	0.18	176.18	0.18
10	175.94	-0.06		**10**	176.45	0.45	176.45	0.45
Average	**176.08**	**0.08**		**Average**	**176.31**	**0.31**	**176.43**	**0.43**
Max	176.66	0.66		**Max**	176.56	0.56	176.56	0.56
Min	175.3	-0.7		**Min**	175.19	-0.81	176.18	0.18
Range	1.36	1.36		**Range**	1.37	1.37	0.38	0.38
Standard deviation	0.45	0.45		**Standard deviation**	0.41	0.41	0.11	0.11
3 SD	1.34	1.34		**3 SD**	1.22	1.22	0.33	0.33

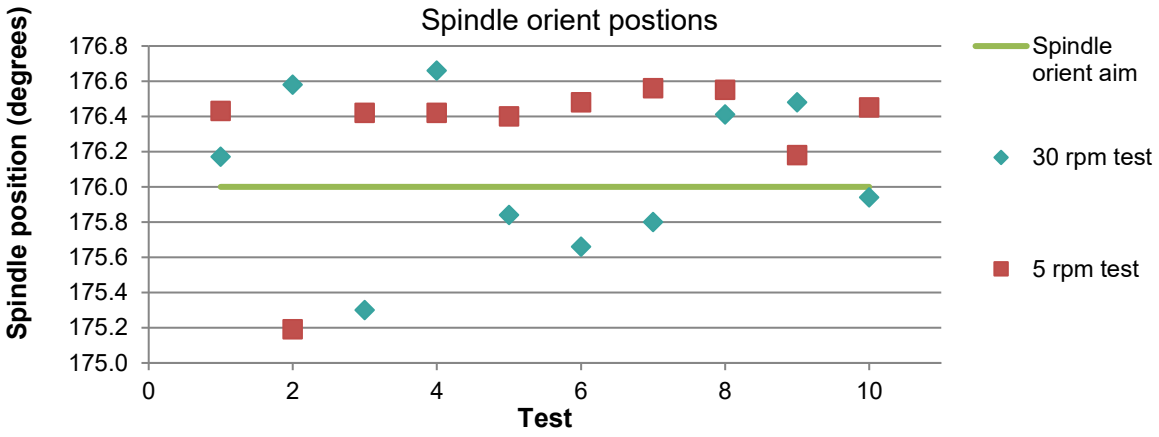
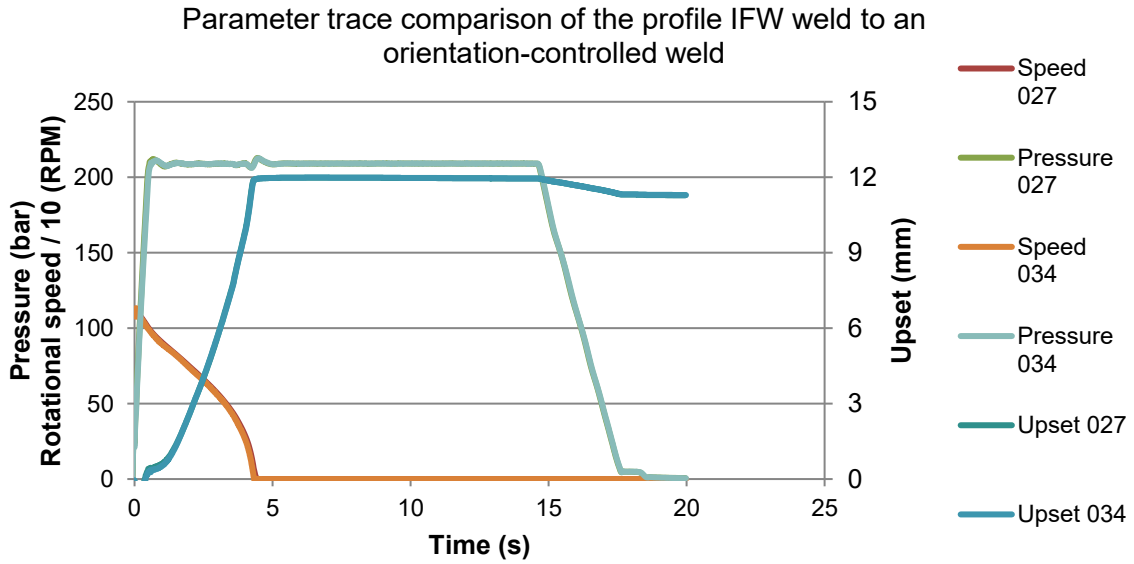


Figure 4-19: Plot showing the final spindle orientation for the pre-welding spindle tests, as measured by the RFW machine, including the target orientation.

4.7.1.2 Weld records

Figure 4-20 shows a comparison of the weld curves from an orientation-controlled weld (RFWCRP80-034) compared to the profile weld (RFWCRP80- 027). Following is the monitored angular spindle position of the orientation-controlled weld (RFWCRP80-034) compared with the targeted spindle position (taken from the profile weld).



--

Figure 4-20: Weld cycle properties for the IFW profile weld (RFWCRP80- 027) and orientation-controlled weld RFWCRP80- 034

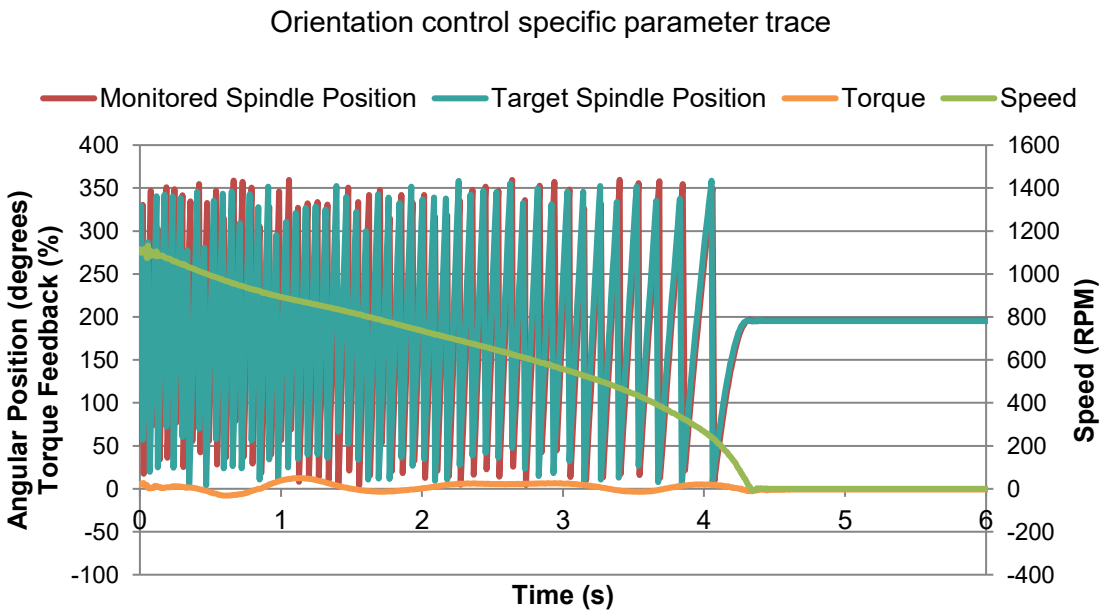


Figure 4-21: Spindle position, motor torque and speed data for orientation-controlled weld RFWCRP80-034, from part contact.

4.7.1.3 Orientation measurement

Table 4-9 and Figure 4-22 show the spindle orientation final position. Figure 4-23 shows the variation between the machine and CMM measurement methods.

Table 4-9: Spindle position data for the IFW profile weld RFWCRP80–027, and the orientation controlled IFW welds RFWCRP80-034, 036 & 037

Orientation measurement comparison				
Weld Number: RFWCRP80-	**Final Spindle Position**	**Machine Data Angular Offset**	**CMM Measured Offset**	**Optivision Angular Offset**
	(degrees)	**(degrees)**	**(degrees)**	**(degrees)**
Profile				
027	195.30	-	-	-
OC Welds				
034	196.16	0.86	0.74	1.33
036	194.95	-0.35	1.85	1.84
037	195.69	0.39	-0.57	-0.46
Average	**195.60**	**0.30**	**0.67**	**0.90**
Maximum Value	196.16	0.86	1.85	1.84
Minimum Value	194.95	-0.35	-0.57	-0.46
Range	1.21	1.21	2.42	2.30
Standard Deviation	0.61	0.61	1.21	1.21
3 SD	1.83	1.83	3.64	3.62

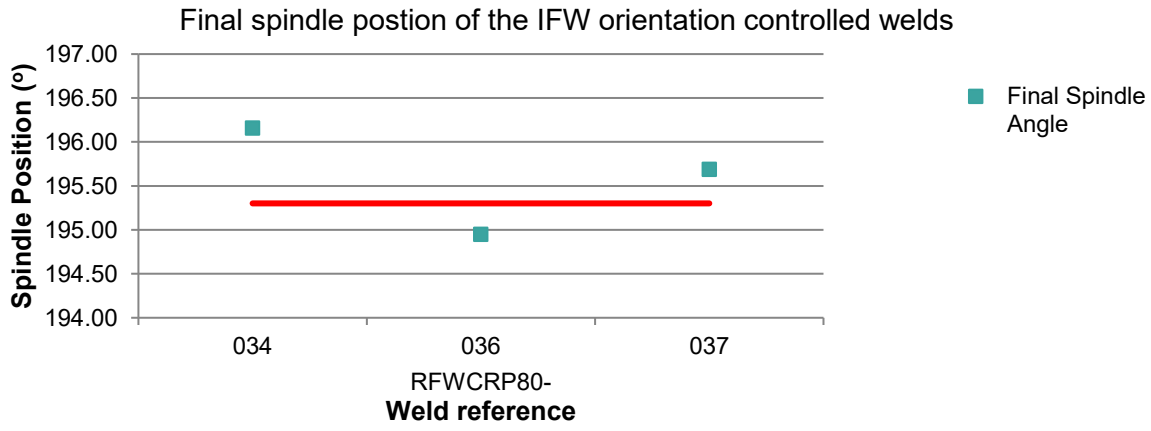


Figure 4-22: Plot showing the final spindle orientation for the orientation-controlled welds RFWCRP80- 034, 036 & 037, as measured by the RFW machine, including a line showing the profile weld orientation that was used as a target.

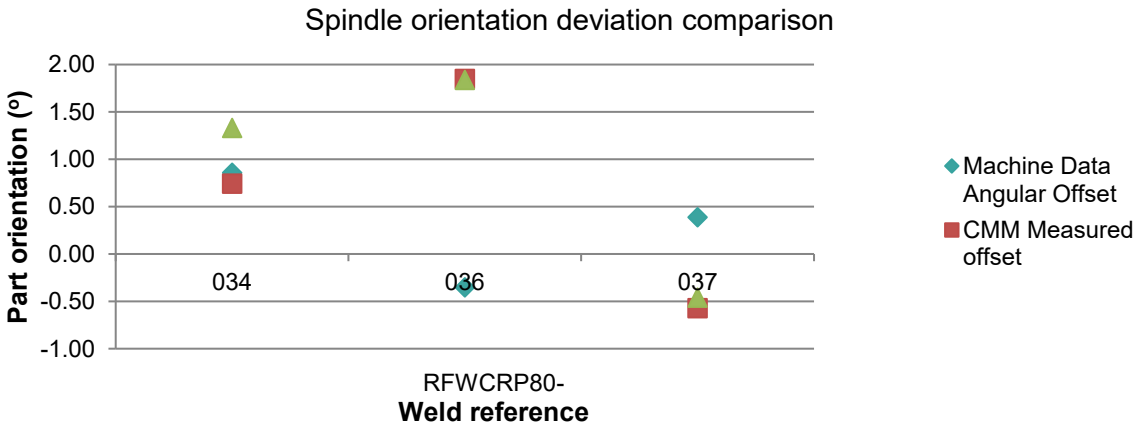


Figure 4-23: Plot showing the offset from the profile spindle position for the orientation-controlled welds RFWCRP80- 034, 036 & 037, as recorded by three different measurement systems in each instance.

4.7.1.4 Upset measurement

Figure 4-24 displays the trends of the nominal weld upset and the orientation-controlled upsets. In the centre is the profile weld. The profile has produced more upset than the nominal welds and the orientation-controlled welds have produced even greater upset. All welds follow the same rough trend of the in-process machine measured upset being ~0.2mm greater than the CMM post-process measurement.

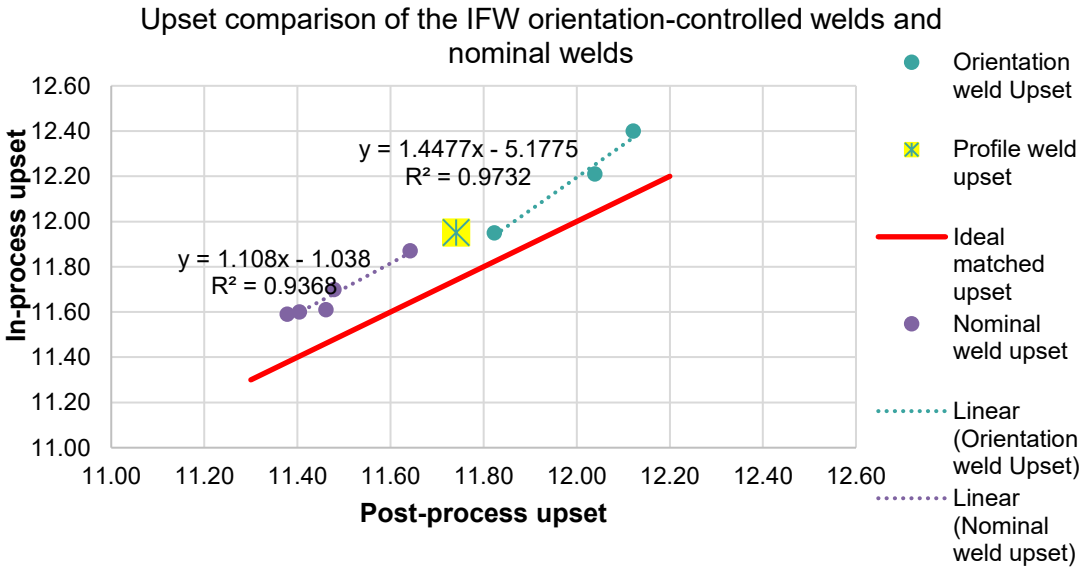


Figure 4-24: Comparison of the in-process and post-process upset measurements of the orientation-controlled welds, the profile weld and the nominal welds

Table 4-10 and Figure 4-25 show how the standard deviation of the results varies between the nominal weld set upset and the orientation controlled upset values.

Table 4-10: Upset values for the IFW profile weld RFWCRP80 - 027, and the orientation controlled IFW welds RFWCRP80 - 034, 036 & 037

Upset measurement comparison and deviations of the IFW orientation-controlled welds				
Weld Number: RFWCRP80-	**Machine Measured Upset**	**Machine Deviation from Profile**	**Cold Measured Upset**	**Cold Measured Deviation from Profile**
	(mm)	**(mm)**	**(mm)**	**(mm)**
Profile				
027	**11.95**		**11.741**	
Modulated Welds				
034	11.95	0.00	11.823	0.08
036	12.40	0.45	12.121	0.38
037	12.21	0.26	12.039	0.30
Average	**12.19**	**0.24**	**11.994**	**0.25**
Maximum Value	12.40	0.45	12.121	0.38
Minimum Value	11.95	0.00	11.823	0.08
Range	0.45	0.45	0.298	0.30
Standard Deviation	0.23	0.23	0.154	0.15
3 SD	0.68	0.68	0.462	0.46

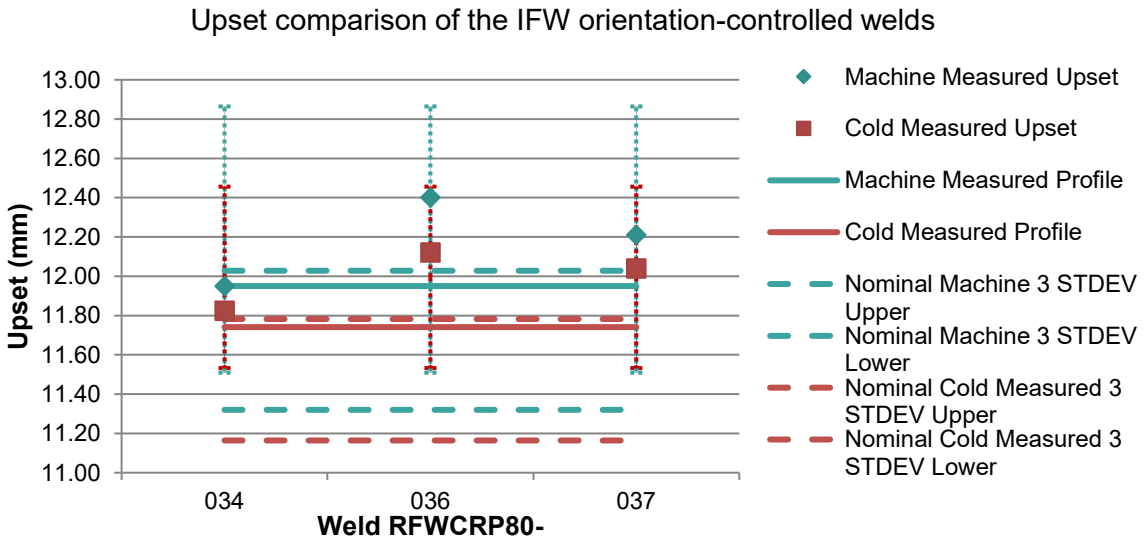


Figure 4-25: A Graph to show both post-process cold and in-process machine measured upset values for orientation controlled welds (RFWCRP - 034, 036 & 037) with error bars of ± 3 SD. Included are the upper and lower upset limits (± 3 SD of the average) for the nominal IFW welds (RFWCRP80 – 006 - 010).

4.7.2 Weld analysis

4.7.2.1 Pre-process orientation analysis

Prior to running the cycle or part loading a spindle test was run. At the end of the spindle test the spindle is rotated, at a speed set in the program, to the final spindle position of the upcoming program. Figure 4-19 shows the variation in spindle position at the end of the spindle tests. For the orientation control welds a spindle orient speed of 30rpm was used. This gave a variation range of 1.36 degrees around the desired spindle orient position. The variation shown in these tests can account for the difference shown between the machine and post weld data. A second set of spindle tests was run with a spindle orient speed of 5 rpm. In Table 4-6 the difference in variation between the two speeds is similar. While the variation in the 30rpm shows weak correlation the variation in the 5rpm test shows a strong correlation with one erroneous result; test two. Without test two the range of results is reduced to 0.38 degrees. For future orientation welds using a low spindle orient speed of 5rpm or less would help to reduce error in the final part orientation when not using keyed parts. Keyed parts or parts mounted into specific tooling aligned to the spindle should not be subject to these loading errors.

4.7.2.2 Weld record analysis

The weld records for the orientation-controlled welds, RFWCRP80- 034, 036 & 037, were typical and representative of the profile IFW weld RFWCRP80-027 (example - Figure 4-20). The curves only show minor variation from the nominal weld. This is expected as the machine is attempting to match a deceleration profile, evident by the slight input and extraction of torque feedback (Manufacturing Technology Inc, 2012).

The spindle position can be seen to lag slightly behind the spindle command position during initial stages of the cycle (Figure 4-21). The feed forward gain parameter is used to help reduce the lag between the two values by scaling the command value to force the spindle position to

equal the original command position. At the final part of the cycle the spindle position begins to overlay the spindle command position more accurately (Manufacturing Technology Inc, 2017b).

4.7.2.3 Orientation analysis

The orientation profile weld finished with a spindle position of 195.30 degrees (Table 4-9). Deviation from the loading position was measured with positive deviation indicating over rotation, while negative deviation shows under rotation. Weld 034 showed the maximum machine measured deviation of 0.86 degrees. Weld 036 showed the smallest with -0.35 degrees, in total this is a range of 1.21 degrees. It should be noted that weld 036 showed the greatest deviation when using the CMM and optivison systems, 1.85 and 1.86 degrees respectively while weld 037 showed the smallest with -0.57 and -0.46 degrees respectively (Figure 4-23). With an average orientation of 195.6 degrees, it shows that further work could be done to improve the accuracy of the feed forward parameter for this material and geometry. The machine recorded a precision of three standard deviations of 1.83 degrees.

While the CMM and optivison systems show correlation there does not appear to be correlation between those results and the machine results. This indicates an extra source of error is present. However, all measurement systems showed that there was an average positive deviation from true alignment. This indicates further work could be done to identify the correct amount of feed forward required to improve the accuracy.

4.7.2.4 Upset analysis

In Figure 4-24 the upset measurements from both the nominal welds and orientation controlled (OC) welds are displayed. The Profile weld is outside the range of the nominal welds therefore the OC welds are expected to produce higher upsets as well. The OC welds produce higher upsets than the nominal welds, but they are also higher than the profile weld putting them outside the nominal weld set three standard deviation limits. All welds, however, appear to

follow the rough trend of recording in-process upsets ~0.2mm greater than the post-process measurements. If the shrinkage was proportional to the upset, there would be an expected difference across all the welds. As there is not it suggests the shrinkage is down to something with less variation, perhaps the weld zone width, however this is not possible to quantify without further study.

The average machine measured upset values for the orientation controlled welded parts was 12.19mm the range of the measurements was 0.45mm. The cold measured upset was slightly lower, with an average of 11.994mm and has a narrower range of 0.298mm. This difference is expected due to contraction as the pieces cool.

These upsets were not representative of the nominal weld set. Figure 4-25 shows that all welds produced upset values outside 3 standard deviations of the nominal weld set (RFWCRP80-006-010), for both measurement methods with an increase in in-process machine measurement range from 0.28mm to 0.45mm. The CMM cold measurement range increased slightly from 0.264mm to 0.298mm.

The maximum deviation from the profile upset was 0.45mm measured on the machine and 0.38mm cold measured with the CMM both from weld 036. However, as the welds are modulating to a profile when the nominal weld three standard deviation limits use the profile weld as the centre point then machine limits become 12.30mm and 11.60mm and the CMM limits become 12.050mm and 11.432mm. Only weld 036 has fallen outside these limits. The increase in upset variation could be due to the machine modulating the position of the spindle to the deceleration curve therefore not taking into account the material variances and changing input of heat due to the torque response (Manufacturing Technology Inc, 2012, 2017b).

4.7.3 Conclusion

Initially an Inertia Rotary Friction Weld (IFW) was produced to be a profile weld (RFWCRP80-027), three welds were undertaken to investigate how the orientation control enhanced

functionality mode would alter the weld record. The intervening welds were used to set the feed forward gain parameter.

The findings from this investigation were compared to the variation from the nominal weld set, with the following conclusions:

1. Using a spindle orient speed below 5rpm can reduce the variation during loading of non- keyed parts.
2. The machine can orientate parts on deceleration to an accuracy of 1.83 degrees (3 standard deviations) when using the in-process measurement. The post weld measurement was 3.64 degrees (3 standard deviation).
3. Some of the discrepancy between in-process and post-process measurement is due to the reliability of accurately loading the parts.
4. Upset variation increased in orientation control mode. In-process variation rose from 0.35mm to 0.65mm and CMM variation up from 0.309mm to 0. 462mm.When the nominal weld limits were applied around the profile weld value, weld 036 was still found to be outside the limits.

The orientation-controlled welds show it is possible to produce welds with up to 1.83 degrees from the profile position. It is recommended to use a low spindle orient speed to reduce error when loading non-keyed parts. In this IFW mode there is a slight increase in variation of the upset from both the machine scale and post weld CMM data.

4.8 Enhanced functionality review

For industrial relevance, the enhanced functionality which had the highest level of control over the welding cycle was chosen for further exploration. The first quality measurement available when welding is the upset measured by the machine (Manufacturing Technology Inc, 2012, 2013b, 2013c).

Orientation control held a variation of 3 standard deviations around the mean upset of 0.68mm, pressure modulation held the variation to 0.05mm while torque modulation contained the variation to 0.03mm. When compared to the nominal weld variation of 0.35mm it is clear to see the effect of pressure and torque modulation actively reduces the variation in the welding cycle able to produce a high standard of repeatable welds as expected. Orientation control in this study has shown an increase in the variation. As the orientation control is following a rotational position profile against a speed profile, the expectation could be that the variation would reduce. However, the results gathered here have shown this to not be the case and make it unsuitable as a control mechanism for further study.

Pressure modulation and torque modulation both dramatically reduced the variation seen in the upset measurements. Pressure modulation is easily added to current machines using a separate upset measurement device and some controller reprograming. The effects of pressure have been studied in multiple papers and reviews (Ates *et al.*, 2007; Chamanfar *et al.*, 2015; Masaaki Kimura *et al.*, 2005; Li *et al.*, 2016; Romero *et al.*, 2009; Uday *et al.*, 2010). In papers concerning continuous drive multi-pressure stage welds are the norm. In inertia multiple pressure stages are not common. Whereas torque modulation is only available on machines with combined inertia and continuous drive modes. The only machines with this capability exist at the MTC. Torque modulation can also be used in other formats. It can be used to modify the energy input at self-defined intervals in the weld cycle or used to automatically scale the transition upset phase based on the weld progression, according to the machine manufacturer Manufacturing Technology, Inc (Manufacturing Technology Inc, 2012,

2016, 2017a, 2017d). On this basis pressure modulation offers the easiest benefit to industry whereas torque modulation offers the chance for completely novel research. Torque modulation was chosen to be explored in greater depth in the following chapters of this thesis.

4.9 Review of the torque modulated welds

The torque modulated welds were down-selected for further investigation based on the potential of the technique and the lack of current research.

4.9.1 Weld data

4.9.1.1 Energy input results

The weld flywheel speed and motor feedback were tracked during the weld allowing calculation of the weld energy rate and the accumulation of the transferred weld energy as shown in Figure 4-26 and Figure 4-27. In both weld sets weld energy can be seen to rise quickly at the start of the cycle during the initial contact and conditioning phases. The weld energy subsequently drops to a near steady state from 1.5s to 4 s. During this phase the torque modulation is activated based on the upset progress of the weld: 0.6mm. From here the rotational speed is controlled to meet pre-set speeds at associated upset amounts. The upset of weld 022 can be seen to be progressing slowly in Figure 4-28, this corresponds with the lower energy input compared to the other welds while also progressing for longer. The extra duration brings the upset and energy consumption of the weld into line with that of the others in the test.

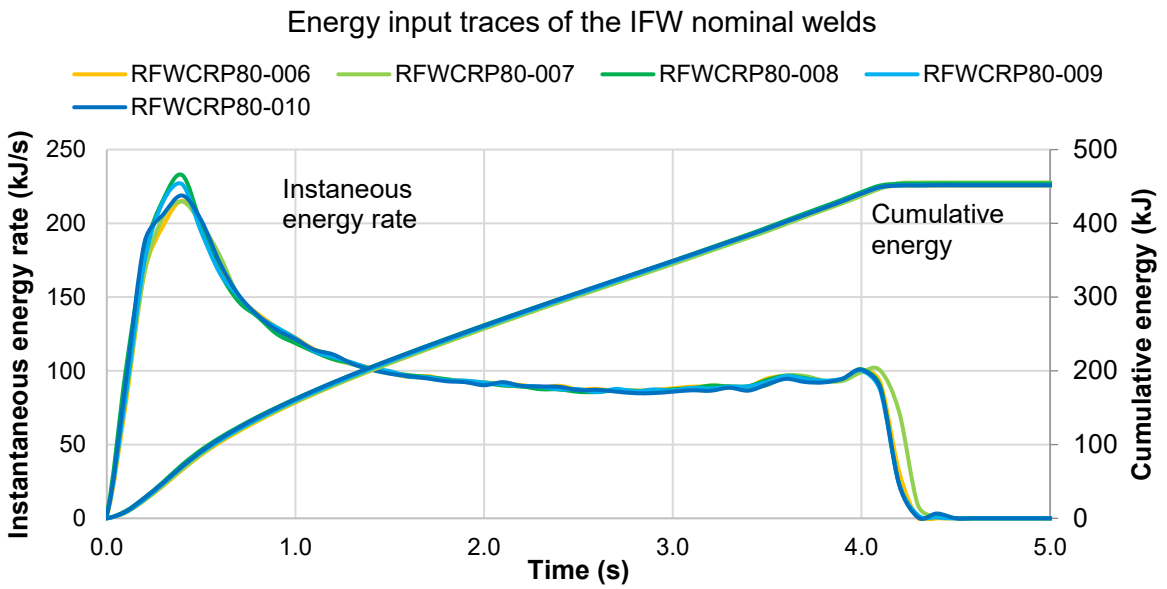


Figure 4-26: Weld energy results showing the energy transfer rate and cumulative energy amounts during the nominal inertia welds.

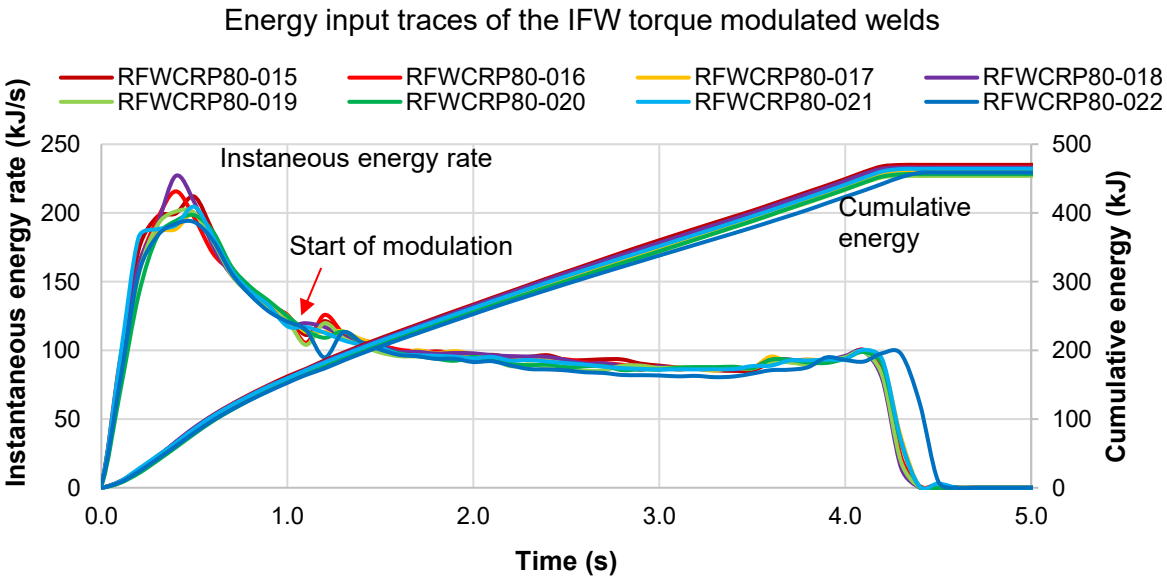


Figure 4-27: Weld energy results showing the energy transfer rate and cumulative energy amounts during the torque modulated inertia welds.

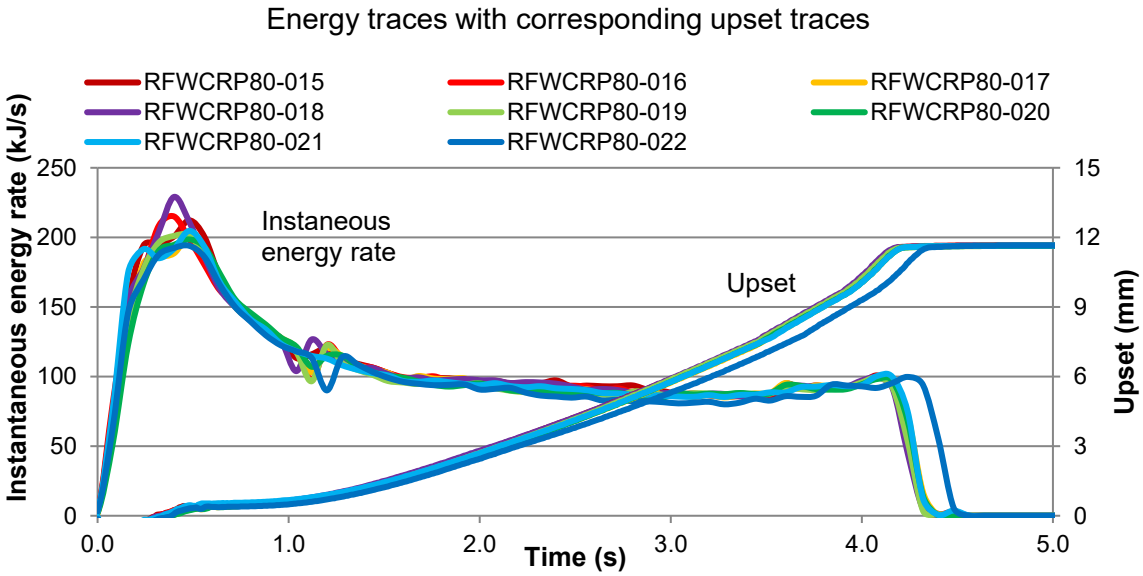


Figure 4-28: Weld energy rates shown alongside the upset progress of the torque modulated inertia welds.

Table 4-11: Nominal and Torque modulated weld energy peak rates and total amounts. Red cells indicate values above the nominal weld three standard deviation upper limit (3SD upper) while yellow cells indicate values below the nominal weld three standard deviation lower limit (3SD lower).

Energy peak rates and totals of the IFW nominal welds		
Weld number:	**Max energy rate**	**Total energy**
RFWCRP80-	**J/s**	**kJ**
6	215257	451.172
7	214773	455.334
8	232679	454.061
9	226431	451.533
10	218860	451.719
Average	**221600**	**452.764**
SD	6934	1.639
3SD	20803	4.916
3SD upper	242403	457.680
3SD lower	200797	447.848

Energy peak rates and totals of the IFW torque modulated welds		
Weld number:	**Max energy rate**	**Total energy**
RFWCRPW80-	**(J/s)**	**(kJ)**
15	211881	469.980
16	215699	466.912
17	199563	462.180
18	226962	466.010
19	201065	453.893
20	198309	456.455
21	204487	464.349
22	193315	458.781
Average	**206410**	**462.320**
SD	10337	5.189
3SD	31011	15.568
3SD upper	237421	477.888
3SD lower	175399	446.752

The torque modulated welds have a greater variation of input energy and input energy rate compared to the nominal welds. This is seen when comparing Figure 4-26 and Figure 4-27. Comparing the nominal welds to the torque modulated welds in Table 4-2 it can clearly be seen that the initial energy peaks during the conditioning phase of five, out of the eight, torque modulated welds were lower than the three standard deviation lower limit. However, in total energy six out of the eight torque modulated welds exceeded the three standard deviation upper limit of the nominal weld's total energy. Variation in maximum energy input rate and total energy was higher in the torque modulated welds indicated by the higher three standard deviations. According to Tumuluru (1984); F. F. Wang *et al.* (2014); Sathiya, Aravindan, and Haq (2007); L. Yang (2010) and others, in theoretical and empirical models, a difference in energy input leads to a resultant difference in upset. These do not take into account all real world variables and so do not produce the natural variation seen in real world production (Manufacturing Technology Inc, 2012). Here, regardless of the source, the variation from weld to weld was being compensated for, producing a more consistent upset.

4.9.2 Microstructural investigations

Three welds were selected from the eight torque modulated welds for further in-depth testing:

- RFWCRP80-019 – Matches profile weld upset according to machine data, within nominal weld energy input limits.
- RFWCRP80-021 – Lowest upset from CMM data, only upset according to CMM to be smaller than the profile and has the smallest initial torque peak.
- RFWCRP80-022 – Largest initial torque peak and furthest from profile weld according to machine data, second closest upset according to CMM results.

Images of the parent material, and weld area morphology were examined and compared to the profile weld. Figure 4-29 shows the samples which are reproduced later at 50x and 500x magnification. No re-entrant notches are visible on any samples while flash

formations, shape and size are comparable between welds. Each produced a larger cross section of flash on the inside diameter in line with that seen in the profile weld.

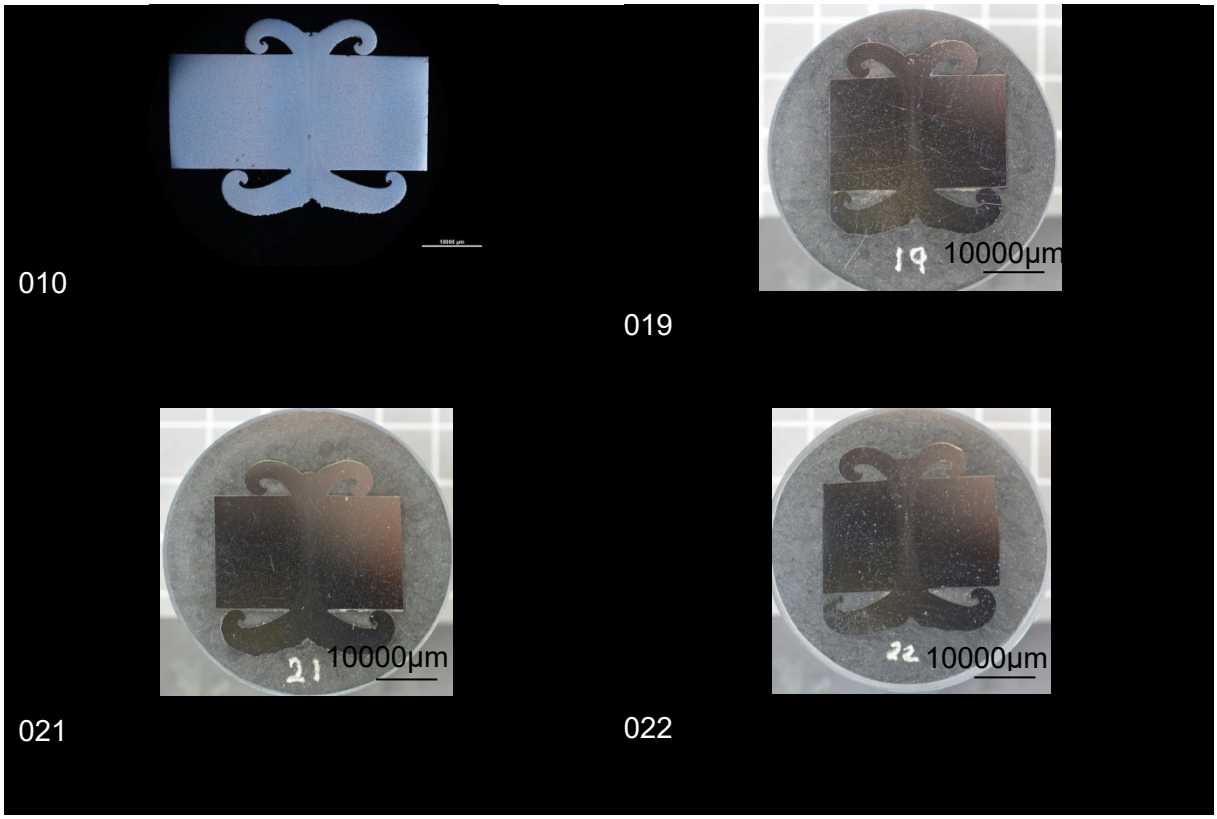
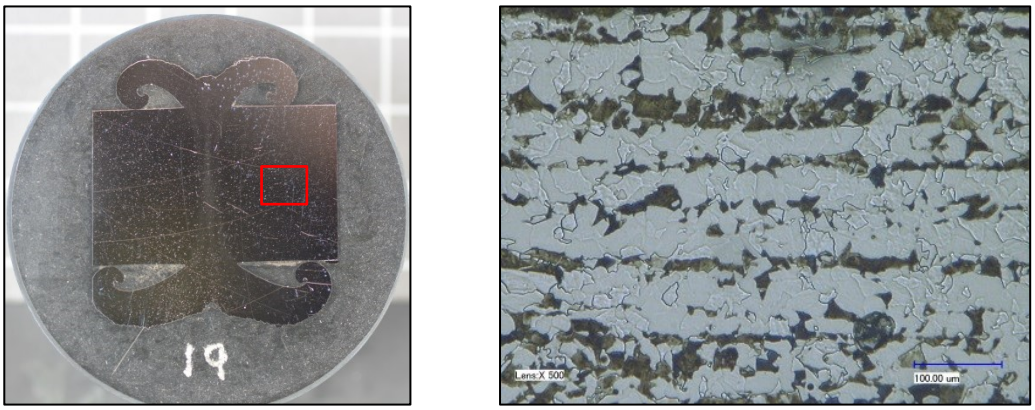


Figure 4-29: Macro-images of IFW nominal weld cross-section, unetched (RFWCRP80- 010, 019, 021 & 022).

4.9.2.1 Microstructure results

The following sections show the micrographs of the weld zone at 50x and 500x magnification post etching. They have been cropped to allow them to fit into the report. Each set contains micrographs of the parent material, ID and OD TMAZ and weld zone prior to ejection into the flash and the TMAZ and weld zone at the centre of the weld. The red boxes indicate the rough area where the higher magnification photos have been taken. Weld 019 has been chosen as a representative weld for comparison.



(a) **(b)**

Figure 4-30: a) mounted sample and b) etched optical micrograph of RFWCRP80-019 parent material at 500x magnification with the white ferrite grains and dark pearlite banding visible, red box is provided for location reference.

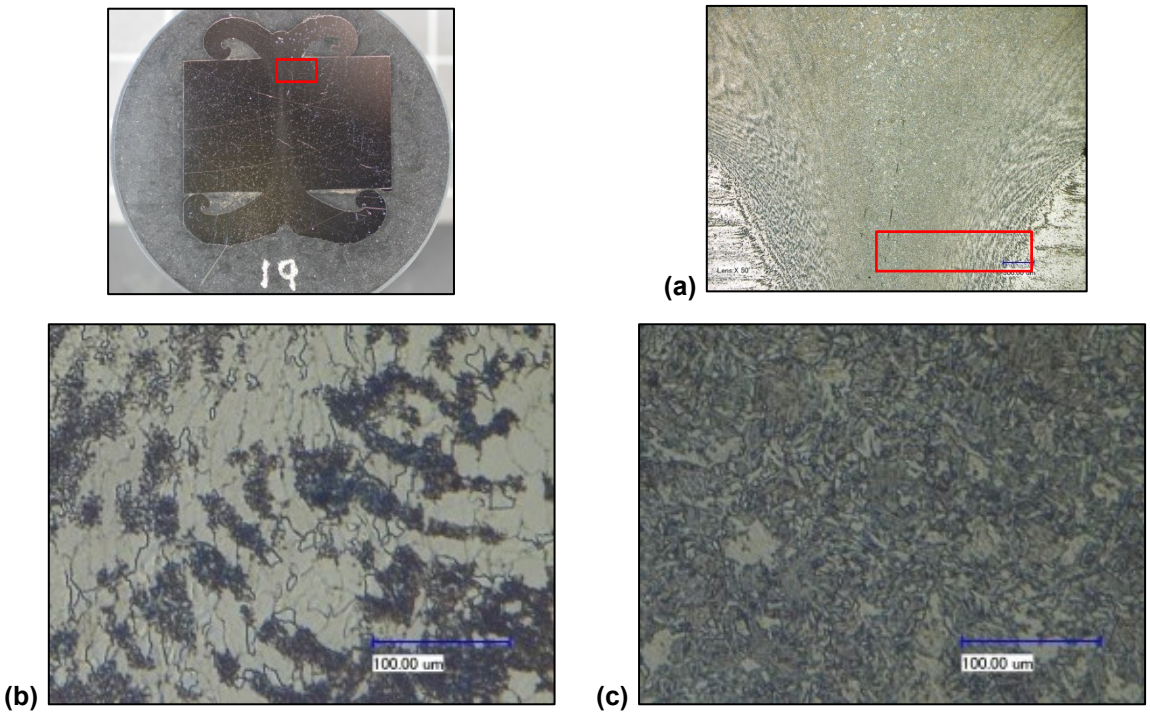


Figure 4-31: Etched optical micrographs of RFWCRP80-019: OD TMAZ to weld line transition with (a) at 50x magnification and (b) TMAZ at 500x magnification (c) weld zone at 500x magnification, weld sample and red boxes are provided for location reference.

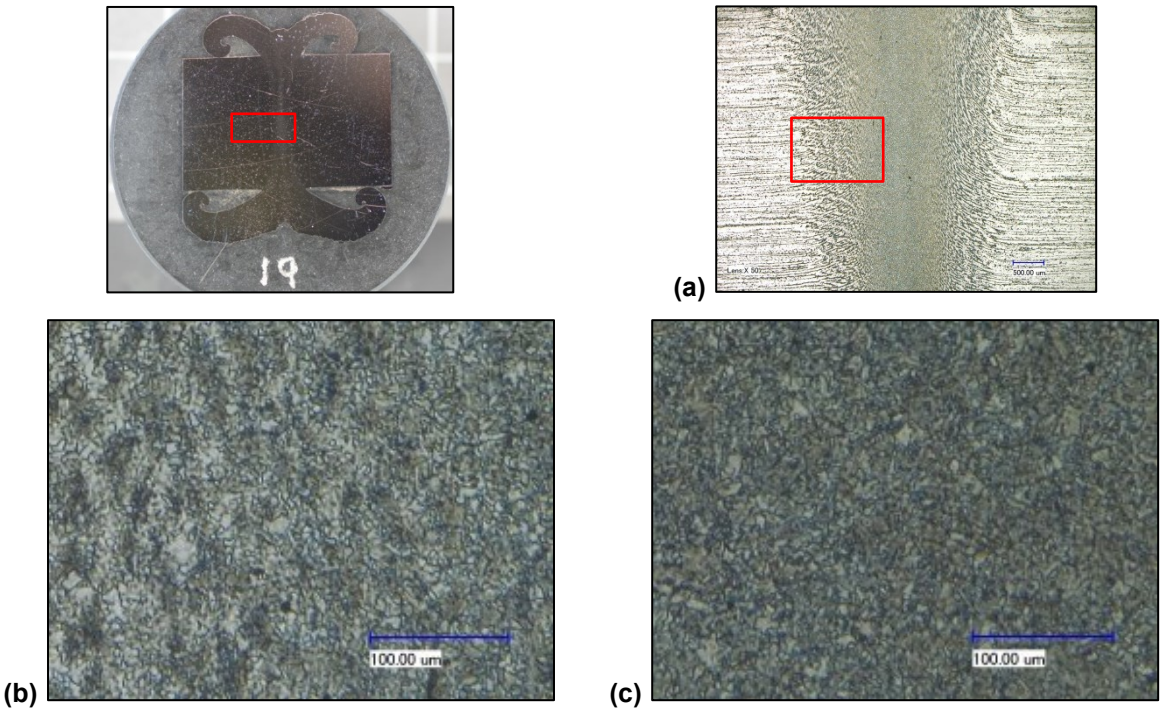


Figure 4-32: Etched optical micrographs of RFWCRP80-019: Centreline weld zones with (a) TMAZ to Weld zone transition at 50x magnification and (b) TMAZ and (c) weld line at 500x magnification, weld sample and red boxes are provided for location reference.

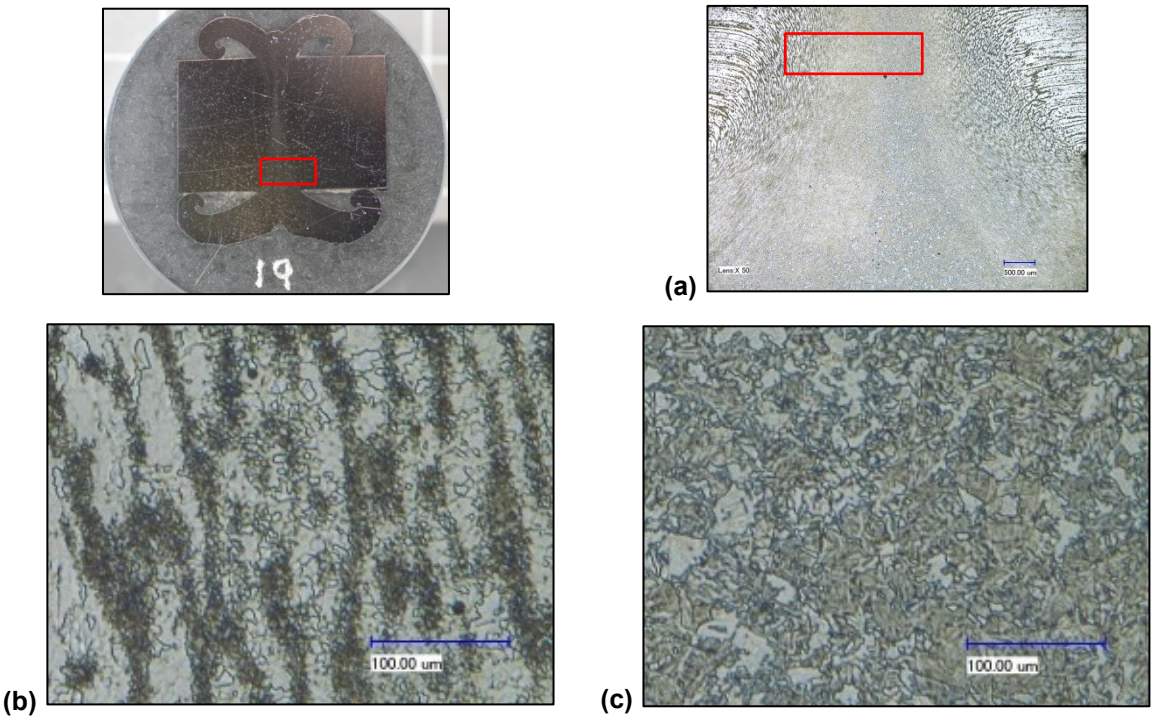


Figure 4-33: Etched optical micrographs of RFWCRP80-019: (a) ID weld overview at 50x magnification, (b, c & d) TMAZ to weld zone to TMAZ transition at 500x magnification, weld sample and red boxes are provided for location reference.

4.9.2.2 Weld zone measurement results

Figure 4-34 details the changing width across the weld zone of the TMAZ region. The three standard deviation limits from the nominal welds show there is more variation as you move towards the outer areas of the weld indicated by the wider gaps between the purple dotted lines. Whereas the torque modulated welds show variation outside the nominal welds three standard deviations at the centre but well within them at the outside and inside diameter locations.

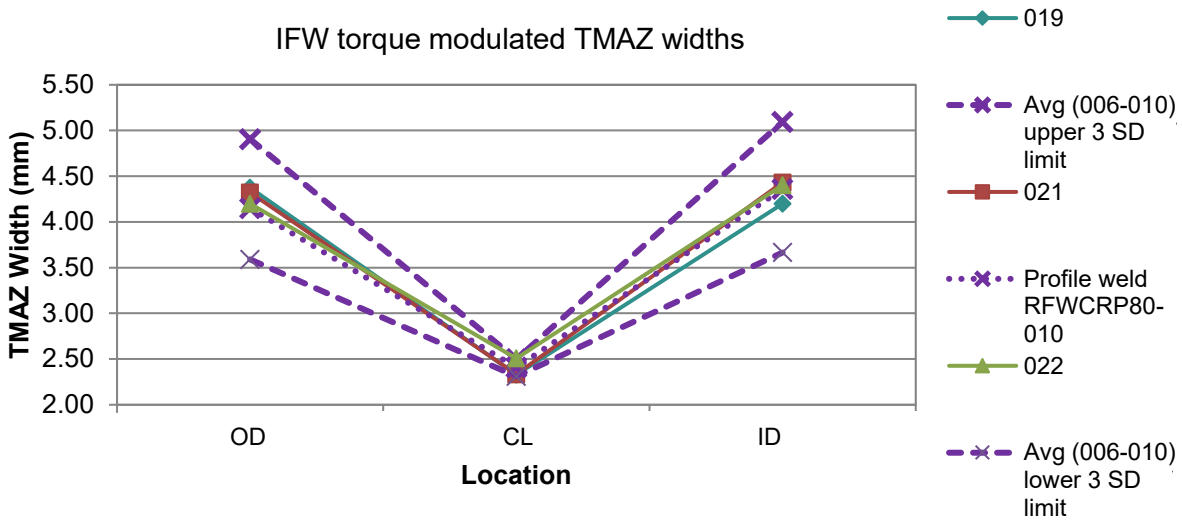


Figure 4-34: Graph to show OD, CL and ID TMAZ widths for IFW torque modulated welds (RFWCRP80- 019, 021 & 022) and for average nominal welds (RFWCRP80- 006-010) with 3 standard deviation error bands.

Figure 4-35 shows the bifurcation locations and widths. Although the widths are uniform and show a reduction in variation compared to the nominal welds the torque modulated welds show a much greater variation in location than the nominal welds. A comparison of the error bars in this graph clearly shows the described trends.

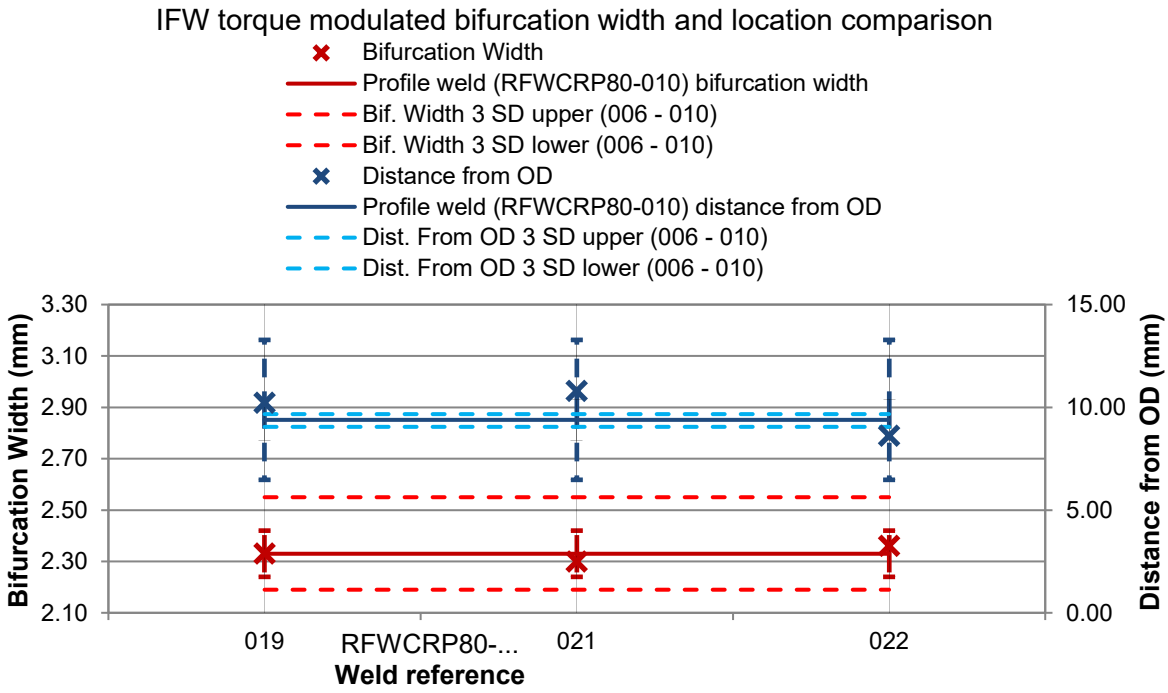


Figure 4-35: Bifurcation width and distance from the OD for IFW torque modulated welds (RFWCRP80- 019, 021 & 022) with 3 standard deviation error bars and for average nominal welds (RFWCRP80- 006-010) with 3 standard deviation error bands of the nominal welds.

Figure 4-36 shows the variation in notch depth between the two sides of the flash. The modulated welds closely match the profile weld RFWCRP80-010.

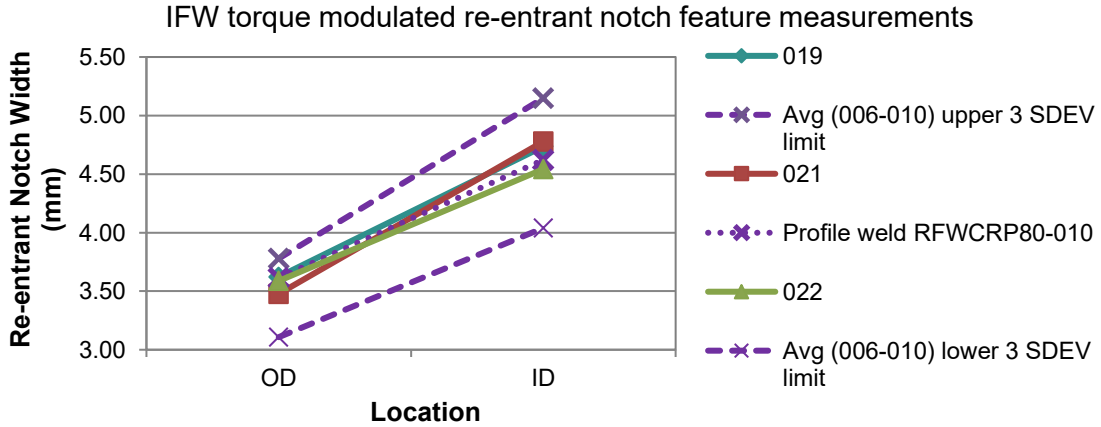


Figure 4-36: Graph to show the OD and ID re-entrant notch depths (where a positive value is representative of a non-re-entrant notch) for IFW torque modulated welds (RFWCRP80- 019, 021 & 022) and for average nominal welds (RFWCRP80- 006-010) with 3 standard deviation error bands.

TMAZ measurements taken from the stitched together micrographs are grouped together in Table 4-12.

Table 4-12: Thermo-mechanically affected zone (TMAZ) width, bifurcation width / location and re-entrant notch (where a positive value is representative of a non-re-entrant notch) measurements taken from IFW torque modulated weld cross-sections (RFWCRP80- 019, 021 & 022).

IFW down-selected torque modulated weld zone feature measurements							
Weld Number: RFWCRP80-	**TMAZ Width (mm)**			**Distance of Bifurcation Location from OD (mm)**	**Bifurcation Width (mm)**	**Depth of Re-entrant Notch Feature (mm)**	
	OD	**CL**	**ID**			**OD**	**ID**
019	4.37	2.33	4.20	10.22	2.33	3.62	4.74
021	4.32	2.33	4.43	10.80	2.30	3.48	4.78
022	4.20	2.51	4.40	8.61	2.36	3.59	4.54
Average	4.30	2.39	4.34	9.88	2.33	3.56	4.69
Maximum Value	4.37	2.51	4.43	10.80	2.36	3.62	4.78
Minimum Value	4.20	2.33	4.2	8.61	2.30	3.48	4.54
Range	0.17	0.18	0.23	2.19	0.05	0.15	0.24
Standard Deviation	0.09	0.10	0.13	1.13	0.03	0.08	0.13
3SD	0.27	0.30	0.38	3.40	0.08	0.23	0.38

4.9.2.3 Hardness testing results

Figure 4-37 details the hardness traces taken across the weld zone. The centreline trace records a slightly higher hardness at the centre of the weld with a much faster rise in comparison to the ID and OD traces.

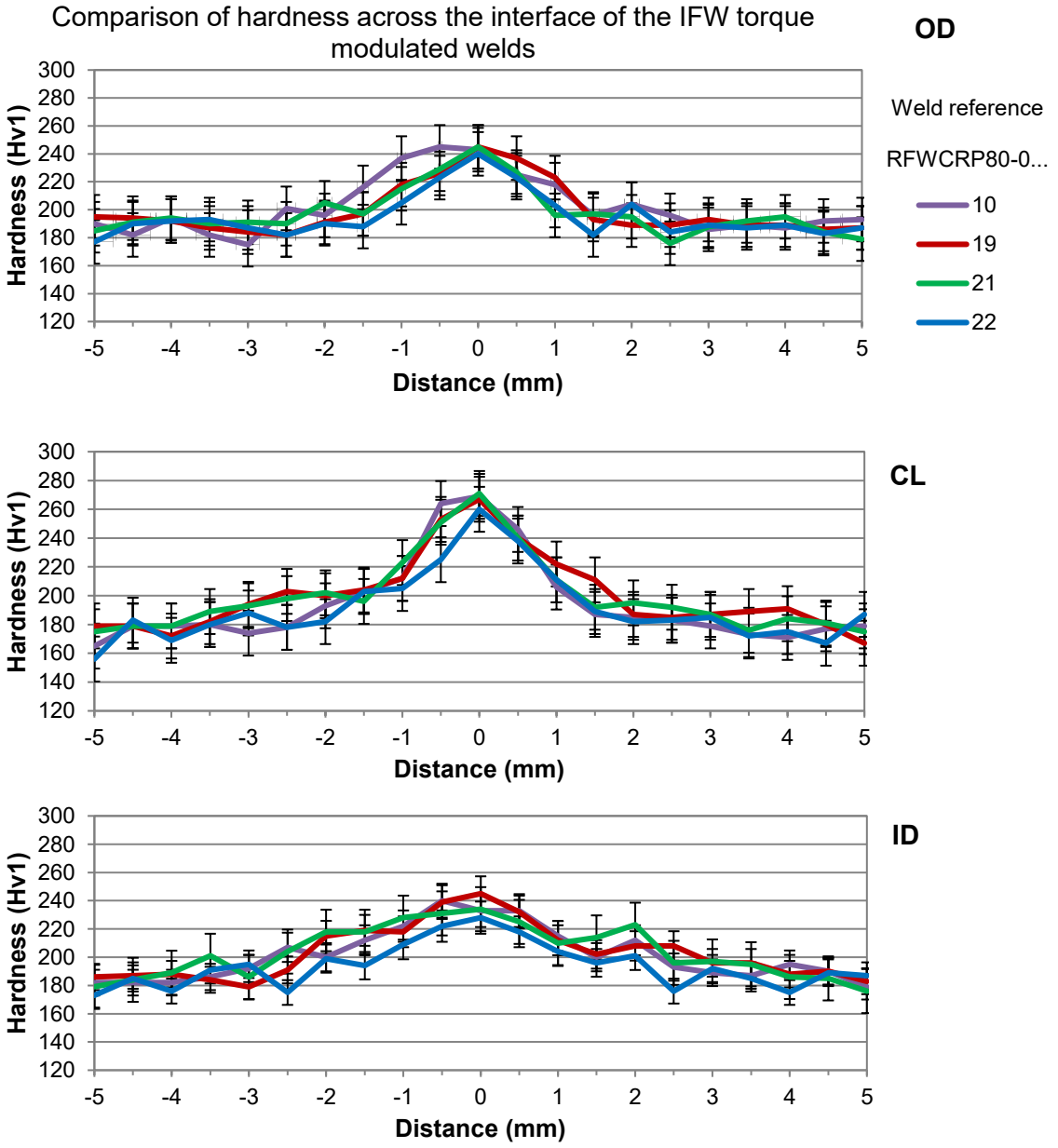


Figure 4-37: Hardness survey traces across the OD, centreline, and ID of the nominal and torque modulated inertia welds. Profile weld - 10 on the graph. Torque modulated welds - 19, 21 & 22 on the graph. 1 standard deviation of all parent material results has been plotted as error bars on all measurements.

The maximum hardness results are compared to the nominal weld three standard deviations and weld 010 in Figure 4-38.

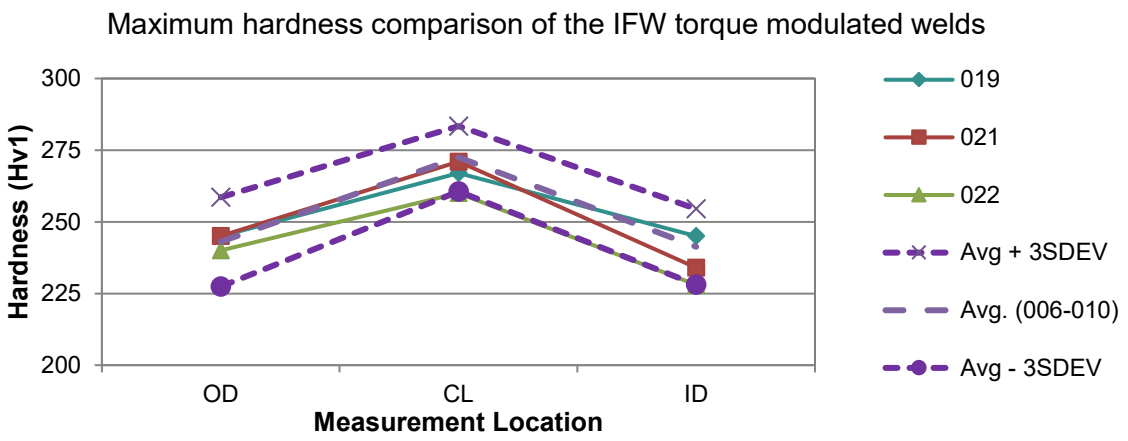


Figure 4-38: Maximum OD, Centreline and ID hardness values for the IFW torque modulated weld cross-sections (RFWCRP80 -019, 021 & 022), the profile weld cross sections (RFWCRP80-010) and average nominal weld cross-sections (RFWCRP80-006-010) with 3 standard deviation limit lines.

4.9.3 Mechanical testing

4.9.3.1 Tensile test results

The following section details the destructive testing results for the three down-selected torque modulated welds. Figure 4-39 displays the stress strain curves from the down-selected torque modulated welds compared to the nominal weld. Weld 020 has a notably higher proof stress, elongating with little stress increase to the UTS while the others begin plastic deformation at a lower proof stress rising faster to a comparable UTS. All welds broke in the parent material away from the weld.

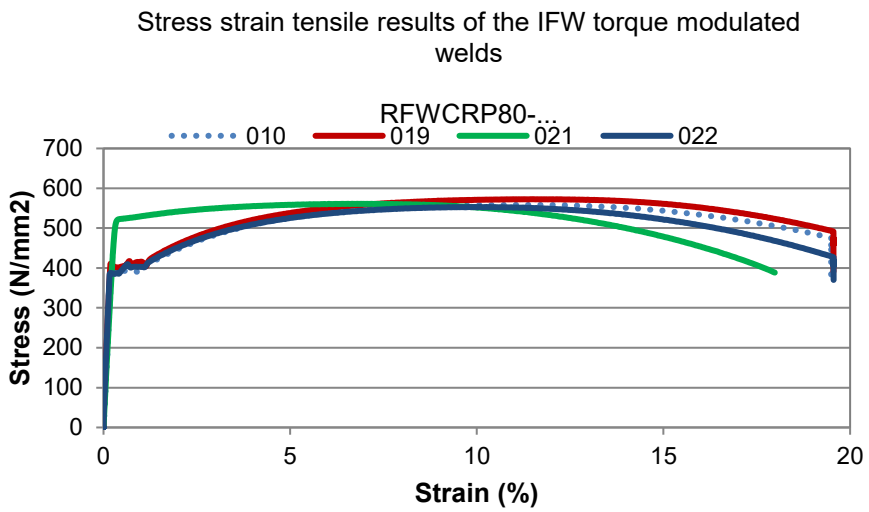


Figure 4-39: IFW torque modulated weld cycle stress strain results from tensile testing (RFWCRP80-019 to 022) compared to the nominal weld (RFWCRP80-010).

Figure 4-40 records the tensile results while showing the three standard deviations. The proof strength of weld 021 causes the major increase in standard deviation compared to the nominal welds.

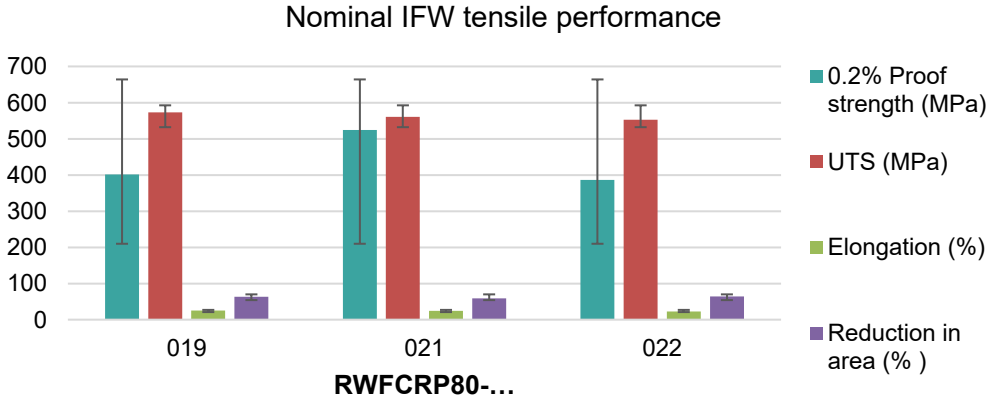


Figure 4-40: IFW torque modulated weld tensile results

4.9.4 Torque modulated weld analysis

4.9.4.1 Weld Data

4.9.4.1.1 Energy input analysis

The energy input from the welder to the weld pieces shows an increased variation of total energy input and peak input rate when torque modulation is employed compared to standard inertia welding. During the initial contact phase torque modulation is not engaged therefore the variation seen in the initial torque peak is natural variation due to minor chances in contact speed, pressure rise and surface condition of the parts (Manufacturing Technology Inc, 2012; Turner *et al.*, 2016). As the torque modulated welds progress after 0.6mm of upset at roughly 0.8 s the remaining energy in the flywheel is artificially altered in proportion to whether the weld is over or under upsetting for the current speed. This can be seen in weld 022 where the deceleration rate was marginally slower than the other welds, however, the upset rate was correspondingly slower therefore it still met the required speed-upset targets except it took the weld longer to complete. By making the weld meet set speed-upset points it can no longer create a matching time-based profile. This also changes the amount of energy lost through inefficiencies, as the primary loss mechanism is proportional to speed (Senkov, Mahaffey, Tung*, et al.*, 2017). At the end of the weld the total input of weld 022 was 458.781kJ only just outside the nominal weld 3 standard deviation limit of 457.680 kJ. As the energy input is lower this would correlate with a lower shear stress value at the interface, as in Figure 4-41. Calculable from rearranging equation (2-21) to make τ_f the output,

$$\tau_f = \frac{3\dot{P}}{2\pi(r_o - r_i)^3 \omega_v} \tag{4-1}$$

Assuming that the system is in a purely plastic regime and in this case the efficiency has already been calculated using flywheel run-downs when calculating $\dot{P}$. The lower energy input and higher rotational speeds give a lower shear stress, visible from 2.5 seconds onwards. The

small bump at the end of a weld cycle, as in weld 021, is sometimes seen in larger machines where the elasticity of the flywheel and spindle mechanism continues to try and rotate when the shear strength of the weld interface is reaching similar levels to the stress applied by the flywheel, prior to the flywheel fully reaching 0 speed. The elasticity of the shaft absorbs the over-rotation, re-winds, and then gives the weld another slight impulse(Kessler *et al.*, 2016). As the measurement apparatus is mounted behind the flywheel, and not at the interface, it records this feature (Manufacturing Technology Inc, 2012; Sketchley, 2013). The stress is high even though the power input rotation is low due to the relatively lower rotational speed at the same time.

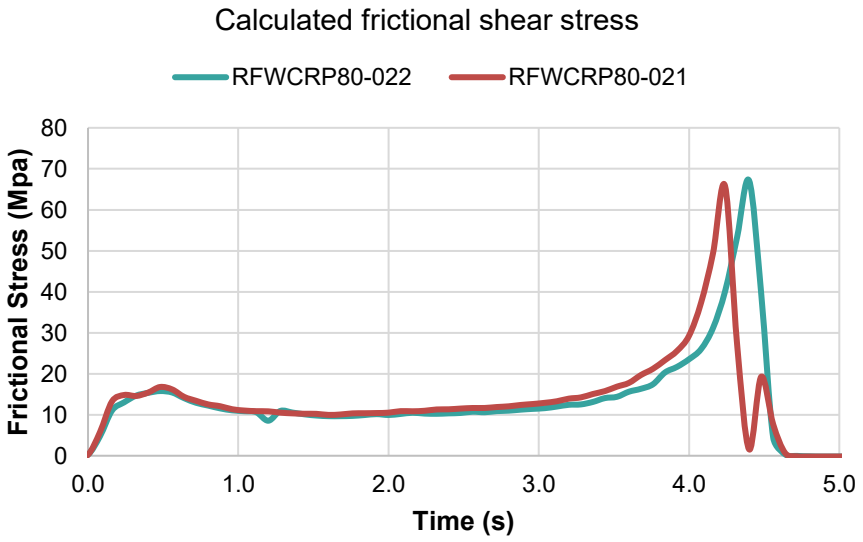


Figure 4-41: **Frictional stress at the interface of two IFW torque modulated welds.**

4.9.4.2 Microstructural investigations

4.9.4.2.1 Microstructure analysis

At 50X magnification the parent material grain structure appeared elongated axially along the length of all the welded parts, parallel to the bulk material hot rolling direction (Figure 4-30). Examination at higher magnifications revealed a pearlite/ferrite grain structure. With parallel

rows of pearlite and ferrite grains matching the standard form of sS355 (Ni & Abdel Wahab, 2017).

Optical analysis of the IFW ID and OD weld zone at 500X magnification for both the nominal weld and torque modulated welds (Figure 4-31 & Figure 4-33) appears to show a transformation to a predominantly bainitic-type structure distinct from the original parent material structure. Previous IFW of steel produced welds with a mainly martensitic centre surrounded by bainite, however the alloy used contained a much greater percentage of carbon leading to the increase in martensite upon cooling Tumuluru (1984). Examination of the centreline IFW micrograph at 50X magnification (Figure 4-32) shows a transformation through the plastically deformed TMAZ to the bond line. The large amounts of plastic deformation in the thermo-mechanically affected zone are obvious from the highly elongated and rotated grains. Transformation from alignment parallel to the rolling direction, in the parent material, to alignment towards the OD and ID parallel to the weld line. Grain alignment perpendicular to the part axis is apparent in the TMAZ at the OD and ID matching similar deformation seen in stainless steel friction welds Satyanarayana *et al.* (2005). At higher magnification, X500, a highly refined and thoroughly mixed structure of ferrite, bainite, and some pearlite can be seen on and around the bond line. The hardness of the welds suggests lower bainite which corresponds to the 330Hv found in the lower bainite regions of welds performed by Tumuluru (1984). The CCT curves of the similar material S355N from Figure 4-42 Ponge (2005) suggest that below 240Hv there should be a mix of ferrite, perlite and bainite. In areas over 240Hv, which is only the bond line on the centre line of the weld, should be a mix of ferrite and bainite. Lower hardness values around 170Hv match with the visible mix of only ferrite and pearlite in the parent material.

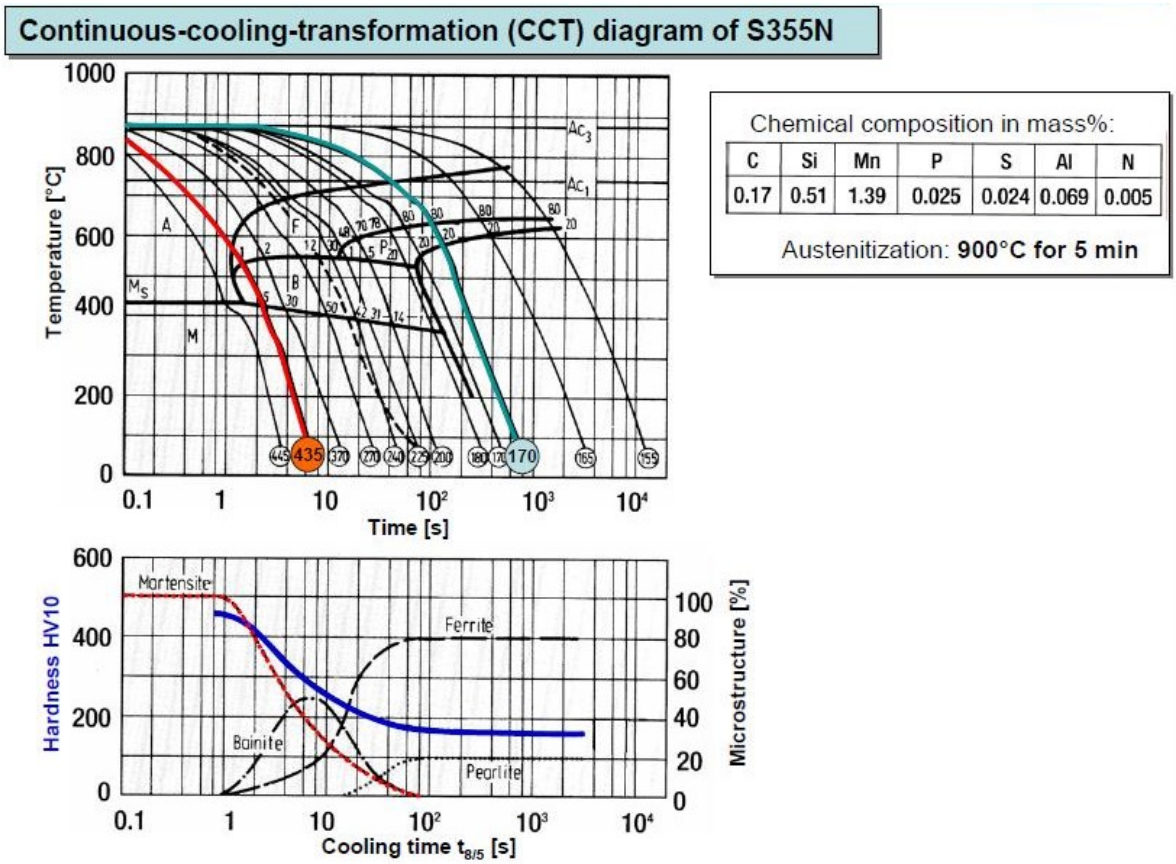


Figure 4-42: Continuous cooling transformation diagram of the structural steel alloy S355N (Ponge, 2005).

The morphology has been refined due to the strain energy and heat energy from the welding process. This has been attributed to continuous dynamic recrystallisation, which is widely believed to be the underlying mechanism for friction welding (M Maalekian, 2007; Uday *et al.*, 2010). This grain structure is visible in the centreline IFW TMAZ optical micrographs for the nominal and torque modulated welds Imaging at 500X magnification of the OD and ID TMAZ shows a larger less refined structure where the trend continues into the weld flash. The larger structure and greater amount of easily visible ferrite suggests slower cooling rates towards the edge of the weld, which is confirmed with the lower hardness traces and larger TMAZ widths.

The micro-scale examination results for RFWCRP80-019, 021 & 022 do not deviate significantly from the nominal IFW weld RFWCRP80-010 and therefore appear to be representative of the torque modulated mode and the standard inertia mode welds.

4.9.4.2.2 Weld zone measurement analysis

The metallographic analysis of the IFW torque modulated welds shows no evidence of incomplete bonding, cracks or other defects across the weld region (Figure 4-29). Flash formation appears similar to welds performed by Tumuluru (1984) and Satyanarayana *et al.* (2005).

Figure 4-34 shows a reduction in variation of the OD and ID TMAZ widths of the torque-modulated welds compared to the nominal welds. This would suggest that the matched speed-upset profiles and the resultant reduced upset variation, Figure 4-12, was also producing a less variable weld zone morphology.

Figure 4-35 shows a reduction in variation of the bifurcation width of the torque-modulated welds, which were nearly identical to the profile weld. The bifurcation locations of the torque-modulated welds were more than three standard deviations of the nominal IFW welds. There is also a slight reduction in variation of the re-entrant notch features of the torque-modulated welds compared to the nominal IFW welds as seen in Figure 4-36.

The macro-scale examination results for RFWCRP80 -019, 021 & 022 do deviate outside of three standard deviations from the nominal welds in some instances, the welds fell outside three standard deviations in up to two out of seven criterions (one for 019 & 021, and two for 022) for each weld. Therefore they do not completely represent a nominal weld in this mode, however as it is only a few criteria and the deviations are not drastic the welds can be described as generally representative. Duffin and Bahrani (1973) found links between rotational speed and weld zone thickness. This suggests that the bifurcation points occurred in welds with different speeds compared to the profile weld however the TMAZ widths being within the three standard deviations of the nominal welds would suggest otherwise.

4.9.4.2.3 Hardness survey analysis

Hardness surveys for the IFW weld cross-section have shown no change in the measured hardness within the TMAZ region (Figure 4-37 & Figure 4-31) when compared to the nominal welds.

Only two of the maximum measured hardness values for the torque modulated welds fell outside of the three standard deviations of the nominal welds, Figure 4-31. Both were from weld 22. The centreline value was 0.6HV below the deviation lower limit of 260.6Hv while the inner diameter was only 0.1Hv below the limit of 280.1Hv. Although the values were outside the process limits it was by a relatively small amount. From the TMAZ measurements, weld 22 was found to be marginally larger at the centre, which could explain the lower hardness values.

Traces across the ID indicates a widening of the weld zone. This correlates with the larger flash size seen in Figure 4-29 and measured in the notch size of Figure 4-36. The wider zone of high hardness would match with the larger flash movement producing a larger cooling effect on the weld zone in comparison to the OD, although the cooling rates would not be as high as at the centre of the weld. Where there was an increased hardness to match a mixed ferrite and bainite structure as seen in the weld zone micrograph, Figure 4-32 and CCT curves, Figure 4-42 (Ponge, 2005).

The results here match those of Handa and Chawla (2014) who continuous drive friction welded a low alloy steel (AISI 1021) to austenitic stainless steel (AISI 304) producing hardness's of 170Hv at 4mm from the weld interface rising to a maximum of 280Hv at the interface under high pressure parameters. The hardness profiles also match those produced by Sathiya, Aravindan, and Haq (2007) when welding ferritic stainless steel. The hardness characteristics for IFW torque modulated weld cross-sections at the OD, centreline and ID appear representative of the nominal welds evaluated.

4.9.4.3 Mechanical testing

4.9.4.3.1 Tensile test analysis

All torque modulated parts fractured in the parent material away from the weld as in the nominal IFW welds. All welds reached the minimum yield stress of 355 Mpa as required of the S355 material, while all UTS's came in within the reported 430-630 range (Gilbert, 2012; West-Yorkshire-Steel, 2018). As the samples broke away from the weld it would appear that the weld has not been detrimental to the materials strength.

Nearly all mechanical test results for RFWCRP80-019 to 022 were within three standard deviations of the nominal IFW welds (RFWCRP80- 006-010) average. Only RFWCRP80-021 had a significantly higher proof stress than the nominal welds and the torque modulated welds. The torque modulated welds appear representative of nominal welds in this IFW mode.

4.10 Conclusion

Initially eight inertia friction welds utilizing torque modulation to a profile weld were undertaken to investigate how this enhanced functionality mode would alter the weld record and metallurgical properties.

Three further welds were down selected for further investigation. The findings from this investigation were compared to within three standard deviations of the nominal weld findings, with the following conclusions:

1. Cold measured and machine measured upset values for the welds showed a reduction in the three standard deviations compared to the nominal weld set. Machine variation was down from 0.35mm to 0.03mm and CMM variation down from 0.309mm to 0.128mm. With further CMM variation reduction to 0.044mm, without RFWCRP80-021.

2. Total energy input increases in variation when torque modulation is employed as the machine is compensating for natural variation in the material.
3. The microstructures of the various regions matched those from the nominal weld 010. With the reduced upset variation coinciding with a reduction in weld zone width variation. Hardness traces matched the general shape of the weld zones and the microstructure within them.

The torque modulated welds undertaken within this study show a reduction in variation of the upset due to the modulated parameters from both the machine scale and post weld CMM data, 91% and 58% respectively. All welds feature one or two TMAZ measurements outside three standard deviations of the nominal welds, but the reduced upset variation and matched upset-speed profiles appear to produce a reduction in weld zone variation from the nominal weld set. The increase in energy variation does not appear to influence the weld zone negatively. Only in one measure is there a major difference and in that case the weld was stronger than the nominal weld set. Using torque modulation appears to increase the weld repeatability of the inertia friction welding process.

5 Microstructural impact and upset accuracy of proportionally modified energy friction welds.

5.1 Aim

To study the influence of mid-cycle energy modification on the weld microstructure and component geometry.

5.2 Introduction

Final length control takes a profile weld and adapts it to the incoming part lengths, based on energy scaling. This is compared to the alternative of setting a friction upset limit in a continuous drive cycle thereby self-adjusting the energy input. Both methods have claimed to produce welds of identical length (Manufacturing Technology Inc, 2012, 2013a, 2017a).While friction limits in continuous drive friction welding (CDFW) are uncommon in the literature, mid-cycle energy modification of inertia friction welding (IFW) has not been studied.

5.3 Summary

This rotary friction welding study was completed as part of the core research project “High Integrity Fabrication Using Near Net Shape Friction Welding Processes”. This study examined two enhanced functionality process control modes that have the potential to further expand the appeal of the process, particularly in the high value manufacturing (HVM) sector. Final length control has the ability to weld parts to a fixed length. Reducing the need for post weld machining or enabling low tolerance parts to be delivered at a cheaper or quicker rate. This can be achieved through an energy scaled inertia cycle or a continuous drive cycle with an exterior fixed burn off point.

The study investigated how the inertia friction weld microstructure responded when a significant proportion of the available weld energy was changed. This was compared to a continuous drive cycle which changed energy input through a proportional friction phase.

Secondly, this study examined which drive mechanisms is more suitable for industry part production.

A total of 54 micro-alloyed (MA) steel welds were produced, using the parameters and geometries established in work package 1 of the CRP. The final length control (FLC) trials produced 8 welds for each mode and geometry combination, resulting in 32 welds.

Weld analysis was completed using visual inspection, weld curve analysis and energy input calculation, upset measurement, metallurgical assessment, and mechanical tests.

In the FLC mode the final length of the part was found to be linearly proportional to the original part size; with final length being 0.081mm smaller in continuous drive and 0.025mm smaller in inertia for every 1mm of extra initial part length. This related to components of nominally 212.2mm total pre-weld length with a final post-weld target length of 206.04mm. A worst case pre-weld sample length of 216.2mm yielded a final CDFW welded sample size of 205.72mm (a worst case error of 0.16% of overall length for starting components 4mm oversize). In this study, when reducing part size the inertia cycle was unable to meet the target when parts were 2mm undersized. In continuous drive the limit was not reached with the parts studied. It is recommended for industrial use that the profile weld is based off the worst case minimal part size scenario therefore the weld cycle is always increasing the energy into the weld instead of reducing it, ensuring the defined final part size is attainable.

SVH40C final length control CDFW welds, samples consistently exhibited a predominantly ferrite and pearlite microstructure regardless of the incoming part length. In IFW, variability was seen in the levels of martensite and bainite formed in the weld zone, resulting in the generation of harder, more brittle regions. Shorter original test pieces correspondingly yielded higher levels of martensite at the weld interface. The choice of welding mode is therefore a balance between dimensional accuracy requirements and microstructural control requirements.

5.4 Enhanced functionality - Final length control in industry

In production, parts arrive having been measured and are accurate within the tolerances specified on the drawings. Depending on the intended use, the tolerances can be in the order of cm's to µm's. The purpose of final length control is to join incoming parts with large tolerances while producing parts to a set length with small tolerances. The alternative is to either specify small tolerances on the incoming parts, which increases their cost, or measure and machine each component to the correct size and tolerance post-welding increasing the production cost and time.

5.5 Objectives

The objective from the weld trial was to understand how the system responds to large changes of energy mid-cycle due to variability of the incoming part size, and the affect this has on the weld in terms of performance, size and shape. Welds performed in inertia and continuous drive modes allow comparison of the options available to consumers. Utilising components in solid and tubular geometry provides a wider understanding, while analysis of the functionality under non-ideal conditions allows further investigation into the torque modulation capability for industrial exploitation.

5.6 Experimental methods

For the final length control trials, the profile weld cycle was taken from the pre-existing nominal weld trials. Table 5-1 details the basic weld matrix and variation in initial part size away from the nominal length of 106.1mm. For each mode, the control system was tested using solid and tubular geometry parts. For each variation in part size two welds were made using the same initial part length.

Table 5-1.Final length control welds summary

Weld matrix of the initial component size								
	IFW				CDFW			
Geometry	Tubular	No. of welds	Solid	No. of welds	Tubular	No. of welds	Solid	No. of welds
Individual part length variation from nominal (mm)	+2	2	+2	2	+2	2	+2	2
	+1	2	+1	2	+1	2	+1	2
	-1	2	-1	2	-1	2	-1	2
	-2	2	-2	2	-2	2	-2	2
Total no. of welds		8		8		8		8

The weld identification system used in the trials is explained in Figure 5-1.

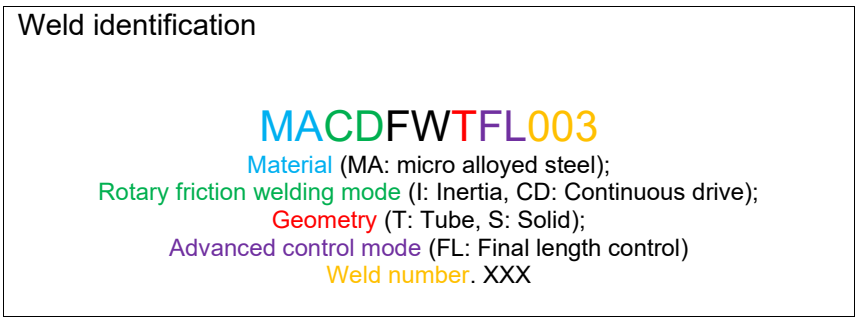


Figure 5-1. Weld identification system.

5.6.1 Materials

In this study the trials welded micro alloyed steel, SVH40C, parts only. Table 3-3 shows the material chemical composition.

The material blanks were machined into tubular and solid geometries. Examples are shown in Figure 3-3.

Table 5-2 summarises the parts geometry. For detailed drawings of the parts, see Appendix (Figure 9-1, Figure 9-2). For the tubular components, an outside diameter of 80mm and a wall thickness of 19mm was chosen. The solid components were given an interface diameter of

60mm. Both were made from oversized billet stock and reduced to 80mm outside diameter over the clamping surface to negate the need for tooling changes when swapping between components. Interface geometries were decided upon with discussion between Manufacturing Technology Inc, Thompsons Friction Welding, Ltd and the Manufacturing Technology Centre (MTC). The selected geometries were to provide compatibility with the M125 machine capabilities and thereby produce a strong weld with enough material to extract samples from. Weld lengths were chosen as sizes above and below the nominal were desired. Examination of the profile welds revealed that 4mm less material would be at the limit of what was capable of being produced from the current parameters. An identical tubular geometry was used in chapter 4. Nissan Motor Company, Ltd were able to provide suitable billet material with ease and therefore reduce the amount of preparatory machining needed.

Table 5-2. Final length control parts geometry summary.

Final length control weld matrix of part geometries				
	Final length control part geometries [mm] - Solid			
Outer diameter	60 +/- 0.05mm			
Wall thickness	-			
Length	108.1 +/- 0.05mm	107.1 +/- 0.05mm	105.1 +/- 0.05mm	104.1 +/- 0.05mm
Weld number	MAIRFWSFL001 MAIRFWSFL002 MACDFWSFL001 MACDFWSFL002	MAIRFWSFL003 MAIRFWSFL004 MACDFWSFL003 MACDFWSFL004	MAIRFWSFL005 MAIRFWSFL006 MACDFWSFL005 MACDFWSFL008	MAIRFWSFL007 MAIRFWSFL008 MACDFWSFL006 MACDFWSFL007
	Final length control part geometries [mm] - Tube			
Outer diameter	80+/- 0.05mm			
Wall thickness	19 +/- 0.05mm			
Length	108.1 +/- 0.05mm	107.1 +/- 0.05mm	105.1 +/- 0.05mm	104.1 +/- 0.05mm
Weld number	MAIRFWTFL001 MAIRFWTFL002 MACDFWTFL001 MACDFWTFL002	MAIRFWTFL003 MAIRFWTFL004 MACDFWTFL003 MACDFWTFL004	MAIRFWTFL005 MAIRFWTFL006 MACDFWTFL005 MACDFWTFL006	MAIRFWTFL007 MAIRFWTFL008 MACDFWTFL007 MACDFWTFL008

5.6.1.1 Material as supplied

The micro alloy steel used in this project is a hypo-eutectoid steel with a typical mixed structure of ferrite and pearlite, as shown in the parent material images in Figure 5-7 to Figure 5-10. From the image taken from the base material we can see that the content of pearlite is slightly higher than the ferrite, giving an average hardness of around 200Hv matching the structure of similar micro alloyed steels Baker (2016); (Işık & Özes, 2016).

5.6.2 Welding process

On the 125T final length control is the welding mode for producing parts of identical length. In inertia mode pressure or torque can be manipulated to change the upset produced scaled from a profile weld. In these trials torque is used to add and subtract energy from the flywheel relative to the change in pre-weld part lengths from the standard profile weld. In the continuous drive mode the burn off point is adjusted relative to the pre-weld part size. This results in a fixed burn off point on the machine's upset measurement scale. This can be taken from the prior welds or arbitrarily set. The accuracy of the length of the components produced was evaluated against any changes in mechanical strength and microstructure.

5.6.2.1 Weld parameters

Each combination had an original set of parameters suggested by the steering group. These were tested and incrementally optimised. From these studies representative welds were chosen to act as profiles by reviewing the upset curves and evaluating the flashes.

For the final length control welds an in-process hot machine measured final length was chosen for the machine to aim for and the average shrinkage from the previous study applied to produce a cold final length target.

Table 5-3. Inertia friction welding final length parameters.

IFW final length control weld parameter matrix			
Geometry		**Solid**	**Tube**
Inertia Weld Parameters	**Weld Speed (RPM)**	2000	2000
	Forge Pressure (MPa)	254.99	184.21
	Total Inertia (kg.m^2)	18.6	18.6

Table 5-4. Continuous drive rotary friction welding parameters.

CDFW final length control weld parameter matrix			
Geometry		**Solid**	**Tube**
Continuous Drive Weld Parameters	**1st Friction Speed (RPM)**	650	800
	2nd Friction Speed (RPM)	486	488
	1st Friction Pressure (MPa)	38.98	57.40
	2nd Friction Pressure (MPa)	124.99	114.80
	Burn Off (mm)	5	8.4
	Forge Pressure (MPa)	169.34	179.51
	Forge Time (s)	6.5	5.0
	Brake Torque (%)	50%	50%
	Machine Inertia (kg.m^2)	18.6	18.6

5.6.3 Weld analysis

5.6.3.1 Weld data analysis

Weld curves were analysed with focus on the following:

- Weld upset
- Pressure at the weld contact interface
- Rotational speed
- Torque feedback
- Burn-off

5.6.3.2 Microstructural assessment

5.6.3.2.1 Visual inspection

As a preliminary method of quality assessment, visual inspection was carried out. Flash shape, volume and aspect were assessed.

5.6.3.2.2 Microstructural Inspection

Sections for metallographic analysis were taken from the weld pieces at the same time as the mechanical testing sample blanks. All metallography analysis samples were prepared and inspected at the MTC. All metallurgical assessment was conducted by the author. Preparation of the samples was conducted by the metallurgy lab at the MTC. Micro images of the weld regions were taken at 50x and 500x magnification once polished and etched. Images focused on the parent material, transition to the heat affected zone (HAZ), transition to the thermo-mechanically affected zone (TMAZ) and the weld region (recrystallised zone) including the bond line.

5.6.3.3 Mechanical testing

Weld samples were delivered to Special Testing, a UKAS test facility with ISO 17025 quality standards. All machining and destructive testing was conducted by Special Testing employees. The methods of destructive testing employed in this study and the standards followed where possible were:

- Tensile testing – ASTM A370 2014
- Bend testing – BS EN ISO 7438 2005
- Charpy testing – ASTM E23 – 12c

5.7 Nominal weld results

These welds were used for comparison against the final length controlled welds. They also provided the target length and profile weld curves the machine used to calculate the adjustments required.

5.7.1 Weld data

5.7.1.1 Weld curves

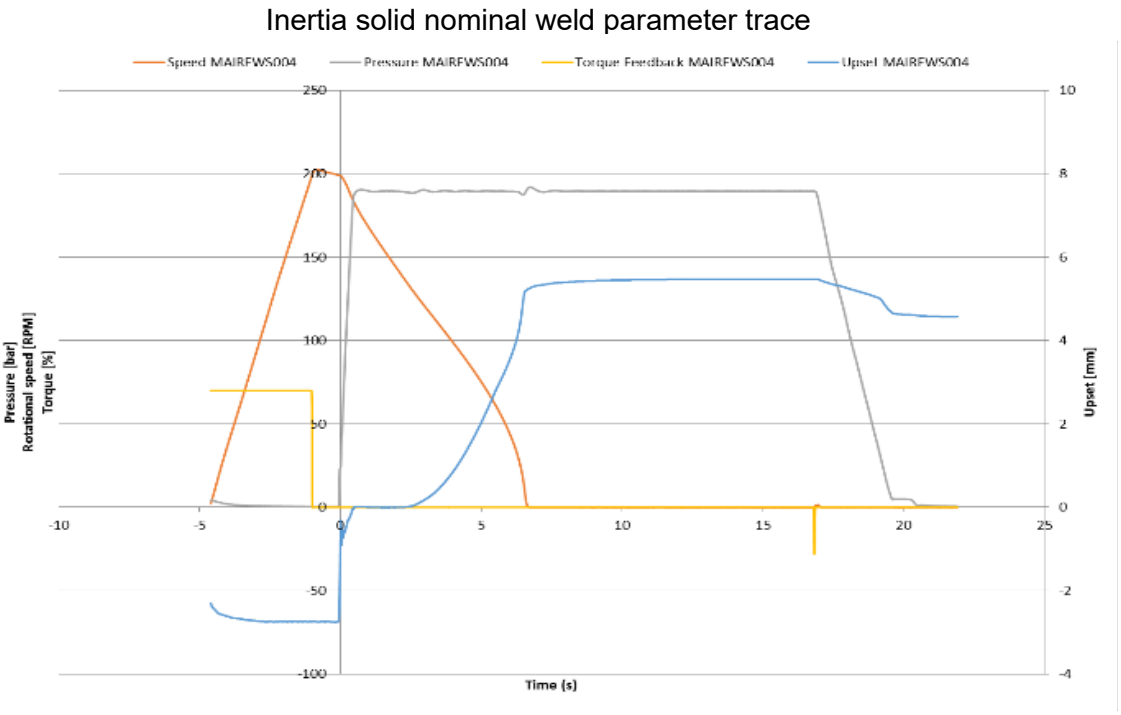


Figure 5-2. Profile parameter weld curves of MAIRFWS004 for the inertia solid components.

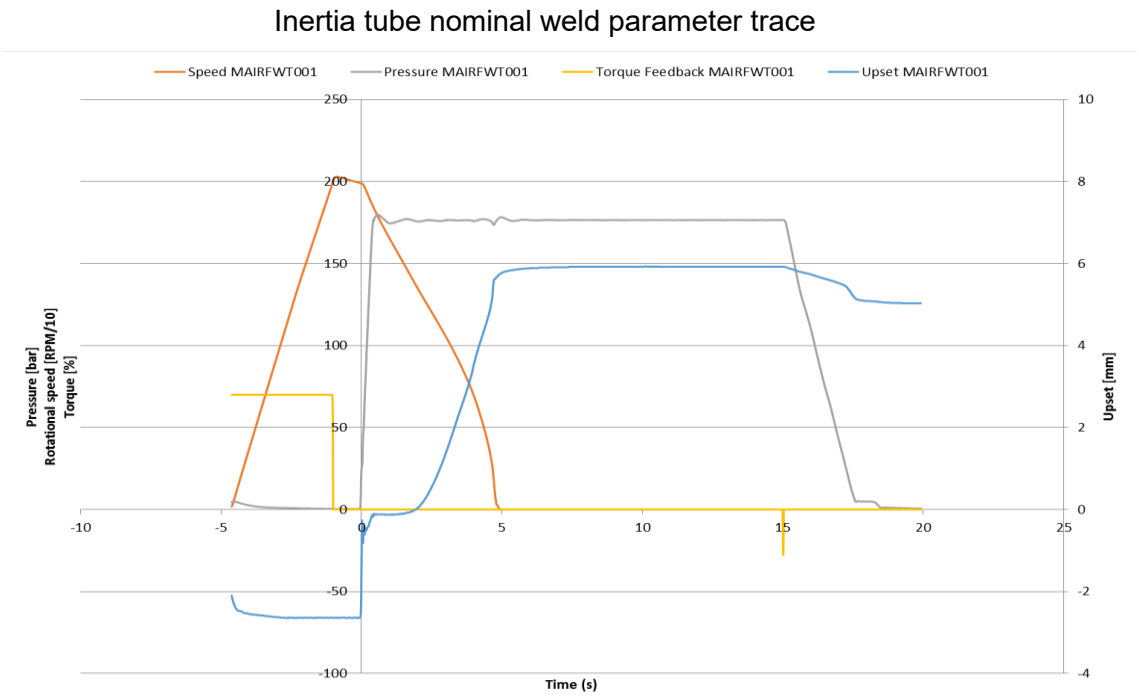


Figure 5-3. Profile parameter weld curves of MAIRFWT001 for the inertia tube components.

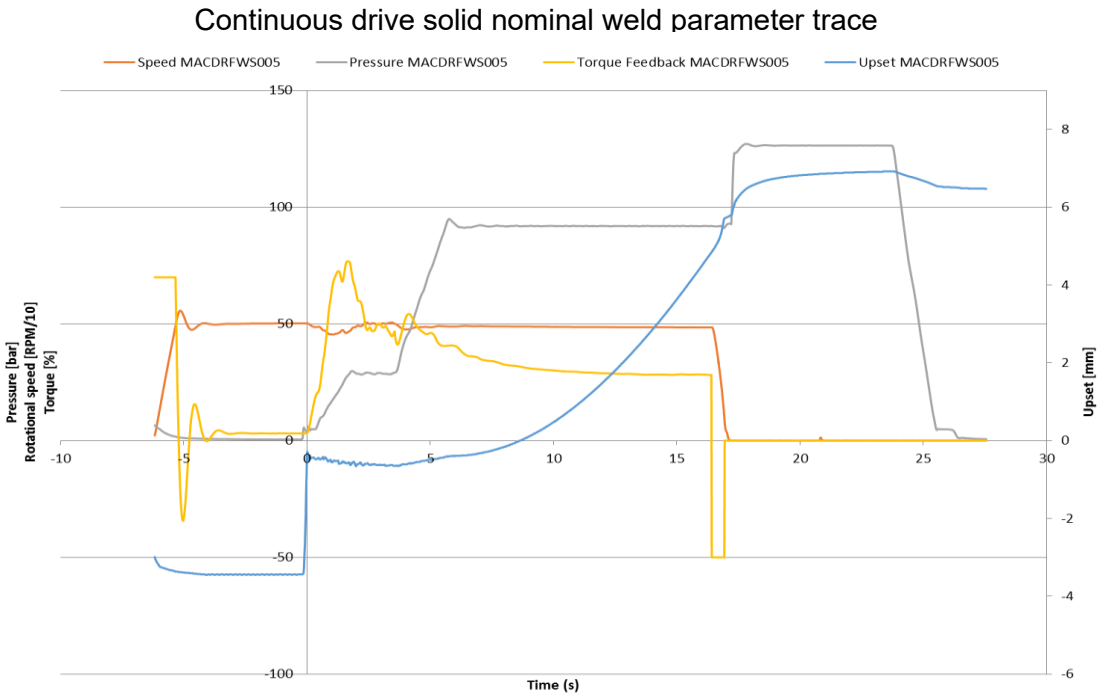


Figure 5-4. Profile parameter weld curves of MACDFWS005 for the continuous drive solid components.

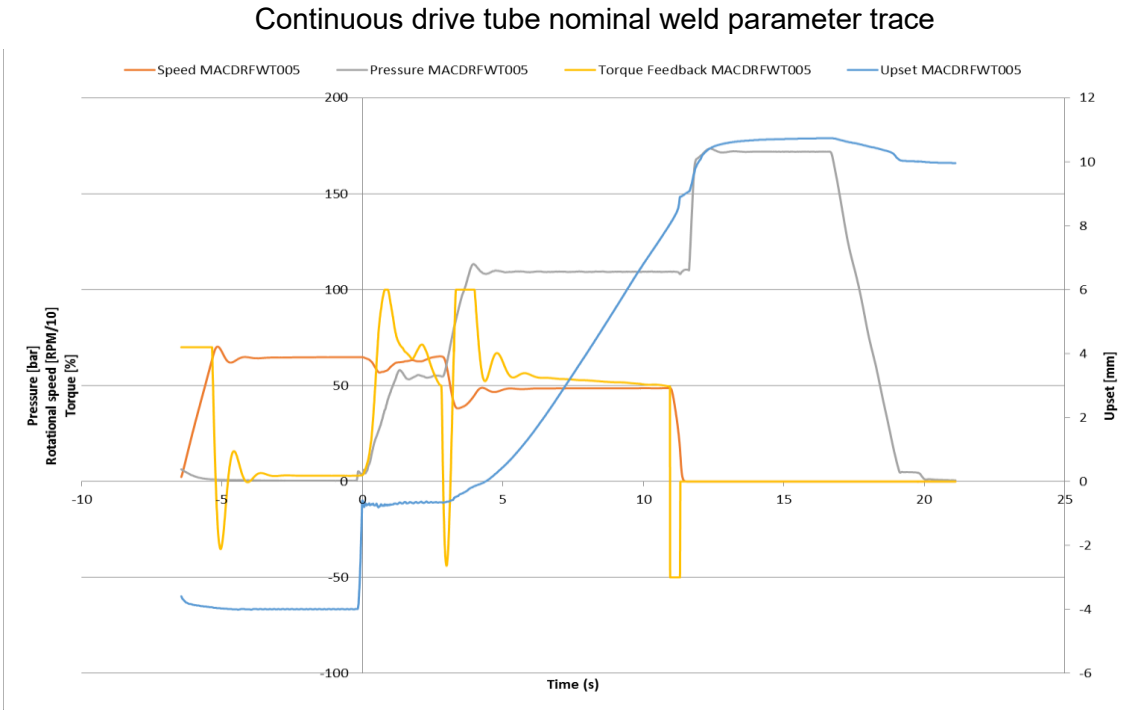


Figure 5-5. Profile parameter weld curve for MACDFWT005, for the continuous drive tube components.

5.7.2 Microstructural Inspection

5.7.2.1 Visual inspection

Welds are shown to indicate the size, shape and texture of the flash produced from nominal parts.

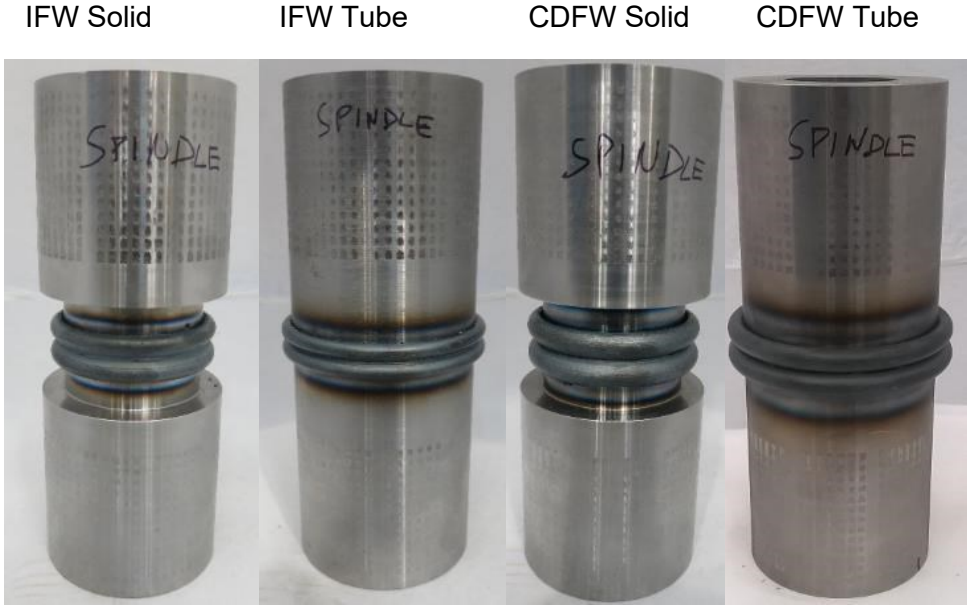


Figure 5-6. Micro-alloyed steel repeated parameter weld samples: a) MAIRFWS001, b) MAIRFWT001, c) MACDFWS005 and d) MACDFWT005.

5.7.2.2 Microstructural results – Micrographs

The micrographs show the microstructure transition of the joints from the parent material through to the weld zone. The weld macro is present to show weld size and shape and locate the area the micrographs were taken (indicated by the red box).

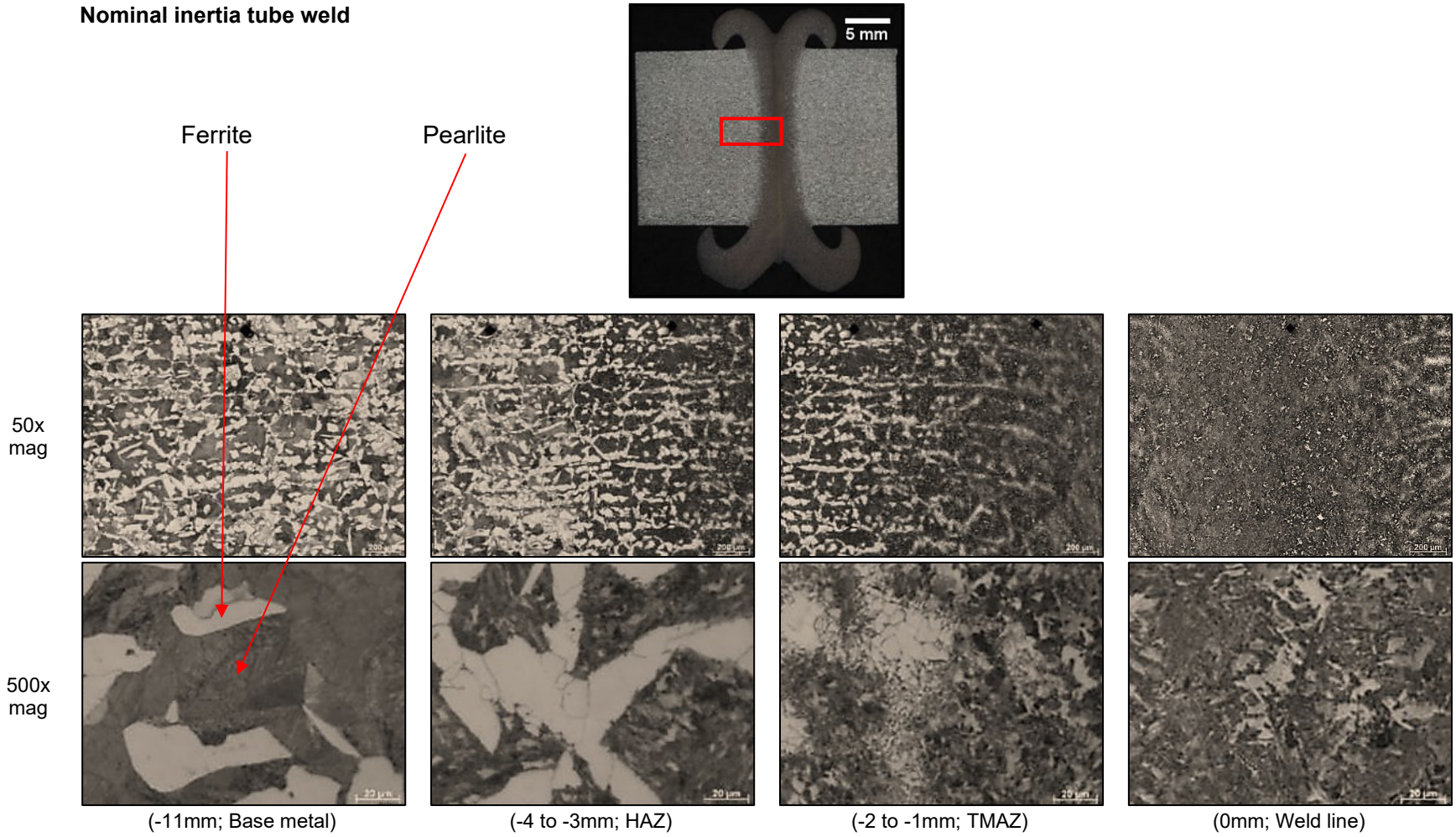
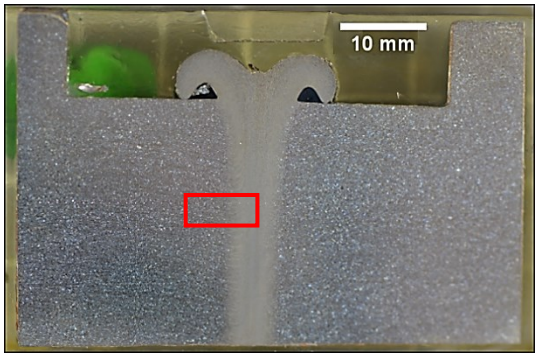
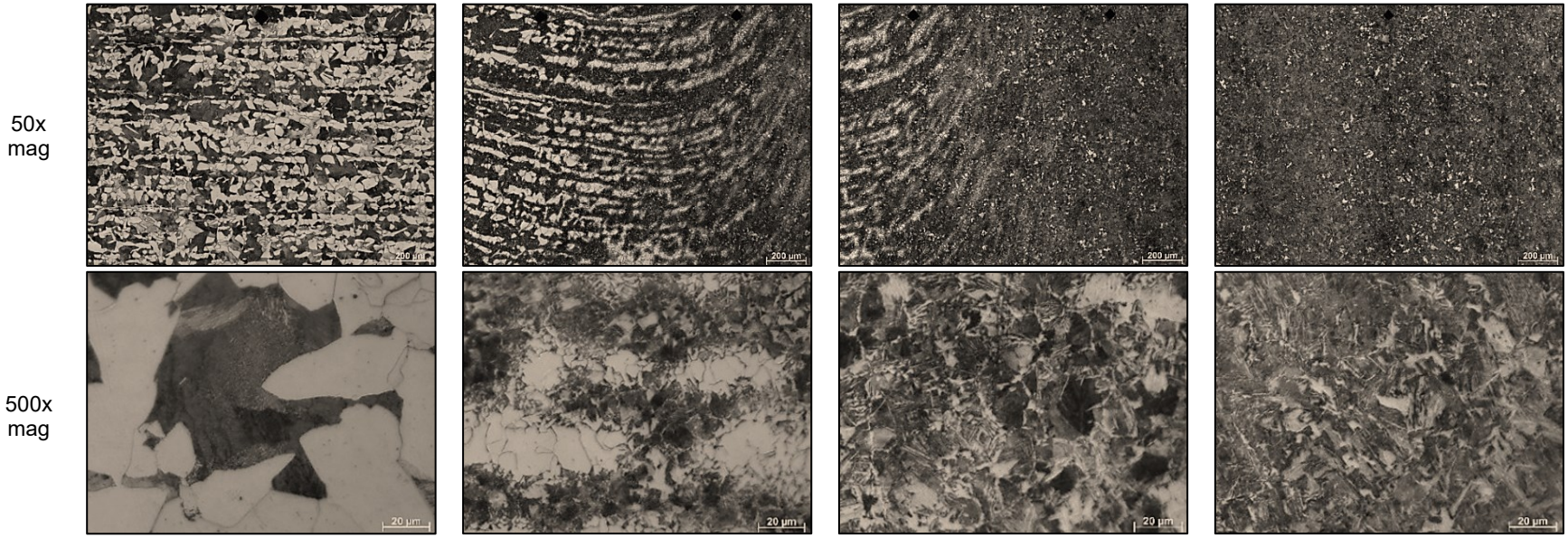


Figure 5-7: The microstructural changes from the parent material to the centre of the weld zone of MAIRFWT 003. Images at 50x and 500x mag (shrunk for reproduction).

Nominal inertia solid weld

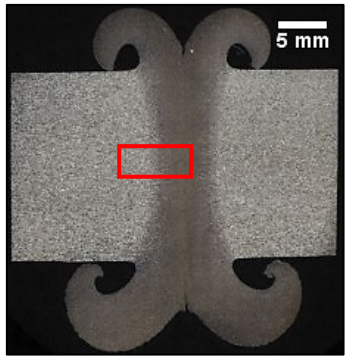




(-25mm; Base metal) (-2mm; HAZ and TMAZ) (-1mm; TMAZ) (0mm; Weld line)

Figure 5-8: The microstructural changes from the parent material to the centre of the weld zone of MAIRFWS 005. Images at 50x and 500x mag (shrunk for reproduction).

Nominal continuous drive tube weld

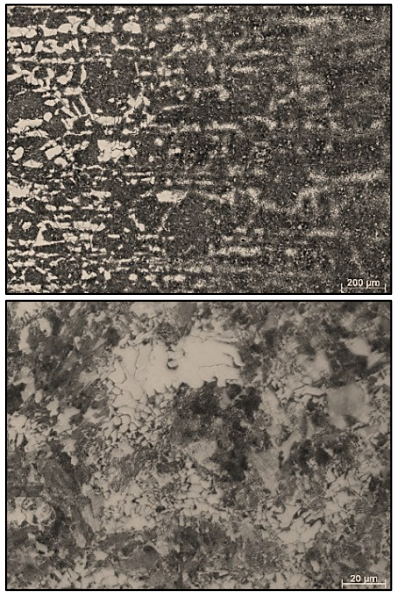


50x mag

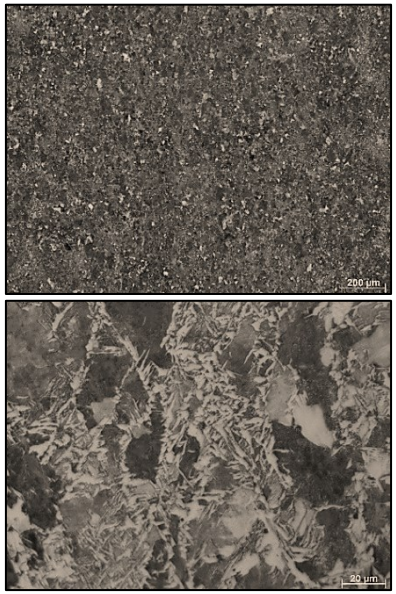
500x mag



(-10mm; Base metal)



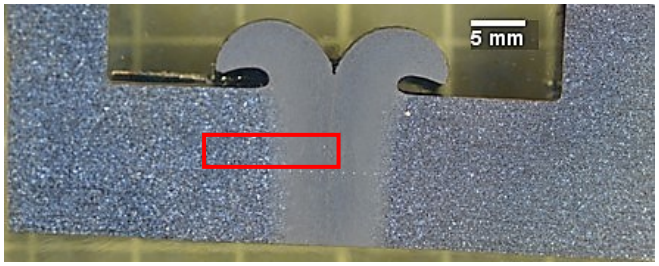
(-2 to -1mm; HAZ and TMAZ)



(0mm; Weld line)

Figure 5-9: The microstructural changes from the parent material to the centre of the weld zone of MACDFWT 005. Images at 50x and 500x mag (shrunk for reproduction).

Nominal continuous drive solid weld



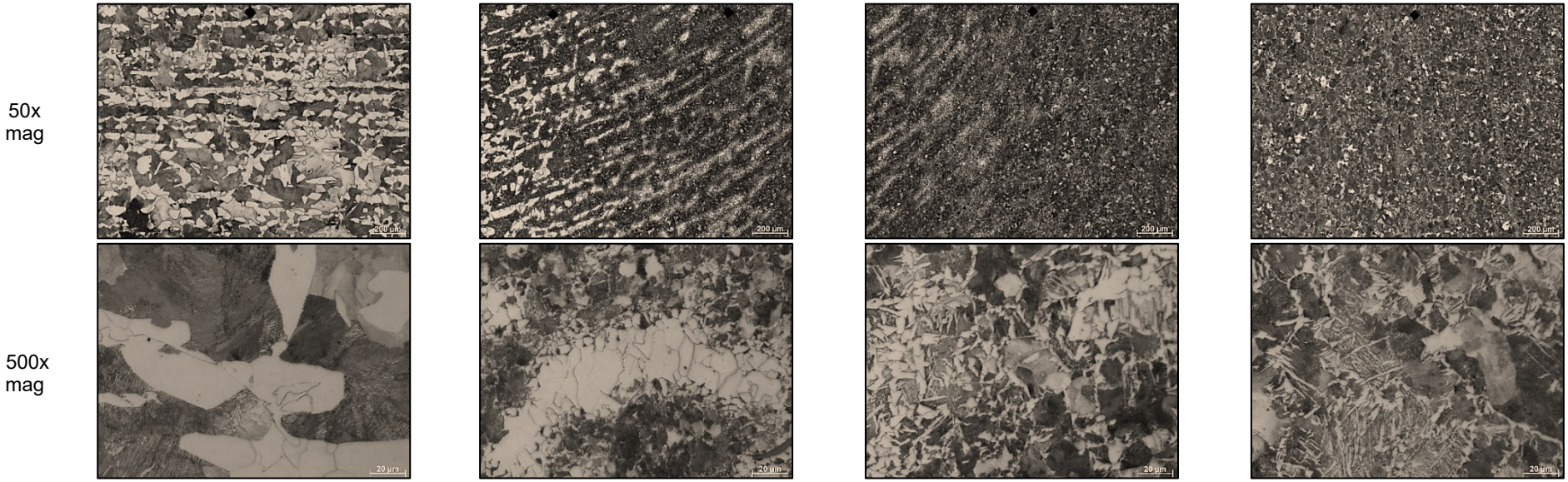


Figure 5-10: The microstructural changes from the parent material to the centre of the weld zone of MACDFWS 006. Images at 50x and 500x mag (shrunk for reproduction).

5.7.2.3 Hardness testing

Displayed are the hardness traces from the centreline of the nominal welds used as profiles for the final length control. Error bars have been calculated from the variation in measurement of the base material. Scales have been matched for easier comparison.

The inertia solid nominal weld appears to show a slight rise in hardness from 5mm either side of the weld line however this is still within the variation seen in the base material. From 2mm a definite increase is seen, broader than the tube weld and only reaching 310Hv1. In the inertia tube weld elevated hardness levels, above the base material variation, can be seen from 3mm either side of the weld line, which recorded a maximum hardness of 346Hv1.

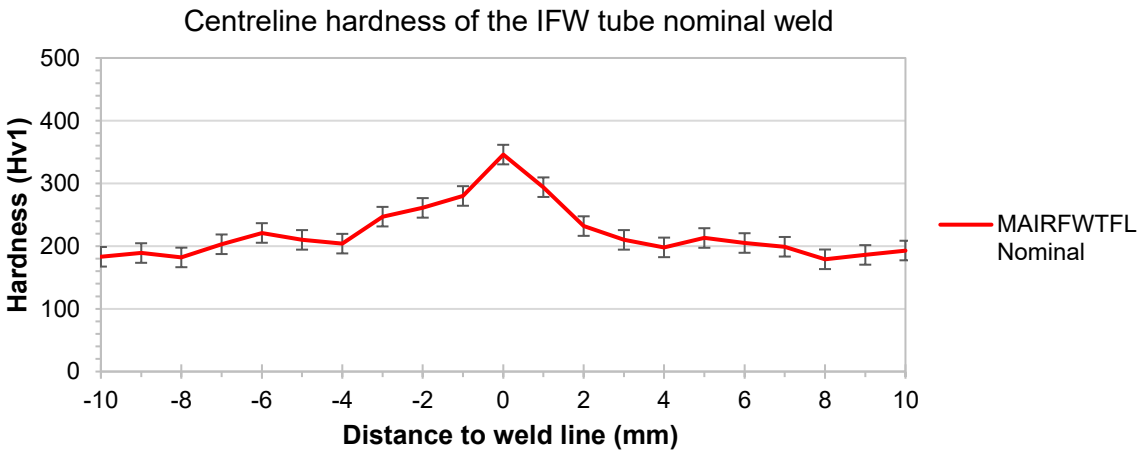


Figure 5-11: Centreline hardness trace of the IFW tube nominal weld. Error bars of 1 standard deviation of the base material measurements displayed.

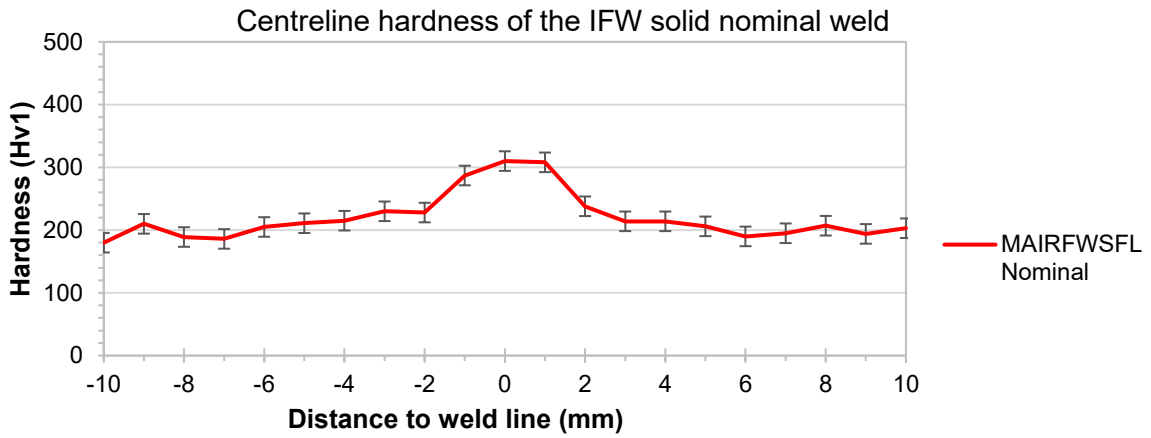


Figure 5-13: Centreline hardness trace of the IFW solid nominal weld. Error bars of 1 standard deviation of the base material measurements displayed.

The continuous drive tube weld exhibits a small rise in hardness visible from 3mm either side, rising to only 276Hv1 on the weld line. In the continuous drive solid component, the weld region shows a limited hardness increase for 4mm across the weld line at ~270Hv1 however the region of elevated hardness extends to 6mm on the left and 8mm on the right with hardness values between 230 and 250Hv1

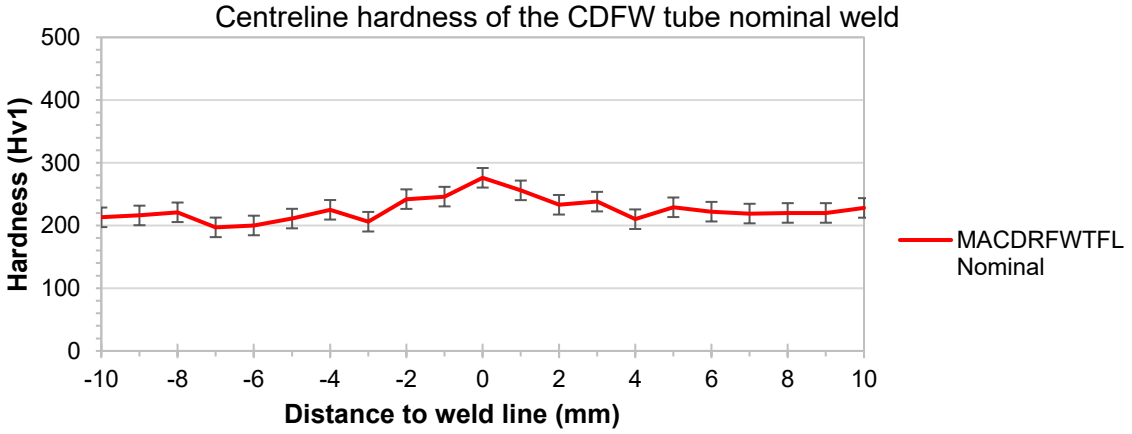


Figure 5-12: Centreline hardness trace of the CDFW tube nominal weld. Error bars of 1 standard deviation of the base material measurements displayed.

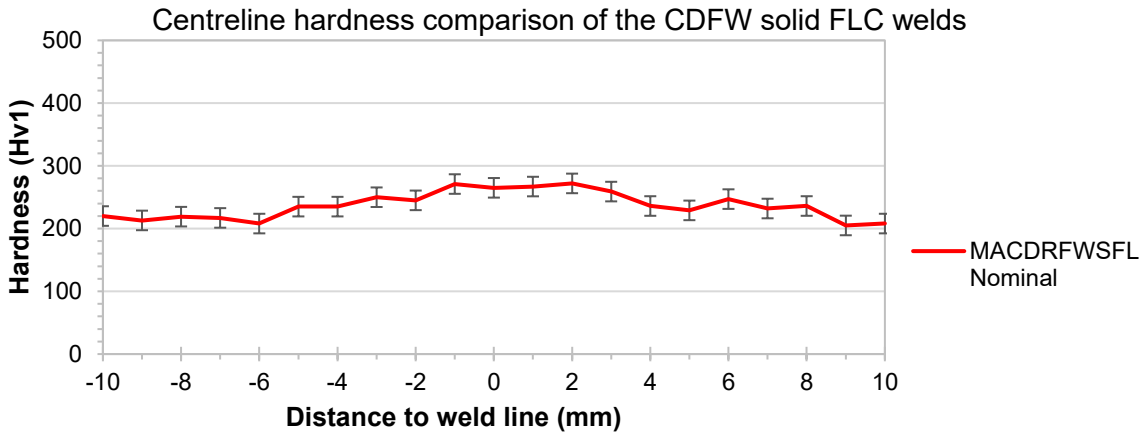


Figure 5-14: Centreline hardness trace of the CDFW solid nominal weld. Error bars of 1 standard deviation of the base material measurements displayed.

5.7.3 Mechanical testing

5.7.3.1 Bend tests

For the bend tests average results of each geometry and mode are shown with the range of results shown by the error bars.

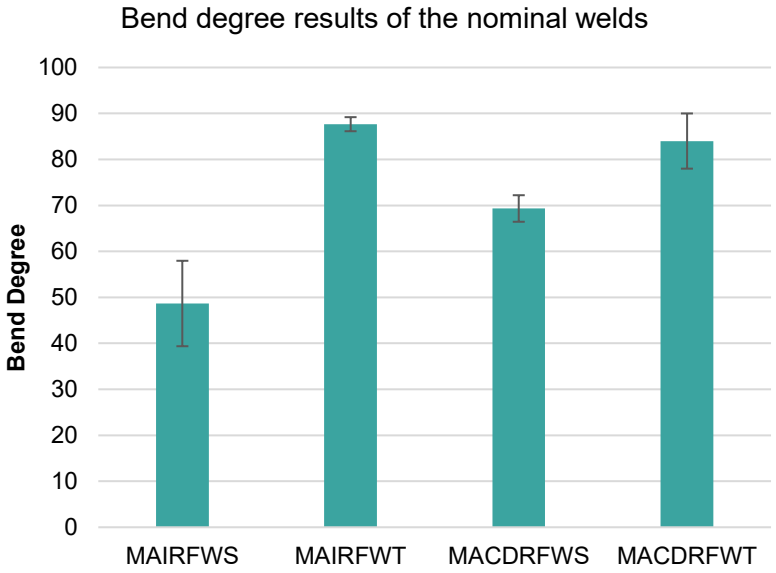


Figure 5-15: Micro-alloyed steel SVH40C average bend test results with error bars.

A correlation is visible between the hardness of the tube welds with narrower but higher hardness peaks and a higher performance in the bend test.

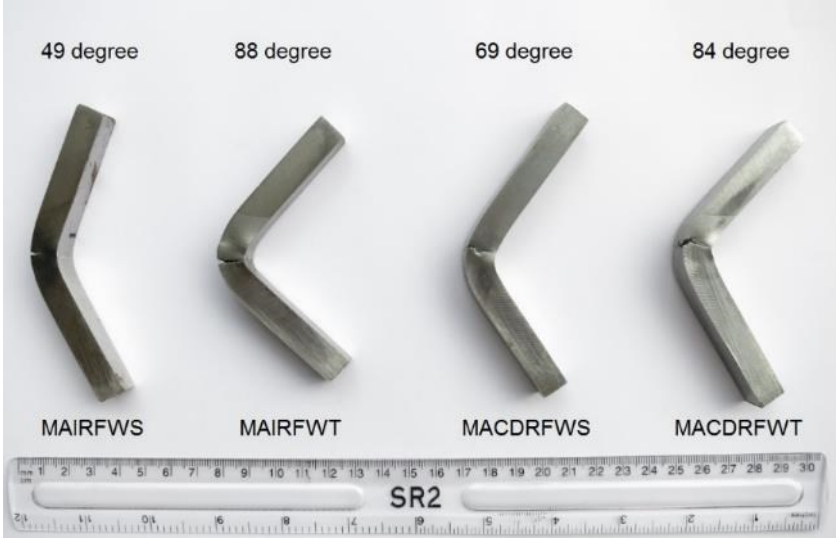


Figure 5-16: Micro-alloyed steel SVH40C nominal weld average bend test pieces.

5.7.3.2 Tensile tests

Tensile test results of the nominal welds are shown with the stress strain curves and primary points graphed. The broken samples are shown indicating the weld zone location. Yield strength results and tensile results show minor differences between the tests. Each tube weld produced a lower proof strength and UTS compared the solid weld in the same mode. However, as the failure location is away from the weld zone and located in the parent material this is unlikely to be indicative of the weld performance and purely normal variation in the parent material. As the point of failure is away from the weld zone it suggests each weld region is stronger than the parent material.

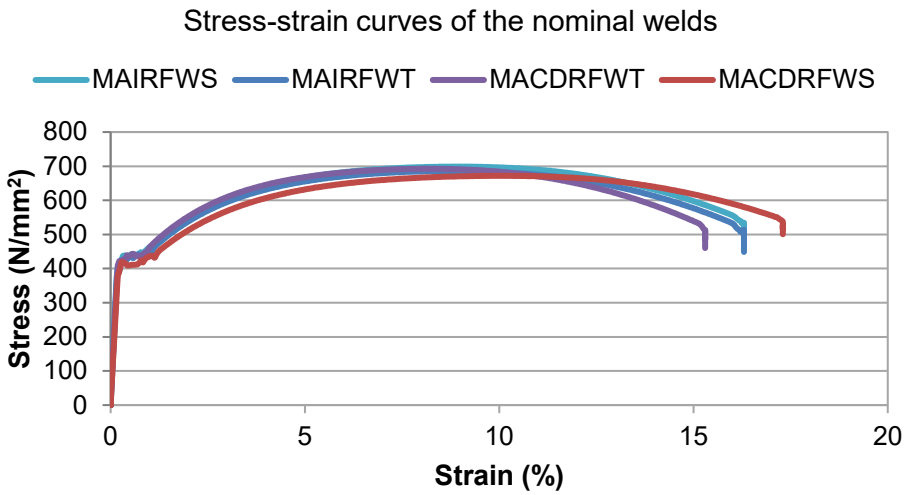


Figure 5-17: Stress strain results from the tensile testing of the nominal welds

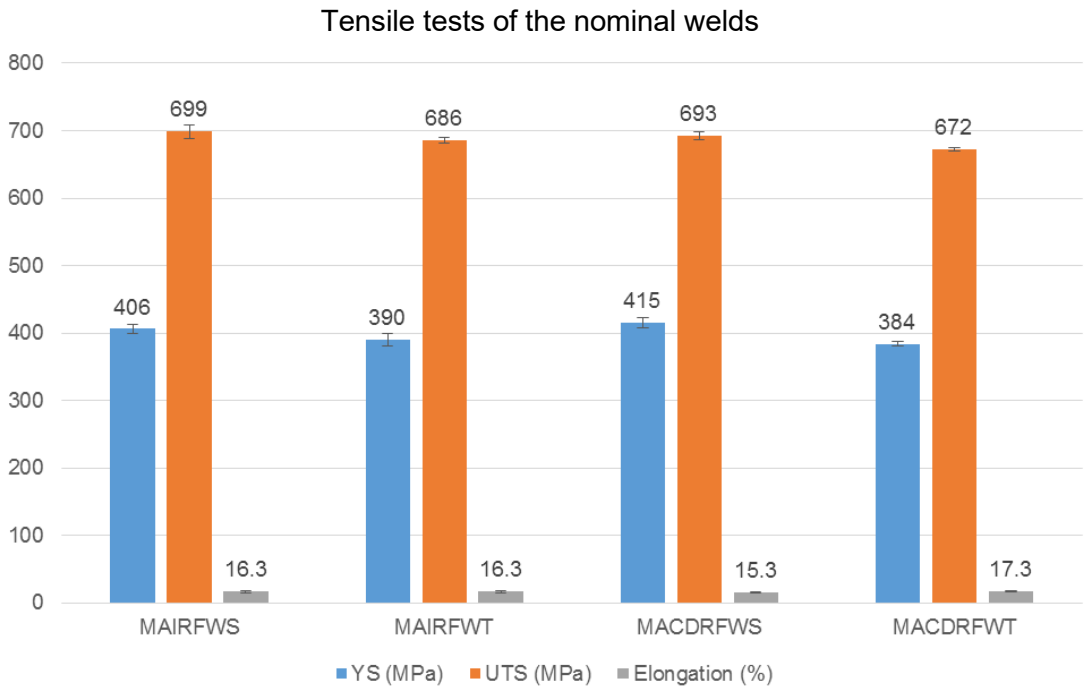


Figure 5-18: Average tensile test results of the micro-alloyed steel SVH40C nominal weld samples including one standard deviation error bars.

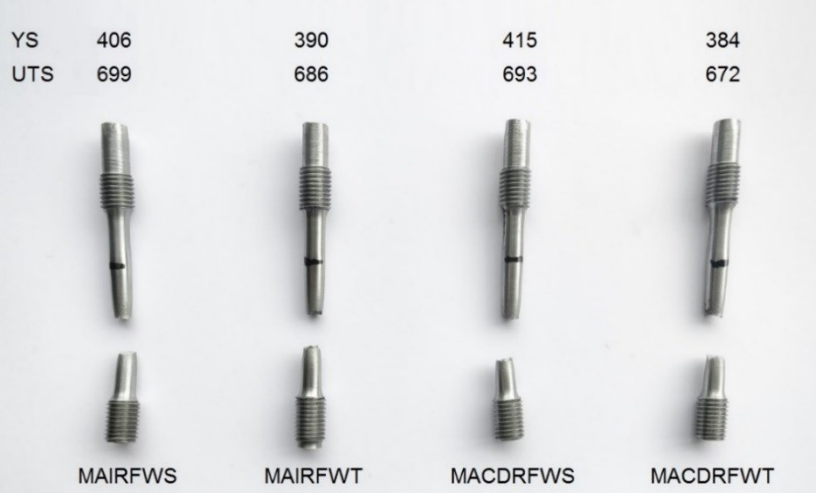


Figure 5-19: Representative micro-alloyed steel SVH40C tensile samples showing failure location. Weld line indicated by black mark.

5.7.3.3 Charpy tests

For the charpy impact tests the average result is shown with the range of the results applied and shown as error bars about the average. In the charpy tests the tube welds outperformed the solid welds. However, the error from the charpy tests could nullify that result. The charpy results also correlate with the bend test results. The tube welds which bent further than the solid welds also absorbed more energy than the solid welds suggesting a more ductile morphology.

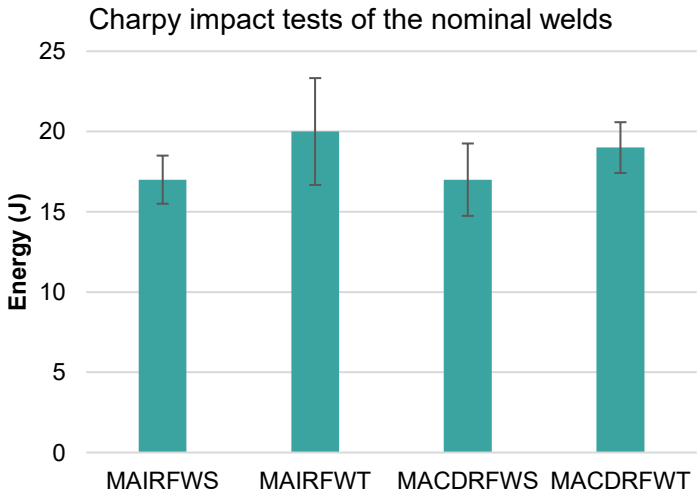


Figure 5-20: Micro-alloyed steel SVH40c nominal weld charpy impact testing results including error bars.

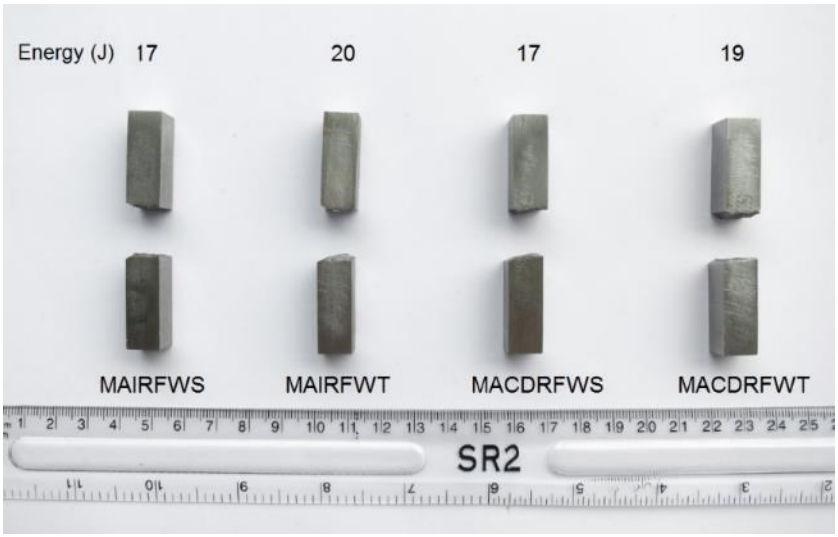


Figure 5-21: Nominal weld average charpy impact test pieces.

5.8 Nominal weld analysis

5.8.1 Weld data

5.8.1.1 Weld curve

The behaviour of the micro-alloyed steel inertia welds display typical traits, matching review work by M Maalekian (2007). The optimal parameters weld curves for solid welds, Figure 5-2, and tube welds, Figure 5-3, are similar and reach cold measurement upsets of 5.74mm and 6.04mm, respectively. Between the welds a maximum variation in upsets of 0.36mm and 0.24mm was seen in the solid and tube geometry, respectively.

Two micro-alloyed steel continuous drive weld curves can be observed in Figure 5-4 (solid welds) and Figure 5-5 (tube welds).

In the CDFW solid weld the second friction speed remained constant, at 486rpm however, a higher first friction speed would have provided more energy to overcome the initial contact torque peak and would have smoothed out the speed undulations when entering the second

friction phase (Manufacturing Technology Inc, 2012). The cold measured upset was 7.01mm. Burn off was triggered at 5.0mm of upset.

For the CDFW tube weld, a higher first friction speed and/or lower first friction pressure would reduce the chance of experiencing the initial 100% torque peak. Longer first friction times and slower pressure ramp ups and speed ramp downs could be employed to reduce the amount of torque variation, as well as limit the amount of 100% torque used. The weld reached a 10.58mm cold upset measurement. Burn off was triggered at 8.4mm of upset. Between the welds a maximum variation in upsets of 0.07mm and 0.03mm was seen in the tube and solid geometries, respectively.

5.8.2 Microstructural analysis

5.8.2.1 Visual inspection

Examples of the repeated parameter welds are shown in Figure 5-6. In all materials the solid components produced larger flash amounts as the material had only one surface from which to exit the interface. The tubes produced smaller flash but on both the OD and ID. The ID flash was larger as the material was squeezed out through a smaller area. The inertia flash produced a tighter curl of flash compared to the continuous drive flash due to the higher pressures, fitting with general parameter effects Linnert (1994).

The only other difference noticed between inertia mode and continuous drive mode welds was the extended heat penetration of the CDFW welds evident from the tempering colouration of the surface, matching the reduced heat input work demonstrated by Romero *et al.* (2009) and suggesting that Duffin and Bahrani (1973) are correct. Flash was symmetrical and free of cracks. No anomalies were found.

5.8.2.2 Weld microstructure

In the nominal inertia tube weld, Figure 5-7, a phase transformation was detected at -4 to -3mm from the weld line (boundary of heat affected zone) due to the large increase in distribution of

the pearlite, with ferrite moving to the grain boundaries. After -2mm the TMAZ zone is visible as the ferrite-pearlite banding is deformed due to material flow during the welding process. Around -1mm the transformation to re-crystallised fine-grained un-tempered martensite begins in the inertia tube weld. In the inertia solid weld, the distribution of un-tempered martensite was less with more bainite visible and correspondingly the weld zone was wider than in the tube weld from a thinner plasticised layer but larger TMAZ and HAZ which would indicate slower cooling rates (Linnert, 1994; I. Woo *et al.*, 2002).

In the continuous drive welds the morphology suggests an even slower cooling rate than the inertia welds visible by the formation of a predominantly bainite mixture on the weld line along with a wider TMAZ and HAZ zone due to the lower pressures used, matching accepted work by Baker (2016); (Kimura *et al.*, 2010; I. Woo *et al.*, 2002).

5.8.2.3 Hardness analysis

Hardness test results for the inertia tube weld showed increased hardness of 250Hv at -2mm and 350Hv at the weld line. This matched with the mixed bainite and martensite microstructure in the weld zone. In the solid welds the centre of the weld is only 310Hv1. This coincided with the increased proportion of bainite visible at the weld zone. Beyond 2mm from the weld zone the hardness drops to 215Hv1 and then back to around 200Hv1 beyond 6mm suggesting that the TMAZ and HAZ is primarily ferrite and pearlite, which matches the micrographs at 3 and 4mm from the weld line.

The continuous drive welds also showed a hardness increase to 250Hv at around -2mm however the centre of the weld did not increase much above this at about 270-280Hv. This agrees with the micrographs where the weld zone is a mix of ferrite, some pearlite and bainite. The combination with the wider zone widths and lower hardness levels suggest a slower cooling rate was experienced in the continuous drive welds (Baker, 2016).

The continuous drive welds showed more ferrite, pearlite and lower bainite in the weld zones along with wider weld zones as seen in the lower and wider hardness trace peaks of Figure 5-9 and Figure 5-10. This again indicates a slower cooling rate compared to the inertia mode while the wider weld zone will be due to the longer process times of the continuous drive mode and the lower relative increase in pressure at forge, leading to the subsequent greater heat penetration away from the bond line (Johnson & Daines, 1973). The slower cooling rate also allowed for greater grain coarsening at the weld zone (Duffin & Bahrani, 1973; I. Woo *et al.*, 2002). However, as the grains are smaller than the parent material it indicates dynamic recrystallisation is occurring, as also observed by Jata and Semiatin (2000), as the grains towards the centre are still relatively small even with the slower cooling rates it would suggest that a continuous recrystallisation mechanism was in play. The inertia tube component can be seen to have a fine grain structure~30μm while at the other end of the scale the continuous drive solid component has a slightly larger mixed grain structure ~ 50μm.

Overall, the weld zones in the micro-alloyed steel components are defined by the deformation and extent of heat penetration away from the bond line: a balance of energy input and conduction as well as other losses. These two factors primarily affect the weld zone width and microstructure, which have direct impacts on the weld piece's mechanical properties.

5.8.3 Mechanical testing

5.8.3.1 Bend test analysis

In the bend test the inertia tube reached a higher level of bend than the Inertia solid. Although the tube weld has a higher hardness and corresponding microstructure the TMAZ width of the tube weld is narrower than the solid weld, ~4mm vs ~8mm. This could suggest that the greater proportion of softer more ductile parent material enabled the tube weld to bend further. A similar phenomenon is seen in copper to aluminium welds conducted by S. Chen *et al.* (2017) and I. Bhamji *et al.* (2012) bend tests clearly show the softer aluminium compensating for the

stiffer less ductile copper and bending preferentially instead of the copper until fractures occurred at the weld interface. The same occurrence is seen in the continuous drive welds, with the softer wider weld zone of the solid weld not bending as much as the harder thinner weld zone of the tube weld.

5.8.3.2 Tensile analysis

As the results are similar, it would suggest the test pieces all broke in the same microstructural area, indicating that regardless of geometry or process mode, the failure point in each sample is the same. Figure 5-19 shows representative samples all breaking at the same distance from the weld beyond the edge of the heat affected zone and in the parent material. This indicates that the microstructure has increased in strength over the weld area to a higher level than the parent material. Similar strengthening of the entire weld zone was seen by Tumuluru (1984) and Sathiya, Aravindan, and Haq (2007). The solid components are noted to have marginally higher tensile strengths and yield stresses than the tubular components. As the main deformation and break is in the parent material this correlation with the other tests is likely to be coincidental.

5.8.3.3 Charpy analysis

The charpy tests show a general trend for the tubular components to be slightly more impact resistant than the solid ones. This corresponds with the more ductile behaviour seen in the bend tests and possibly relates to the lower yield stress as noted in the tensile tests. However, the difference of only 2 – 3 J is within the variation seen within the group testing and so is not statistically significant. All test pieces broke at the weld interface and didn't deviate towards the parent material, indicating that the weld interface is more brittle than the surrounding material, Figure 5-21, as also seen by Tumuluru (1984) and C. Bennett *et al.* (2007).

5.9 Final length control results

5.9.1 Weld data

5.9.1.1 Weld curve results

Weld curves have been plotted from the machine collected data. The adjustment for the part length can be seen in the speed and torque traces in inertia welding with positive increases for oversized parts and speed reductions for undersized parts. In the continuous drive components it appears that the second friction phase is being adjusted however this is actually triggered by the forge fixture meeting a trigger point (Manufacturing Technology Inc, 2012).

5.9.1.1.1 Inertia mode results

In the inertia mode proportional torque input is seen dependant on the combined initial size of the components. This is followed by torque modulated deceleration, which is based on the nominal weld curve, to meet the required calculated upset. In the parts -2mm less than nominal the braking torque continues through into the forge phase until the rotation stops indicating the final length was not met as there was not enough material to upset. This occurs in both the tube and solid geometry.

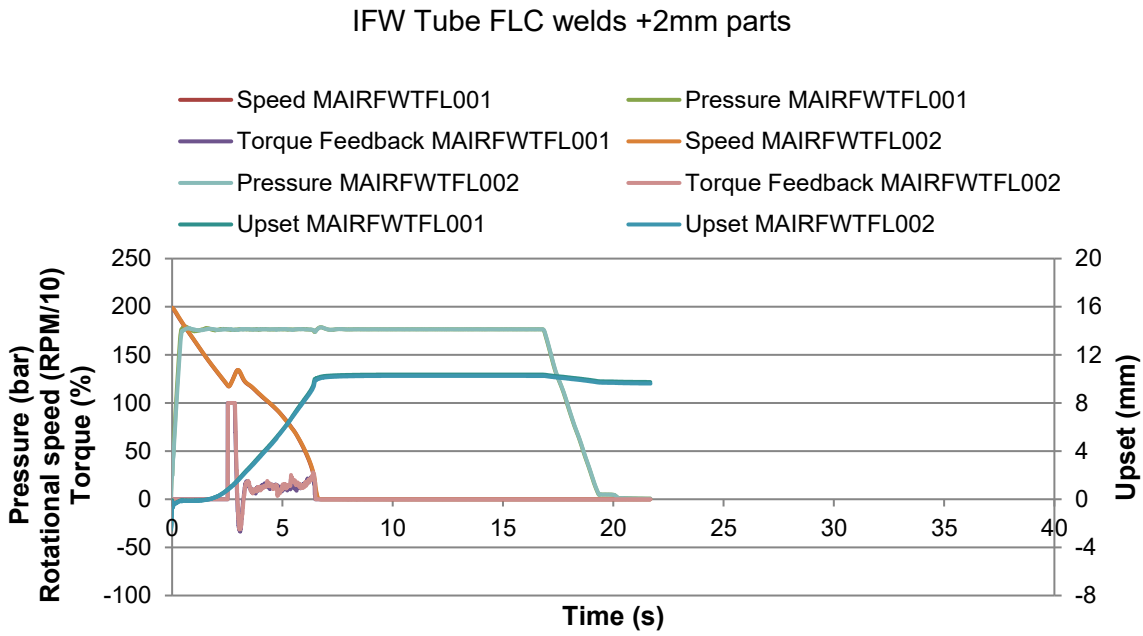


Figure 5-22: Parameter weld curves for a) MAIRFWTFL001, and b) MAIRFWTFL002, both from components +2mm greater than nominal.

Positive torque input can be seen increasing the weld speed and then modulating the remaining deceleration with respect to the upset produced.

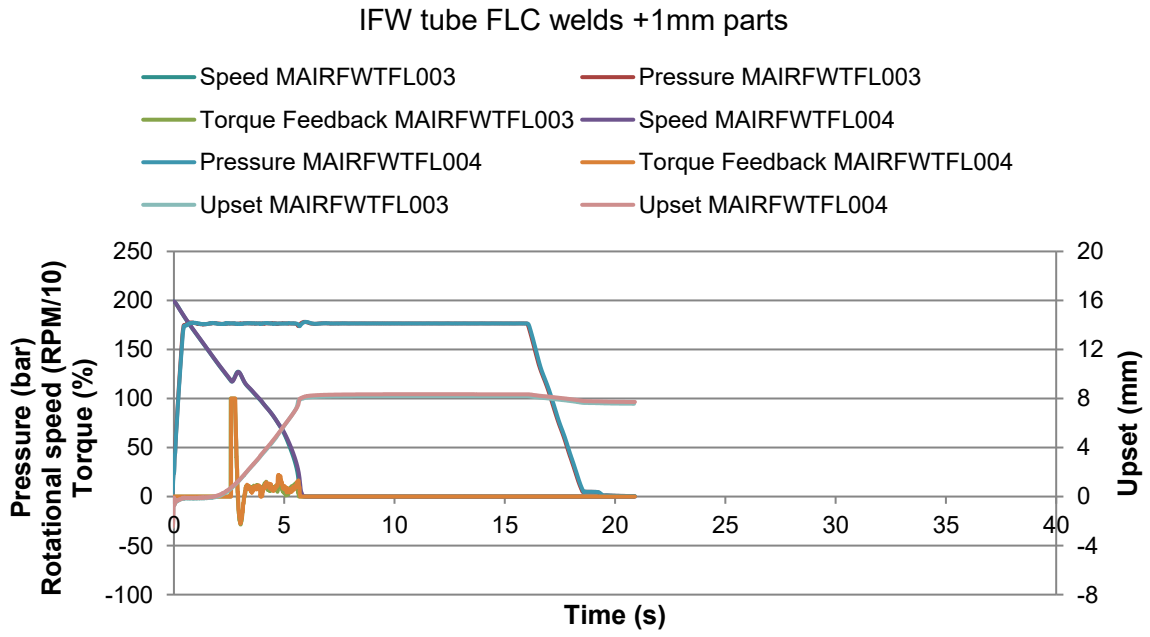


Figure 5-23: Parameter weld curves for a) MAIRFWTFL003, and b) MAIRFWTFL004 both from components +1mm greater than nominal.

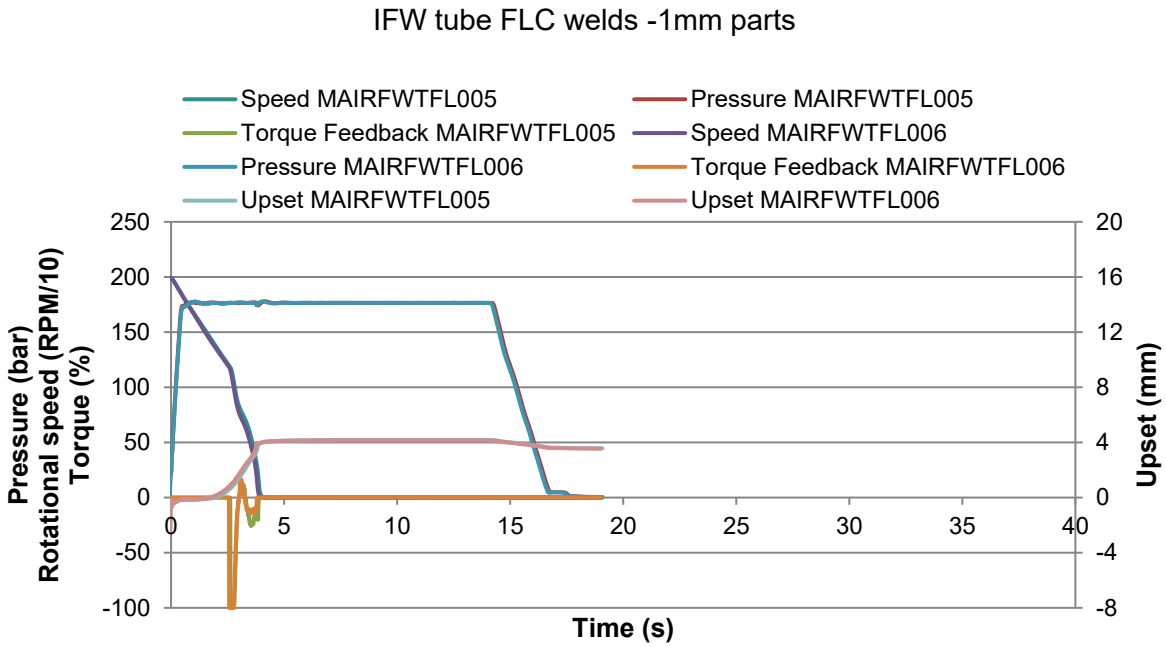


Figure 5-24: Parameter weld curves for a) MAIRFWTFL005, and b) MAIRFWTFL006, both from components -1mm less than nominal.

Continued braking can be seen from the start of the modulation in the parts 2mm less than nominal.

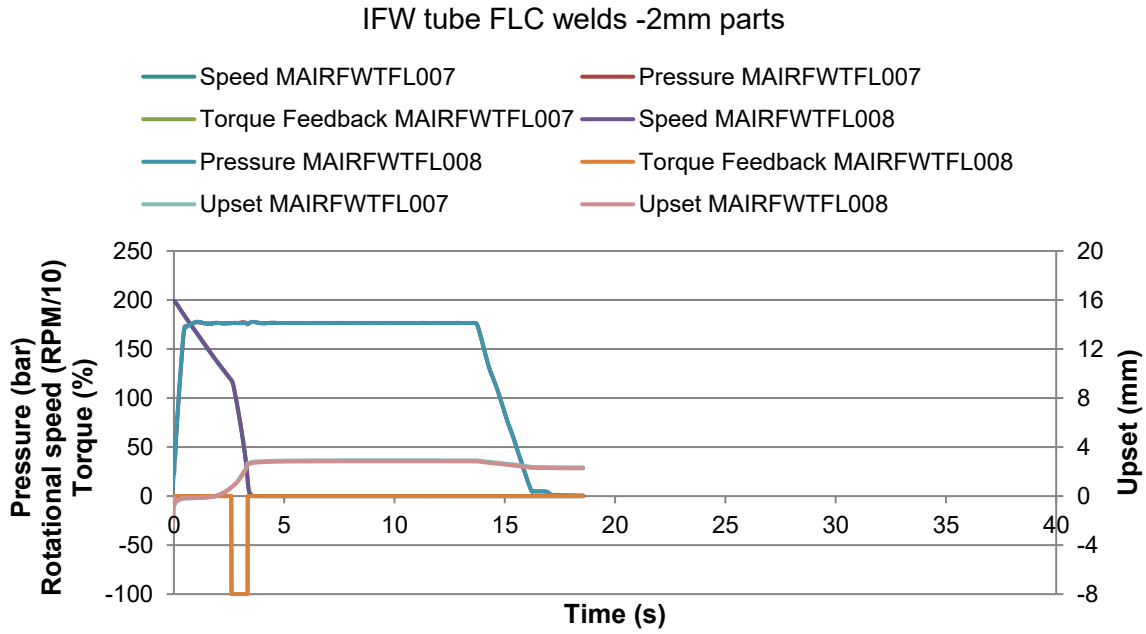


Figure 5-25: Parameter weld curves for a) MAIRFWTFL007, and b) MAIRFWTFL008, both from components -2mm less than nominal.

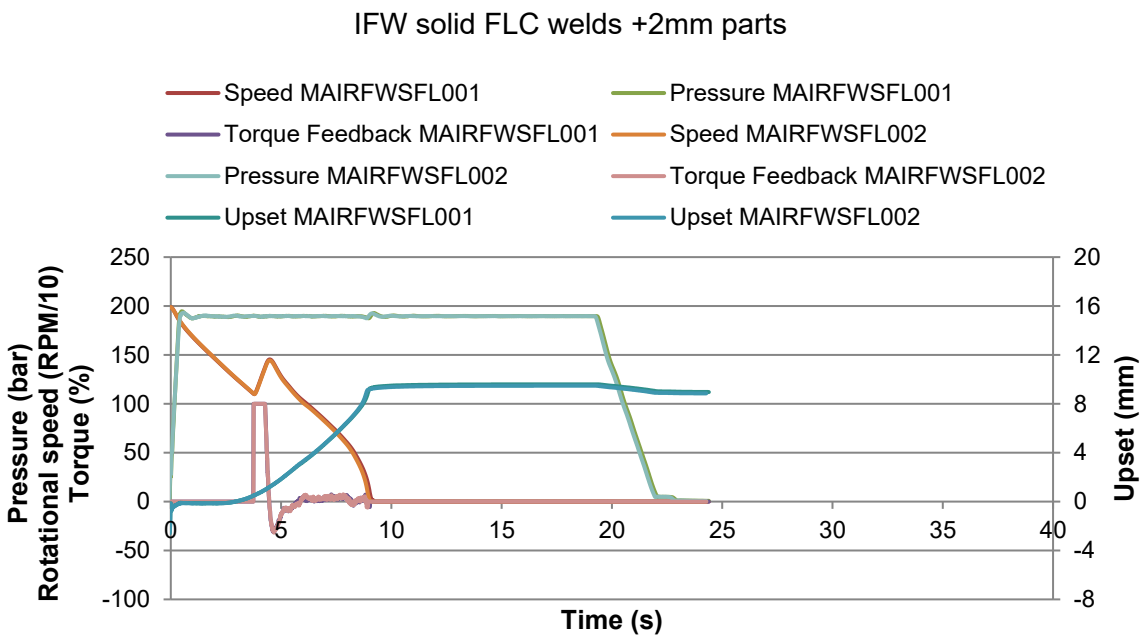


Figure 5-26: Parameter weld curves for a) MAIRFWSFL001, and b) MAIRFWSFL002, both from components +2mm greater than nominal.

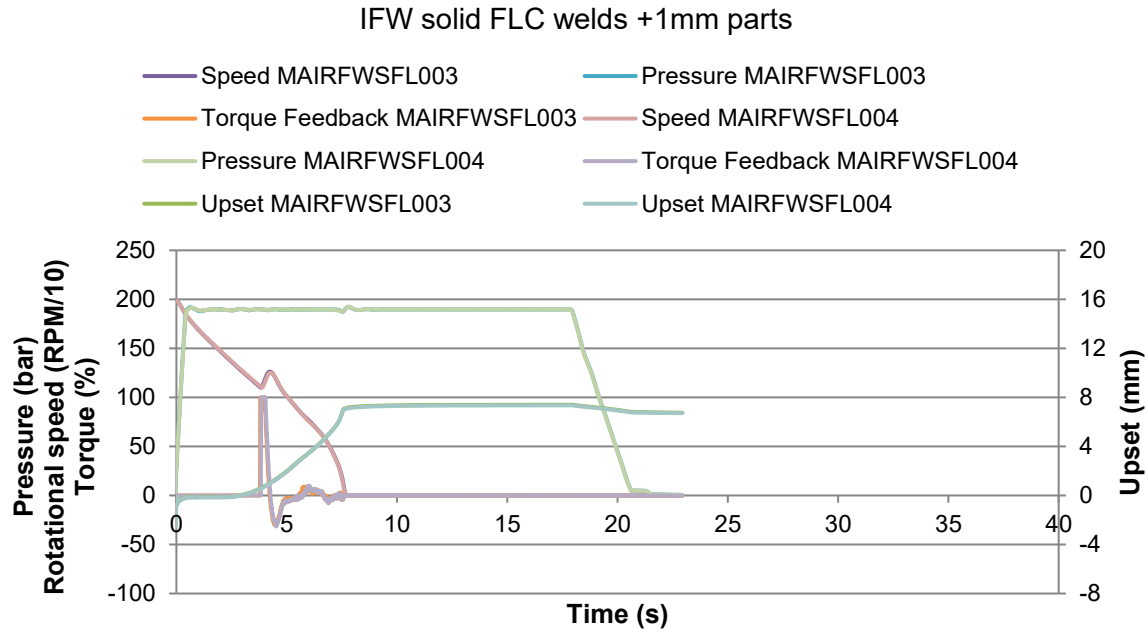


Figure 5-27: Parameter weld curves for a) MAIRFWSFL003, and b) MAIRFWSFL004, both from components +1mm greater than nominal.

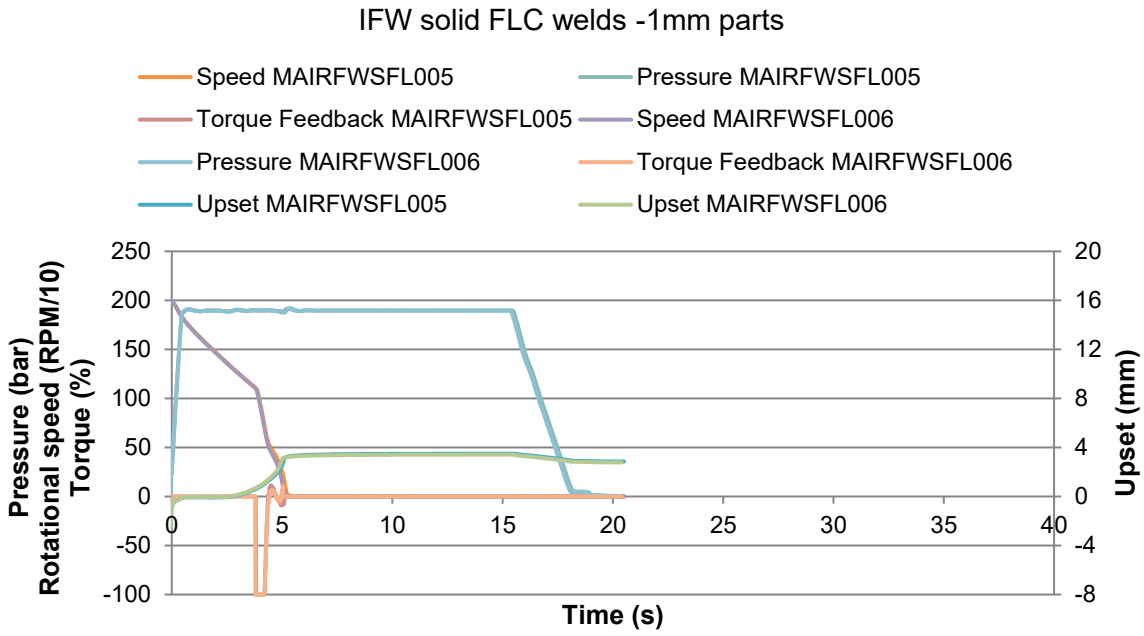


Figure 5-28: Parameter weld curves for a) MAIRFWSFL005, and b) MAIRFWSFL006, both from components -1mm less than nominal.

The braking torque can be seen continuing throughout the weld cycle from the start of the manipulation in the welds with parts 2mm less than nominal.

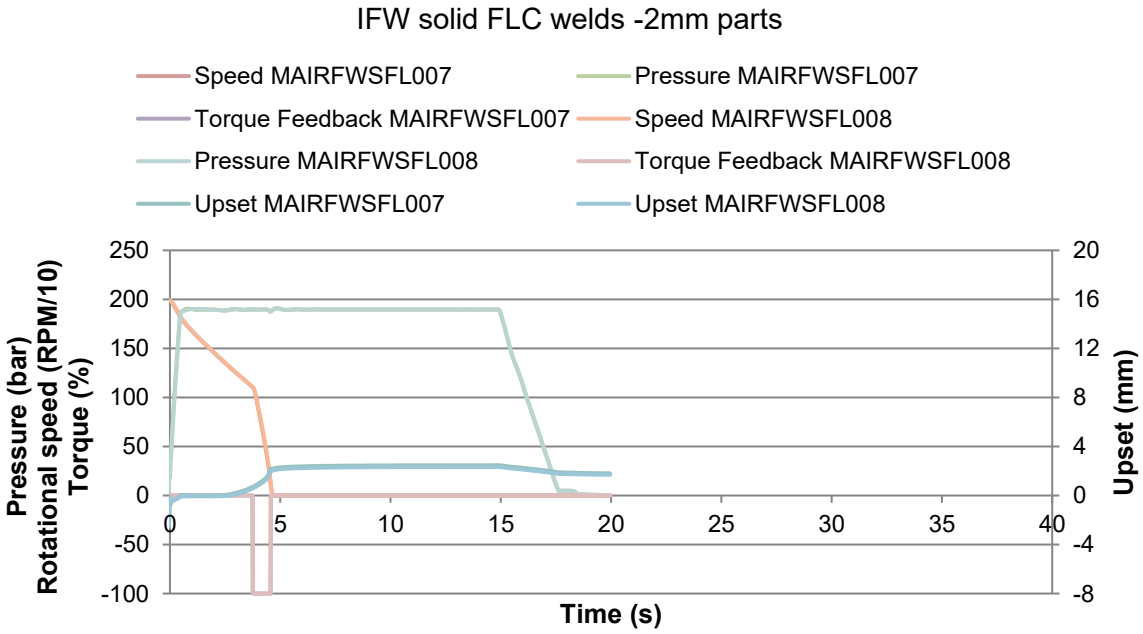


Figure 5-29: Parameter weld curves for a) MAIRFWSFL007, and b) MAIRFWSFL008, both from components -2mm less than nominal.

5.9.1.1.2 Continuous drive mode results

In continuous drive the first weld MACDRFWTFL001 showed an extended time at 100% torque feedback, when transitioning to 2nd friction speeds and pressures. To reduce the stress on the machine the 1st friction speed was increased and the time at 1st friction was extended, Figure 5-30. This reduced the time at 100% torque feedback and made the transfer into the upsetting transition phase more immediate. However, the gain parameters in the machine still caused an undershoot of spindle speed. A potential better solution would have been to increase the ramp time between the 1st and 2nd friction phases allowing for more accurate control with the set gain parameters. As minimal upset is produced during the 1st friction phase due to very low interface pressure it can be assumed that the interface was in a conditioning phase. Some extra heat energy would have penetrated the material behind the interface in MACDRFWTFL002, softening the material, as evidenced by the immediate transition to upsetting upon starting 2nd friction compared to the gradual increase seen in the previous weld. However, later in the 2nd friction phase the upset rates were identical thereby suggesting that any impact from the change in 1st friction had ceased. Longer ramp times can be seen in the solid component, Figure 5-34 to Figure 5-37, where combined with a smaller diameter the machine reached 50% torque feedback as a maximum.

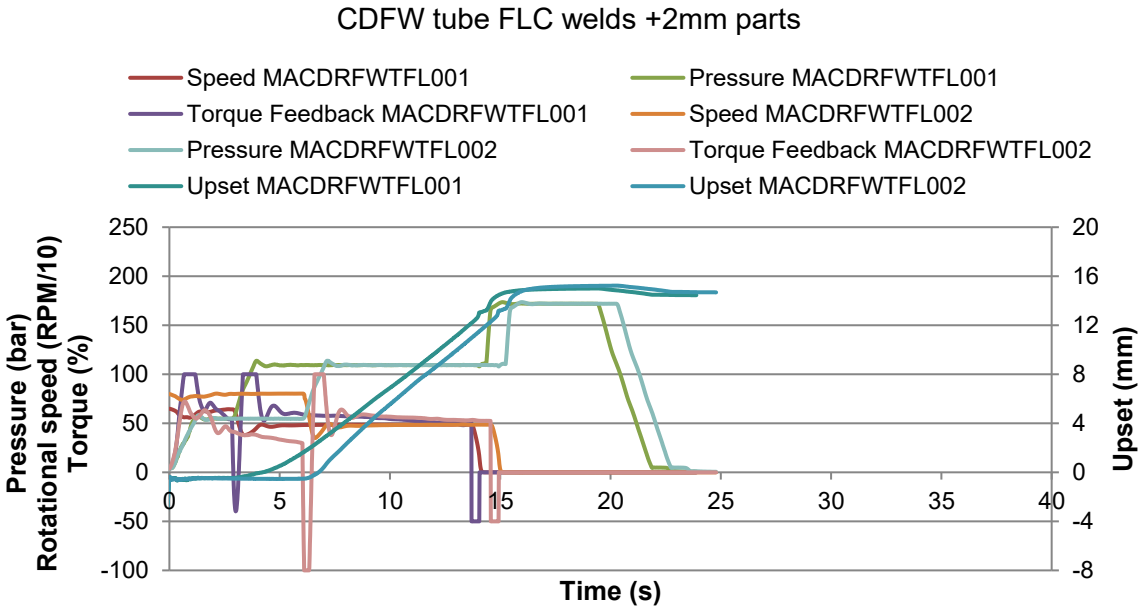


Figure 5-30: Parameter weld curves for a) MACDRFWTFL001, and b) MACDRFWTFL002, both from components +2mm greater than nominal.

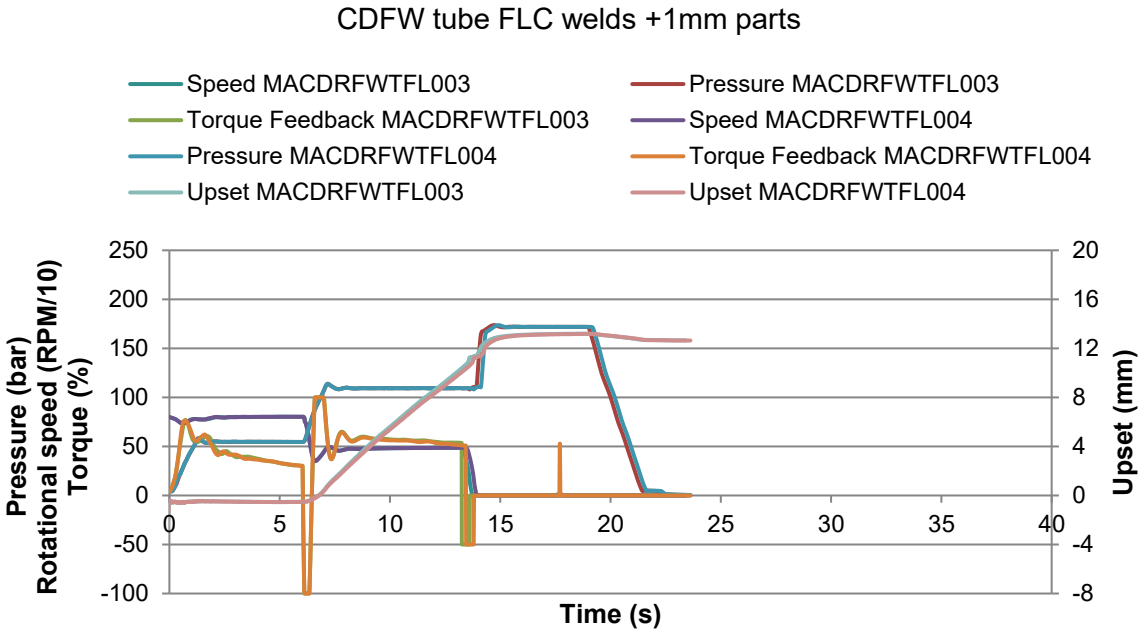


Figure 5-31: Parameter weld curves for a) MACDRFWTFL003, and b) MACDRFWTFL004, both from components +1mm greater than nominal.

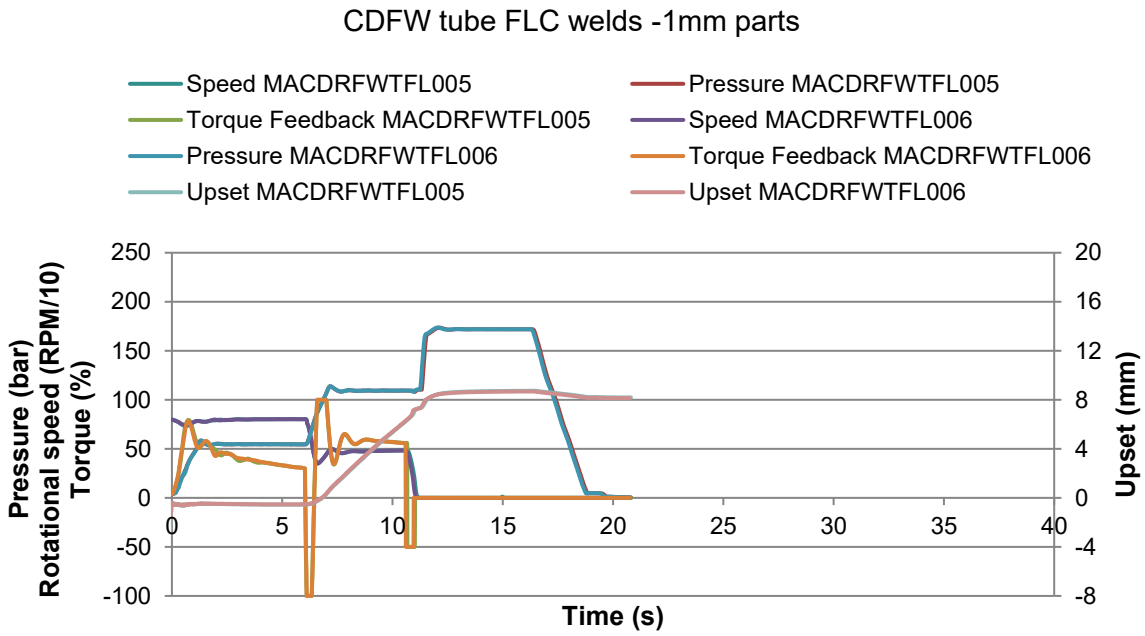


Figure 5-32: Parameter weld curves for a) MACDFWTFL005, and b) MACDFWTFL006, both from components -1mm less than nominal.

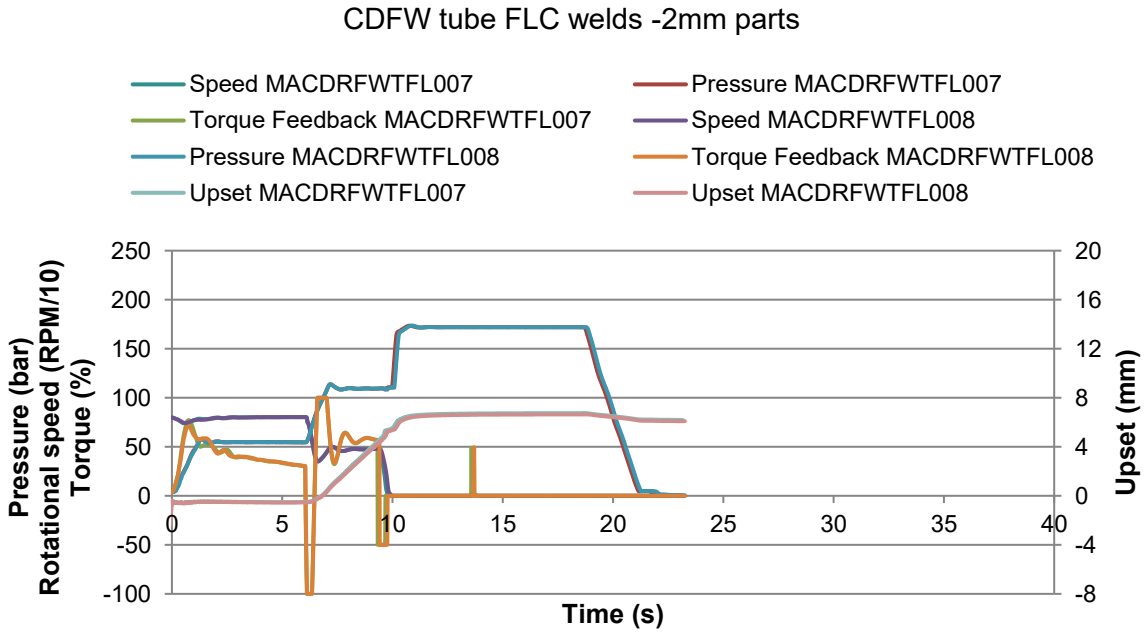


Figure 5-33: Parameter weld curves for a) MACDRFWTFL007, and b) MACDRFWTFL008, both from components -2mm less than nominal.

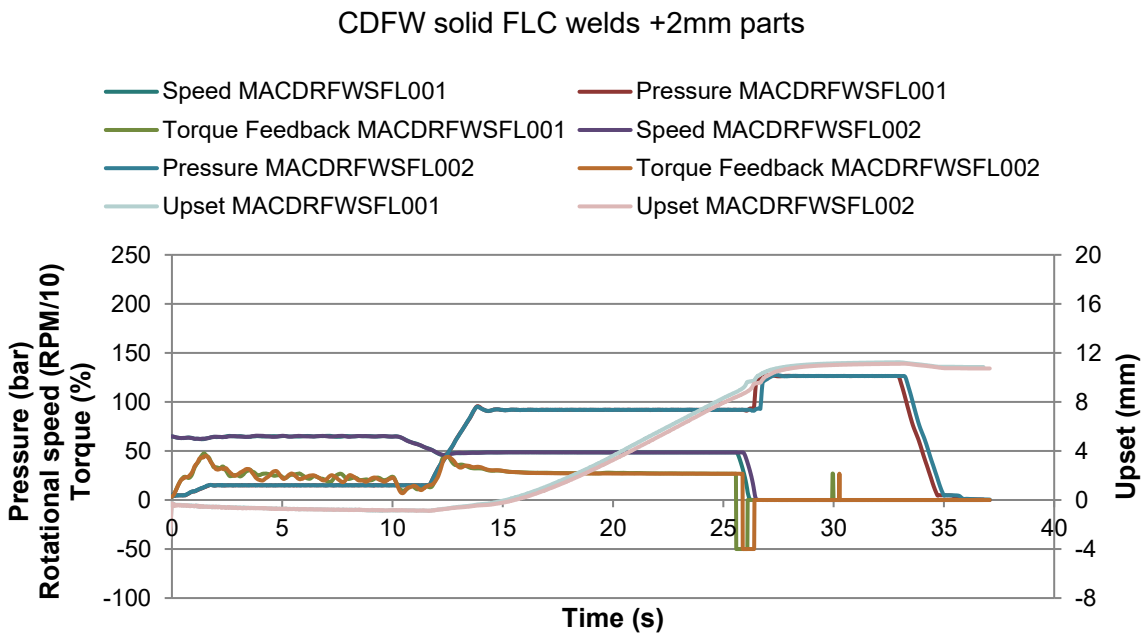


Figure 5-34: Parameter weld curves for a) MACDRFWSFL001, and b) MACDRFWSFL002, both from components +2mm greater than nominal.

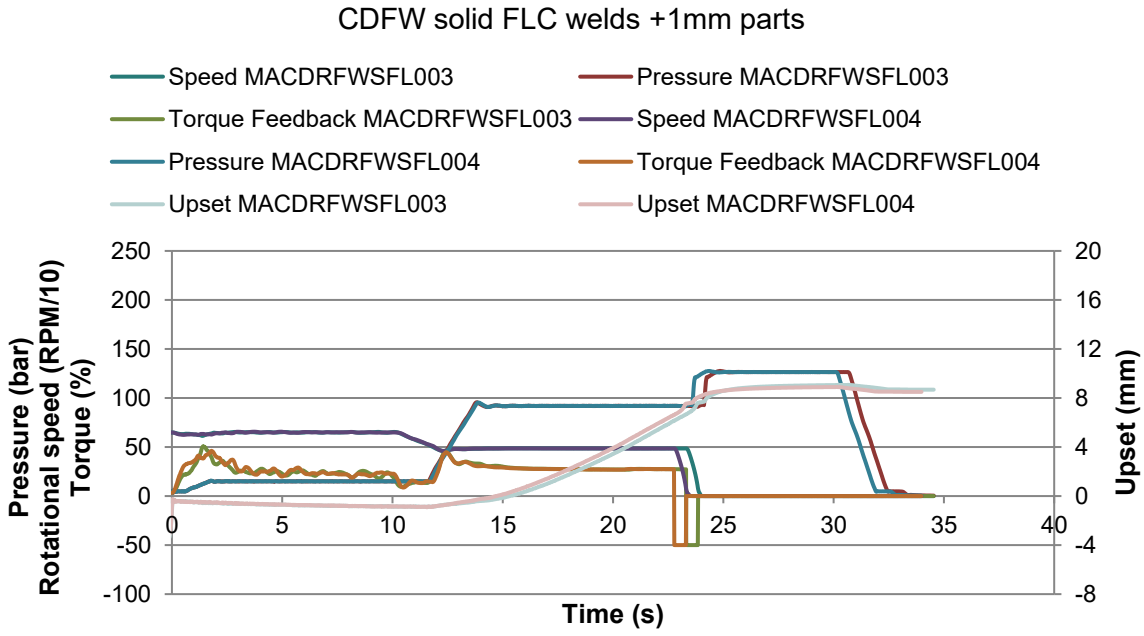


Figure 5-35: Parameter weld curves for a) MACDRFWSFL003, and b) MACDRFWSFL004, both from components +1mm greater than nominal.

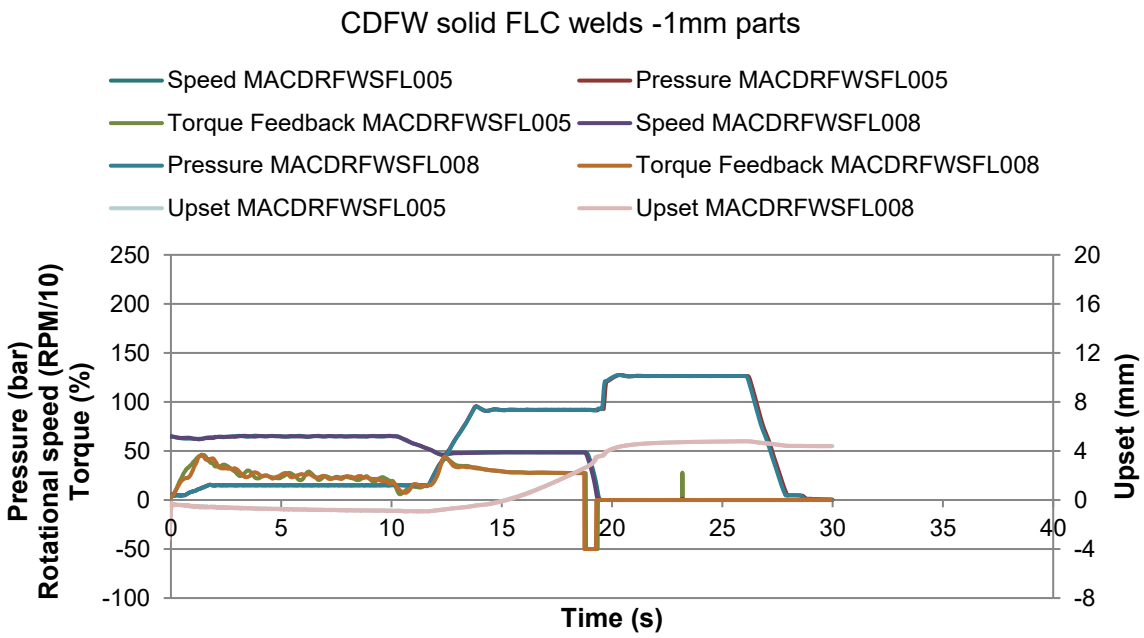


Figure 5-36: Parameter weld curves for a) MACDRFWSFL005 and b) MACDRFWSFL008, both from components -1mm less than nominal.

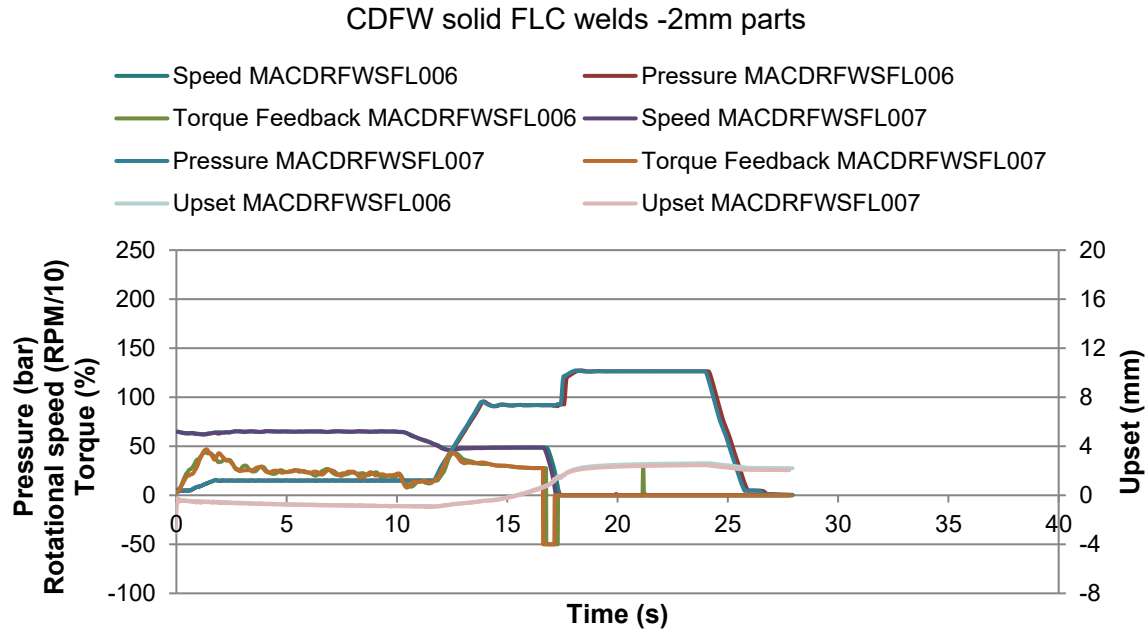


Figure 5-37: Parameter weld curves for a) MACDRFWSFL006, d b) MACDRFWSFL007, from components -2mm less than nominal.

5.9.1.2 Component length

The following graphs have been plotted with the hot final length the machine used as a parameter taken from a representative profile weld from the nominal welds. Additionally, the average shrinkage due to cooling from the nominal welds was applied to the hot target length to produce a cold target length. This allowed comparison of the post-process cold actual measurement of the final length control welds against a component made from ideal part lengths. Pre-weld lengths of the combined parts are plotted against the final length of the welded part. Trends have been applied where possible to calculate the relationship.

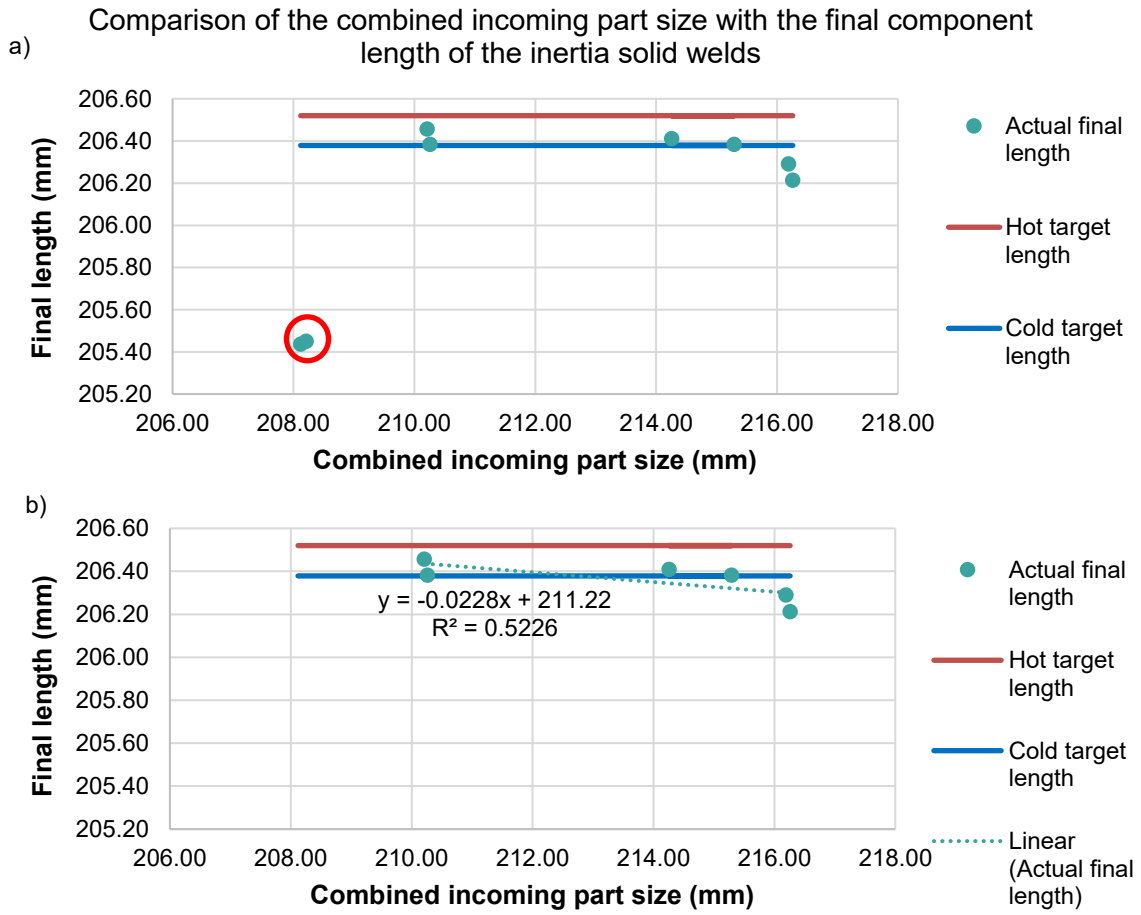


Figure 5-38: Inertia solid final length control cold measurements compared to the targets, a) with the undersized part welds included outlined in a red circle, b) with the undersized part welds removed and a linear trend line applied.

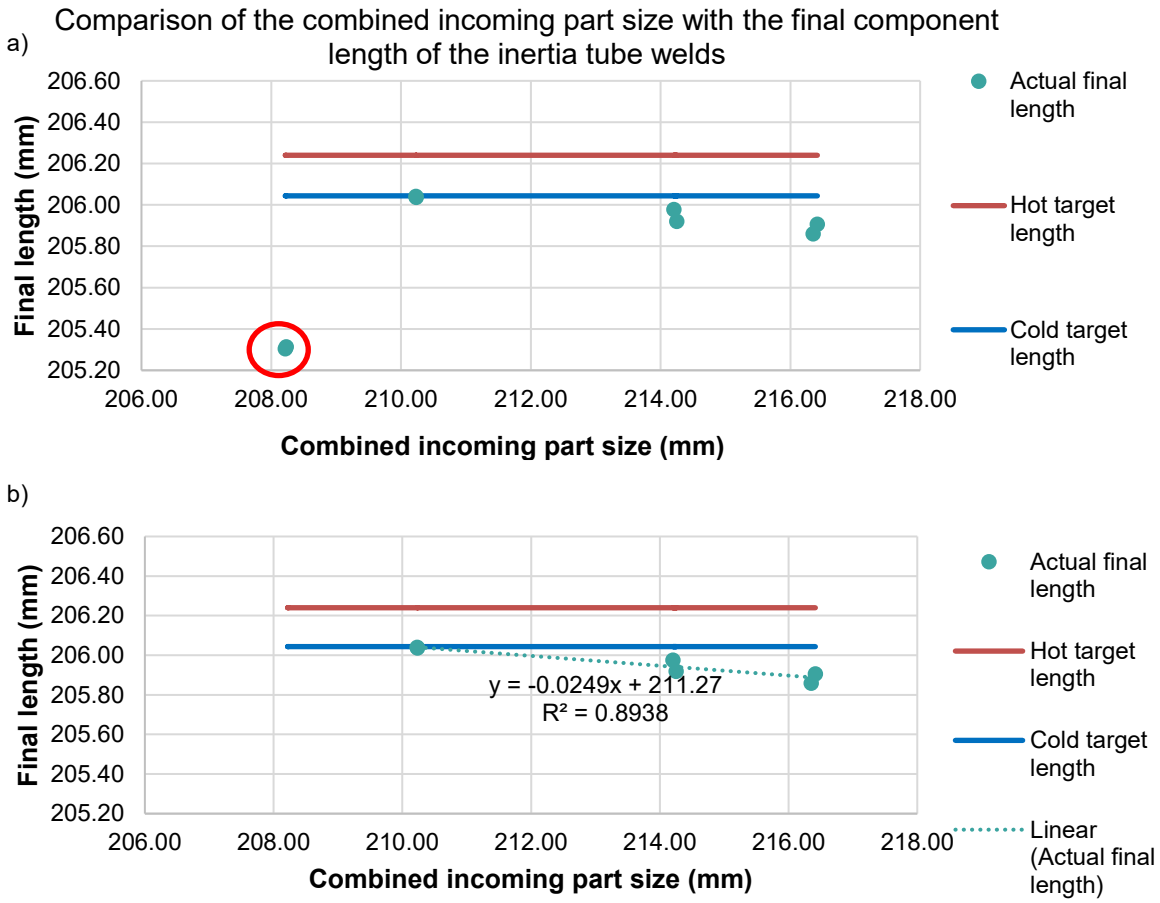


Figure 5-39: Inertia tube final length control cold measurements compared to the targets, a) with the impossible welds included outlined in a red circle, b) with the impossible welds removed and a linear trend line applied.

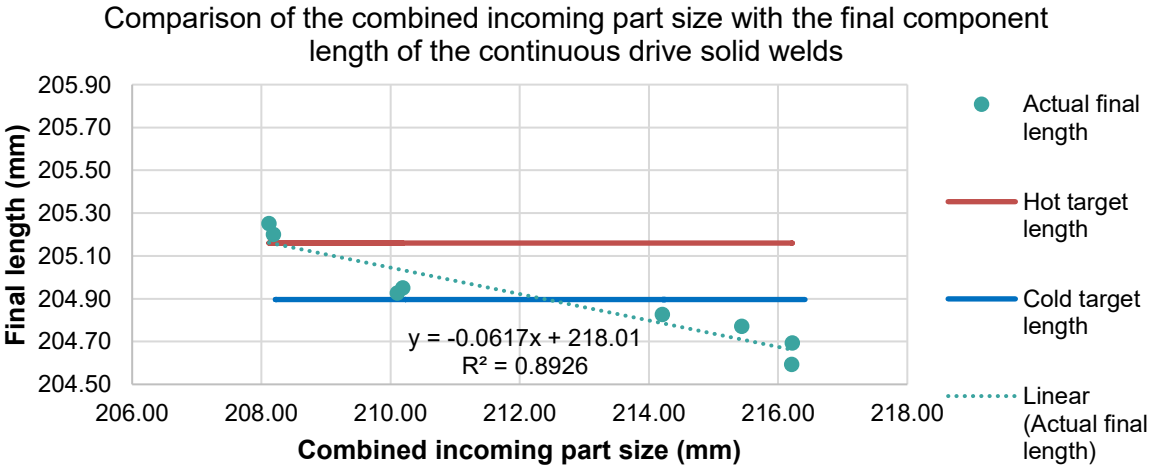


Figure 5-40: Continuous drive solid final length control cold measurements compared to the targets.

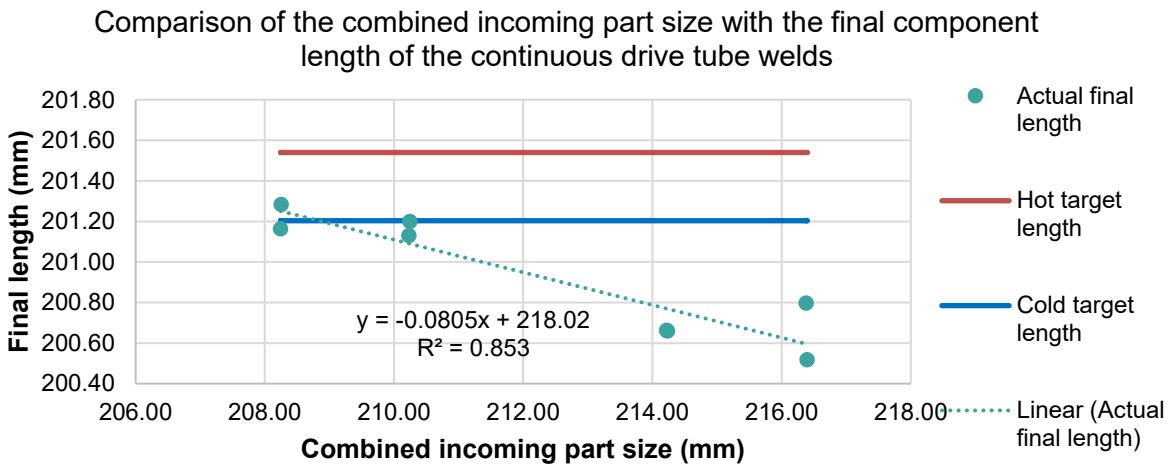


Figure 5-41: Continuous drive tube final length control cold measurements compared to the targets.

5.9.1.3 Energy input results

Solid geometry IFW FLC weld energy rates and cumulative energy amounts are shown in Figure 5-42. A high initial peak rate is shown of 140-150kJ/s during conditioning of the interface. This decreases rapidly to around 35kJ/s where the remaining energy is modified. In the longer two weld sets the energy rate continues at a rough steady state of 35kJ/s until 0.5 s before rotation ceased.

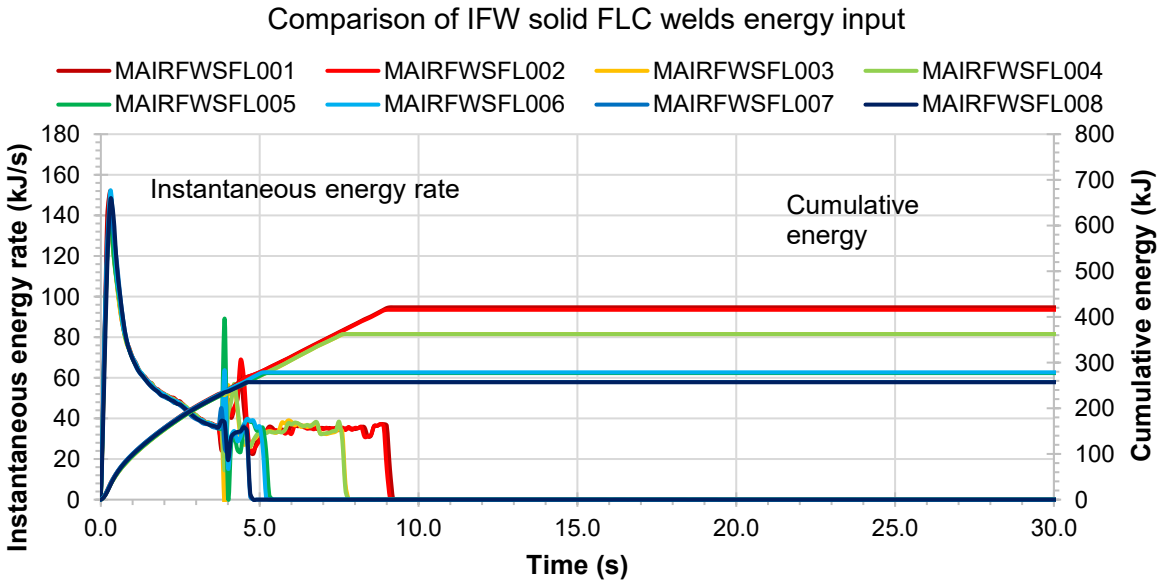


Figure 5-42: The energy input rate and cumulative energy of the IFW solid FLC welds.

Tube geometry IFW FLC weld energy rates and cumulative energy amounts are shown in Figure 5-43. Similar to the inertia solid welds, a high initial peak rate is seen of 118 to 136kJ/s dropping steadily to 60kJ/s when the energy is then modified dependant on remaining length. The weld set with the shortest parts are seen to drop rapidly to a stop while the remaining weld sets show a rate of around 60kJ/s until just before the rotation stops.

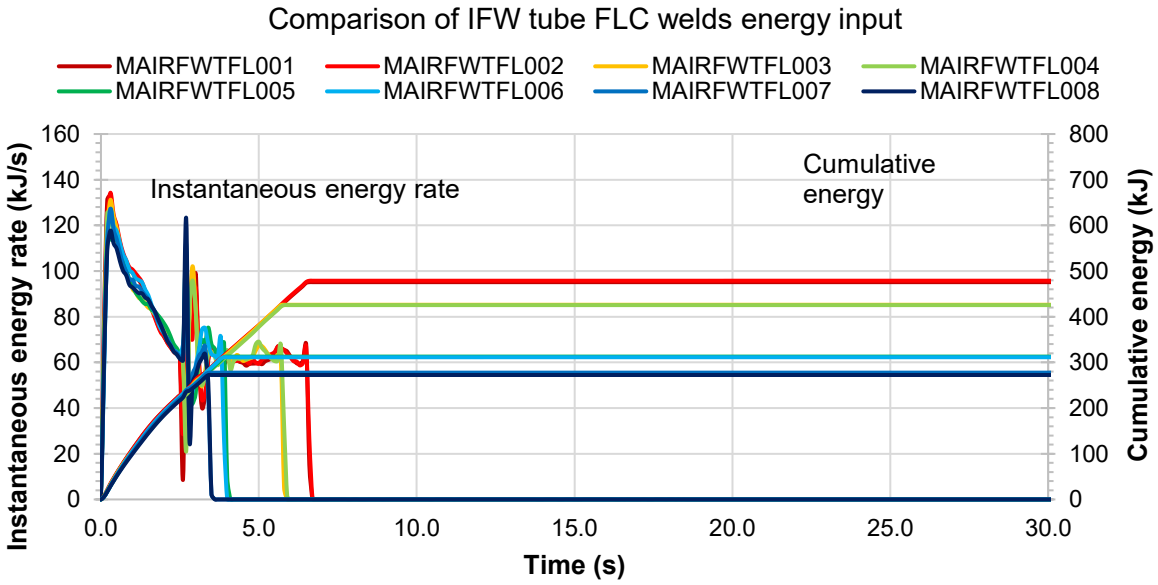


Figure 5-43: The energy input rate and cumulative energy of the IFW tube FLC welds.

Solid geometry CDFW FLC weld energy rates and cumulative energy amounts are shown in Figure 5-44. The energy input rate varies during the 1st friction phase (up to 12 seconds) while transferring to a steady input state in the 2nd friction phase. This continues until the friction phase upset trigger is reached whereupon braking occurs. The energy input ceases here but the weld is still in the forge phase.

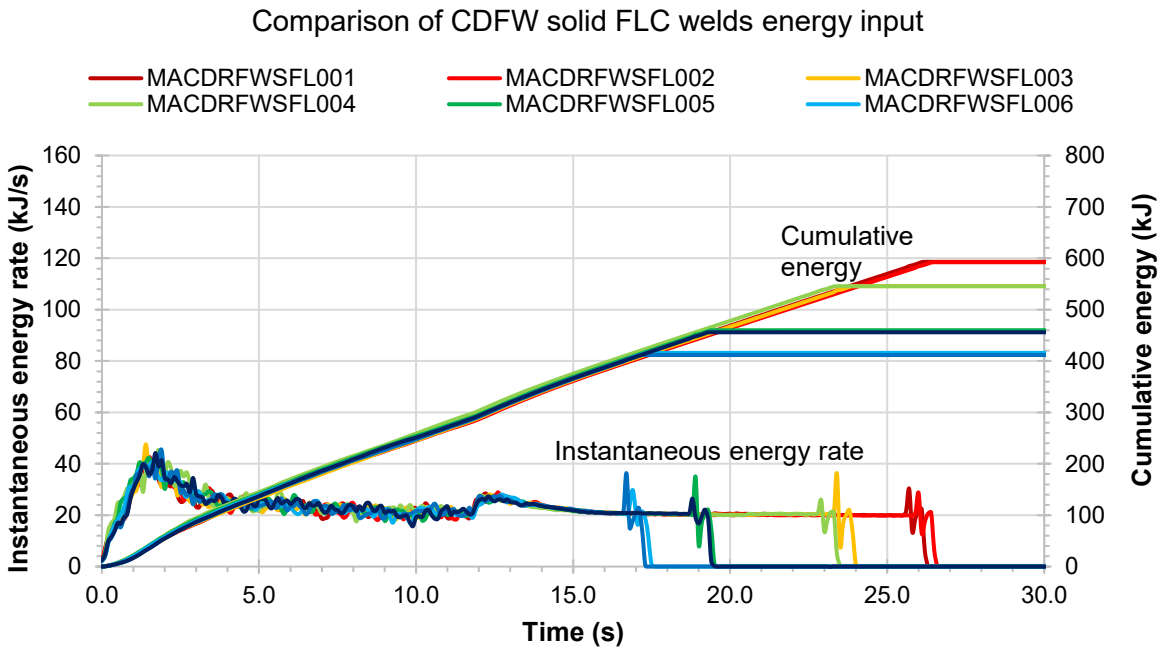


Figure 5-44: The energy input rate and cumulative energy of the CDFW solid FLC welds.

Tube geometry CDFW FLC weld energy rates and cumulative energy amounts are shown in Figure 5-45. The energy input rate varies during the 1st friction phase (up to 7 seconds) while transferring to an almost steady input state in the 2nd friction phase. The input rate is slightly bowed instead of horizontal, producing a marginally non-linear cumulative energy trace.

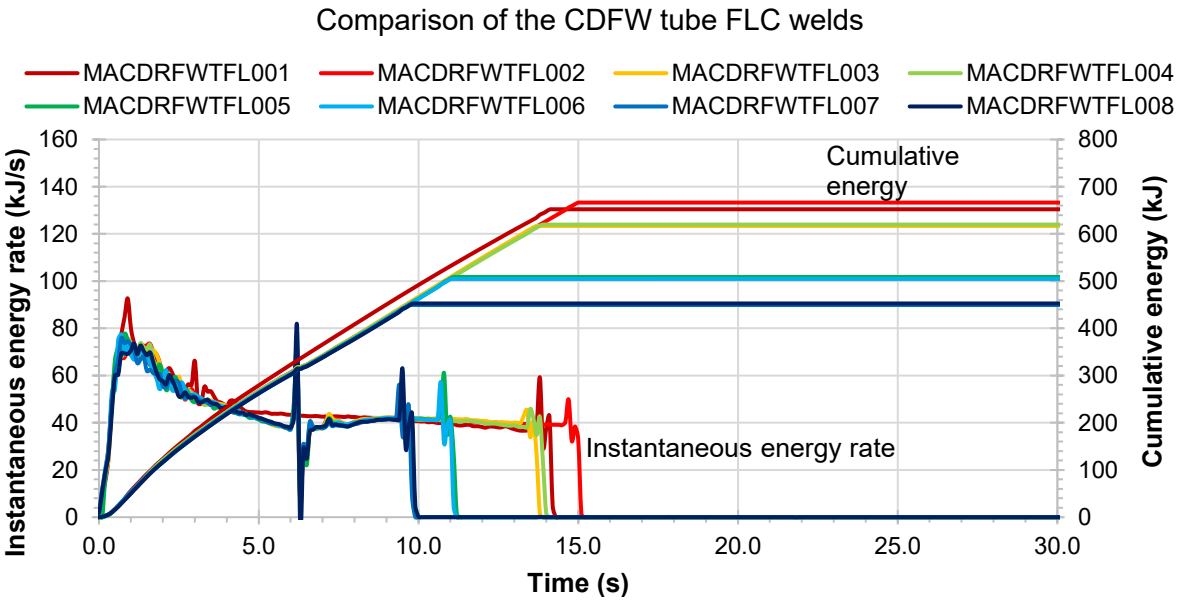


Figure 5-45: The energy input rate and cumulative energy of the CDFW tube FLC welds.

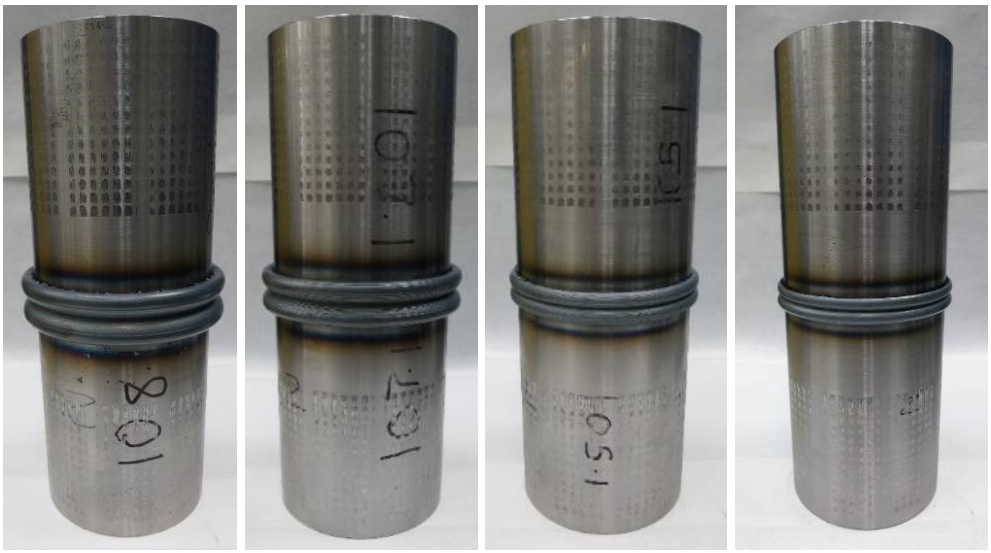
5.9.2 Microstructural results

Each weld is presented with a full cross section cut through, and microstructure development from the parent material into the recrystallised zone at 50x and 500x magnification.

5.9.2.1 Visual inspection

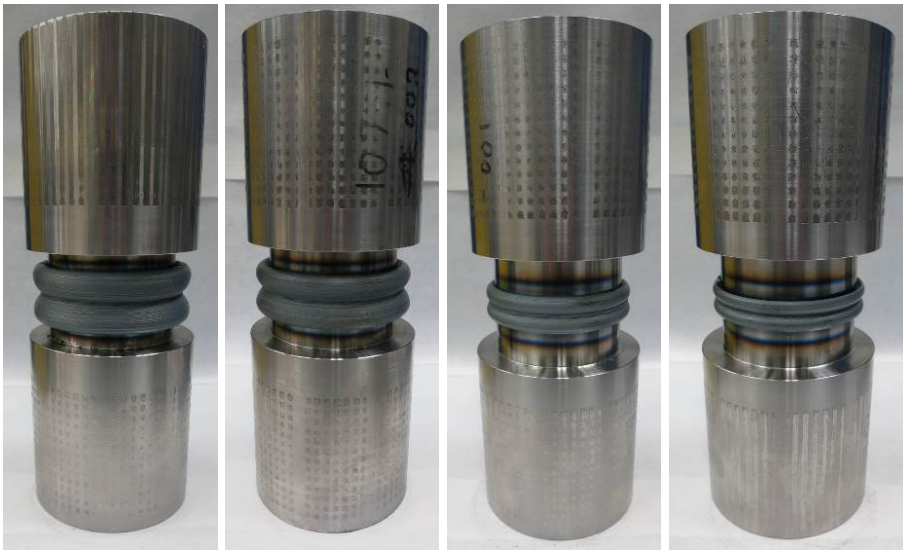
One of each pair are shown below for comparison of flash size, shape and texture.

Flash size increases with incoming part size. It is also possible to see tempering colours above and below the flash. Solid welds produced proportionally larger flash due to the single surface for the material to exit onto.



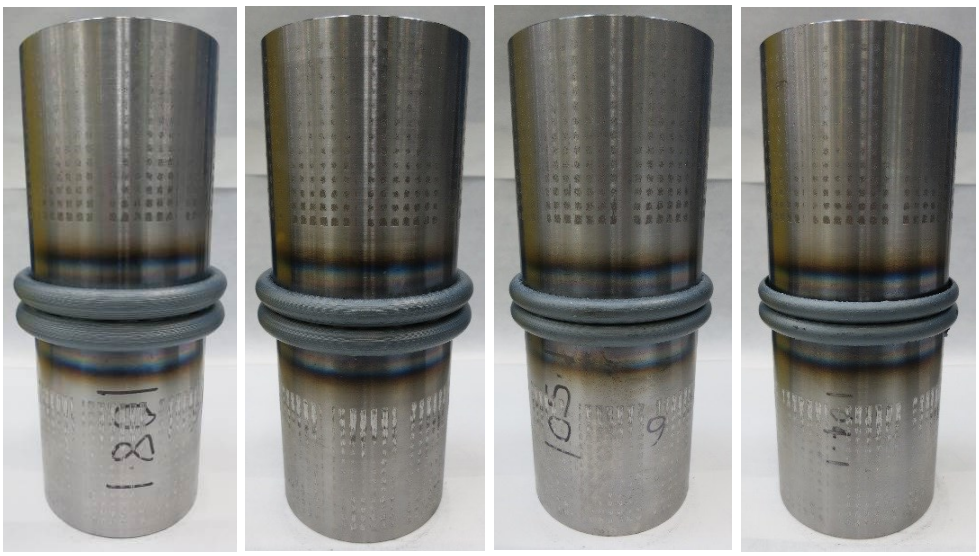
a) b) c) d)

Figure 5-46: Micro alloyed steel inertia rotary friction welding final length control weld tubes: a) MAIRFWTFL001 with part length 108.1mm, b) MAIRFWTFL003 with part length 107.1mm, c) MAIRFWTFL005 with part length 105.1mm, and d) MAIRFWTFL007 with part length 104.1mm.



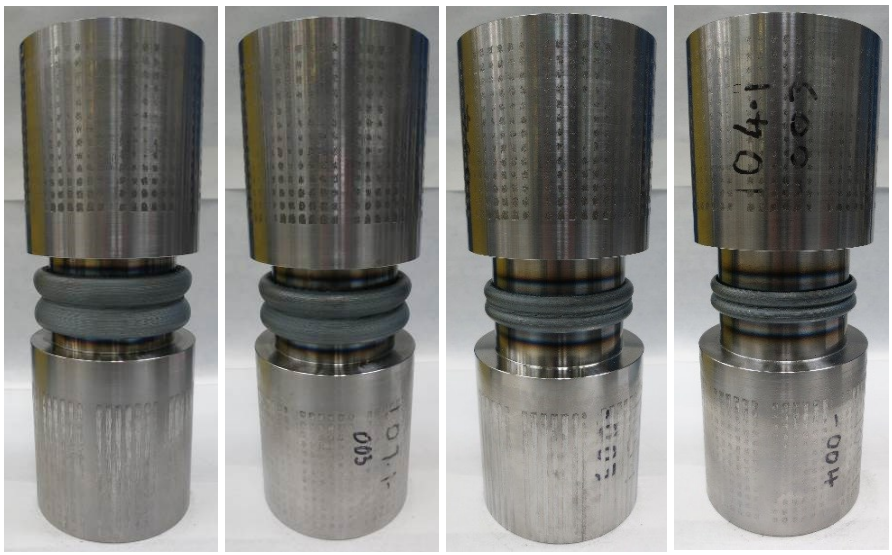
a) b) c) d)

Figure 5-47: Micro alloyed steel inertia rotary friction welding final length control weld solids: a) MAIRFWSFL001 with part length 108.1mm, b) MAIRFWSFL003 with part length 107.1mm, c) MAIRFWSFL005 with part length 105.1mm, and d) MAIRFWSFL007 with part length 104.1mm.



a) b) c) d)

Figure 5-48: Micro alloyed steel continuous drive rotary friction welding final length control weld tubes: a) MACDFWTFL001 with part length 108.1mm, b) MACDFWTFL003 with part length 107.1mm, c) MACDFWTFL005 with part length 105.1mm, and d) MACDFWTFL007 with part length 104.1mm.



a) b) c) d)

Figure 5-49: Micro alloyed steel continuous drive rotary friction welding final length control weld solids: a) MACDFWSFL001 with part length 108.1mm, b) MACDFWSFL003 with part length 107.1mm, c) MACDFWSFL005 with part length 105.1mm, and d) MACDFWSFL007 with part length 104.1mm.

5.9.2.2 Micrographs

The micrographs show optical microscope images from the parent material through to the weld line.

5.9.2.2.1 Inertia solid welds

.

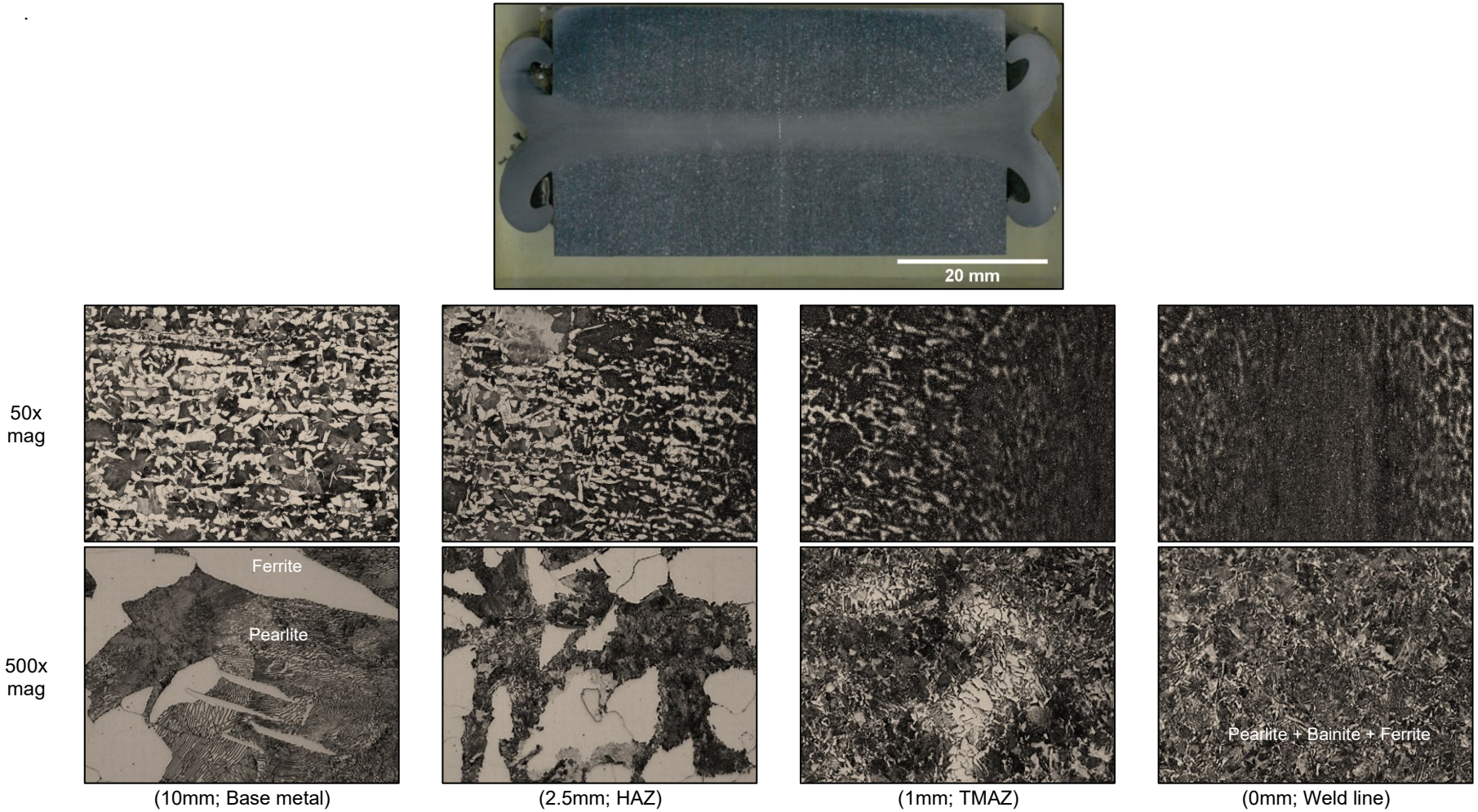


Figure 5-50: The microstructural changes from the parent material to the centre of the weld zone of MAIRFWSFL001. Images at 50x and 500x mag (shrunk for reproduction).

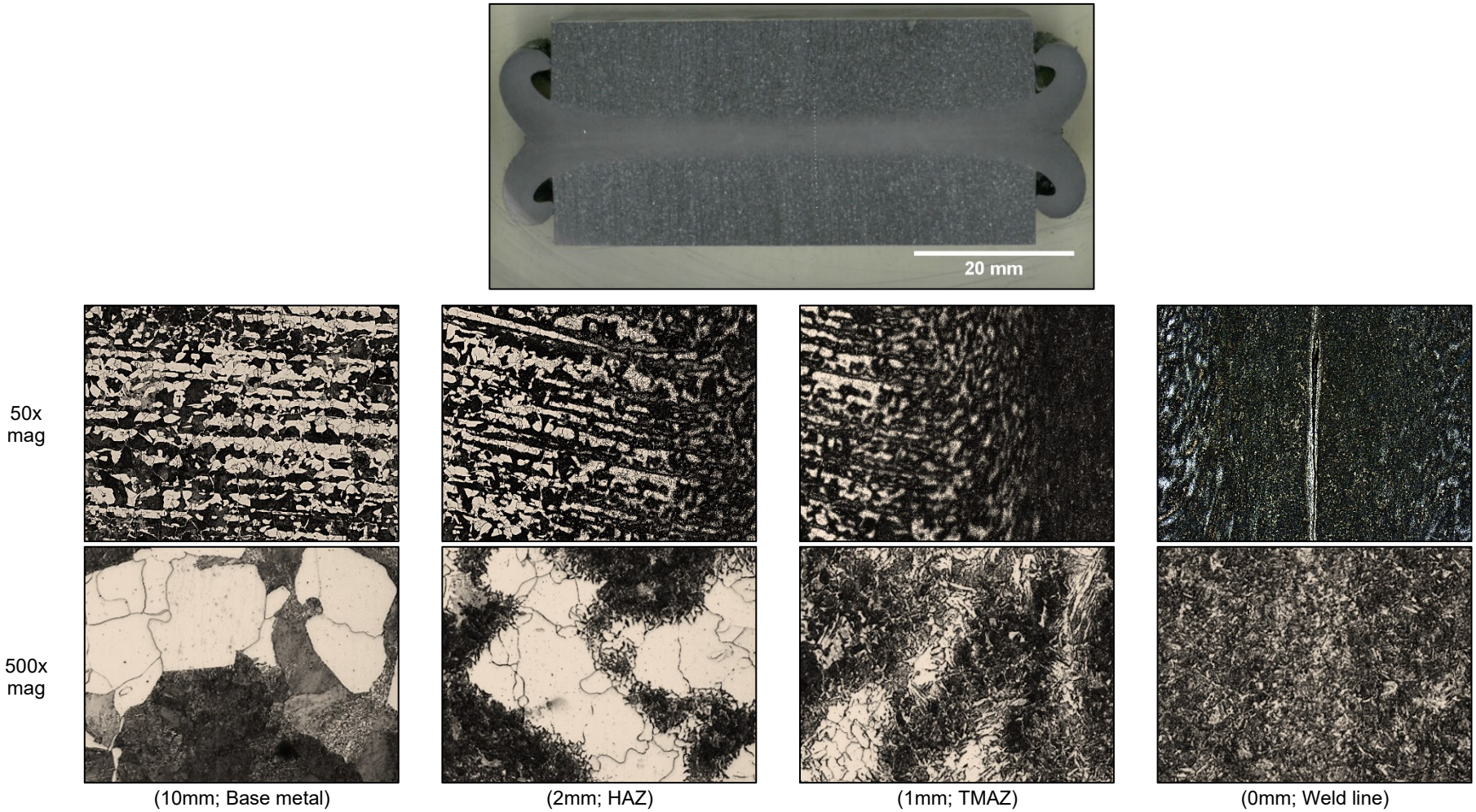


Figure 5-51: The microstructural changes from the parent material to the centre of the weld zone of MAIRFWSFL003. Images at 50x and 500x mag (shrunk for reproduction).

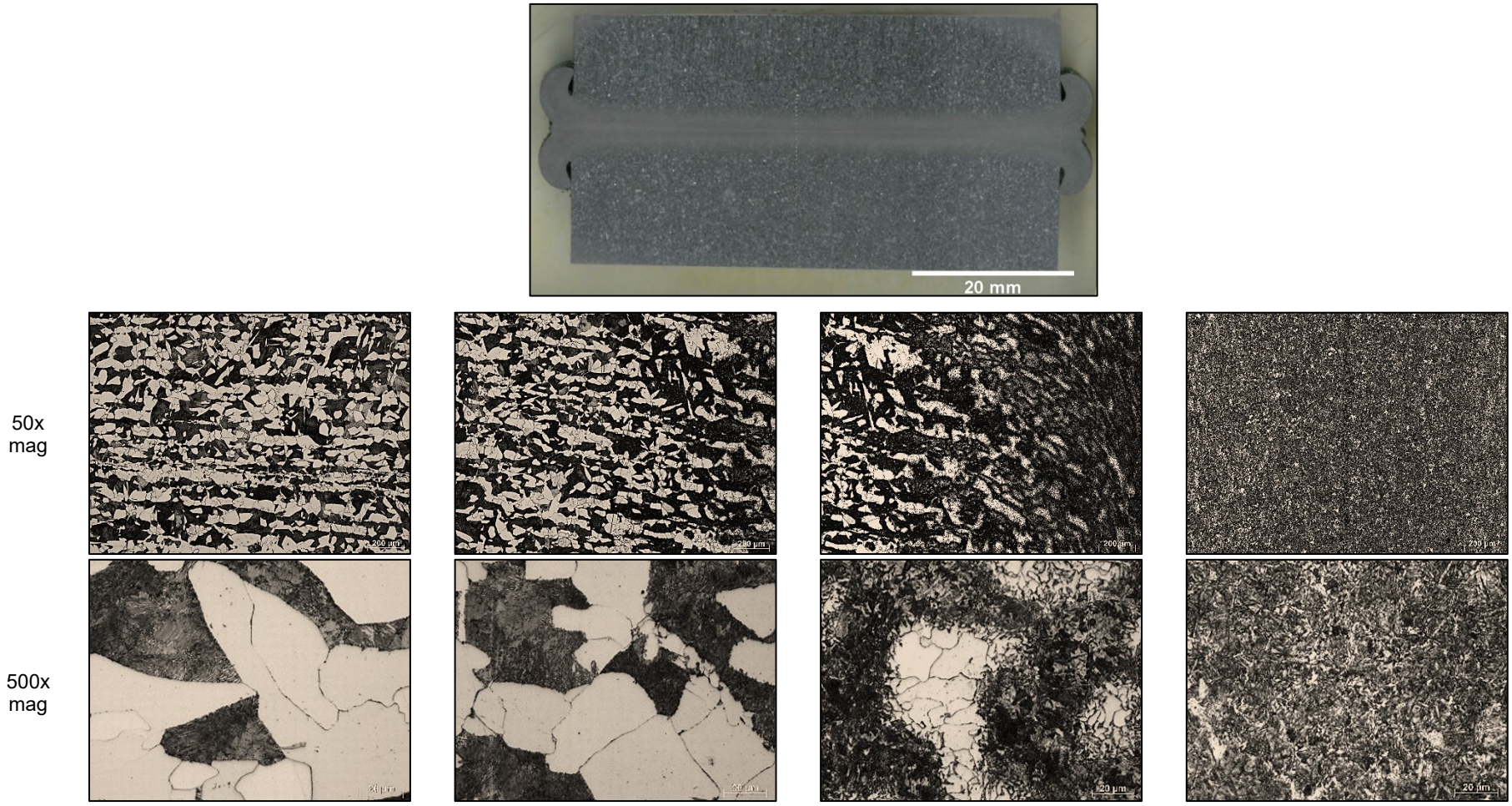


Figure 5-52: The microstructural changes from the parent material to the centre of the weld zone of MAIRFWSFL005. Images at 50x and 500x mag (shrunk for reproduction).

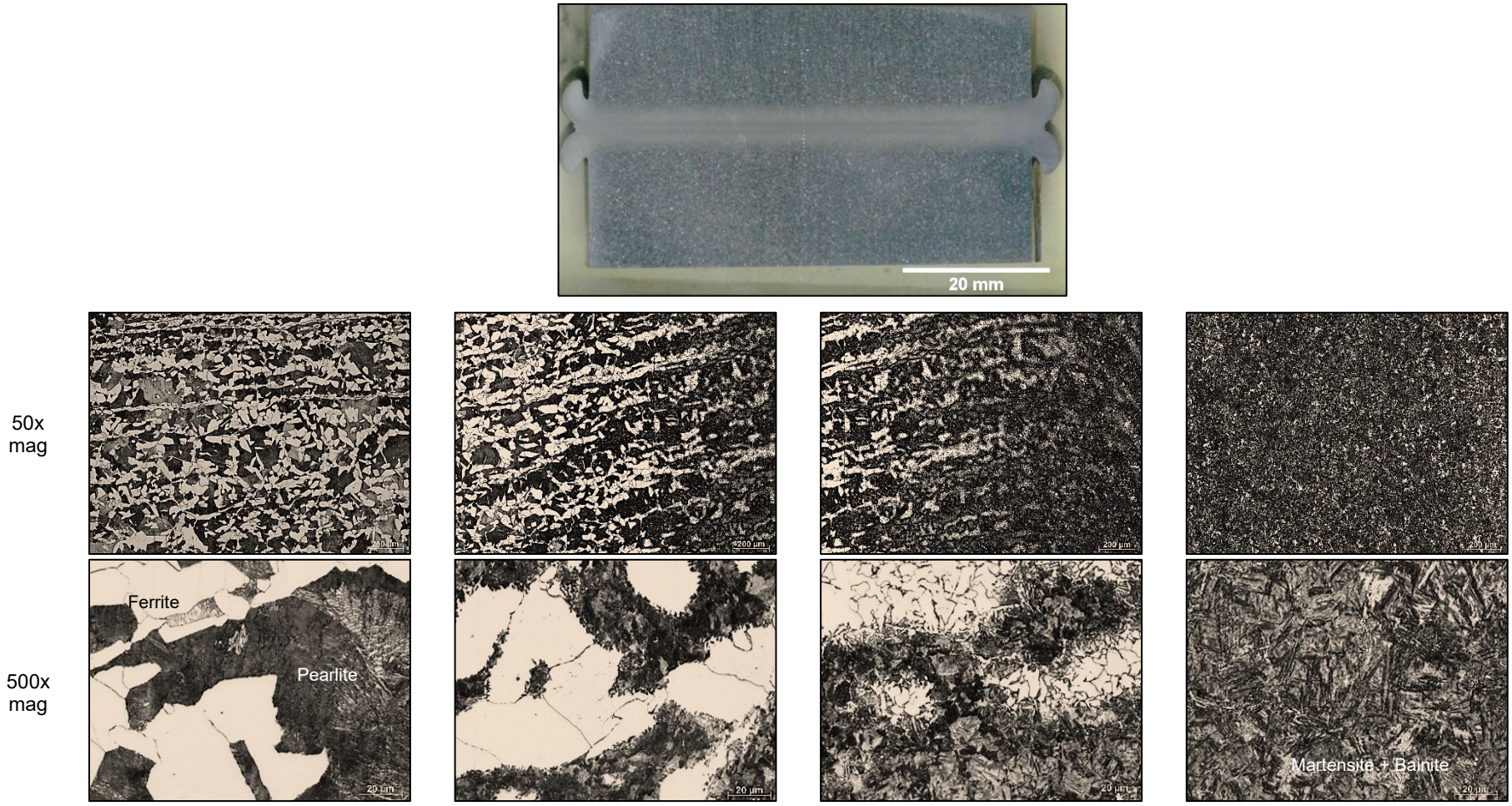


Figure 5-53: The microstructural changes from the parent material to the centre of the weld zone of MAIRFWSFL007. Images at 50x and 500x mag (shrunk for reproduction).

5.9.2.2.2 Inertia tube welds

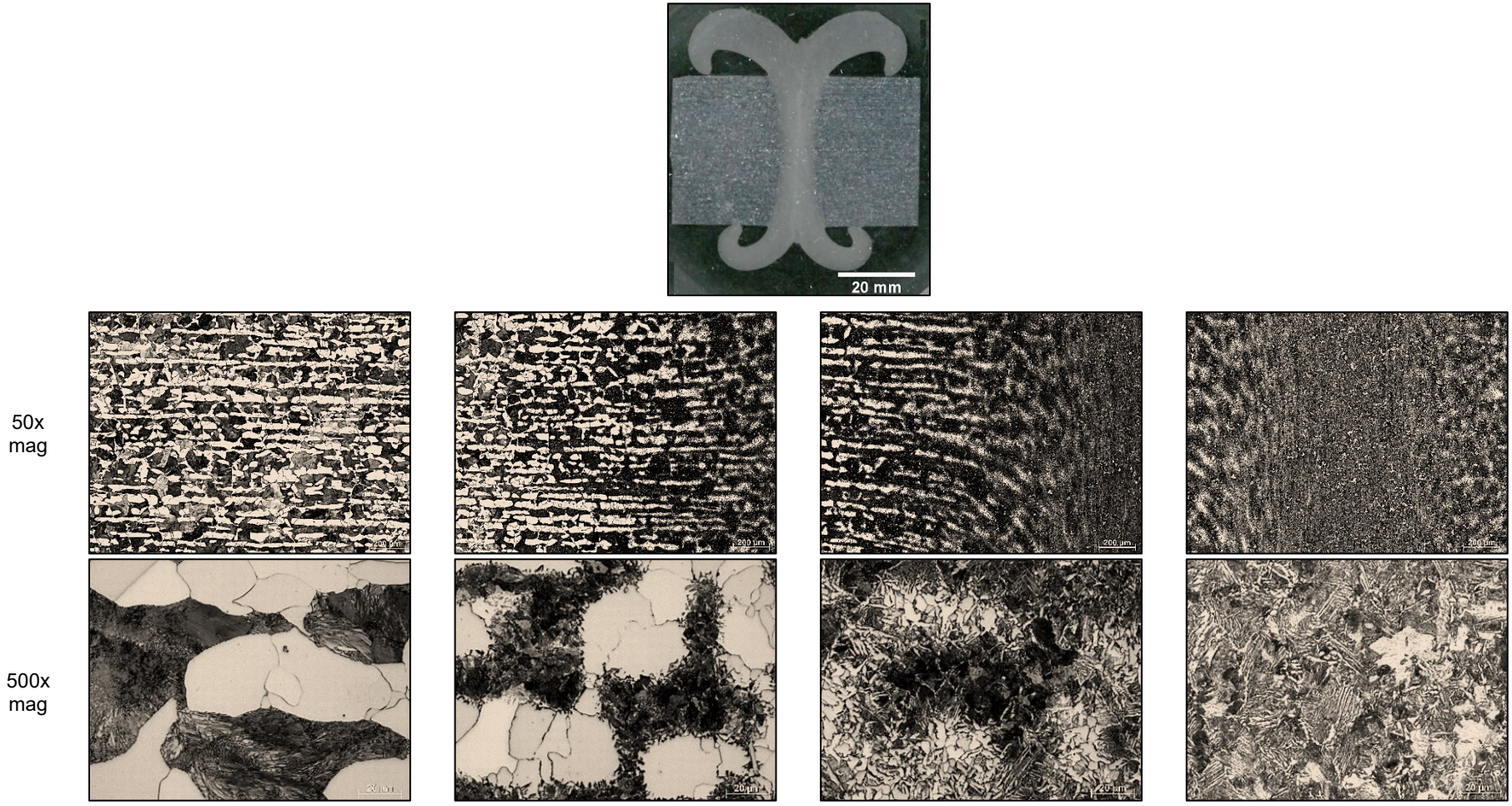


Figure 5-54: The microstructural changes from the parent material to the centre of the weld zone of MAIRFWTFL001. Images at 50x and 500x mag (shrunk for reproduction).

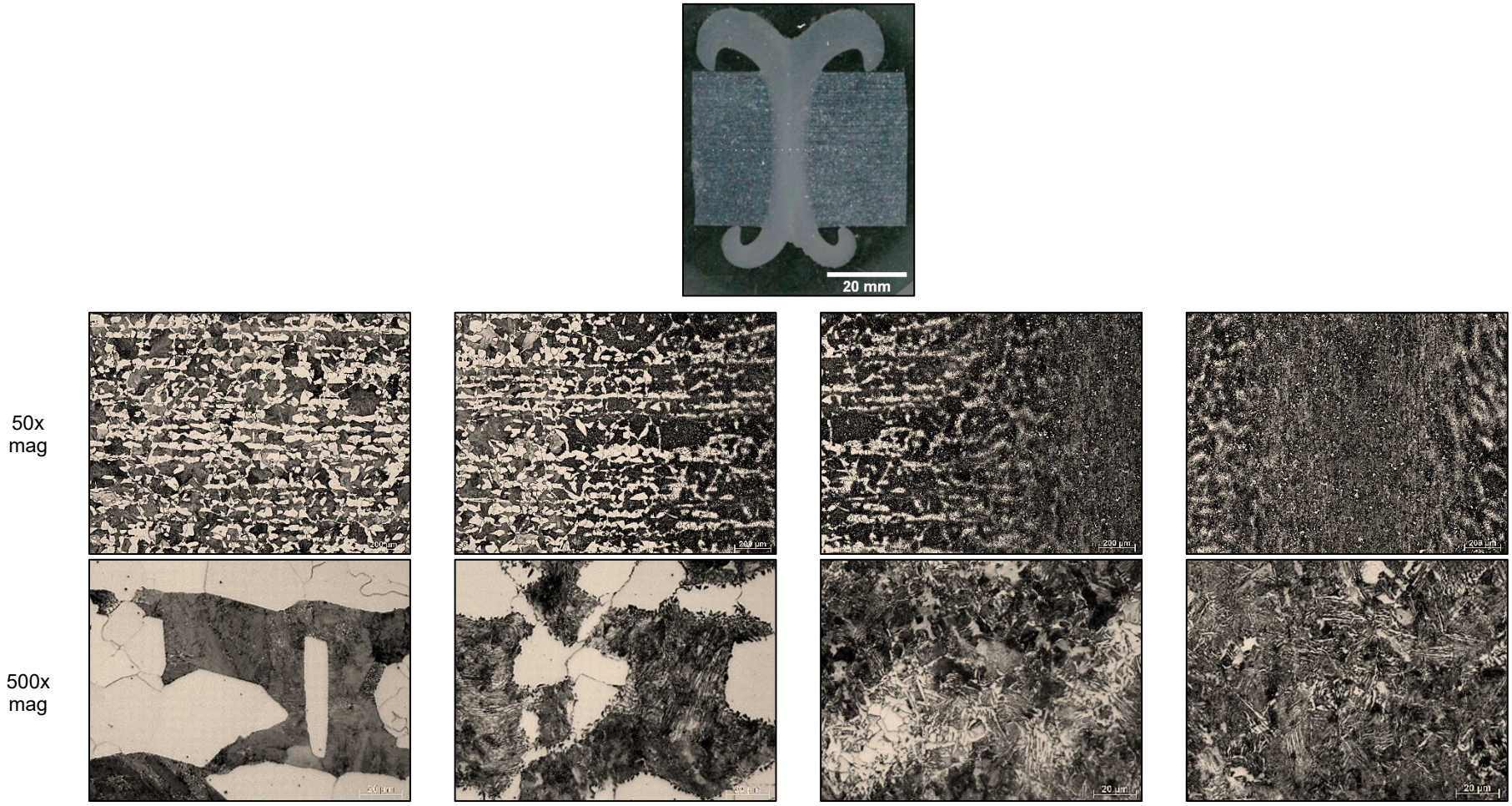


Figure 5-55: The microstructural changes from the parent material to the centre of the weld zone of MAIRFWTFL003. Images at 50x and 500x mag (shrunk for reproduction).

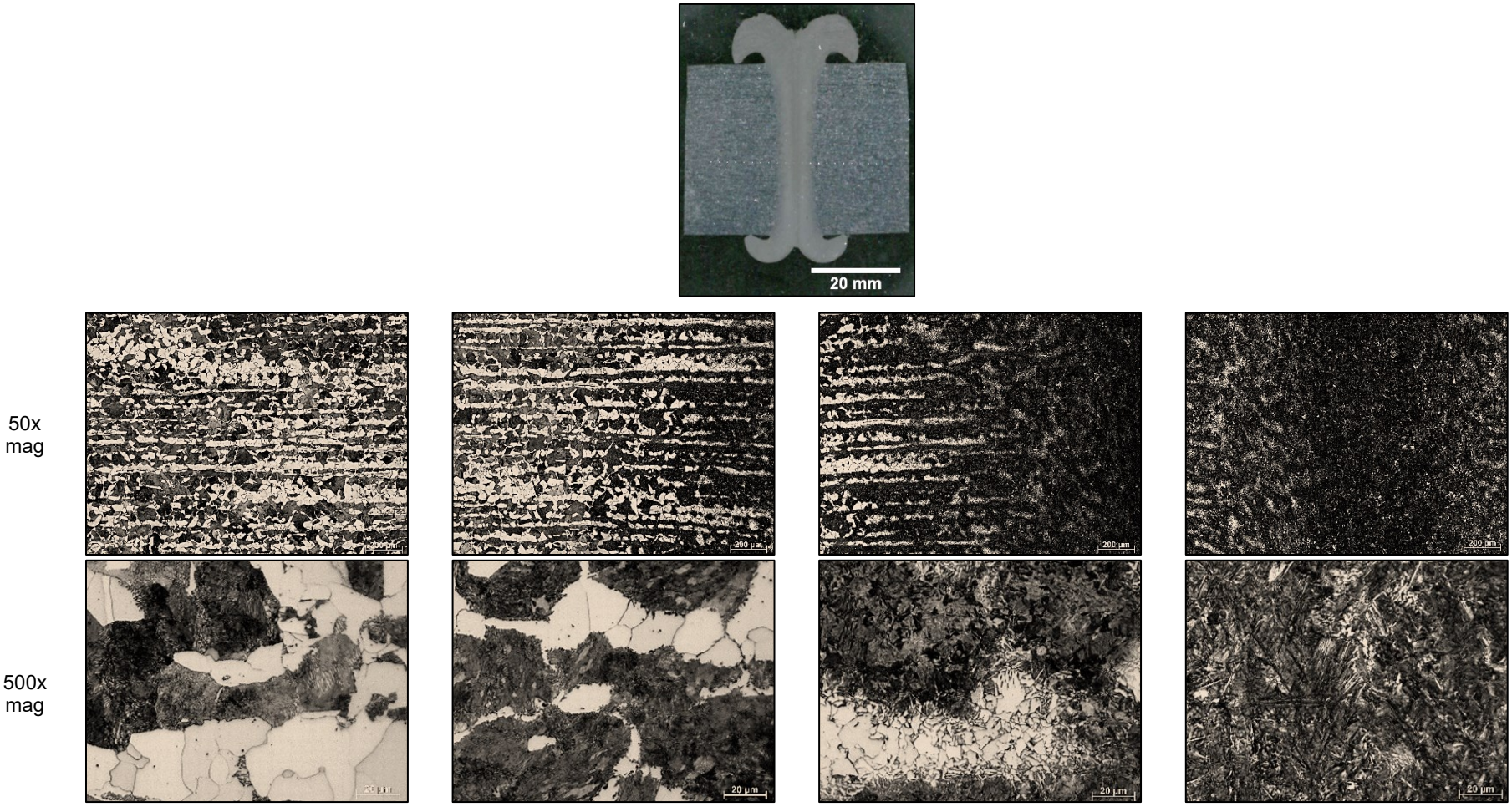


Figure 5-56: The microstructural changes from the parent material to the centre of the weld zone of MAIRFWTFL5. Images at 50x and 500x mag (shrunk for reproduction).

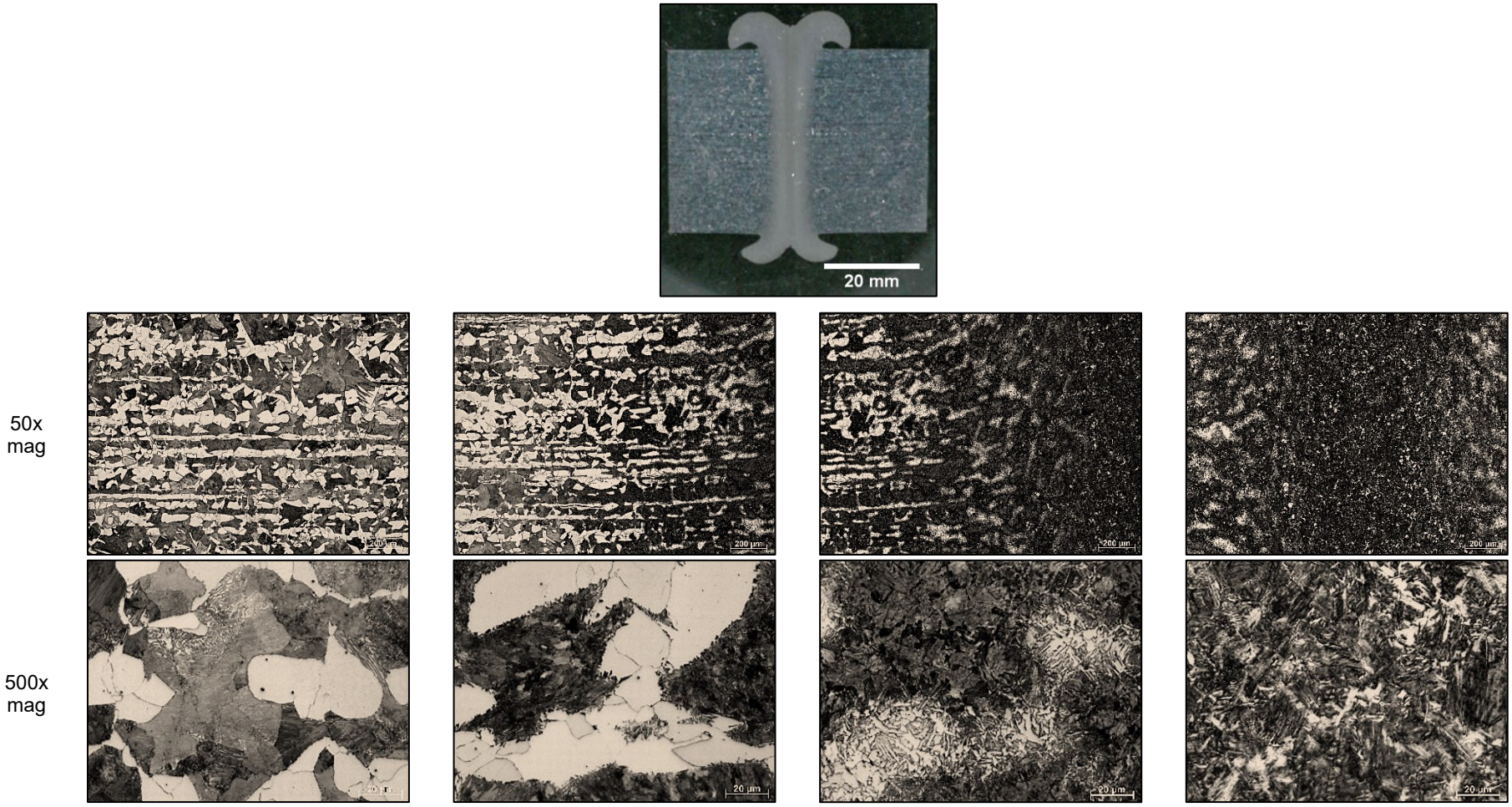


Figure 5-57: The microstructural changes from the parent material to the centre of the weld zone of MAIRFWTFL7. Images at 50x and 500x mag (shrunk for reproduction).

5.9.2.2.3 Continuous drive solid welds

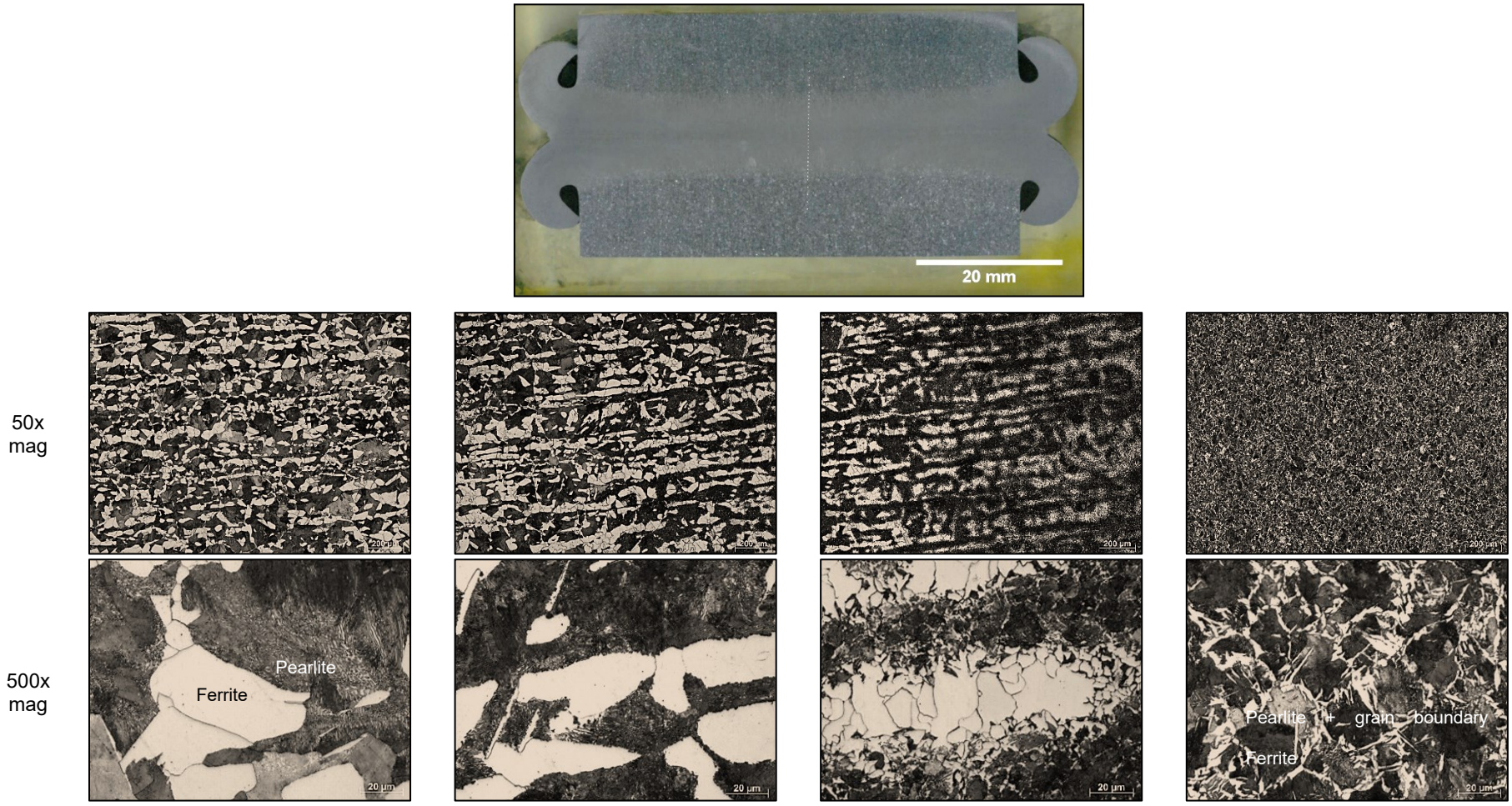


Figure 5-58: The microstructural changes from the parent material to the centre of the weld zone of MACDFWSFL1. Images at 50x and 500x mag (shrunk for reproduction).

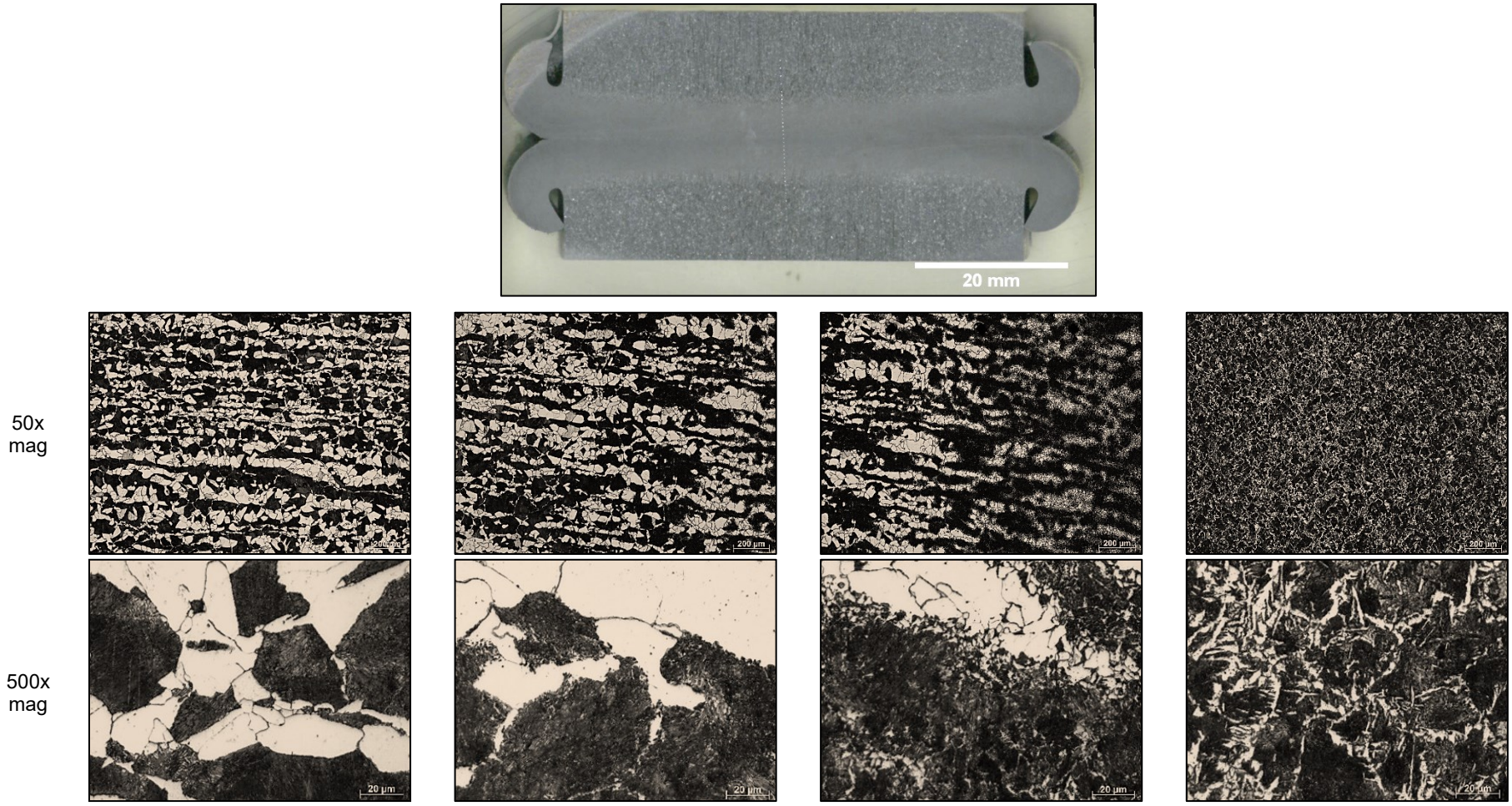
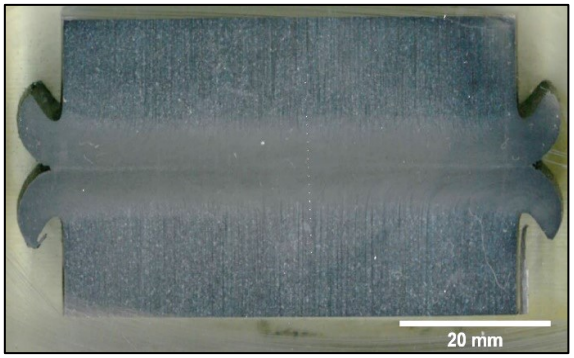


Figure 5-59: The microstructural changes from the parent material to the centre of the weld zone of MACDFWSFL3. Images at 50x and 500x mag (shrunk for reproduction).



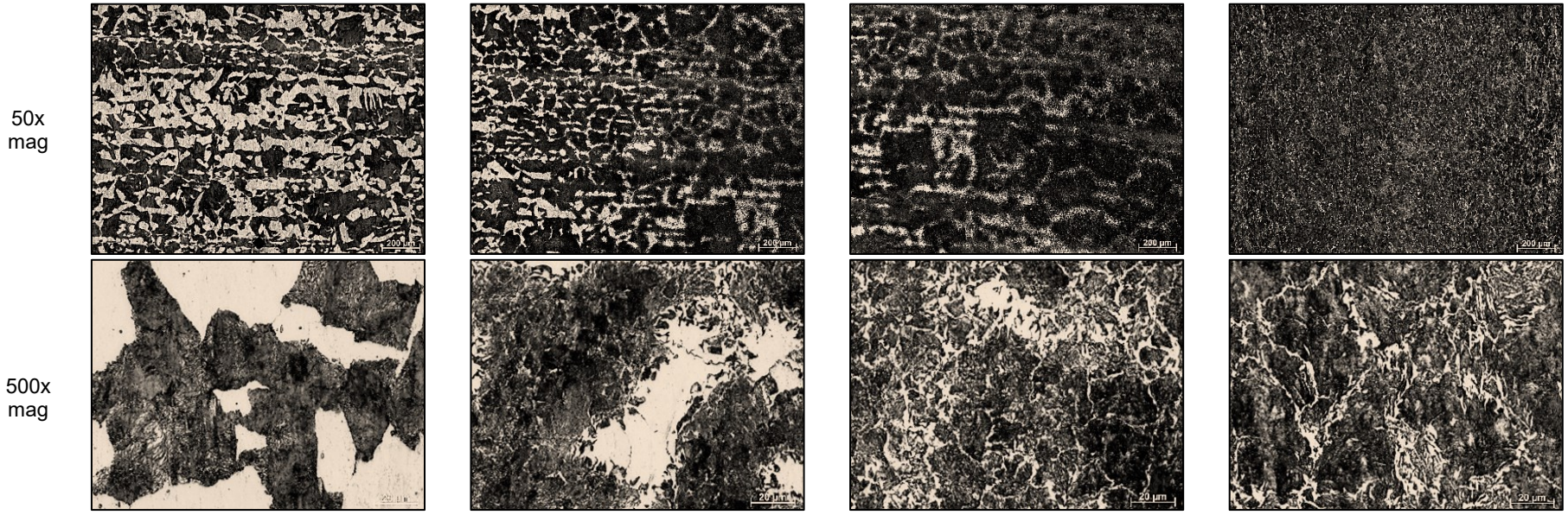


Figure 5-60: The microstructural changes from the parent material to the centre of the weld zone of MACDFWSFL5. Images at 50x and 500x mag (shrunk for reproduction).

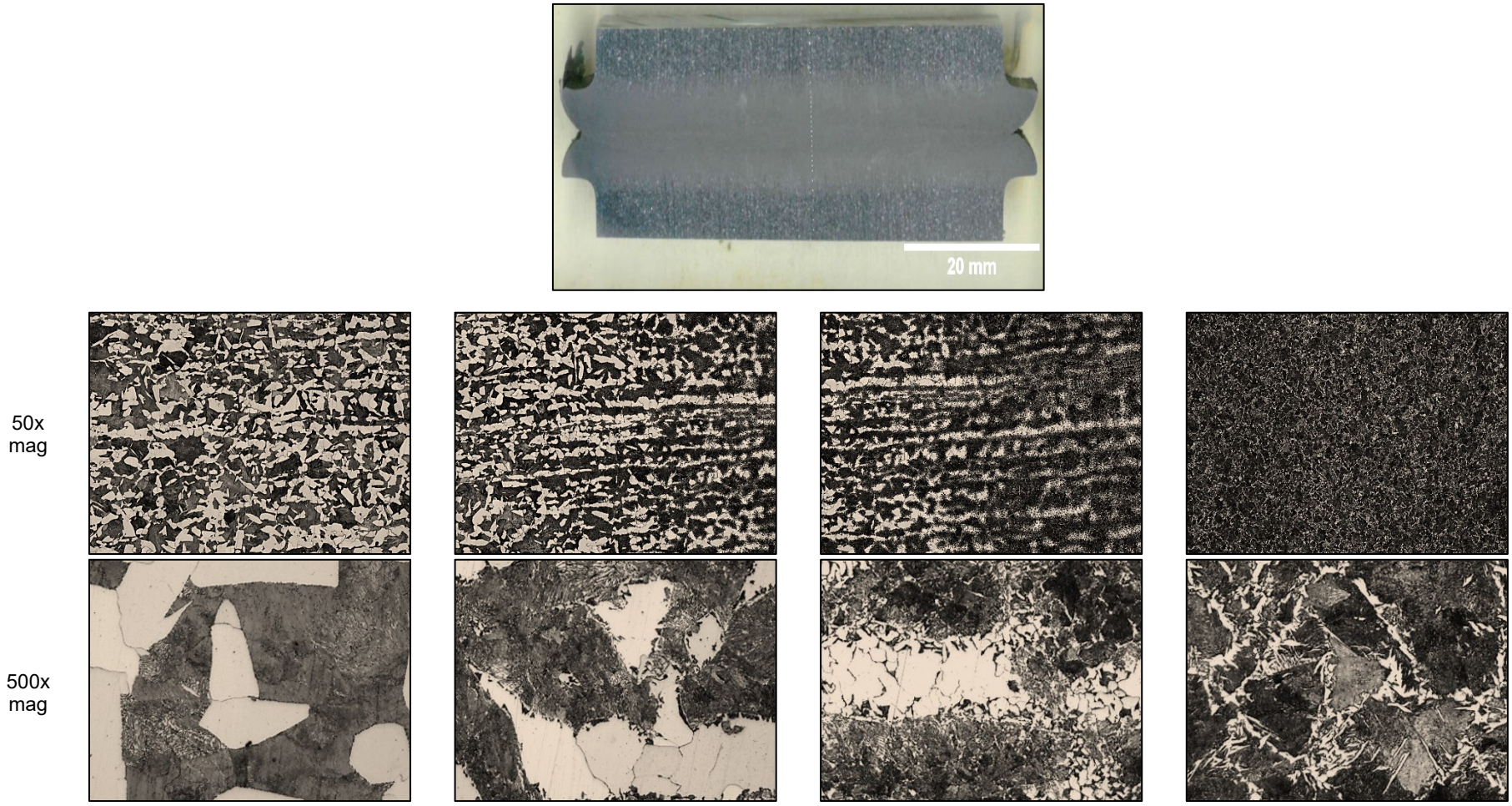


Figure 5-61: The microstructural changes from the parent material to the centre of the weld zone of MACDFWSFL7. Images at 50x and 500x mag (shrunk for reproduction).

5.9.2.2.4 Continuous drive tube welds



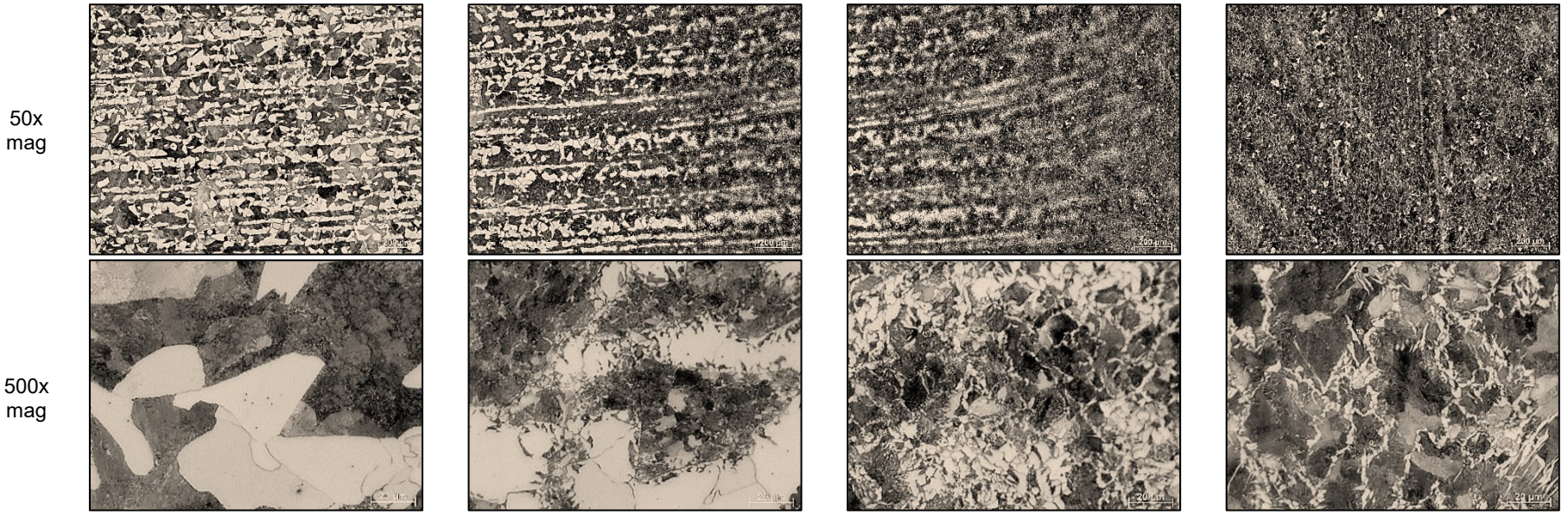
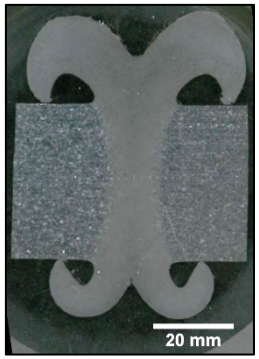


Figure 5-62: The microstructural changes from the parent material to the centre of the weld zone of MACDFWTFL1. Images at 50x and 500x mag (shrunk for reproduction).



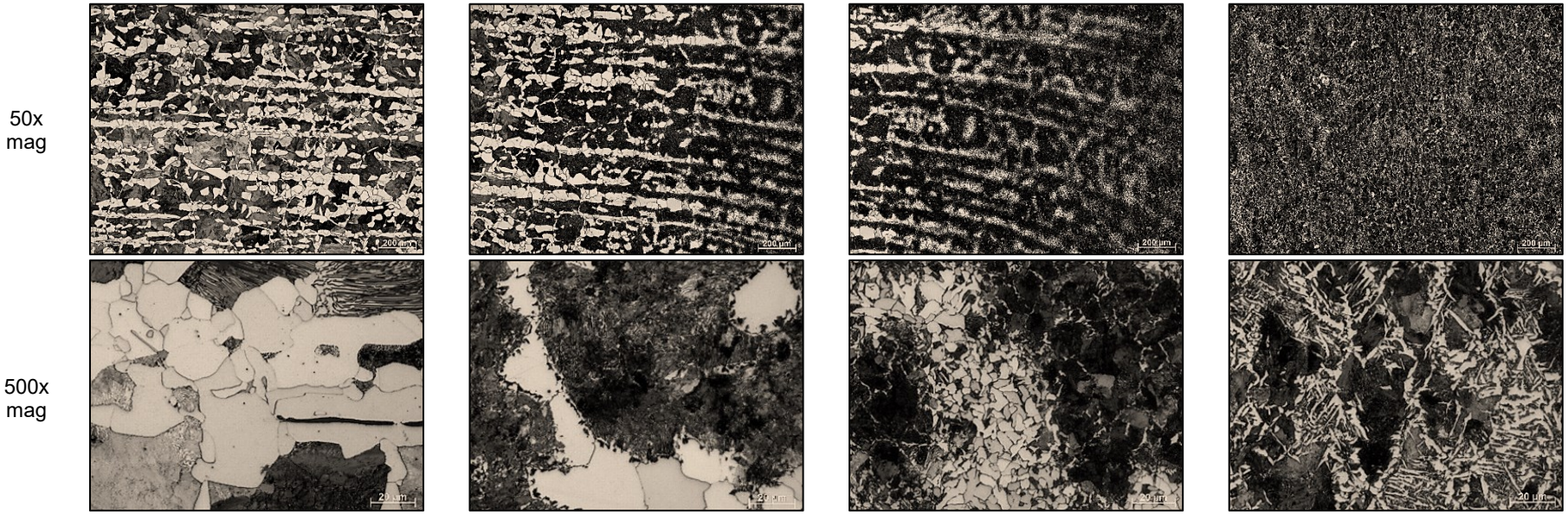


Figure 5-63: The microstructural changes from the parent material to the centre of the weld zone of MACDFWTFL3. Images at 50x and 500x mag (shrunk for reproduction).

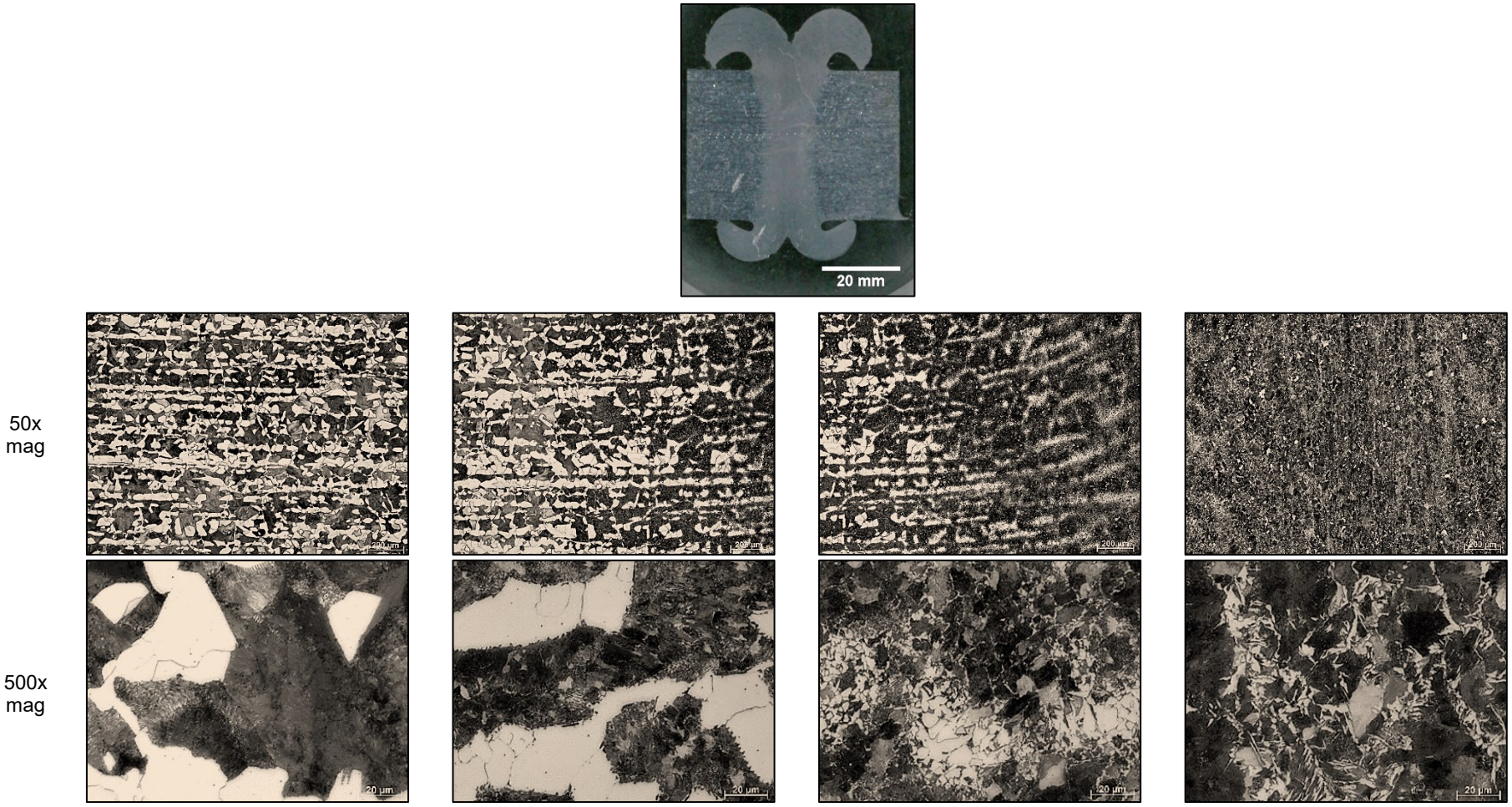


Figure 5-64: The microstructural changes from the parent material to the centre of the weld zone of MACDFWTFL5. Images at 50x and 500x mag (shrunk for reproduction).

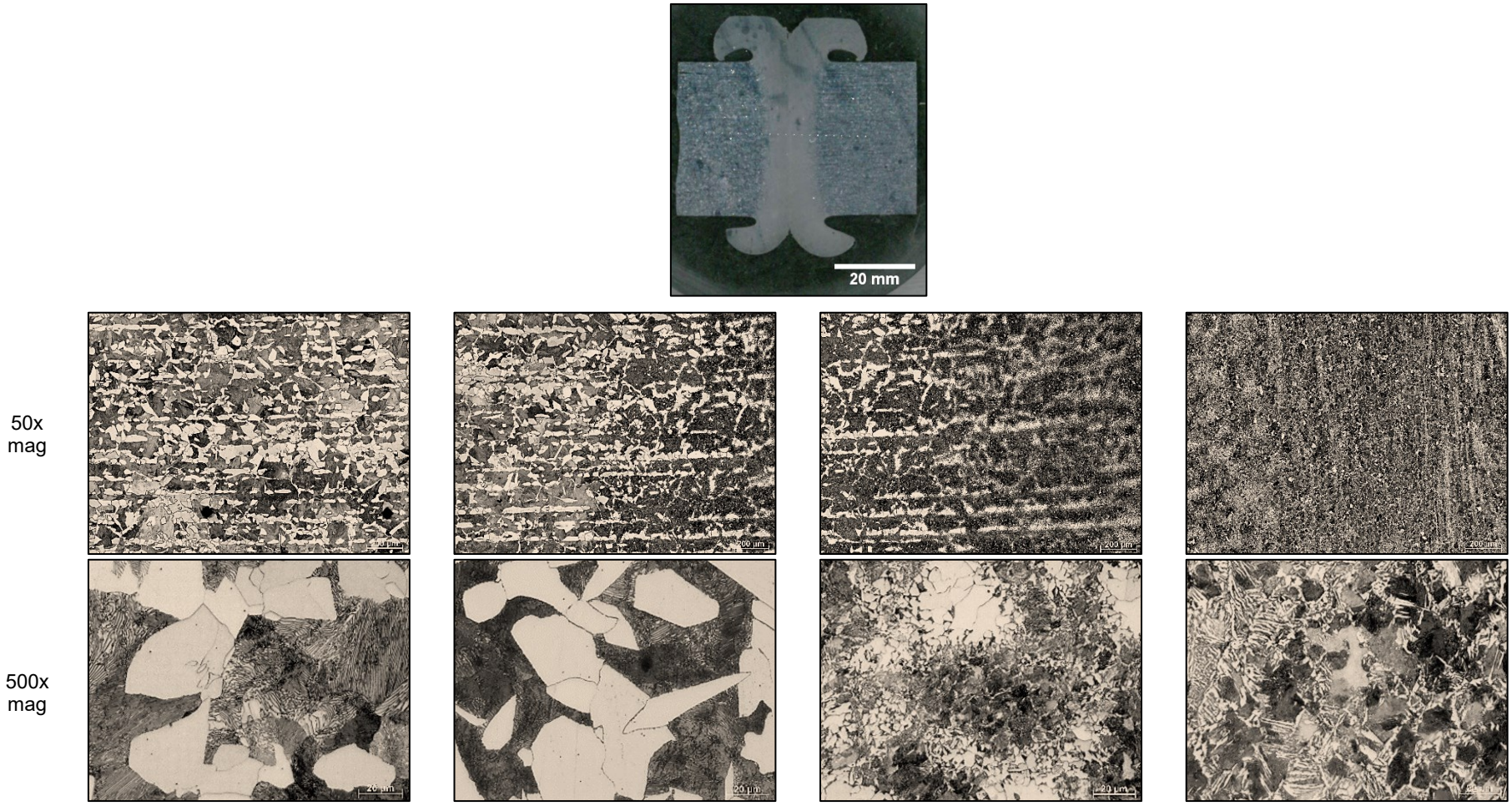


Figure 5-65: The microstructural changes from the parent material to the centre of the weld zone of MACDFWTFL7. Images at 50x and 500x mag (shrunk for reproduction).

5.9.2.3 Hardness Results

Presented are the centreline hardness traces of the final length control welds. Each mode is shown with a single trace for each component length. The nominal weld is included for comparison.

5.9.2.3.1 Inertia solid welds

In the inertia solid welds, the shortest component weld displayed a marked increase in hardness. MAIRFWSFL007 reached 480Hv1 at the centreline. While both the +1mm and -1mm welds reached 370Hv1. The weld with the longest components produced the lowest hardness at 325Hv1. All of which were higher than the nominal weld at 310Hv1.

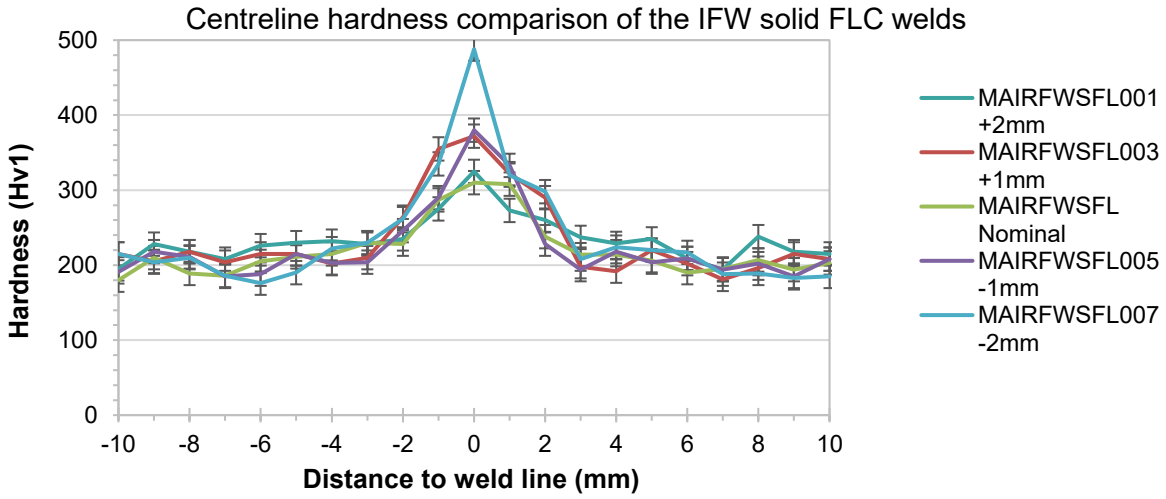


Figure 5-66: Comparison of the inertia solid final length control welds centreline hardness traces. 1 standard deviation error bars from the base material measurements displayed.

5.9.2.3.2 Inertia tube welds

In the inertia tube final length controlled welds, the hardness corresponds with the initial part length. The two shorter components produced weld line centres of ~ 450Hv1, while the nominal weld centre was 346Hv1. The longer components both produced centres of ~320Hv1.

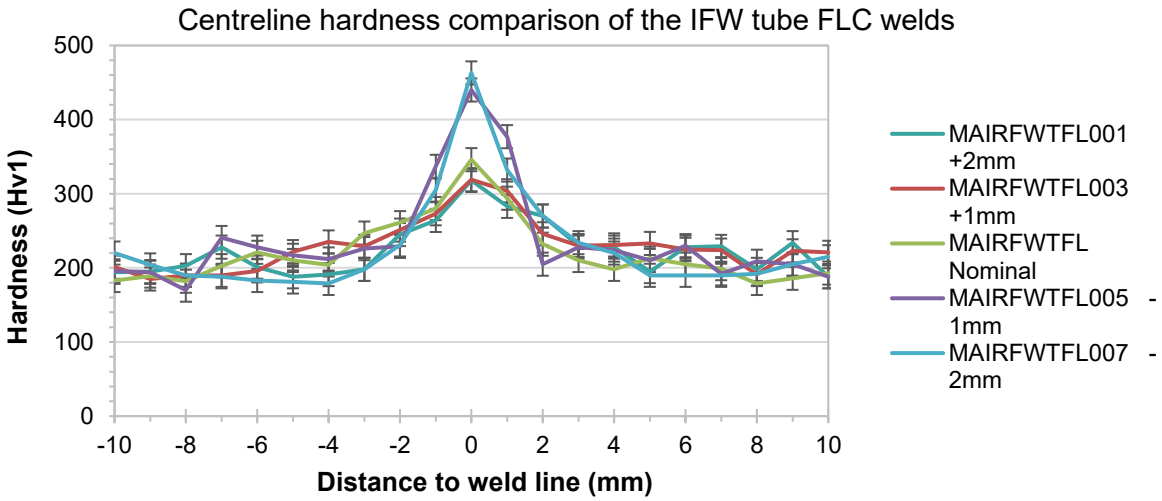


Figure 5-67: Comparison of the inertia tube final length control welds centreline hardness traces. 1 standard deviation error bars from the base material measurements displayed.

5.9.2.3.3 Continuous drive solid welds

The continuous drive solid welds all displayed a wide flat topped hardness zone with a slight increase of ~60-70Hv1 regardless of initial part size.

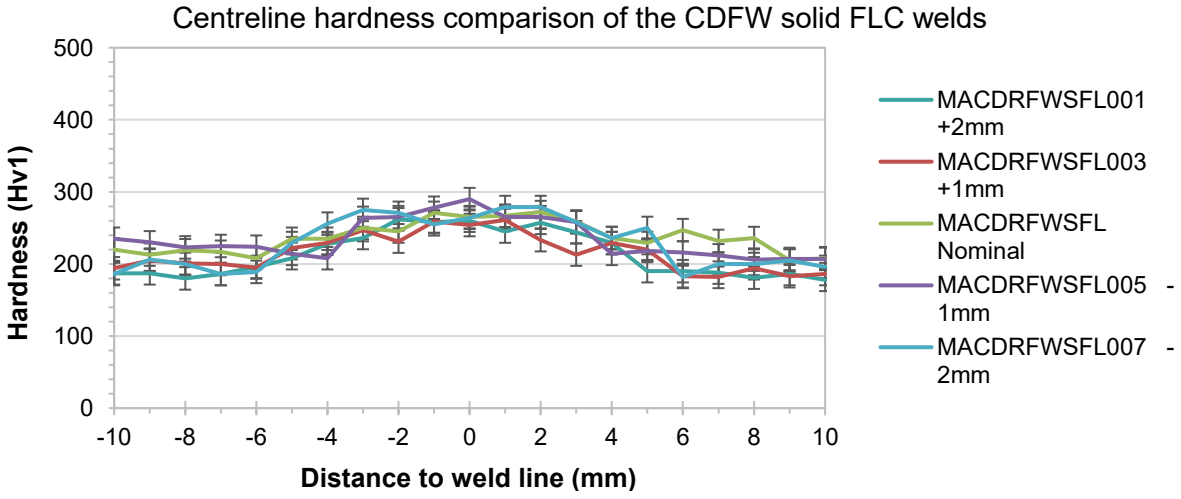


Figure 5-68: Comparison of the continuous drive solid final length control welds centreline hardness traces. 1 standard deviation error bars from the base material measurements displayed.

5.9.2.3.4 Continuous drive tube welds

The continuous drive tube welds displayed a small area of increased hardness across the weld zone with a maximum increase of ~100Hv1. The +1mm weld recorded a marginally higher hardness weld zone compared with the other welds, however, when combined with the error of the measurements it does not appear significant.

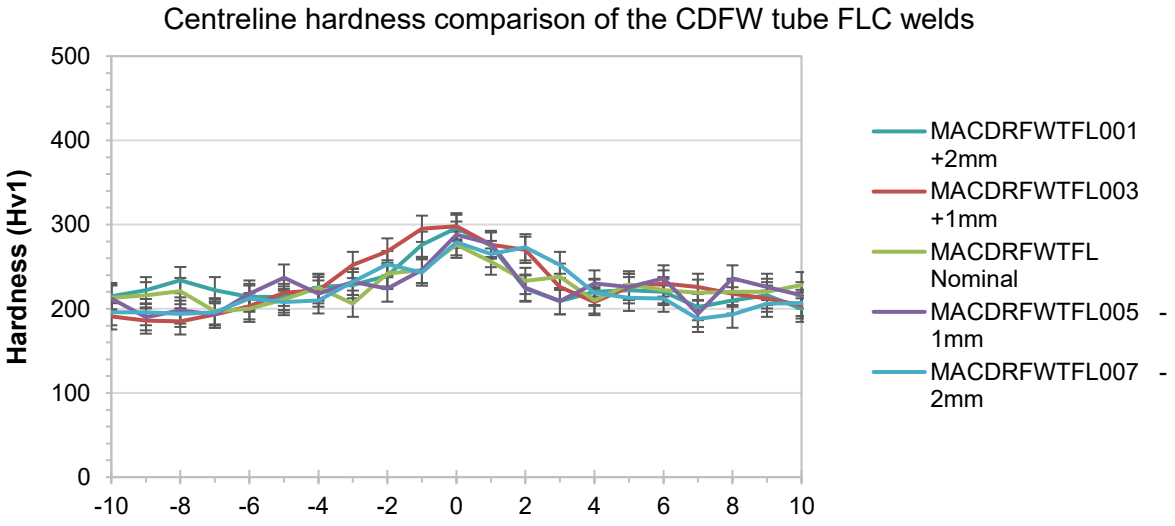


Figure 5-69: Comparison of the continuous drive tube final length control welds centreline hardness traces. 1 standard deviation error bars from the base material measurements displayed.

5.9.3 Mechanical testing

5.9.3.1 Bend tests results

3-point bend testing of sectioned pieces revealed a general trend of tube welds producing less variation and on average a higher degree of bend.

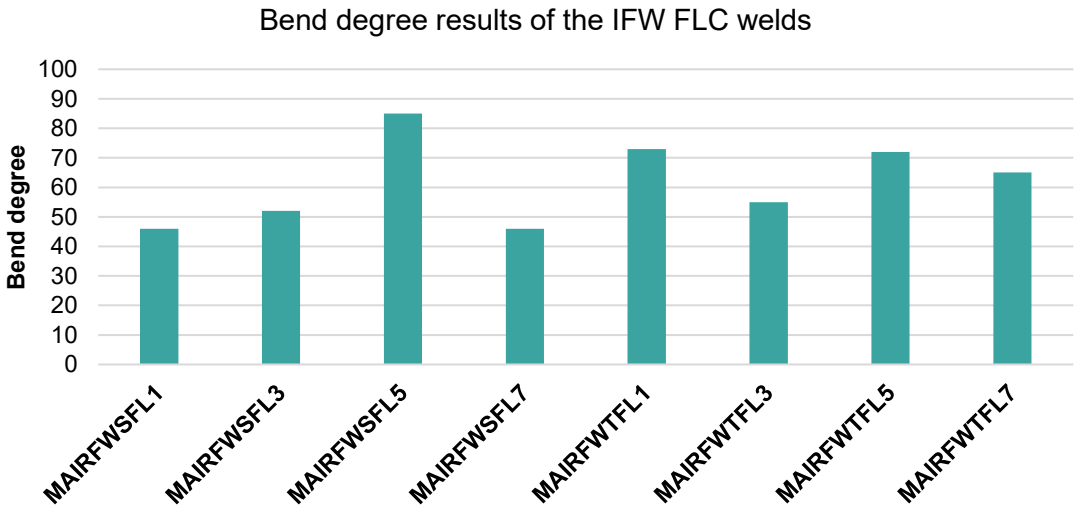


Figure 5-70: Bend test results of inertia rotary friction final length control welds.

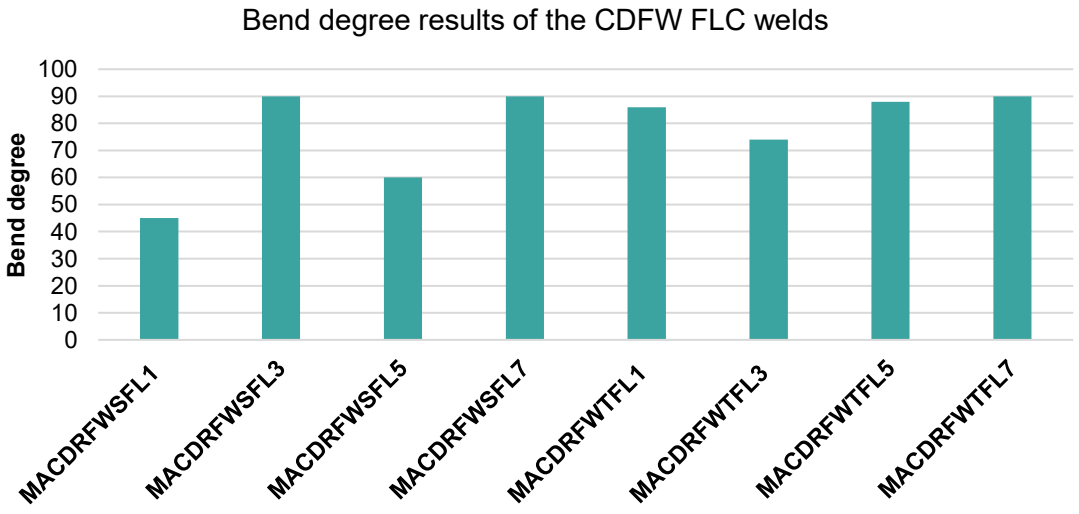


Figure 5-71: Bend test results of continuous drive rotary friction final length control welds.

5.9.3.2 Tensile tests results

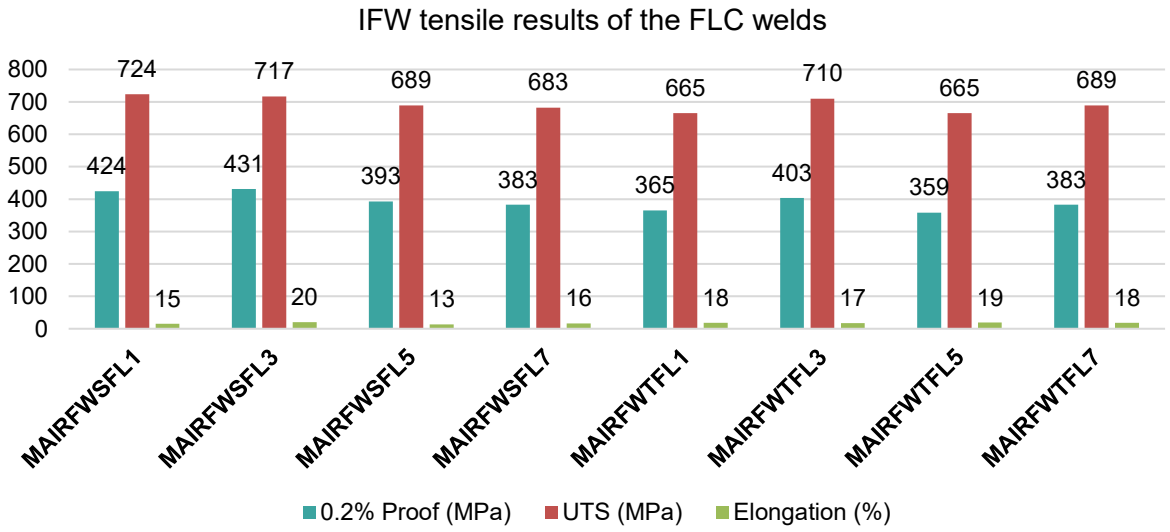


Figure 5-72: Tensile test results of inertia rotary friction final length control welds.

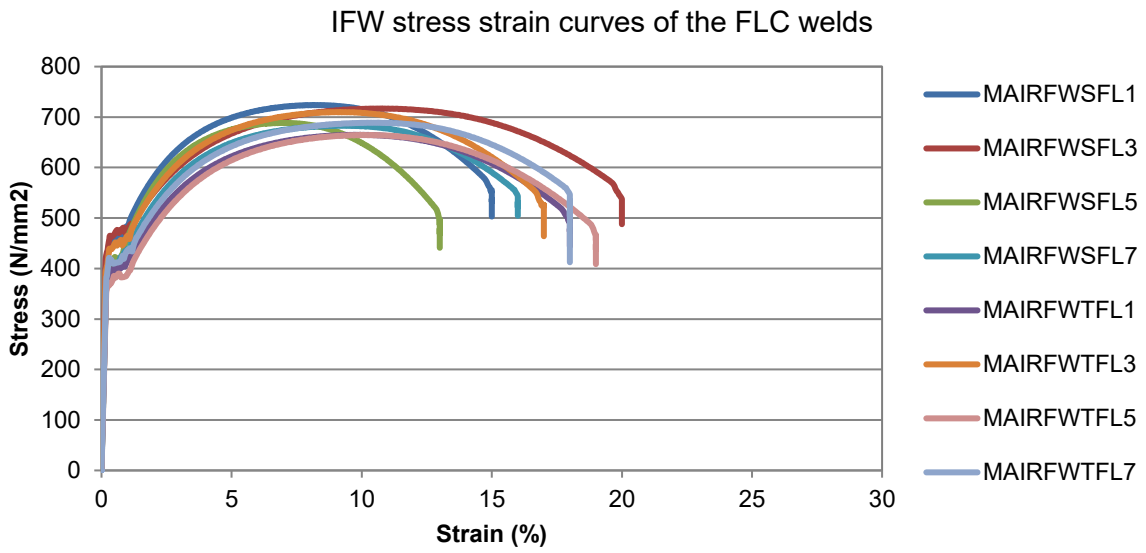


Figure 5-73: Stress strain curves of the inertia rotary friction final length welds

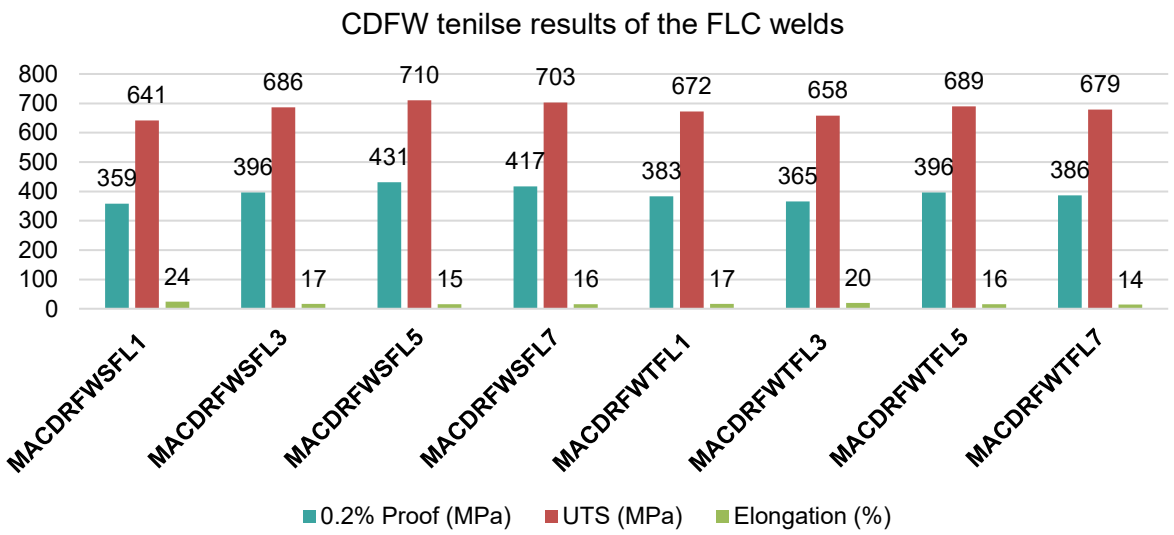


Figure 5-74: Tensile test results of continuous drive rotary friction final length control welds.

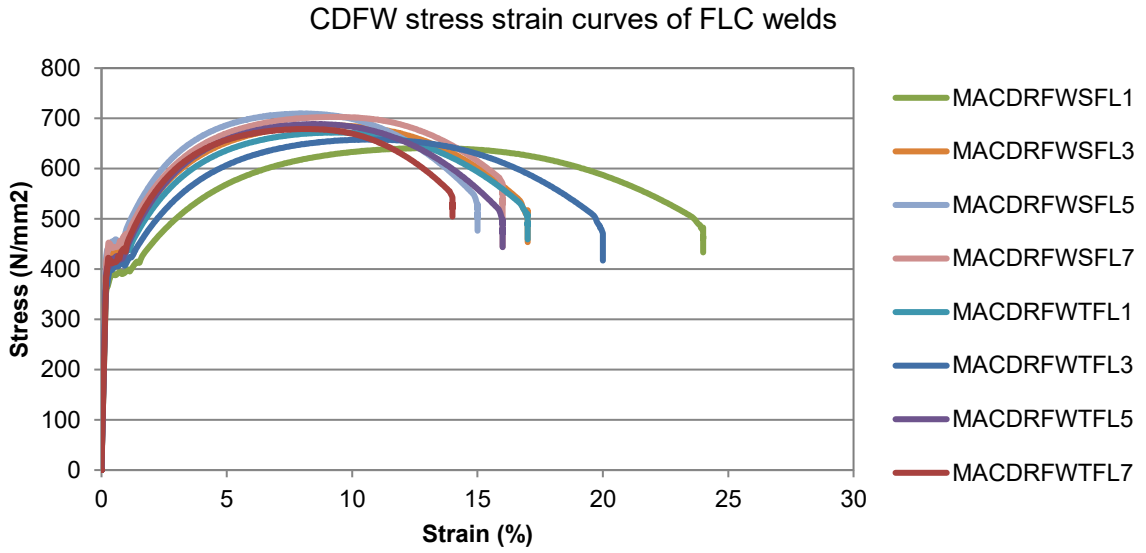


Figure 5-75: Stress strain curves of the continuous drive rotary friction final length welds

5.9.3.3 Charpy impact tests results

As the charpy tests included three samples the average is shown with the range indicated by the error bars.

In the inertia solid welds there was a weak trend for longer initial parts to produce slightly higher impact toughness. In the inertia tube welds there was a strong trend for longer initial parts to produce higher impact toughness. The continuous drive welds produced a weak trend in the opposite direction, with shorter incoming parts generally reaching a higher impact toughness.

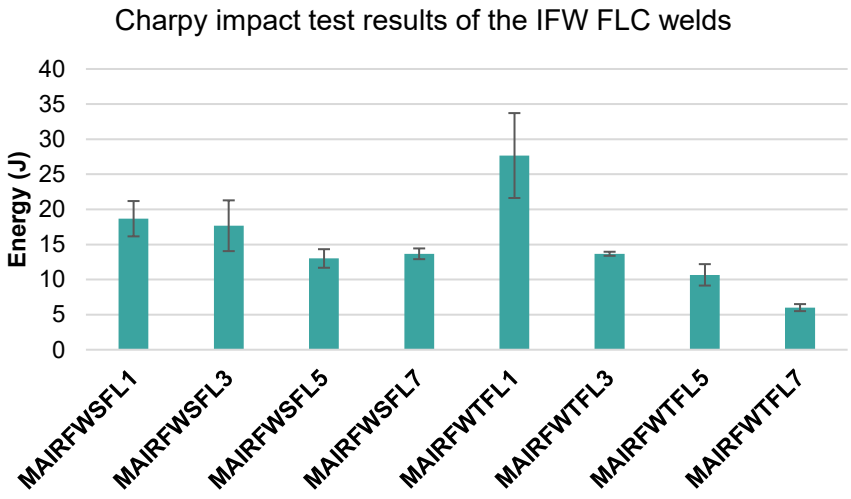


Figure 5-76: Charpy impact test results of inertia rotary friction final length control welds.

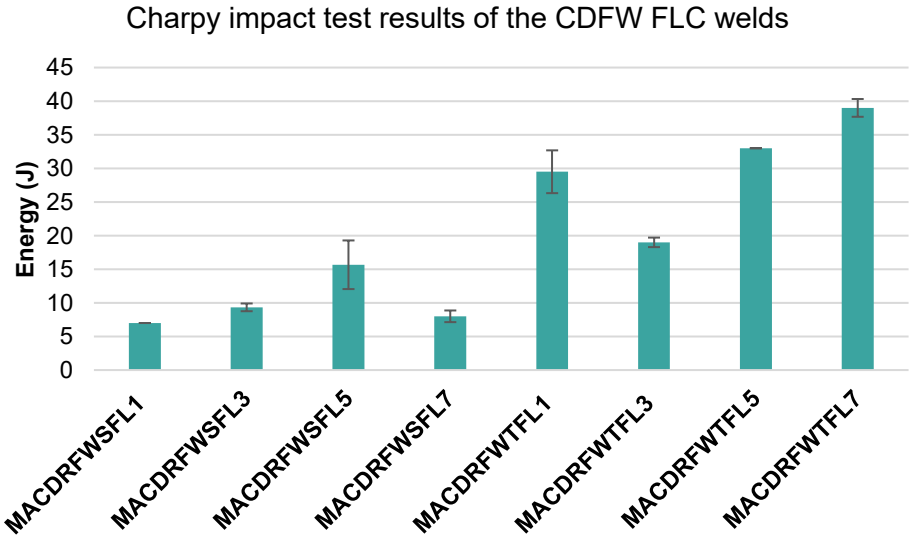


Figure 5-77: Charpy impact test results of continuous drive rotary friction final length control welds.

5.10 Final length control analysis

5.10.1 Weld curve analysis

5.10.1.1 Inertia mode analysis

The weld curves for the inertia tube welds showed distinct proportional responses to the change in incoming part size. Oversized parts required extra energy to generate more upset. This was seen in the weld curves as acceleration spikes in the spindle deceleration. The size of the spike being proportional to the increase in energy required to produce the extra upset (Manufacturing Technology Inc, 2012, 2017a, 2017d). Undersized parts required a proportionally reduced amount of energy to produce the same part length. This can be seen as an exaggerated deceleration during the deceleration curve. Once sufficient energy was removed the braking action was removed and the system then modulated the remaining deceleration to ascertain the desired upset. In MAIRFWTFL007 & 008 the braking continued until all speed was removed, which indicated that the brake system could not remove enough energy from the flywheel system for the final length target to be met. In this case the reduction in part length required was larger than the scalable linear upset region from the nominal weld. The system continued to brake through the remaining deceleration instead of modulating the deceleration to meet the required upset.

The inertia tube components, Figure 5-22 to Figure 5-25, showed an identical trend to the solid components, Figure 5-26 to Figure 5-29. Oversize components required additional energy input to produce extra upset. Undersized components were capable of producing characteristic welds showing all phases, providing that the smaller initial part length still allowed the required upset to be generated from conditioning and forging phases of the profile, such as in Figure 5-24 and Figure 5-25. Un-characteristic phases were produced when the initial part size was too short for the upset from conditioning and forging phases to be produced and meet the

required final length. In this case the braking of the spindle to remove energy from the transition phase continued into the forging phase and undersized components were produced.

The scaling could occur from earlier in the cycle, but this would be harder as the conditioning and initial heating phases did not have a linear energy-upset relationship. The speed could be modified earlier in the cycle in an effort to allow greater variation however this could result in a lack of heating occurring before the brake is applied and the material would not be in a quasi-stable state suitable for producing sound welds (Manufacturing Technology Inc, 2012, 2017a, 2017d). The undersized components also risked not cleaning the interface, potentially leaving inclusions in the weld on the bond line McAndrew *et al.* (2015)

5.10.1.2 Continuous drive mode analysis

The weld curves for the continuous drive tube welds are shown in Figure 5-30 to Figure 5-33. In continuous drive the burn off point was set as a fixed point on the machine (Manufacturing Technology Inc, 2012).

Each weld continues to extrude material during the friction phases until a fixed point on the machine was reached. Variations in upset were from the effect of the forge pressure on the resultant state of the material at the end of second friction. The welds spending longer in the second friction phase produced more upset during the forging phase. The longer second friction phase would allow greater heat penetration into the part from the interface creating a larger region of plasticised material. This plasticised material would be extruded along with the interface material as the pressure rose during the forge phase I. Woo *et al.* (2002).

There is a slight difference in parameters between MACDFWTFL001 and the other welds. In subsequent welds the first friction time was extended, and the first friction speed was increased to reduce torque loading upon part contact. As a result, the welds transitioned to a linear upset rate quicker. This parameter change would increase the initial interface temperature and heat

penetration into the parts Özdemir *et al.* (2007), Healy *et al.* (1976) and (Healy *et al.*, 1976; Özdemir *et al.*, 2007); Turner *et al.* (2016)

The solid component welds for CDFW exhibited similar traits as the tube component welds, Figure 5-34 to Figure 5-37 The welds starting with longer parts undergo longer second friction stages which produce more upset during the forging phase. The solid components enter the linear upset state slower than the tubes due to the challenge of heating parts of components with low rotational speeds such as at the centre Linnert (1994). The shortest components just enter the linear upset stable state before switching straight away into the forge as the burn off point is quickly reached. If shorter parts had been used then the linear upset phase would have been missed and miss-sized components would be produced as in the inertia cycles.

5.10.2 Component final length measurement analysis

As seen in the weld curves the inertia weld axial measurements show that there must be enough material to upset for the weld curves to produce standard conditioning, transition and forging phases. The transition stage is then scaled accordingly. If enough material does not exist, the transition and forging phase do not match that of the nominal weld preventing the control system from reaching the required final length.

The shortest initial parts (-2mm variation) have undergone too much upset and hence are shorter than required. These are highlighted in Figure 5-38 & Figure 5-39 as “undersized part”. Once the minimum initial part size has been met the control system produced final lengths proportional to the initial length. Both showed a trend of longer pre-weld components producing over upset components and hence shorter than ideal final lengths. The solid components showed a trend gradient of -0.0228 while the tubes showed -0.0249. With respect to the trend, it can be stated that for every 1mm of extra initial part length the inertia solid mode produces parts 0.023mm shorter while the inertia tube mode produced parts 0.025mm shorter. The solid mode would have produced an exact part length at 212.28mm, 0.08mm greater than the

nominal initial part size. The tube parts would have produced an exact part length at 210.04mm, 2.16mm shorter than the nominal initial part size.

The continuous drive control system did not show that the minimum initial part length had been reached in this study. The smallest initial parts completed welding without failure. Failure would be indicated from weld curves when the burn off point is reached during first friction. Again, a trend was shown towards longer cycles producing greater upset and hence shorter parts. The trend is stronger in the continuous drive components (Figure 5-40 & Figure 5-41) showing a gradient of -0.0617 for the solid components and -0.0805 for the tube components. The trends show for continuous drive solid components every 1mm of extra initial part size produces a final component 0.062mm smaller. An exact final length would have been produced with initial parts 212.48mm long, 0.28mm longer than nominal. The continuous drive tube program would produce a weld 0.081mm shorter for every 1mm of initial part length. Both solid components would have produced ideal part lengths with initial part sizes very close to the nominal part size of 212.2mm, while the tube components would require an initial part size several millimetres shorter than nominal. The continuous drive solid shows up to 0.28mm variation for the same initial part size which could explain the lower trend line. The inertia solid welds have a smaller max variation of 0.06mm difference but it would also allow the trend line to match the ideal size with nominal initial part sizes.

5.10.3 Energy analysis

In the inertia welds while the cycle was not able to always weld to an exact final length there was a strong correlation between the upset produced and the energy the cycle put into the weld. In the Inertia solid welds, the post process upset measurement trend suggests that 0.0369mm of upset is created for every kilojoule of energy. Extending the line backwards also suggests a minimum of 203kJ of energy is required for the weld to move from conditioning to producing upset. In the tube welds the gradient is very similar as is the minimum energy. Taking the start point of upset generation from the weld cycle curves the energy traces show

that conditioning takes ~158kJ for the inertia tube welds and ~184kJ for the inertia solid welds. The discrepancy is due to the linear trend also including the energy in the forge phase where the upset rate increases in the final moments of rotation.

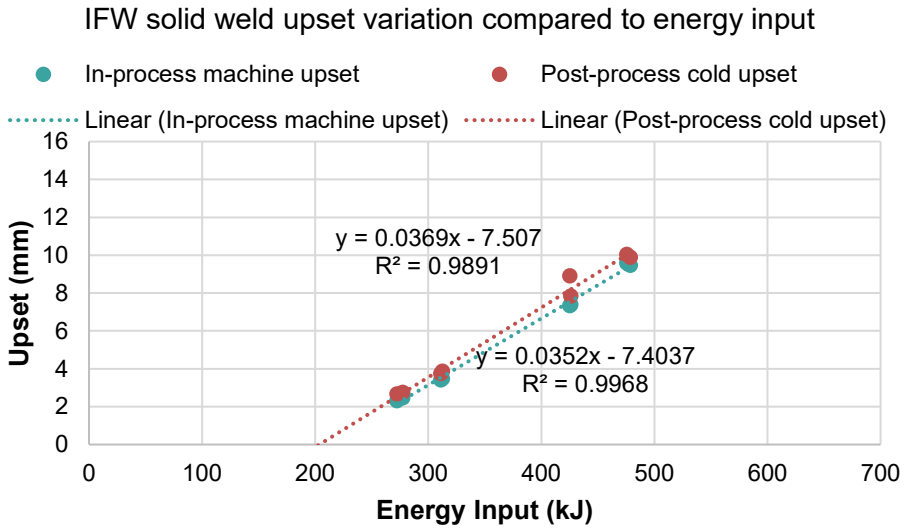


Figure 5-78: In-process and post-process upset measurements of the IFW solid final length control welds plotted against the total weld energy input

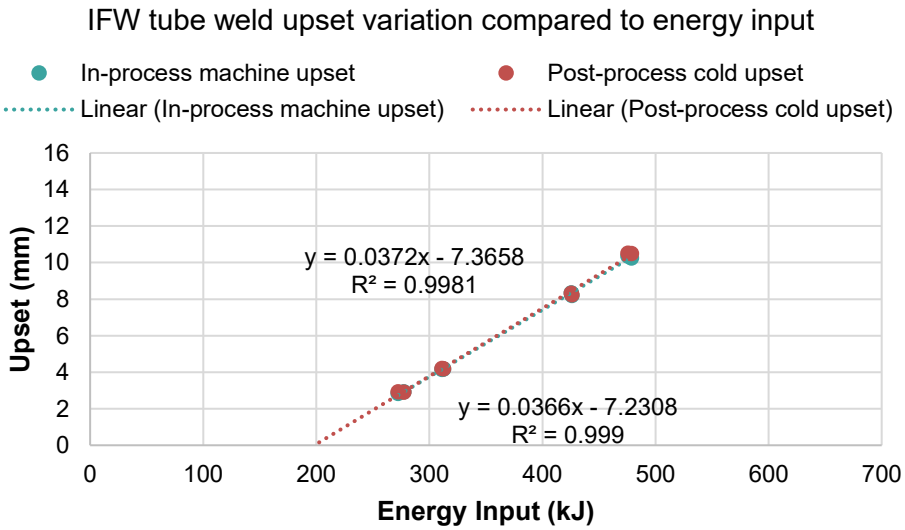


Figure 5-79: In-process and post-process upset measurements of the IFW tube final length control welds plotted against the total weld energy input

In the continuous drive welds the trends show that once welding the process is more efficient with 0.495mm of upset produced in the solid weld, and 0.413mm of upset produced in the tube weld for every kilojoule of energy. However, extending the trend backwards shows a minimum energy requirement of 352kJ for the solid weld and 284kJ for the tube welds.

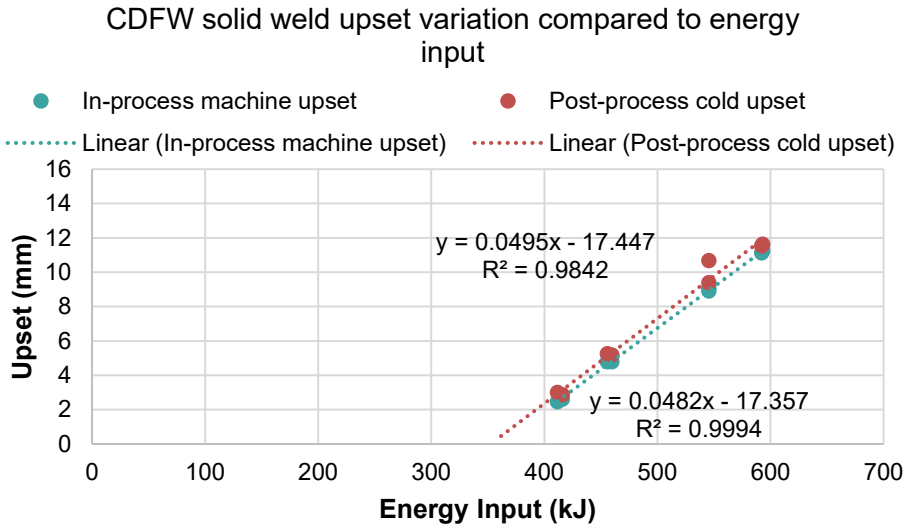


Figure 5-81: In-process and post-process upset measurements of the CDFW solid final length control welds plotted against the total weld energy input

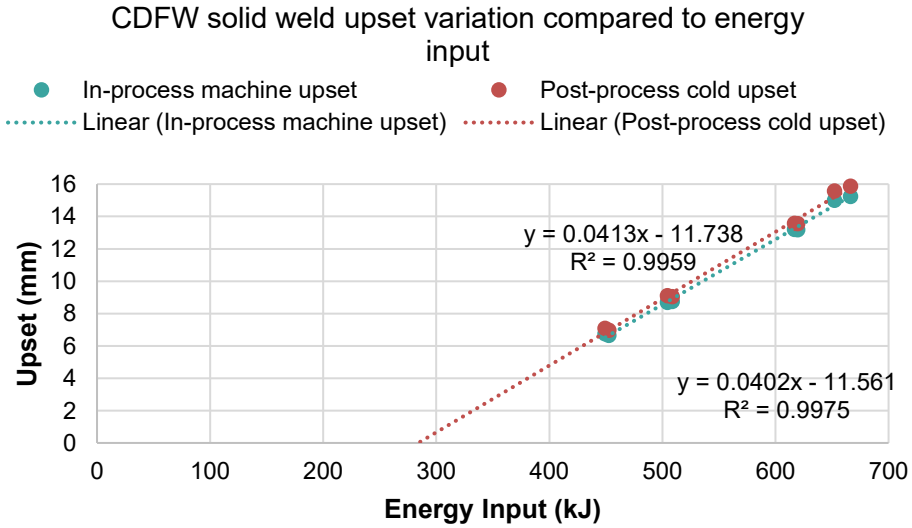


Figure 5-80: In-process and post-process upset measurements of the CDFW tube final length control welds plotted against the total weld energy input

From the point of upset production, which corresponds to the switch to the 2nd friction phase, the energy traces calculated 316kJ for the conditioning of the CDFW tube welds and 284kJ for the solid welds. The similarity between the solid measurements can be attributed to the slow rotational speed and low input rate where limited energy is transferred during deceleration and the smooth transitions between phases making tracking of the weld energy easier, as evidenced by the smaller sudden variations to the energy input rate.

5.10.4 Microstructural analysis

5.10.4.1 Visual inspection analysis

All welds produced flash proportional to the amount of upset required to produce parts of similar lengths.

The inertia tubes exhibited characteristic tight curls of flash growing proportional to the pre-weld part size (M Maalekian, 2007; Uday *et al.*, 2010). Tempering colours can be seen just above the flash showing how far the heat near the surface penetrated the component. No cracking was present.

The inertia solid components showed greater amounts of flash as the material can only move to the outside diameter. Again, no cracks were seen, and tempering colours were visible on the exterior of the part but slightly further from the weld, than on the tube welds due to the greater amount of energy and reduced surface area for the heat to escape through.

The continuous drive tubes showed looser curling flash and tempering colours further into the base material of the part probably due to the lower pressures involved. At the very centre of the weld the effect of the forge pressure can be seen creating a small join between the two sides of the flash. The longer upsetting parts have a larger flash and a larger bridge between the two flash curls matching those described by Linnert (1994). Cracking is also not seen.

The continuous drive solids showed the largest flash curls. Like the tubes they displayed tempering colours further away from the weld line than the inertia components. This will be due to the lower pressures used in the process allowing the heat to penetrate the material further before being ejected along with the flash. This matches work on the thermal profile of Ti-6Al-4V which presented larger and hotter plasticised zones when inertia welding with lower pressures Turner *et al.* (2016). Cracking was also not seen.

5.10.4.2 Inertia solid analysis

The inertia solid components show variation in hardness at the weld centre and weld shape depending on pre-weld part length. Each weld shows a similar weld zone width of ~6mm at the centre visible from the macrographs and the hardness traces. However, the width and shape of the weld zone at the outside diameter changes with upset. Greater upsetting welds displayed wider zone widths, with the cone shape expanding further into the centre of the component, producing a concaved weld zone such as Figure 5-50. Welds that upset very little appeared to produce a constant width across more of the diameter. The cone shape was thinner and smaller such as in Figure 5-53. Figure 5-82 shows a diagram of the phenomenon. The change in weld zone shape was due to the change in energy midway through the cycle. Similar weld shapes have been seen in the inertia welding of low-alloy pipes (Tumuluru, 1984). The change in shape was attributed to changes in initial rotational velocity however, this ignored the change of energy due to the change in rotational speed. As the conditioning phases of the FLC welds are the same and thereby the steady state thermal profiles of these welds are also the same the change in weld shape cannot come from a change in the interface layer which could have been the case in the low-alloy pipe welds due to the change in initial rotational speed and weld time (Özdemir *et al.*, 2007; Turner *et al.*, 2016; I. Woo *et al.*, 2002). Therefore, the change in weld shape is likely due to the change in energy.

Diagram of the changing weld shape in the inertia welds

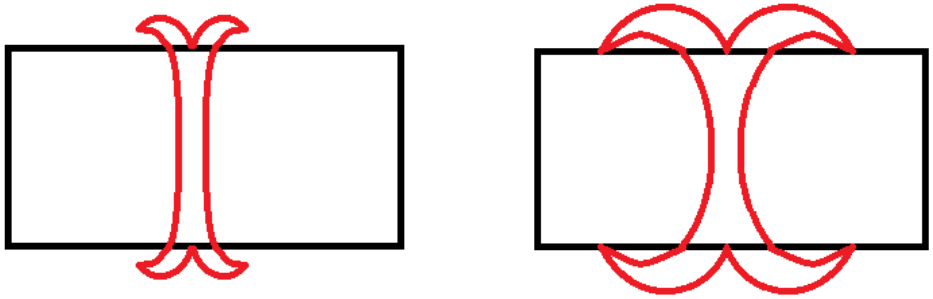


Figure 5-82: a) low energy - weld zone is thin and even across most of the weld sample with small amounts of flash b) high energy - large changes in weld zone width across the weld sample with larger amounts of flash thereby distorting the edge of the weld zone near the flash (adapted from Linnert (1994) with results seen in the work above).

The difference in energy input would also influence the thermal history of the weld. For instance Turner *et al.* (2016) produced parts with temperature profiles dependant on the rotational speed. Along with Duffin and Bahrani (1973) suggesting a change in the plasticised layer thickness at different speeds along with a matching temperature profile. The higher speeds and higher associated interface temperatures would lead to more curved and wider weld zones. As seen here in the higher energy welds. Where the welds are held at a higher speed for longer.

With respect to the microstructure parts with greater upset produce lower max hardness (320Hv for MAIRFWSFL001 Figure 5-50) with a fine grain mixed pearlite, lower bainite and a small amount of retained ferrite. As the upset reduced the max hardness increased and the morphology changed. The ferrite disappeared along with nearly all the pearlite. Bainite increased and in the smallest upset welds some martensite was also visible. The increase in bainite and martensite at the expense of the ferrite and pearlite would explain the increase of the max hardness, up to 500Hv, in the smallest upset weld MAIRFSFL007, Figure 5-53. As the morphology of this material is dependent on cooling rate (Baker, 2016; Ponge, 2005) it

would suggest that the greater pre-weld length parts have been subjected to a slower cooling rate while the shorter pre-weld components have undergone a faster cooling rate. This is most likely due to that fact that the heat from the interface has had a chance to permeate into the base material reducing the temperature gradient away from the weld zone. In the shorter pre-weld components, which experienced short amounts of upset and shorter welding cycle times the heat from the interface would not have diffused into the parent material leaving a large temperature gradient and a strong driving force for a fast cooling rate. This is backed up by the thinner HAZ widths and higher hardness's at the centre of the welds measured.

5.10.4.3 Inertia tube analysis

Similar traits occur in the inertia tube compared to the inertia solid components. The oversized components produced more upset which resulted in a very concaved weld zone with the largest width at the inside diameter and smallest near the centre. The two oversized welds both displayed a weld zone hardness of 320Hv and had a matching predominantly bainite microstructure (Figure 5-54 & Figure 5-55). The shorter components experienced shorter cycle times as energy was extracted from the weld by the brake. This produced steadily less concave weld zones with thinner widths towards the edge of the sample. The hardness values of 440Hv and 460Hv for 005 and 007 respectively indicate a faster cooling rate with a resultant morphology consisting of increased levels of mixed martensite and some bainite (Figure 5-56 & Figure 5-57) (Baker, 2016; Ponge, 2005).

5.10.4.4 Continuous drive solid analysis

All solid welds showed a similar microstructure and weld zone regardless of the length of pre-weld part. Each weld achieved a max hardness of around 270Hv with the HAZ expanding 5mm either side of the bond line. This is similar to the nominal welds. The ferrite and pearlite base material is seen to change while approaching the weld zone with the percentage of pearlite increasing while the ferrite decreases. Some Lower bainite is also visible around the bond line. Grain size is reduced in the weld zone due to recrystallisation (Ćirić & Radović, 2005; Jata &

Semiatin, 2000; M Maalekian, 2007). In the TMAZ away from the weld zone, the material had undergone minimal deformation with the prior morphology slightly deformed but still visible in the resulting recrystallised structure.

The similar microstructures suggest similar thermal histories. The weld cycle curves show the larger pre-weld parts undergoing proportionally longer second friction phases and also producing greater upset during the forging phase. This suggests that the forge is leaving the same amount of material at the same temperature in the weld zone regardless of second friction duration. This will be due to the forge pressure being able to extrude material that is above a critical temperature and hence below a critical yield stress. It is possible to conclude that the linear upset produced during second friction is advancing through the part slower than heat is conducted away from the interface at such a difference that a hot zone is being created behind the weld zone. The longer the second friction stage is applied the greater the amount of material in the hot zone, which is above the critical temperature to be extruded by the forge pressure. Once the forge pressure is applied, all material above the critical temperature, and correspondingly below the critical yield stress (the forging stress) is removed leaving a weld zone at a set temperature regardless of the length of second friction. A situation similarly seen until friction pressures were increased to the point where an advancing hot zone was not created Masaaki Kimura *et al.* (2005).

5.10.4.5 Continuous drive tube analysis

The continuous drive tube shows similarities to the solid components. Primarily down to the matching method of length control. A slight variation is seen with the longer pre-weld components producing slightly higher weld line hardness, 290 - 300Hv1 compared to the undersized components producing a hardness of 280 - 290Hv1, however as the base material shows a variation of roughly 30Hv1 this is not significant. The hardness trace corresponded with the ferrite and pearlite base material beginning to recrystallise in the TMAZ with the prior morphology evident even though deformed. Closer to the bond line the percentage of pearlite

increased with retained ferrite around the pearlite grains with some lower bainite present. The HAZ extends roughly to 2-3mm. This matched the nominal welds with ideal length parts with a standard burn off.

5.10.5 Mechanical testing analysis

5.10.5.1 Bend test analysis

Bend test results of inertia rotary friction final length control welds and continuous drive rotary friction final length control welds are shown in Figure 5-70 and Figure 5-71, respectively. In the bend test results some scatter is present. As shown in Figure 5-70, the inertia FLC solid components mostly achieved a minimum of 45º while part 005 erroneously achieved 88º. The tubular components achieved a higher average of 65º with a variation either side of only 10º. This could be explained by the tubular components generally showing a slightly thinner weld zone than the solid components even though they were generally harder. Allowing a greater degree of bend to be performed by the larger amount of softer HAZ and parent material incorporated in the region subjected to the bend as seen in copper to aluminium welds (I. Bhamji *et al.*, 2012); S. Chen *et al.* (2017). However, from the optical images of the weld zones the incoming part size influenced the resultant microstructure with wider zones attributed to longer parts. When compared to the hardness trace the region of increased hardness appears to be the same width regardless of component length. This could explain the trend for the tube samples to outperform the solid samples as the region of increased hardness extends 2mm either side of the weld in the tube welds and 3mm either side in the solid welds.

Figure 5-71 shows the bend test results of continuous drive rotary friction final length control welds. It can be seen from this figure that the solid components show variation from 45º to the maximum angle of 90º. On average they achieved 72º. The tube components showed less total variation of only 74º to 90º with an average of 85º. The nominal tube weld reached 84 º in line with the FLC welds. With similar microstructures at the weld zone with an increase in

pearlite and some bainite seen correlating with the slight rise in hardness of all the welds to ~290Hv1 and the matching weld zone sizes, the low variation of the CDFW FLC tube welds is expected. The variation presented by the solid components was more than expected, when correlated with the consistency of the hardness traces and weld zone widths. In the CDFW welds the narrower regions of weld hardness correlate with improved bend results. The CDFW tube welds had increased hardness up to 3mm from the weld line while the solid welds had an increased hardness up to 6mm from the weld line. With the performing better on average than the solid welds. The improvement of the CDFW welds over the IFW welds can be attributed to the reduction in hardness of the welded regions in combination with the weld zone widths.

5.10.5.2 Tensile analysis

Tensile test results of inertia rotary friction final length control welds and continuous drive rotary friction final length control welds are shown in Figure 5-72 and Figure 5-74, respectively. It can be seen from Figure 5-72 that the tensile tests show slight variation in the UTS, yield strength and elongation across all the inertia welds. No correlation exists between the bend results and the UTS or weld zone widths. Hardness values and the microstructure also do not correlate.

As the welds broke away from the bond line in the parent material matching the failure location of the nominal welds, this suggests the FLC tensile variation is the inherent variation in the parent material. However, it does prove that the weld region is stronger than the parent material as would be expected with the change in microstructure and grain refinement (Moat *et al.*, 2008; Rollet, 2007; Sathiya, Aravindan, & Noorul Haq, 2007).

The continuous drive welds show similarities to the inertia welds. As shown in Figure 5-74, the tensile results show some scatter in the UTS, yield strength and elongation but as they all broke away from the weld line in the parent material this suggests the variation is due to natural variation of the parent material. As the tests broke away from the weld line it shows that the weld is not the weakest part of the test piece (Ragu Nathan *et al.*, 2015).

5.10.5.3 Charpy impact analysis

Charpy impact test results of inertia rotary friction final length control welds and continuous drive rotary friction final length control welds are shown in Figure 5-76 and Figure 5-77, respectively. As the charpy test directly tests the impact strength of the microstructure at the notch tip variations in notch placement will provide variations in result.

As can be seen from Figure 5-76, in both the solid and tube inertia components the charpy tests show a correlation between shorter upsets of parts and lower energy absorption. This matches with the harder and more brittle microstructures also seen in the weld zones of the shorter parts and matches previous welds from the literature Ragu Nathan *et al.* (2015).

For continuous drive rotary friction final length control welds, the charpy impact tests show low absorption from the weld zone in the solid components, around 10J. The shortest upset part MACDFWSFL007 has a slightly harder weld zone microstructure of 300Hv, which relates to the slightly higher performance seen in the charpy tests. The tube components show a higher energy absorption but with greater scatter around the 30J mark.

5.11 Conclusions and recommendations

This study evaluated the capabilities of the enhanced functionality, final length control. Welds were created in inertia and continuous drive modes and made from tubular and solid samples.

The study showed that when choosing a final length control mode, the product requirements should be considered in order to achieve the best performance. When the length of the part is the most critical factor then the Inertia mode should be used. The welds produced differed by 0.025mm for every millimetre of difference from the nominal profile compared to 0.081mm in continuous drive. If consistent weld performance is the upmost criteria, then continuous drive mode should be used. The consistent upset rate in the 2nd friction phase followed by the forge

pressure produced welds with matching weld microstructures, hardness profiles and performance.

This study demonstrated that initial pre-weld components of between 208mm and 216mm could be CDFW welded to the final length of 206mm with a maximum deviation from the desired length of 0.16%. The deviation in final length was also found to be directly proportional to the original variation in component length.

Final length control in continuous drive has shown a trend to increase the variation from the desired part length by 0.081mm for every millimetre difference from the nominal part size desired length. Continuous drive mode showed a greater ability to accept weld parts of varying length due to the 1st friction phase of the process consuming less material when conditioning the weld interface. However, as the dimensional control of the process is stopped at the end of the 2nd friction phase the resulting upset from the forge phase is proportional to the length of time / distance of material consumed during the second friction phase. This resulted in a greater variation of final part sizes. Though the consistent forge phase produced identical microstructures regardless of the pre-weld part sizes.

Final length control in inertia welded samples achieved variation from the desired part length by 0.025mm for every millimetre difference from nominal part size. However, there were limits to this capability when the amount of energy required to be extracted from the weld was greater than the amount in the weld to shorten the upset and the final length couldn't be achieved. Microstructures in welds above the standard amount of upset were not greatly affected. Welds below the minimum amount still created full bonds. The cycle matched the similar low heat input cycle demonstrated by M. Kimura, M. Kusaka*, et al.* (2005a); Kimura *et al.* (2003). In both scenarios the welds made it through the initial conditioning phase suggesting that the wear and seizure phases seen by Kimura *et al.* (2010) at the interface occurred within the welds seen here. When approaching the minimum capable welding length an increase in hardness

is seen in the weld zone as the cooling rates are increased due to the reduced amount of hot material created, enabling the formation of regions of martensite in rapidly cooled regions as also seen by Sathiya, Aravindan, and Haq (2007).

5.12 Industrial recommendations

When using final length control it is worth considering several factors.

First, the primary performance criteria should be decided for the part.

- If part length is critical then inertia mode should be used as this provides a greater degree of accuracy.
- If weld performance is critical and part length is secondary then continuous drive should be used as it produced welds of matching microstructure, weld width, hardness profile and mechanical performance regardless of the incoming part size.

When setting up the process the profile weld should be based on the smallest incoming part size. The smallest part size should provide enough material for a weld cycle to upset and still meet the final length requirement. Both Inertia and continuous drive were able to cope with oversized parts but in this study parts 2mm less than the nominal profile caused length inaccuracies in the inertia weld cycle and was near the limit of acceptable part sizes in the continuous drive cycle. Smaller parts also caused large changes to the produced microstructure and hardness traces when in inertia mode which can affect the performance of the component.

5.13 Future work

The final length control work conducted in this study can be used to further the development of components in a production route with large variability of incoming part sizes: helping to reduce deviation in feature measurements which would reduce machining time and improve

production rates. Further work may develop processing algorithms that can reduce final part size variation.

6 Impact of simulated inertias upon the residual stress in inertia friction welded Ti-6Al-4V.

6.1 Aim

To evaluate the impact of artificial deceleration profiles on the weld energy input and associated residual stress state.

6.2 Summary

Three welding cycles were created using the enhanced capabilities of the M125T rotary friction welder. Initially a set of nominal welds were produced, utilising the torque braking feature of the machine's electric motor, to create a suitable amount of upset. Secondly, a set of welds with a higher initial speed and large amounts of brake torque were made to simulate a weld with a smaller flywheel inertia than fitted, while matching the nominal upset. Thirdly, a set of welds containing torque braking and torque injection were used to produce a weld that initially simulated a small flywheel, then switching to a large flywheel mid-weld, whilst still matching the previous cycle upsets. The contour method was used to compare the residual stresses created during the welds, while temperature probes and energy traces were used to help analyse the impact of the various cycles on the weld microstructure.

6.3 Research approach

Herein the application of the torque modulation capability is analysed with respect to its ability to simulate various inertial states and modify the resulting weld morphology. This builds on the work conducted within chapter 5 where energy was modified mid-cycle, in some cases to the limit of the cycle, with the aim of understanding the impact of the cycle on the material state. The work within chapter 6 explores entirely novel welding cycles with the aim of evaluating their influence on the final stress state to reduce post processing. The created weld cycles

substantially modify the rate of energy delivered to the weld, utilising a pre-determined upset-deceleration profile to alter the upset rates in the later stages of the weld, thereby controlling the heat input into the surrounding material and the associated residual stresses.

6.4 Experimental background

It has been shown that pressure had a direct impact on the residual stresses and textures found in linear friction welds of Ti-6Al-4V Romero *et al.* (2009). Increasing the pressure used by a factor of nine lead to randomised textures and a strong reduction in residual stresses across the weld zone. It was suggested the randomized textures were due to interface deformation occurring at a cooler temperature; in the α + β phase instead of the more normal, hotter, β phase. However, increasing the pressure on a weld by nine times is not always practical. Yield strengths and physical machine limitations can prevent this application. Being able to recreate the higher pressure's lower interface temperature and higher upset speed through an alternative method could be more industrially viable.

Higher pressures are linked to faster upset rates by McAndrew *et al.* (2015) which were also linked to lower rubbing (rotational) speeds by Healy *et al.* (1976), who showed there was an optimal low rotational speed, in continuous drive mode, for a maximum upset rate. This fits with the parameter-weld zone relationships shown in Figure 2-1 Linnert (1994).

It was also noted that the greatest upset rate was produced at the end of the inertia cycle when the rotational speeds were lowest, and the flywheel was decelerating faster than earlier in the cycle. Low rotational speeds were originally suggested as the alternative to the high pressures however these are known to produce centre defects in solid bar geometries (Linnert, 1994; M Maalekian, 2007). A phenomenon where at the centre of the interface the surface velocity is reduced to zero. Therefore, the centre point relies upon heat transfer from the faster moving interface areas. If the heat transfer is insufficient the centre will not form a sufficiently plastic layer able to join the two interfaces. A solution is to use a tube geometry at the interface. Low

rotational speeds also require a large amount of inertia to be used to generate a similar upset with potentially comparable variations in upset as seen in previous chapter standard welds.

Conversely, a reduction in heat-affected-zone (HAZ) size with increasing speed was witnessed Avinash *et al.* (2007), similar to the reduction in thermo-mechanically-affected-zone (TMAZ) width I. Woo *et al.* (2002), potentially indicating a reduction of heat into the base material. A reduction in contact zone width with increasing rotational speed was observed when continuous drive welding stainless steel joints Özdemir *et al.* (2007), but this also increased HAZ widths due to increased heat dissipation into the adjacent material. Potentially this was due to the use of a time-based friction limit instead of an upset based friction limit. The increase in upset rate would decrease the time to reach the original amount of upset and potentially change the amount of heat dissipation.

It has been suggested that the contact zone thickness and surrounding layers are dependent on rotational speed Duffin and Bahrani (1973), through the idea of a fragmenting surface. Low speeds produced large fragments upon initial contact plasticizing into a thick contact layer resulting in higher torques. High speeds produced small fragments and hence plasticized into a thin contact layer. The thicker plasticized layer of the low-speed weld would allow for a greater amount of material to be ejected as the weld progresses, thereby producing high upset rates and associated steep temperature gradients reducing the heat input into the material and the TMAZ thicknesses. High speed welds would have lower upset rates and more time for the heat to penetrate the base material, hence a larger TMAZ region. High speeds were linked to the same phenomenon’s as low pressures and vice versa as seen in more general parameter relationships Linnert (1994).

6.5 Experimental methodology

To test both scenarios two welding cycles were proposed as opposing cycles. One with a simulated high inertia and one with a simulated low inertia. Both could be compared back to a nominal weld in the centre, Figure 6-1.

For the high inertia weld cycle initially, it would need to prevent centre defects and not stall therefore a two-part torque modulated profile was created which would also reduce upset variation. It consisted of a faster than normal initial deceleration, simulating a small amount of inertia and allowing for nominal starting speeds, followed by a slower deceleration due to torque input simulating a larger amount of inertia. High pressures and low speeds are known to produce large initial torque peaks, hence the use of low first friction pressures and higher first friction speeds in continuous drive welds to prevent motor stall outs (Manufacturing Technology Inc, 2012). This cycle would also provide information, in comparison to the nominal weld starting at the same speed and the high-speed weld with the same initial braking torque, on contact zone width dependence on initial speed or if it could be altered during the weld.

Weld cycle diagrams of the tested simulated inertia cycle

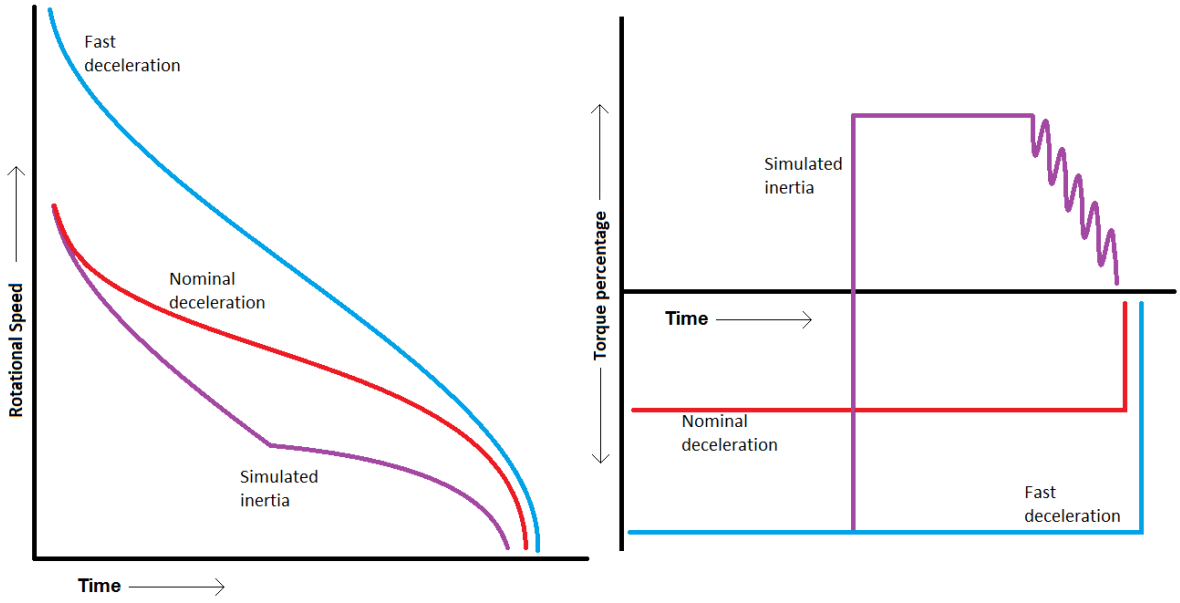


Figure 6-1: Schematic diagram of the tested weld cycles showing the intended deceleration and predicted torque profiles.

To test the opposing scenario a weld profile using much greater speeds was created with a fast deceleration profile utilising a constant braking torque to simulate a smaller inertial mass in the system. The same initial braking torque was used as in the two-part inertia weld.

Table 6-1: Weld parameters developed through prior testing

Enhanced cycle weld parameters				
Weld	**Machine inertia (kgm^2)**	**Initial speed (RPM)**	**Interface Pressure (MPa)**	**Torque profile**
Nominal	68.6	1600	40.32	-40% constant
Fast Deceleration	68.6	2200	40.32	-80% constant
Simulated inertia	68.6	1600	40.32	-80% till 444 rpm, followed by proportional deceleration copy of nominal till 0rpm for matching upset.

Parts consisted of 80mm outer diameter (OD), 20mm inside diameter (ID) and 50mm height. Keyways were machined into the rear face to transfer torque through to the backup owing to the small clamping area, as can be seen in Figure 6-2.



Figure 6-2: Photo of the welded components clearly showing the keyway machined into the rear of the parts and the small clamping area visible from the collet marks on the surface.

An array of pre/post-weld geometry, weld cycle, properties and metallurgy were recorded, inspected and analysed. Results were used to understand the impact various welding cycles had on the microstructure and performance of Titanium 6Al-4V components.

In total four welds of each cycle type were produced. The fourth weld of each cycle underwent temperature measurement. Four K-type thermocouples were imbedded into slots on the outer diameter of the non-rotating fixture part, 6mm ,8mm, 10mm and 12mm back from the initial interface. Slots were created using electro-discharge machining. Slots measured 3mm wide and 3mm deep. All slots were spaced equally apart on the circumference to measurement interference from the neighbouring thermocouple and slot. Thermocouples were supported with high temperature resistant tape. Measurements were recorded on a National Instruments data logger with cold junction compensation. A schematic of the modified fixture weld part is shown in Figure 6-3.

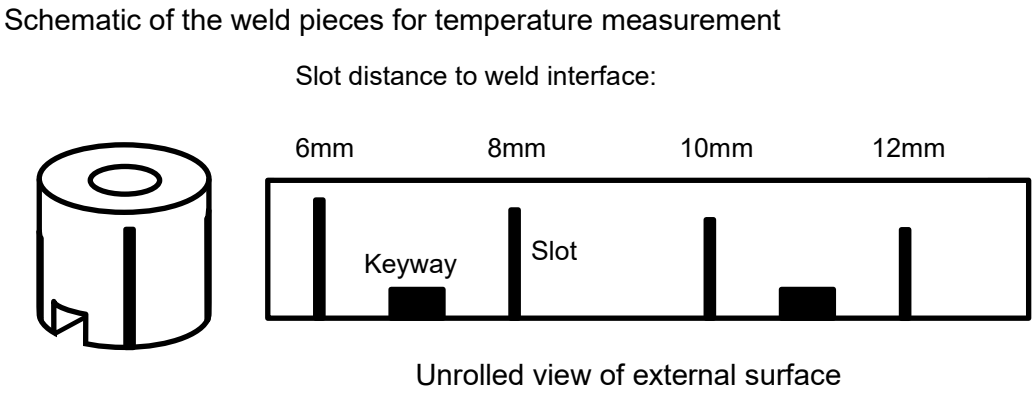


Figure 6-3: Schematic diagram of tracked weld pieces for temperature measurement (not to scale).

Residual stress measurements were conducted at the University of Coventry in the engineering department, using the newly acquired contour method capability by Prof Xiang Zhang and Dr Bilal Ahmed.

6.6 Results

6.6.1 Weld data

6.6.1.1 Weld records

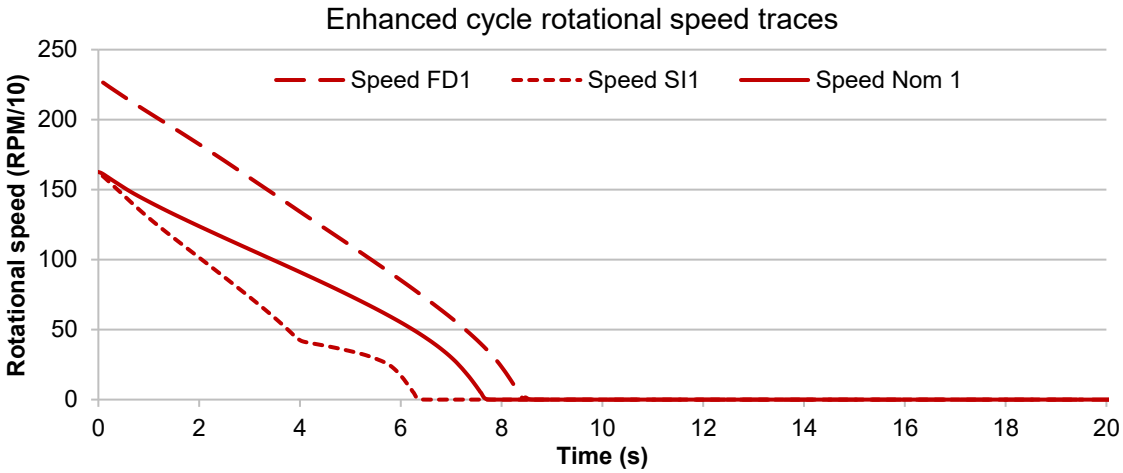


Figure 6-4: Weld traces of the rotational speed of representative cycles for comparison.

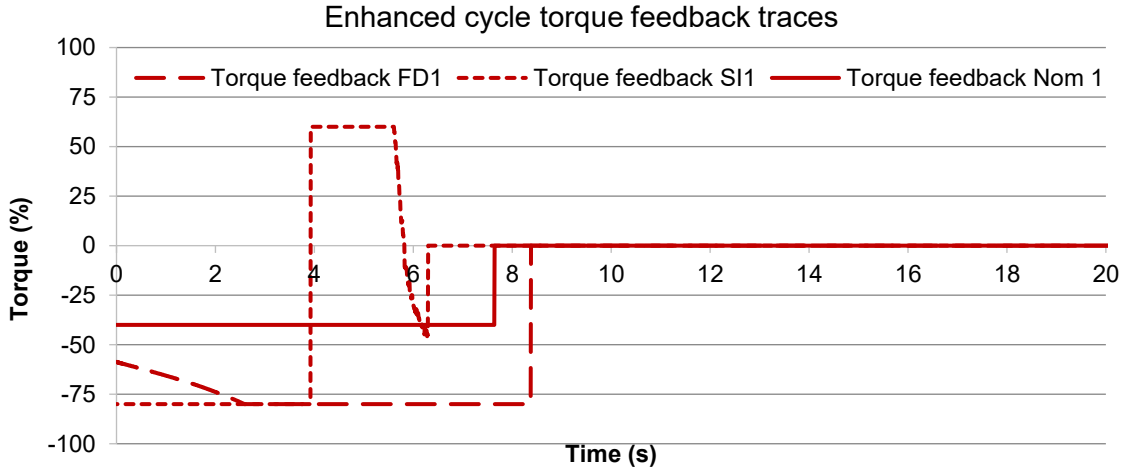


Figure 6-5: Weld traces of the torque feedback percentage of representative cycles for comparison.

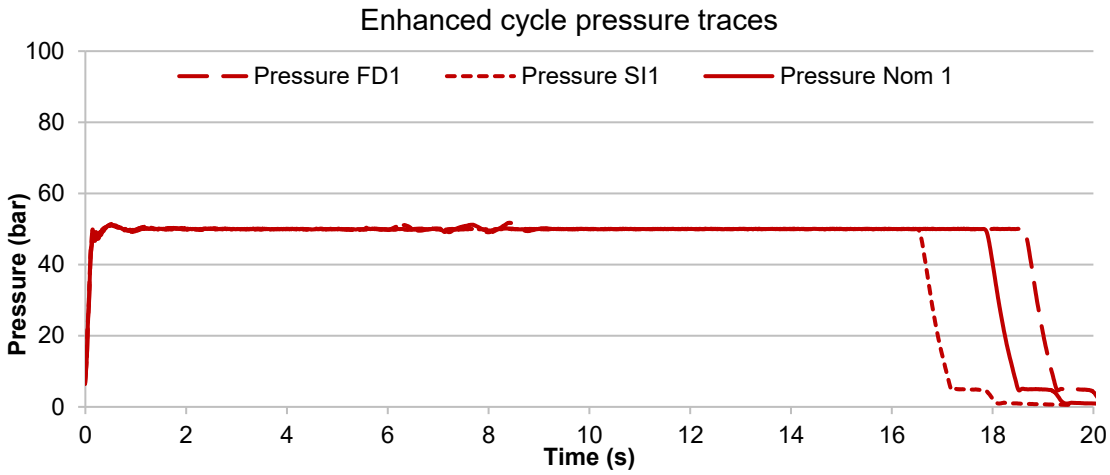


Figure 6-6: Weld traces of the machine pressure of representative cycles for comparison.

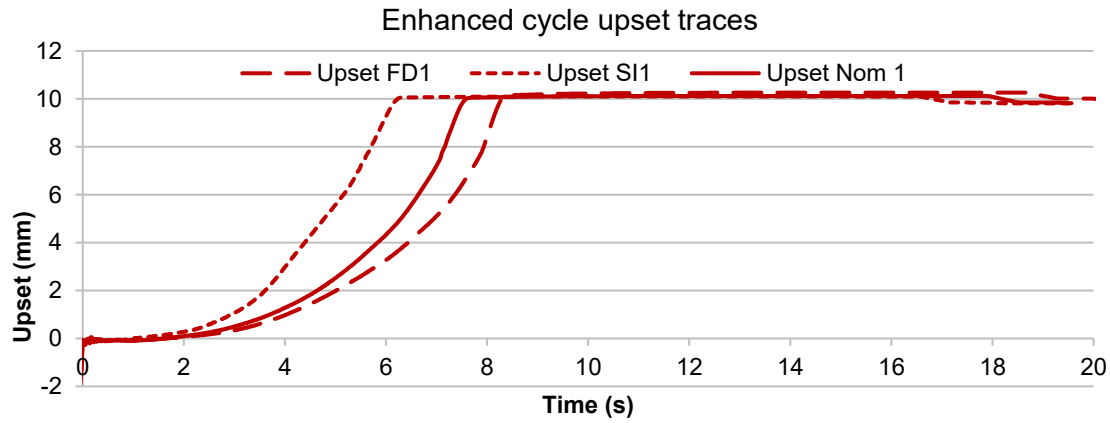


Figure 6-7: Weld traces of the upset of representative cycles for comparison.

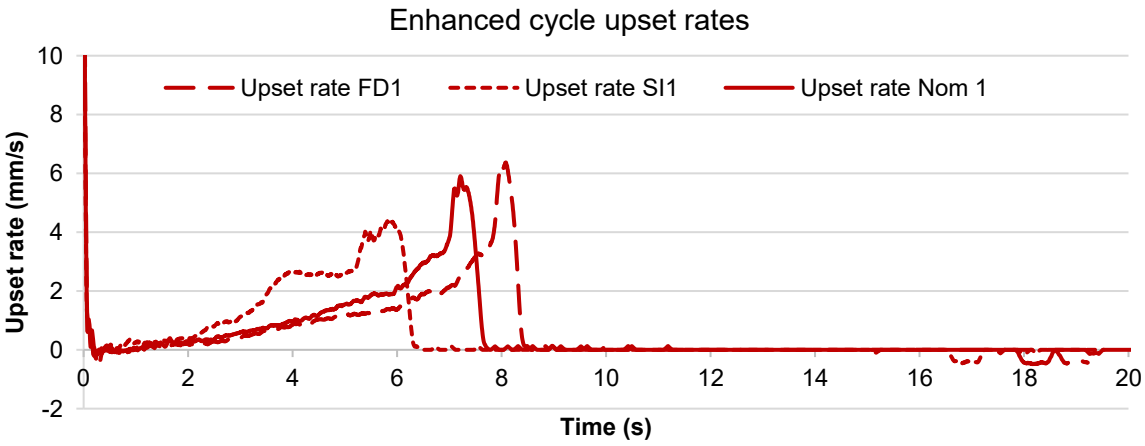


Figure 6-8: Weld traces of the upset rate (smoothed) of representative cycles for comparison.

6.6.1.2 Upset measurement

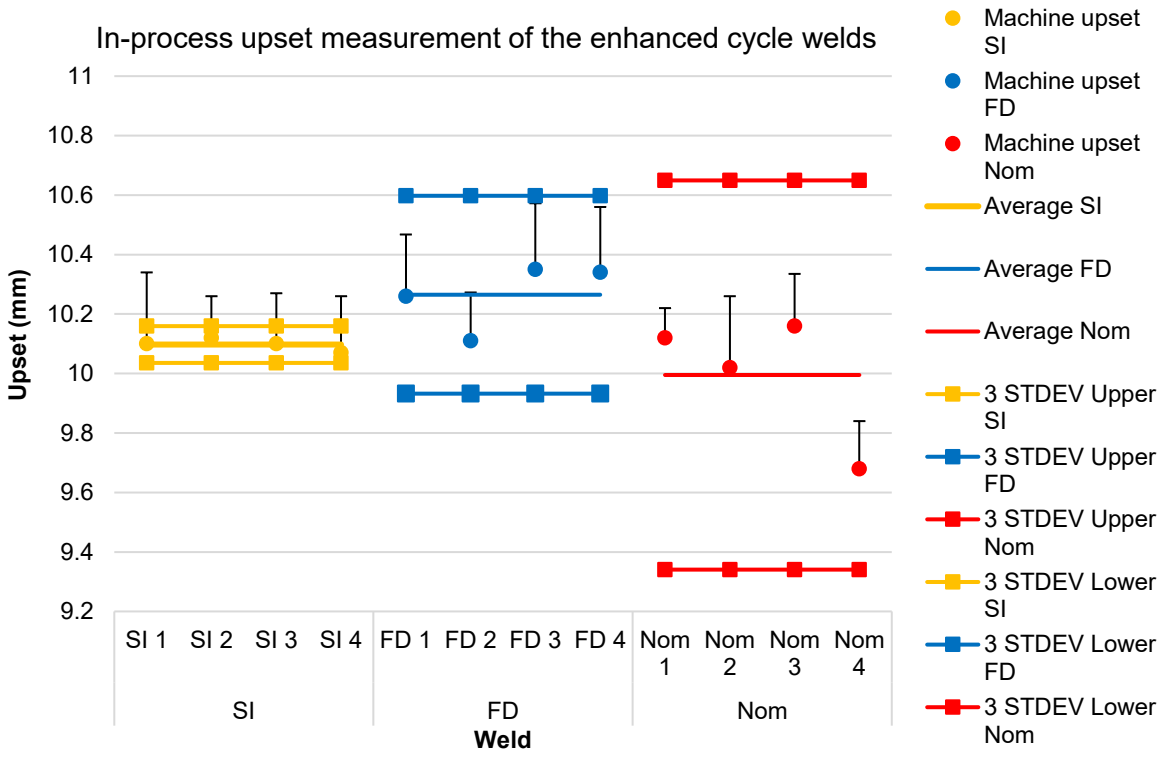


Figure 6-9: Machine upset measurements for each weld including the average and three standard deviation upper and lower lines. The error bars indicate measurement deviation of the machine to the post weld measurement. Resolution of the machine measurement was +/- 0.01mm. Resolution of the post weld height gauge measurement was +/-0.01mm.

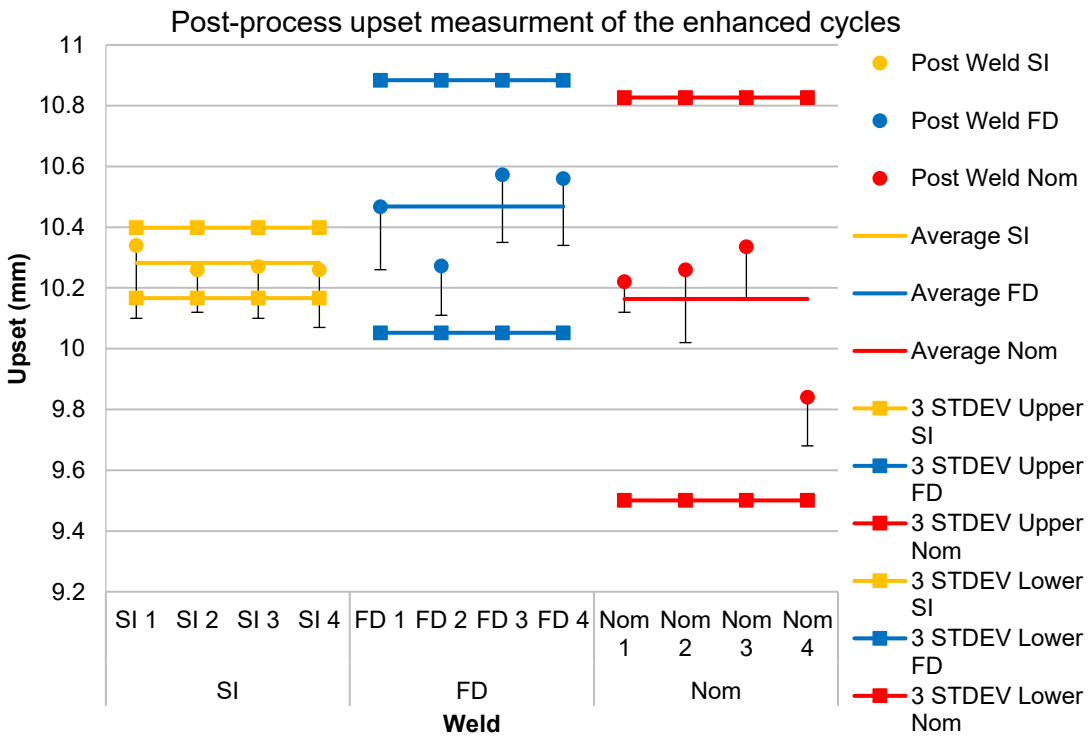


Figure 6-10: Post weld upset measurements for each weld including the average and three standard deviation upper and lower lines. The error bars indicate measurement deviation of the post weld to the machine measurement. Resolution of the post weld height gauge measurement was +/-0.01mm.

6.6.1.3 Energy input

The energy input of the welds are shown. The initial peak looks similar with the welds separating after 2.7s. The similar initial peak suggests the conditioning of the weld requires the same amount of energy regardless of weld speed. In the later stages of the weld the energy input rates show a definitive difference with the higher rates of the SI weld compared to the lower rates of the FD weld. However, as the rotation is coming to stop all welds approach the same energy input rate.

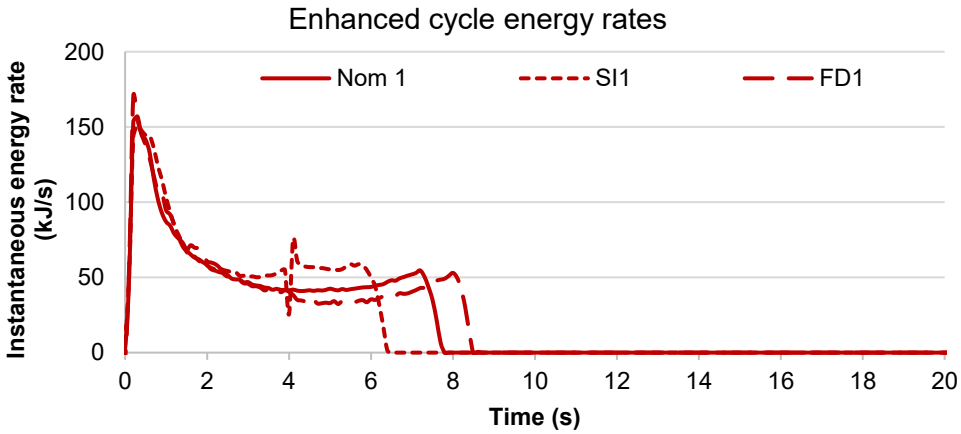


Figure 6-11: Calculated instantaneous energy input traces of the representative welds from each cycle.

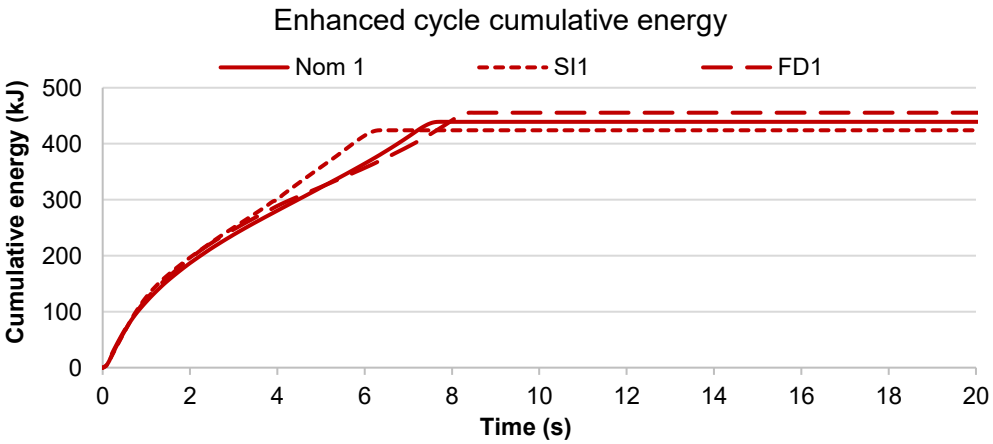


Figure 6-12: Calculated cumulative energy input traces of the representative welds from each cycle.

6.6.1.4 Weld temperatures

Weld temperatures for the 8mm probe and 12mm. The 6mm and 10mm probes both experienced movement during the weld and failed to stay in contact with the surface sufficiently to get accurate measurements.

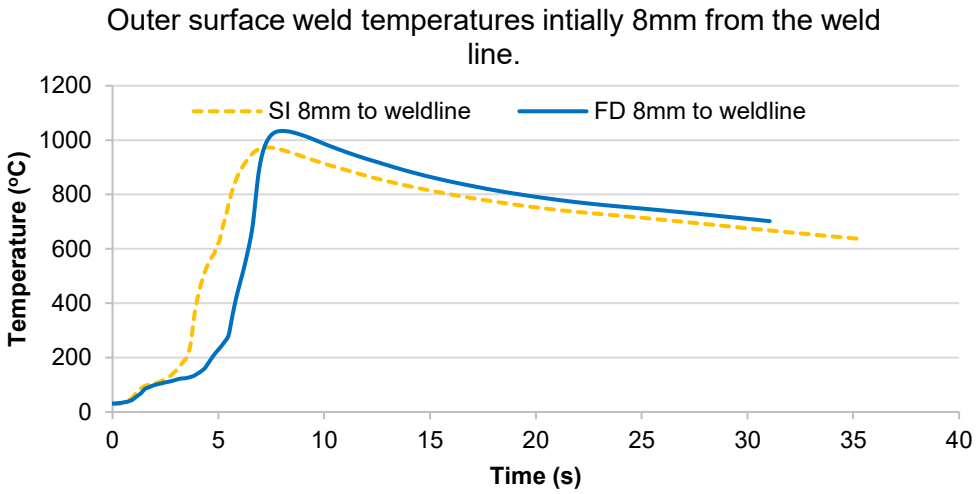


Figure 6-13: Temperature traces of the simulated inertia and fast deceleration weld 4's starting at 8mm from the weld line.

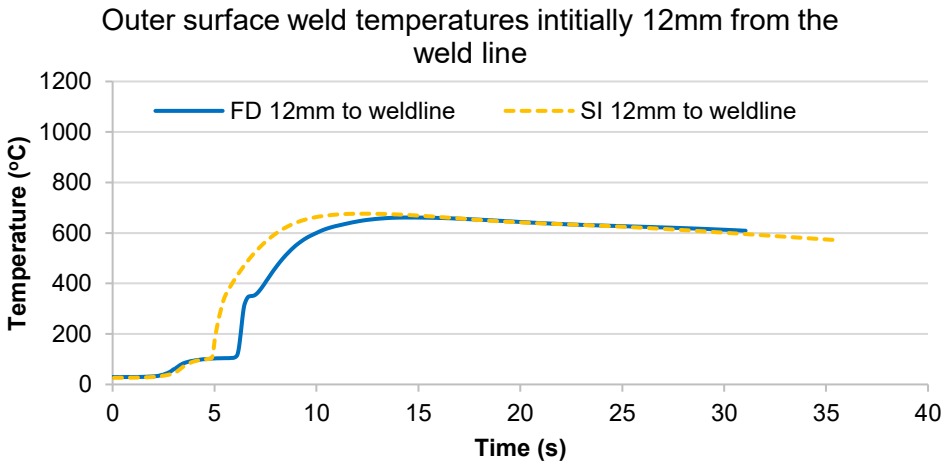


Figure 6-14: Temperature traces of the simulated inertia and fast deceleration weld 4's starting at 12mm from the weld line.

6.6.2 Microstructural examination

6.6.2.1 Visual results

The three enhanced cycle welds are displayed. Close up photos of the weld flash have been included to show the difference in the exterior flash texture and colouring from the three cycles.



Figure 6-15: Comparison of the three weld modes. Fast deceleration on the left, Nominal in the centre and Simulated inertia on the right.

The simulated inertia cycle has a rough textured flash throughout.



Figure 6-16: Close up of the simulated inertia weld flash.

The fast deceleration flash is smooth at the top and bottom of the flash curl on the material first ejected. Lines of striations in the mid-flash are visible becoming rough at the centre. The initial flash has a gold sheen.



Figure 6-17: Close up of the fast deceleration weld flash.

The nominal flash shows some gold sheen with more striations further from the centre of the weld than the fast deceleration sample but less rough than the simulated inertia sample.



Figure 6-18: Close up of the nominal weld flash.

6.6.2.2 Optical micrographs

6.6.2.2.1 Simulated inertia

The simulated inertia weld zone is displayed created from a mosaic of micrographs taken at 50x magnification. The curved weld zone can be seen spanning the tube wall. The ID flash has filled the internal volume and so has been directed down the shaft in either direction. In doing so it has created a wider weld zone. The OD flash has formed a characteristic curled shape. The grain size of the weld zone can be seen to increase rapidly when approaching the ID and especially the OD. The widmanstätten weld line microstructure is consistent through all welds.

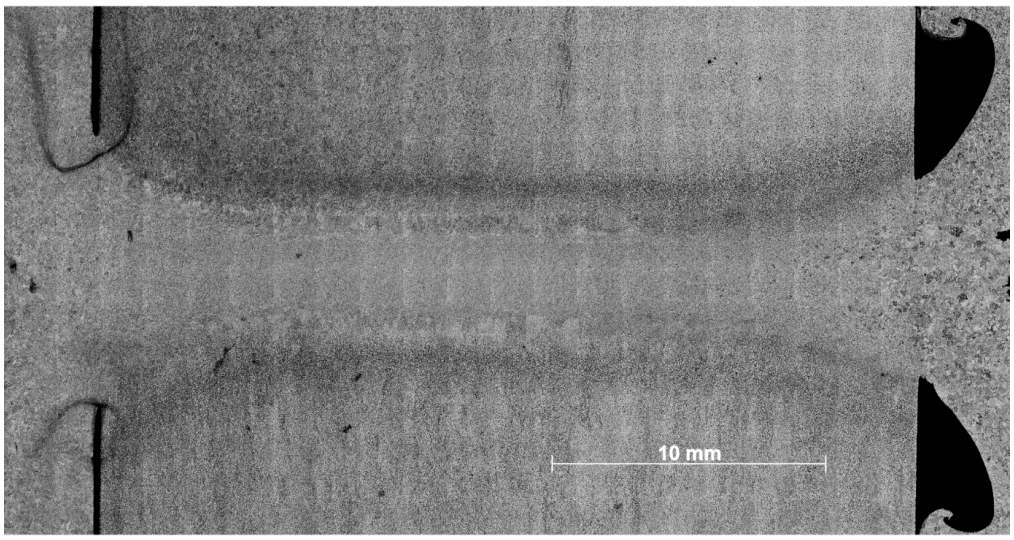


Figure 6-19: Simulated inertia weld zone mosaic image at 50x magnification (resized).

The following micrographs are shown with a reduced full weld zone mosaic to indicate the location of the micrographs.

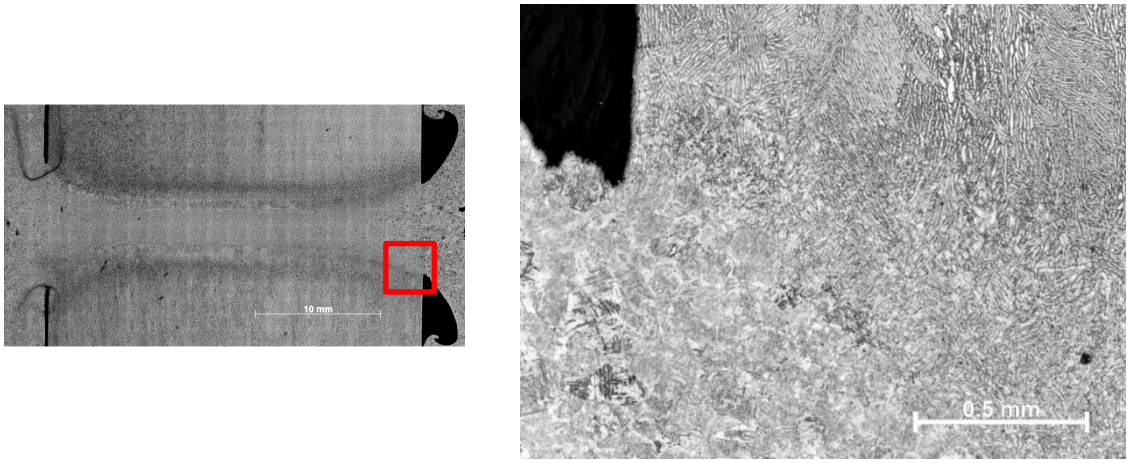


Figure 6-20: Simulated inertia TMAZ transition to weld zone from the outside diameter at 50x magnification.

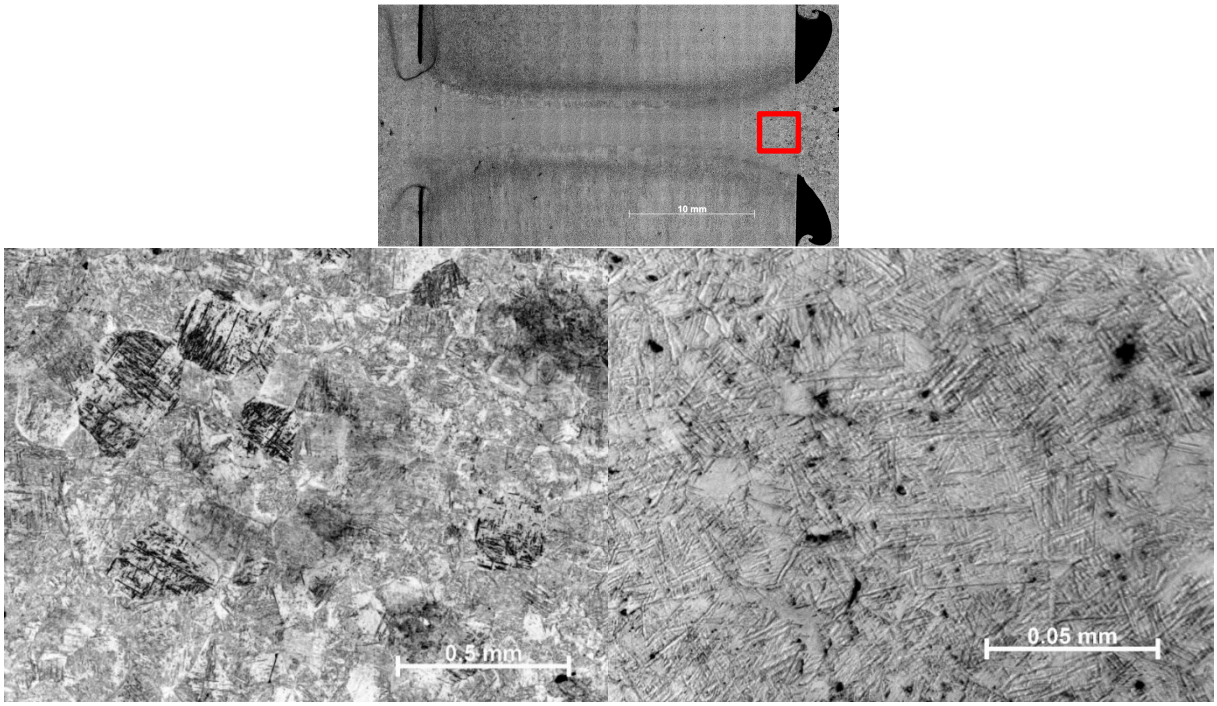


Figure 6-21: Simulated inertia weld zone from the outside diameter at 50x magnification on the left and 500x magnification on the right.

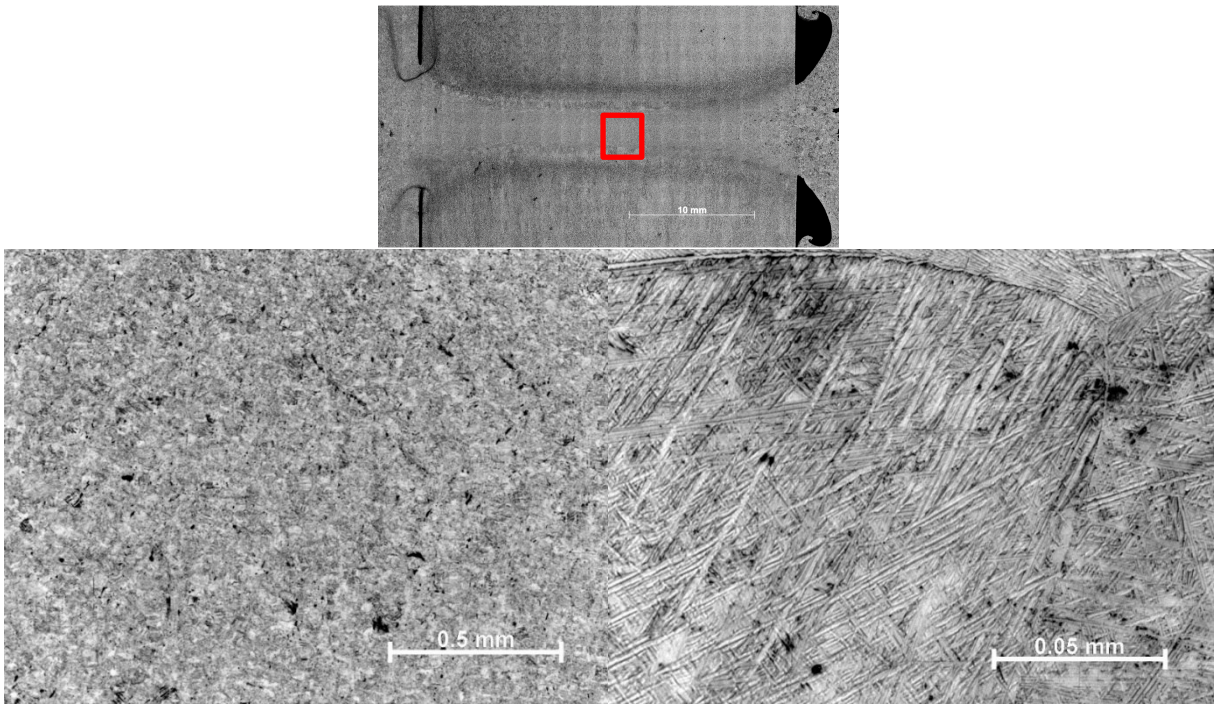


Figure 6-22: Simulated inertia weld zone from the centre line at 50x magnification on the left and 500x magnification on the right.

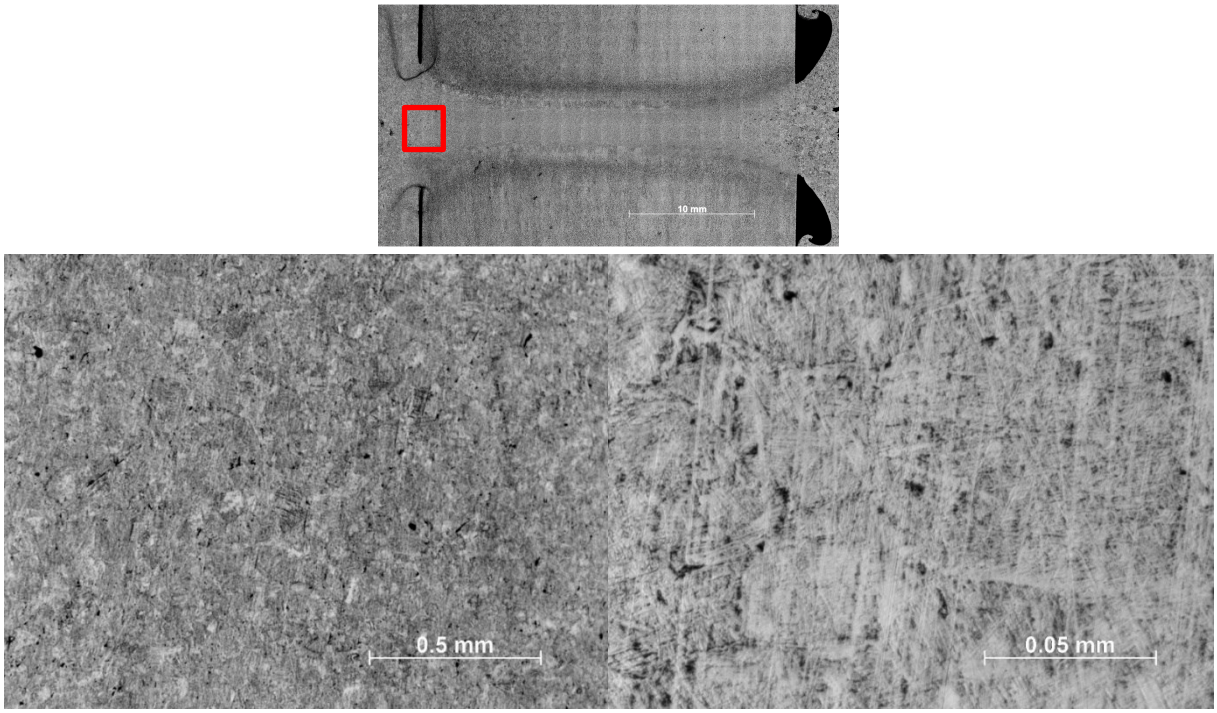


Figure 6-23: Simulated inertia weld zone from the inside diameter at 50x magnification on the left and 500x magnification on the right.

6.6.2.2.2 Fast deceleration

The fast deceleration weld zone is displayed created from a mosaic of micrographs. The ID flash has created a visibly wider weld zone. The grain size of the weld zone has increased near the ID and OD. The rough surface at the centre of the flash can be seen on the right.

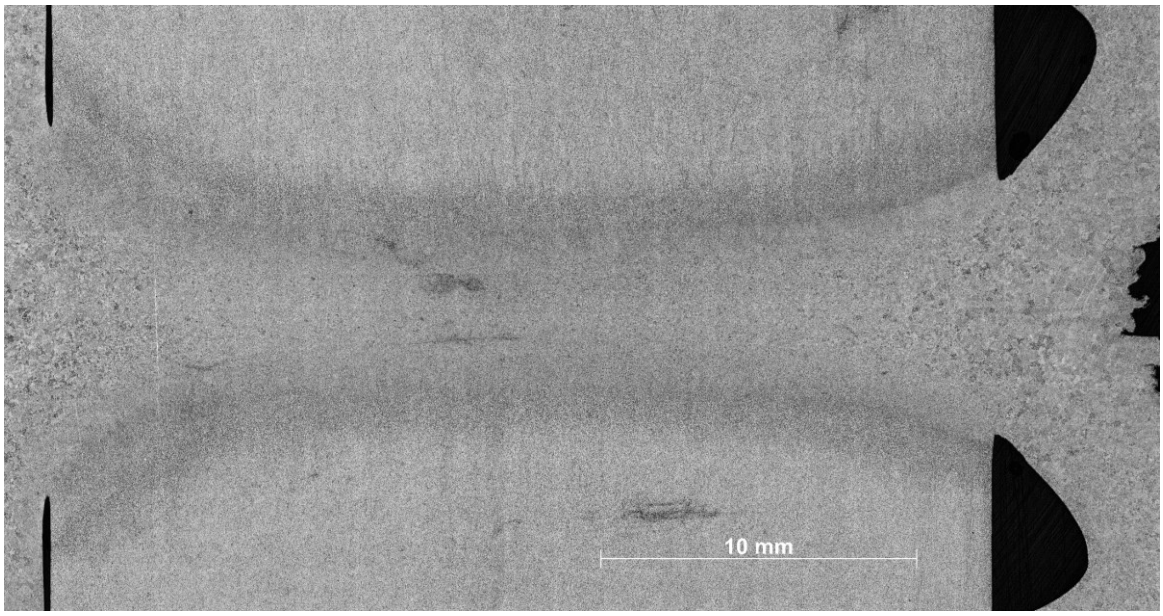


Figure 6-24: Fast deceleration weld zone mosaic image at 50x magnification (resized).

The following micrographs are shown with a reduced full weld zone mosaic to indicate the location of the micrographs.

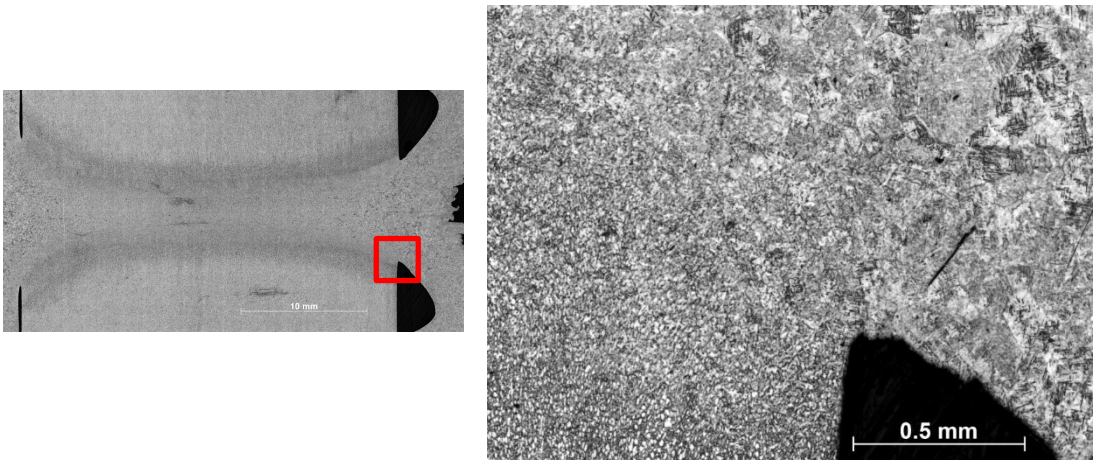


Figure 6-25: Fast deceleration TMAZ transition to weld zone and flash from the outside diameter at 50x magnification.

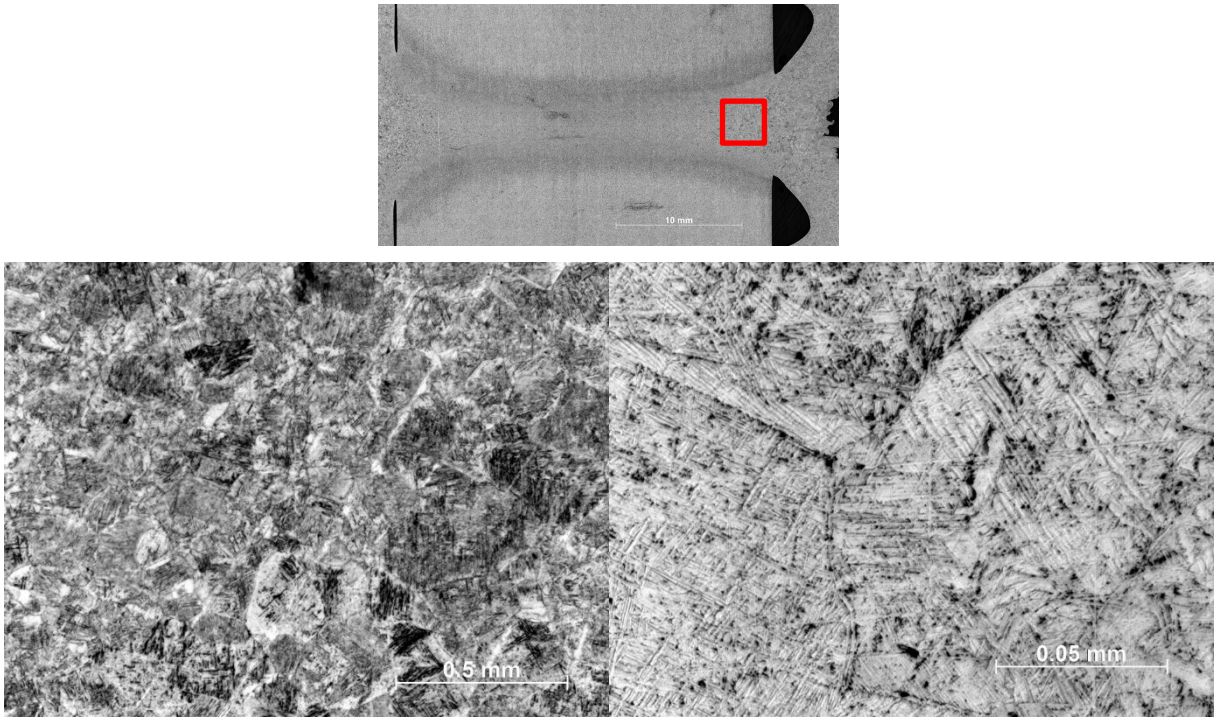


Figure 6-26: Fast deceleration weld zone from the outside diameter at 50x magnification on the left and 500x magnification on the right.

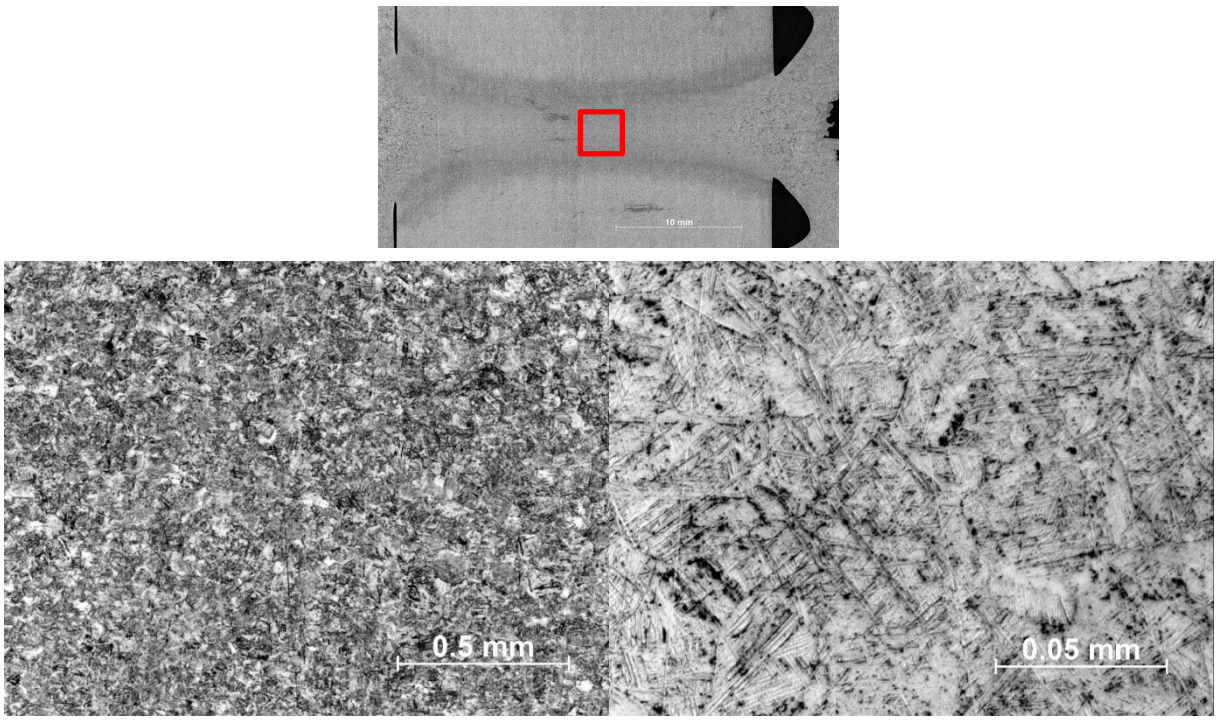


Figure 6-27: Fast deceleration weld zone from the centre line at 50x magnification on the left and 500x magnification on the right.

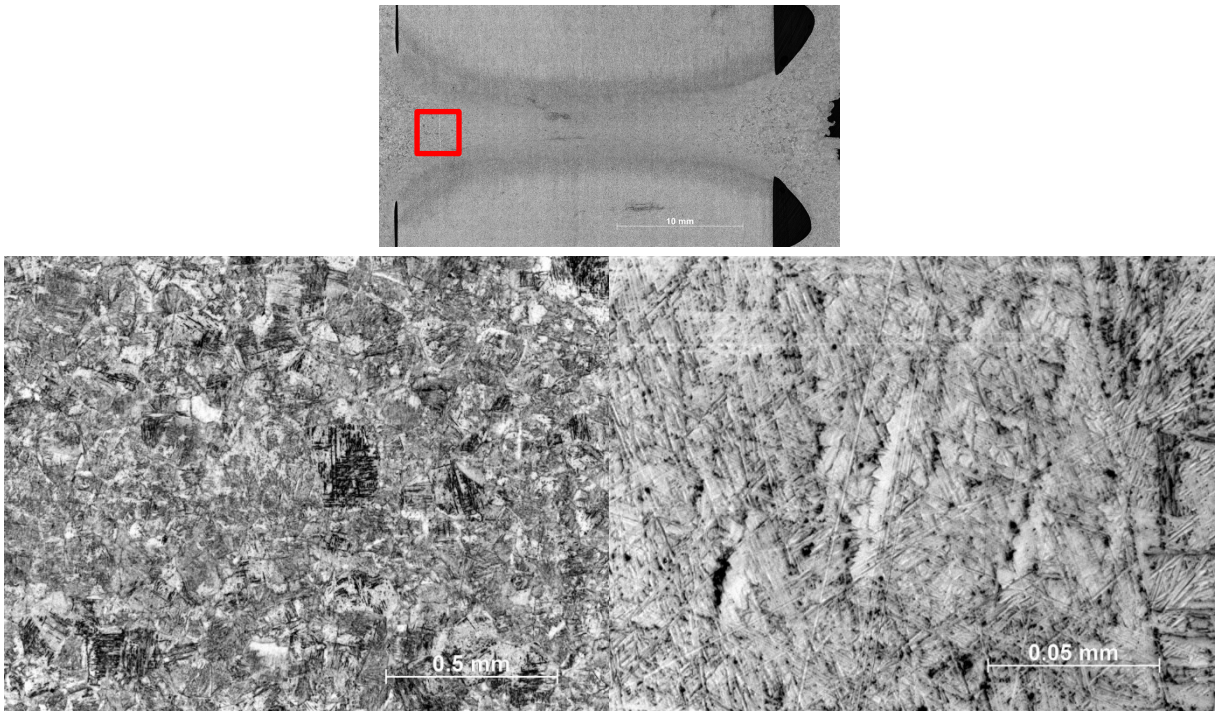


Figure 6-28: Fast deceleration weld zone from the inside diameter at 50x magnification on the left and 500x magnification on the right.

6.6.2.2.3 Nominal

The nominal weld zone is displayed created from a mosaic of micrographs. The ID flash has created a visibly wider weld zone at the ID while the centre section of the weld zone appears parallel. The rough surface at the centre of the flash can be seen on the exterior of the OD flash.

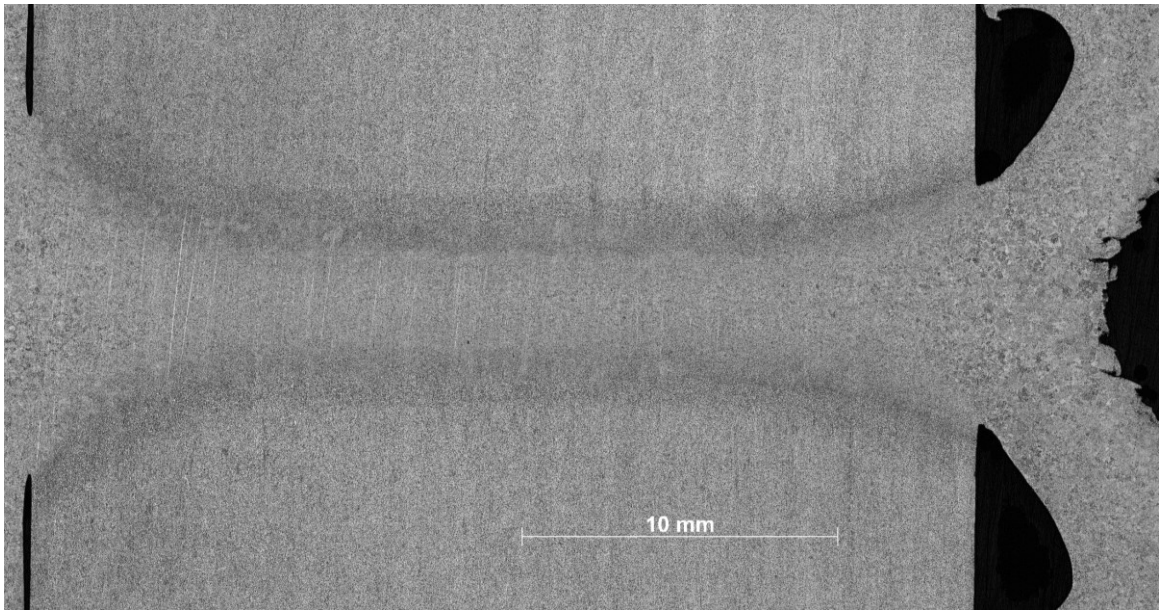


Figure 6-29: Nominal weld zone moasic image at 50x magnification (resized).

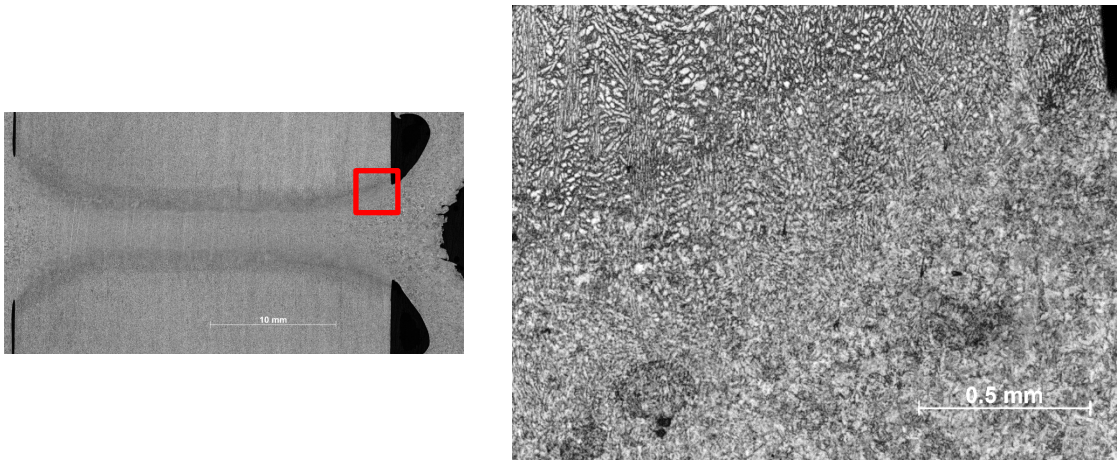


Figure 6-30: Nominal weld zone to TMAZ transition from the OD at 50x magnification.

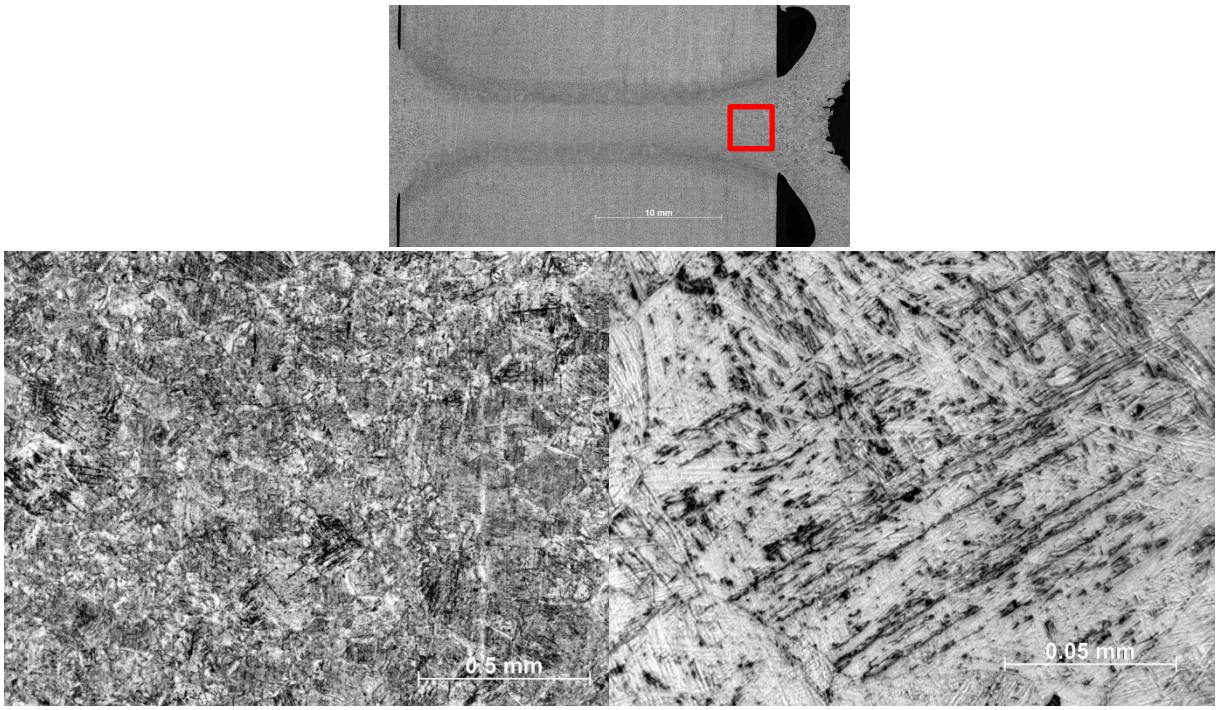


Figure 6-31: Nominal weld zone from the outside diameter at 50x magnification on the left and 500x magnification on the right.

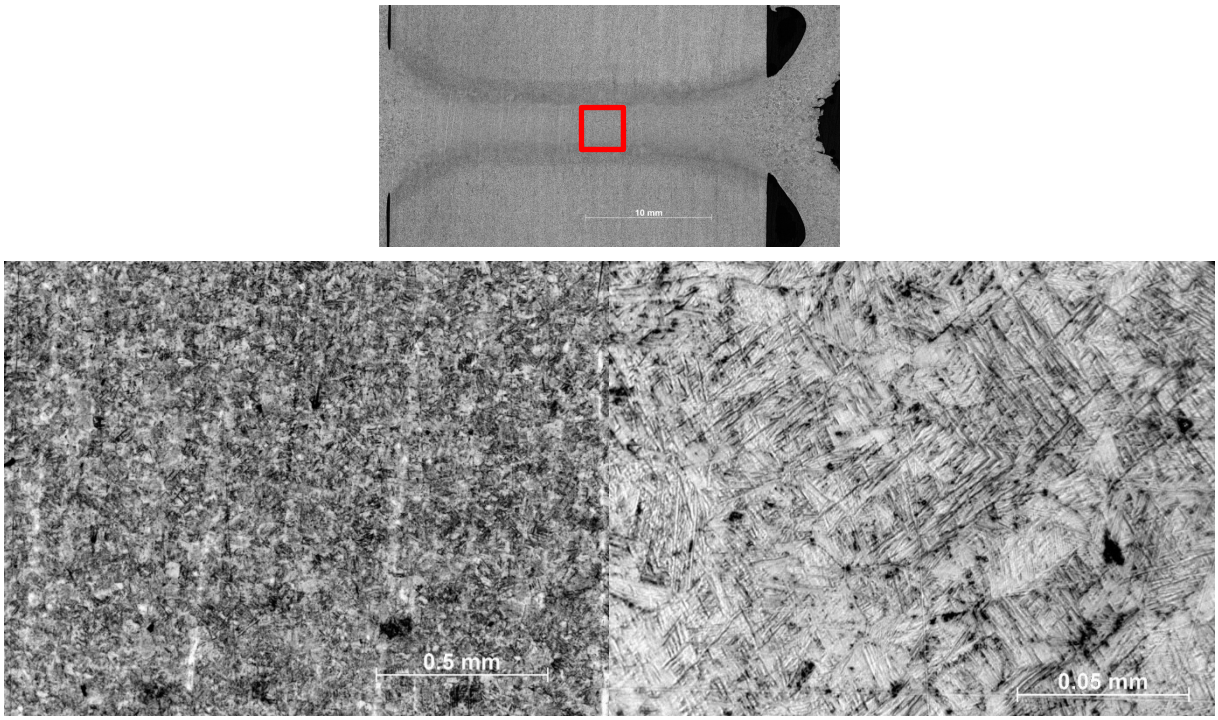


Figure 6-32: Nominal weld zone from the centre line at 50x magnification on the left and 500x magnification on the right.

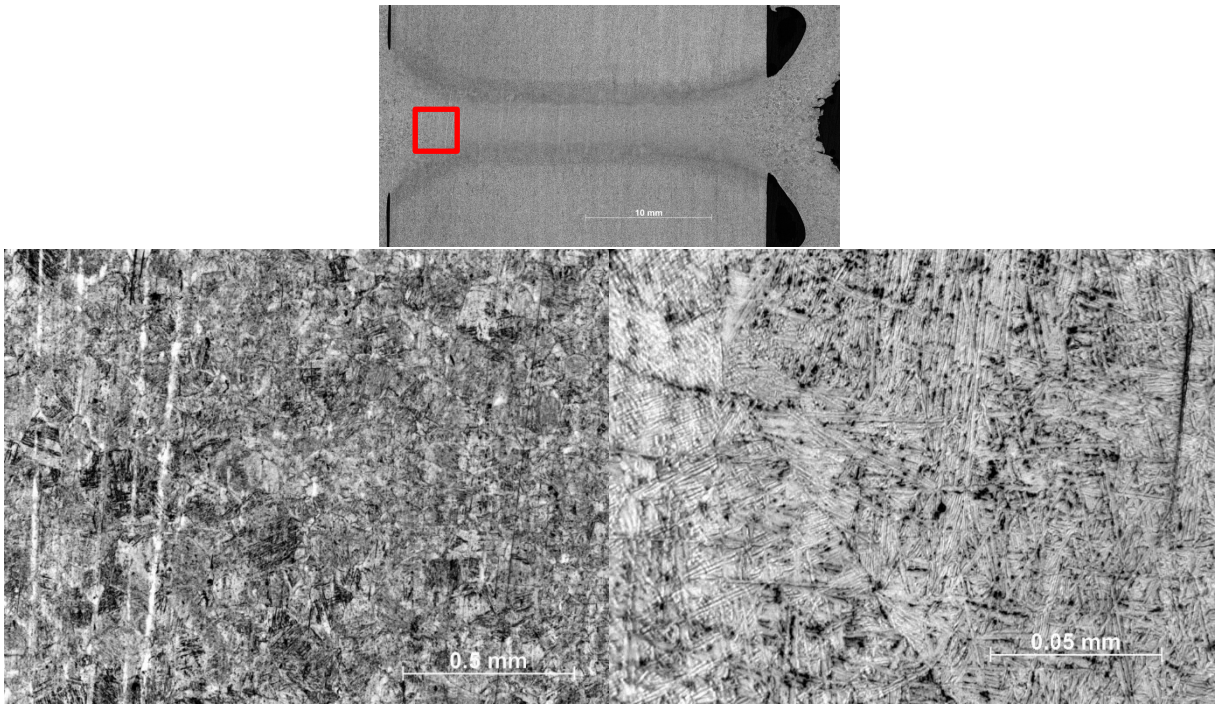


Figure 6-33: Nominal weld zone from the inside diameter at 50x magnification on the left and 500x magnification on the right.

6.6.2.3 Weld zone widths

The weld zone width data shows the curved nature of the zones directly behind the weld interface.

Table 6-2: TMAZ widths across the weld zone.

Weld zone widths								
Measurement location (mm)		**(OD) 0**	**5**	**10**	**(CL) 15**	**20**	**25**	**(ID) 30**
Simulated Inertia	**Recrystallised zone**	7.15	4.05	3.84	3.04	3.17	3.64	9.87
	TMAZ	12.2	8.93	7.77	7.43	7.58	8.7	16.72
Fast Deceleration	**Recrystallised zone**	8.05	4.71	4.36	3.61	4.15	5.03	11.72
	TMAZ	12.84	9.34	8.23	7.49	7.93	9.87	16.57
Nominal	**Recrystallised zone**	7.56	4.22	3.33	3.11	3.32	4.51	11.35
	TMAZ	11.16	7.69	6.68	7.08	7.07	8.58	15.09

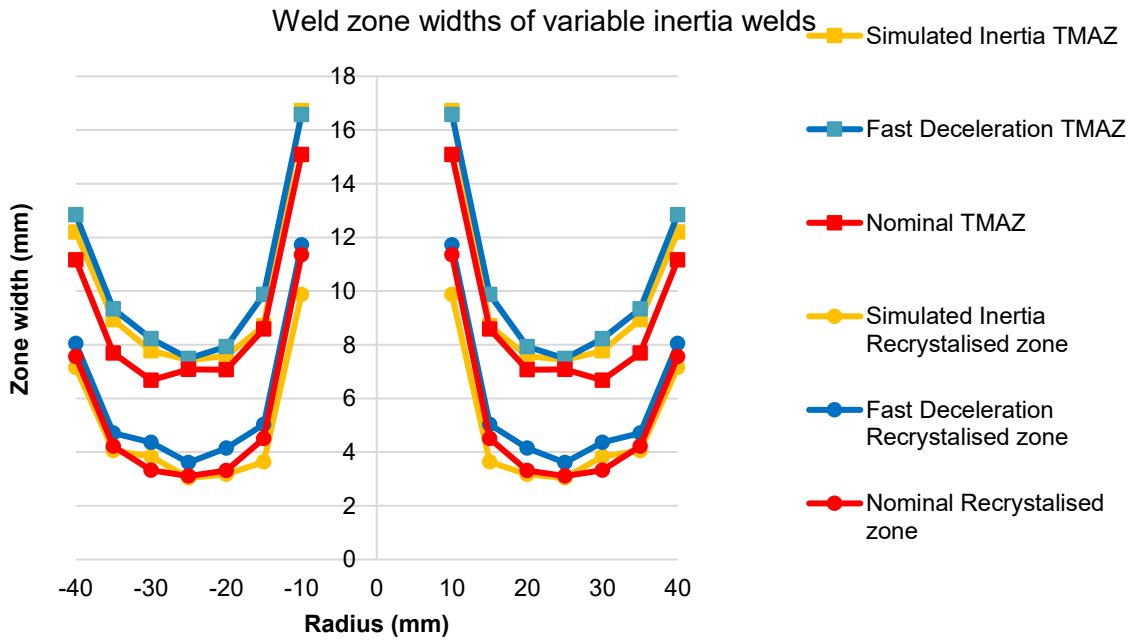


Figure 6-34: Results of the weld region measurements from the optical micrograph mosaics. As the test pieces are cylindrical, the data has been flipped and repeated to provide a through thickness view.

6.6.2.4 Hardness mapping

Presented are the hardness maps: a 2d contour plot of the thirty offset hardness traces and calculated interstitial data points. Individual erroneous results have been smoothed out to prevent impacting the surrounding interstitial points.

Traces of the ID, CL and OD have been plotted separately for comparison. The parent material measurements of all the welds were used to find the standard deviation error in the measurements. The parent material upper standard deviation is added to the traces to help identify when the hardness values are above the parent material norm.

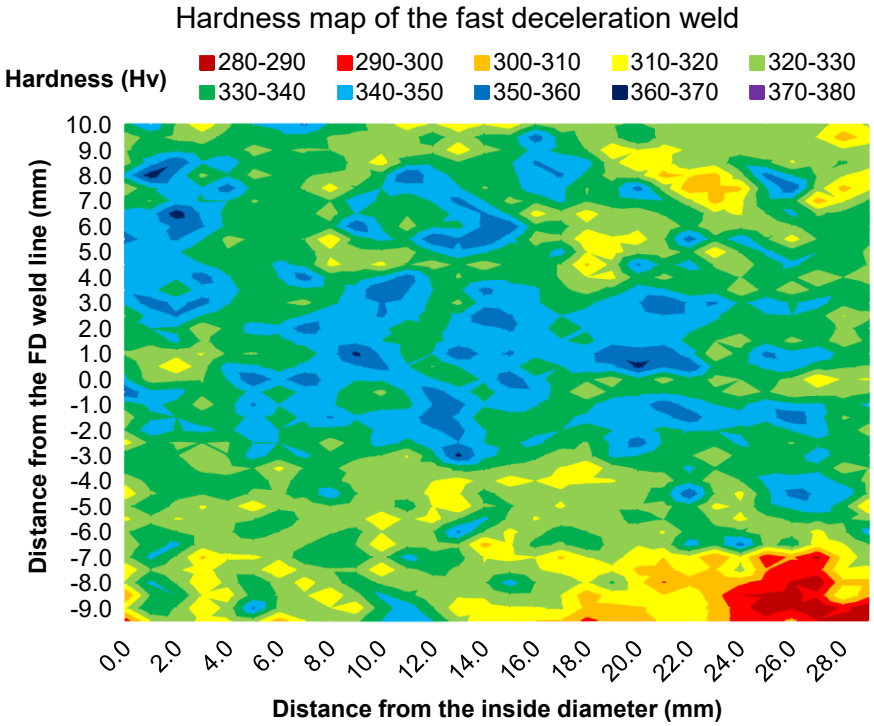


Figure 6-35: Contour map of the fast deceleration hardness survey.

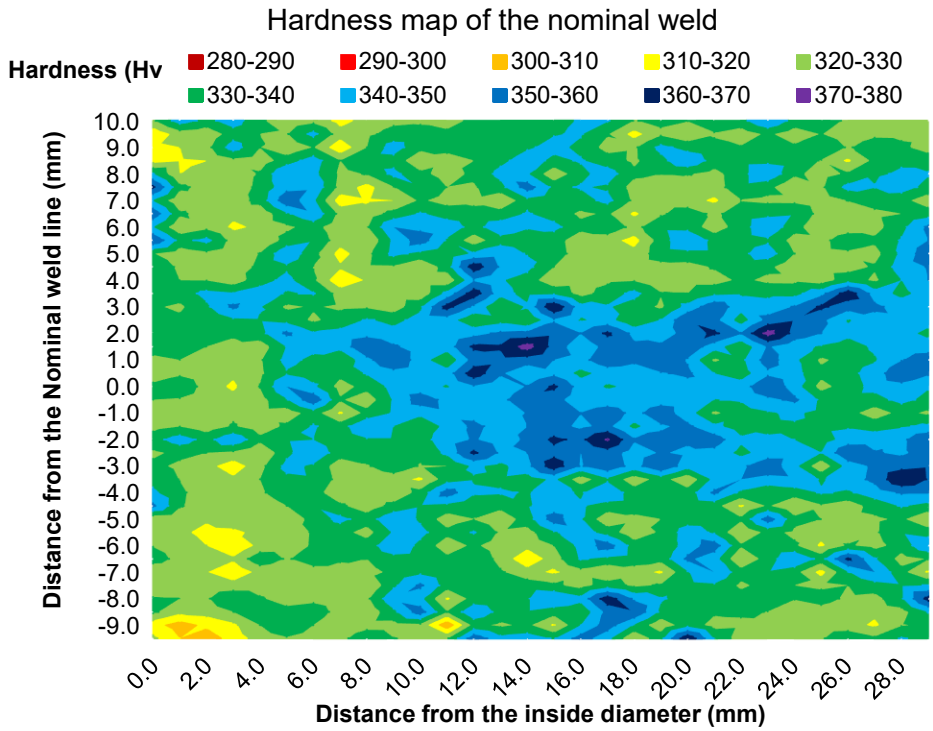


Figure 6-36: Map of the nominal hardness survey.

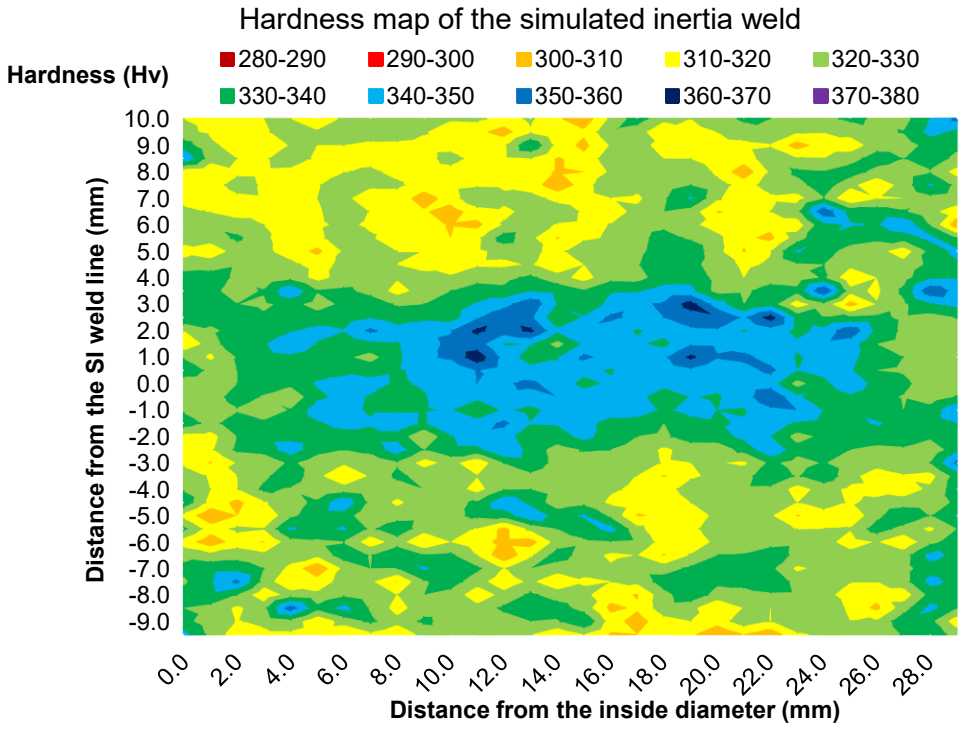


Figure 6-37: Map of the simulated inertia hardness survey.

For easier direct comparison the OD, CL and ID traces have been plotted.

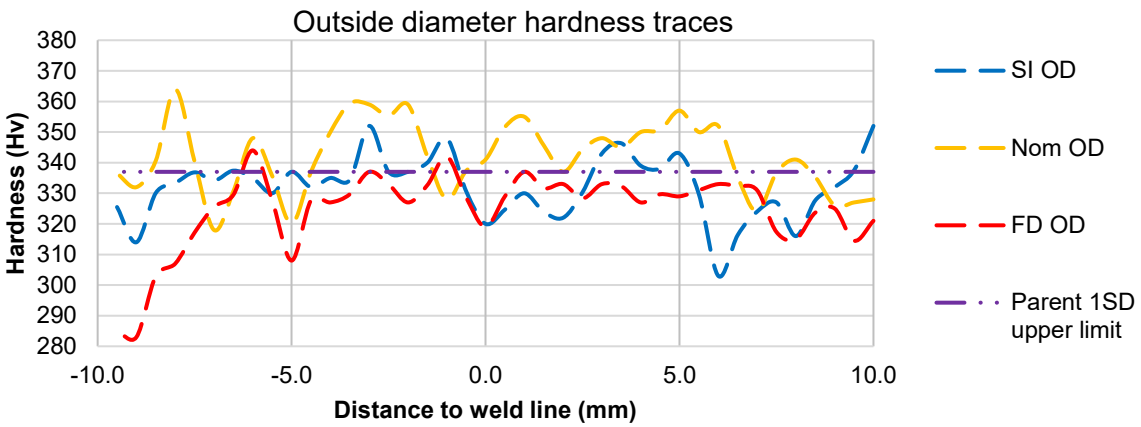


Figure 6-38: Hardness trace across the weld zone at the outer diameter.

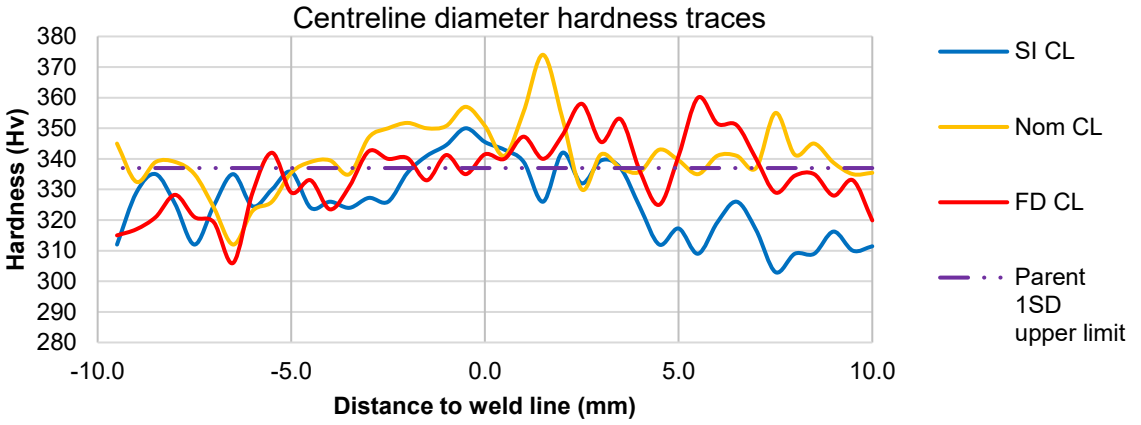


Figure 6-39: Hardness trace across the weld zone at the centre line.

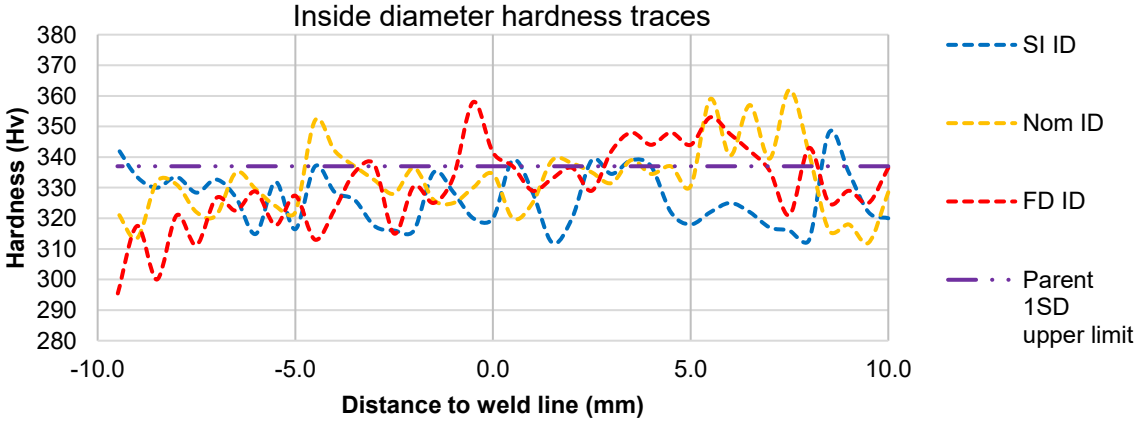


Figure 6-40: Hardness trace across the weld line at the inside diameter

.

6.6.3 Residual Stress measurements

6.6.3.1 Hoop Stress

Hoop stresses have been plotted on a sectioned view of a post weld component. At the displayed surface, the stresses are perpendicular to it. Tensile stresses are positive and compressive stress are negative.

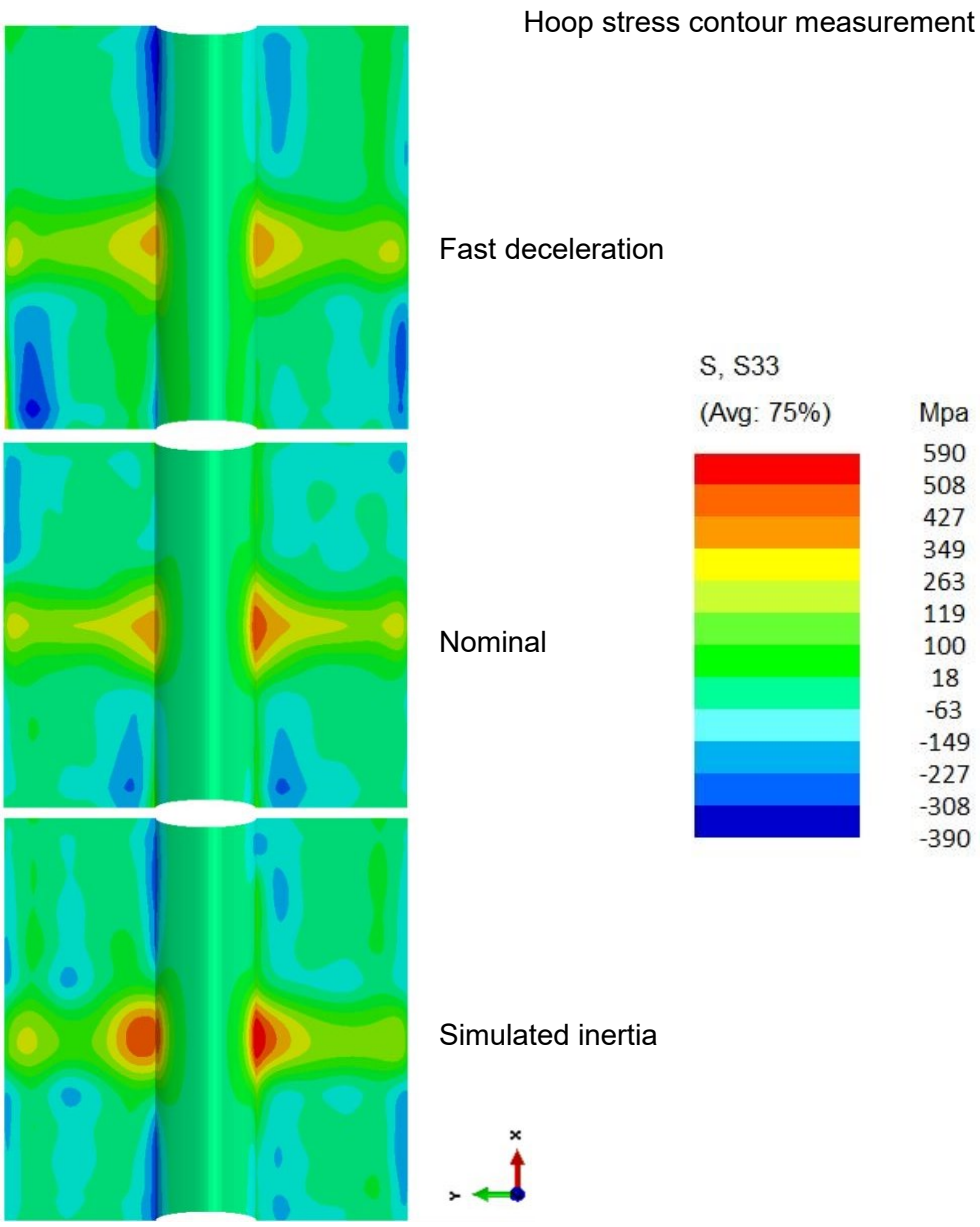


Figure 6-41: Hoop stresses from the three cycles shown as coloured areas on the mesh map.

For a more direct comparison the hoop stresses have been plotted across the weld line.

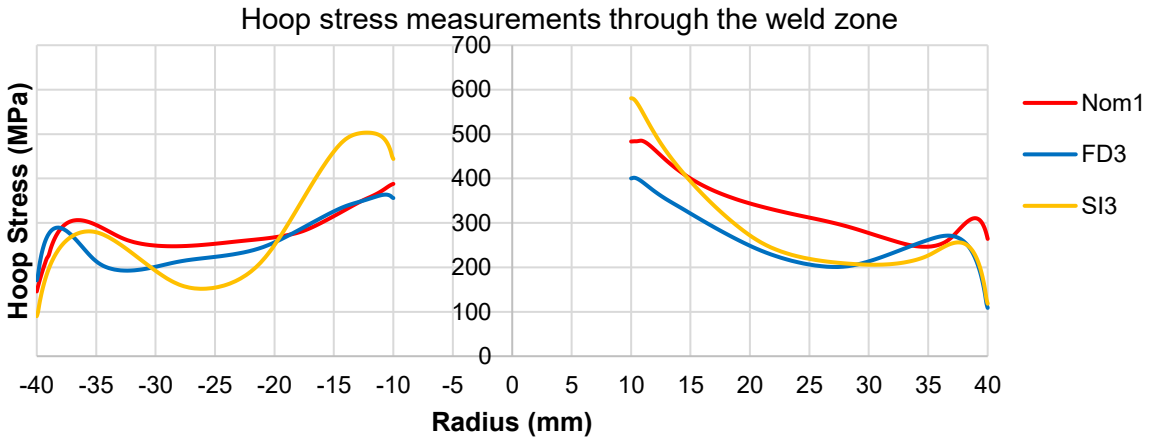


Figure 6-42: Hoop stress measurements across the weld diameter through the contact zone from the contour method. The drop in stress visible in the simulated inertia ID at -15 to -10mm was caused by a wire snap on the EDM machine at the -14mm point.

The wire of the EDM broke during the cut of the SI weld. The restart of the cut can be seen in the surface.

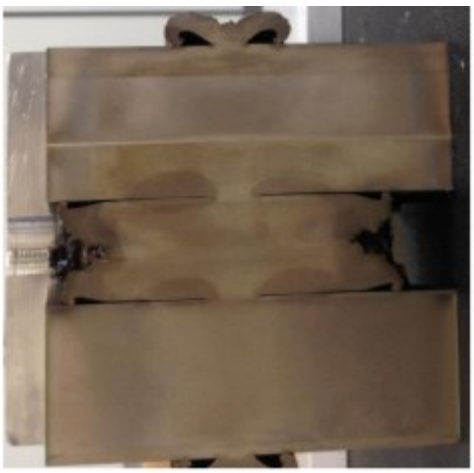


Figure 6-43: Evidence of the wire cut restarting due to the wire breakage in the simulated inertia sample. Visible in the upper portion as the light-coloured line.

6.6.3.2 Axial stress

The axial stress is plotted as a contour map over the interface area with the stresses acting perpendicular to the displayed plane. Tensile stresses are positive and compressive stresses are negative.

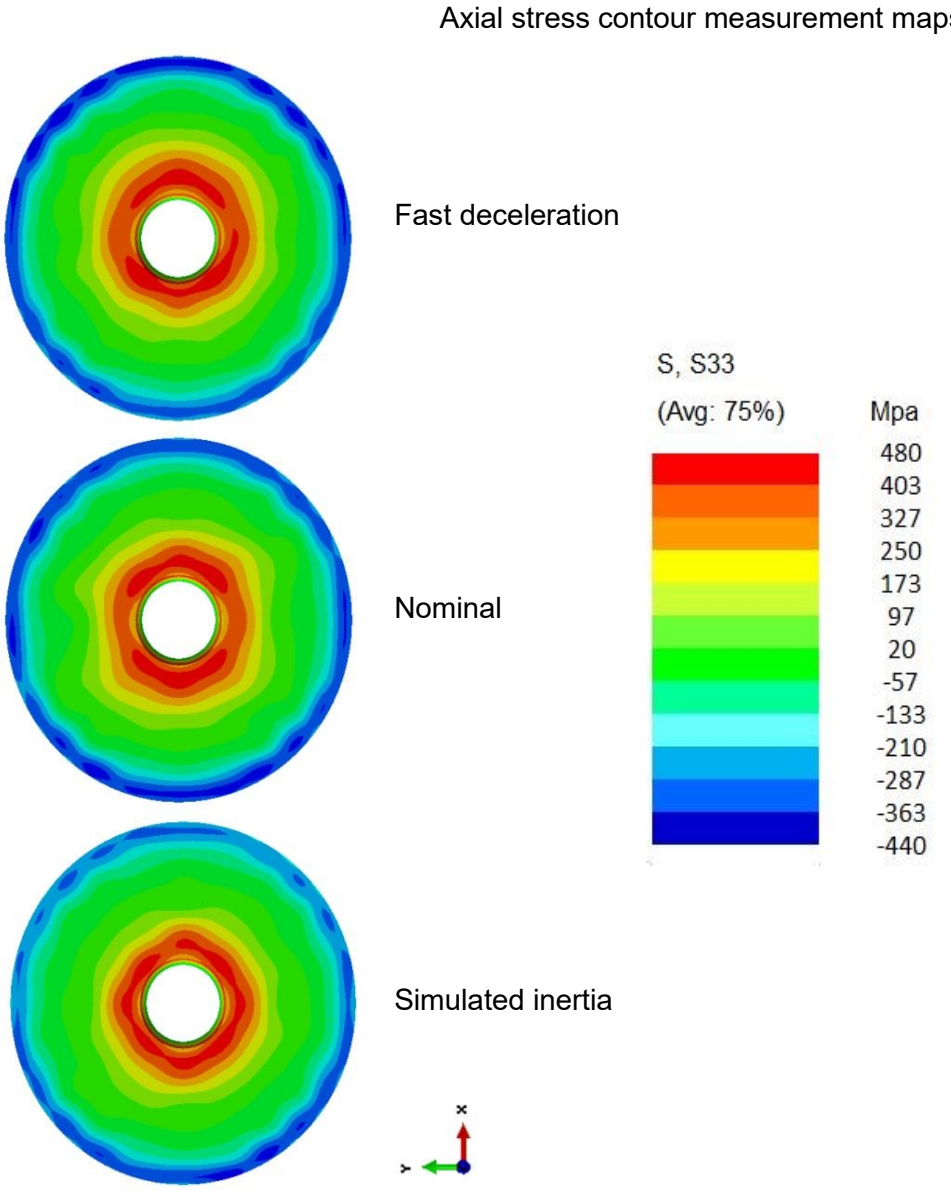


Figure 6-44: Axial stresses from the three cycles shown as coloured areas on the part map.

For a more direct comparison the axial stresses have been plotted across a single diameter. The diameter is horizontal when referenced to the contour map above.

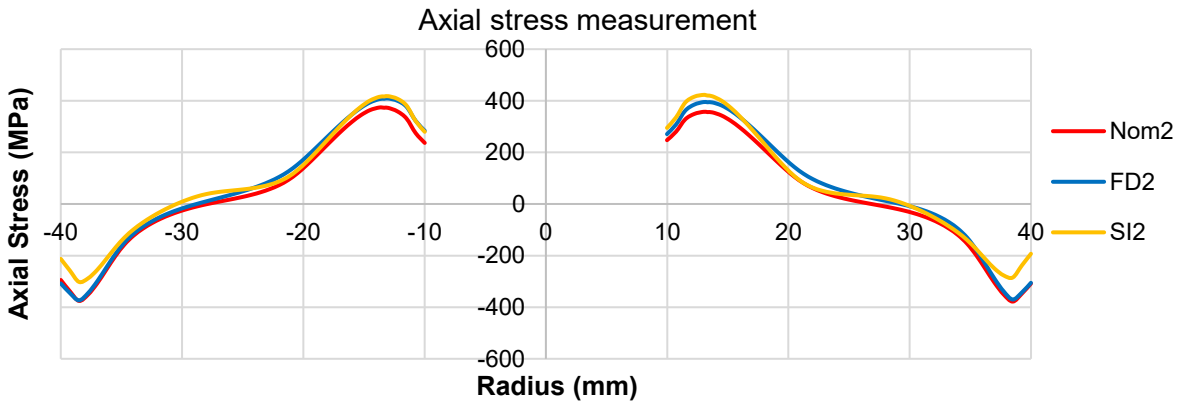


Figure 6-45: Axial stress measurements from across the horizontal weld diameter relative to the above orientation.

6.7 Analysis

6.7.1 Weld data

6.7.1.1 Weld records

Between the weld sets only minor variations were visible except in the case of the temperature probe welds where differences can be seen; see Figure 9-3, Figure 9-4, Figure 9-5 and Figure 9-6 in the Appendix. To compare the weld sets the first weld from each cycle was plotted. Figure 6-4 shows the deceleration of the flywheel. The fast deceleration weld clearly starts at a higher rotational speed and takes the longest time to become stationery. The simulated inertia weld has a similar initial deceleration to the fast deceleration weld, after four seconds the deceleration is reduced imitating the presence of a larger flywheel.

Figure 6-5 shows the torque feedback percentage. The nominal weld at a constant -40%, the simulated inertia weld with the initial -80% turning to a positive amount when simulating the larger flywheel and modulating when matching the pre-set deceleration-upset points. The fast deceleration weld was designed to use -80% throughout but due to the high speeds at the start

of the cycle, the machine automatically employed a lower braking torque initially, increasing the value back to -80% when possible.

Figure 6-6 shows the matching machine pressure throughout each cycle, showing each weld had no deviations from the set pressure. Figure 6-7 presents the resulting upset created by each weld cycle. The simulated inertia cycle transitions from the conditioning phase to the equilibrium phase the quickest suggesting the most efficient processing of the weld interface. Each weld reaches a similar amount of upset with the SI weld completed first, the nominal second and the FD weld last.

Figure 6-8 details the upset rate of each cycle. The traces have been smoothed with an eleven point double simple moving average. This removed noise but did not obscure the main trend. The SI weld clearly reaches a steady state equilibrium. The nominal weld and FD welds do not, instead displaying an increased upset acceleration during this phase. From six to seven seconds in the nominal weld and from seven to seven point eight in the fast deceleration weld. Each weld also displays a peak upset rate right before the cycle end. The peaks displayed, rise and become narrower with the higher deceleration rates. The widest and lowest peak comes from the SI weld while the tallest and narrowest peak belongs to the FD weld. The high amount of upset rate at the start of the cycle is the two component parts coming into contact.

The simulated inertia welds produced closely matching upset amounts, due to the ability of the program to compensate for over or under upsetting welds. This can be seen in Figure 9-3 where SI4 has a lower upset rate after the torque switches to a positive input compared to the other welds. In response, the torque is held at a higher level until the required upset has been reached for that rotational speed. This extends the weld cycle. Prior to this point the weld is tracking similar to the others and should not have been influenced by the extra ~1.3mm pre-weld gap, thereby it can be supposed that the difference came from the material or the slightly different heat flow due to the channels in the outer surface.

Figure 9-4 details the weld records of the fast deceleration welds showing marked similarity between all weld cycles. Only minor deviations can be noted across the upset trace with FD4 showing the most deviation during the weld and FD2 reaching the shortest upset.

Nominal welds are recorded in Figure 9-5. Good agreement is shown between the first three welds, with Nom4 recording a larger pre-weld gap by ~0.6mm and a lower total upset by ~0.5mm. Speed and pressure traces are identical to the three previous welds. The larger pre-weld gap was due to a slight program error by the author. This however, made no impact on the initial starting conditions of the weld as the components made contact at 1626.5rpm compared to: 1625.56 for Nom 1, 1624.7 for Nom 2 and 1625.56 for Nom3.

6.7.1.2 Upset measurement

The upset results show a marked difference in variation, Figure 6-9 and Figure 6-10. Figure 6-9 details the machine measured results showing the simulated inertia's smallest variation and the nominal welds largest variation based on three standard deviations around the average. The error bars show the difference to the post weld measurements. In all cases, the machine recorded a smaller upset than the post weld measurement but there is no correlation between the deviation and amount of upset. Figure 6-10 details the post weld upset measurement calculated from pre- and post-weld height gauge measurements. These follow the variation trends of the machine but record higher amounts of upset possibly due to the machine not including the contraction of the part due to cooling. All have attempted to meet the same upset amount within the capabilities of a few setup welds. The simulated inertia welds showed the smallest variation as expected due to the torque modulation driving the weld towards a pre-determined upset, whereas the fast deceleration and nominal welds used a set amount of deceleration torque feedback resulting in a greater variation as seen in Chapter 4. The greater variation of the nominal weld compared to the fast deceleration weld comes from the Nominal 4 weld which is 0.38mm (post weld measurement) below the nearest weld. This is possibly due to the slightly greater gap between the rotating and non-rotating components

prior to welding. This would have reduced the energy available for welding, as it would take longer for the machine to bring the parts into contact, connecting at a lower initial speed and therefore lower total energy.

6.7.1.3 Energy input

Figure 6-11, Figure 6-12 show the instantaneous and cumulative energy input of the simulated inertia, fast deceleration, and nominal welds for comparison. In the Appendix Figure 9-7, Figure 9-8 and Figure 9-9 show all the calculated energy traces from each set of welds. Of the simulated inertia welds, all produced peak inputs between 150 and 171KJ/s and cumulatively 420 to 433KJ. SI4 has a longer cycle which throughout inputs less energy per second but overall inputs a higher cumulative amount compared to the other SI welds. Among the fast deceleration welds, FD4 produces a lower initial instantaneous energy peak of 148KJ/s, compared to a range of 166 to 183KJ/s, reducing the total amount of energy delivered to the weld, 449KJ compared to between 456 and 459KJ. Nominal welds produced on average the lowest peak input at between 141 and 158KJ/s and the median total energy input between 433 and 441KJ. The fast deceleration weld cycle delivered the most amount of energy to the titanium parts with the simulated inertia cycle delivering the least. The fast deceleration weld cycle also produced the highest peak input rate while the nominal weld cycle delivered the lowest peak input rate. When taken over the time for the weld to start upsetting the peak energy rate feeds into the energy for conditioning of the weld interface. Figure 6-46 shows the conditioning energy taken from the point upsetting starts to occur. The FD welds required the highest amount of energy to condition the interface due to the high initial energy peak and longer time to transition through to producing upset. Although the SI and Nominal welds take different amounts of time to start upsetting, Figure 6-7, and have different initial energy peaks the conditioning phase requires similar energy. Compared to similar inertia friction welding (IFW) Ti-6Al-4V welds, where the rotational speeds were similar but the inertia was lower (Turner *et al.*, 2016), the initial rotational speed was shown to have limited input upon

conditioning of the interface. The weld at similar parameters (ω_v = 185 rad/s, I = 18.6 kgm^2 p_i = 40Mpa) was measured using 194.8kJ for conditioning, which is slightly more than the Nominal and SI welds, which because of the torque braking used during the cycles have a simulated inertia less than the 68.6 kgm^2 flywheel combination used. However direct comparison is not possible as the geometry is not revealed in the study.

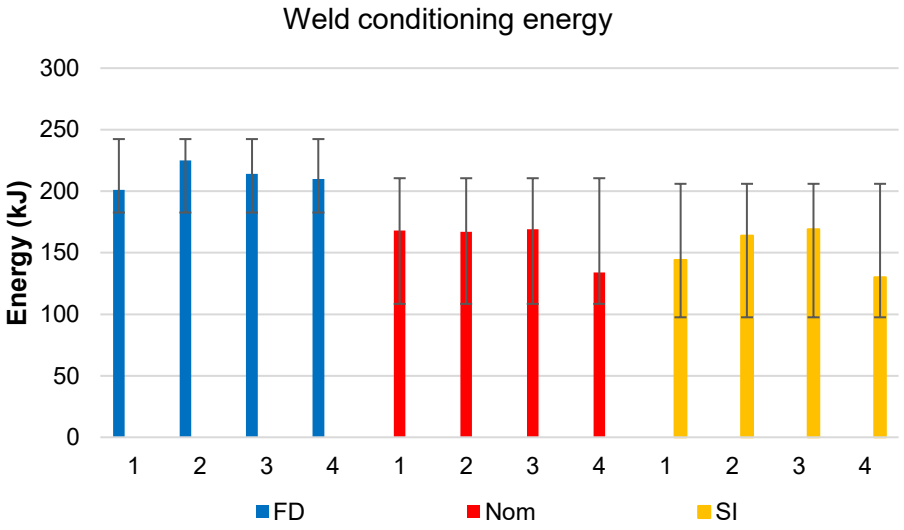


Figure 6-46: The conditioning energy of the enhanced cycles.

From the energy input it is possible to determine the apparent coefficient of friction at the interface using equation (2-14) rearranged

$$\mu = \frac{\dot{P}}{\frac{2}{3}\pi p_i \omega_v (r_o - r_i)^3} \tag{6-1}$$

With r_o being the external radius and r_i the internal radius of the tubular weld. Representative cycles have been taken and plotted in Figure 6-47. This assumes that the cycle is purely in a coulombic friction regime. The curves are similar to those calculated from welding Inconel 718 (C. Bennett *et al.*, 2007). In that instance the initial drop in coefficient was attributed to the rising temperature and therefore reducing stress while the rise towards the end of the cycle

was related to an increase in thickness of the plasticised layer, due to the slowing rotation, a phenomenon noted in continuous drive friction welding (CDFW) (Duffin & Bahrani, 1973), thereby increasing the frictional forces with the switch occurring at a critical velocity. As the apparent coefficient of friction is related to the frictional stress directly through the applied pressure

$\tau_f = \mu p_i$, equation (2-16), the value of the frictional stress at the interface can be calculated, Figure 6-48.

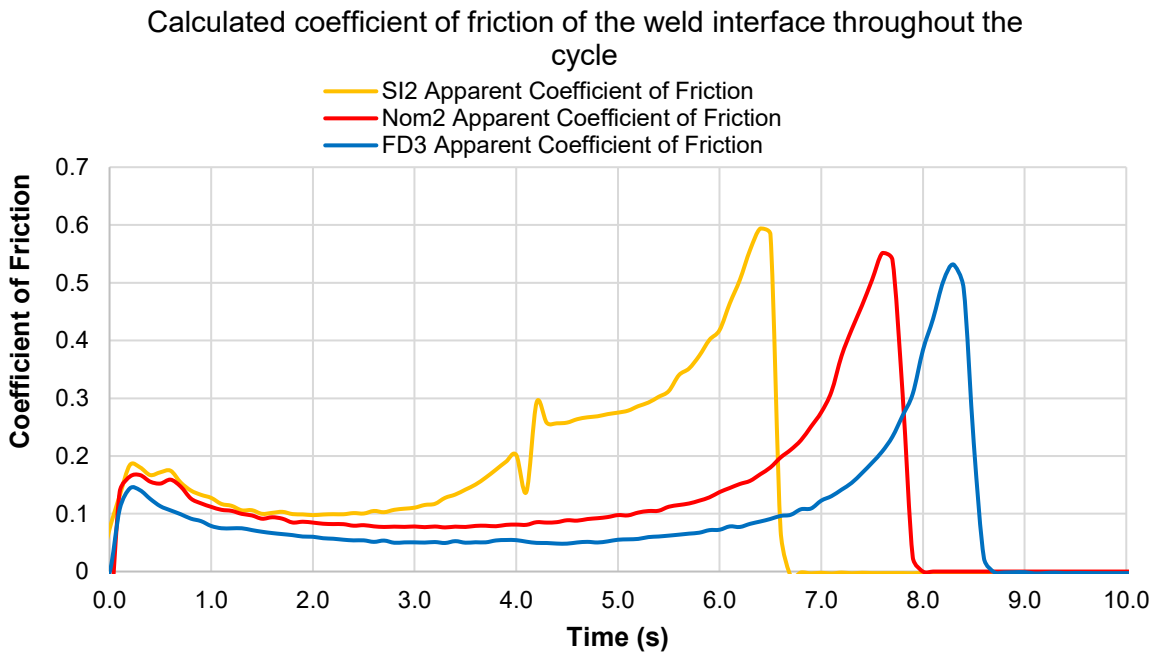


Figure 6-47: Apparent coefficients of friction determined from the weld parameters and calculated input power. A representative weld from each cycle is shown.

Each weld exhibits a small initial stress peak dropping during the bulk of the cycle and rising steeply to a stress peak just before the end of the weld. The initial stress peaks are of similar magnitude with the Simulated Inertia being the largest and the final deceleration weld the smallest. As these welds are experiencing different decelerations and rotational speeds it seems to agree with Bennett et. al. (2007) that stage 1 is not highly dependent on the rotation of the part. After two seconds into the weld the SI weld starts to increase the coefficient of

friction and therefore frictional stress, the Nominal weld starts to see an increase after four seconds and the Fast deceleration after five. The SI weld slows the increase when the motor injects extra energy into the weld slowing the deceleration. Each exhibits a similar stress peak level during the final second of deceleration, further agreeing with Bennett et. al. (2007) that the 3rd stage of the weld occurs below a critical angular velocity. Each peak is similar in amplitude, however, a trend can be seen where the longer welds have a lower peak. Further research would be needed to confirm or contradict this. When the apparent coefficient of friction is plotted against angular velocity, Figure 6-49, all the welds followed the same pattern when below 75 rad/s (716rpm). In the case of the Nominal weld and SI weld which start at the same initial velocity the two are matched across the entire weld with the SI weld only slightly higher throughout. The nominal and FD welds overlay directly below 75 rad/s.

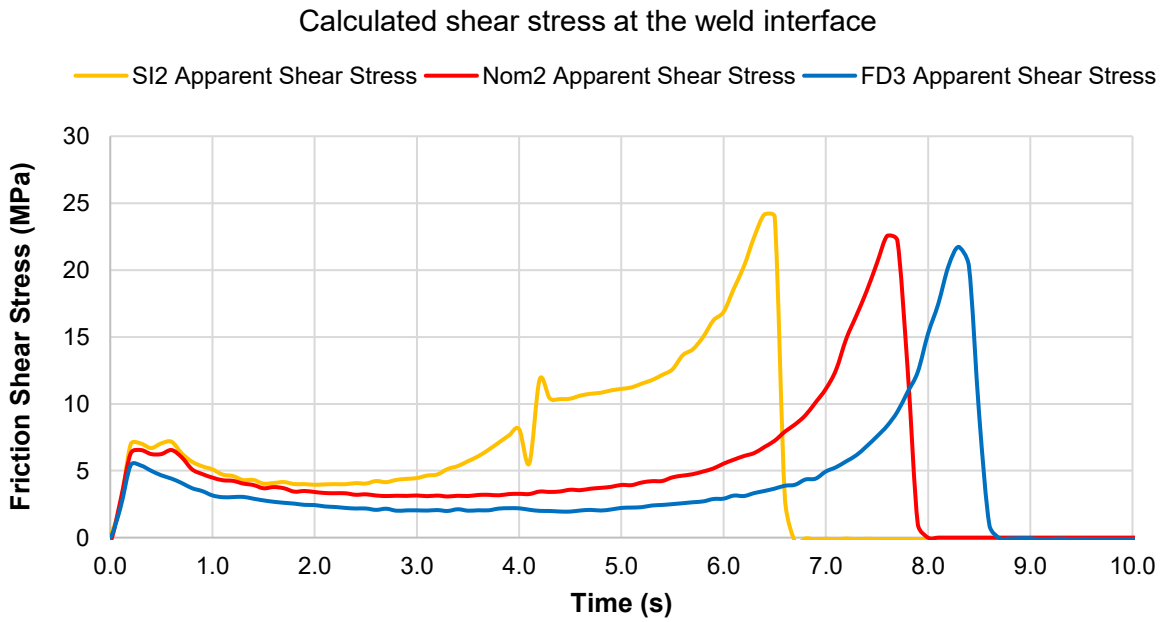


Figure 6-48: Apparent shear stress values across the weld interface derived from the power input.

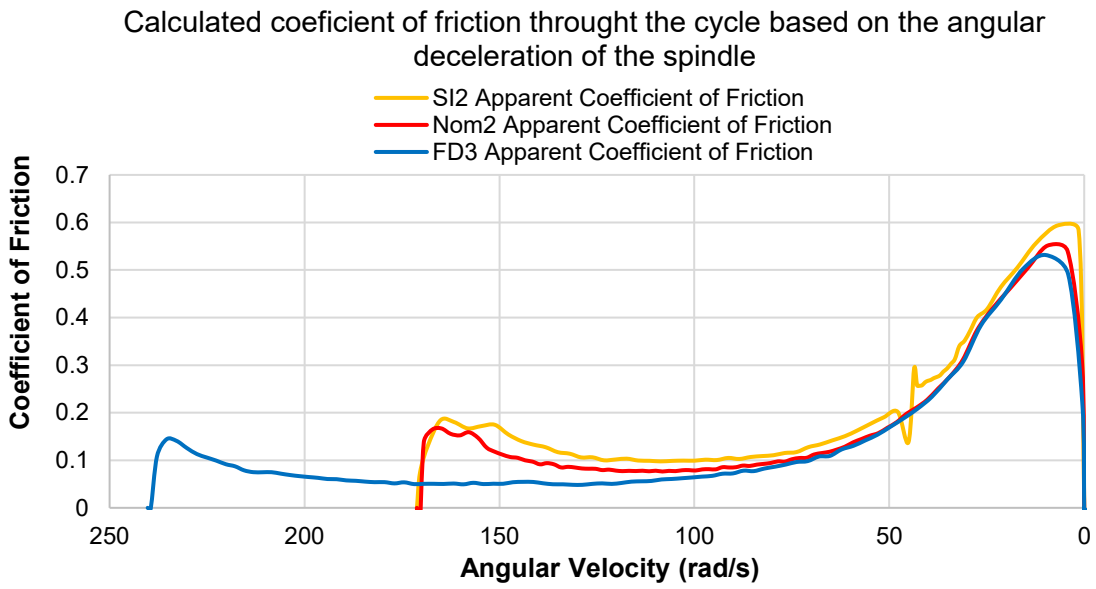


Figure 6-49: Apparent coefficient of friction plotted against angular velocity.

Plotting the coefficient of the representative welds against upset shows how the interface condition was changing as material was ejected. Having the point at which the coefficient of friction of all welds converged at 75 rad/s from Figure 6-49 plotted also shows how much material was ejected after the welds decelerated from the same point of rotational speed. In Figure 6-7 the upset appears to start at ~2s after initial contact. At this point the welds are at substantially different rotational speeds, as in Figure 6-4, suggesting the initial conditioning is time and possibly pressure dependant rather than speed or inertia dependant. All welds displayed a drop in the coefficient of friction during the conditioning phase after which the coefficient rises as more material is ejected. With the SI weld reaching the critical 75 rad/s speed first the coefficient of friction rises in that weld earlier with the nominal weld second and the FD weld last. This corresponds with the earlier increase in upset rate, Figure 6-8, and rise in power input, Figure 6-11.

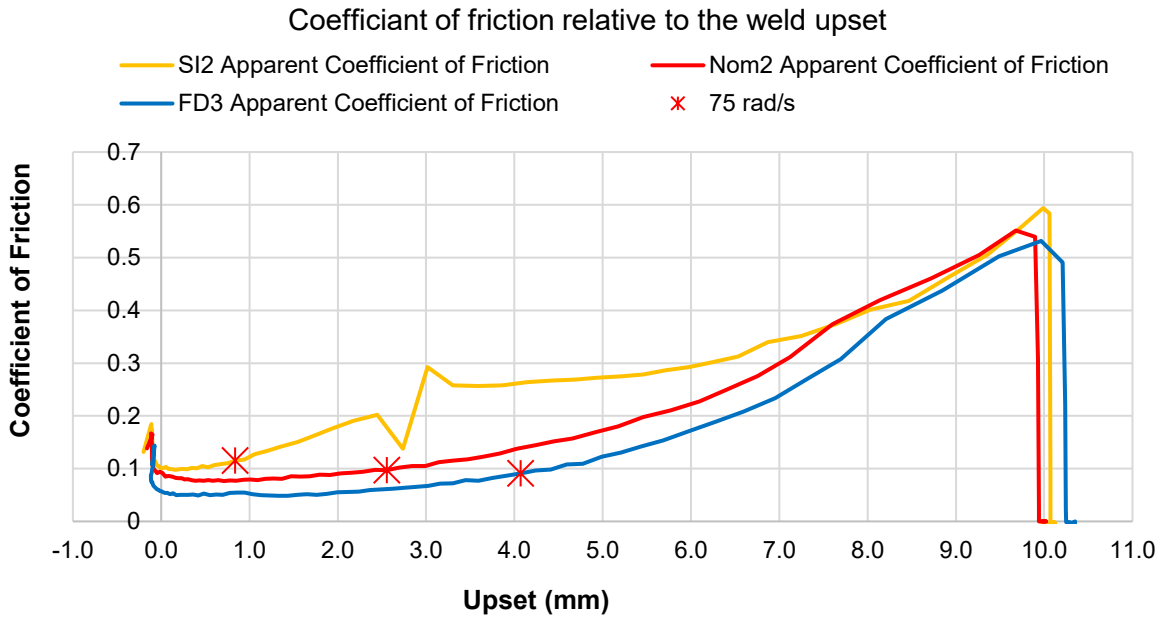


Figure 6-50: Apparent coefficient of friction plotted against upset, with 75 rad/s marked on each line with a red star.

6.7.1.4 Weld temperatures

The simulated inertia results appear to have under-recorded the 6mm probe temperature, Figure 9-10 in the Appendix, as it was reading a temperature less than that of the 8mm probe. The most likely cause would be due to probe movement preventing full contact of the probe tip with the slot channel end, reducing the effectiveness of the probe and relying on conduction through the side of the probe. The same appears to have occurred on the 10mm probe at about 5s when the trace slows it's rise and begins tracking similar to the 12mm probe. This is based on the idea that the 8mm probe and 12mm probe from both the simulated inertia weld and fast deceleration weld, Figure 9-11, peak at roughly similar temperatures. The temperature gradients and peak temperatures of the 6mm and 10mm probes do not coincide with the readings from the other probes.

From the temperature records, it can be seen that the simulated inertia weld rose in temperature slower and peaked sooner, just after 7s, compared with the fast deceleration weld peaking after 8s. The start of the temperature increase also occurred sooner in the simulated

inertia welds. Due to the uncertainty about the simulated inertia probe results at 6 and 10mm, only the 8 and 12mm probes can be directly compared. In the simulated inertia weld the 8mm probe peaked at 972°C after 7.35s while the 12mm probe reached 676°C after 12.30s. In the fast deceleration weld the 8mm probe reached 1033 °C after 8.00s while the 12mm probe reached 661°C after 14.35s.

When temperature is plotted against the corresponding upset, Figure 6-51, there is a dramatic difference in the later stages of progression of each weld. Initially, at the 8mm probes the temperature rises with the upset movement of the parts in each weld equally until the probes are 6.45mm from the interface where the fast deceleration weld temperature rises steeply compared to the simulated inertia weld's lower gradient. The same phenomenon is also visible in the 12mm probe but after the temperature rises initially to 100°C. This suggests that the conditioning phase and initial upset of the two cycles are similar. To begin with the temperature in the material is increasing steadily as the weld starts and begins to eject material from the interface. After ~1.5mm of upset the temperature in the fast deceleration weld increases rapidly with little upset occurring. Energy from the interface appears to be propagating from the fast deceleration weld interface without the same progression in expelled material as the simulated inertia weld. This would suggest that in these welds temperature does not have a strong influence on the upset rate. A situation seen in Figure 6-52 where the fast deceleration weld reaches a much higher upset rate compared to the simulated inertia weld after it has risen to its peak temperature, while the simulated inertia weld temperature rises with a small increase in temperature.

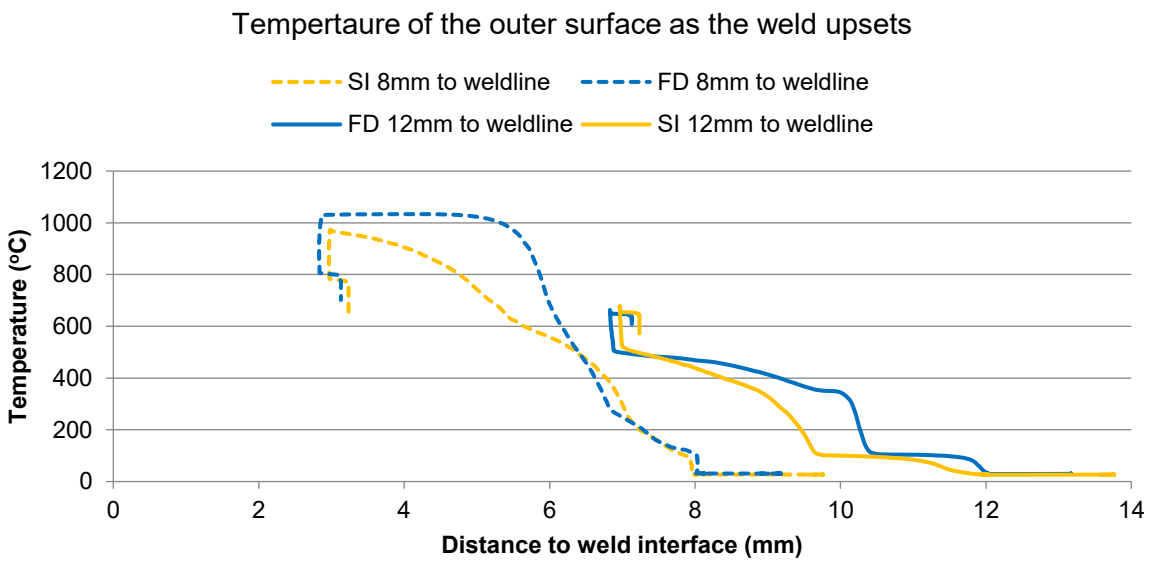


Figure 6-51: Probe temperatures plotted against the distance to the approaching weld interface.

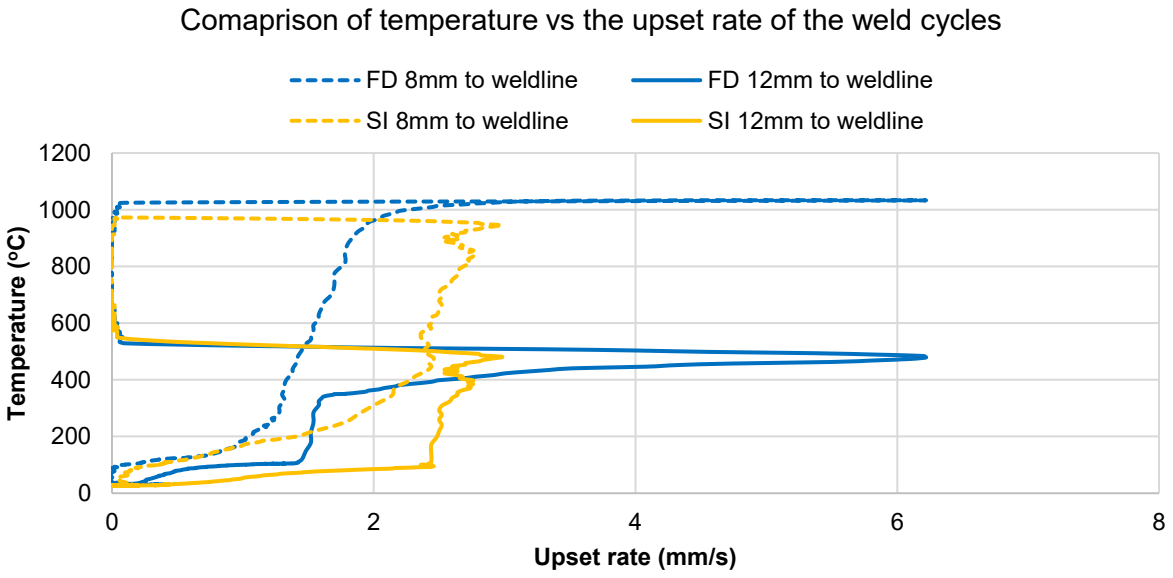


Figure 6-52: Temperature vs upset rate of the simulated inertia and fast deceleration weld.

Calculating the temperature rates throughout the weld produces Figure 6-53. Heating rates of the 8mm probe differ with the simulated inertia weld reaching a max of 622°C/s whereas the

fast deceleration weld reached 750°C/s. Further from the weld at the 12mm probe the simulated inertia weld reaches 697°C/s compared to 745°C/s for the fast deceleration weld.

Of the cooling rates both welds peak around -30°C/s with the simulated inertia reaching -28°C/s compared to the fast deceleration welds -35°C/s. The SI 8mm probe experiences cooling after 7.4s and the FD 8mm after 7.9s. Beyond this both welds tend to a cooling rate of ~-7°C/s, 30 seconds after the weld starts. As both welds reach similar temperatures, have the same surface area and were produced in room temperature air no major discrepancy would be expected.

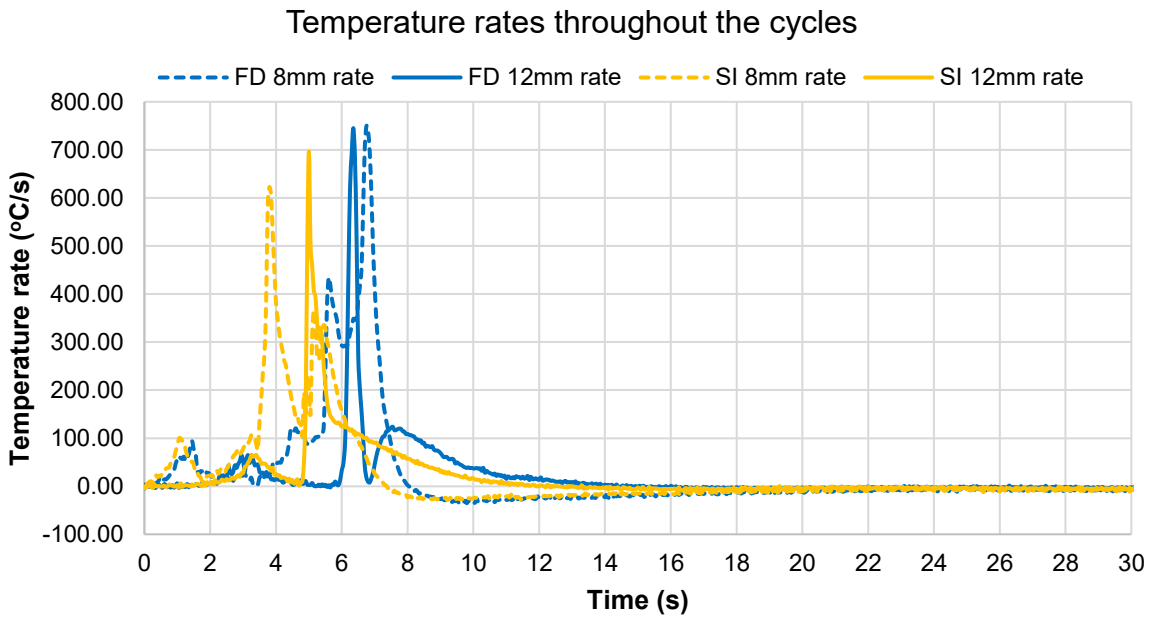


Figure 6-53: Rate of temperature change of the 8mm and 12mm probes throughout the weld cycles.

6.7.2 Microstructural examination

6.7.2.1 Visual

Overall, all cycles produced visually similar amounts of flash on the outside diameter, probably due to the very similar amounts of upset. With no evidence of re-entrant notches, it suggests a full bond has occurred across the interface. All three cycles displayed matching colour

changes of a purple with gold flecks on the outer most flash moving to pink and onto a dark yellow in the centre, Figure 6-15. However, the three cycles produced distinctly visible textures in the flash. The simulated inertia cycle flash, Figure 6-16, produced a rough texture across the entire flash. The fast deceleration cycle produced a smooth initial flash transitioning to rough at the purple to pink transition. The purple initial flash also contained more gold specks, Figure 6-17. While the nominal cycle transitioned from rough to smooth marginally before the purple to pink transition, Figure 6-18, gold speck density was also noted to be between the two other cycles. The colours match similar IFW Ti-6Al-4V welds Turner *et al.* (2016).

6.7.2.2 Optical micrographs

From Figure 6-19, Figure 6-24 and Figure 6-29, which show the mosaic images of the weld zones at 50x magnification, the shape of the weld zones can be seen along with indications of grain size transitions. All welds featured a reduced grain size along the weld line and in the surrounding material, defined as the recrystallised zone. The grains increased in size approaching the internal and outer diameter flash material. Banding of a transition zone from the weld zone to the base material can clearly be seen on the mosaics, made up of the TMAZ and HAZ. The TMAZ/HAZ banding on either side of the recrystallised zone diverges towards the edge of the sample where material has been ejected and formed flash. On the outer diameter, all welds displayed the characteristic curled flash in both directions away from the weld line. On the internal diameter, the flash has filled the internal cavity thereby preventing any formation of a curled shape. A point to note is that even with the internal cavity filling with flash at no point does it connect with the base material of the weld piece. Instead, the internal flash extends in both directions towards the backup tooling, maintaining a slim gap (~0.5mm) between the flash and base materials, as also seen by Adams and Miller (2013). The flash material contains enlarged grains in comparison to the rest of the material. Suggesting reduced strain energy and cooling rates as the material is no longer in the weld zone therefore sub-

grain rotation is reduced with the remaining heat energy being used for grain growth (Callister Jr, 1994).

All welds displayed a widmanstätten structure within the recrystallised zone. At the outer and inner diameter, the colonies are far larger and grouped together into larger grains (~0.1-0.25mm) The transition to smaller colonies found at the centreline of the weld zone occurs as the weld zone stops narrowing when moving away from the flash material. Throughout the weld zone and welding parameters the size of the underlying individual lath microstructure does not appear to significantly change thickness or length.

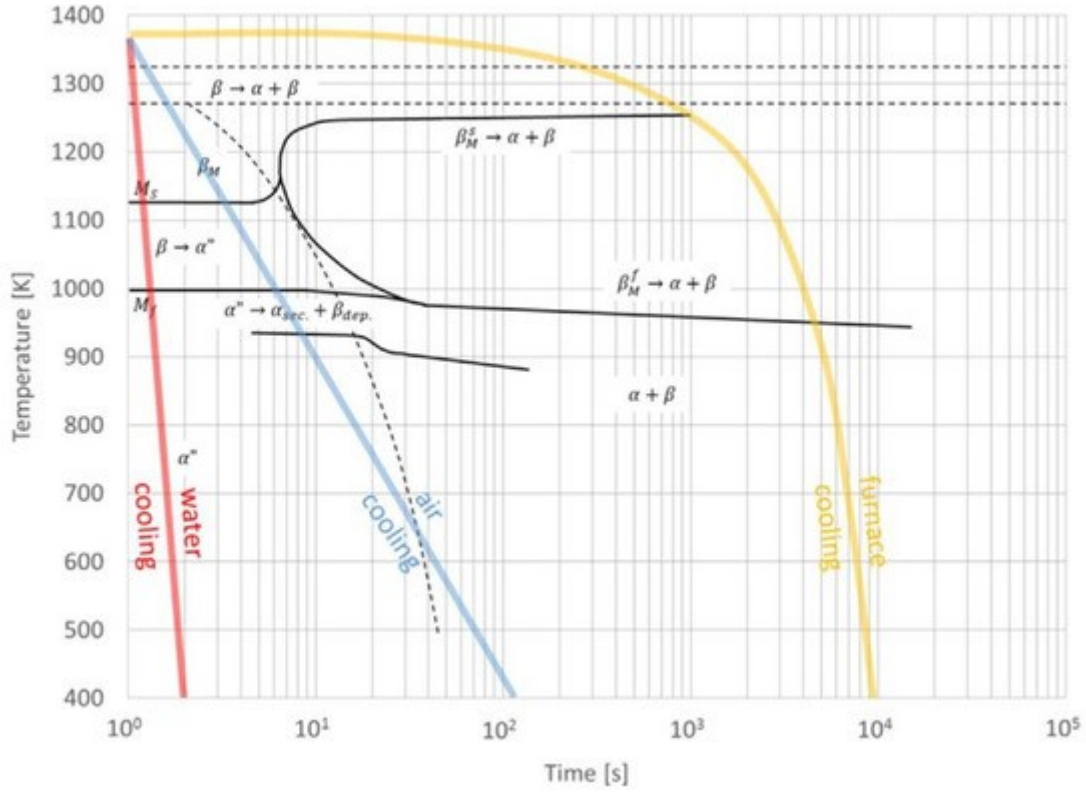


Figure 6-54: Continuous cooling curves of Ti-6Al-4V with air cooling estimated at ~20°C/s (Zhong *et al.*, 2020).

6.7.2.3 Weld zone widths

The weld zone measurements come from the mosaic images of the weld zone at 50x magnification. The microscope uses a scaled line to measure the distance between chosen pixels on the image. As the measurements are of microstructural transitions, there is a

subjective element, which would differ between researchers. In this study one researcher (the author) was used to take all measurements potentially reducing the variability in this study.

Table 6-2 details the measured widths of the microstructural zones visible from the etched micrograph. These have been plotted in Figure 6-34 to allow for comparison and analysis. The TMAZ/HAZ widths are largest at the internal diameter followed by the outside diameter with the smallest width being at the centre of the annulus. Of the TMAZ/HAZ widths, the fast deceleration and simulated inertia widths are similar with the simulated inertia recording slightly smaller widths. The nominal weld produced TMAZ/HAZ widths noticeably smaller than the other two welds. Of the weld zone widths, the simulated inertia and nominal welds produced similar and noticeably smaller widths compared to the fast deceleration welds, except within 5mm of the inside diameter where the nominal weld zone width increases to the same as the fast deceleration weld.

6.7.2.4 Hardness Mapping

The fast deceleration map indicates a general hardness across the surveyed area of 330Hv to 340Hv with few areas of higher hardness. There is a noticeable area of lower hardness <300Hv in the lower right corner of the survey while the upper and lower edges of the survey exhibit slightly lower hardness than the central region at ~320Hv.

The nominal map shows a harder central region extending towards the right-hand edge (coinciding with the outside diameter) generally >340Hv. The surrounding area consists of a hardness mostly between 315Hv and 335Hv with localised hard spots as hard and sometimes harder than the central region, which do not appear to be in keeping with the surrounding values.

The simulated inertia map displays an obvious wide central region of high hardness mostly above 340Hv centred on the bond line. Areas of low hardness above and below the bond line

are markedly lower from 300Hv to 325Hv, only rising above 325Hv when nearing the central region and occasional local points.

Notably the hardness mapping does not coincide with the weld zone widths seen in the macro images. Instead, correlation is seen between the hardness and the grain morphology with the reduction in hardness of the weld zone towards the ID and OD coinciding with the increase in grain size. This is consistent across all three welds.

6.7.3 Residual stress measurements

From the contoured mesh map of hoop stresses, Figure 6-41, it can be seen that across the weld line in each weld the peak stresses were found towards the inside diameter. Secondary peaks were visible towards the outside diameter. The stresses did not exactly mirror across the weld surface, as is clearly visible in Figure 6-42, which could be attributed to variances in material flow, cooling paths or similar but without further investigation would be difficult to confirm. A definite cause of the simulated inertia internal diameter stress results not matching on both sides of the weld was due to the EDM wire breaking during the cut, visible by the light shaded horizontal line in Figure 6-43. The stresses presented match in form with those measured and modelled by others (Grant *et al.*, 2009; Iracheta *et al.*, 2015)

The simulated inertia cycle produced the highest peak hoop stresses at the inside diameter, and some of the lowest stresses at the outside diameter and centre line points. The nominal weld cycle produced similar profiles to the fast deceleration cycle but at slightly higher stress levels. The fast deceleration cycle generally produced the lowest stress levels towards the inside diameter, dropping towards the centre line roughly at the same gradient as the nominal cycle with a similar small peak towards the outside diameter. Further work to measure the temperature profiles at the ID and CL would allow linking between the thermal strains caused during and after welding in the initial cooling phase

6.8 Discussion

It is worth noting that each weld 4, performed at a later date due to the complexity of the thermocouple rig, deviated from the earlier welds. The simulated inertia weld 4 had an elongated cycle due to a slow upset rate at the final deceleration stage, overall consuming more energy. The fast deceleration weld 4 consumed less energy than the others even with matching weld profiles and upsets. While nominal weld 4 produced less upset but consumed the same amount of energy. As both SI4 and Nom4 started with slightly larger pre-weld gaps the lack of upset could come from reduced energy available to them, as some would be consumed within the time taken for the two parts to be brought into contact. However, this should have been mitigated in the SI weld by the SI profile dictating the speed-upset points.

From a cycle point of view the fast deceleration cycle and nominal cycle could have been controlled by the torque modulation software, which would have reduced the upset variation within each cycle set and between the cycle sets. However, this could have led to greater deviations in deceleration rates as experienced by SI4.

It is known that a flywheel decelerating faster is having energy transferred away from it at a faster rate than one decelerating slower (Manufacturing Technology Inc, 2012). The energy equations take into account the motor input and friction of the system and show that even with simulated increased deceleration at the start of the weld (Si welds vs nominal) there is no increase of energy into the weld with similar amounts of energy required for conditioning in each.

The longer time spent initially at lower temperatures of the fast deceleration weld compared to the simulated inertia weld suggests a difference within the conditioning phase. The lower initial speed of the simulated inertia weld appears to move through the conditioning phase quicker, which was also observed by (Healy *et al.*, 1976) and Özdemir *et al.* (2007). As the temperature rises sooner than in the fast deceleration weld, while also having reduced heat flow into the

part, this would also suggest a more efficient transition through the conditioning phase potentially due to a lower temperature at the interface. Kimura *et al.* (2010) suggested a change in interface progression due to pressure differences, which could be applied here as an increase in speed can compensate for a reduction in pressure, with respect to energy absorbed into the weld (Linnert, 1994; W. Liu *et al.*, 2013) but more work would be needed to ascertain if this is correct.

As the temperature results are not from a steady state process nor do the probes measure the temperature at the interface the comparison to the literature is complicated. The steady state thermal profiles by Turner *et al.* (2016) of stage II predict a lower interface temperature for a lower initial speed but greater heat penetration into the part, matching the work by McAndrew *et al.* (2015). This initially fits with the higher peak temperatures seen in the fast deceleration welds. However, in the final part of the weld cycle the simulated inertia weld speed is increased above that of the fast deceleration welds and it is arguable that the peak temperatures recorded are from the later part of the cycle as the probes move towards the interface rather than track the temperature at the interface. Without being able to track the temperature distribution axially along the weld component and through the cycle it is difficult to conclude whether the second part of the cycle influenced the temperature profile created by the initial part of the cycle.

Residual stresses were linked to the build-up of thermal strains created upon cooling straight after the rotational movement has ceased Iracheta *et al.* (2015). Figure 6-53 shows a much higher heating rate experienced by the fast deceleration weld but also a slightly higher cooling rate experienced by the fast deceleration weld. This would suggest that on the outside diameter the fast deceleration welds should have higher levels of stress. This fits with the measurements on both sides of the weld in the hoop stresses, in Figure 6-42 and the axial stresses, in Figure 6-45.

With respect to the residual stress results the similar profiles between the nominal cycle and fast deceleration cycle could be due to similar thermal profiles or material movement due to their matching style of cycle with a natural deceleration. The change in deceleration of the simulated inertia cycle, as well as potentially changing the distribution of heat energy into the component, could influence the material movement and hence the residual stresses. Full cycles with differing parameters have shown variances in material movement as shown by Linnert (1994) and Turner *et al.* (2016) producing welds with varying shapes of recrystallised zone and flash formation. Parameters have also been shown to influence residual stress, by Romero *et al.* (2009), if sufficiently altered to manipulate the generation of heat at the interface, as seen by McAndrew *et al.* (2015) and Zulu and Mashinini (2018).

Diagram of the potential heat flow from the weld interface

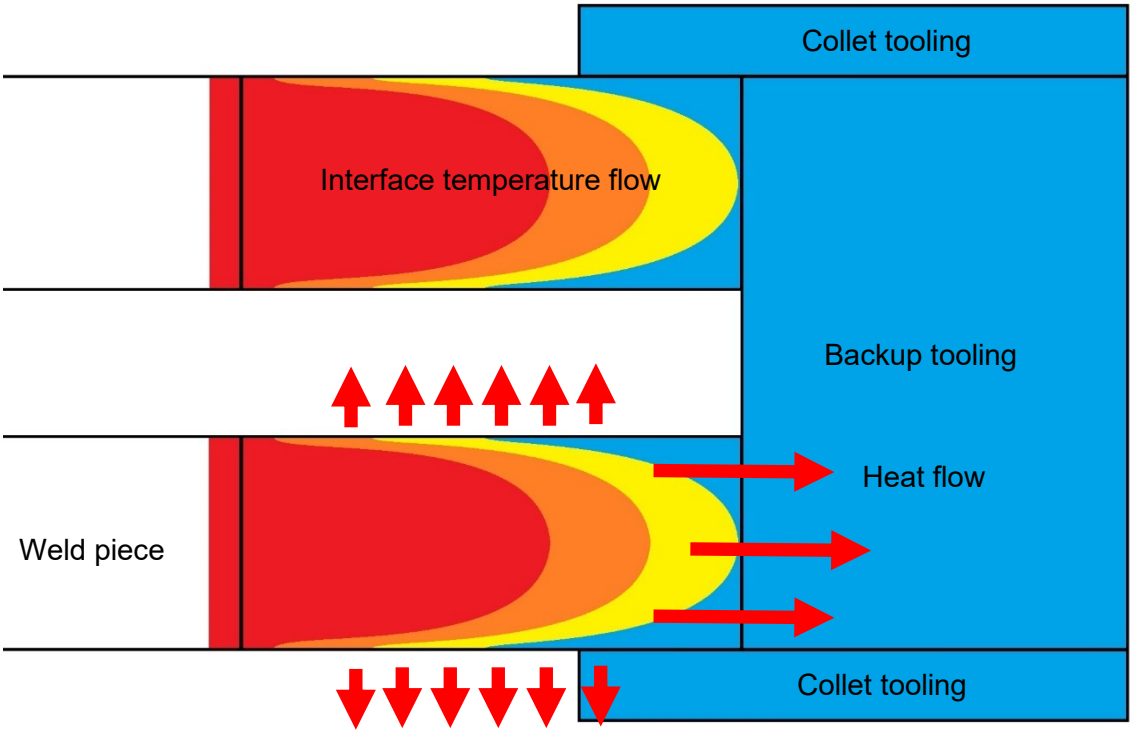


Figure 6-55: Cut through diagram of the weld pieces and tooling displaying the potential temperature flow from the interface through the part. Red indicating higher temperatures with orange ,yellow and blue indicating progressivly colder temperatures.

The weld zone widths correlate with the residual stresses though the part. The wider widths appearing at the outer and inner diameter. Iracheta *et al.* (2015) suggested that the mean diameter would correlate with the lower stresses due to a reduced cooling rate. Away from the interface, the results in Figure 6-41 from the contour map, show a lower stress level matching the slower cooling rate seen in the 12mm temperature probe, suggesting this is indeed the case. The wider weld zone areas of the ID and OD matching the residual stresses would come from the larger of area of hot material that needs to cool. As this larger area cools, it will contract straining the material at the outer surfaces more than the material at the centre of the weld. With the ID having the proportionally widest zone widths and resultant stresses, followed by the OD and then centreline, it suggests weld zone width is a factor as well as cooling rates in this scenario.

As the inside diameter is much smaller than the outer diameter the material has less space to eject material onto creating a larger flash formation. In this case the inside diameter is so small that the ejected material fills the central cavity in doing so widening the ejection area and creating wider weld zones and TMAZ/HAZ zones at the inside diameter. This concentration of hot material at the ID would be expected to slow the cooling rate and thereby reduce the residual stresses Iracheta *et al.* (2015), instead the stress state increases potentially due to the large amount of material movement creating a large area of thermal strain which combined offsets the expected slower cooling rates.

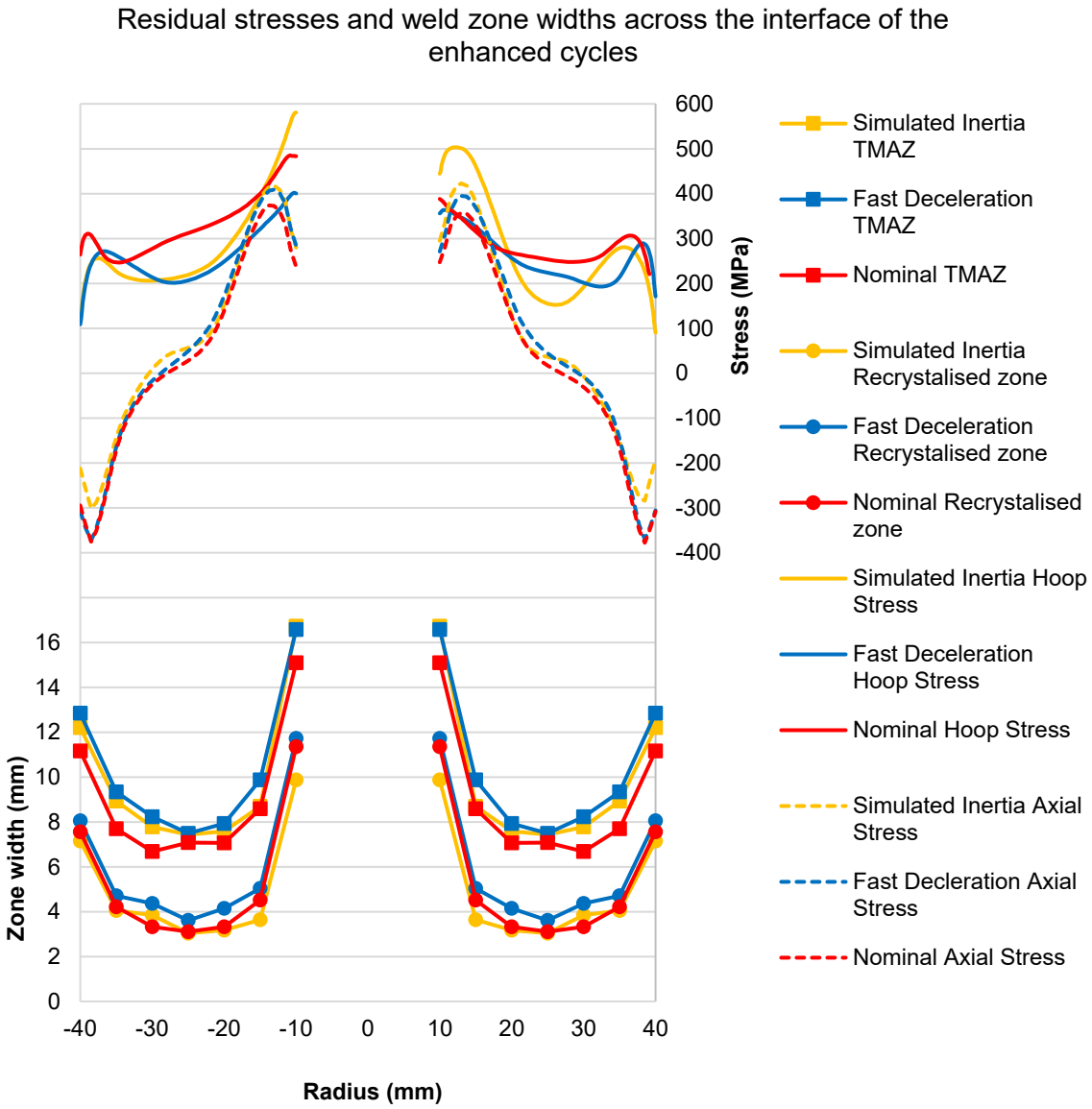


Figure 6-56: Residual stress measurements compared to the weld zone widths across the weld interface.

In comparison to the TMAZ/HAZ width, there are no strong correlations apart from the previous link between width and magnitude. There is a weak correlation between the residual stresses on the left side of the weld and the TMAZ width which matches with the state seen in FE models of the process (Iracheta *et al.*, 2015).

It is also possible that the component geometry played a role in the resulting outcomes. The ID stresses are much greater than those of the OD correlating with the flash build up on the ID. It reached a point where the material became a plug rather than the classic curled formation potentially increasing the ejection area of material on the ID. This geometric consequence could have had such an influence that towards the ID the variation that might have been introduced by the differing cycles could have been covered by geometry influences.

Axially the stresses inversed between the ID and OD, balancing out, while remaining less than those of the hoop direction aligning with results seen in IFW of other materials (Grant *et al.*, 2009; Karadge *et al.*, 2011; Moat *et al.*, 2009; Preuss *et al.*, 2006).

The hardness contour maps all show a centre section of each weld with increased hardness. The CCT curves of Ti-6Al-4V, from Sieniawski *et al.* (2013), suggest that for hardness's over 352Hv phases of martensite microstructure should be visible. It also suggests that a faster cooling rate was experienced compared to the surrounding material at the ID and OD. This would counteract the suggestions from the residual stress measurements. A more likely scenario is the increase in hardness is due to a mixture of grain refinement and work hardening from dynamic recrystallisation. Continuous dynamic recrystallisation has been noted as the primary mechanism in the rotary friction weld zone by many (I. Bhamji *et al.*, 2012; Ćirić & Radović, 2005; Fu & Du, 2006; Jata & Semiatin, 2000; M Maalekian, 2007; Tchein *et al.*, 2018; Uday *et al.*, 2010)

The enlarged grains of the flash material are possibly due to the interaction of material flow. The reduction in material movement could reduce recrystallisation allowing grain growth to occur. The enlarged grains are visible extending into the recrystallised zone within the part. This phenomenon is least visible in the simulated inertia parts prompting suggestions of increased material movement as it would aid recrystallisation and prevent grain growth. This would especially be the case at extended low rotational speeds where the OD is still

experiencing deformation of the material while the material at the centre is moving at speeds close to zero. Similar to the idea proposed by Kimura *et al.* (2010) in high pressure situations where wear followed by seizure develops at the OD initially and successively works inwards once each annulus reaches the seizure state.

The curvature of the flash also correlates with the weld zone widths at the outer diameter. The simulated inertia weld produced the tightest curling flash and the narrowest recrystallised zone while the fast deceleration weld produced the least curled flash from the widest recrystallised zone. Although flash shape can be seen to alter directly with parameters, (H.-Y. Chen *et al.*, 2015; Linnert, 1994; Turner *et al.*, 2016) little has been done to link parameters to flash shape in any material. From the welds here it would suggest upset rate is a primary contributing factor. With slower upset rates / narrower recrystallised zones producing smoother more curled flash due to larger differences in flow stress from the outer edge to the inner edge of the flash and smaller particle transference between the faying surfaces(Duffin & Bahrani, 1973). More work would be needed to clarify this phenomenon, but it might help give a greater understanding to the quality of the weld prior to destructive testing. This might match up well with the transitions seen in the surface roughness of the flash. It would appear that the cycle has a definite impact on the flash surface either through rotational speed or upset rate. However, as noted, little work has been conducted into flash formation to weld property relationships.

6.9 Conclusions

With the aim of producing welds with identical upset, cycle manipulation was introduced to see if changes could be made to the weld morphology of the component. On average, between the weld sets, there was a difference of 0.3mm in upset where the simulated inertia welds produced the least variation due to the controlled nature of the cycle, for further reductions torque modulation could have been used across all weld sets but it would have altered the deceleration characteristics of the nominal and fast deceleration welds.

1. From a visual perspective, the cycles made distinct changes to the flash surface and formation.
2. The nature of the cycle can result in changes to the energy input rate and total consumed energy in the weld.
3. The cycle can have a direct impact on the heat flow within a component, evident from temperature measurements and energy calculations.
4. The cycle will influence the morphology of the weld zones but geometry of the component can have a large impact, making it hard to identify cycle specific impacts.
5. Residual stresses within Ti-6Al-4V rotary friction welds (RFW) can be linked to weld zone widths through cooling rates and associated thermal strains.
6. Welds in all cycles presented with a widmanstätten morphology while the specific cycle had an impact on the hardness of the weld zone.

More work is required to explore enhanced cycles and their impact on the weld structure. There are opportunities to push the cycles to further extremes or add extra stages. Potentially using pressure to modify the weld behaviour as well as the cycles features here could be beneficial, however, through this study it appears that some impact can be made.

7 Conclusion

The focus of this thesis has been to assess the utility of enhanced control approaches during friction welding through understanding and exploiting the new developments in control systems, known as enhanced functionalities, explore ways to improve the manufacturing process when using rotary friction welding. Here the main outcomes of each section are recapped along with suggested areas of further study.

7.1 Inertia welding enhanced functionality capability assessment

7.1.1 Pressure modulation

Pressure modulation was able to reduce variation in weld repeatability down from 0.35mm to 0.05mm when measured in-process, however a separate upset measurement device is required which isn't affected by tooling compression as the post process measurement only showed a reduction from 0.309mm down to 0.175mm. Pressure modulation would be easily retro-fitable to many machines with a control system upgrade and a secondary upset measurement device.

7.1.2 Orientation control

The system in this study achieved an accuracy of +/- 1.83^{o} however this was increased with errors in part loading and pre-orientation to only 3.64^{o}. Slowing the spindle pre-orient speed down to 5rpm was found to help improve accuracy.

While in orientation control the upset repeatability was reduced from 0.35mm variation to 0.65mm measured in-process. Therefore, this process was only suitable for producing rotationally accurate parts.

7.1.3 Torque modulation

Torque modulation showed the most upset variation reduction of the three functionalities with in-process measurement down from 0.35mm to 0.03mm and CMM variation down from

0.309mm to 0.128mm with scope for further reduction in the CMM measurement due to an erroneous outlier.

Torque modulation most accurately controlled the weld cycle and is currently only available on machines with combined inertia and continuous drive modes. On this basis torque modulation offered the chance for completely novel research.

7.2 Proportionally modified energy friction welds

This study evaluated the capabilities of the final length control (FLC) system looking at the influence mid-cycle energy modification had on the weld structure, this was compared to a continuous drive cycle with a component length based friction to forge based trigger

Due to the differing capabilities of the continuous drive friction welding (CDFW) and inertia friction welding (IFW) modes, this study recommends aligning the critical factors of the part production to the welding cycle, choosing between component length and weld performance.

IFW FLC samples achieved a lower variation of component length compared to CDFW. Actual part length deviated from the desired part length by 0.025mm for every millimetre the incoming parts differed from the nominal part size. CDFW achieved a variation of 0.081mm.

If weld microstructure is of more importance, then CDFW FLC should be used, as it produced matching microstructures and performances regardless of incoming part size. IFW welds were affected by the incoming part size especially when undersized which caused the microstructure to present more bainite and even some martensite thereby creating a harder weld zone with a different performance to the nominal weld as seen in bend and charpy tests.

However, there were limits to this capability when the amount of energy required to be extracted from the weld was greater than the amount in the weld to shorten the upset and the final length couldn’t be achieved. When approaching the minimum capable welding length an

increase in hardness is seen in the weld zone as the cooling rates are increased due to the reduced amount of hot material created, enabling the formation of regions of martensite in rapidly cooled regions.

Further work may develop processing algorithms that can reduce final part size variation through a hybrid cycle combining the equal energy conditioning ability of the CDFW cycle with the accuracy of an inertia deceleration. Differences in microstructure could also potentially be compensated for.

7.3 Simulated inertia impact upon residual stress

Weld cycle manipulation was investigated in order to see if microstructural changes could be made to a welded component through artificial deceleration profiles for comparison welds of equal upset were created. On average, between the weld sets, there was a difference of 0.3mm in upset where the simulated inertia welds produced the least variation due to the controlled nature of the cycle, for further reductions torque modulation could have been used across all weld sets but it could have altered the deceleration characteristics of the nominal and fast deceleration welds as in SI4.

The cycles clearly show differences during upset as evidenced on the flash produced, this is confirmed looking at the temperature results, energy calculations and upset rates. The resulting change in the weld zone widths was linked to the residual stresses measured through thermal strains but more work needs to be done to characterise the temperature profile of the weld material in the final moments of the rotation phase and into cooling where the majority of the residual stresses are formed

7.4 Enhanced functionalities and potential industrial applications

7.4.1 Torque modulation

Torque modulation is available in multiple forms: Final length control and simulated inertia both utilise torque modulation in their operation. In its standard form a reduction in upset variation can be achieved by adjusting the rotational speed relative to the achieved upset. This is done multiple times during a cycle essentially tracking and adjusting the weld's progress. The reduction in variation can be used where accuracy across the weld area is important to the application. This could either be due to metallurgical reasons such as ensuring a consistent weld material performance or a metrology reason where the amount of material consumed is important. High value materials or sensitive materials with a narrow parameter window are ideal candidates to be welded in this fashion.

7.4.2 Final length control

Final length control includes the length of the part in the control of the weld. Instead of welding to a specific upset the weld is adjusted to reach a calculated upset dependent on the part lengths to ensure an overall length once welded. This form of welding is ideal to remove incoming part variance in a production process. An example would be rough castings which would require large amounts of machining prior to use. Through welding the amount of pre-machining can be reduced or even completely removed saving on component cost and production time.

7.4.3 Simulated inertia

Simulated inertia works on modifying the rotational speeds to appropriate various inertia amounts. This modification is ideal for altering the cycle to draw out or enhance certain characteristics of the weld cycle. For instance, parts which are known to have a dirty interface could simulate a larger flywheel initially to maintain higher speeds throughout the conditioning and heating phases. The central idea being that phases of the weld can be identified and either

extended or reduced to enhance a metallurgical trait. In the case of this thesis the final deceleration phase has been modified to identify its impact upon residual stresses.

7.5 Final conclusion

Through the work presented in this thesis, the modification of the friction weld cycle, predominantly the inertia cycle, can be used to enhance the process. Material performance can be controlled, while part variation can be reduced, production routes simplified and costs decreased. More work is needed to identify optimum cycles for residual stress reduction however, the work here has proven that torque manipulation can influence the residual stress state of Ti-6Al-4v friction welds.

8 Bibliography

Adams, A., & Miller, D. (2013). *Characterization and Optimization of Rotational Friction Welding for Small Stainless Steel Tubes* (Vol. 2).

AFW. (2016, 27/10/2016). Cost Reduction & Efficiency Gains. Retrieved from https://www.teamafw.com/cost-reduction-efficiency-gains/

Ahmad, B., & Fitzpatrick, M. E. (2016). Minimization and Mitigation of Wire EDM Cutting Errors in the Application of the Contour Method of Residual Stress Measurement. *Metallurgical and Materials Transactions A, 47*(1), 301-313. doi:10.1007/s11661-015-3231-7

Ahmed, T., & Rack, H. J. (1998). Phase transformations during cooling in α+β titanium alloys. *Materials Science and Engineering: A, 243*(1–2), 206-211. doi:http://dx.doi.org/10.1016/S0921-5093(97)00802-2

Alaneme, K. K., & Okotete, E. A. (2019). Recrystallization mechanisms and microstructure development in emerging metallic materials: A review. *Journal of Science: Advanced Materials and Devices, 4*(1), 19-33. doi:https://doi.org/10.1016/j.jsamd.2018.12.007

Alavala, C. R. (2016). Evaluation of parametric significance in friction welding process for AA2024 and Zr705 alloy using finite element analysis. *International Journal of Engineering Research & Technology, 5*(1), 84-89.

Alloypipes. (2012, 14/01/2012). BAOSTEEL SVH40C HIGH STRENGTH STEEL APPROVED BY DONGFENG NISSAN. Retrieved from http://alloypipes.over-blog.com/page/3

Altenkirch, J., Steuwer, A., Peel, M., Richards, D. G., & Withers, P. J. (2008). The effect of tensioning and sectioning on residual stresses in aluminium AA7749 friction stir welds. *Materials Science and Engineering: A, 488*(1), 16-24. doi:https://doi.org/10.1016/j.msea.2007.10.055

aluMatter. (2010). Retrieved from http://aluminium.matter.org.uk/content/html/eng/default.asp?catid=64&pageid=10003 14345

Ananthapadmanaban, D., Rao, V. S., Abraham, N., & Rao, K. P. (2009). A study of mechanical properties of friction welded mild steel to stainless steel joints. *Materials & Design, 30*(7), 2642-2646.

Ates, H., Turker, M., & Kurt, A. (2007). Effect of friction pressure on the properties of friction welded MA956 iron-based superalloy. *Materials & Design, 28*(3), 948-953.

Attallah, M. M., & Preuss, M. (2012). 2 - Inertia friction welding (IFW) for aerospace applications A2 - Chaturvedi, M.C *Welding and Joining of Aerospace Materials* (pp. 25-74): Woodhead Publishing.

Attallah, M. M., Preuss, M., Bouchareon, C., Steuwer, A., Daniels, J. E., Hughes, D. J., . . . Baxter, G. J. (2012). Microstructural and residual stress development due to inertia friction welding in Ti-6246. *Metallurgical and Materials Transactions A, 43*(9), 3149-3161.

Avinash, M., Chaitanya, G., Giri, D. K., Upadhya, S., & Muralidhara, B. (2007). *Microstructure and mechanical behavior of rotary friction welded titanium alloys.* Paper presented at the Proceedings of world academy of science, engineering and technology.

Bache, M. R., & Evans, W. J. (2001). Impact of texture on mechanical properties in an advanced titanium alloy. *Materials Science and Engineering A, 319*(321), 409 - 414.

Baker, T. N. (2016). Microalloyed steels. *Ironmaking & Steelmaking, 43*(4), 264-307. doi:10.1179/1743281215Y.0000000063

Bennett, C., Attallah, M., Preuss, M., Shipway, P., Hyde, T., & Bray, S. (2013). Finite element modeling of the inertia friction welding of dissimilar high-strength steels. *Metallurgical and Materials Transactions A, 44*(11), 5054-5064.

Bennett, C., Hyde, T., & Williams, E. (2007). Modelling and simulation of the inertia friction welding of shafts. *Proceedings of the Institution of Mechanical Engineers, Part L: Journal of Materials Design and Applications, 221*(4), 275-284.

Bennett, C. J., Attallah, M. M., Preuss, M., Shipway, P. H., Hyde, T. H., & Bray, S. (2013). Finite Element Modeling of the Inertia Friction Welding of Dissimilar High-Strength Steels. *Metallurgical and Materials Transactions A, 44*(11), 5054-5064. doi:10.1007/s11661-013-1852-2

Bennett, C. J., Hyde, T. H., & Williams, E. J. (2007). Modelling and simulation of the inertia friction welding of shafts. *Proceedings of the Institution of Mechanical Engineers, Part L: Journal of Materials: Design and Applications, 221*(4), 275-284. doi:10.1243/14644207JMDA154

Bhamji, I., Moat, R. J., Preuss, M., Threadgill, P. L., Addison, A. C., & Peel, M. J. (2012). Linear friction welding of aluminium to copper. *Science and Technology of Welding and Joining, 17*(4), 314-320. doi:10.1179/1362171812Y.0000000010

Bhamji, I., Preuss, M., Threadgill, P., & Addison, A. (2011). Solid state joining of metals by linear friction welding: a literature review. *Materials Science and Technology, 27*(1), 2-12.

Bhole, S. D. (1991). Interface properties in friction welding: a technical note. *Welding Journal, 82*(7), 168-170.

Böhme, D., Appel, L., & Cramer, H. (2009). Joint of Titanium/Titanium/Steel by Friction Welding with Continuous Drive. *Innovative technologies for joining advanced materials*.

Bouchard, P. J., Ledgard, P., Hiller, S., & Hosseinzadh Torknezhad, F. (2012). Making the cut for the contour method.

Bowen, A. W. (1978). The influence of crystallographic orientation on the fracture toughness of strongly textured Ti-6Al-4V. *Acta Metallurgica, 26*(9), 1423-1433. doi:https://doi.org/10.1016/0001-6160(78)90157-8

BSI. (2000). BS EN ISO 15620:2000 Welding. Friction welding of metallic materials. https://shop.bsigroup.com/: British Standards Institution.

BSI. (2004). Hot rolled products of structural steels. Technical delivery conditions for normalized/normalized rolled weldable fine grain structural steels *Heat-treatable steels*. www.shop.bsigroup.com: British Standards Institution,.

BSI. (2019). BS EN ISO 15620:2019

Welding. Friction welding of metallic materials. https://shop.bsigroup.com: British Standards Institution.

Bueckner, H. F. (1973). Field singularities and related integral representations. In G. C. Sih (Ed.), *Methods of analysis and solutions of crack problems: Recent developments in fracture mechanics Theory and methods of solving crack problems* (pp. 239-314). Dordrecht: Springer Netherlands.

Callister Jr, W. (1994). Materials Science and Engineering: An Introduction, Wiley. *College/msci/callister39551X/links. html*.

Caterpillar. (2020). INNOVATION IN WELDING: THE CATERPILLAR INERTIA WELDER. *From the Vault.* Retrieved from https://www.caterpillar.com/en/company/history/archive/innovation-in-welding.html

Celik, S., & Ersozlu, I. (2009). Investigation of the mechanical properties and microstructure of friction welded joints between AISI 4140 and AISI 1050 steels. *Materials & Design, 30*(4), 970-976.

Chamanfar, A., Jahazi, M., & Cormier, J. (2015). A review on inertia and linear friction welding of Ni-based superalloys. *Metallurgical and Materials Transactions A, 46*(4), 1639-1669.

Chaturvedi, M. C. (2011). *Welding and joining of aerospace materials*: Elsevier.

Chen, H.-Y., Fu, L., Zhang, W.-Y., & Liu, F.-J. (2015). Radial Distribution Characteristics of Microstructure and Mechanical Properties of Ti–6Al–4V Butt Joint by Rotary Friction

Welding. *Acta Metallurgica Sinica (English Letters), 28*(10), 1291-1298. doi:10.1007/s40195-015-0325-6

Chen, S., Dong, H., Li, P., Niu, S., Yu, L., & Ji, H. (2017). *Microstructure and mechanical property of aluminum/copper dissimilar friction welded joints: Sound aluminum/copper dissimilar joints can be produced with continuous drive friction welding after a 2-h postweld heat treatment at 100°C* (Vol. 96).

Chen, Y., Ashwell, R., Santos, P., Yang, J., Ward, A., Styles, A., & Edmonds, H. (2016). *High integrity fabrication using near net shape friction processing. D1.1 & D 1.2 RFW weld trials baseline, mechanical and metallurgical assessment.* High integrity fabrication using near net shape friction processing. CRP Report. Component Technology. Manufacturing Technology Centre. Manufacturing Technology Centre - Core Research Programme.

Ćirić, R., & Radović, N. (2005). Dynamic recrystallization in M2 tool steel during friction welding. *Metalurgija, 11*(4), 315-319.

D'Alvise, L. (2002). *Development of a finite element model for the simulation of the inertia friction.* (PhD), France ,.

D'Alvise, L., Massoni, E., & Walløe, S. (2002). Finite element modelling of the inertia friction welding process between dissimilar materials. *Journal of Materials Processing Technology, 125*, 387-391.

Denton, A., & W. Ashcroft, N. (1991). *Vegard's law* (Vol. 43).

Dey, H., Ashfaq, M., Bhaduri, A., & Rao, K. P. (2009). Joining of titanium to 304L stainless steel by friction welding. *Journal of Materials Processing Technology, 209*(18), 5862-5870.

Doherty, R., Hughes, D., Humphreys, F., Jonas, J., Jensen, D. J., Kassner, M., . . . Rollett, A. (1997). Current issues in recrystallization: a review. *Materials Science and Engineering: A, 238*(2), 219-274.

Duffin, F. D., & Bahrani, A. S. (1973). Frictional behaviour of mild steel in friction welding. *Wear, 26*(1), 53-74. doi:https://doi.org/10.1016/0043-1648(73)90150-6

English, C. (1995). Inertia welding of jet engine components: transition from electron beam welding to inertia welding for a titanium alloy fan disk. *Fabtech International'95., 2*, 1237-1250.

Frankel, P. (2017, 14/11/2017). [Discussion on figure presentations within a paper.].

Frankel, P., Preuss, M., Steuwer, A., Withers, P., & Bray, S. (2009). Comparison of residual stresses in Ti–6Al–4V and Ti–6Al–2Sn–4Zr–2Mo linear friction welds. *Materials Science and Technology, 25*(5), 640-650.

Fu, L., & Du, S. G. (2006). Effects of external electric field on microstructure and property of friction welded joint between copper and stainless steel. *Journal of Materials Science, 41*(13), 4137-4142. doi:10.1007/s10853-006-6224-5

Fuji, A., North, T., Ameyama, K., & Futamata, M. (1992). Improving tensile strength and bend ductility of titanium/AISI 304L stainless steel friction welds. *Materials Science and Technology, 8*(3), 219-235.

Fukumoto, S., Inoue, T., Mizuno, S., Okita, K., Tomita, T., & Yamamoto, A. (2010). Friction welding of TiNi alloy to stainless steel using Ni interlayer. *Science and Technology of Welding and Joining, 15*(2), 124-130.

Fukumoto, S., Tsubakino, H., Okita, K., Aritoshi, M., & Tomita, T. (1998). Microstructure of friction weld interface of 1050 aluminium to austenitic stainless steel. *Materials Science and Technology, 14*(4), 333-338. doi:10.1179/mst.1998.14.4.333

Gan, W. M., Hofmann, M., Ventzke, V., Randau, C., Huang, Y. D., Kriele, A., . . . Mueller, M. (2017). *Microstructure and Residual Stress in Rotary Friction Welded Dissimilar Metals of AA7020 Aluminium Alloy with 316L Steel.* Paper presented at the MAterials Science Forum.

Gilbert, N. (2012). Structural Steel - S235, S275, S355 Chemical Composition, Mechanical Properties and Common Applications. Retrieved from https://www.azom.com/article.aspx?ArticleID=6022

Grant, B., Preuss, M., Withers, P., Baxter, G., & Rowlson, M. (2009). Finite element process modelling of inertia friction welding advanced nickel-based superalloy. *Materials Science and Engineering: A, 513*, 366-375.

Guo, Y., Attallah, M. M., Chiu, Y., Li, H., Bray, S., & Bowen, P. (2017). Spatial variation of microtexture in linear friction welded Ti-6Al-4V. *Materials Characterization, 127*(Supplement C), 342-347. doi:https://doi.org/10.1016/j.matchar.2017.03.019

Guo, Y., Chiu, Y., Attallah, M. M., Li, H., Bray, S., & Bowen, P. (2012). Characterization of dissimilar linear friction welds of α-β titanium alloys. *Journal of Materials Engineering and Performance, 21*(5), 770-776.

Handa, A., & Chawla, V. (2014). Investigation of mechanical properties of friction-welded AISI 304 with AISI 1021 dissimilar steels. *The International Journal of Advanced Manufacturing Technology, 75*(9), 1493-1500. doi:10.1007/s00170-014-6238-0

Hashmi, S. (2014). *Comprehensive materials processing*: Newnes.

Healy, J. J., McMullan, D. J., & Bahrani, A. S. (1976). Analysis of frictional phenomena in friction welding of mild steel. *Wear, 37*(2), 265-278. doi:https://doi.org/10.1016/0043-1648(76)90033-8

Heidarzadeh, A., Kazemi-Choobi, K., Hanifian, H., & Asadi, P. (2014). 3 - Microstructural evolution. In M. K. B. Givi & P. Asadi (Eds.), *Advances in Friction-Stir Welding and Processing* (pp. 65-140): Woodhead Publishing.

Heng, z., Qingbin, L., & Yaole, X. (2015). *The microstructure and texture analysis of Ti-6Al-4V alloy through linear friction welding*. Paper presented at the International Conference on Materials, Environmental and Biological Engineering 2015. http://www.atlantis-press.com/proceedings/mebe-15/17810

Hirst, W., & Lancaster, J. K. (1960). The influence of speed on metallic wear. *Proceedings of the Royal Society of London. Series A. Mathematical and Physical Sciences, 259*(1297), 228.

Huang, K., & Logé, R. E. (2016). A review of dynamic recrystallization phenomena in metallic materials. *Materials & Design, 111*, 548-574. doi:https://doi.org/10.1016/j.matdes.2016.09.012

Iracheta, O., Bennett, C. J., & Sun, W. (2015). A sensitivity study of parameters affecting residual stress predictions in finite element modelling of the inertia friction welding process. *International Journal of Solids and Structures, 71*, 180-193. doi:10.1016/j.ijsolstr.2015.06.018

Işık, E., & Özes, Ç. (2016). Determination of the Mechanical Properties of Friction Welded Tube Yoke and Tube Joint. *Advances in Materials Science and Engineering, 2016*, 8918253. doi:10.1155/2016/8918253

Jata, K., & Semiatin, S. (2000). *Continuous dynamic recrystallization during friction stir welding of high strength aluminum alloys*. Retrieved from

Johnson, T. K., & Daines, J. W. (1973). *Society of Manufacturing Engineers / A comparison of the capabilities of continuous drive friction and inertia welding /. Tech Paper No. AD73-221*. Michigan: Society of Manufacturing Engineers /.

Kallee, S., & Nicholas, D. (1999). *Friction and forge welding processes for the automotive industry* (0148-7191). Retrieved from

Karadge, M., Grant, B., Withers, P. J., Baxter, G., & Preuss, M. (2011). Thermal Relaxation of Residual Stresses in Nickel-Based Superalloy Inertia Friction Welds. *Metallurgical and Materials Transactions A, 42*(8), 2301-2311. doi:10.1007/s11661-011-0613-3

Karadge, M., Preuss, M., Lovell, C., Withers, P. J., & Bray, S. (2007). Texture development in Ti–6Al–4V linear friction welds. *Materials Science and Engineering: A, 459*(1), 182-191. doi:https://doi.org/10.1016/j.msea.2006.12.095

Kerridge, M., & Lancaster, J. K. (1956). The stages in a process of severe metallic wear. *Proceedings of the Royal Society of London. Series A. Mathematical and Physical Sciences, 236*(1205), 250.

Kessler, M., Suenger, S., Haubold, M., & Zaeh, M. F. (2016). Modeling of upset and torsional moment during inertia friction welding. *Journal of Materials Processing Technology, 227*, 34-40. doi:https://doi.org/10.1016/j.jmatprotec.2015.07.024

Kim, Y. C., Fuji, A., & North, T. H. (1995). Residual stress and plastic strain in AI51 304L stainless steel/titanium friction welds. *Materials Science and Technology, 11*(4), 383-388. doi:10.1179/mst.1995.11.4.383

Kimura, M., Choji, M., Kusaka, M., Seo, K., & Fuji, A. (2006). Effect of friction welding conditions on mechanical properties of A5052 aluminium alloy friction welded joint. *Science and Technology of Welding and Joining, 11*(2), 209-215. doi:10.1179/174329306X89242

Kimura, M., Inoue, H., Kusaka, M., & Kaizu, K. (2010). Analysis method of friction torque and weld interface temperature during friction process of steel friction welding. *Journal of Solid Mechanics and Materials Engineering, 4*(3), 401-413. doi:https://doi.org/10.1299/jmmp.4.401

Kimura, M., Kusaka, M., Seo, K., & Fuji, A. (2005a). Improving joint properties of friction welded joint of high tensile steel. *JSME International Journal Series A Solid Mechanics and Material Engineering, 48*(4), 399-405.

Kimura, M., Kusaka, M., Seo, K., & Fuji, A. (2005b). Joining phenomena during friction stage of A7075-T6 aluminium alloy friction weld. *Science and Technology of Welding and Joining, 10*(3), 378-383. doi:10.1179/174329305X40723

Kimura, M., Nakamura, S., Kusaka, M., Seo, K., & Fuji, A. (2005). Mechanical properties of friction welded joint between Ti–6Al–4V alloy and Al–Mg alloy (AA5052). *Science and Technology of Welding and Joining, 10*(6), 666-672. doi:10.1179/174329305X57455

Kimura, M., Ohtsuka, Y., Kusaka, M., Seo, K., & Fuji, A. (2005). *Effect of Friction Time and Friction Pressure on Tensile Strength of Welded Joint for Medium and High Carbon Steels by Low Heat Input Friction Welding Method* (Vol. 23).

Kimura, M., Seo, K., Kusaka, M., & Fuji, A. (2003). Observation of joining phenomena in friction stage and improving friction welding method. *JSME International Journal Series A Solid Mechanics and Material Engineering, 46*(3), 384-390.

Kumar, B. (2013). A review on blisk technology. *Int. J. Innov. Res. Sci. Eng. Technol, 2*(13531358.11).

Kumar, N., Mishra, R. S., & Baumann, J. A. (2014). Chapter 1 - Introduction. In N. Kumar, R. S. Mishra, & J. A. Baumann (Eds.), *Residual Stresses in Friction Stir Welding* (pp. 1-4). Boston: Butterworth-Heinemann.

Li, W., Vairis, A., Preuss, M., & Ma, T. (2016). Linear and rotary friction welding review. *International Materials Reviews, 61*(2), 71-100. doi:10.1080/09506608.2015.1109214

Linnert, G. E. (1994). Welding Metallurgy, Carbon and Alloy Steels, Vol. 1. Fundamentals. *American Welding Society, Welding Metallurgy, Carbon and Alloy Steels, 1*, 940.

Lippold, J., & Odegard, B. (1984). Technical note: Microstructural evolution during inertia friction welding of austenitic stainless steels. *Weld. J, 63*, 35s-38s.

Liu, C., & Dong, C.-l. (2014). Internal residual stress measurement on linear friction welding of titanium alloy plates with contour method. *Transactions of Nonferrous Metals Society of China, 24*(5), 1387-1392. doi:https://doi.org/10.1016/S1003-6326(14)63203-9

Liu, W., Wang, F., Yang, X., & Li, W. (2013). Upset Prediction in Friction Welding Using Radial Basis Function Neural Network. *Advances in Materials Science and Engineering, 2013*, 9. doi:10.1155/2013/196382

Lombard, H., Hattingh, D. G., Steuwer, A., & James, M. N. (2009). Effect of process parameters on the residual stresses in AA5083-H321 friction stir welds. *Materials Science and Engineering: A, 501*(1), 119-124. doi:https://doi.org/10.1016/j.msea.2008.09.078

Lovin, J., Adams, R., Kuruzar, D., & Spindler, D. (2004a). US Patent No. 7080770. Google Patents.
Lovin, J., Adams, R., Kuruzar, D., & Spindler, D. (2004b). US Patent No. 7080770. JUSTIA Patents / Google Patents: B. T. LLP.
Luo, J., Xiang, J., Liu, D., Li, F., & Xue, K. (2012). Radial friction welding interface between brass and high carbon steel. *Journal of Materials Processing Technology, 212*(2), 385-392.
Lütjering, G. (1998). Influence of processing on microstructure and mechanical properties of (α+β) titanium alloys. *Materials Science and Engineering: A, 243*(1), 32-45. doi:https://doi.org/10.1016/S0921-5093(97)00778-8
Maalekian, M. (2007). Friction welding–critical assessment of literature. *Science and Technology of Welding and Joining, 12*(8), 738-759.
Maalekian, M., Kozeschnik, E., Brantner, H. P., & Cerjak, H. (2008). Comparative analysis of heat generation in friction welding of steel bars. *Acta Materialia, 56*(12), 2843-2855. doi:http://dx.doi.org/10.1016/j.actamat.2008.02.016
Mahaffey, D. W., Senkov, O. N., Shivpuri, R., & Semiatin, S. L. (2016). Effect of Process Variables on the Inertia Friction Welding of Superalloys LSHR and Mar-M247. *Metallurgical and Materials Transactions A, 47*(8), 3981-4000. doi:10.1007/s11661-016-3600-x
Manufacturing Technology Inc. (2012). *M125T Instruction Manual*. Instruction Manual. High Integrity Fabrication. Manufacturing Technology Centre. Recieved upon purchase of machine.
Manufacturing Technology Inc. (2013a, 2017). Direct Drive Friction Welding. Retrieved from http://www.mtiwelding.com/direct-drive-friction-welding.html
Manufacturing Technology Inc. (2013b). Inertia Friction Welding. Retrieved from http://www.mtiwelding.com/inertia-friction-welding.html
Manufacturing Technology Inc. (2013c, 2017). Inertia Friction Welding. Retrieved from http://www.mtiwelding.com/inertia-friction-welding.html
Manufacturing Technology Inc (Producer). (2016, 7/6/2018). Rotary Friction Welding Upset Control - Part 2. *MTI Whiteboard Wednesdays*. Retrieved from https://www.youtube.com/watch?v=id2v94QuHnE&list=PLMKVGv43Qd32YooMkSejXAG2R601JYwjF&index=12
Manufacturing Technology Inc (Producer). (2017a, 5/6/2018). Dynamic Profile Modification. *MTI Whiteboard Wednesdays*. [Video] Retrieved from https://www.youtube.com/watch?v=0u0m0qEVB7c
Manufacturing Technology Inc (Producer). (2017b, 6/5/2018). Radial Position Control Techniques. *MTI Whiteboard Wednesday*. [Video] Retrieved from https://www.youtube.com/watch?v=vL4_Y_GJZsc&index=22&list=PLMKVGv43Qd32YooMkSejXAG2R601JYwjF
Manufacturing Technology Inc (Producer). (2017c, 5/6/2018). Upset Control - Pressure Modulation. *MTI Whiteboard Wednesdays*. [Video] Retrieved from https://www.youtube.com/watch?v=ZgU-zrZqJlU&index=13&list=PLMKVGv43Qd32YooMkSejXAG2R601JYwjF
Manufacturing Technology Inc (Producer). (2017d, 5/6/2018). Upset Control - Torque Modulation. *MTI Whiteboard Wednesdays*. [Video] Retrieved from https://www.youtube.com/watch?v=UN35feK--r0
McAndrew, A. R., Colegrove, P. A., Addison, A. C., Flipo, B. C. D., & Russell, M. J. (2014). Energy and Force Analysis of Ti-6Al-4V Linear Friction Welds for Computational Modeling Input and Validation Data. *Metallurgical and Materials Transactions A, 45*(13), 6118-6128. doi:10.1007/s11661-014-2575-8
McAndrew, A. R., Colegrove, P. A., Addison, A. C., Flipo, B. C. D., & Russell, M. J. (2015). Modelling the influence of the process inputs on the removal of surface contaminants

from Ti–6Al–4V linear friction welds. *Materials & Design (1980-2015), 66*, 183-195. doi:https://doi.org/10.1016/j.matdes.2014.10.058
McAndrew, A. R., Colegrove, P. A., Bühr, C., Flipo, B. C. D., & Vairis, A. (2018). A literature review of Ti-6Al-4V linear friction welding. *Progress in Materials Science, 92*, 225-257. doi:https://doi.org/10.1016/j.pmatsci.2017.10.003
Metric-Metal. (2018). CARBON FLAT BAR (RECTANGULAR BAR) S355. Retrieved from http://www.metricmetal.com/product/carbon/carbon-flat-bar-rectangular-bar-s355/
Milton, B. H., & Lynn, V. R. E. (1966). Friction welding: Google Patents.
Milton, B. H., & Robert, M. B. (1968). Friction welding: Google Patents.
Mishra, R. S., & Ma, Z. (2005). Friction stir welding and processing. *Materials Science and Engineering: R: Reports, 50*(1), 1-78.
Moat, R. J., Hughes, D. J., Steuwer, A., Iqbal, N., Preuss, M., Bray, S., & Rawson, M. (2009). Residual stresses in inertia-friction-welded dissimilar high-strength steels. *Metallurgical and Materials Transactions A, 40*(9), 2098-2108.
Moat, R. J., Karadge, M., Preuss, M., Bray, S., & Rawson, M. (2008). Phase transformations across high strength dissimilar steel inertia friction weld. *Journal of Materials Processing Technology, 204*(1), 48-58.
Morris, B. R., & Bernard, H. M. (1969). Friction welding: Google Patents.
Morton, W. (1944). Method of welding: Google Patents.
MTI. (2012). *M125 Friction Welder Operating Manual*.
NASA. (2014). Friction Stir Welding.
Nessler, C., Rutz, D., Eng, R., & Vozzella, P. (1971). Friction welding of titanium alloys. *Welding Journal, 50*(9), 379-385.
Nguyen-Dinh, X. (2001). Friction welding interlayer and method for joining gamma titanium aluminide to steel, and turbocharger components thereof: Google Patents.
Ni, J., & Abdel Wahab, M. (2017). A numerical kinematic model of welding process for low carbon steels. *Computers & Structures, 186*, 35-49. doi:https://doi.org/10.1016/j.compstruc.2017.03.009
Özdemir, N., Sarsılmaz, F., & Hasçalık, A. (2007). Effect of rotational speed on the interface properties of friction-welded AISI 304L to 4340 steel. *Materials & Design, 28*(1), 301-307.
Pagliaro, P., Prime, M. B., Swenson, H., & Zuccarello, B. (2010). Measuring Multiple Residual-Stress Components using the Contour Method and Multiple Cuts. *Experimental Mechanics, 50*(2), 187-194. doi:10.1007/s11340-009-9280-3
Pang, J., Preuss, M., Withers, P., Baxter, G., & Small, C. (2003). Effects of tooling on the residual stress distribution in an inertia weld. *Materials Science and Engineering: A, 356*(1), 405-413.
Paventhan, R., Lakshminarayanan, P. R., & Balasubramanian, V. (2011). Fatigue behaviour of friction welded medium carbon steel and austenitic stainless steel dissimilar joints. *Materials & Design, 32*(4), 1888-1894. doi:https://doi.org/10.1016/j.matdes.2010.12.011
Pederson, R. (2002). *Microstructure and Phase Transformation of Ti-6Al-4V.* (Licentiate Thesis), Lulea University of Technology. Retrieved from https://www.diva-portal.org/smash/get/diva2:991369/FULLTEXT01.pdf
Peters, M., Gysler, A., & LÜtjering, G. (1984). Influence of texture on fatigue properties of Ti-6Al-4V. *Metallurgical and Materials Transactions A, 15*(8), 1597-1605. doi:10.1007/bf02657799
Ponge, D. (2005). Continuous cooling transformations. In cct.jpg (Ed.), (pp. Structural Materials: Steels. Talk presented at Marie Curie Summer School on Knowledge Based Materials. Hürtgenwald, Germany. 08-08-2005 - 2017-2008-2005). https://www.scribd.com/document/135823772/Steels-Ponge-Marie-Curie-Summer-School: Scribd.

Preuss, M., Withers, P., & Baxter, G. (2006). A comparison of inertia friction welds in three nickel base superalloys. *Materials Science and Engineering: A, 437*(1), 38-45.
Prime, M. B. (2001). CROSS-SECTIONAL MAPPING OF RESIDUAL STRESSES BY MEASURING THE SURFACE CONTOUR AFTER A CUT. *Jounral of Engineering MAterials and Technology, 123*, 162-168.
Prime, M. B., Gnäupel-Herold, T., Baumann, J. A., Lederich, R. J., Bowden, D. M., & Sebring, R. J. (2006). Residual stress measurements in a thick, dissimilar aluminum alloy friction stir weld. *Acta Materialia, 54*(15), 4013-4021. doi:https://doi.org/10.1016/j.actamat.2006.04.034
Prime, M. B., & Gonzales, A. (2000). *THE CONTOUR METHOD: SIMPLE 2-D MAPPING OF RESIDUAL STRESSES*: ; Los Alamos National Lab., NM (US).
Raabe, D. (2017). introduction to Titanium Alloys. Retrieved from http://www.dierk-raabe.com/titanium-alloys/
Ragu Nathan, S., Balasubramanian, V., Malarvizhi, S., & Rao, A. G. (2015). Effect of welding processes on mechanical and microstructural characteristics of high strength low alloy naval grade steel joints. *Defence Technology, 11*(3), 308-317. doi:https://doi.org/10.1016/j.dt.2015.06.001
Reddy, N. S., Lee, Y. H., Park, C. H., & Lee, C. S. (2008). Prediction of flow stress in Ti–6Al–4V alloy with an equiaxed α+β microstructure by artificial neural networks. *Materials Science and Engineering: A, 492*(1), 276-282. doi:https://doi.org/10.1016/j.msea.2008.03.030
Richards, M. (2009, 23/10/2009). Friction is good for Thompson. *Machinery*.
Rollet, A. D. (Producer). (2007, 27/11/2014). The Effect of Grain Size on Strength and Toughness. *Microstructure-Properties*. Retrieved from http://neon.mems.cmu.edu/rollett/27301/L5A_GrainSize_HallPetch_05Oct07.pdf
Romero, J., Attallah, M., Preuss, M., Karadge, M., & Bray, S. (2009). Effect of the forging pressure on the microstructure and residual stress development in Ti–6Al–4V linear friction welds. *Acta Materialia, 57*(18), 5582-5592.
Roters, F., Raabe, D., & Gottstein, G. (2000). Work hardening in heterogeneous alloys—a microstructural approach based on three internal state variables. *Acta Materialia, 48*(17), 4181-4189.
Sahin, M. (2005). Joining with friction welding of high-speed steel and medium-carbon steel. *Journal of Materials Processing Technology, 168*(2), 202-210. doi:https://doi.org/10.1016/j.jmatprotec.2004.11.015
Sahin, M., & Erol Akata, H. (2004). An experimental study on friction welding of medium carbon and austenitic stainless steel components. *Industrial Lubrication and Tribology, 56*(2), 122-129. doi:https://doi.org/10.1108/00368790410524074
Sathiya, P., Aravindan, S., & Haq, A. N. (2007). Effect of friction welding parameters on mechanical and metallurgical properties of ferritic stainless steel. *The International Journal of Advanced Manufacturing Technology, 31*(11-12), 1076-1082.
Sathiya, P., Aravindan, S., Haq, A. N., & Paneerselvam, K. (2009). Optimization of friction welding parameters using evolutionary computational techniques. *Journal of Materials Processing Technology, 209*(5), 2576-2584. doi:http://dx.doi.org/10.1016/j.jmatprotec.2008.06.030
Sathiya, P., Aravindan, S., & Noorul Haq, A. (2007). Effect of friction welding parameters on mechanical and metallurgical properties of ferritic stainless steel. *The International Journal of Advanced Manufacturing Technology, 31*(11), 1076-1082. doi:https://doi.org/10.1007/s00170-005-0285-5
Sathiya, P., Aravindan, S., Noorul Haq, A., & Paneerselvam, K. (2006). Optimization of friction welding parameters using simulated annealing. *Indian Journal of Engineering & Materials Sciences, 13*, 37-44.

Satyanarayana, V. V., Madhusudhan Reddy, G., & Mohandas, T. (2005). Dissimilar metal friction welding of austenitic–ferritic stainless steels. *Journal of Materials Processing Technology, 160*(2), 128-137. doi:http://dx.doi.org/10.1016/j.jmatprotec.2004.05.017

Seli, H., Ismail, A. I. M., Rachman, E., & Ahmad, Z. A. (2010). Mechanical evaluation and thermal modelling of friction welding of mild steel and aluminium. *Journal of Materials Processing Technology, 210*(9), 1209-1216. doi:http://dx.doi.org/10.1016/j.jmatprotec.2010.03.007

Selvamani, S. T., Palanikumar, K., Umanath, K., & Jayaperumal, D. (2015). Analysis of friction welding parameters on the mechanical metallurgical and chemical properties of AISI 1035 steel joints. *Materials & Design (1980-2015), 65*, 652-661. doi:https://doi.org/10.1016/j.matdes.2014.09.056

Senkov, O. N., Mahaffey, D. W., & Semiatin, S. L. (2017). Effect of process parameters on process efficiency and inertia friction welding behavior of the superalloys LSHR and Mar-M247. *Journal of Materials Processing Technology, 250*(Supplement C), 156-168. doi:https://doi.org/10.1016/j.jmatprotec.2017.07.020

Senkov, O. N., Mahaffey, D. W., Tung, D. J., Zhang, W., & Semiatin, S. L. (2017). Efficiency of the Inertia Friction Welding Process and Its Dependence on Process Parameters. *Metallurgical and Materials Transactions A, 48*(7), 3328-3342. doi:10.1007/s11661-017-4115-9

Sieniawski, J., Ziaja, W., Kubiak, K., & Motyka, M. (2013). Microstructure and mechanical properties of high strength two-phase titanium alloys (pp. 69-80).

Sketchley, P. (2013). [Discussion on welding of Ti-64].

Smith, W. F., & Hashemi, J. (2003). Fundamentals of Materials Science and Engineering. *McGraw Hill, New York*.

Staron, P., Koçak, M., Williams, S., & Wescott, A. (2004). Residual stress in friction stir-welded Al sheets. *Physica B: Condensed Matter, 350*(1, Supplement), E491-E493. doi:https://doi.org/10.1016/j.physb.2004.03.128

Su, J.-Q., Nelson, T., Mishra, R., & Mahoney, M. (2003). Microstructural investigation of friction stir welded 7050-T651 aluminium. *Acta Materialia, 51*(3), 713-729.

Taban, E., Gould, J. E., & Lippold, J. C. (2010). Dissimilar friction welding of 6061-T6 aluminum and AISI 1018 steel: Properties and microstructural characterization. *Materials & Design, 31*(5), 2305-2311.

Tchein, G. J., Jacquin, D., Coupard, D., Lacoste, E., & Girot Mata, F. (2018). Genesis of Microstructures in Friction Stir Welding of Ti-6Al-4V. *Metallurgical and Materials Transactions A, 49*(6), 2113-2123. doi:10.1007/s11661-018-4568-5

Threadgill, P. L., & Russel, M. J. (2007). *Friction welding of near net shape preforms in Ti-6Al-4V*. Paper presented at the 11th World Conference on titanium (Ti-2007), Kyoto - Japan. http://www.twi-global.com/technical-knowledge/published-papers/friction-welding-of-near-net-shape-preforms-in-ti-6al-4v-june-2007/

Tumuluru, M. (1984). A parametric study of inertia friction welding for low alloy steel pipes. *Welding Journal, 63*(9), 289-294.

Turner, R. P., Howe, D., Thota, B., Ward, R. M., Basoalto, H. C., & Brooks, J. W. (2016). Calculating the energy required to undergo the conditioning phase of a titanium alloy inertia friction weld. *Journal of Manufacturing Processes, 24*, 186-194. doi:https://doi.org/10.1016/j.jmapro.2016.09.008

TWI. (2014). Benefits and Advantages. Retrieved from http://www.twi-global.com/capabilities/joining-technologies/friction-processes/friction-stir-welding/benefits-and-advantages/

TWI. (2021). WHAT IS RESIDUAL STRESS? *Technical Knowledge - FAQ*. Retrieved from https://www.twi-global.com/technical-knowledge/faqs/residual-stress

TWI. (2021). WHAT IS RESIDUAL STRESS? *Technical Knowledge - FAQ*. Retrieved from https://www.twi-global.com/technical-knowledge/faqs/residual-stress

Uday, M., Ahmad Fauzi, M., Zuhailawati, H., & Ismail, A. (2010). Advances in friction welding process: a review. *Science and Technology of Welding and Joining, 15*(7), 534-558.
Vairis, A., Papazafeiropoulos, G., & Tsainis, A.-M. (2016). A comparison between friction stir welding, linear friction welding and rotary friction welding. *Advances in Manufacturing, 4*(4), 296-304.
VEQTER Ltd. (2018). Contour. *Residual Stress Measurement.* Retrieved from http://www.veqter.co.uk/residual-stress-measurement/contour
Volpp, T., Göring, E., Kuschke, W.-M., & Arzt, E. (1997). Grain size determination and limits to Hall-Petch behavior in nanocrystalline NiAl powders. *Nanostructured materials, 8*(7), 855-865.
Wang, F. F., Li, W. Y., Li, J. L., & Vairis, A. (2014). Process parameter analysis of inertia friction welding nickel-based superalloy. *The International Journal of Advanced Manufacturing Technology, 71*(9-12), 1909-1918.
Wang, K., & Lin, W. (1974). Flywheel friction welding research. *Welding Journal, 53*(6), 233s-241s.
Wang, L., Preuss, M., Withers, P., Baxter, G., & Wilson, P. (2005). Energy-input-based finite-element process modeling of inertia welding. *Metallurgical and Materials Transactions B, 36*(4), 513-523.
Wei, L. Y., & Nelson, T. (2011). *Correlation of microstructures and process variables in FSW HSLA-65 steel* (Vol. 90).
West-Yorkshire-Steel. (2018). S355 S355J2 S355J2+N Steel. Retrieved from https://www.westyorkssteel.com/carbon-steel/s355/
Williams, S. W., & Steuwer, A. (2010). 8 - Residual stresses in friction stir welding. In D. Lohwasser & Z. Chen (Eds.), *Friction Stir Welding* (pp. 215-244): Woodhead Publishing.
Wisbey, A., Wallis, I. C., Ubhi, H. S., Sketchley, P., Ward-Close, C. M., & Threadgill, P. L. (1999). *Mechanical Properties of Friction Welds in High Strength Titanium Alloys*. Paper presented at the Titanium '99', 9th World Titanium Conference, St. Petersburg, Russia. http://www.twi-global.com/technical-knowledge/published-papers/mechanical-properties-of-friction-welds-in-high-strength-titanium-alloys-june-1999/
Woo, I., Aritoshi, M., & Kikuchi, Y. (2002). Metallurgical and Mechanical Properties of High Nitrogen Austenitic Stainless Steel Friction Welds. *ISIJ International, 42*(4), 401-406. doi:https://doi.org/10.2355/isijinternational.42.401
Woo, W., Feng, Z., Wang, X. L., Brown, D. W., Clausen, B., An, K., . . . David, S. A. (2007). In situ neutron diffraction measurements of temperature and stresses during friction stir welding of 6061-T6 aluminium alloy. *Science and Technology of Welding and Joining, 12*(4), 298-303. doi:10.1179/174329307X197548
Wu, W., Zhu, L. Y., Wu, G. F., & Xu, H. B. (2011). *Study on Performance of Inertia Radial Friction Welding of Copper-Alloy to 35CrMnSi Steel.* Paper presented at the Advanced Materials Research.
Yang, L. (2010). *Modelling of the inertia welding of inconel 718.* (PhD), University of Birmingham, Birmingham.
Yang, Y.-C., Chen, W.-L., & Lee, H.-L. (2011). A Nonlinear Inverse Problem in Estimating the Heat Generation in Rotary Friction Welding. *Numerical Heat Transfer, Part A: Applications, 59*(2), 130-149. doi:10.1080/10407782.2011.540965
Yates, A. (2015). *The effect of microstructure on mechnical properties in inertia welded titanium 6-4.* (Master of Research), Univeristy of Birmingham, http://etheses.bham.ac.uk/5856/2/Yates15MRes.pdf.
Zhang, Q. Z., Zhang, L. W., Liu, W. W., Zhang, X. G., Zhu, W. H., & Qu, S. (2006). 3D rigid viscoplastic FE modelling of continuous drive friction welding process. *Science and Technology of Welding and Joining, 11*(6), 737-743. doi:10.1179/174329306X153222

Zhang, Y., Prathiar, S., Fitzpatrick, M. E., & Edwards, L. (2005). Residual Stress Mapping in Welds Using the Contour Method. *MAterials Science Forum, 490-491*, 294-299. doi:10.4028/www.scientific.net/MSF.490-491.294

Zhong, C., Liu, J., Zhao, T., Schopphoven, T., Fu, J., Gasser, A., & Schleifenbaum, J. H. (2020). Laser metal deposition of Ti6Al4V—a brief review. *Applied Sciences, 10*(3), 764.

Zulu, M., & Mashinini, P. M. (2018). *Process optimization of rotary friction welding of Ti-6Al-4V alloy rods* (Vol. 430).

9 Appendix

9.1 Chapter 5

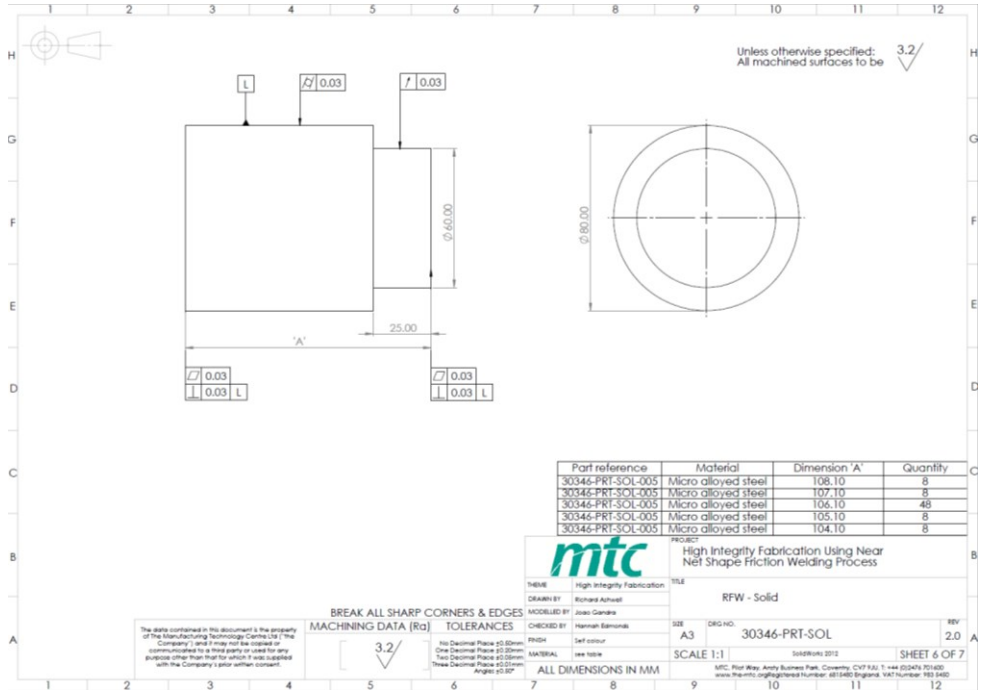


Figure 9-1. Part drawings: Solid MA steel.

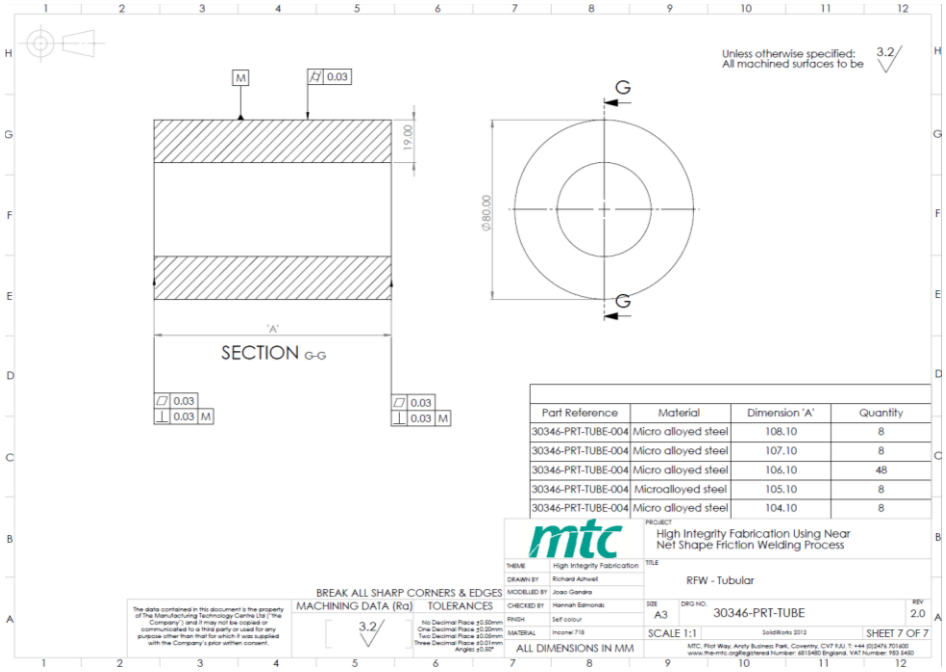


Figure 9-2. Part drawings: Tubular MA steel.

9.2 Chapter 6



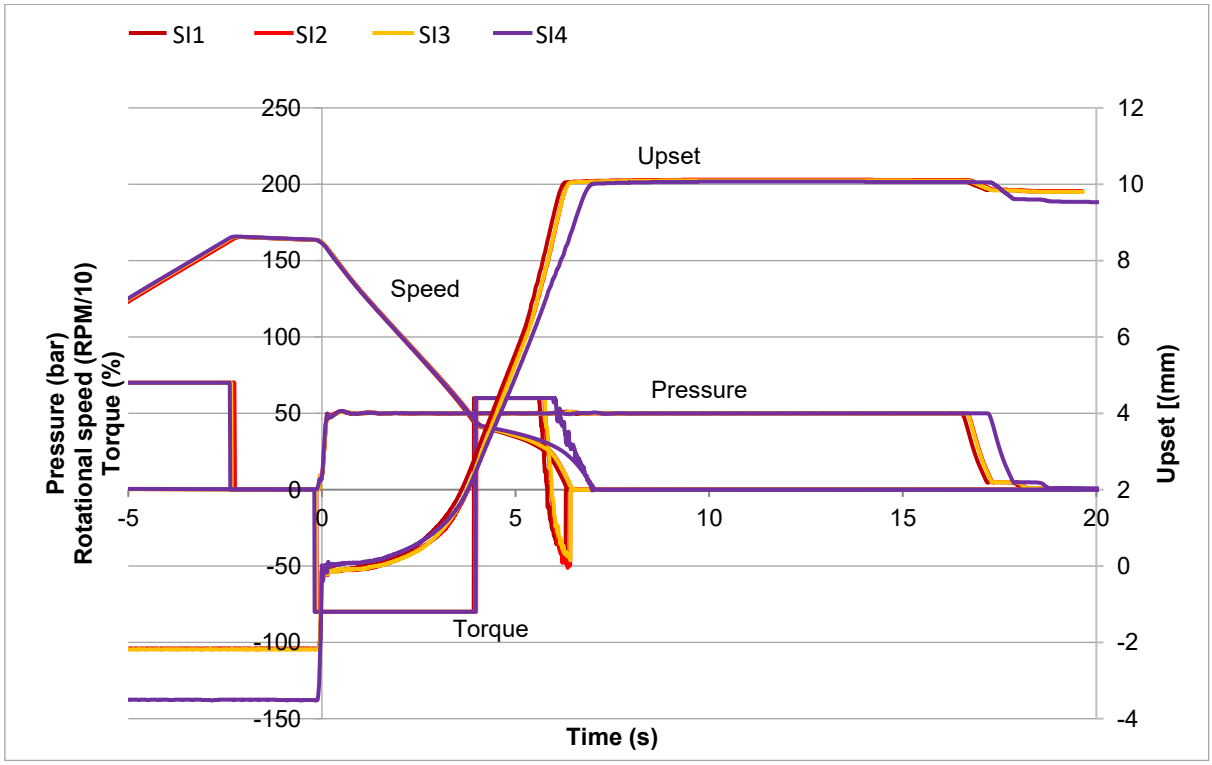


Figure 9-3: Weld traces of the simulated inertia cycles.

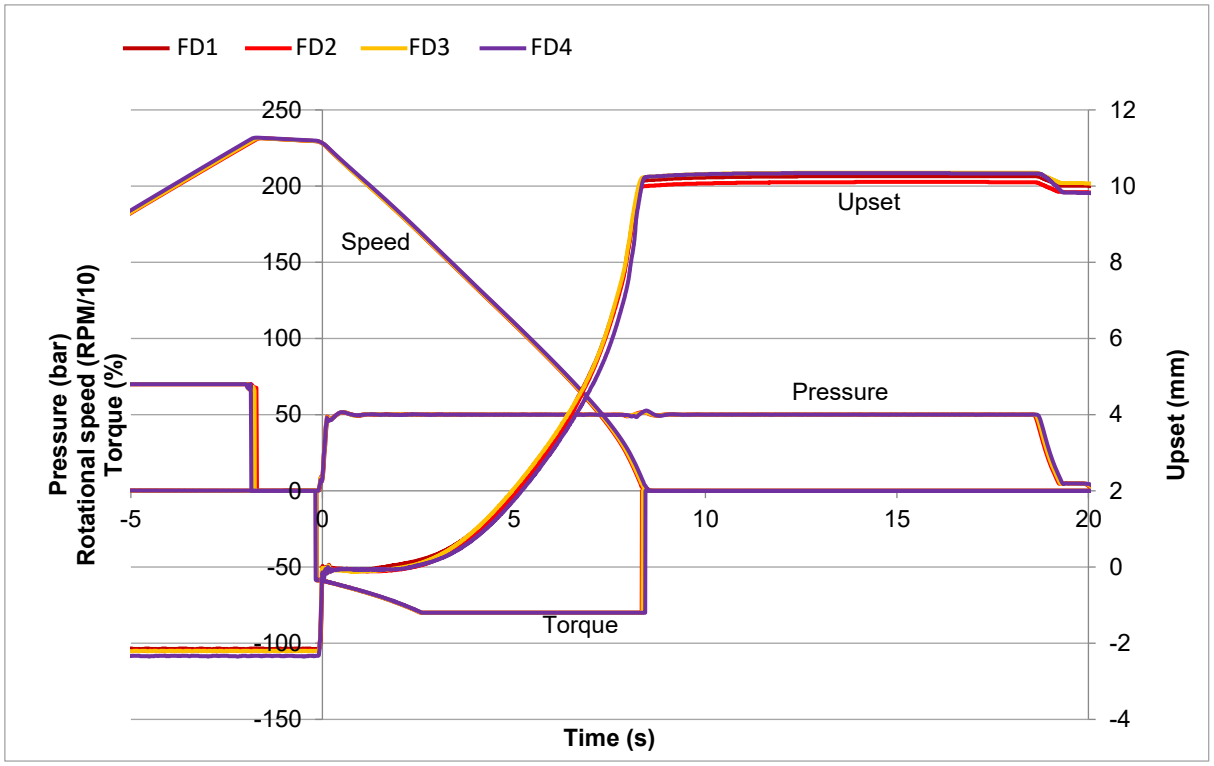


Figure 9-4: Weld traces of the fast deceleration cycles.

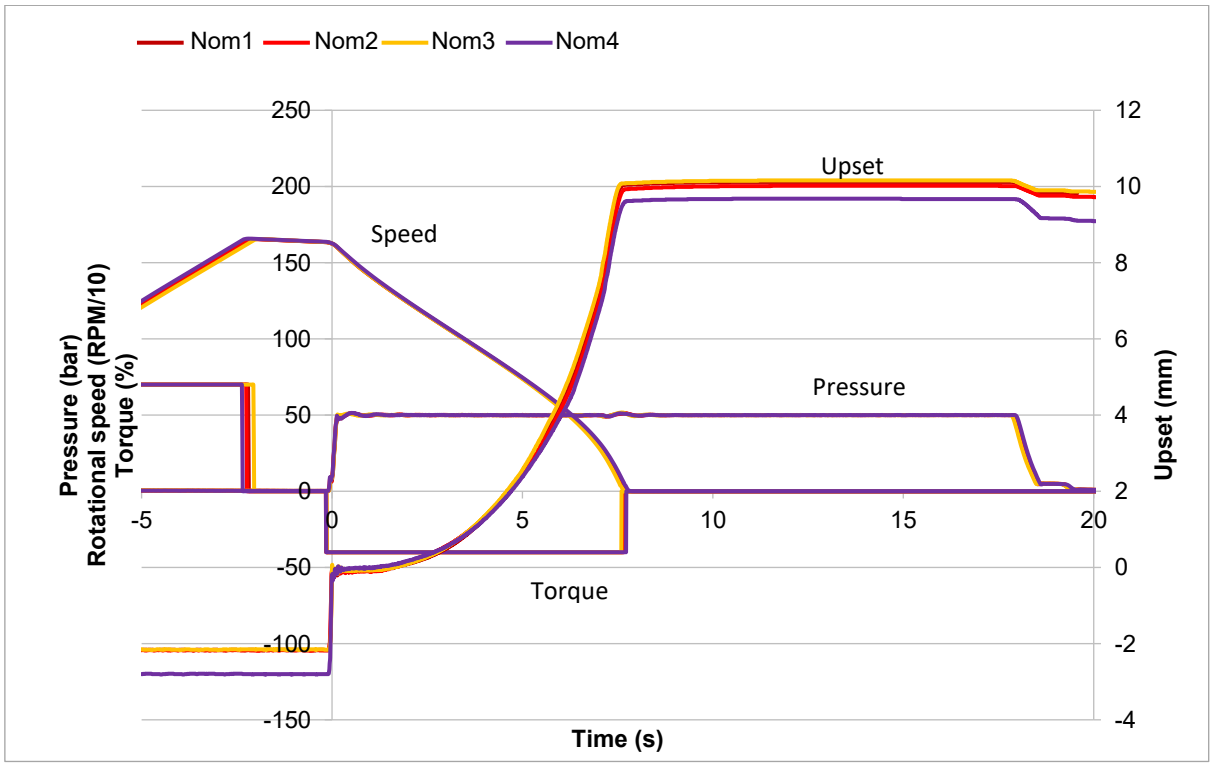


Figure 9-5: Weld traces of the nominal weld cycles.

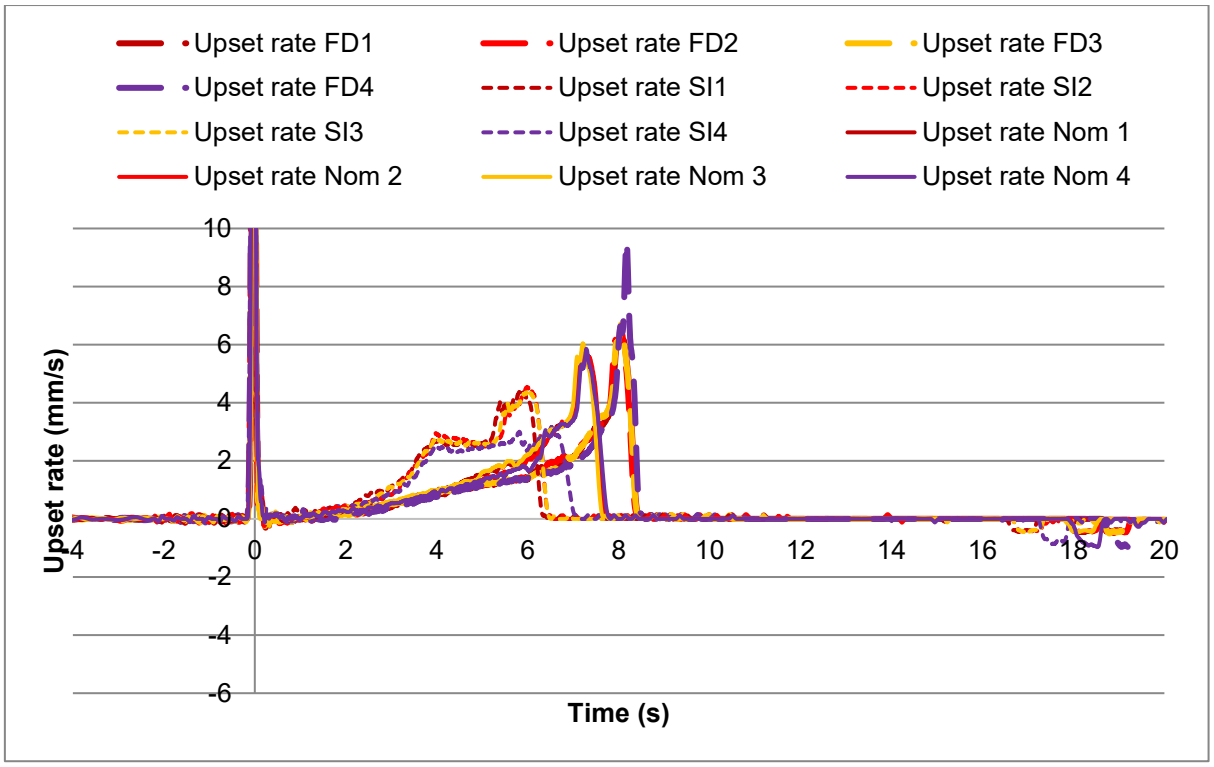


Figure 9-6: Collection of the upset rate from each weld cycle for comparison.

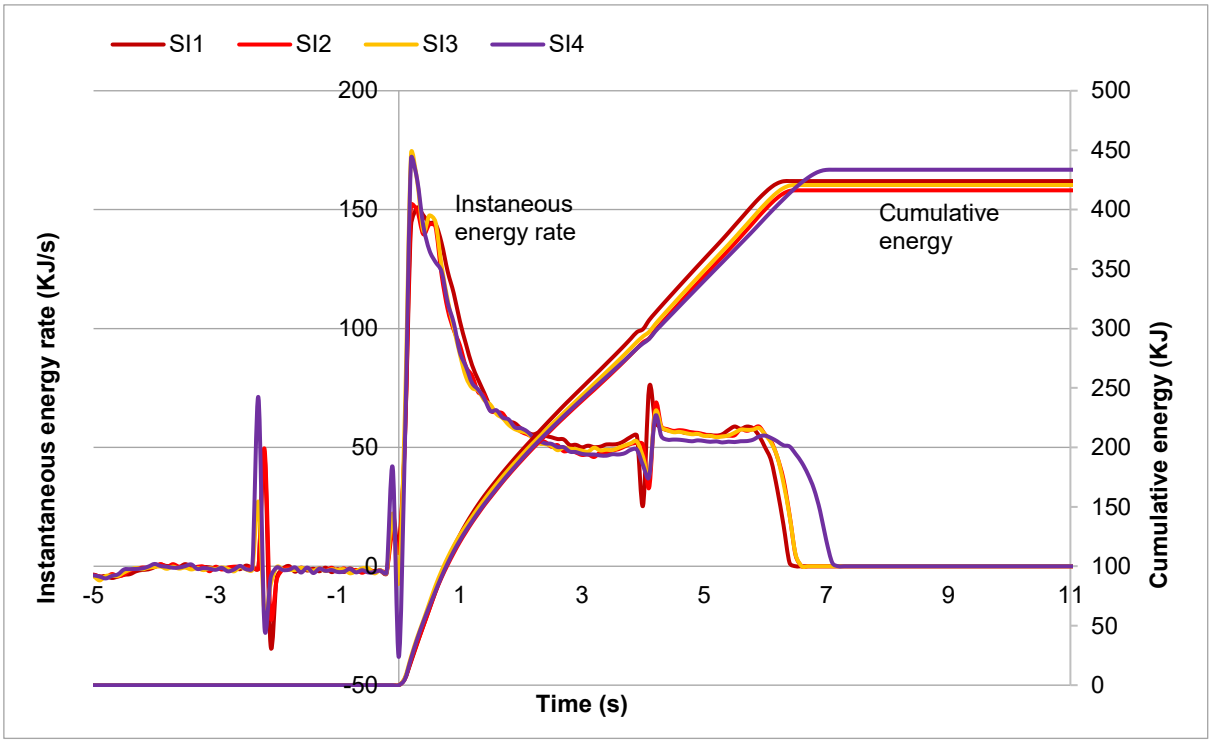


Figure 9-7: Calculated energy data from the simulated inertia cycles.

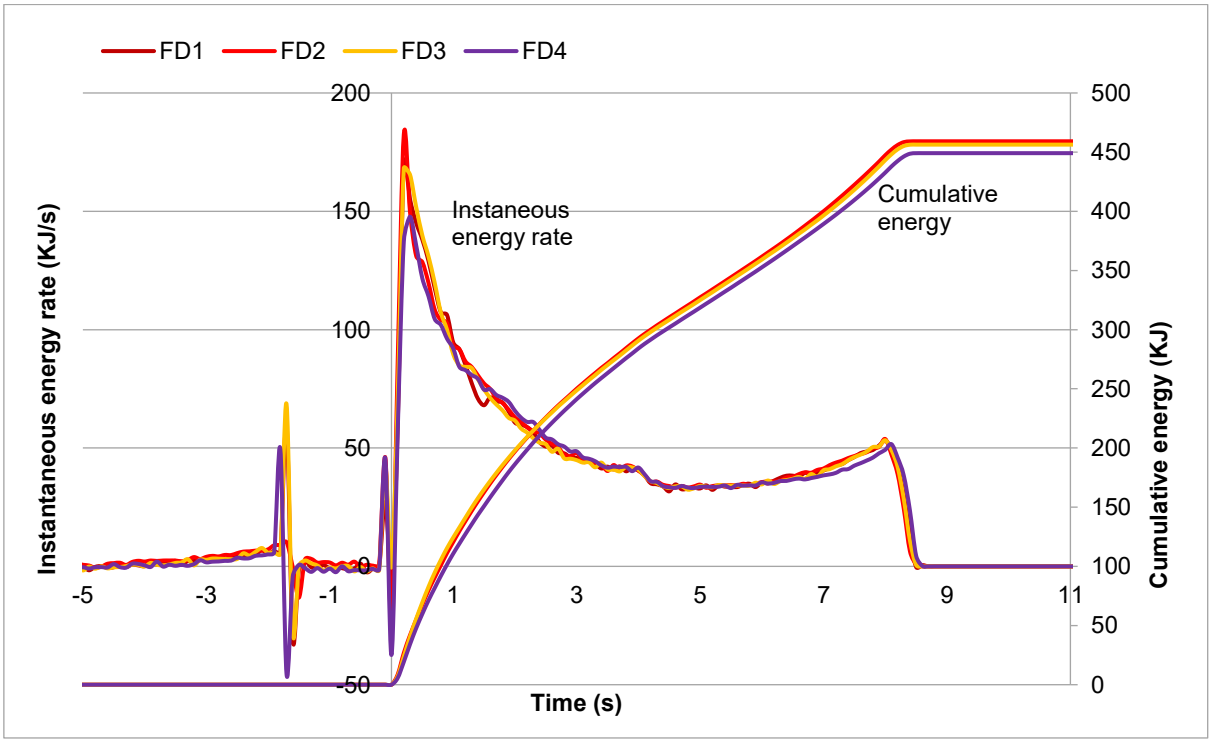


Figure 9-8: Calculated energy data from the fast deceleration weld cycles.

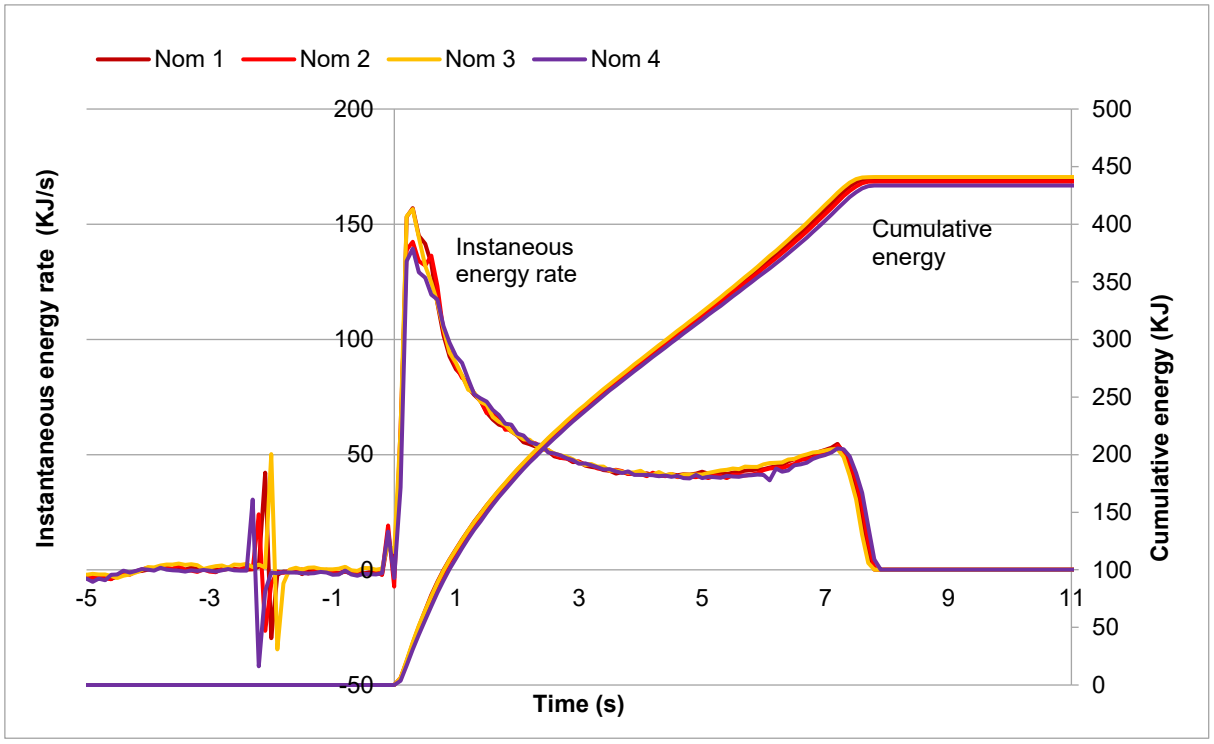


Figure 9-9: Calculated energy data from the nominal weld cycles.

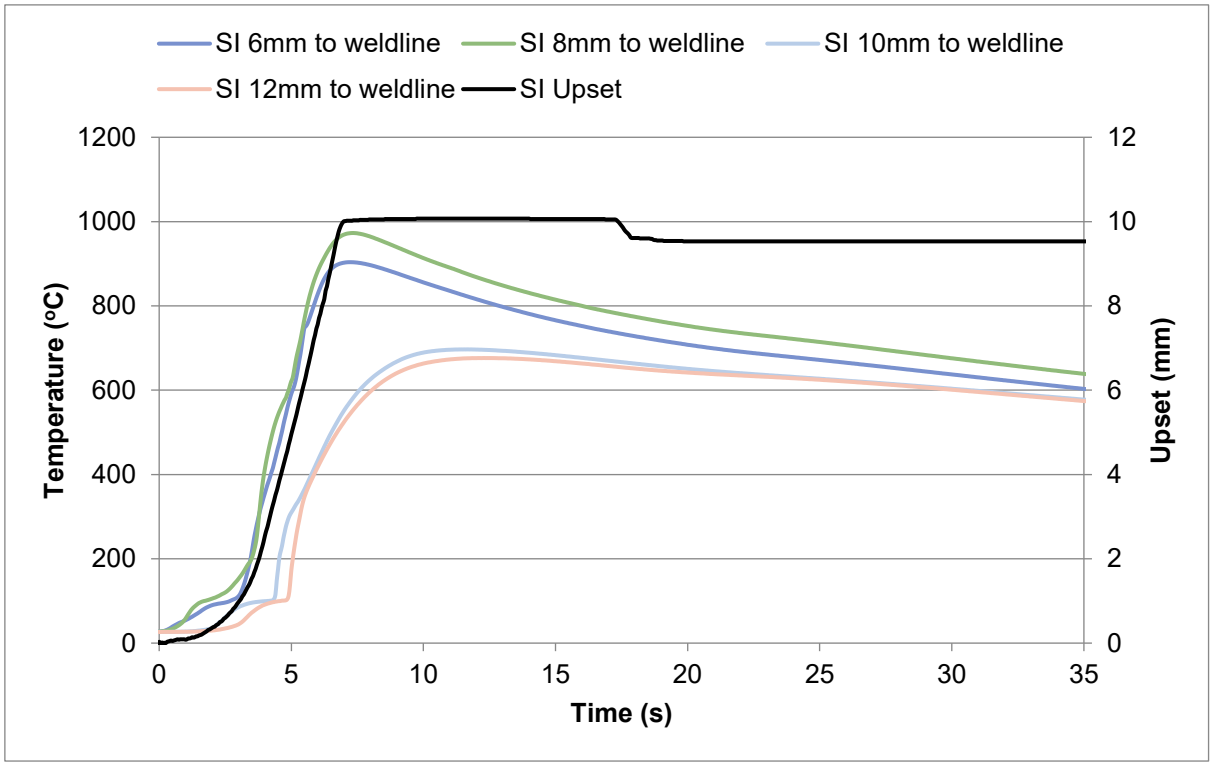


Figure 9-10: Temperature traces from SI4 during the simulated welding cycle, denoted by their initial position from the weld line. Compared against the upset curve from the same weld.

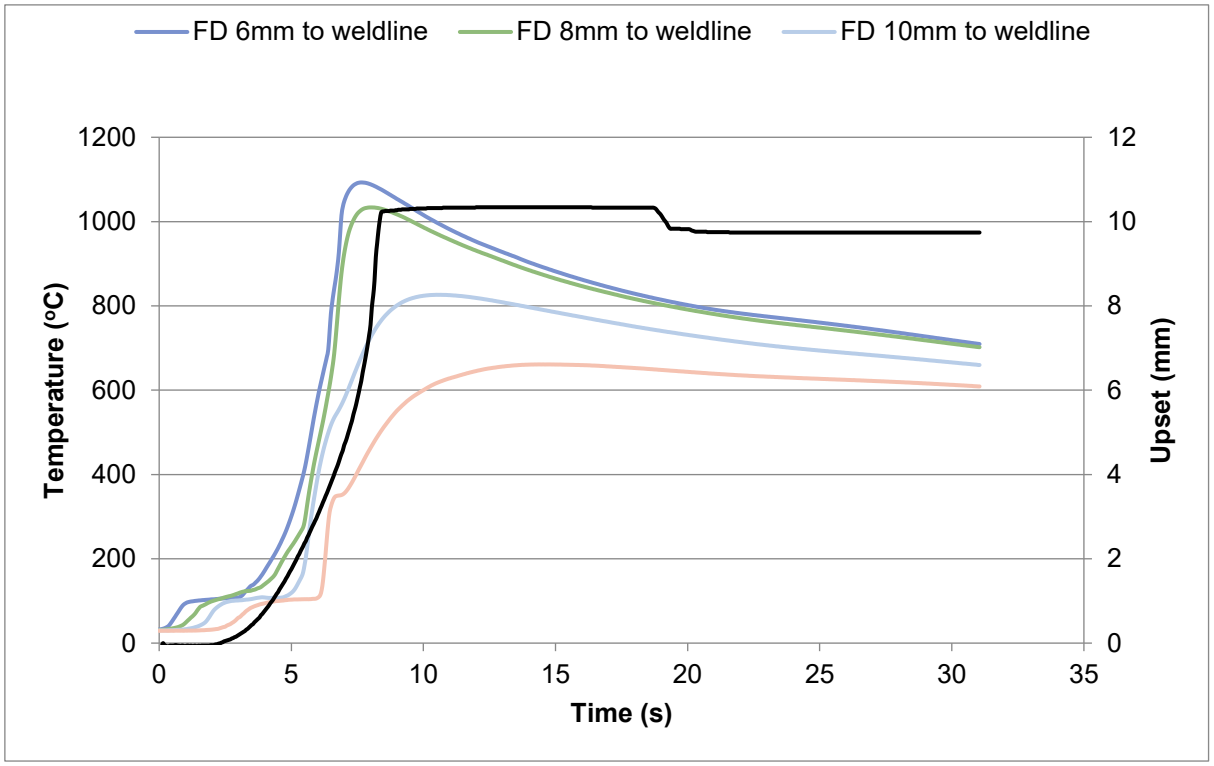


Figure 9-11: Temperature traces from FD4 during the fast deceleration welding cycle, denoted by their initial position from the weld line. Compared against the upset curve from the same weld.